

# Spectroscopy and photochemistry of transition metal complexes: a quantum chemical study



Dissertation

zur Erlangung des akademischen Grades doctor rerum naturalium

(Dr. rer. nat.)

vorgelegt dem Rat der Chemisch-Geowissenschaftlichen Fakultät der

Friedrich-Schiller Universität Jena

von Daniel Escudero Masa

geboren am 15.05.1984 in Palma de Mallorca, Spanien

---

1. Gutachter:

2. Gutachter:

3. Gutachter:

Tag der öffentlichen Verteidigung

## Abstract

Transition metal complexes possess unique chemical, photoredox and spectroscopical properties that makes them promising candidates as light harvesting antennae or photocatalytic centers in many photochemical devices, such as e.g. Ru(II) polypyridyl complexes in dye sensitized solar cells. The knowledge of the photochemical properties of these complexes is therefore of paramount importance to optimize their performance in these devices. To this aim, the computation of excited states and photochemical properties can provide useful hints to guide molecular design strategies. Unfortunately, the description of electronic excited states is still far from routine, as compared to ground state studies, and even more that of systems containing metal atoms.

The present work focuses on the computation of the spectroscopic and photochemical properties of transition metal complexes. First, a benchmark study on the excited states of a Ru(II) polypyridyl complex with quantum chemical and TD-DFT methods is presented. After electronic excitation, the possibilities that a molecule has for deactivating are plenty and usually such relaxation processes compete one to each other. The second main part of this thesis is then devoted to disentangling photophysical and photochemical mechanisms on several Ru(II) polypyridyl and Pt complexes with the help of quantum chemical calculations. Thereby, some photophysical properties, such as e.g. radiative decay rates have been computed to rationalize e.g. the fine-tuning in the emissive properties. Other photochemical studies dealing with the emissive properties of Ir complexes, which are used as phosphors in organic light-emitting diodes, are also presented along this thesis. Finally, in order to get information about quantum yields and lifetimes of the excited states, ab-initio excited state reaction dynamical studies

are mandatory. This is still a challenge for transition metal complexes and in this thesis we have performed model surface-hopping molecular dynamics simulations in a small organic system, i.e. 2H-Azirine, which shows wavelength dependent C-N and C-C bond photoactivation.

## Acknowledgements

Without the human, scientific and financial support this thesis would have not been possible. It is time therefore, to acknowledge all the people who directly or indirectly have made feasible its ending. I want to begin the acknowledgments section thanking both of my parents: **Maria Victoria** and **Antonio Luis**. They have always believed in me, giving me support in all my decisions and encouraging me with their example to face life in all the situations. You are my guidelines and there are no words to express my gratitude to you. Special mention deserve also my two brothers, **Antonio Jorge** and **Ismael**. Thank you guys, for being always there! Even though in the last years the distance did not allow us to share many moments together, you put a smile in my face with each of your words, anecdotes and successes in life. I am very grateful as well to the rest of my big family: cousins, uncles, grandparents, etc. Especially to my grandmother **Victoriana**, thank you very much grandma for taking care of me doing socks and scarfs for the cold winter!

My most sincerely gratitude to my supervisor, **Prof. Dr. Leticia González**, who gave me the opportunity to join her group in Jena by October 2007. I have learned many things from you and you will be my scientific guideline in the future. Also deserve special mention **Dr. Dirk Bender**, for his patience with my computer problems and the kindly help with translation issues. What about the rest of past and present members of the AG González, thank you very much **Dr. Inés Corral**, **Dr. Marta Labuda**, **Dr. Jesús González-Vázquez**, **Dr. Julien Guthmuller**, **Dr. Guillermo Pérez-Hernández**, **Dr. Philipp Marquetand**, **Daniel Kinzel**, **Hartmut Preuss**, **Stephan Kupfer**, **Verónica Leyva**, **Mariana Assmann**, **Martin Richter** and **Cristian Buendía** for the great

moments that we have shared together. My sincere gratitude to all of you for the scientific support; specially to Jesús, who introduced me in the fascinating world of mixed quantum-classical molecular dynamics; as well as for the personal support, specially to Guille, who made my life much more easier in the very beginning of my PhD, and to Vero, for making easier and funnier the every-day routine.

It is time to thank the experimental partners. This thesis would have not been feasible without the nice interaction between theory and experiments. All my gratitude to the groups of **Prof. Dr. Weigand**, **PD. Dr. Mohr**, **Prof. Dr. Schubert** and **Prof. Dr. Holder**. Specially, I will like to mention here Thomas Weisheit for the work concerning Pt complexes and Benjamin Schulze, Bobby Happ, Beatrice Beyer, Dr. Christoph Ulbricht and Dr. Andreas Winter for the work regarding Ru(II) polypyridyl and Ir(III) cyclometalated complexes. I would also like to express my gratitude to my students who encouragingly participated from my research projects and contributed to this thesis, special mention deserve Leon Freitag, Mariana Assmann, Anne Pospiech, Martin Richter, Jörg Hildebrandt, Sebastian Mai and Martin Thomas. Very special mention deserve also my friends. Specially, all the past and former members from the Spanisch Stammtisch: Raúl, Valentina, Catha, Emilio, Bea, Guille, Ana, Anna, Ainara, Pini, Katrin S., Katrin H., Jutta, Fernando, Eliseo, Alejandro, Sabrina, Vaneza, Christian, Sarahi, Edward, Ale, Kiara... Thank you all for the great experiences that we have lived together. I will never forget you. I am also very grateful to other friends around the world: Marcos, Arturo, Jetro, Alex... Even though you may not know it, you indirectly contribute to this thesis. Finally, I will like to thank the financial support during the thesis. All my gratitude to the Carl-Zeiss Stiftung and the Fundació Sa Nostra.

# Contents

<b>List of Figures</b>	<b>vii</b>
<b>List of Tables</b>	<b>xi</b>
<b>1 Preface</b>	<b>1</b>
<b>2 Introduction</b>	<b>5</b>
2.1 Photophysics and photochemistry of TM complexes . . . . .	5
2.1.1 Photophysics and photochemistry of selected complexes . . . . .	9
2.2 Light-triggered applications involving TM complexes . . . . .	14
2.2.1 Artificial photosynthesis . . . . .	15
2.2.2 DSSCs technology . . . . .	18
2.2.3 OLEDs technology . . . . .	22
2.2.4 Green synthesis by sunlight . . . . .	24
2.3 Goals of this thesis . . . . .	26
<b>3 Computational methods for TM complexes</b>	<b>27</b>
3.1 Quantum chemistry: some basics . . . . .	29
3.1.1 From Hartree-Fock to multiconfigurational methods . . . . .	30
3.1.2 Methods based on Density Functional Theory . . . . .	34
3.2 Ab-initio excited state molecular dynamics: the trajectory surface hopping method. . . . .	37
<b>4 Results</b>	<b>39</b>
4.1 Assessing the excited states of TM complexes and organic dyes . . . . .	41
4.1.1 Benchmarking the excited states of TM complexes with RASPT2 and TD-DFT methods: the case of a Ru(II)bypyridyl complex . . . . .	41

## CONTENTS

---

4.1.2	Computing the excited states of organic compounds with quantum chemical and TD-DFT methods: HESAB dyes as a case study	46
4.2	Selected applications of related Ru(II)polypyridyl complexes: a computational insight into their photophysics and photochemistry	50
4.2.1	Ru(CNC) <sub>2</sub> <sup>2+</sup> complex and its potential use for photosensitizer applications: a DFT and TD-DFT study of the underlying photophysical and photochemical processes	50
4.2.2	Fine tuning of the excited state lifetimes of Ru(II)polypyridyl complexes.	52
4.3	Cyclometalated Ir(III) complexes: a theoretical insight into their emissive properties	56
4.4	Insights from TD-DFT and DFT calculations into the photochemical bond-activation on (bisphosphane)( $\mu^2$ tolane)Pt <sup>0</sup> complexes	59
4.5	Quantum chemical studies and ab-initio excited state molecular dynamics in 2H-Azirines.	66
<b>5</b>	<b>Appended publications</b>	<b>71</b>
5.1	RASPT2/RASSCF vs range-separated/hybrid DFT methods: assessing the excited states of a Ru(II)polypyridyl complex	73
5.2	Spectroscopic properties of azobenzene-based pH indicator dyes: a quantum chemical and experimental study	105
5.3	A heteroleptic bis(tridentate) ruthenium(II) complex of a click-derived abnormal carbene pincer ligand with potential for photosensitizer application	117
5.4	N-Heterocyclic donor- and acceptor-type ligands based on 2-(1H-[1,2,3]triazol-4-yl)pyridines and their ruthenium(II) complexes	123
5.5	Phenyl-1H-[1,2,3]triazoles as new cyclometalating ligands for Ir(III) complexes	138
5.6	Structure-property relationship of red- and green-emitting iridium(III) complexes with respect to their temperature and oxygen sensitivity	150
5.7	Selective carbon-carbon bond cleavage of 2,2'-dibromotolane <i>via</i> photolysis of its appropriate (diphosphine)Pt <sup>0</sup> complex in the solid state	162



---

5.8	Substituent effects on the light-induced C-C and C-Br bond activation in (bisphosphine)( $\eta^2$ -tolane)Pt <sup>0</sup> complexes. A TD-DFT study . . . . .	166
5.9	Photochemical behavior of (diphosphine)( $\eta^2$ -tolane)Pt <sup>0</sup> complexes. Part A: Experimental considerations in solution and in the solid state . . . . .	175
5.10	Photochemical behavior of (diphosphine)( $\eta^2$ -tolane)Pt <sup>0</sup> complexes. Part B: An insight from DFT calculations . . . . .	188
<b>6</b>	<b>Conclusions and Outlook</b>	<b>199</b>
<b>7</b>	<b>Zusammenfassung</b>	<b>201</b>
	<b>References</b>	<b>205</b>

## CONTENTS

---

# List of Figures

2.1	Main adiabatic and non-adiabatic events in photochemical processes . . .	7
2.2	a) $[\text{Ru}(\text{bpy})_3]^{2+}$ complex. b) $[\text{Ru}(\text{tpy})_2]^{2+}$ complex. c-d) Schematic representation of the states involved in the main photochemical processes of $[\text{Ru}(\text{bpy})_3]^{2+}$ (c) and $[\text{Ru}(\text{tpy})_2]^{2+}$ (d) complexes. . . . .	11
2.3	Main components (light-harvesting antennae and OEC) of PSII, with a closer zoom into the $\text{Mn}_4\text{Ca}$ cluster. . . . .	14
2.4	Main components of a tryad-based (D-P-A) artificial photosynthesis device . . . . .	17
2.5	a) Dendrimer structure. b) Phorphyrin-fullerene dyad (D-A). c) Blue dimer compound. d) One component system. . . . .	17
2.6	a) Schematic representation of a typical DSSC device. b) Approximate energy diagram of a conventional DSSC. Processes highlighted. 1) Regeneration of the dye by the redox shuttle. 2) Electron injection into the semiconductor. 3) Charge collection in the anode. . . . .	19
2.7	a) Schematic representation of an OLED device. 1) Electron-hole recombination and concomitant exciton formation. b) Typical homoleptic and heteroleptic Ir(III) complexes used as phosphors in OLED devices. . . . .	22
2.8	a) Oxidative reaction and reductive elimination. b) Chemical structure of $(\text{Bisphosphane})(\mu^2\text{tolane})\text{Pt}^0$ complexes. c) Chemical structure of 2H-Azirines. . . . .	26
3.1	a) CASSCF classification of the MO orbitals. b) RASSCF classification of the MO orbitals. . . . .	33

## LIST OF FIGURES

---

4.1	Chemical structure of complex 1. Adapted from Escudero et. al. <i>J. Chem. Theory and Comp.</i> , <b>2011</b> , submitted. . . . .	42
4.2	Chemical structure of the 2/2 <sup>-</sup> -7/7 <sup>-</sup> HESAB dye compounds here investigated. Adapted from Escudero et. al. <i>J. Chem. Theory and Comp.</i> , <b>2011</b> , 7, 1062. . . . .	46
4.3	UV-vis absorption spectra of 2(solid) and 2 <sup>-</sup> (dashed). a) Experimental spectrum normalized to 1 in arbitrary units, b) RI-CC2//RI-BP86, c) RI-BP86//RI-BP86, d) PBE0//PBE0, e) PCM-PBE0//PBE0 and f) PCM-PBE0//PCM-PBE0. The theoretical spectra are convoluted with a Lorentzian function with a full width at half-maximum of 60 nm: the corresponding transitions are marked with vertical lines. Adapted from Escudero et. al. <i>J. Chem. Theory and Comp.</i> , <b>2011</b> , 7, 1062. . . . .	47
4.4	Experimental (top) and PCM-PBE0//PBE0 (bottom) spectra of neutral (solid) and anionic (dashed) compound. The theoretical spectra are convoluted with a Lorentzian function with a full width at half-maximum of 60 nm; the transitions are marked with vertical lines indicating its character. Adapted from Escudero et. al. <i>J. Chem. Theory and Comp.</i> , <b>2011</b> , 7, 1062. . . . .	48
4.5	a) Chemical structure of complex 8. b) Schematic representation of the main orbital interactions between the mesoionic carbene ligand and the tpy-Ru(II) fragment. The symmetry of the interacting orbitals is assigned in brackets. Adapted from Schulze et. al. <i>Chem. Eur. J.</i> , <b>2011</b> , 17, 5494. . . . .	51
4.6	a) Calculated and measured UV-Vis absorption spectra and measured emission spectra of complex 8. b) Spin-density plot of the T <sub>1</sub> state. c) Energy-level scheme of the lowest excited states of complex 8 at both the S <sub>0</sub> and T <sub>1</sub> optimized geometries. Adapted from Schulze et. al. <i>Chem. Eur. J.</i> , <b>2011</b> , 17, 5494. . . . .	53
4.7	Chemical structure of complexes 9-10. . . . .	54

---

4.8	Jablonski diagrams of complex 10 (a) and complex 9 (b). PCM-TD-B3LYP/6-31G* singlet-singlet and singlet-triplet vertical excitations vertical excitations. The main absolute SOC values ( $\text{cm}^{-1}$ ) and the main radiative mechanism ( $k_r$ ) are highlighted. Adapted from Escudero et al. <b>2011</b> , submitted. . . . .	56
4.9	Chemical structure of the cyclometalated Ir(III) complexes 11-17. Adapted from publications Beyer et al. <i>Organometallics</i> , <b>2009</b> , <i>28</i> , 5478 and Tian et al. <i>Eur. J. Inorg. Chem.</i> , <b>2010</b> , 4875. . . . .	57
4.10	Schematic representation of the TD-DFT and $\Delta$ -SCF approaches to reproduce the emission spectra maxima. . . . .	58
4.11	C-C and C-Br bond cleavage pathways taking place in complex 18 via irradiation with sunlight. Complex 19 does not undergo photochemical bond cleavage. . . . .	61
4.12	a) Chemical structure of (dppbe)( $\mu^2$ tolane)Pt <sup>0</sup> 20-33 complexes. . . . .	61
4.13	a) TD-BP86/TZVP simulated UV/Vis spectra of complexes 18 and 19. . . . .	63
4.14	TD-DFT UV-Vis spectra of complexes 18, 20-24. The main electronic transitions are highlighted. Adapted from Escudero et al. <i>Phys. Chem. Chem. Phys.</i> , <b>2009</b> , <i>11</i> , 4593. . . . .	64
4.15	a) Energy diagram of the thermal reductive elimination beginning from the C-C activated products leading to complexes 21 (blue), 30 (red) and 31 (green), calculated at the B2GP-PLYP/6-311G**//RI-BP86/TZVP level of theory. Relative free Gibbs energies are given in $\text{kcal mol}^{-1}$ with respect to complexes R. b) Energy diagram of the thermal reductive elimination beginning from the C-Br activated product leading to complex 21 (blue), calculated at the B2GP-PLYP/6-311G**//RI-BP86/TZVP level of theory. Relative free Gibbs energies are given in $\text{kcal mol}^{-1}$ with respect to complexes R1. Main distances are in angstroms. Adapted from Escudero et al. <i>Dalton Trans.</i> , <b>2010</b> , <i>39</i> , 9505. . . . .	65
4.16	Global photochemical and thermal reactivity of complex 21. . . . .	66
4.17	a) General scheme of 2H-azirine photochemistry: C-C and C-N bond cleavage. b) Chemical structure of compound 34. . . . .	67

## LIST OF FIGURES

---

4.18 Photochemical pathways beginning from the $S_1$ (a) and $S_2$ (b) states. Relevant CoIn geometries are also included. The distances are in angstroms. 68	
4.19 C-C bond distance versus time for a sample of trajectories launched from the $S_1$ state. The distances are in angstroms. . . . .	68
4.20 Representative a) and b) trajectories launched from the $S_2$ state leading to the $S_2$ state. . . . .	69

# List of Tables

4.1	Selected TD-DFT electronic transitions energies in eV compared to the experimental values. Values in brackets correspond to the PCM-TD-DFT values . . . . .	43
4.2	Relative MS-CASPT2 and MS-RASPT2(n,l,m;i,j,k) electronic transitions energies, $\Delta E$ (in eV), of the main electronic excitation of complex 1, at different levels of theory . . . . .	44
4.3	Experimental emission data of complexes 9-10 obtained in $\text{CH}_2\text{Cl}_2$ solution	54
4.4	Lowest singlet-triplet theoretical emission energies by means of TD-DFT and $\Delta$ -DFT approaches . . . . .	58

## GLOSSARY

---

### List of abbreviations:

**UV:** ultraviolet  
**TM:** transition metal  
**OLED:** organic light-emitting diode  
**DSSC:** dye sensitized solar cell  
**MC:** metal-centered  
**CT:** charge-transfer  
**LMCT:** ligand-to-metal charge-transfer  
**MLCT:** metal-to-ligand charge-transfer  
**IL:** intra-ligand  
**LLCT:** ligand-to-ligand charge-transfer  
**PES:** potential energy surface  
**CoIn:** conical intersection  
**ISC:** intersystem crossing  
**IC:** internal conversion  
**SOC:** spin-orbit coupling  
**TD-DFT:** time-dependent density functional theory  
**GS:** ground state  
**NIR:** near-infrared  
**PSII:** photosystem II  
**OEC:** oxygen evolving complex  
**HOMO:** highest occupied molecular orbital  
**LUMO:** lowest unoccupied molecular orbital  
**HESAB:** 2-hydroxyethylsulfonyl azobenzene  
**HF:** Hartree-Fock  
**MP:** many-body perturbation  
**CC:** coupled cluster  
**DKH:** Douglas-Kroll-Hess  
**ZORA:** zeroth-order regular approximation  
**RECP:** relativistic effective core potentials  
**DFT:** Density Functional Theory



**UDFT:** Unrestricted Density Functional Theory  
**TISE:** time-independent Schrödinger equation  
**CI:** Configuration Interaction  
**MO:** molecular orbital  
**FCI:** Full Configuration Interaction  
**CSF:** configuration state function  
**CIS:** Configuration Interaction Singles  
**CISD:** Configuration Interaction Singles and Doubles  
**MCSCF:** Multiconfigurational self-consistent field  
**PEH:** Potential energy hypersurface  
**CASSCF:** Complete active space self-consistent field  
**RASSCF:** Restricted active space self-consistent field  
**SA:** State Average  
**MR:** multireference  
**CASPT2:** Second-order perturbative complete active  
**xc:** exchange correlation  
**LSDA:** local spin-density approximation  
**GGA:** generalized-gradient approximation  
**mGGA:** meta-generalized gradient approximation  
**TDSE:** time-dependent Schrödinger equation  
**PCM:** polarizable continuum model  
**AEE:** adiabatic emission energy  
**EWG:** electron withdrawing group  
**EDG:** electron donor group  
**MEP:** Minimum Energy Path

## GLOSSARY

---

# 1

## Preface

Photochemistry (in its global meaning, including photophysics) is the discipline that studies the interaction of light with matter, either atoms or molecules. From a philosophical view, already in the Bible there are references to this relevant natural phenomenon. Namely, when God states: "Let there be light" is highlighted the importance of light and its concomitant interaction with nature. As a matter of the fact, it is through the photosynthetic processes that takes place in green plants that life on Earth is maintained. Other beautiful examples in biology are the chemistry of vision, which is initiated by a photochemical reaction, or phototropism in plants. Photochemical processes are also involved in many environmental events occurring in soil, sea and atmosphere; like e.g. the striking regulation of ozone levels in the stratosphere through absorption of ultraviolet (UV) radiation.

Despite its importance, molecular photochemistry is a relatively young field. Starting in the middle of the last century, photochemistry began to be extensively studied, mainly experimentally, in parallel to the advances achieved in spectroscopic techniques. In a first stage the major developments were associated to organic photochemistry and this is reflected in the seminal books that reviewed the progress and challenges of the excited states and photochemistry of organic compounds in the 70's.(1, 2) Investigations of the photophysics and photochemical processes of transition metal (TM) complexes were by that time more scarce. However, the photosensitivity of metal complexes was known for a long time, as e.g. the effect of light on AgCl and its applications in photography, which began to be exploited in the 1830s.(3) Historically, the beautiful colors that TM complexes exhibit have attracted the interest of the scientific community

## 1. PREFACE

---

because important information about coordination number and spin configuration as well as about ionicity/covalency of the ligand-metal bonds can be extracted. Thereby, the interpretation of the UV-Vis spectra of TM complexes began around the 1950s, with the development of the ligand field theory(4, 5) and the first attempts to rationalize the charge-transfer bands.(6, 7) Early stage studies on TM photochemistry by that time were dealing with ligand photosubstitution reactions and photoredox decompositions of simple TM complexes. These photochemical studies have evolved with the years to solve more complicated issues (such as the determination of quantum yields and luminescence lifetimes or the study of energy and electron transfer) and also in more complicated systems (as e.g. bimolecular and supramolecular systems). The combination of ideas of supramolecular chemistry and photochemistry has lead in the last decade of the past century to important applications and light-triggered functionalities. Among them, light-triggered molecular motors(8) and machines,(9, 10) solar-energy conversion,(11) organic-light emitting diodes (OLEDs) technology(12) and green synthesis by sunlight(13) are the most challenging ones. TM complexes, due to their unique ground and excited state properties have become invaluable components of many of these devices and machines; acting as e.g. light-harvesting antennas or catalytic centers.

Among the stated above applications, solar-energy conversion is going to be of vital importance for the coming generations. Light from the sun is the ideal source of energy. It is, among the clean and renewable energies, the only one which is readily available.(14) Much effort is therefore dedicated to develop technologies which harness solar energy efficiently. Still, solar-based technologies can not compete economically to fossil fuels.(15) Among them, dye-sensitized solar cells(16) (DSSCs) and artificial photosynthesis(17, 18) have attracted much attention in the last years. Interestingly, TM compounds are often light-active components in such devices. To get an insight into the excited states properties and into the photochemical processes after light absorption, quantum chemical and dynamical studies are a perfect complement to spectroscopic measurements. They provide hints not only regarding the nature of the excited states but also on the mechanisms, either of radiative or non-radiative nature, after light excitation. Such knowledge could be of striking importance to optimize the efficiency of solar energy conversion.

---

This thesis is framed in the study of the photophysical and photochemical characteristics of several TM complexes mainly with the help of quantum chemical methods. Many of the studies have been performed in close cooperation with several experimental groups that synthesized and characterized spectroscopically some of the compounds: the group of Prof. Dr. Weigand (IAAC, FSU Jena), Prof. Dr. Schubert (IOMC, FSU Jena), Prof. Dr. Holder (Bergische Universitaet, Wuppertal) and PD. Dr. Mohr (Fraunhofer-Institute, Regensburg). Particularly, the following TM complexes have been studied and are included in this thesis:

- i) Ru(II) polypyridyl complexes, as suitable candidates for light-harvesting antennas in DSSC cells.
- ii) Ir(III) cyclometalated complexes, prone to act as triplet emitters in OLED devices.
- ii) (Bisphosphane)( $\eta^2$ -tolane)Pt<sup>0</sup> complexes, which undergo photochemically promoted C-C bond activation in a selective manner.

Additionally, the photophysical and photochemical properties of several organic compounds have been also studied, namely 2H-Azirines and acidochromic azobenzene-related dyes.

The rest of this thesis is structured in introduction, theoretical methods and summary of the results. The scientific contributions which resulted from this PhD work are appended in Chapter 5. Other publications obtained during the course of this work are also mentioned in Chapter 5.

## 1. PREFACE

---

## 2

# Introduction

This introduction is structured in two main parts. In the first one the photophysics and photochemistry of TM complexes, emphasizing on the photophysical properties of Ru(II) polypyridyl complexes is discussed. The second section comprises all the light-triggered applications which are at the core of this thesis, namely artificial photosynthesis, DSSCs and OLEDs technology as well as green synthesis by sunlight.

## 2.1 Photophysics and photochemistry of TM complexes

The main five types of electronic transitions, which can be found in coordination chemistry are the following:

- i) Metal-centered (MC) excitations as e.g. d-d electronic transitions. They are in principle strictly not permitted by Laporte rules<sup>1</sup> in centrosymmetric environments but partially allowed due to vibronic and spin-orbit couplings and thus, exhibiting generally lower extinction coefficients as compared to charge-transfer (CT) transitions. These excitations are responsible for instance for the blue color of Cu(II) water solutions.
- ii) ligand-to-metal charge transfer (LMCT) excitations. They involve promotion of electrons from occupied ligand orbitals to the partially empty d shell of the metal. They are low-lying states when at least one of the ligands is easy to oxidize and

---

<sup>1</sup>The Laporte Rule states that electronic transitions that conserve either symmetry or asymmetry with respect to an inversion center are forbidden.

## 2. INTRODUCTION

---

the metal is easy to reduce. Such transitions are responsible for instance for the intense purple color of the permanganate anion.

- iii) metal-to-ligand charge transfer (MLCT) excitations. These transitions involve excitations from metal d-based orbitals to low-lying empty orbitals located on the ligand, typically of  $\pi^*$  character. They are expected at the low-energy regime when the metal is easy to oxidize and the ligand is easy to reduce, as in Ru(II) polypyridyl complexes.
- iv) intra-ligand (IL) transitions, involving excitation between ligand-based orbitals which are located on the same ligand. They are usually present in the UV-Vis spectrum of the ligands without complexation.
- v) ligand-to-ligand charge transfer (LLCT) states. These transitions involve orbitals located in different ligands.

Due to the presence of many kinds of electronic excitations the description of the UV-Visible spectra of TM complexes is less simple than for organic molecules. The correspondence in going from electronic configurations to states is also more complicated, especially in highly symmetric complexes (i.e. due to degenerate molecular orbitals) or in the case of open-shell ground state configurations, which typically render excited states with certain double or multiple excitation character. In principle, and following the selection rules for UV-Vis spectroscopy, transitions between states of different multiplicity are strictly forbidden. Symmetry selection rules determine the intensities of the absorption bands. On the other hand, and leaving aside predictive theories such as ligand field theory, electronic structure calculations of excited states have become nowadays a very important complement to spectroscopic techniques. State-of-the-art calculations, being the multiconfigurational methods the best suited to deal with TM spectroscopy, allow to accurately describe, in terms of energies and intensities, the UV-Vis absorption bands of these complexes (see Chapter 3 for a detailed discussion).

Until now we have discussed the photophysical, i.e. vertical, processes of TM complexes. On the other hand, the photochemical events are those occurring typically after light absorption. In Figure 2.1 are represented several plausible photochemical pathways. To this aim, some potential energy curves corresponding to several electronic



## 2.1 Photophysics and photochemistry of TM complexes

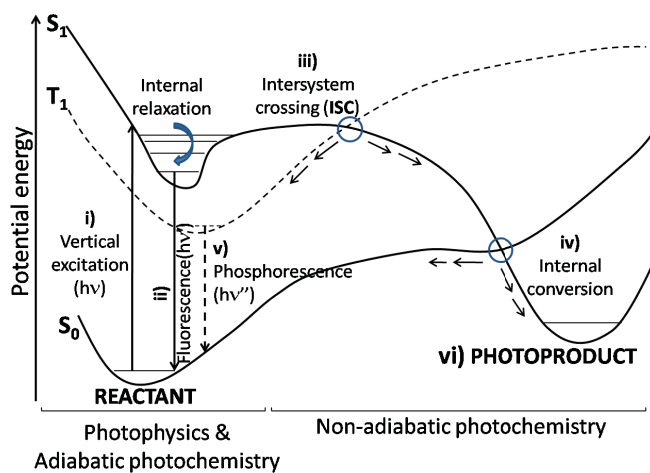


**Figure 2.1:** Main adiabatic and non-adiabatic events in photochemical processes

states ( $S_0$ ,  $S_1$  and  $T_1$ ) have been represented. After Franck-Condon vertical excitation i) to the singlet excited states, nuclear relaxation can lead to several radiative or non-radiative pathways. Before discussing them, it is useful to distinguish first between adiabatic and non-adiabatic (or diabatic) photochemical processes, depending whether these occur on the same potential energy surface (PES) or not. Nowadays it is well-accepted that both adiabatic and non-adiabatic processes are ubiquitous in photochemistry. The excited state molecule might relax *via* vibrational relaxation (mediated by solvent deactivation and molecular collisions) to a minimum on the singlet potential energy surface. From there, emission of a photon could take place ii), that is fluorescence. It may happen as well that the excited state molecule has enough vibrational energy to reach other regions of the PES. Eventually, in the vicinity of a surface crossing (non-adiabatic photochemistry), population transfer between two electronic states can take place *via* coupling of the electron motion to the nuclear and/or spin motion. Surface crossings are mediated by Conical Intersections (CoIns)(19, 20). The importance of CoIns in organic photochemistry as efficient photochemical funnels for radiationless deactivation mechanisms on a subpicosecond scale and/or in photochemical transformations is nowadays well established.(21)

Surface crossings are classified in intersystem crossings (iii, ISC) or internal conversion (iv, IC), depending whether they involve states of different multiplicity (e.g. singlet-triplet crossing) or states of the same multiplicity (e.g. singlet-singlet crossing),

## 2. INTRODUCTION

---

respectively. For TM atoms the photochemical picture allows for full complexity. The increased spin-orbit couplings (SOC) due to the metal atoms as compared to main group chemistry, makes the formally forbidden singlet-triplet transitions substantially enhanced. The ISC rates  $k_{ISC}$  can be obtained, in principle, from the Fermi's Golden Rule, see equation (2.1)

$$k_{ISC} = \frac{2\pi}{\hbar} |\langle T | \hat{H}_{SO} | S \rangle|^2 \rho(E), \quad (2.1)$$

where  $\hat{H}_{SO}$  is the spin-orbit coupling operator and  $\rho(E)$  is the density of states in the final electronic states.(2) For TM complexes, and oppositely to organic chemistry, ISC processes may occur in an ultrafast manner and very efficiently. Exemplarily, in the well characterized experimentally  $[\text{Ru}(\text{bpy})_3]^{2+}$  (bpy=2,2'-bipyridine) complex, ISC takes place in less than 100 fs and almost with the unity of quantum yield.(22) Therefore, triplet excited states have a protagonist role in the photochemistry of TM complexes. Once the triplet excited states are populated, alternative deactivation pathways are opened up, as e.g. vibrational relaxation to a minimum on the triplet excited state surface from where emission of a photon takes place, v) that is phosphorescence. Finally, to conclude the description of the photochemical reactions described in Fig.2.1, the radiationless pathways may lead again to the ground state PES, yielding either a photoproduct vi) or recovering the ground state initial reactant without chemical transformation. The branching ratio reactant/photoproduct will be determined, among other effects, by the nature of the CoIn (sloped or peaked CoIn).(23)

Computational photochemistry exploted ca. 20 years ago with the pioneering work of Robb and Olivucci.(21) Nowadays, it is well accepted that CoIns mediate all type of chemical events, from e.g. pericyclic photoreactions to ultrafast deactivation in DNA. In the last 10 years and parallel to the boom of time-resolved femtosecond spectroscopy,(24) a number of computational strategies are readily available to complement stationary quantum chemical calculations with time-dependent properties. Dynamical calculations allow, in principle, to be quantitative with experimental quantum yields and with time scales. It is fair noting that these theoretical studies (either of "static" or "dynamic" nature) have been mainly focused on organic compounds. Computational studies on the photochemistry of TM complexes(25) are more scarce due to their intrinsic complexity (see Section 3 for further details). Consequently, many

## 2.1 Photophysics and photochemistry of TM complexes

---

challenges in TM spectroscopy and photochemistry are open up from a computational point of view.

In the following subsection the photophysics and photochemistry of selected Ru(II) polypyridyl complexes is described, since they are at the core of this thesis. The photochemical properties of Ir and Pt complexes will be also briefly commented and compared to the Ru(II) polypyridyl complexes.

### 2.1.1 Photophysics and photochemistry of selected complexes

Ru(II) polypyridyl complexes have been extensively investigated due to their unique chemical, redox and photophysical properties.(11, 26, 27) Particularly, Ru(II) polypyridyl complexes feature chemical stability and ability to undergo redox reactions both in the ground and the excited states. From a photochemical point of view, they show very interesting properties to be exploited in light-based functionalities. Therefore, the number of photophysical studies on Ru(II) polypyridyl complexes has increased considerably during the last 30 years. Ru(II) polypyridyl complexes absorb considerably in the UV-Vis region and exhibit long-lived and intense luminescence. Among Ru(II) polypyridyl complexes, the prototype compound  $[\text{Ru}(\text{bpy})_3]^{2+}$ , see Fig 2.2a is certainly the most studied complex. In an early stage, much effort was put in aspects of supramolecular photochemistry and static photophysical properties. In the last years and with the development of femtosecond transient-absorption spectroscopy, important additional information of the underlying photochemical processes could be extracted. Thus, it has been shown that upon excitation of the  $[\text{Ru}(\text{bpy})_3]^{2+}$  complex to the first singlet excited states (absorption maximum around 450 nm) ultrafast ISC occurs in less than 100 fs in an "horizontal" manner, leading to the formation of triplet states with near-unity quantum yield.(22, 28) Therefore, relaxation processes are dominated by the decay from the triplet excited states rather than by spin-allowed fluorescence or IC from the excited singlet states. Both low-lying singlet and triplet excited states have been theoretically assigned using time-dependent density functional theory (TD-DFT), as singlet and triplet metal-to-ligand charge transfer ( $^1\text{MLCT}$  and  $^3\text{MLCT}$ , respectively) states.(29) Thus, the ultrafast nature of the ISC processes is not surprising, since strong spin-orbit couplings are expected for the states with participation of the metal ion. From 300 fs onwards,(22) the transient-absorption spectrum remains without changes. Hence, the  $^3\text{MLCT}$  manifold decays to the lowest triplet excited state *via*

## 2. INTRODUCTION

---

IC and vibrational relaxation processes. Once the lowest triplet excited state is populated, eventually phosphorescence can take place (again due to strong SOC), recovering the ground state reactant without chemical transformation.(11, 30)

The luminescence rates as well as the efficiency of the phosphorescence process are strongly dependent on the sample conditions (i.e. solvent), room temperature as well as ligand modification. Currently, one of the major goals on Ru(II) polypyridyl chemistry is to optimize its photophysical properties profiting at the same time from desirable architectures to potentially build photochemical devices. In this sense, the  $[\text{Ru}(\text{bpy})_3]^{2+}$  complex present optimal photophysical properties, with long-lived excited states at room temperature of ca. 1  $\mu\text{s}$ .(26) However, the construction of  $[\text{Ru}(\text{bpy})_3]^{2+}$ -based polynuclear systems implies some undesirable design drawbacks. Thus, the use of tris-bidentate architectures induces the creation of diastereoisomers, and furthermore additional substitution of the bpy ligands will lead in principle to facial and meridional isomers.(31) In such isomer constructions, electron and energy transfer processes do not proceed with a well-defined directionality, which is in principle desired to exercise control over these processes on a nanometer scale. Instead, it has been seen that complexes based on tridentate ligands, as e.g. 2:2':6',2''-terpyridine (tpy) are prone to yield isomer-free linear assemblies for vectorial electron transfer(31, 32, 33) in multiunit assemblies. Unfortunately, the bis-tridentate  $[\text{Ru}(\text{tpy})_2]^{2+}$  complex (see Fig 2.2b) has an excited-state lifetime of only 0.25 ns at room temperature.(33) The short lifetimes of the excited states of  $[\text{Ru}(\text{tpy})_2]^{2+}$  are usually rationalized in terms of the thermal population of non-emissive triplet excited states, typically of metal-center ( $^3\text{MC}$ ) character.(34, 35) Thus, in this complex, the modification of the octahedral environment around the Ru center by the pincer tpy ligand leads to a weak ligand field which in turn determines the stabilization of the  $^3\text{MC}$  states. In Fig 2.2c-d the schematic representation of the excited state diagrams for the prototype  $[\text{Ru}(\text{bpy})_3]^{2+}$  and  $[\text{Ru}(\text{tpy})_2]^{2+}$  complexes are represented, respectively. When the  $^3\text{MC}$  states are highly accessible at room temperature, as in the case of the latter compound (Fig 2.2d), ultrafast radiationless deactivation *via* the ISC channel to the ground state PES follows. Indeed, this fast deactivation channel is associated not only to radiationless deactivation to the ground state but is also related to the opening of other photochemical reactivity channels, as e.g. solvolysis or anation(36) as well as reactivity towards biomolecules.(37) As it has been recently theoretically elucidated,(35) two major facts

## 2.1 Photophysics and photochemistry of TM complexes

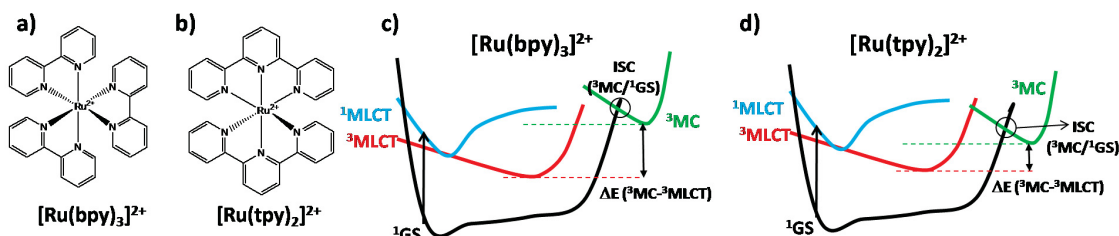


**Figure 2.2:** a)  $[\text{Ru}(\text{bpy})_3]^{2+}$  complex. b)  $[\text{Ru}(\text{tpy})_2]^{2+}$  complex. c-d) Schematic representation of the states involved in the main photochemical processes of  $[\text{Ru}(\text{bpy})_3]^{2+}$  (c) and  $[\text{Ru}(\text{tpy})_2]^{2+}$  (d) complexes.

determine the fast deactivation channels in these complexes; namely, the presence of small  ${}^3\text{MC}$ - ${}^3\text{MLCT}$  energy gaps and the accessibility from the  ${}^3\text{MC}$  state to the  ${}^1\text{GS}$  PES. Exemplarily, a minimum energy  ${}^3\text{MC}/{}^1\text{GS}$  ISC point has been located theoretically for the  $[\text{Ru}(\text{bpy})_3]^{2+}$  complex.<sup>(38)</sup> Such ISC geometrical structures features a distorted geometry bearing non-bonded nitrogen atoms, which might explain the observed photochemical reactions in these complexes, as e.g. the solvolysis reactions. As we stated before, in the  $[\text{Ru}(\text{bpy})_3]^{2+}$  complex the radiative mechanisms (i.e. phosphorescence) is preferred to the non-radiative deactivation pathways. Such behavior can be straightforwardly rationalized in terms of the considerable  ${}^3\text{MC}$ - ${}^3\text{MLCT}$  energy gaps (see 2.2c), even though still some temperature-dependent behavior of the luminescence lifetime has been observed for the  $[\text{Ru}(\text{bpy})_3]^{2+}$  complex. Oppositely, for the  $[\text{Ru}(\text{tpy})_2]^{2+}$  complex, such gap is considerably reduced and hence determining the preference for non-radiative pathways rather than radiative emission processes.

The phosphorescence quantum yield ( $\Phi_p$ ) of Ru(II) polypyridyl complexes is a subtle balance between the radiative decay ( $k_r$ ) and the non-radiative decay ( $k_{nr}$ ) rates.<sup>(2)</sup> Assuming a temperature independent behavior of the  $k_r$  value, the  $\Phi_p$  is defined by equation (2.2).

$$\Phi_p = \frac{k_r}{k_r + k_{nr}^{obs}} \quad (2.2)$$

The  $k_{nr}^{obs}$  value is the observed non-radiative decay rate, which can be expressed as

$$k_{obs}^{nr} = k_{nr} + k_{nr}(T), \quad (2.3)$$

## 2. INTRODUCTION

---

which is a sum of the  $k_{nr}$ , i.e. the temperature independent non-radiative decay rate and the temperature dependent rate ( $k_{nr}(T)$ ). This, in turn, can be expressed as an Arrhenius type equation, as shown in equation (2.4)

$$k_{nr}(T) = Ae^{\frac{-E_a}{RT}} \quad (2.4)$$

where  $E_a$  stands for the activation barrier for the thermal population of the  $^3\text{MC}$  state from the  $^3\text{MLCT}$  state, as discussed before.(39) This expression explains the temperature dependence of the luminescence lifetimes of complexes with thermally accessible  $^3\text{MC}$  states.

In order to achieve longer lifetimes of Ru(II) polypyridyl complexes, several design strategies have been proposed in the literature, mainly directed towards achieving increased  $^3\text{MC}$ - $^3\text{MLCT}$  energy gaps. To this aim, the use of i) cyclometalating and other strong donor ligands,(40, 41, 42), ii) ligands with extended  $\pi$  systems(43, 44, 45) and iii) ligand substitution(33, 46) has been proposed in the literature, with more or less success. Some of these strategies, namely the use of abnormal carbene ligands, are contemplated in this thesis. In those cases where the radiationless deactivation mechanisms involving the  $^3\text{MC}$  state are efficiently suppressed, the  $k_{nr}(T)$  component can be neglected from equation 2.3. In such situations, it has been observed that the non-radiative decay rates from the  $^3\text{MLCT}$  states to the ground state are determined by large vibrational overlap between both PES. In a simplified description of the  $k_{nr}$ , it usually exhibits an energy gap law like dependence,(47, 48) see equation (2.5)

$$k_{nr} \propto -e^{\beta\Delta E}, \quad (2.5)$$

where  $\Delta E$  stands for the  $^3\text{MLCT}$ - $^1\text{GS}$  energy gap, which can be approximated as the emission energy. In principle, diminished energy gaps (i.e.  $\Delta E$ ) yield larger non-radiative decay rates. The  $\beta$  parameter depends on the structural distortions going from the  $^1\text{GS}$  minimum to the emitting  $^3\text{MLCT}$  equilibrium geometry. In a simplified manner we can also state that the more distortions occur, the bigger the  $k_{nr}$  becomes. It has been seen that such exponential dependence of the  $k_{nr}$  with increasing energy-gaps holds for a series of related Ru(II) and Os(II) polypyridyl complexes, since the deactivation modes remain common within the series.(49, 50) Such modes have been

## 2.1 Photophysics and photochemistry of TM complexes

---

typically assigned with the help of low-temperature experiments,(48, 51, 52, 53) to medium-frequency ring-stretching vibrations, ranging from  $1000\text{cm}^{-1}$  to  $1600\text{cm}^{-1}$ .

The radiative rates  $k_r$  of Ru(II) polypyridyl complexes can be derived from a Strickler-Berg expression(54) *via* the following equation (2.6):

$$k_r^\alpha (T_m \rightarrow S_0) = \frac{\eta^2}{1.5} \left[ \sum_n \frac{\left| \langle T_m^\alpha | \hat{H}_{SO} | S_n \rangle \right|}{\chi_n^{0.5} |(\chi_n - 1)|} \cdot f^{0.5} \right]^2 \quad (2.6)$$

As it can be seen in Eq. 2.6, the  $k_r$  are obtained for each triplet ( $T_m$ ) participating in the phosphorescence emission and what is more, there is a rate component for each spin sublevel ( $\alpha$ ) of the triplet excited state,  $T_m$ . All the contributions with the interacting  $n$  singlet states are summed up.  $\chi_n$  stands up for the  $S_n/T_m$  energy ratio, whilst  $\eta$  corresponds to the refractive index of the medium. Finally, the  $k_r$  depends on the SOC matrix elements and on the singlet to singlet associated oscillator strengths,  $f$ . It is worth noting that the individual phosphorescence rates for the three possible spin sublevels can only be experimentally determined in the limit of large fine-structure splittings and low temperatures. At room temperatures only weighted phosphorescence rates can be measured, these can be straightforwardly obtained through equation (2.7).

$$\overline{k_r} = \frac{1}{3} \sum_\alpha k_r^\alpha \quad (2.7)$$

Summarizing, as it can be deduced from Equation 2.6 three factors influence the phosphorescence rates: i) the SOC matrix elements, ii) the energy difference between the manifold of singlet and triplet excited states, and iii) finally the oscillator strengths.

As it will be discussed on the following sections of this introduction, and due to the potential applications of Ru(II) polypyridyl dyes in light-triggered devices, there is a strong need of developing complexes that feature long lifetimes of their excited states. Furthermore, complexes capable of absorbing a larger fraction of the sun light, i.e achieving near-infrared (NIR) absorption through more intense  $^1\text{MLCT}$  states are desired. As we stated above, to achieve longer lifetimes of Ru(II) polypyridyl complexes, several synthetic strategies have been proposed. We note that the strategies based on the single optimization of only one of these desired photophysical features might result in a worst global photochemical behavior for potential applications. Exemplarily, in those complexes designed to yield NIR absorption (by lowering the energy of the

## 2. INTRODUCTION

---

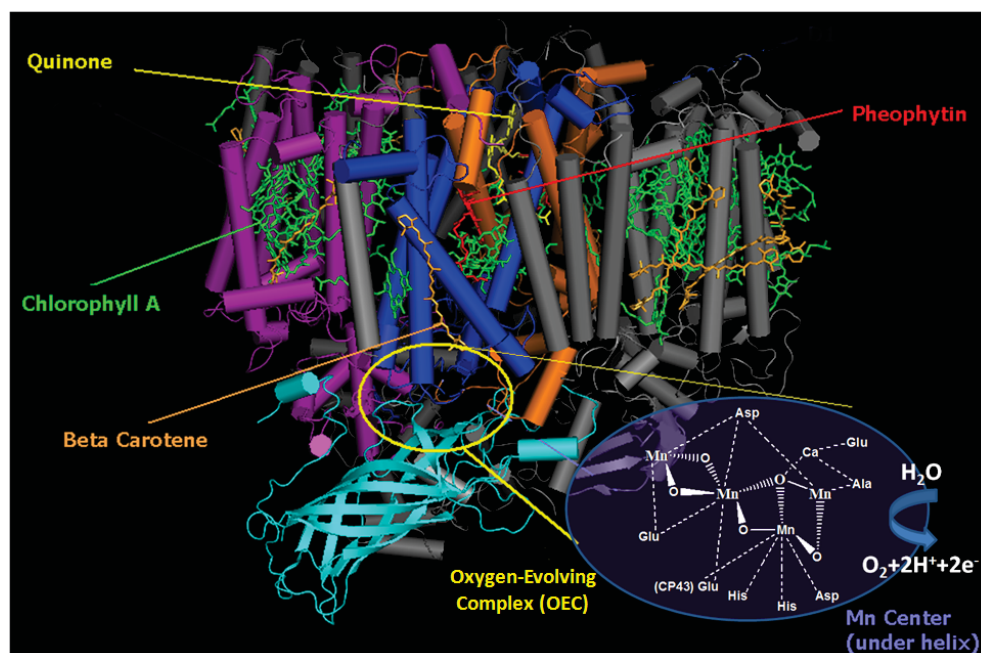


**Figure 2.3:** Main components (light-harvesting antennae and OEC) of PSII, with a closer zoom into the Mn<sub>4</sub>Ca cluster.

<sup>1</sup>MLCT states) it is usually seen that lower <sup>3</sup>MLCT states are also obtained, thus harming the excited state lifetimes due to the energy-gap law dependence.

Pt and Ir complexes, which are also at the core of this thesis, present very similar photophysical properties as compared to Ru(II) polypyridyl complexes. We just note here that ISC processes could be even faster, since larger SOC are expected for 5d transition metal atoms.

## 2.2 Light-triggered applications involving TM complexes

In the last decades an increasing effort has been put into the development of technologies which harness solar energy efficiently. This revolution has been stimulated by the urgent need for substituting the non-renewable sources of energies, i.e. fossil fuels, and by the human desire to mimic the photosynthetic processes taking place in green plants. Many functional artificial photosynthetic molecular devices have been proposed, being mainly inspired in the photosystem II (PSII), see Fig 2.3.

Two main components can be found in PSII, namely the light-harvesting antennae



## 2.2 Light-triggered applications involving TM complexes

---

and the oxygen-evolving complex (OEC). The secondary light-harvesting antennae, i.e. Chlorophyll A and Beta Carotene chromophores, absorb sunlight and transfer efficiently energy (*via* the Förster mechanism) to the primary chromophore, the complex P680. The excited P680 complex transfers an electron to an acceptor cofactor, namely the plastoquinone. The electron hole in the reaction center triggers the concomitant reactions that finally lead to the oxidation of water to O<sub>2</sub> in the OEC complex.<sup>(55)</sup> Interestingly, the OEC core is composed by a Mn<sub>4</sub>Ca cluster.<sup>(56)</sup> So, it seems that nature has selected metal atoms as active components in photosynthetic processes. Metal atoms are present not only in the photocatalytic reaction centers (i.e. the Mn<sub>4</sub>Ca cluster) but also in the light-harvesting antennae (e.g. Chlorophyll chromophores are constituted by a chlorin ring with a Mg atom at the center of the ring). Therefore, it is not surprising that TM complexes have had in the last decades a protagonist role in the main artificial supramolecular strategies to harness solar energy. Another important lesson to learn from nature is that for the achievement of efficient energy conversion a very precise organization in the spatial organization of the different components as well as in energy and time dimensions is needed.

In the following subsections some of these bio-inspired based-technologies are described; namely artificial photosynthesis, dye-sensitized solar cells (DSSCs) technology, OLEDs technology and green synthesis by sunlight.

### 2.2.1 Artificial photosynthesis

As we stated above, there is an urgent need in the modern society to substitute fossil fuels. Future fuels must be extracted from abundant, inexpensive raw materials such as carbon dioxide and water. It is precisely the latter, due to a combination of different factors, the most promising one. In the water splitting reaction, molecular oxygen and hydrogen are released, according to Eq. (2.8):



Obviously reaction (2.8) does not occur spontaneously upon light excitation. Therefore, water must be previously sensitized because sunlight does not electronically excite the water molecule. By mimicking the PSII chemistry, several artificial photosynthetic systems have been proposed. In the natural systems the complex spatial organization of

## 2. INTRODUCTION

---

the different components is mainly driven by intricate intermolecular interactions. This complexity is out of reach for the synthetic chemists and therefore covalent bonding is employed to connect the different subunits in artificial photosystems.(57) The general features that such devices must contain are the following:(58)

- i) A Light-harvesting antenna complex capable of absorbing sunlight and transfer energy in an efficient manner.
- ii) A reaction center for photoinduced charge-separation. The minimal reaction center should contain an electron-donor and an electron-acceptor unit.
- iii) Catalyst as one-to-multiple electron interfaces between the charge-separated state and the primary substrate.
- iv) A membrane to provide physical separation of the products might be also needed.

In Fig 2.4 a plausible artificial photosynthetic system is represented. In such a device, the primary chromophore P can induce charge-separation donor-acceptor (i.e.  $D^+-A^-$ ) through direct absorption of light or *via* mediated energy transfer from the secondary light-harvesting antennae. Directionality towards the primary chromophore in the energy transfer process is therefore a must to achieve efficiency (organization in space dimension). In this respect, it is worth mentioning that the solar radiation spectrum covers from the near-UV region to the near-IR region. Therefore, in order to absorb a larger fraction of the incident light, the use of different chromophores with different maximum absorption peaks covering the whole solar radiation spectrum is of crucial importance. The antennae effect in supramolecular arrays is only suitable if an organization not only in space but also in time and energy dimensions concur.(58) Thus, the energy transfer rates should occur fast enough before competing radiative or non-radiative deactivation takes place (organization in time dimension). Additionally, the energy of the acceptor excited state has to be lower, or at least equal, to the energy of the excited state of the donor (organization in energy dimension). Due to a combination of synthetic and functionalization advantages, dendrimer structures(59) (see Fig 2.5a) are currently the most promising supramolecular strategy for the construction of artificial antennae.(30, 60) As a consequence, TM complexes-based dendrimers,(30, 61) porphyrin-based dendrimers(62, 63) as well as organic-based dendrimers(64, 65) have been proposed in the literature as light-harvesting antennae in artificial photosystems.

## 2.2 Light-triggered applications involving TM complexes

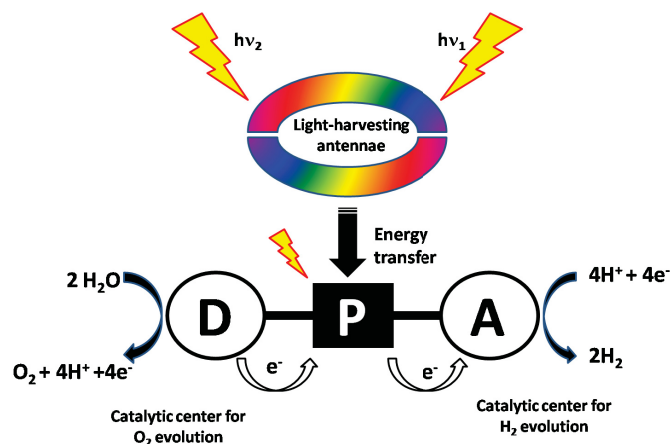


**Figure 2.4:** Main components of a tryad-based (D-P-A) artificial photosynthesis device

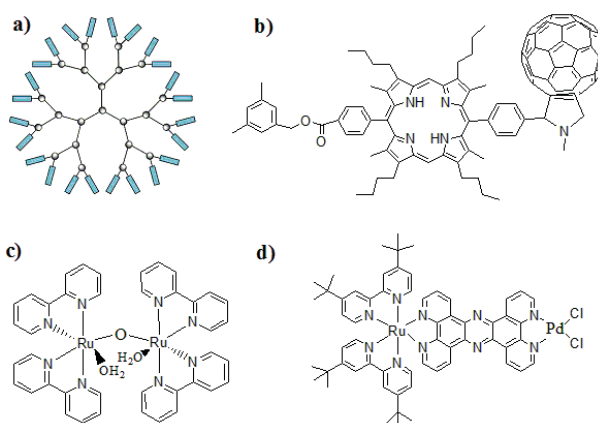


**Figure 2.5:** a) Dendrimer structure. b) Phorphyrin-fullerene dyad (D-A). c) Blue dimer compound. d) One component system.

Regarding the charge-separation center, several architectures have been proposed, mainly based on dyads (D-A)(66, 67) or tryads (e.g. D-P-A, see in Fig 2.4)(68, 69, 70). All the proposed architectures rely on the conversion of light energy to redox energy. Accordingly, and in order to avoid charge recombination processes, the quantum yields of electron transfer should be high and long-lived lifetimes for these states are desired. The phorphyrin-fullerene (see Fig 2.5b) moiety is often used as a charge-separation device since it fulfills both requirements.(70)

In the design of an artificial photosystem device one of the major problems that one has to face is the design of the catalytic centers. Particularly, the major bottleneck is the water oxidation catalyst. The water oxidation implies a four-electron process

## 2. INTRODUCTION

---

whilst the photoinduced charge separation is a one-electron process, and both processes must be coupled. To this aim, the design of multielectron redox catalysts capable of releasing electrons in a stepwise manner and oxidizing water in a concerted way is of vital importance.(71) Again nature astonishes us with its beautiful know-how, i.e. the  $\text{Mn}_4\text{Ca}$  cluster, which acts as a "pool of electrons". The major advances during the last years in what multielectron redox catalysts concerns have been associated to the development of bimolecular approaches, particularly in the use of dinuclear Ru complexes,(72, 73) like the blue dimer compound(74) (see Fig 2.5c). Such systems are capable of oxidizing water to dioxygen, but still the reaction rates are not comparable to those obtained in the oxygen evolving complex of PSII.

Leaving aside bottom-up approaches in the design of artificial photosystems, currently there is an increased effort to develop one-component systems,(75, 76, 77) like the one shown in Fig 2.5d. In such a device the photo-redox reaction center (i.e. a light-harvesting antenna and the charge-separation reaction center) is directly linked to the catalytic center through a redox-active bridge. Such intramolecular approaches have been exploited with an integrated evolving  $\text{H}_2$  catalytic center, like the dichloro-Pd moiety shown in Fig 2.5d,(75) and using as primary font of electrons other species instead of water, as e.g. triethylamine. Thus, upon light excitation production of  $\text{H}_2$  is observed.

### 2.2.2 DSSCs technology

In 1991 Grätzel and coworkers published a DSSC device(16) based on nanocrystalline  $\text{TiO}_2$ , that was exhibiting a 7% of sunlight conversion efficiency. Since then, DSSCs have attracted much attention as they offer the possibility of inexpensive and remarkable efficiency ratios.(78, 79) Fig 2.6a represents schematically a typical DSSC. The cell is constituted by transparent conduction oxide electrodes. The photoanode is composed of  $\text{TiO}_2$  nanoparticles, which are covered with a thick film that scatter photons back into the transparent film.(80, 81) The dye is usually covalently linked to the  $\text{TiO}_2$  nanoparticles *via* carboxylate moieties. After light excitation of the dye, it rapidly injects an electron into the semiconductor. The dye will be consequently regenerated (i.e. reduced) through a redox shuttle, typically the pair  $\text{I}_3^-/\text{I}_2$ , which is part of the electrolyte solution. As in other conventional batteries, anode and cathode are placed at different sides of the liquid conductor, namely the electrolyte. In Fig 2.6b is represented

## 2.2 Light-triggered applications involving TM complexes

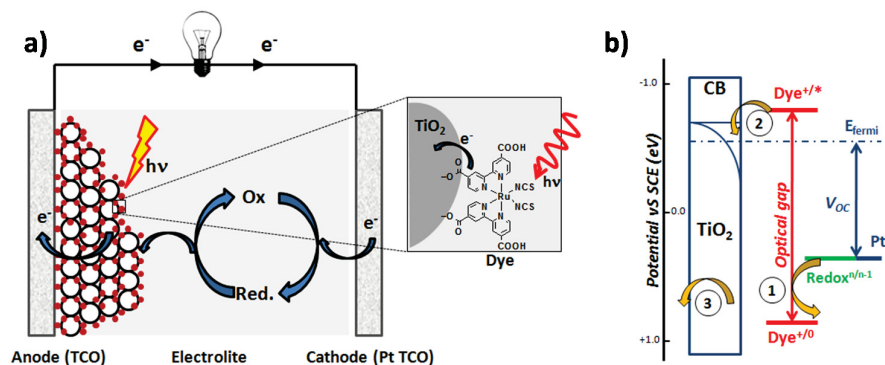


**Figure 2.6:** a) Schematic representation of a typical DSSC device. b) Approximate energy diagram of a conventional DSSC. Processes highlighted. 1) Regeneration of the dye by the redox shuttle. 2) Electron injection into the semiconductor. 3) Charge collection in the anode.

an approximate energy diagram of a typical DSSC. The electron movement in a DSSC is represented with arrows. From an energetic point of view it is crucial that the HOMO/LUMO dye's energy levels are aligned with those of the TiO<sub>2</sub> conduction band as well as with respect to the redox shuttle. An energetic alignment, like the one shown in Fig 2.6b ensures that electron injection and dye regeneration takes place. There are mainly three processes that compete with the electron transfer processes and thwart the successful operation of DSSC. First, the excited state dye could undergo internal deactivation (either of radiative or non-radiative nature) before transferring an electron to the semiconductor photoanode. Second, the injected electron could recombine with the oxidized dye before the dye is regenerated by the redox shuttle. Finally, the injected electron could even be directly intercepted by the redox shuttle.

The improvement of the sunlight conversion efficiencies has been the major bottleneck in the development of these devices, reaching current records of ca. 11%(82, 83). The overall solar conversion efficiency (i.e.  $\eta$ ) is a subtle balance of many variables. It is usually expressed by equation (2.9)

$$\eta = \frac{J_{SC} \times V_{OC} \times FF}{P_{in}}, \quad (2.9)$$

where  $P_{in}$  stands for the total solar incident power. FF (i.e. the fill factor) depends on the diode quality factor and typical values range between 0.75 and 0.85. There is

## 2. INTRODUCTION

---

little room for the improvement the latter variable and therefore, the focus for optimizing efficiencies has been mainly put on increasing the other two parameters, the short-circuit current density ( $J_{SC}$ ) and the open-circuit photovoltage,  $V_{OC}$ .(78) It is worth noting that DSSC comprises four main components, which are i) the dye, ii) the redox shuttle, iii) a dark electrode and iv) a semiconductor photoanode. Such components have been individually optimized to maximize the efficiency ratio. Unfortunately, the global device efficiency is hardly improved by single substitution of one of the components. It is very likely that in order to make significant improvements, at least two or three components should be interchanged simultaneously. In the following, we will briefly discuss several guidelines in order to increase the device efficiencies:

- i) Increasing the  $J_{SC}$  value. The most obvious way to increase the  $J_{SC}$  value is to absorb a greater fraction of the incident sunlight. Ru(II)polypyridil dyes absorb strongly in the near UV-region and moderately in the visible region. Therefore, the design of dyes that absorb in the near-IR region is vital since, as we stated above, the solar radiation spectrum covers from the near-UV region to the near-IR region. The optical gap of the dye (see 2.6b) should be then reduced, either by lowering the LUMO energy level (we note that it should be lowered without harming the electron injection into the conduction band of the photoanode(84)) or by raising the HOMO level. Hence, low-energy  $^1MLCT$  and  $^3MLCT$  states are desired. This strategy might indirectly enhance other non-desired photochemical events on the dye, since as stated by the energy gap-law(47), non-radiative deactivation pathways are enhanced exponentially with decreased energy gaps of the responsible excited states. Whether these deactivation pathways compete with the electron injection still is a question of debate and needs further study, since different injection dynamic time-scales have been observed in Ru(II)polypyridyl-based DSSC's.(84) Another striking point of Ru(II)polypyridyl dyes is that their absorption bands usually present low extinction coefficients, and therefore hundreds of adsorbed dye monolayers are required to collect all the incident light. Large semiconductor surfaces areas are consequently employed, fact that could induce further drawbacks. Indeed, it has been seen that interception rates scale super-linearly with surface areas whilst absorption scales only linearly.(85) This fact remarks the benefits that increased absorptivity of the dye could induce in

## 2.2 Light-triggered applications involving TM complexes

---

the development of future DSSC's, particularly in the design of photoanodes with reduced surface areas. In line with this, the search for dyes that address both spectral coverage and absorptivity issues has led in the last years to DSSC's devices based on organic dyes, like indoline(86) or coumarin(87) dyes. Such DSSC's currently compete in terms of efficiency, costs and chemical stability with Ru(II)polypyridyl-based DSSC's. The major drawback of the organic dyes, as compared to the Ru(II) dyes, is the lower lifetimes of their excited states that might enhance recombination processes, although this fact could not be so important if ultrafast electron injection dynamics is achieved.

- ii) Increasing the  $V_{OC}$  value. The  $V_{OC}$  is the difference between the Nernstian potential of the solution and the semiconductor's quasi-Fermi level ( $E_{fermi}$  in 2.6b). Since there is little room for biasing the semiconductor level, the most straightforward way to increase the  $V_{OC}$  value is shifting the solution potential to more positive values (see 2.6b).(88) It is fair to note that an overpotential between the redox shuttle and the dye is needed for guaranteeing the regeneration of the dye at an acceptable rate. To this aim, searching for redox couples exhibiting more positive potentials than the well known  $I_3^-/I_2$  pair, while maintaining enough overpotential with respect to the dye, is crucial. Furthermore, the bad performance of  $I_3^-/I_2$ -based cells sensitized with highly-polarizable organic dyes(89) as compared to conventional Ru(II)polypyridyl dyes and the complicated regeneration processes of the latter dyes with the  $I_3^-/I_2$  redox pair, and which mechanism is still uncertain,(90, 91) opens the range of potential substitutes of this redox pair. Indeed, substituted cobalt polypyridyl complexes(92, 93), copper complexes(94) as well as pseudohalogen redox couples, like the  $(SeCN)_2/(SeCN)^-$  pair,(95) have shown promising efficiencies in different DSSC's.

Summarizing, the efficiency in DSSC's is a subtle balance of many variables. The main components of the cells should be interchanged simultaneously, very often in a try-and-error manner, to improve efficiencies. Nevertheless it is expected that the records in efficiency will exceed the 16% in the following years.(78)

## 2. INTRODUCTION

---

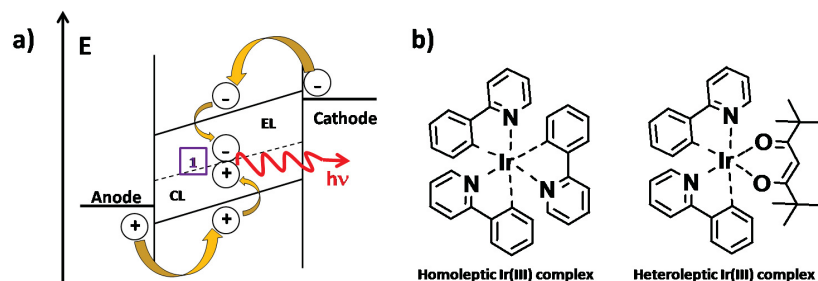


**Figure 2.7:** a) Schematic representation of an OLED device. 1) Electron-hole recombination and concomitant exciton formation. b) Typical homoleptic and heteroleptic Ir(III) complexes used as phosphors in OLED devices.

### 2.2.3 OLEDs technology

While DSSC use sunlight to produce electricity, there is also an increasing interest from the scientific community to efficiently produce the reverse process, namely the transformation of electricity into light. As a consequence OLED technology has exploited in the last years,(96, 97) mainly due to their low energy consumption and high color reproduction and fidelity. A simplified representation of a typical monolayer OLED is shown in Fig 2.7a. It is fair noting that multilayer architectures are usually used in order to improve injection and transporting properties. A typical device comprises an anode, several organic layers and a cathode. Such devices can be extremely thin, flat and transparent. They are even capable of being built up on flexible substrates.(96, 98, 99) The host material of the layers (usually composed by organic polymers) is a semiconductor where hole and electron transport takes place. Cyclometalated Ir(III) complexes, like the one shown in Fig 2.7b, are usually employed in OLED technology as dopants of the host material. When a voltage is applied, holes are injected in the HOMO level of the material and electrons are transferred into the LUMO level. Both hole and electrons will be transported to the opposite electrode. Eventually, while being transported on the host material, interaction between hole and electron may occur, process which can be followed by their recombination and formation of an exciton.(97, 99, 100) Deactivation of an exciton leads finally to the emission of a photon, see Fig 2.7a.

As we stated above, Ir(III) complexes are usually used as dopants in such devices due to their optimal photophysical properties and their versatility to tune the emission color by varying the attached ligands.(101, 102) Concerning their photophysical



## 2.2 Light-triggered applications involving TM complexes

---

properties, besides their chemical stability, these complexes feature very high quantum yields of phosphorescence, due to enhanced SOCs for the Ir atom, and relatively short phosphorescence lifetimes. Furthermore, the triplet-triplet annihilation processes at higher currents are deactivated, as compared to parent  $\text{Pt}^{II}$  complexes. Consequently, high quantum efficiencies can be achieved. In principle an internal efficiency of 100% can be theoretically achieved when using these phosphors, which in any case cannot be improved within a fluorophore exciton-based device.<sup>(96)</sup> Current records of external efficiency lay nevertheless around 20%,<sup>(103, 104)</sup> due to the limited charge transporting capabilities of the host materials. In Fig 2.7b are shown some typical Ir(III) complexes, used as phosphors in OLED devices. Tris-cyclometalated homo- and heteroleptic complexes (see e.g. an homoleptic tris-cyclometalated complex in 2.7b) and neutral bis-cyclometalated derivatives with ancillary ligands such as acetylacetonate (as in the case of the heteroleptic complex shown in 2.7b) are the typical phosphors in OLED devices.<sup>(105, 106, 107)</sup> The emission color of these complexes can be varied from blue to red by adapting the coordinated ligand system (either by substitution of the cyclometalated as well as the ancillary ligand).<sup>(101, 102, 108, 109)</sup>

So far, the efficiencies of green triplet emitters are usually better than the ones for red<sup>(110)</sup> and blue ones<sup>(111)</sup> The poor performance of the red emitters can be straightforwardly understood in terms of the energy-gap law. The design of efficient blue emitters is even more challenging, since the lowest-lying emitting states usually lay close in energy to non-emissive states, typically of multiconfigurational character (see section 2.1.1), which become thermally accessible and harm the phosphorescence efficiencies. Many effort has been therefore put during the last years on the designing of efficient blue emitters.<sup>(112)</sup>

For all the stated reasons, cyclometalated Ir(III) complexes are the most efficient and versatile class of phosphors in multicolor OLEDs as well as in white OLEDs assemblies. Furthermore, they can be employed in biomedical imaging<sup>(113)</sup> as well as active components in sensor devices,<sup>(114)</sup> since it has been seen that the phosphorescence of these complexes is sensitive towards oxygen (and therefore to barometric pressure) and temperature.<sup>(114, 115, 116)</sup>

## 2. INTRODUCTION

---

### 2.2.4 Green synthesis by sunlight

As we have seen along this introduction, storage of solar energy is one of the main challenges in the near future. A rather unexploited way to store sunlight energy, as compared to the rest of applications, is the photoinduced transformation of new chemical bonds, that is, synthesis by sunlight.(13, 117, 118) Promisingly, photochemical reactions could be used instead of toxic or expensive chemicals reagents in the production of industrially chemicals and/or to overcome activation barriers without an external source of energy. Furthermore, no residues in the reaction mixture are obtained. For all the stated reasons, synthesis by sunlight is a promising field of green and eco-sustainable chemistry.(119) The major drawbacks of synthesis promoted by sunlight are the following: i) the variability of the sunlight flux according to weather and geographic conditions, ii) the poor absorption of the solar emission by the reagents (typically organic reagents that mainly absorb on the near UV-region) and finally iii) the poor versatility of the field to tackle all kind of chemical reactions, and therefore narrowing its potential applications. This drawback is on the other hand an advantage since photochemistry opens up the possibility of non-available thermal pathways and/or selective chemical transformations. From a technical point of view, either solar concentration systems(120) and solar reactor systems without prior concentration have been studied.(117) Currently, the three most promising group of reactions to be promoted by sunlight are: i) reactions involving Fischer carbene complexes,(121, 122) ii) chromoarene derivatives(123, 124, 125) as well as ii) reactions involving carbonyl containing compounds (e.g. ketones, cyclohexadienones or quinones).(126, 127, 128, 129) In many of these examples of reactions promoted by sunlight, high quantum yields combined with remarkable chemical selectivity have been achieved.

We note that coordination of organic ligands to metal centers (like e.g. in the chromoarene derivatives) opens up the possibility of matching in a better extent the solar spectra as compared to the bare organic ligands (*via* the creation of typically low-lying CT bands involving the metal center, which are absent in the ligands by themselves). Furthermore, new photochemical pathways arise upon metal coordination, which could be interesting to be exploited from a synthetic point of view. Particularly, one of those potential uses of sunlight in synthetic strategies involving transition metal

## 2.2 Light-triggered applications involving TM complexes

---

atoms is in what C-C bond activation concerns. Since C-C bond activation is in the context of this thesis, it will be in the following briefly reviewed.

C-C bond cleavage has attracted the interest of the chemists due to its potential use in organic synthesis, catalysis and pharmaceutical research. Due to its intrinsic inertness, the activation of C-C bonds is a challenging subject yet far from practical use. Several strategies have been developed(130, 131, 132, 133, 134, 135) to this aim, most of them based on the use of transition metal complexes or strained molecules. From the viewpoint of microscopic reversibility it is quite reasonable to consider that C-C bond activation by a metal (oxidative reaction, see Figure 2.8a) is the reverse reaction of C-C bond formation (i.e. reductive elimination). C-C bond activation is thermodynamically much less favored than C-C bond formation, since two weak metal-carbon bonds (ca. 20-30 kcal/mol per bond) are formed at the expense of a relatively stable C-C bond (ca. 90 kcal/mol).(135) Therefore, two main strategies to yield C-C bond activated products have been proposed, that are either increasing the energy of the starting materials (by using strained 3- or 4-membered rings)(136, 137, 138, 139) or lowering the energy of the C-C bond cleaved products, which is very likely the case for activation with metal atoms.(140, 141, 142) Still, relatively few examples can be found in the literature for the activation of unstrained C-C bonds.(143, 144, 145) To make the things more complicated, C-C bond activation usually competes with C-H bond cleavage, either kinetically(146, 147) or thermodynamically.(140) The use of photons opens up the possibility for surmounting the high activation barriers of C-C bond activation reactions, even leading to photoproducts in a selective manner.(145, 148) On the other hand, photochemical reactions are rather more complicated than thermal ones. In this sense the forecast of possible photoproducts or reaction mechanisms is not straightforward. Quantum chemical and molecular dynamics involving excited states are therefore helpful tools to unravel photochemical reactions which in turn allow for a better design of the starting photomaterial. Throughout this thesis we have studied the selective C-C bond activation of several compounds:

- i) In collaboration with the experimental group of Prof. Weigand (IAAC, FSU Jena) we have explored the photochemical pathways in (bisphosphane)( $\mu^2$ -tolane)Pt<sup>0</sup> complexes; see 2.8b, who undergo selective C-C bond activation upon sunlight irradiation.

## 2. INTRODUCTION

---

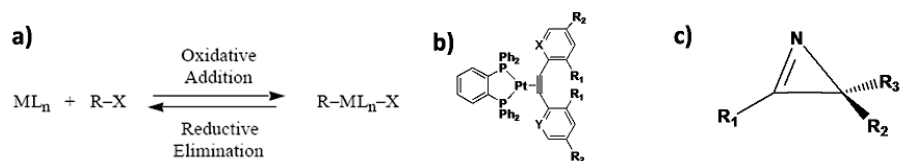


**Figure 2.8:** a) Oxidative reaction and reductive elimination. b) Chemical structure of (Bispophane)( $\mu^2$ tolane)Pt<sup>0</sup> complexes. c) Chemical structure of 2H-Azirines.

- ii) Additionally, the wavelength-selective C-C bond activation in a small strained molecule, i.e. 2H-Azirines (see 2.8c), has been studied.

Summarizing, due to the limitations already highlighted, it is very likely that the use of sunlight as energy source in the industrial synthesis of chemicals will play only a limited role in the near future. Nevertheless, the potential finding of new photochemical pathways that do not occur under thermal conditions in conjunction with the increased concern for green chemistry will make this field more appealing in the near future.

### 2.3 Goals of this thesis

This thesis is devoted to the study of the photophysical and photochemical properties of TM complexes and organic compounds, which are of paramount interest for photosensitizer application in e.g solar energy applications. The main goals of this thesis are:

- i) Benchmarking the excited states of TM complexes and organic compounds with quantum chemical and TD-DFT methods.
- ii) Disentangling the photochemical deactivation pathways, either of radiative or non-radiative nature, after light absorption. To this aim, quantum chemical calculations as well as ab initio excited state molecular dynamics have been performed.

Ru(II)polypyridyl complexes, Ir(III) cyclometalated complexes, (bispophane)( $\mu^2$ -tolane)Pt<sup>0</sup> complexes as well as 2-hydroxyethylsulfonyl azobenzene (HESAB) dyes and 2H-azirines have been object of study. The results can be found in the fourth chapter. The third chapter is devoted to the description of the quantum chemical and molecular dynamics methods employed in this thesis.

### 3

# Computational methods for TM complexes

The study of ground and excited state properties of TM complexes using computational methods is a challenging topic, being particularly more difficult than for organic and main group chemistry. In general, the main challenges when computing TM complexes include the following:

- i) The size. Metal complexes are typically large, involving many atoms and electrons, and therefore are computationally very demanding.
- ii) State degeneracies. Degeneracies play an important role in transition metal complexes, and not only between electronically excited state potential energy surfaces (as e.g. in the case of CoIns), but also near-degenerate electronic ground states are sometimes found, typically in several open-shell situations. Among these situations we note e.g. the antiferromagnetic interactions in metal clusters or the problematic with non-innocent ligands, as e.g NO and corrole ligands(149, 150, 151, 152). In these problematic cases, the Hartree Fock (HF) wavefunction will likely fail to predict the correct ground state, hence making it a bad guess for other single-reference post-HF correlated methods, such as many-body perturbation (MP) theory or coupled cluster (CC) theory, which would in principle require high level of excitations with larger basis sets to overcome such errors. We can state therefore that single-reference methods, i.e. those based on a HF

### 3. COMPUTATIONAL METHODS FOR TM COMPLEXES

---

wavefunction, are often unreliable for transition metal complexes. These situations make preferable the use of a multiconfiguration wavefunction (see below), which properly deal with the non-dynamical correlation effects. This fact is a great shortcoming, since multiconfigurational methods are computationally very demanding.

- iii) Dynamical correlation effects. As in organic and main group chemistry, dynamical correlation is compulsory to achieve a quantitatively comparison with the experiment. Multiconfigurational methods including dynamical correlation are therefore desired.
  
- iv) Relativistic effects. A proper relativistic treatment is mandatory in TM complexes. The most important relativistic effects can be divided mainly into the scalar-relativistic and SOC effects, which are spin-independent and spin-dependent phenomena, respectively. Obviously, a proper description of relativistic effects would in principle demand the use of the 4-component Dirac's theory, which is currently limited to small molecular systems. Beyond the 4-component Dirac's theory, which may be in principle combined with a multiconfigurational wavefunction but leads to lengthy and complex calculations, it has been seen that quite accurate results can be obtained transforming the 4-component Dirac operator into a 2-component form. Thus, two of the most used today transformations are the second order Douglas-Kroll-Hess (DKH) Hamiltonian(153, 154, 155) and the zeroth order regular approximation (ZORA)(156) Hamiltonian, which have been successfully implemented into multiconfigurational methods. Both Hamiltonians can be divided into a scalar part and a SOC part. The scalar part includes contributions to the one-electron Hamiltonian by introducing the mass-velocity term which modifies the potential close to the nucleus. Scalar-relativistic effects can also be included in a non-relativistic treatment *via* replacing the core electrons with relativistic effective core potentials (RECPs). For the first row transition metal compounds (3d) the scalar-relativistic effects dominate, and calculations can be safely performed by just considering these effects, either in a relativistic or non-relativistic framework. For heavier atoms, SOC effects are more important. Furthermore, the calculation of SOCs are indispensable for the interpretation of many spectroscopic phenomena, such as intersystem crossing rates, g-tensors,

zero-field splitting, etc. Within the DKH and ZORA Hamiltonians, there is a true two-component term, which mainly accounts for the SOC effects.

Due to all the facts mentioned above, the most appropriate formalism to describe the ground state and excited state properties of TM complexes seems to be the multiconfigurational one, when including a proper description of relativistic effects. Controversially, density functional theory (DFT) methods are widely spread for studying TM complexes, due to its easy handling and computational cheapness. Indeed, DFT methods succeed in describing ground state properties, specially in those cases where long-range correlation effects are not mandatory,<sup>(157)</sup> but special care is needed when computing the excited states properties with TD-DFT (see section 3.1.2).

To study the ground and excited states properties of TM complexes, in this thesis wavefunction-based methods as well as density-based methods (i.e. DFT and TD-DFT) have been extensively used. Among the wavefunction methods, mainly multiconfigurational methods have been employed. The aim of section 3.1 is neither to present the basics of quantum chemistry nor to provide a descriptive review of the quantum chemical methods. For completeness we refer the reader to cornerstone books on the basis of quantum chemistry.<sup>(158, 159)</sup> In Section 3.2 a mixed quantum-classical molecular dynamics method, namely the trajectory surface hopping method, is briefly introduced.

## 3.1 Quantum chemistry: some basics

After the Born-Oppenheimer approximation, the electronic time-independent Schrödinger equation (TISE) is given by

$$\hat{H}_{el} |\Psi_{el}^i(r_a; R_A)\rangle = \varepsilon_{el}^i(R_A) |\Psi_{el}^i(r_a; R_A)\rangle, \quad (3.1)$$

where  $\hat{H}_{el}$  is the electronic Hamiltonian,  $|\Psi_{el}^i(r_a; R_A)\rangle$  stands for the electronic wavefunction and  $\varepsilon_{el}^i(R_A)$  for the electronic energy of a given  $i$ -th electronic state.

Once the stationary electronic Schrödinger equation 3.1 is solved, the sum of the electronic energy,  $\varepsilon_{el}^i(R_A)$  and the nuclear repulsion,  $\hat{V}_{nu,nu}(R_A)$  for a fixed nuclear configuration  $R_A$  yields the potential energy for a  $i$ -th given electronic state, see Eq (3.2).

$$\hat{V}_{el}^i(R_A) = \varepsilon_{el}^i(R_A) + \hat{V}_{nu,nu}(R_A) \quad (3.2)$$

### 3. COMPUTATIONAL METHODS FOR TM COMPLEXES

---

#### 3.1.1 From Hartree-Fock to multiconfigurational methods

The HF method, while it is remarkably successful in the first-principles determination of molecular electronic wavefunctions and properties of closed-shell electronic ground states, has also its limitations. Among these situations where HF clearly fails the most cumbersome are: i) bond dissociations, ii) multiconfigurational situations, iii) excited states and iv) degenerate situations, such as CoIns. The underlying reason is the lack of electron correlation effects. On the one hand, the HF approximation relies on averages: it does not consider the instantaneous coulombic interactions between electrons, nor does it take into account the quantum chemical effects on electron distribution because the effect of the  $n-1$  electron is averaged (i.e. dynamical correlation effects are missing). On the other hand, in many chemical situations the use of a single determinant is inadequate because there is a number of near-degenerate electronic configurations, which are required to describe the chemical process (i.e. non-dynamical correlation effects are missing). This lack of correlation in the HF method has led to the development of post-HF methods, either of variational or perturbational nature, which aim to recover the lack of electron correlation. Since only multiconfigurational methods will be used in this thesis, they will be briefly described in the following.

The simplest and most straightforward method to deal with the correlation energy error is the Configuration Interaction (CI) method. In this method the single determinant HF wavefunction is extended to a wavefunction composed of a linear combination of many determinants in which the coefficients are variationally optimized. The new determinants can be created by e.g. promoting an electron from an occupied molecular orbital (MO) ( $a$ ) to a virtual MO ( $p$ ) of a preceding HF calculation, hence leading to a singly excited determinant denoted as  $|\psi_a^p\rangle$ . Analogously, a double excitation from  $a$  to  $p$  and simultaneously from  $b$  to  $q$ , i.e.  $|\psi_{ab}^{pq}\rangle$ , generates a doubly excited determinant. Accordingly, triply, quadruply, ...,  $N$ -tuply excited determinants can be set up. Thus, the Full Configuration Interaction (FCI) vector can be extended to all possible excitations, leading to equation (3.3):

$$|\Phi_{FCI}\rangle = C_{HF} |\psi_{HF}\rangle + \sum_{a,p} C_a^p |\psi_a^p\rangle + \sum_{\substack{a<b \\ p<q}} C_{ab}^{pq} |\psi_{ab}^{pq}\rangle + \sum_{\substack{a<b<c \\ p<q<r}} C_{abc}^{pqr} |\psi_{abc}^{pqr}\rangle + \dots \quad (3.3)$$



where  $|\psi_{HF}\rangle$  stands for the HF zeroth-order wavefunction and the C's are the expansion coefficients. Given a trial function as 3.3 we can find the corresponding energies by using the linear variational method. If a complete basis set is employed, the  $\epsilon_{FCI}$  corresponds to the exact energy. However, FCI calculations are rarely performed since it is computationally impossible to handle an infinite basis set of N-electron Slater determinants. In the practice they are limited to very small molecules in conjunction with small basis sets.

Thereby, attempts to reduce the number of configuration state functions (CSF's)<sup>1</sup> lead in the past to truncated CI methods. They are based on the intuitive assumptions that highly n-tuple excitations are very likely not to considerably contribute to the energies and molecular properties. Among them, the Configuration Interaction Singles (CIS) and Configuration Interaction Singles and Doubles (CISD) have been extensively employed. These methods are based on a CI expansion of singly and singly-doubly excited determinants, respectively. CISD has been a popular approach to the calculation of correlation energies and one-electron properties, which are certainly good described at this level of theory. We note that corrections on the correlation energies are mainly recovered by double excitations (which mix directly with  $|\psi_{HF}\rangle$ , oppositely to single excitations, as a consequence of Brillouin's theorem). However, single excitations are needed for a proper description of one-electron properties, such as dipole moments. One of the drawbacks of truncated CI methods is that they are not size consistent. On the other hand, the multideterminantal description of the CI-vector enables the calculation of excited states. Among the CI truncated methods for the calculation of excited states, CIS has been extensively used. The orthogonalization of the states is the essence of the CIS technique, that involves diagonalization of the CI matrix formed from the HF reference and all single excited configurations. The final outcome is a set of energy eigenvalues associated with eigenvectors in which the coefficients of the singly excited determinants characterize the electronic states. The CIS results are qualitatively useful, with the exception of excited states with multiconfigurational character. The flaws of CIS technique are on the other hand well recognized,(160) being related to the lack of most basic correlation effects.

---

<sup>1</sup>We note that a CSF is a symmetry-adapted linear combination of Slater determinants, which is constructed to have the same quantum numbers as the global wavefunction.

### 3. COMPUTATIONAL METHODS FOR TM COMPLEXES

---

The difficulty to treat excited states lead to the development of multiconfigurational methods. In the multiconfiguration self-consistent field (MCSCF) method not only the expansion coefficients but also the MOs coefficients are optimized variationally. Designing a MCSCF calculation is though a tough work. One different solution is obtained from each of the possible multiconfigurational wavefunctions, which should be selected in the way, that first, enables the proper description of the studied process in all regions of the potential energy hypersurface (PEH) and, second, ensures that a balanced selection of the reference CIs has been chosen. In this sense the Complete active space self-consistent field (CASSCF) method,(161, 162) developed by Roos and coworkers, enables the use the chemical intuition to reduce *a priori* the number of CSF's included in the MCSCF approach. The selection of the active space (i.e active electrons and orbitals) in a CASSCF calculation is crucial. Indeed, it requires a prior exploration of the chemistry being examined.

In the CASSCF method the MOs are classified in three categories: inactive, active and virtual orbitals (see Fig 3.1a). The inactive orbitals are those MO of lowest energy which are doubly occupied in all the CASSCF configurations. They are also optimized in the variational process but treated as in the restricted HF function. Virtual MO orbitals are of very high energy and are unoccupied in all CASSCF configurations whilst the active orbitals should be those responsible of the description of the chemical process. Hence, the CASSCF wavefunction is formed by a linear combination of all possible configurations that can be built by distributing the chosen active electrons among the selected active orbitals (i.e. a FCI treatment within the active space). One important issue when computing electronic excited states as higher roots of the Hamiltonian, is to assure the orthogonality of the wavefunctions. This is particularly true in the case of close-lying excited states, where contamination between the states might take place. In CASSCF (or RASSCF, see below) this is achieved by getting simultaneously several states that belong to the same symmetry into a State-Average (SA)-CASSCF (or SA-RASSCF) calculation, where a functional of energy is defined as an average of a certain number of states with an associated weight. As an outcome of the SA-CASSCF/RASSCF calculation a set of average orbitals and a number of orthogonal wavefunctions equal to the number of roots used in the average process are obtained. For all the stated reasons the State-average approach is recommended.

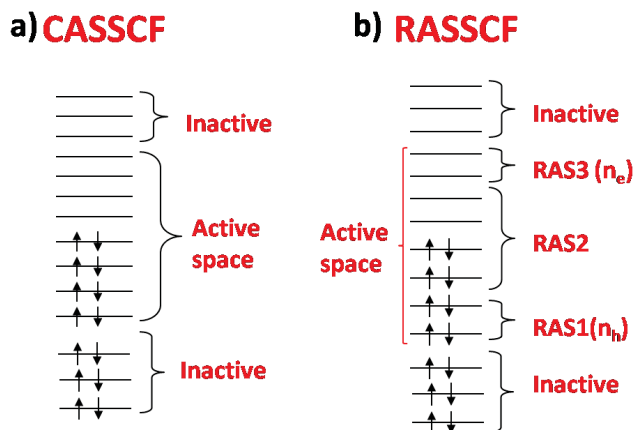


**Figure 3.1:** a) CASSCF classification of the MO orbitals. b) RASSCF classification of the MO orbitals.

One of the major shortcomings of the CASSCF method is that there are technical limits in the size of the CAS active space (the current limit is ca. 16-14 electrons/orbitals). In this sense, a refinement of the CASSCF method that allows extending the number of active electrons/orbitals, by restricting the CI excitation level and without expense of computational cost, is the Restricted active space SCF (RASSCF) method.(163, 164) The underlying assumption is that highly n-tuple excitations are very likely not to considerably contribute to recover correlation effects (we recall to truncated CI methods). Thus, in the RASSCF method the active space is subdivided into RAS1, RAS2 and RAS3 subspaces, see Fig 3.1b. Whereas RAS2 is equivalent to the active space in CASSCF, the RAS-CI is built restricting the number of holes in RAS1 and particles in RAS3, typically to two or three. With the RASSCF method it is possible to address the excited states of larger systems, such as extended  $\pi$  systems or TM complexes, as seen in section 4.1.1 of this thesis.

The correlation energy added by a CASSCF/RASSCF treatment is mainly of non-dynamic nature. Sometimes, depending on the system and the electronic state, such contribution represents an important fraction of the total correlation energy. However, the description of the correlation effects at the CASSCF/RASSCF levels of theory is hardly good enough to obtain spectroscopic accuracy since the electronic states are differently affected to dynamical correlation effects. Thus, the remaining correlation effects (i.e. dynamical correlation effects) have to be added on top of the multicon-

### 3. COMPUTATIONAL METHODS FOR TM COMPLEXES

---

figurational or multireference (MR) wavefunction. One of the most elegant ways to recover such deficiencies is applying a perturbative treatment on a multiconfigurational wavefunction. In the CASPT2 method(165, 166) second order Moller-Plesset perturbation theory is applied to a reference wavefunction.<sup>1</sup> Very recently, an extension of the CASPT2 method has been developed to include RAS references, that is the so-called RASPT2 approach.(167) In situations where strong mixing between the SA-CASSCF/RASSCF states occurs it is recommended to use the multi-state CASPT2/RASPT2 (MS-CASPT2/RASPT2)(168). An effective Hamiltonian matrix is constructed where the diagonal elements correspond to the CASPT2 (or RASPT2) energies and the off-diagonal elements introduce the coupling to second order in the dynamic correlation energy. Subsequent diagonalization of this Hamiltonian produces a set of new wavefunctions and energies. Summarizing, the CASPT2//CASSCF (or RASPT2//RASSCF) approach (either in its single-state or MS fashion) is a powerful tool in spectroscopy and photophysics, capable of handling all kind of chemical situations, since it relies on a multiconfigurational wavefunction, in an accurate manner.

#### 3.1.2 Methods based on Density Functional Theory

DFT is based on the Hohenberg and Kohn theorems.(169) The basic idea behind DFT is that the energy of an electronic system can be written as a functional of the electron density,  $\rho$ . The variational principle is also verified and allows to determine the true electronic ground state density which minimizes the energy functional. The second cornerstone idea in the development of DFT was introduced by Kohn and Sham who proposed a way to determine the electron density for a set of interacting electrons.(170) The difficulty within such formulation is that the form of the functional is unknown, in particular  $E_{xc}[\rho]$ , which is the exchange-correlation (xc) part.

Thereby, numerous schemes have been developed to obtain approximate forms for the functional for the xc energy. From the initial local spin-density approximation (LSDA) to the generalized-gradient approximation approximation (GGA) or the meta-generalized gradient approximation (mGGA), many schemes are currently available

---

<sup>1</sup>For a exhaustive treatment of many-body perturbation theory we refer the reader to A. Szabo and N. S. Ostlund, Modern quantum chemistry: introduction to advanced electronic structure, Macmillan, New York (1982).

for the construction of hundreds of different xc functionals.<sup>1</sup> One of the promising or popular approaches was the development of hybrid functionals. In such schemes, the xc energy is expressed as a linear combination of a variety of different proposals, including the HF exchange (exact exchange) with density functional exchange. Among them, the most widely used hybrid functional is the B3LYP, introduced by Becke,(171) and it mixes exact HF-exchange part with other DFT exchange-correlation functional parts arising from the B88,(172) the Lee-Yang-Parr(173) (LYP) and the VWM(174) functionals, see in equation (3.4) the form of the xc functional for B3LYP.

$$E_{xc}^{B3LYP} = (1 - a_x)E_x^{LSDA} + a_0E_x^{HF} + a_xE_x^{B88} + (1 - a_c)E_c^{VWN} + a_cE_c^{LYP}, \quad (3.4)$$

where the parameters  $a_0 = 0.20$ ,  $a_x = 0.72$  and  $a_c = 0.81$  are fitting parameters based on experimental molecular atomisation energies.

Since the computational cost of DFT in its present form is much lower than that for any other method that describes correlation, it has become widely used among the computational community. However, DFT shows severe problems and the applicability of many functionals to various problems is not broad but rather specialized. Among these problems we remark the self-interaction-error(175, 176) and the lack of adequately describing long-range correlation effects, e.g London dispersion.(177, 178) Recent attempts to overcome such deficiencies has led to the development of double-hybrid functionals,(179) which combine DFT semilocal correction with MP2-like second-order correction, or the DFT-D approach,(180) where an additional empirical correction for long-range dispersion effects is added.

For further details in DFT theory we refer the reader to cornerstone books.(181, 182, 183)

**Methods based on DFT for the calculation of excited states:** Among them we note the  $\Delta$ -SCF(184, 185) and time-dependent DFT (TD-DFT) methods.(186) The  $\Delta$ -SCF method consist in performing DFT/UDFT calculations for both ground and excited states and get the energy difference. Such approach is only possible when the

---

<sup>1</sup>We refer the reader to W. Koch and M. C. Holthausen, A Chemist's guide to Density Functional Theory, Wiley-VCH, Weinheim (2001)

### 3. COMPUTATIONAL METHODS FOR TM COMPLEXES

---

electronic states of interest belong to different irreducible representations or have different spin, since otherwise the problem of variational collapse typically prevents an equivalent SCF description for excited states.  $\Delta$ -SCF calculations at the DFT level of theory provides good estimations of singlet-triplet splittings,(157) and have been used along this thesis to get e.g. photophysical properties such as emission maxima.

The most popular extension of DFT to the calculation of excited states is the TD-DFT approach. As other propagator methods it is based on the solution of the frequency-dependent polarizability equation. Thus, if a molecule is subjected to a linear electric field  $E$ , that is fluctuating such that:

$$E = r \cos(\omega t), \quad (3.5)$$

where  $r$  is the position vector in one dimension,  $t$  is time and  $\omega$  is the frequency of the fluctuation, it can be demonstrated that the frequency-dependent polarizability is given by equation (3.6):

$$\langle \alpha \rangle_{\omega} = \sum_{i \neq 0}^{states} \frac{|\langle \Psi_0 | r | \Psi_i \rangle|^2}{\omega - (E_i - E_0)} \quad (3.6)$$

where the numerator of each term in the sum corresponds to the transition dipole moments and the denominator involves the frequency and the energies of ground and excited states. Using linear response theory it is possible to obtain the poles of the expression, that is, the values for which the frequency corresponds to the excitation energies and the denominator goes to zero, whereas the residues provide the numerators, in this case the one-photon absorption matrix elements. Hence, the procedure avoids the calculation of the explicit states.

The behavior of TD-DFT relies on the frequently erratic performance of the heavy parametrized functionals. The procedure can be, however, generally applied to study simple absorption and emission spectra, provided that an accuracy below 0.5 eV is not required. Otherwise, the flaws of the method/functionals are well known: i) poor description of CT and Rydberg states,(187, 188) ii) lack of multiconfigurational character(189) and iii) impossibility to cope with degenerate situations, such as CoIns.(190) Items ii) and iii) are difficult to solve within a TD-DFT framework in its adiabatic approximation. Concerning item i), the failure of TD-DFT in CT situations is attributed to to the incorrect long-range behavior of the current xc functionals(191, 192) and

### 3.2 Ab-initio excited state molecular dynamics: the trajectory surface hopping method.

---

spurious solutions with errors amounting to a few eV might be obtained for some molecular systems with some functionals. Attempts to improve accuracy on CT and Rydberg situations while maintaining good quality for the local excitations has led to the development of range-separated functionals. Thus, short-range exchange is treated using a local functional whilst long-range exchange is mainly treated using exact exchange. These schemes lead for instance to the LC- $\omega$ PBE(193) and CAM-B3LYP functionals.(194) The performance of several functionals to treat the excited states of TM complexes is assessed in section 4.1.1.

### 3.2 Ab-initio excited state molecular dynamics: the trajectory surface hopping method.

The theoretical treatment of the time-dependent nonadiabatic phenomena for molecular systems is a great challenge in many levels, from the description of the excited states to the time propagation of their properties. In principle, a complete description of such systems would require solving the full time-dependent Schrödinger equation (TDSE) including both electronic and nuclear degrees of freedom. This is however, unfeasible for systems of more than three atoms and more than one electronic state. To tackle this problem, several semiclassical approaches have been developed.

The basic idea behind the mixed quantum-classical molecular dynamics methods is that the nuclei are treated as classical particles whilst the electrons are treated quantum mechanically. For details in mixed quantum-classical molecular dynamics methods we refer the reader to the seminal reviews (195), (196) and (197). In the trajectory surface hopping method,(198) the adiabatic and non-adiabatic processes are splitted. Thereby, the adiabatic dynamics of the nuclei is propagated classically (i.e. following the Newton's equations of motion) on single Born-Oppenheimer PEH. As we have seen along this chapter, the excited states problematic require high ab-initio multiconfigurational methods to build accurate PEH. On the other hand, in order to take into account non-adiabatic effects, the trajectory can jump from one to another state. To this aim, the most common algorithm is the fewest-switches method proposed by Tully.(199) Such algorithm provides a probability of hopping at each time-step along the trajectory.

### 3. COMPUTATIONAL METHODS FOR TM COMPLEXES

---

The statistical character obtained with wave-packets propagations is recovered in the trajectory surface hopping method by preparing an ensemble of semiclassical trajectories, characterized by a set of initial conditions. The trajectory surface hopping methodology has been extensively used to simulate e.g. relaxation dynamics *via* CoIn's.(196)



## 4

# Results

This chapter is organized as follows. Section 4.1 deals with the computation of the excited states of TM complexes and organic compounds with quantum chemical and TD-DFT methods. In section 4.1.1 a TD-DFT and RASPT2 benchmark study of the excited states of a prototypical Ru(II)polypyridyl complex, namely *trans*(Cl)-Ru(bpy)Cl<sub>2</sub>(CO)<sub>2</sub>, is presented. As we stated in the introduction, Ru(II)polypyridyl complexes are prone to act as light-harvesting antennas in artificial photosynthesis devices and DSSCs. One of our goals is to provide useful hints about how tackle TM complexes with the powerful RASPT2/RASSCF protocol. Additionally, the performance of several TD-DFT flavors is studied. Hence, the second main goal in this subsection is evaluating which of the current xc functionals in the frame of TD-DFT methodology is more suited to describe the excited states of Ru(II)polypyridyl complexes. The low-lying excited states responsible of the main UV-Vis experimental bands of *trans*(Cl)-Ru(bpy)Cl<sub>2</sub>(CO)<sub>2</sub> are assigned as <sup>1</sup>MLCT and <sup>1</sup>IL excited states. As we have discussed along this thesis, the accurate description of CT states, which are also ubiquitous in organic chemistry, is particularly difficult with TD-DFT methods. Therefore, in Section 4.1.2, we have investigated the performance of several TD-DFT flavors for describing the CT excited states of some organic compounds, specifically in 2-hydroxyethylsulfonyl azobenzene (HESAB) acidochromic dyes. One of the main efforts in this subsection has been put into unravel the effect of solvation into the photophysical properties of the dyes. This work has been done in cooperation with the experimental group of PD. Mohr (Fraunhofer Institute, Regensburg), who synthesized and recorded the experimental UV-Vis spectra of the dyes.

## 4. RESULTS

---

In Section 4.2 some selected applications of some Ru(II)polypyridyl complexes are presented. The first application (subsection 4.2.1) involves the Ru(tpy)(CNC) $_2^{2+}$  complex, which is a bis-tridentate Ru(II)complex bearing a tpy ligand and a 2,6-bis(1,2,3-triazolylidene)pyridine moiety, herein denoted as CNC ligand. Such complex, which still benefits from tpy-related chemistry (we refer the reader to section 2.1.1), exhibits long-lived excited states and has a potential use as a photosensitizer. In subsection 4.2.2, the photophysical properties of some tris-bidentate Ru(II)complexes bearing bis(4,4'-dimethyl-2,2'-bipyridine) and a 2-(1*H*-1,2,3-triazol-4-yl)pyridine ligand are studied. Substitution of the 2-(1*H*-1,2,3-triazol-4-yl)pyridine ligand by an electron-donor or an electron-withdrawing substituent leads to a fine tuning of the emissive properties of these complexes. Along this section the photophysics of these complexes is studied with the help of quantum chemical calculations. Since we are interested in modeling the underlying mechanisms after light excitation, i.e. photochemical processes, some qualitative and quantitative analysis of several properties, as e.g radiative rates, are presented along this section. To this aim, and based in the benchmark studies done in Section 4.1, TD-DFT and multiconfigurational calculations have been performed. These contributions have been done in close cooperation with the experimental group of Prof. Schubert (IOMC, FSU Jena), who synthesized, chemically analyzed and studied by means of spectro-electrochemical techniques the Ru(II) polypyridyl complexes herein presented.

In Section 4.3 the focus is put in the emissive properties of Ir(III) complexes. As we stated in Section 2.2.3, cyclometalated Ir(III) complexes exhibit optimal photophysical properties to be exploited in OLED technology. We have theoretically rationalized the emissive properties of these complexes with the help of TD-DFT methods, emphasizing in the versatility of these complexes to tune the emission color by varying the attached ligands. These studies were done in collaboration with the experimental groups of Prof. Dr. Holder (Bergische Universitaet, Wuppertal) and Prof. Schubert (IOMC, FSU Jena).

In Section 4.4 we present the studies concerning the sunlight promoted C-C and C-Br bond activation taking place in (bisphosphane)( $\mu^2$ tolane)Pt $^0$  complexes. Along a series of complexes, it is experimentally observed a radical tune of the photochemical reactivity by substituting the tolane ring with different moieties at different positions. We have examined and elucidated the origin of the different photochemical reactivity

## 4.1 Assessing the excited states of TM complexes and organic dyes

---

(either leading to C-C, C-Br bond activation or absence of photoreactivity) for all the complexes *via* an exhaustive analysis of the vertical TD-DFT calculated spectra. Additionally, it has been observed that the photochemical oxidative reaction is reversible under thermal conditions. Therefore, ground state DFT studies have been also performed to unravel the mechanism of the thermal reductive elimination reactions. Modeling C-C bond activation involving 5d transition metal atoms with conventional DFT methods is a difficult task, due to the lack of dispersion effects in such methodologies. To overcome such deficiencies, double-hybrid DFT functionals (see Section 3.1.2), which exhibit a good performance in similar prototype reactions,(200) have been also used. TD-DFT calculations and mechanistic ground DFT studies provide a global understanding of the experimental evidences. These studies were done in close cooperation with the group of Prof. Weigand (IAAC, FSU Jena).

Finally in Section 4.5 we present a quantum chemical study and ab-initio excited state molecular dynamics of a small organic compound, namely 2H-Azirine. Dynamical simulations are mandatory to obtain time-resolved information as well as to confirm the "static" photochemical pathways obtained with quantum chemical calculations. In this sense, it has been seen that the minimum energy CoIn structure might not be the key geometry at which non-adiabatic transfer takes place.(201) Thus, crossing points located higher in energy might be more accessible and then may also be efficient funnels. It would have been desired to perform this kind of simulations in TM complexes, but the large active spaces required for these complexes with multiconfigurational methods make its study with molecular dynamics unaffordable. Therefore, in this thesis we concentrate exemplarily in 2H-Azirines, which exhibits an interesting photochemistry to be evaluated with ab-initio excited state molecular dynamics.

## 4.1 Assessing the excited states of TM complexes and organic dyes

### 4.1.1 Benchmarking the excited states of TM complexes with RASPT2 and TD-DFT methods: the case of a Ru(II)bpyridyl complex

As we have discussed along this thesis, the proper description of the excited states of TM complexes is a difficult task since a balanced description of different excitations is needed. In this subsection a state-of-the-art RASPT2 study on a Ru(II)bpyridyl

## 4. RESULTS

---

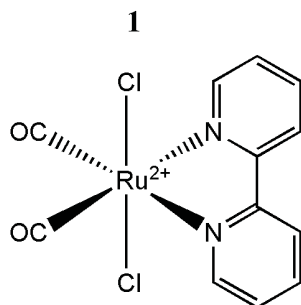


**Figure 4.1:** Chemical structure of complex 1. Adapted from Escudero et. al. *J. Chem. Theory and Comp.*, **2011**, submitted.

complex, namely the *trans*(Cl)-Ru(bpy)Cl<sub>2</sub>(CO)<sub>2</sub> (complex 1 depicted in Fig. 4.1) is presented. The performance of TD-DFT methods is also assessed. The inclusion of solvent and spin-orbit effects is also addressed. These results can be found in full detail in the appended article Escudero et. al. *J. Chem. Theory and Comp.*, **2011**, submitted. The most important findings are summarized as follows:

**i) Evaluating the performance of different range-separated and hybrid functionals including solvent effects.**

The description of CT states is one of the major bottlenecks of the TD-DFT methods. Few examples are found in the literature assessing the performance of TD-DFT methods on TM-complexes.<sup>(202)</sup> Here, different flavors of TD-DFT are evaluated. Specifically, we have employed the following functionals: i) several hybrid functionals with an increasing amount of exact exchange in the following order: B3LYP (20% of exact exchange), PBE0 (25%) and B3LYP-35 (35%), ii) the meta-hybrid M06 and M06-2X functionals (with 27% and 54% of exact exchange, respectively), iii) the pure functional PBE and iv) the long-range corrected CAM-B3LYP and LC- $\omega$ PBE functionals.

In Table 4.1 selected TD-DFT electronic excitations of complex 1 (PCM-TD-DFT<sup>1</sup> values between brackets) are collected and compared to the experimental values. These states (i.e. the 3 <sup>1</sup>A<sub>1</sub>, 4 <sup>1</sup>B<sub>2</sub> <sup>1</sup>MLCT states and the 5 <sup>1</sup>B<sub>2</sub> <sup>1</sup>IL state) are those responsible of the main UV-Vis absorption bands of complex 1. For benchmarking purposes a <sup>1</sup>MC state is also tabulated in Table 4.1. Inclusion

---

<sup>1</sup>We note that the polarizable continuum model, i.e. PCM, is employed to simulate solvent effects.

## 4.1 Assessing the excited states of TM complexes and organic dyes

**Table 4.1: Selected TD-DFT electronic transitions energies in eV compared to the experimental values. Values in brackets correspond to the PCM-TD-DFT values.**

	M06	CAM-B3LYP	PBE0	B3LYP	PBE	Exp
1 $^1B_1$ ( $^1MC$ )	2.99 (3.00)	3.39 (3.38)	3.31 (3.34)	3.25 (3.30)	3.09 (3.19)	-
3 $^1A_1$ ( $^1MLCT$ )	2.48 (3.47)	3.43 (4.41)	2.60 (3.51)	2.41 (3.42)	1.56 (2.50)	3.52
5 $^1B_2$ ( $^1IL$ )	4.29 (4.18)	4.67 (4.53)	4.44 (4.32)	4.29 (4.21)	4.02 (3.94)	3.96
4 $^1B_2$ ( $^1MLCT$ )	3.35 (4.42)	4.51 (5.71)	3.49 (4.49)	3.25 (4.36)	2.19 (3.21)	4.13

of solvent effects is mandatory to get spectroscopic accuracy, since e.g. the MLCT states are blue-shifted by ca. 1 eV as compared to the gas phase values, regardless of the functional. Therefore, only the PCM-TD-DFT values are discussed herein. All the functionals perform reasonably well for describing the  $^1MC$  state ( $1\ ^1B_1$ ) in terms of energies and oscillator strengths but acute problems are found in the description of the  $^1MLCT$  states. As it can be seen in Table 4.1, these states are only accurately calculated with hybrid functionals with an intermediate amount of exact exchange, such as B3LYP, PBE0 and M06. The errors in the MLCT states exceed in some cases 1 eV (as in the case of the pure PBE functional) indicating the importance of choosing a proper functional. The  $^1IL$  state is also better described with PBE, B3LYP, M06 or PBE0, rather than with functionals containing high percentage of exact exchange or with the range-separated CAM-B3LYP functional.

Summarizing, a balanced description of all kind of excited states of Ru(II)-polypyridyl complexes can be best obtained with M06 in first place and B3LYP or PBE0 in second place. On the other hand, it is surprising that the CAM-B3LYP functional, which is *a priori* designed to deal with CT situations, does not improve the results. Very likely, the bad performance of CAM-B3LYP for describing  $^1MLCT$  states is due to the short distance between the donor and acceptor moieties.

### ii) Assessing the RASPT2 method: Evaluating the optimal RAS partition.

As stated in section 3.1.1 the recently developed RASPT2/RASSCF method enables the treatment of larger active spaces by restricting the number of highly n-tuply determinants in the zeroth-order wavefunction. Despite its promising

## 4. RESULTS

computational advantages, the use of this method is far from straightforward and there is an urgent need to find systematic strategies about how to choose the proper partition of the active space and the level of excitations.

**Table 4.2: Relative CASPT2 and RASPT2( $n,l,m;i,j,k$ ) electronic transitions energies,  $\Delta E$  (in eV), of the main electronic excitation of complex 1, at different levels of theory, compared to the available experimental data**

States	MS-CASPT2 (14,13)	MS-RASPT2 (16,2,2;8,0,8)	MS-RASPT2 (16,2,2;2,11,3)	MS-RASPT2 (16,2,2;3,9,4)	MS-RASPT2 (22,2,2;6,9,6)	Exp
1 $^1B_1$ ( $^1MC$ )	3.49	3.36	3.31	3.23	3.55	-
3 $^1A_1$ ( $^1MLCT$ )	3.35	4.32	3.35	3.92	3.83	3.52
5 $^1B_2$ ( $^1IL$ )	4.49	4.83	4.87	4.19	4.30	3.96
4 $^1B_2$ ( $^1MLCT$ )	4.75	4.57	4.62	3.96	4.61	4.13
Number CSFs	183150	73108	2230837	557036	3890064	

In Table 4.2, the main MS-CASPT2 and MS-RASPT2 electronic transitions energies for the most important states of complex 1 are compiled. As it can be seen the energy of the strong band experimentally centered at ca. 3.96 eV is overestimated by the MS-CASPT2(14,13) calculations by 0.5 eV. The RAS calculations aim at improving the accuracy of these results by introducing additional orbitals more economically. Two main computational strategies are herein considered, namely **a)** changing the RAS1/2/3 partition or **b)** allowing to different level of excitations within the RAS1/3. In the case of strategy **b)** slightly improvements are achieved.<sup>1</sup> Therefore, only strategy **a)** is commented on the following.

**a.1)** Firstly, a correlation shell of three orbitals was considered. Leaving the RAS2 empty while allowing to SDTQ excitations within the RAS1/3 subspaces leads to the MS-RASPT2(16,4,4;8,0,8) calculations.<sup>2</sup> This cheapest computational strategy (as reflected by the decreased number of CSFs) unfortunately does not yield balanced results. It seems therefore that for describing the excited states of TM-complexes a non-vacant RAS2 subspace is needed.

<sup>1</sup>See the appended publication for details.

<sup>2</sup>In the RAS calculations, the RAS( $n,l,m;i,j,k$ ) notation is employed, where  $n$  is the number of active electrons,  $l$  the maximum of holes in the RAS1,  $m$  the maximum of electrons in RAS3, and  $i, j$  and  $k$  stand for the number of orbitals in RAS1, RAS2 and RAS3, respectively.

## 4.1 Assessing the excited states of TM complexes and organic dyes

---

**a.2)** Moving three correlation orbitals plus a pair of  $\pi\pi^*$  orbitals that was not participating in the main excited states into the RAS1/3 subspaces and allowing to SD excitations leads to the MS-RASPT2(16,2,2;2,11,3) calculations. As it can be seen in Table 4.2, the results are hardly improved despite the expense of computational cost (e.g. the number of CSFs increases by more than one order of magnitude in comparison to the MS-CASPT2(14,13) calculations). Therefore, we turn our attention to redefine the RAS partition.

**a.3)** An additional pair of  $\pi\pi^*$  orbitals that was neither participating in the main excited states of complex 1 is moved to the RAS1/3 subspaces. Hence, the RAS2 subspace is composed by the orbitals involved in the main excited states and only those. By allowing to SD excitations we get the MS-RASPT2(16,2,2;3,9,4) calculations. As it can be seen in Table 4.2 the number of CSFs is reduced by a factor of 10 in comparison to the MS-RASPT2(16,2,2;2,11,3) calculations. Very interestingly, we note that the results with the more economic MS-RASPT2(16,2,2;3,9,4) level of theory are more accurate than all the previous ones. Thus, the errors with the experimental peaks in the main electronic excited states (i.e. the  $5^1B_2$  and the  $3^1B_2$  states) are considerably reduced, assuming the solvent shifts obtained at the PCM-TD-DFT level of theory. Unfortunately, the  $3^1A_1$  state (assuming a solvent blue-shift of ca. 1 eV) is not good described.

**a.4)** Inclusion of further correlation orbitals leads to the MS-RASPT2(22,2,2;6,9,6) calculations. The results are hardly improved with respect to the MS-RASPT2(16,2,2;3,9,4) ones. Thus, we believe that a first correlation shell in combination with SD excitations within the RAS1/RAS3 is sufficient for describing in a balanced way the excited states of TM-polypyridyl complexes.

In conclusion, it seems particularly difficult to provide hints about how to obtain an accurate and balance description of all types of excited states of TM complexes simultaneously in the frame of RASPT2 calculations. The effect of different partitions should be then considered when studying other TM-polypyridyl complexes alike.

## 4. RESULTS

---

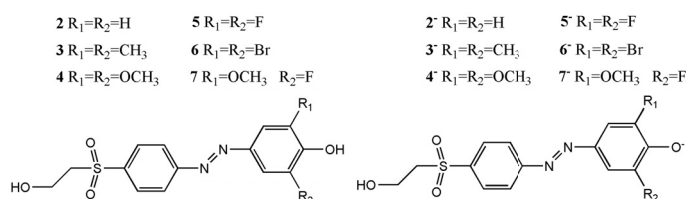


**Figure 4.2:** Chemical structure of the 2/2<sup>-</sup>-7/7<sup>-</sup> HESAB dye compounds here investigated. Adapted from Escudero et. al. *J. Chem. Theory and Comp.*, **2011**, *7*, 1062.

### 4.1.2 Computing the excited states of organic compounds with quantum chemical and TD-DFT methods: HESAB dyes as a case study

As we have seen for complex 1 one of the major shortcomings of TD-DFT comes from the description of CT states. Indeed, it has been seen that the errors can exceed 5 eV in some situations.<sup>(203)</sup> CT events are also ubiquitous in organic dyes. Seminal works show that the long-range corrected CAM-B3LYP functional and hybrid functionals with intermediate percentages of exact exchange, such as PBE0 (25%), in combination with solvent effects, are best suited to describe CT states (in terms of intensities and energies).<sup>(204, 205)</sup> Conjugated organic dyes are typical cases where CT transitions and local excitation coexist. On the other hand, their excited states are more simply to treat than those of TM complexes. Therefore, they are an adequate "scenario" to further evaluate the performance of different TD-DFT flavors as well as to assess the effects of solvation on the electronic excitation energies and their associated intensities. In this subsection the excited states of several acidochromic azobenzene-related compounds (see the 2-7 HESAB compounds and its deprotonated counterparts 2<sup>-</sup>-7<sup>-</sup>, depicted in Fig 4.2) are studied with TD-DFT and quantum chemical methods. Additionally, the effect of solvation on both the electronic excitation energies as well as on the geometries is assessed. These results can be found in the appended article Escudero et al. *J. Chem. Theory and Comp.* **2011**, *7*, 1062. The most important findings are summarized as follows:

- i) **Assessing the performance of several functionals on the excited states of HESAB compounds.** In Fig 4.3 the UV-Vis spectra of the pair of bare complexes 2/2<sup>-</sup> with different theoretical approaches are displayed and compared



## 4.1 Assessing the excited states of TM complexes and organic dyes

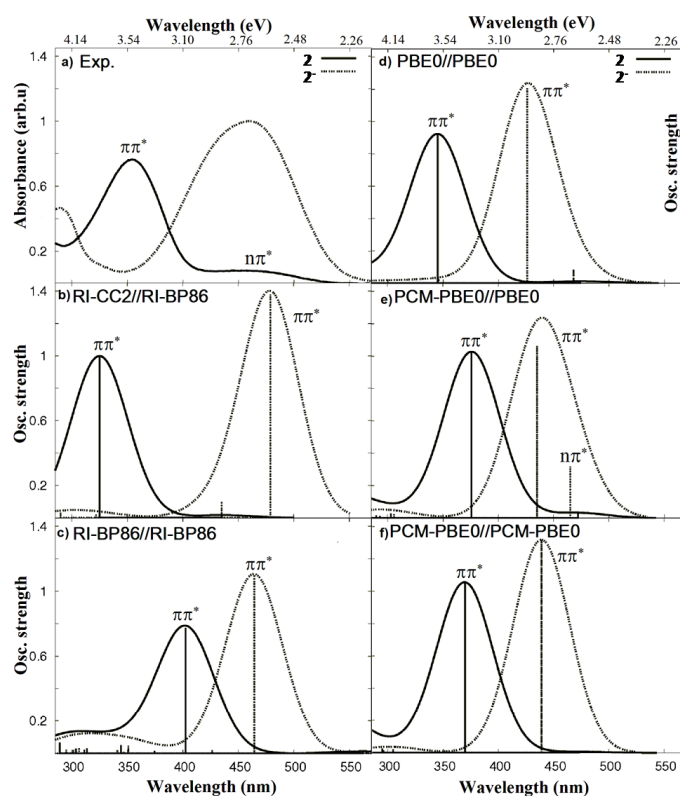


**Figure 4.3:** UV-vis absorption spectra of **2** (solid) and **2<sup>-</sup>** (dashed). a) Experimental spectrum normalized to 1 in arbitrary units, b) RI-CC2//RI-BP86, c) RI-BP86//RI-BP86, d) PBE0//PBE0, e) PCM-PBE0//PBE0 and f) PCM-PBE0//PCM-PBE0. The theoretical spectra are convoluted with a Lorentzian function with a full width at half-maximum of 60 nm: the corresponding transitions are marked with vertical lines. Adapted from Escudero et. al. *J. Chem. Theory and Comp.*, **2011**, *7*, 1062.

## 4. RESULTS

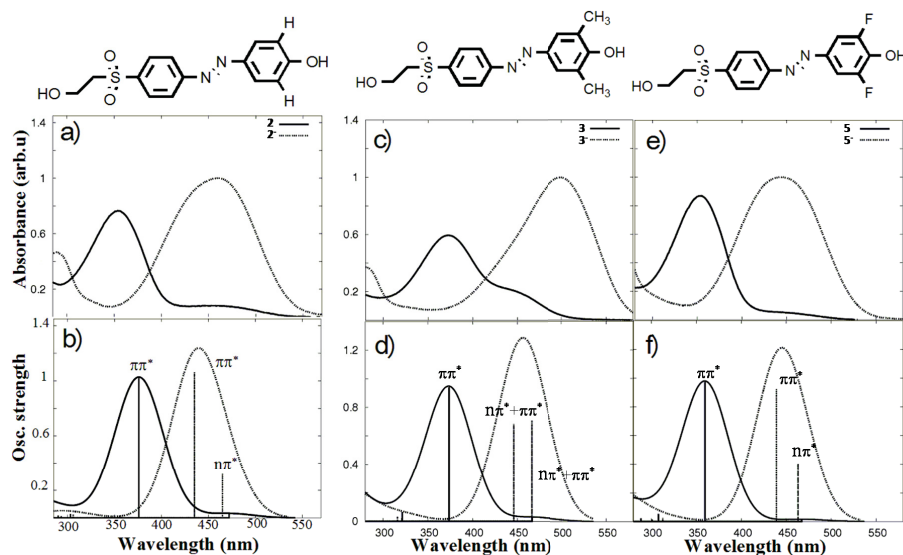


**Figure 4.4:** Experimental (top) and PCM-PBE0//PBE0 (bottom) spectra of neutral (solid) and anionic (dashed) compound. The theoretical spectra are convoluted with a Lorentzian function with a full width at half-maximum of 60 nm; the transitions are marked with vertical lines indicating its character. Adapted from Escudero et. al. *J. Chem. Theory and Comp.*, **2011**, 7, 1062.

to the experimental one. The UV-Vis spectrum of **2** is characterized by a weak  $n\pi^*$  state ( $S_1$ ) followed by a strong  $\pi\pi^*$  state ( $S_2$ ), which is the spectroscopic state (see the experimental spectrum in Fig 4.3a). The most accurate RI-CC2/TZVP method delivers  $n\pi^*$  and  $\pi\pi^*$  states in good agreement with the experimental peaks. The maximum deviations amount to ca. 0.4 eV and are probably due to the exclusion of the solvent. At the RI-BP86/TZVP level of theory, the  $S_2$   $\pi\pi^*$  state of **2** is red-shifted by ca. 0.8 eV with respect to the RI-CC2 value, clearly illustrating the energetic underestimations of CT states by pure functionals (see Fig 4.3c). With the hybrid functional PBE0 (25% of exact exchange) the errors with the experiment in the  $S_2$   $\pi\pi^*$  states of **2** and **2**<sup>-</sup> are considerably reduced, amounting only to ca. 0.15 eV.

### ii) Addressing solvent effects on the excited states of HESAB compounds.

In view of the accurate energetic estimations with the PBE0 functional the effects of solvation are evaluated at this level of theory. In Fig 4.3e and Fig 4.3f the TD-DFT spectra of compounds **2/2**<sup>-</sup> calculated including solvent effects only in the

## 4.1 Assessing the excited states of TM complexes and organic dyes

---

computation of the excitation energies, herein denoted as PCM-PBE0//PBE0 values, and both in the energies and geometries, i.e. the PCM-PBE0//PCM-PBE0 computational approach, respectively are shown. Concerning the excitation energies, one can clearly see that the errors with respect to the experiment are reduced when solvent effects are considered, being well below 0.1 eV with both methodologies. The description of the intensities deserves additional attention, specially in the case of the  $n\pi^*$  states. Unexpectedly, the best agreement with the experiment is found with the PCM-PBE0//PBE0 approach, which yields increased oscillator strengths for the  $n\pi^*$  excitations. Indeed, the weak experimental  $n\pi^*$  band is only reproduced within the latter methodology (see Fig 4.3e). A likely explanation roots to the geometry of the compounds. When considering bulk solvent effects on the optimization of the geometries, slightly more planar optimized structures are obtained. This planarization affects strongly the intensities of the  $n\pi^*$  states. We believe that the flat nature of the potential energy surface in the vicinity of the planarization region prevents the molecule from remaining planar under the experimental conditions. Thereby, the PBE0 geometries are accidentally more realistic than the PCM-PBE0 geometries. In view of these facts, the PCM-PBE0//PBE0 protocol was selected to study the spectroscopic properties of the rest of substituted HESAB compounds.

- iii) **Analyzing substitution effects on the spectroscopic properties of HESAB dyes.** Having analyzed the basic spectral properties of the neutral and anionic forms of the reference compounds  $2/2^-$ , we evaluated how the electronic transitions are modulated by substitution on the phenol moiety. The effect of substitution by electron donor groups ( $3/3^-$  and  $4/4^-$  compounds), electron acceptor groups ( $5/5^-$  and  $6/6^-$  compounds), and both electron donor and electron acceptor substituents ( $7/7^-$ ) have been analyzed, see Fig 4.2. For the sake of simplicity here we will focus on the methyl substituted  $3/3^-$  pair of compounds and on the fluorine substituted  $5/5^-$  pair of compounds. For a detailed description of the rest of compounds we refer the reader to the appended article. In Fig 4.4 the experimental and PCM-PBE0//PBE0 theoretical spectra of compounds  $3/3^-$  and  $5/5^-$  are compared with respect to the bare  $2/2^-$  reference compounds. In the electron-donor substituted compounds ( $3/3^-$ ), both the neutral and the anionic

## 4. RESULTS

---

forms show red-shifted peaks in comparison to the unsubstituted compounds. An inverse trend is observed in the studied electron-withdrawing derivatives; i.e. peaks are blue-shifted with respect to the unsubstituted compounds. These trends are observed both in the theoretical and experimental spectra. We note that the spectroscopic states responsible of the main UV-Vis bands are of the same nature as in the bare compounds. The energetic shifts in the spectroscopic  $\pi\pi^*$  states are rationalized theoretically in terms of the stabilization/destabilization of the orbital levels due to electronic effects upon substitution.

### 4.2 Selected applications of related Ru(II)polypyridyl complexes: a computational insight into their photophysics and photochemistry

#### 4.2.1 Ru(CNC)<sub>2</sub><sup>2+</sup> complex and its potential use for photosensitizer applications: a DFT and TD-DFT study of the underlying photophysical and photochemical processes

The heteroleptic Ru(tpy)(CNC)<sub>2</sub><sup>2+</sup> complex **8** depicted in Fig 4.5a possesses very interesting photophysical properties to be exploited in photosensitizer applications. It has been synthesized, chemically analyzed and studied by means of spectro-electrochemical techniques in the group of Prof Schubert (IOMC, FSU Jena). Herein we will focus on the theoretical analysis. For a detailed description of the experiments we refer the reader to the joint experimental-computational appended publication Schulze et al. *Chem. Eur. J.*, **2011**, *17*, 5494. We note that this scientific contribution was selected for a back cover.

As we emphasize in Section 2.1.1, the use of Ru(II)polypyridyl complexes based in the tpy ligand is preferred for photosensitizer applications as compared to the bpy chemistry.<sup>(32, 33)</sup> The use of tpy-based Ru(II) complexes implies also some drawbacks, since these complexes usually yield diminished excited state lifetimes. As stated in Section 2.1.1 one of the main strategies in order to achieve longer lifetimes of the excited states of tpy-based Ru(II) complexes is to obtain increased <sup>3</sup>MC-<sup>3</sup>MLCT energy gaps. To this aim, herein an abnormal/mesoionic carbene pincer ligand, i.e. the CNC ligand, was used. The mesoionic carbene ligands provide superior  $\sigma$ -donating and only

## 4.2 Selected applications of related Ru(II)polypyridyl complexes: a computational insight into their photophysics and photochemistry

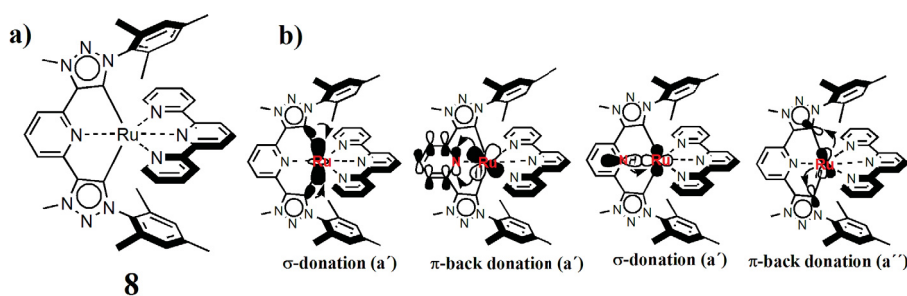


**Figure 4.5:** a) Chemical structure of complex 8. b) Schematic representation of the main orbital interactions between the mesoionic carbene ligand and the tpy-Ru(II) fragment. The symmetry of the interacting orbitals is assigned in brackets. Adapted from Schulze et. al. *Chem. Eur. J.*, **2011**, *17*, 5494.

moderate  $\pi$ -accepting properties that ideally would lead to strongly destabilized  $^3MC$  states and a maintained  $^3MLCT$  energy. Our theoretical analysis has been focused on:

- i) **Analyzing the bonding mechanisms of the abnormal carbene to the ruthenium center.** To this aim, energy-decomposition analysis (EDA)(206, 207) was performed. The EDA (BP86-ZORA/TZP) calculation revealed that the interaction energy between the carbene and the ruthenium(II)-tpy fragment is  $-256 \text{ kcal mol}^{-1}$ . Former EDA calculations of normal and abnormal imidazolynes yield interaction energies of  $-60$  to  $-70 \text{ kcal mol}^{-1}$  for a single ruthenium carbene bond.(208) Assuming these values for a tridentate system still leaves a significant energy difference, meaning that the CNC pincer ligand enables very strong ruthenium-abnormal carbene bonds. The global interaction energy stems roughly 1:1 from covalent and ionic interactions. Concerning the covalency of the bond, strong  $\sigma$ -donating as well as  $\pi$ -accepting interactions contribute to the global energy (see Fig 4.5b for the most relevant interactions).
- ii) **Examination of the UV-Vis absorption spectrum of complex 8.** To this aim, TD-DFT calculations were performed. In Fig 4.6a the calculated PCM-TD-B3LYP/6-31G\* UV-Vis absorption spectrum is represented and compared to the experimental one. The experimental emission spectrum is also presented in Fig 4.6a. The calculated UV-Vis absorption spectrum is slightly blue-shifted in comparison to the measured spectrum, but both are consistent in shape.<sup>1</sup> The

<sup>1</sup>We recall that a good agreement between the calculated and the measured UV-Vis spectra of

## 4. RESULTS

---

low-energy band, which peaks experimentally at ca. 463 nm, is due to excitations of MLCT character involving both the tpy and the CNC ligands.  $^1IL$  states are mainly responsible of the two intense bands peaking at ca. 300 nm (the most important excitations are highlighted in Fig 4.6a).

**iii) Analysis of the photochemical events after excitation of the lowest-lying excited states.** Complex 8 exhibits high quantum yields of emission, which are comparable to those obtained in the  $[\text{Ru}(\text{bpy})_3]^{2+}$  complex. The room-temperature emission is characterized by a slow and monoexponential decay, thus arising from a single phosphorescent triple state. To shed some light into the emission phenomena we performed further DFT and TD-DFT calculations. Thus, the lowest triplet excited state was optimized with unrestricted density functional theory (UB3LYP/6-31G\*). Additionally TD-DFT singlet-triplet excitations were computed at both the  $S_0$  and the  $T_1$  optimized geometries. The analysis of the spin density at the  $T_1$  geometry clearly reveals that this state is of  $^3\text{MLCT}$  character and involves the CNC ligand, see Fig 4.6b. In Fig 4.6c the energy-level scheme of the lowest PCM-TD-B3LYP/6-31G\* singlet and triplet excited states involved in the photochemical deactivation processes are depicted. Thereby, the longest-wavelength  $^1\text{MLCT}$  absorption involves the tpy ligand, whereas, the  $^3\text{MLCT}$  emission originates from the carbene ligand after redistribution of electron density in the course of vibrational relaxation and ISC. Remarkably, due to the strong  $\sigma$  donation, the  $^3\text{MC}$  states are of very high energies, achieving exemplarily  $^3\text{MC}$ - $^3\text{MLCT}$  energy gaps of  $32 \text{ kcal mol}^{-1}$  at the  $T_1$  optimized geometry. Accordingly, the  $^3\text{MC}$  states are hardly populated thermally and therefore, the radiationless deactivation is efficiently suppressed in complex 8 (see Fig 4.6c).

### 4.2.2 Fine tuning of the excited state lifetimes of Ru(II)polypyridyl complexes.

As stated in section 2.1.1 when the radiationless deactivation mechanisms involving the  $^3\text{MC}$  states are suppressed, the non-radiative decay rates from the  $^3\text{MLCT}$  states are determined by the energy-gap law dependence (Eq. 2.5). In such situations a

---

Ru(II)polypyridyl complexes has been obtained within the B3LYP functional rather than with CAM-B3LYP.

## 4.2 Selected applications of related Ru(II)polypyridyl complexes: a computational insight into their photophysics and photochemistry

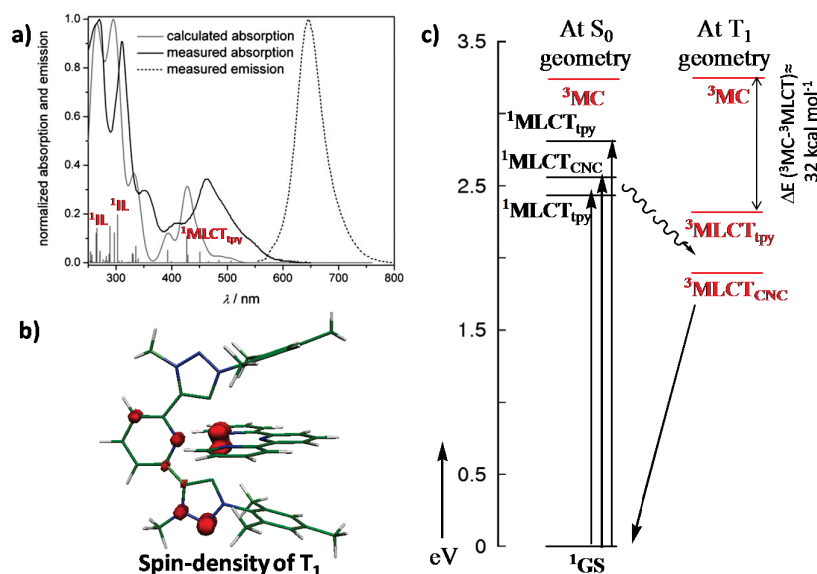


**Figure 4.6:** a) Calculated and measured UV-Vis absorption spectra and measured emission spectra of complex 8. b) Spin-density plot of the  $T_1$  state. c) Energy-level scheme of the lowest excited states of complex 8 at both the  $S_0$  and  $T_1$  optimized geometries. Adapted from Schulze et. al. *Chem. Eur. J.*, **2011**, *17*, 5494.

fine tuning of the excited state lifetimes and consequently of the quantum yields of phosphorescence (i.e.  $\Phi_p$ ) is feasible, by e.g. ligand modification. This is the case of the Ru(II) polypyridyl complexes 9 and 10 depicted in Fig 4.7. Substitution of the phenylacetylene moiety attached to the 2-(1*H*-1,2,3-triazol-4-yl)pyridine ligand by an electron-withdrawing ( $-\text{NO}_2$ ) or an electron-donor ( $-\text{OC}_6\text{H}_{13}$ ) group leads to complex 9 and 10, respectively. Such peripheral modification results in a very different photophysical behavior. Thus, the  $\Phi_p$  of complex 9 is ca. 5-fold bigger as compared to the one of complex 10 in dichloromethane (i.e.  $\text{CH}_2\text{Cl}_2$ ) solution. Additionally, it is observed a solvent dependence on the phosphorescence properties of complexes 9-10, as reflected by the lower  $\Phi_p$  values obtained in acetonitrile ( $\text{CH}_3\text{CN}$ ) solutions for both complexes. Herein, we will concentrate on the emission properties obtained in  $\text{CH}_2\text{Cl}_2$  solution. In Table 4.3 the experimental emission data in  $\text{CH}_2\text{Cl}_2$  are collected. The complexes 9-10 were synthesized, chemically analyzed and studied by means of spectroelectrochemical techniques in the group of Prof. Schubert (IOMC, FSU Jena). All these results can be found in the following publications: Happ et al. *J. Org. Chem.*, **2010**, *75*, 4025. Additionally, a publication is currently under preparation. The main findings can be

## 4. RESULTS

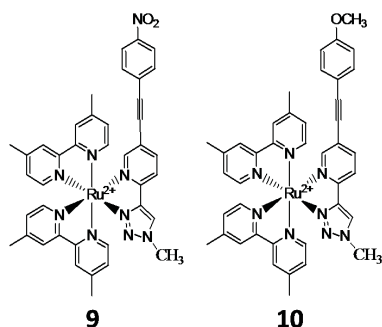


**Figure 4.7:** Chemical structure of complexes 9-10.

summarized as follows:

**Table 4.3:** Experimental emission data of complexes 9-10 obtained in  $\text{CH}_2\text{Cl}_2$  solution

Complex	$\lambda_{ems}$ [ $\text{CH}_2\text{Cl}_2$ , nm(eV)]	$\Phi_P$ [ $\text{CH}_2\text{Cl}_2$ ]
9	647(1.92)	0.022
10	594 (2.09)	0.005

**i) Substitution effects: Tuning the  $\Phi_p$  values of complexes 9 and 10.** As stated in section 2.1 the  $\Phi_p$  is a subtle balance of the radiative ( $k_r$ ) and the non-radiative ( $k_{nr}$ ) decay rates (see Eq. 2.2). The computation of the  $k_{nr}$  is a challenging objective far from being trivial. On the other hand, the  $k_r$  can be easily computed with equations 2.6 and 2.7. Such equations have been successfully used to compute the radiative rates of other TM complexes.(209, 210, 211) The  $k_{nr}$  values raise exponentially with decreasing  $T_1$ - $S_0$  energy gaps, as deduced from equation 2.5. If we compare the emission energies (i.e.  $T_1$ - $S_0$  gaps) of complexes 9 and 10 we can see that lower energy gaps are obtained for complex 9 (see Table 4.3). That results in bigger  $k_{nr}$  values for complex 9. If we do not consider the  $k_r$  values, then larger  $\Phi_p$  values are obtained for complex 10 than for complex 9. Oppositely, it is observed that ca. 5-fold bigger  $\Phi_p$  values are obtained for complex 9 (see Table 4.3). There must be therefore a compensating effect on the  $\Phi_p$  that explains this behavior. Consequently, the  $k_r$  were computed. To this aim, we have propose a mixed TD-DFT/CASSCF theoretical approach to



## 4.2 Selected applications of related Ru(II)polypyridyl complexes: a computational insight into their photophysics and photochemistry

---

compute the phosphorescence rates, i.e. the vertical energies and its associated oscillator strengths are computed at the PCM-TD-B3LYP/6-31G\* level of theory whilst the SOC matrix elements are evaluated with a SA-CASSCF(8,7)/ANO-S wavefunction. In Figure 4.8 the Jablonski diagrams of complexes 9 and 10 are presented. The main PCM-TD-B3LYP/6-31G\* singlet-singlet and singlet-triplet electronic excitations computed at the  $S_0$  geometry as well as the involved PCM-TD-B3LYP/6-31G\* triplet excited states at the  $T_1$  geometry are highlighted in Fig. 4.8. The absolute SOC elements ( $\text{cm}^{-1}$ ) between the manifold of singlet and triplet excited states are also included. One can see that the biggest SOC elements are obtained, as expected, for the interaction between  $^1\text{MLCT}$  and  $^3\text{MLCT}$  states. In Fig 4.8 is also highlighted the highest  $k_r(T_m \rightarrow S_0)$  obtained for each complex. The analysis of all the computed  $k_r$  values reveals that in the case of complex 9 the biggest rate corresponds to the  $k_r(T_7 \rightarrow S_0)$  value, which amounts to  $5.4 \times 10^7 \text{ s}^{-1}$ . In the case of complex 10, the highest rate arises from the  $k_r(T_4 \rightarrow S_0)$  value, amounting to  $3.0 \times 10^6 \text{ s}^{-1}$ . The latter is ca. one order of magnitude smaller. The underlying reason of these findings can be easily understood by looking at Fig. 4.8. In complex 9 more  $^1\text{MLCT}$  states are excited under the  $\lambda_{exp}$  as compared to the electron-donor substituted complex 10. Moreover, the interaction between the  $^1\text{MLCT}$  and the  $^3\text{MLCT}$  takes place in a more horizontal manner in complex 9, hence favoring the efficient population of the  $^3\text{MLCT}$  states. Thus, electron-donor substitution of the 2-(1*H*-1,2,3-triazol-4-yl)pyridine ligand leads to a stabilization/destabilization of the  $\pi$  and  $\pi^*$  related orbital and consequently less  $^1\text{MLCT}$  states are available to be populated. Summarizing, we have explained the experimental evidence of bigger yields for complex 9 in terms of the differences in the computed  $k_r$  values for complexes 9 and 10, that finally leads to an overall compensation on the  $\Phi_p$  values, as we stated above.

- ii) **Solvent effects on the  $\Phi_p$  values.** The emissive behavior of complexes 9 and 10 is highly dependent on the solvent. Thus, the solvent not only biases the  $\Phi_p$  values but also shifts the emission maxima of both complexes. We have found that the rationalization of the solvent effects on the  $\Phi_p$  values can be mainly derived, oppositely to substitution effects, from the energy gap-law dependence(Eq. 2.5).

## 4. RESULTS

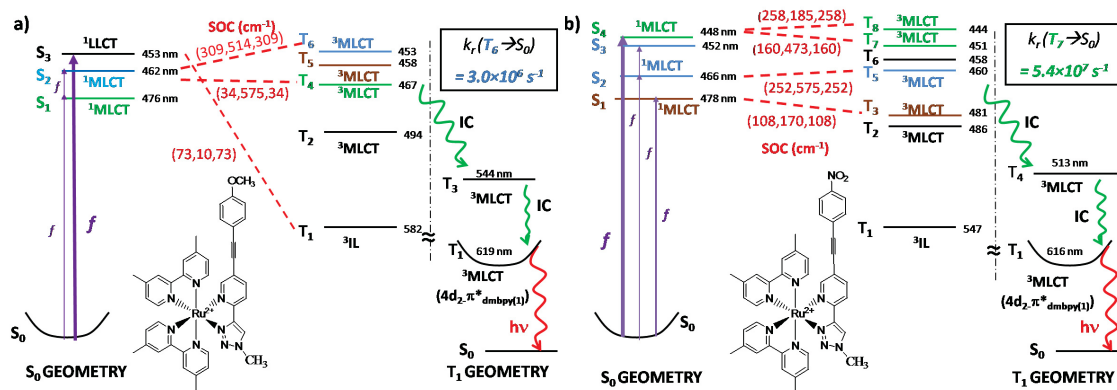


**Figure 4.8:** Jablonski diagrams of complex 10 (a) and complex 9 (b). PCM-TD-B3LYP/6-31G\* singlet-singlet and singlet-triplet vertical excitations vertical excitations. The main absolute SOC values (cm<sup>-1</sup>) and the main radiative mechanism ( $k_r$ ) are highlighted. Adapted from Escudero et al. **2011**, submitted.

### 4.3 Cyclometalated Ir(III) complexes: a theoretical insight into their emissive properties

In this section the main focus is put in the interpretation of emission properties and in the design of efficient blue phosphors. To this aim the cyclometalated Ir(III) complexes 11-17 depicted in Fig 4.9 have been studied in close cooperation with the experimental groups of Prof Schubert (IOMC, FSU Jena) and Prof. Holder (Bergische Universitaet, Wuppertal). The results can be found in the appended articles Beyer et al. *Organometallics*, **2009**, *28*, 5478 and Tian et al. *Eur. J. Inorg. Chem.*, **2010**, 4875.

To simulate the emission spectra maxima several computational strategies have been considered, namely  $\Delta$ -SCF and TD-DFT approaches. Particularly, the following strategies have been employed, (see Fig 4.10):

- i) TD-DFT singlet-triplet gap calculations performed at the ground state geometry (S<sub>0</sub>). See item 1 in Fig 4.10.
- ii) TD-DFT singlet-triplet gap calculations performed at the lowest triplet excited state geometry (T<sub>1</sub>). See item 2 in Fig 4.10.
- iii) Computing the AEE, i.e. adiabatic emission energies, values. This is calculated as the energy difference between the first triplet excited state at its optimized

### 4.3 Cyclometalated Ir(III) complexes: a theoretical insight into their emissive properties

---

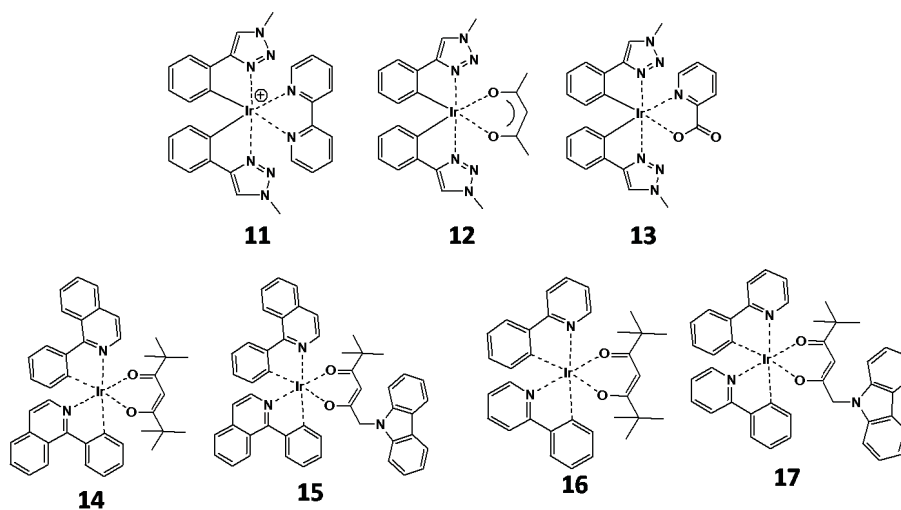


**Figure 4.9:** Chemical structure of the cyclometalated Ir(III) complexes 11-17. Adapted from publications Beyer et al. *Organometallics*, **2009**, *28*, 5478 and Tian et al. *Eur. J. Inorg. Chem.*, **2010**, 4875.

geometry and the closed-shell ground state at the same geometry (using UDFT energies, we recall the reader to section 3.1.2). See item 3 in Fig 4.10.

The main results obtained for these complexes can be summarized as follows:

- i) **Evaluation of the different TD-DFT and  $\Delta$ -SCF approaches to compute the emission maxima.** In Table 4.4 the phosphorescence emission maxima of complexes 11-13 obtained with different theoretical approaches are tabulated and compared to the experimental value. Both the TD-DFT singlet-triplet electronic excitation energies and the  $\Delta$ -SCF energies are computed in the presence of  $\text{CH}_2\text{Cl}_2$ . As it can be seen all the theoretical approaches predict the emissive state ( $T_1$ ) to be of MLCT character. In the  $\Delta$ -SCF procedure (3), the underlying character of the lowest triplet excited state is assigned through the analysis of the spin density at the lowest triplet excited state geometry. On the contrary for the TD-DFT approaches, the character of the lowest triplet excited state is assigned through the analysis of its main configuration. Interestingly, the PCM-TD-B3LYP/TZVP values at the  $S_0$  geometry show blue-shifted phosphorescence peaks in comparison to the experiment, in particular for complex 13 where this blue-shift amounts to ca. 0.6 eV. Blue-shifted peaks are inherent within this

## 4. RESULTS

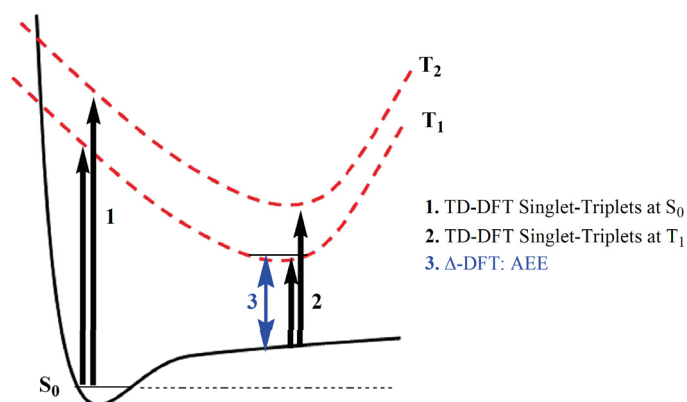


**Figure 4.10:** Schematic representation of the TD-DFT and  $\Delta$ -SCF approaches to reproduce the emission spectra maxima.

approach since the relaxation to the lowest triplet excited state is not allowed. On the contrary, the PCM-TD-B3LYP/TZVP values at the  $T_1$  geometry are in closer agreement with the experiment, with the maximum deviation amounting to ca. 0.39 eV (complex 12). Finally, the AEE values match perfectly the phosphorescence emission maxima of cyclometalated Ir(III) complexes 11-13, yielding complex 13 the major deviation with the experiment, which only amounts to ca. 0.27 eV. We are confident that the two latter approaches are the best ones to simulate the phosphorescence spectra. Indeed, similar conclusions can be extracted through the analysis of complexes 14-17.<sup>1</sup>

**Table 4.4:** Lowest singlet-triplet theoretical emission energies by means of TD-DFT and  $\Delta$ -SCF approaches

	Exp.	AEE /Character	TD-DFT at $S_0$	TD-DFT at $T_1$
11 [Ir(a) <sub>2</sub> (bpy)] <sup>+</sup>	560	581 / <sup>3</sup> MLCT	505 / <sup>3</sup> MLCT	648 / <sup>3</sup> MLCT
12 [Ir(a) <sub>2</sub> (acac)]	435	476 / <sup>3</sup> MLCT	413 / <sup>3</sup> MLCT	504 / <sup>3</sup> MLCT
13 [Ir(a) <sub>2</sub> (pic)] <sup>+</sup>	527	472 / <sup>3</sup> MLCT	422 / <sup>3</sup> MLCT	500 / <sup>3</sup> MLCT

### ii) How do we achieve efficient blue phosphors? A theoretical insight into the blue-shifts arising from ligand substitution in complexes 11-13.

The use of the phenyl-1*H*-[1,2,3]triazole (a) cyclometalating ligand instead of the

<sup>1</sup>For a detailed analysis of the phosphorescence spectra of these complexes we refer the reader to the appended publication Tian et al. *Eur. J. Inorg. Chem.*, **2010**, 4875.

#### 4.4 Insights from TD-DFT and DFT calculations into the photochemical bond-activation on (bisphosphane)( $\mu^2$ tolane)Pt<sup>0</sup> complexes

---

widely used 2-phenylpyridine (ppy) ligand in general cause a spectral blue shift, as the results for these complexes in comparison to their known 2-phenylpyridinato analogues reflect. Among the ancillary ligands herein employed, i.e. bipyridine (bpy), acetylacetonate (acac) and picolate (pic), the acac ligand in combination with the (a) cyclometalating ligand results in the most blue-shifted phosphorescence peak. As stated in section 2.2.3, one of the major goals in OLED chemistry is obtaining efficient blue-emitters phosphors. We have rationalized the blue-shifts along this series of complexes by examining the energies of the LUMOs energies, since the HOMO levels are mostly maintained. Thus, in the acac complex 12 the LUMO is of  $\pi_{acac}^*$  character and it is destabilized as compared to the analogous  $\pi^*$  orbital of complexes 11 and 13. This effect can be rationalized in terms of the conjugation effect over the ancillary ligand, which is not feasible in the  $\pi_{acac}^*$  related orbital. These studies reveal that there is an increasing possibility of color-tuning through changing the ancillary or cyclometalating ligands. Indeed, the results for complexes 14-17 (not shown here, see Tian et al. *Eur. J. Inorg. Chem.*, **2010**, 4875) are also illustrative of this fact.

#### 4.4 Insights from TD-DFT and DFT calculations into the photochemical bond-activation on (bisphosphane)( $\mu^2$ tolane)Pt<sup>0</sup> complexes

The studies herein presented were motivated by the experimental findings in the group of Prof. Weigand (IAAC, FSU Jena) that by irradiating with sunlight the (bisphosphane)( $\mu^2$ tolane)Pt<sup>0</sup> complex 18 depicted in Fig 4.11, a rare example of selective C-C bond activation in the solid state was observed. In solution, selectivity was lost and C-Br bond activation products were also observed. Interestingly, C-C bond activation is not observed when the bromine substituents are not present, see compound 19 in Fig 4.11, neither in solution nor in the solid state. These findings motivated the study of further (bisphosphane)( $\mu^2$ tolane)Pt<sup>0</sup> derivatives, bearing different tolane substitution as well as different bisphosphane ligands (see the complexes depicted in Fig 4.12a-c). For a detailed description of these studies we refer the reader to the appended publications: i) Petzold et al. *Dalton Trans.*, **2008**, 1979; ii) Escudero et al. *Phys. Chem.*

## 4. RESULTS

---

*Chem. Phys.*, **2009**, *11*, 4593; iii) Weisheit et al. *Dalton Trans.*, **2010**, *39*, 9493; and iv) Escudero et al. *Dalton Trans.*, **2010**, *39*, 9505.

The main findings can be summarized as follows:

**i) TD-DFT studies on  $(\mu^2\text{tolane})\text{Pt}^0$  complexes: deciphering the reasons for C-C and C-Br bond activation.** Firstly, we aimed at rationalizing the astonishingly different photochemical behavior of compounds 18 and 19. TD-BP86/TZVP calculations were performed to simulate their UV-Vis absorption spectra and to assign the main electronic transitions that promote the observed rearrangement. As seen in Fig 4.13, whereas in complex 19 the main electronic transitions correspond to  $\pi_{alk}\pi_{phe}^*$  transitions, in complex 18 the most intense peaks are of  $d_{Pt}\pi_{alk}^*$  character.<sup>1</sup> Through the analysis of these evidences we put forward the hypothesis that the  $d_{Pt}\pi_{alk}^*$  states were responsible of the observed photochemical rearrangement in complex 18. Hence, depopulation of the  $d_{Pt}$  orbitals and concomitant population of the antibonding  $\pi_{alk}^*$  leads to a destabilization of the alkyne group *via* additional  $\pi$ -back donation, which weakens the hapto-coordination of the Pt to the tolane group and ultimately promote the observed C-C bond cleavage product in compound 18. These results were published in the appended article Petzold et al. *Dalton Trans.*, **2008**, 1979. Indeed, further joint experimental-theoretical studies in complexes 26-33 confirmed these hypothesis. Hence, the complexes which are prone to undergo C-C bond activation processes are those having intense  $d_{Pt}\pi_{alk}^*$  bands. Regarding C-Br bond activation, both the weakening of the hapto-coordination plus a weakening in the C-Br bond after light irradiation should take place simultaneously. We have rationalized the latter process in the bromine substituted compounds by localizing several intense MLCT and LLCT transitions of  $d_{x^2-y^2}\sigma_{C-Br}^*$  and  $\pi_{alk}^*\sigma_{C-Br}^*$  character. These evidences can be found in Escudero et al. *Dalton Trans.*, **2010**, *39*, 9505.

**ii) Steric or electronic? Understanding C-C and C-Br bond activation.**

---

<sup>1</sup>Methodologically we found (as we stated in previous sections) that pure functionals (as e.g. BP86) tend to underestimate the electronic excitation energies of the CT states. As we already discussed in section 4.1.1, this holds true for true long-range CT situations. In practise, short-range CT states with overlap of the interacting orbitals are common within these complexes. Therefore, we are still confident that in this case the description of the CT states is not hampered by the use of pure functionals.

#### 4.4 Insights from TD-DFT and DFT calculations into the photochemical bond-activation on (bisphosphane)( $\mu^2$ tolane)Pt<sup>0</sup> complexes

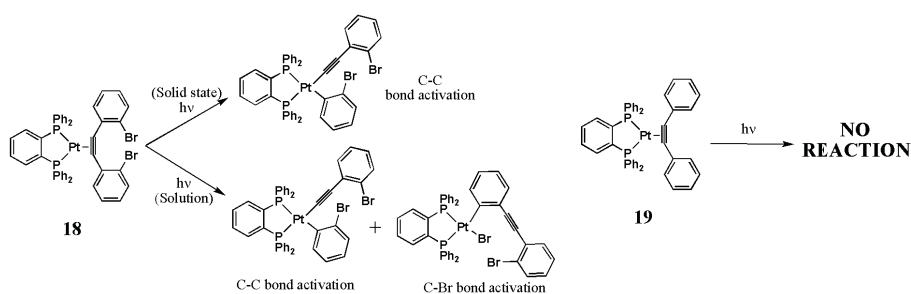


**Figure 4.11:** C-C and C-Br bond cleavage pathways taking place in complex 18 via irradiation with sunlight. Complex 19 does not undergo photochemical bond cleavage.

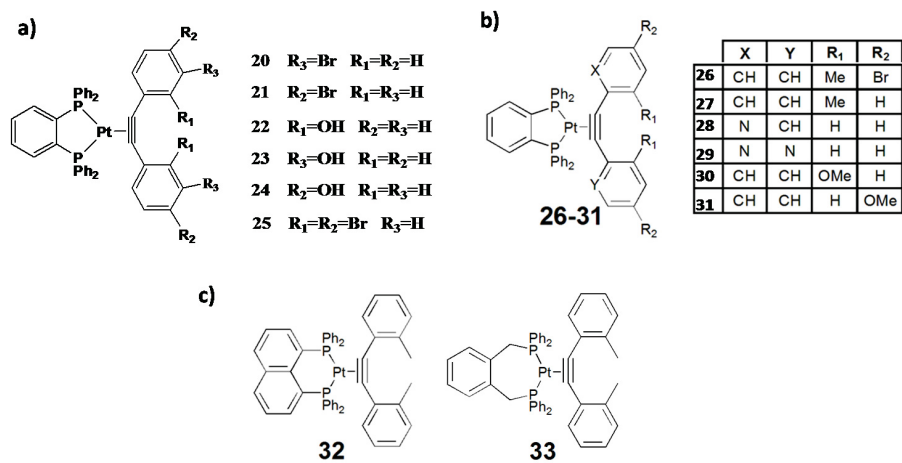


**Figure 4.12:** a) Chemical structure of (dppbe)( $\mu^2$ tolane)Pt<sup>0</sup> 20-33 complexes.

## 4. RESULTS

---

Based on the previous findings we aimed at understanding whether the different photochemical reactivity stems from a pure electronic effect or it is a consequence of the steric constraints imposed by ligand substitution. The steric effects can be illustrated as follows. By comparing the X-ray structures of e.g. 18 and 19 one can clearly see that *ortho*(2,2')-disubstitution in 18 leads to steric hindrance between both bromine ligands, which ultimately affect the planarity of the tolane ring and could eventually influence the UV-Vis absorption properties. To this aim, in a second contribution (see the appended contribution Escudero et al. *Phys. Chem. Chem. Phys.*, **2009**, *11*, 4593), we dealt with the study of the ground and excited state properties of several (dppbe)( $\mu^2$ tolane)Pt<sup>0</sup> (dppe=1,2-bis(diphenylphosphino)benzene) complexes, which are shown in Fig 4.12b. Particularly, we considered complexes 18, 20 and 21 by substituting some position of the tolane ring with an electron-withdrawing group (EWG), i.e. bromine, in *ortho*(2,2'-), *meta*(3,3'-) and *para*(4,4'-) positions, respectively. Likewise, an analogous series of complexes 22, 23 and 24 are obtained with an electron-donor group (EDG), i.e. hydroxyl, in the corresponding positions. Additionally, complex 25 was also studied, which exhibits bromine substitution in both *ortho*(2,2'-) and *para*(4,4'-) positions.

The calculated UV-Vis spectra of complexes 18 and 20-24 are shown in Fig 4.14. The main electronic excitations in these complexes are of MLCT, LLCT and IL character. As a general remark one can clearly see that the UV-Vis spectra of the complexes are more robust with respect to the substitution pattern than to the electronic nature of the substituent. As seen in Fig 4.14, e.g. the spectra of the *ortho*-derivatives resemble more one another in greater extent than within the electron-donating/withdrawing series. In what the photochemical "active" states responsible for the photochemical reactivity is concerned, i.e. the MLCT transitions of  $d_{Pt}\pi_{alk}^*$  character, several interesting points arise. As we stated above, such MLCT states are not found (or are mainly dark states) in the unsubstituted compound 19. An exhaustive analysis of these MLCT excitations in complexes 18 and 20-25 reveals that they are predominant and more intense in electron-withdrawing substituted compounds, as well as in *ortho*-derivatives (see the  $d_{Pt}\pi_{alk}^*$  excitations in Fig 4.14). Regarding the C-Br bond activation we also localized intense transitions involving  $\sigma_{C-Br}^*$  orbitals.



#### 4.4 Insights from TD-DFT and DFT calculations into the photochemical bond-activation on (bisphosphane)( $\mu^2$ tolane)Pt<sup>0</sup> complexes

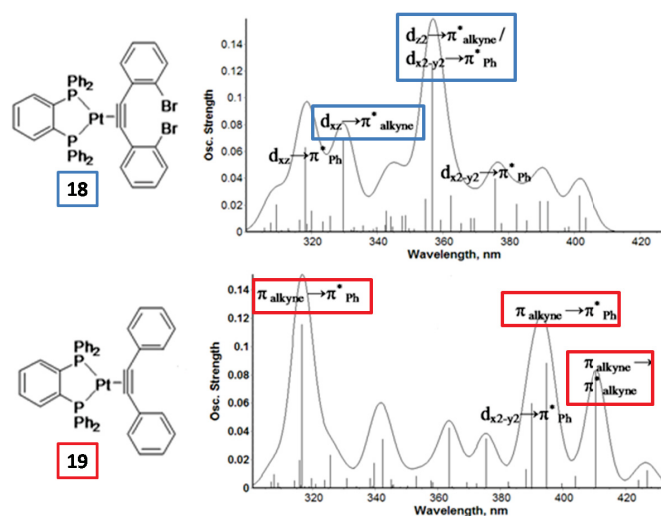


**Figure 4.13:** a) TD-BP86/TZVP simulated UV/Vis spectra of complexes 18 and 19.

Summarizing, it seems that both the pattern substitution and the electronic nature of the substituent play an important role in determining the presence or absence of the photochemical active MLCT states of  $d_{Pt}\pi_{alk}^*$  character. Indeed, additional joint experimental-theoretical studies in complexes 26-31 confirmed these hypothesis (see appended publication Escudero et al. *Dalton Trans.*, **2010**, 39, 9505). In this latter publication, the effect of changing the bisphosphane ligand was also analyzed (see complexes 32-33 in Fig 4.12c). Only complex 32, which bears a similar P-Pt-P bite angle as compared to the 18-26 series, possesses intense  $d_{Pt}\pi_{alk}^*$  excitations and accordingly undergoes photochemical C-C bond activation.

iii) **Backwards thermal reductive elimination reactions.** To provide insights into the selectivity of the photochemical and backwards thermal reductive elimination, i.e. (Pt<sup>2</sup> to Pt<sup>0</sup>), DFT studies on the ground state were performed.

It is observed experimentally that the photochemical C-C bond activation is reversible under thermal conditions, even though the forward reaction does not proceed thermally. Interestingly, the C-Br photochemical bond activation reaction taking place in the bromine substituted compounds 21 and 26 is irreversible under thermal conditions. To understand these results we performed DFT ground state calculations which allowed elucidating the mechanism underlying the ther-

## 4. RESULTS

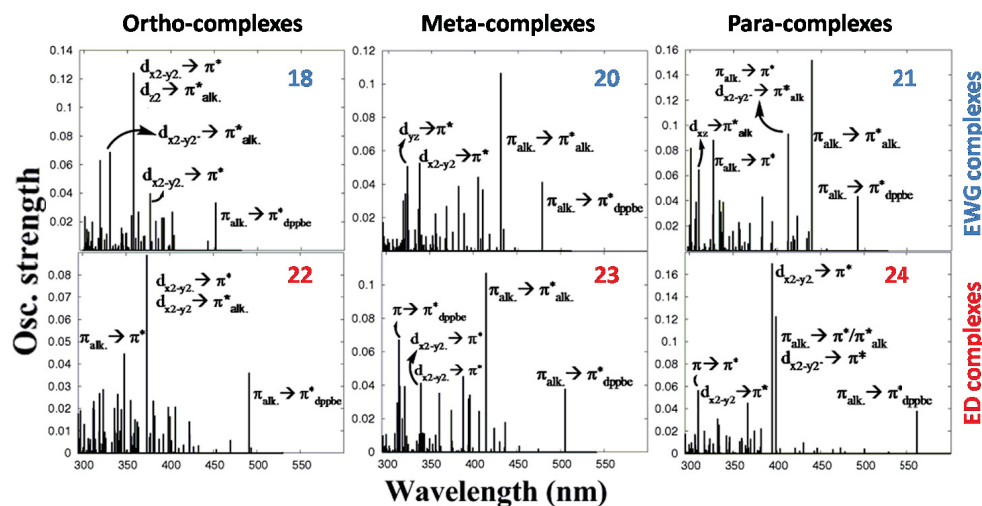


**Figure 4.14:** TD-DFT UV-Vis spectra of complexes 18, 20-24. The main electronic transitions are highlighted. Adapted from Escudero et al. *Phys. Chem. Chem. Phys.*, **2009**, *11*, 4593.

mal backwards reactions. The C-C bond activated products have been optimized in the EWG complex 21 and in the EDG complexes 30 and 31. The thermal reductive elimination dealing with the C-Br bond activation has been studied in complex 21. Gas phase Gibbs free energies ( $\Delta G$ ) as well as activation barriers ( $\Delta G^\ddagger$ ) of the reactions have been obtained at the B3LYP/6-311G\*//RI-BP86/TZVP and B2GP-PLYP/6-311G\*//RI-BP86/TZVP levels of theory.

In Fig 4.15a the energetic profiles of the thermal reductive eliminations for complexes 21, 30 and 31 beginning from the C-C bond activated reactants is shown. In Fig 4.15b the energetic profile for the thermal reductive elimination beginning from the C-Br activated complex 21 is depicted. Several stationary points have been located in the potential energy surfaces of the complexes. The thermal pathway beginning from the C-C bond activated products is exothermic for all the herein considered complexes regardless the pattern and electronic nature of the substituents. B2GP-PLYP activation barriers range from 30 to 35 kcal/mol in agreement to the experimental activation barriers for C-C bond cleavage reactions for similar (bisphosphane)( $\mu^2$ tolane)Pt<sup>0</sup> complexes.(148) The B3LYP activation barriers are underestimated by ca. 10 kcal/mol, very likely due to the lack of long-range correlation effects (see section 3.1.2). The thermal pathway beginning

#### 4.4 Insights from TD-DFT and DFT calculations into the photochemical bond-activation on (bisphosphane)( $\mu^2$ tolane)Pt<sup>0</sup> complexes

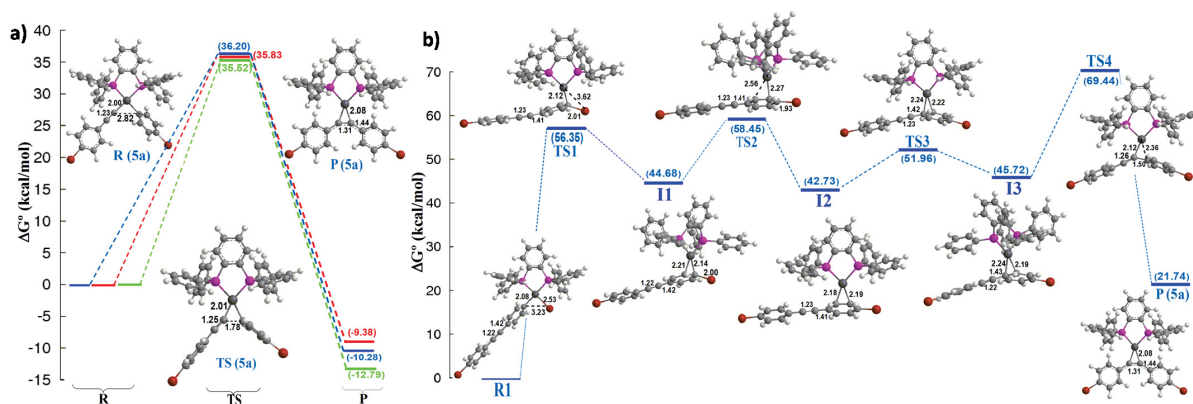


**Figure 4.15:** a) Energy diagram of the thermal reductive elimination beginning from the C-C activated products leading to complexes 21 (blue), 30 (red) and 31 (green), calculated at the B2GP-PLYP/6-311G\*//RI-BP86/TZVP level of theory. Relative free Gibbs energies are given in kcal mol<sup>-1</sup> with respect to complexes R. b) Energy diagram of the thermal reductive elimination beginning from the C-Br activated product leading to complex 21 (blue), calculated at the B2GP-PLYP/6-311G\*//RI-BP86/TZVP level of theory. Relative free Gibbs energies are given in kcal mol<sup>-1</sup> with respect to complexes R1. Main distances are in angstroms. Adapted from Escudero et al. *Dalton Trans.*, **2010**, 39, 9505.

from the C-Br bond activated product of complex 21 is endothermic. Accordingly, C-Br photoactivation is thermally irreversible. We have localized several intermediates and transition states along the reaction coordinate (see 4.15b), being the C-Br bond activated product the global minimum.

- iv) **Summary of the photochemical and thermal reactions on (bisphosphane)( $\mu^2$ tolane)Pt<sup>0</sup> complexes.** A summary of the photochemical and thermal reaction pathways for both the C-C and C-Br bond activation pathways is shown in Fig 4.16, exemplarily for complex 21. C-X bond cleavage reactions (oxidative reactions) do not proceed thermally due to the associated high activation barriers. Upon sunlight irradiation, excitation to specific electronic states with enough energy to overcome these barriers promote C-X bond cleavage reactions. The backward thermal reaction (reductive elimination reaction) takes place only in the C-C bond and an exothermic profile is obtained. On the contrary, the reductive elimination beginning from the C-Br bond activated product does not proceed thermally since an endothermic profile is obtained. We point here that the dual thermal/photochemical reactivity of (bisphosphane)( $\mu^2$ tolane)Pt<sup>0</sup> com-

## 4. RESULTS

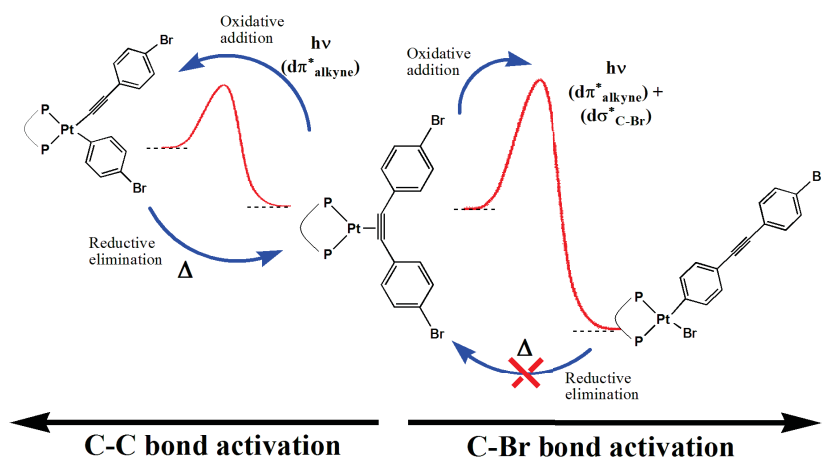


Figure 4.16: Global photochemical and thermal reactivity of complex 21.

plexes is not only interesting from a synthetic point of view but could also be profited to design molecular machines and sensors, based on the different spectral changes along these reactions.

### 4.5 Quantum chemical studies and ab-initio excited state molecular dynamics in 2H-Azirines.

Aiming at understanding C-C and C-N bond photoactivation in small systems, quantum chemical calculations and ab initio excited state molecular dynamics simulations have been performed on 2H-Azirines. Experimentally, it has been observed that selective C-C or C-N bond cleavage depending on the wavelength and on the substituent takes place(212) (see Fig 4.17a). For the sake of simplicity, only the bare 2H-azirine (34) depicted in Fig 4.17b has been studied herein.

The results are currently under preparation for publication. The main findings on the photochemistry of 2H-Azirines are the following:

- i) **The photochemical deactivation pathways in 2H-Azirines investigated with quantum chemistry.** A previous theoretical study(213) on compound 34 assigned the  $S_1$  ( $n\pi^*$ ) state as responsible of the photochemical pathway leading C-C bond activation. On the other hand, the C-N bond cleavage product is obtained after excitation of the intense  $S_2$  ( $\pi\pi^*$ ) state. For the latter process

## 4.5 Quantum chemical studies and ab-initio excited state molecular dynamics in 2H-Azirines.

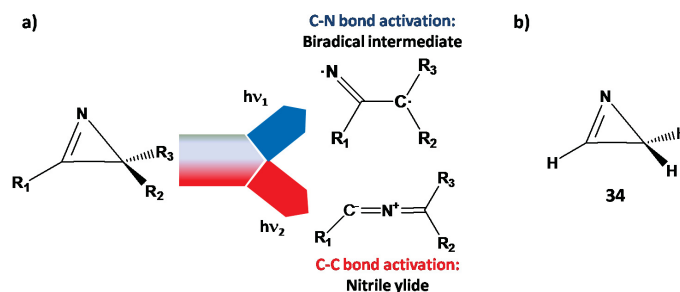


**Figure 4.17:** a) General scheme of 2H-azirine photochemistry: C-C and C-N bond cleavage. b) Chemical structure of compound 34.

the photodeactivation mechanism was not completely characterized. In order to locate stationary points (such as e.g. minima or CoIns) we have performed CASSCF(6,5) and MR-SDCI(10,9) calculations, for the  $S_1$  and  $S_2$  pathways, respectively. Additionally, Minimum Energy Path (MEP) calculations connecting the located stationary points and leading to the photoproducts have been performed at the same level of theory. In Fig 4.18a-b the photochemical deactivation pathways after Franck-Condon excitation of the  $S_1$  and  $S_2$  states are depicted. The minimum energy CoIns structures are also included. Regarding the  $S_1$  pathway, we can clearly see that the C-C bond is completely activated at the  $S_1/S_0$  CoIn (see 4.17a). The nitrile ylide (photoproduct) lies almost isoenergetically to the reactant. A more complicated photochemical picture is obtained for the  $S_2$  pathway. After excitation of the intense  $\pi\pi^*$  state relaxation on the PEH leads to a  $S_2/S_1$  CoIn, where the C-N bond is almost broken (see 4.17b). Afterwards, another  $S_1/S_0$  CoIn is found, which bears an enlarged C-H distance. Hydrogen migration to the adjacent carbon finally leads to the biradical intermediate, as demonstrated by the MEP calculation. Thus, the mechanism of the photochemical C-N bond activation in compound 34 is rather more complicated than a simple C-N bond cleavage, since it also involves hydrogen migration. This fact may have stereochemical consequences in the photoproducts of substituted 2H-Azirines.

- ii) **Confirming the photochemical pathways in 2H-azirines by ab-initio excited state molecular dynamics simulations.** Dynamical simulations are mandatory to obtain time-resolved information as well as to confirm the "static" photochemical pathways obtained with quantum chemical calculations. Addition-

## 4. RESULTS

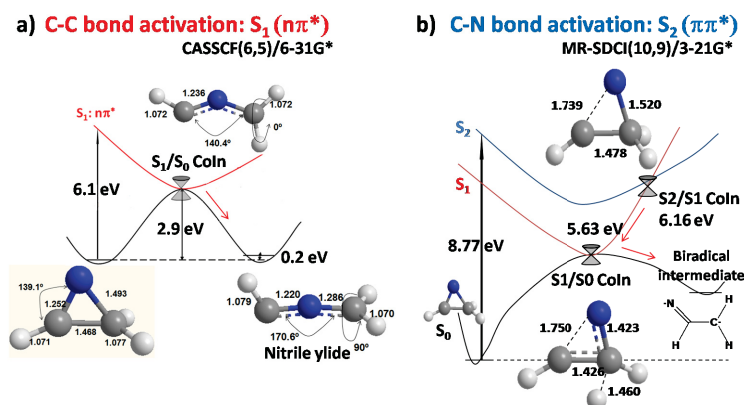


**Figure 4.18:** Photochemical pathways beginning from the  $S_1$  (a) and  $S_2$  (b) states. Relevant CoIn geometries are also included. The distances are in angstroms.

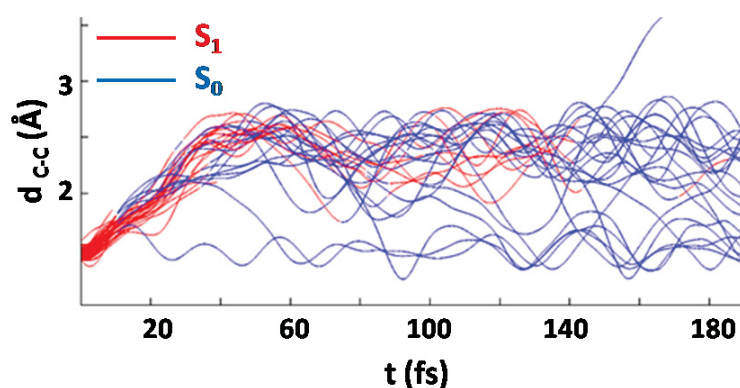


**Figure 4.19:** C-C bond distance versus time for a sample of trajectories launched from the  $S_1$  state. The distances are in angstroms.

ally, provided a big ensemble of trajectories, estimations of quantum yields can be derived from the simulations. To these aims, ab-initio excited state molecular dynamics simulations have been performed on compound 34. The potentials were computed "on-the-fly" at the same level of theory of the quantum chemical calculations. Specifically, 100 and 50 trajectories were launched from the (i)  $S_1$  and (ii)  $S_2$  pathways, respectively.

i) The analysis of the trajectories beginning in  $S_1$  reveals that the deactivation to the ground state occurs in an ultrafast manner. Hence, the non-adiabatic population transfer takes place in around 40 fs, mainly through geometries that resemble the CoIn geometry. In Fig 4.19, the C-C distance ( $d_{C-C}$ ) of a sample

## 4.5 Quantum chemical studies and ab-initio excited state molecular dynamics in 2H-Azirines.

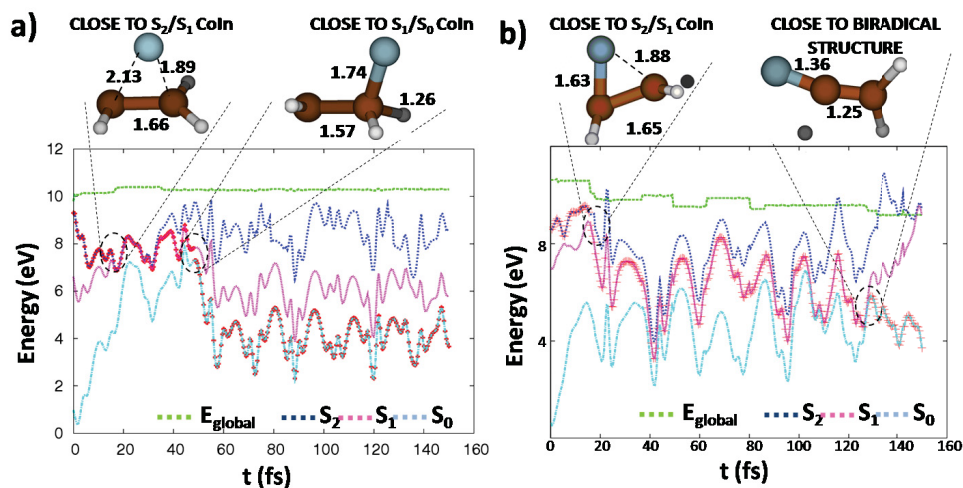


**Figure 4.20:** Representative a) and b) trajectories launched from the  $S_2$  state leading to the  $S_2$  state.

of trajectories is plotted against time. By the end of the simulations (ca. 180 fs), two products were obtained: i) a product yielding  $d_{C-C} > 2 \text{ \AA}$  (corresponding to the formation of the photoproduct, i.e nitrile ylide) and structures bearing  $d_{C-C} < 2 \text{ \AA}$  (i.e. recovering the 2H-azirine). The ratio photoproduct/reactant is ca. 1:1.

ii) The analysis of the trajectories launched from the  $S_2$  is rather more complicated than the one obtained for the  $S_1$  state. A common feature for all the trajectories is that they first deactivate very rapidly through structures close to the minimum energy  $S_2/S_1$  CoIn. In Fig 4.20a-b two representative trajectories leading to the biradical are depicted. Trajectory **a)** leads to the biradical through C-N bond activation and concomitant migration of hydrogen, in accordance to the "static" picture obtained from quantum chemical calculations. Oppositely, trajectory **b)** leads also to the biradical but without migration of hydrogen. Presumably, the region in the surrounds of the  $S_2/S_1$  CoIn determines which is the preferred deactivation pathway, since as it can be seen in Fig 4.20, whilst in trajectory **a)** the C-N is already activated in the case of trajectory **b)** this feature is not observed. The ratio between both pathways is ca. 1:1.

## 4. RESULTS

---



## 5

# Appended publications

The scientific publications which resulted from this PhD work are appended in this Chapter in the following order:

- i) RASPT2/RASSCF vs range-separated/hybrid DFT methods: assessing the excited states of a Ru(II)polypyridyl complex. Escudero, D.; González, L. **J. Chem. Theory and Comput.** Submitted, (2011).
- ii) Spectroscopic properties of azobenzene-based pH indicator dyes: a quantum chemical and experimental study. Escudero, D.; Trupp, S.; Bussemer, B.; Mohr, G.; González, L. **J. Chem. Theory and Comput.** *7*, 1062, (2011).
- iii) A heteroleptic bis(tridentate) ruthenium(II) complex of a click-derived abnormal carbene pincer ligand with potential for photosensitizer application. Schulze, B.; Escudero, D.; Friebe, C.; Siebert, R.; Görls, H.; Köhn, U.; Altuntas, E.; Baumgaertel, A.; Hager, M. D.; Winter, A.; Dietzek, B.; Popp, J.; González, L.; Schubert, U. S. **Chem. Eur. J.** *17*, 5494, (2011)
- iv) N-Heterocyclic donor- and acceptor-type ligands based on 2-(1H-[1,2,3]triazol-4-yl)pyridines and their ruthenium(II) complexes. Happ, B.; Escudero, D.; Hager, M. D. Friebe, C.; Winter, A.; Altuntas, E.; González, L.; Schubert, U. S. **J. Org. Chem.**, *75*, 4025, (2010).
- v) Phenyl-1H-[1,2,3]triazoles as new cyclometalating ligands for Ir(III) complexes. Beyer, B.; Ulbricht, C.; Escudero, D.; Friebe, C.; Winter, A.; González, L.; Schubert, U. S. **Organometallics**, *28*, 5478, (2009).

## 5. APPENDED PUBLICATIONS

---

- vi) Structure-property relationship of red- and green-emitting iridium(III) complexes with respect to their temperature and oxygen sensitivity. Tian, N.; Lenkeit, D.; Pelz, S.; Fischer, L. H.; Escudero, D.; Schiewek, R.; Klink, D.; Schmitz, O. J.; González, L.; Schäferling, M.; Holder, E. **Eur. J. Inorg. Chem.**, 4875, (2010).
- vii) Selective carbon-carbon bond cleavage of 2,2'-dibromotolane *via* photolysis of its appropriate (diphosphine) $Pt^0$  complex in the solid state. Petzold, H.; Weisheit, T.; Görls, H.; Breitzke, H.; Buntkowsky, G.; Escudero, D.; González, L.; Weigand, W. **Dalton Trans.**, 1979, (2008).
- viii) Substituent effects on the light-induced C-C and C-Br bond activation in (bisphosphine)( $\eta^2$ -tolane) $Pt^0$  complexes. A TD-DFT study. Escudero, D.; Assmann, M.; Pospiech, A.; Weigand, W.; González, L. **Phys. Chem. Chem. Phys.**, 11, 4593, (2009).
- ix) Photochemical behavior of (diphosphine)( $\eta^2$ -tolane) $Pt^0$  complexes. Part A: Experimental considerations in solution and in the solid state. Weisheit, T.; Escudero, D.; Petzold, H.; Görls, H.; González, L.; Weigand, W. **Dalton Trans.**, 39, 9493, (2010).
- x) Photochemical behavior of (diphosphine)( $\eta^2$ -tolane) $Pt^0$  complexes. Part B: An insight from DFT calculations. Escudero, D.; Weisheit, T.; Weigand, W.; González, L. **Dalton Trans.**, 39, 9505, (2010).

Some additional publications, which are not part of this thesis, but have been produced during the course of this work are mentioned in the following:

- i) Progress and challenges in the calculation of electronic excited states. González, L.; Escudero, D.; Serrano-Andrés, L. **Chem. Phys. Chem.**, Submitted, (2011)
- ii) Mechanistic studies on the alcoholysis and aminolysis of [(MeZn) $_{2\eta}$ -N(H)*t*Bu- $\eta$ -N(CH<sub>2</sub>Py)<sub>2</sub>]. Kahnes, M.; Richthof, J.; Görls, H.; Escudero, D.; González, L.; Wsterhausen, M. **J. Organomet. Chem.**, 695, 280, (2010).
- iii) Design of acidochromic dyes for facile preparation of pH sensor layers. Mohr, G. J.; Müller, H.; Bussemer, B.; Stark, A.; Carofiglio, T.; Trupp, S.; Heuermann, R.; Henkel, T.; Escudero, D.; González, L. **Anal. Bional. Chem.**, 392, 1411, (2008).

**5.1 RASPT2/RASSCF vs range-separated/hybrid DFT methods:  
assessing the excited states of a Ru(II)polypyridyl complex**

---

**5.1 RASPT2/RASSCF vs range-separated/hybrid DFT  
methods: assessing the excited states of a Ru(II)polypyridyl  
complex**

Submitted to Journal of Chemical Theory and Computation.

**RASPT2/RASSCF vs range-separated/hybrid DFT methods:  
assessing the excited states of a Ru(II)bipyridyl complex.**

Journal:	<i>Journal of Chemical Theory and Computation</i>
Manuscript ID:	ct-2011-00311y.R1
Manuscript Type:	Article
Date Submitted by the Author:	27-Jun-2011
Complete List of Authors:	Escudero, Daniel; Friedrich-Schiller-Universität Jena, Institut für Physikalische Chemie González, Leticia; Friedrich-Schiller Universität Jena, Institut für Physikalische Chemie

SCHOLARONE™  
Manuscripts

1  
2  
3  
4  
5  
6  
7  
8  
9  
10  
11  
12  
13  
14  
15  
16  
17  
18  
19  
20  
21  
22  
23  
24  
25  
26  
27  
28  
29  
30  
31  
32  
33  
34  
35  
36  
37  
38  
39  
40  
41  
42  
43  
44  
45  
46  
47  
48  
49  
50  
51  
52  
53  
54  
55  
56  
57  
58  
59  
60

# RASPT2/RASSCF vs range-separated/hybrid DFT methods: assessing the excited states of a Ru(II)bipyridyl complex.

*Daniel Escudero<sup>a</sup>, Leticia González<sup>a\*</sup>*

<sup>a</sup>Institut of Physikalische Chemie, Friedrich-Schiller Universität, Helmholtzweg, 4, Germany;

e-mail: [leticia.gonzalez@uni-jena.com](mailto:leticia.gonzalez@uni-jena.com)

1  
2  
3  
4  
5 **Abstract.** The excited states of the *trans(Cl)-Ru(bpy)Cl<sub>2</sub>(CO)<sub>2</sub>* (bpy = bipyridyl) transition metal (TM)  
6  
7 complex are assessed using the newly developed second order perturbation theory restricted active  
8  
9 space (RASPT2/RASSCF) method . The delicate problem of partitioning the RAS subspaces (RAS1,  
10  
11 RAS2 and RAS3) is addressed, being the choice of the RAS2 the bottleneck to obtain a balanced  
12  
13 description of the excited states of different nature when TMs are present. The level of excitations  
14  
15 within the RAS1 and RAS3 subspaces is also examined. Singles and doubles excitations are found to be  
16  
17 enough to recover most of the dynamical correlation, provided an adequate choice of the RAS2 is  
18  
19 selected. The performance of different flavors of time-dependent density functional theory (TD-DFT)  
20  
21 including pure, hybrid, meta-hybrid and range-separated functionals in the presence of solvent effects is  
22  
23 also evaluated. It is found that none of the functionals can optimally describe all the excited states  
24  
25 simultaneously. However, the hybrid M06, B3LYP and PBE0 functionals seem to be the best  
26  
27 compromise to obtain a balanced description of the excited states of *trans(Cl)-Ru(bpy)Cl<sub>2</sub>(CO)<sub>2</sub>*, when  
28  
29 comparing with the experimental spectrum. The conclusions obtained in this molecule should pave the  
30  
31 road to properly treat excited states of larger Ru-polypyridyl complexes, which are of particular interest  
32  
33 in supramolecular chemistry.  
34  
35  
36  
37  
38  
39  
40

## 41 1. Introduction

42  
43  
44  
45 Ru(II) polypyridyl complexes and related compounds are promising candidates as light harvesting  
46  
47 antennas in hot research areas, such as artificial photosynthesis,<sup>1</sup> light driven catalysis (i.e sunlight  
48  
49 driven splitting of water)<sup>2</sup> or dye sensitised solar cells (DSSCs),<sup>3</sup> due to a combination of optimal  
50  
51 chemical, electrochemical and photophysical properties. The identification and characterization of the  
52  
53 lowest-lying excited states is therefore a challenging task of paramount importance to guide the design  
54  
55 of molecular functional materials. To get an insight into the photophysical properties of these  
56  
57 complexes the use of accurate *ab initio* multiconfiguration methods, as for example, the well-  
58  
59 established second order perturbation theory complete active space,<sup>4</sup> CASPT2/CASSCF, protocol, is  
60

1  
2  
3 highly desirable. Due to the extensive size of such transition metal (TM) complexes and the need of  
4  
5 large active spaces able to handle all the static correlation, such calculations are yet pretty much at the  
6  
7 limit of the current computational resources and not very much extended. Up to our knowledge there are  
8  
9 only a few examples of CASPT2/CASSCF studies on TM-polypyridyl complexes, e.g. on  $[\text{Fe}(\text{bpy})_3]^{2+}$ ,<sup>5</sup>  
10  
11 or  $[\text{Re}(\text{bpy})(t\text{-stpy})]^+$ .<sup>6</sup> Despite the considerable effort involved in these studies, they involve reduced  
12  
13 CAS reference wave functions with active spaces that might not be extensive enough to account for all  
14  
15 the desired correlation effects. The restricted active space method (RASSCF)<sup>7</sup> and its PT2 extension  
16  
17 (RASPT2)<sup>8</sup> are very appealing because allow using considerable larger active spaces than the  
18  
19 CASPT2/CASSCF protocol. However, due to the three different partitions of the active space, a number  
20  
21 of open questions can be raised regarding its systematic use. In particular, it is not straightforward how  
22  
23 the active orbitals in the RAS subspaces should be best distributed or until which level of excitation the  
24  
25 results can be considered converged. Recently, Gagliardi and coworkers have performed an extensive  
26  
27 number of RASPT2/RASSCF calculations mainly in organic dyes,<sup>9,10</sup> clearly illustrating that the  
28  
29 selection of the RAS spaces requires careful calibration. In the case of simple oligomeric  $\pi$ -conjugated  
30  
31 systems, the computationally cheapest strategy is leaving the RAS2 empty while allowing for singles,  
32  
33 doubles, triples and quadruple (SDTQ) excitations within the RAS1 and RAS3 subspaces. This simple  
34  
35 recipe allows for an accurate description of ionization potentials and lowest-lying excited states of many  
36  
37 organic systems<sup>9</sup> but unfortunately it cannot be extrapolated to more complicated systems, neither of  
38  
39 organic character, like free base porphins,<sup>10</sup> nor of inorganic nature, like Cu(I)- $\alpha$ -ketocarboxylate  
40  
41 complexes.<sup>11</sup> From this perspective, there is an urge to calibrate the RASSCF approach in TM  
42  
43 complexes, which otherwise are typically treated by means of density functional theory (DFT) and its  
44  
45 time-dependent version (TD-DFT).<sup>12</sup>  
46  
47  
48  
49  
50  
51  
52  
53

54 The compromise between low computational cost and accuracy obtained with DFT is in general  
55  
56 remarkable and therefore a huge number of TM ground state studies are found in the literature.<sup>13</sup> The  
57  
58 success of DFT describing ground state properties is however not comparable to the success of TD-DFT  
59  
60 for the study of excited states. TD-DFT is known to have difficulties in describing Rydberg states,

1  
2  
3 charge-transfer (CT) excitations<sup>14</sup> as well as doubly or highly excited-states.<sup>15</sup> Attempts to improve the  
4 description of CT and Rydberg excitations, while maintaining good quality for local excitations, has led  
5 to the development of hybrid functionals with intermediate percentage of exact exchange, such as  
6 PBE0,<sup>16</sup> and range-separated hybrid functionals, such as LC- $\omega$ PBE<sup>17</sup> or CAM-B3LYP<sup>18</sup>, which have  
7 been shown to perform reasonably well describing CT of organic dyes.<sup>19</sup> CT events are common in TM  
8 spectroscopy; however, more challenging is that the calculation of the UV-Vis spectra of complex TM  
9 systems also requires a balanced description of local excitations and d-d transitions. Despite these  
10 difficulties, TD-DFT is indiscriminately employed due to its simplicity and apparent black-box  
11 behavior, in particular for large systems such as Ru(II) polypyridyl complexes,<sup>20</sup> which are otherwise  
12 out of reach from more accurate ab initio methods. Few examples are found in the literature assessing  
13 the performance of TD-DFT on TM-complexes.<sup>21</sup> However, up to our knowledge, there is no evaluation  
14 of the performance of DFT functionals to describe the excited states of TM-polypyridyl and related  
15 complexes.

16  
17  
18  
19  
20  
21  
22  
23  
24  
25  
26  
27  
28  
29  
30  
31  
32  
33 In this contribution we present a RASPT2/RASSCF study of the electronically excited states of  
34 *trans(Cl)-Ru(bpy)Cl<sub>2</sub>(CO)<sub>2</sub>* for which experimental data is available for comparison.<sup>22,23</sup> This complex  
35 serves as an example of this general class of systems. It displays different types of excited states and  
36 thus represents a challenge for computational chemistry. Different partition schemes of the RAS  
37 subspaces (RAS1, RAS2 and RAS3) as well as the level of excitations in the RAS1 and RAS3  
38 subspaces are evaluated. The conclusions reached with this molecular system will provide hints about  
39 how to study similar TM-compounds, therefore extending the possibilities of RASPT2/RASSCF to  
40 larger TM-polypyridyl complexes. Additionally, and based on the experimental results, the performance  
41 of TD-DFT using different functionals in solution is analyzed. Particularly, the behavior of several  
42 hybrid, meta-hybrid, pure and long-range corrected functionals in describing the different types of  
43 excitations present in TM complexes is examined and discussed. The conclusions should help to make a  
44 adequate choice of the functional when studying very large TM-polypyridyl complexes that cannot be  
45 treated within the RASPT2/RASSCF protocol.



## 2. Computational details

The *trans*(Cl)-Ru(bpy)Cl<sub>2</sub>(CO)<sub>2</sub> complex **1** (see Figure 1) was optimized in its electronic ground state under the C<sub>2v</sub> symmetry constraint at the B3LYP/6-31G\* level of theory. Relativistic effects in the Ru atom were considered using the ECP-28-mwb pseudopotential.<sup>24</sup> The complex has been characterized as a true minimum by calculating the Hessian at the same level of theory.

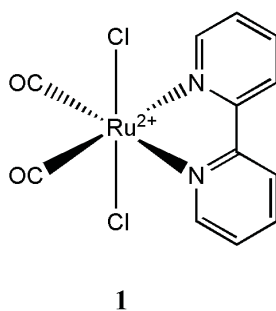


**Figure 1.** Chemical structure of *trans*(Cl)-Ru(bpy)Cl<sub>2</sub>(CO)<sub>2</sub>, complex **1**.

Single point CASPT2/CASSCF and RASPT2/RASSCF calculations were performed on the C<sub>2v</sub> geometry. These calculations were done with the ANO-rcc-VTZP basis set.<sup>25</sup> Scalar relativistic effects were considered using a standard second order Douglas-Kroll-Hess (DKH) Hamiltonian.<sup>26</sup> Cholesky decomposition of the electron repulsion integral matrix<sup>27</sup> was used, then reducing the computational times and disk storage needs. In the CAS calculations, the traditional notation is used, namely CAS(*n*,*j*) where *n* is the number of electrons included in the active space and *j* is the number of active orbitals. In the RAS calculations, the RAS(*n*,*l*,*m*; *i*,*j*,*k*) notation is employed, where *n* is the number of active electrons, *l* the maximum of holes in the RAS1, *m* the maximum of electrons in RAS3, and *i*, *j* and *k* the number of orbitals in RAS1, RAS2 and RAS3, respectively.

The choice of the active orbitals for the CASSCF/RASSCF calculations is made in terms of the standard rules for TM compounds.<sup>28,29</sup> Important correlation effects due to the covalency of the Ru metal-ligand bonds *via*  $\sigma$  and  $\pi$  bonding interactions are considered by including some relevant  $\sigma$

1  
2  
3 orbitals involving the Ru atom and also the chlorine atoms ( $n_{\text{Cl-a}_1}$  orbital) or the bpy and the CO ligands  
4 ( $\sigma_{\text{CO-bpy}}$  orbitals, in Figure 2). Relevant  $\pi$  bonding interactions are taken into account by including  $\pi^*_{\text{CO}}$   
5 orbitals and lone pairs of the chlorines atoms ( $n_{\text{Cl-b}_1}$  orbital). In principle we follow the advice given by  
6 Pierloot<sup>30</sup> that all orbitals with an important contribution of d character should be included in the active  
7 space. Since Ru is a 4d atom, the “double-shell” effect is not as indispensable as for 3d atoms; therefore,  
8 this external shell is not considered here for the sake of computational saving. In some sense, these  
9 correlation effects are partially recovered upon inclusion of other orbitals, such as the  $\pi^*_{\text{CO}}$  orbitals,  
10 which possess some contribution of 5d character. The intershell effects, i.e. those due to semi-core  
11 electrons, are very important for the 4d and 5d series and thus they have been inherently considered by  
12 using the ANO-rcc basis set that is optimized to include such correlation effects. Other valence orbitals,  
13 such as the  $\pi_{\text{CO}}$  orbitals and some  $\pi_{\text{bpy}}/\pi^*_{\text{bpy}}$  orbital pairs are not included in our calculations since a full  
14 valence electron treatment is out of reach for CASPT2 and even for RASPT2 calculations in the  
15 complex **1**. The strategy followed here is to include many of the orbitals that in principle contribute to  
16 static correlation, but to a lesser extent, in the RAS1 and RAS3 subspaces, while, as we will show,  
17 RAS2 should only include the indispensable orbitals involved in the main excited states (low-lying and  
18 high-lying) of **1**; these are the five 4d orbitals and the  $\pi_{\text{bpy}}/\pi^*_{\text{bpy}}$  orbitals. These orbitals are involved in  
19 the main metal-centered (MC), metal-to-ligand charge transfer (MLCT) and intra-ligand (IL) states of **1**.  
20 This strategy allows dealing with larger active spaces and consequently bigger TM-complexes than  
21 those feasible with CASSCF. All the relevant orbitals are depicted in Fig. 2.  
22  
23  
24  
25  
26  
27  
28  
29  
30  
31  
32  
33  
34  
35  
36  
37  
38  
39  
40  
41  
42  
43  
44  
45  
46

47 Specifically, the active spaces for the different calculations were constructed as follows:

48  
49 i) Small CAS active space. It is composed of the five 4d orbitals of the Ru atom and a balanced set of  
50 four frontier  $\pi_{\text{bpy}}/\pi^*_{\text{bpy}}$  pair of orbitals, see figure 2. This active space is used in the CASSCF(14,13)  
51 calculations.  
52  
53  
54

55  
56 ii) Inclusion of correlation effects to the small CAS active space. A relevant  $n_{\text{Cl}}$  orbital with important  
57  $\sigma$  character, involving lone pairs of the chlorine and the Ru center (see  $n_{\text{Cl-a}_1}$  in Fig. 2) as well as two  
58  $\pi^*_{\text{CO}}$  orbitals ( $\pi^*_{\text{CO-b}_1}$  and  $\pi^*_{\text{CO-a}_2}$ ) are included in the active space through the RAS1 and RAS3  
59  
60

subspaces. Such selection was made in terms of the higher metal d contributions of such orbitals. Additionally, a pair of  $\pi_{\text{bpy}}/\pi_{\text{bpy}}^*$  orbitals (namely the  $\pi_{\text{bpy}}-2a_2/\pi_{\text{bpy}}^*-2a_2$  orbitals, see Fig. 2) is shifted to the RAS1 and RAS3 subspaces, respectively, because the corresponding occupation numbers were higher/lower than 1.95/0.05. This active space is used in the RASSCF(16,2,2;2,11,3), RASSCF(16,3,3;2,11,3) and RASSCF(16,3,4;2,11,3) calculations. For comparison, a calculation where the RAS2 subspace is empty and all the active orbitals are assigned to the RAS1 and RAS3 subspaces is also performed, RASSCF(16,4,4;8,0,8). For the same reason as before, an additional pair of  $\pi_{\text{bpy}}/\pi_{\text{bpy}}^*$  orbitals (namely the pair  $\pi_{\text{bpy}}-1b_1/\pi_{\text{bpy}}^*-1a_2$ ) was moved into the RAS1/3 subspaces, leading to the RASSCF(16,2,2;3,9,4) calculation.

iii) Additional correlation effects: Based on the RAS(16,2,2;3,9,4) active space, additional correlation orbitals were considered. Again, such selection was done paying attention to the metal d contribution of the included orbitals: in the RAS1 an additional  $n_{\text{Cl}}$  orbital ( $n_{\text{Cl}}-b_1$ ) and two  $\sigma_{\text{CO-bpy}}$  orbitals ( $\sigma_{\text{CO-bpy}}-a_1$  and  $\sigma_{\text{CO-bpy}}-b_2$ ) were included and the two remaining  $\pi_{\text{CO}}$  orbitals ( $\pi_{\text{CO}}^*-a_1$  and  $\pi_{\text{CO}}^*-b_2$ ) were put in the RAS3 (see Fig. 2). In these calculations the two  $\pi_{\text{bpy}}/\pi_{\text{bpy}}^*$  orbital pairs,  $\pi_{\text{bpy}}-2a_2/\pi_{\text{bpy}}^*-2a_2$  and  $\pi_{\text{bpy}}-1b_1/\pi_{\text{bpy}}^*-1a_2$ , were maintained in the RAS1/3 subspaces because they do not play a role in the low- and high-lying excited states. This partition leads to a RASSCF(22,2,2;6,9,6) calculation.

The CASSCF/RASSCF calculations presented herein are done as state-average (SA-CASSCF/RASSCF) with equal weights. The subsequent CASPT2 calculations are reported as single-state (SS-) and multi-state (MS-CASPT2).<sup>31</sup> The RASPT2 results are only reported in the MS fashion. The number of roots employed in each irreducible representation is specified in the corresponding Table caption. Oscillator strengths were calculated at both the SA-CASSCF, MS-CASPT2 and MS-RASPT2 levels of theory through the RAS State Interaction method.<sup>32</sup> The core shell orbitals were kept frozen in the CASPT2 calculations in order to avoid BSSE errors. In all our CASPT2/RASPT2 calculations an IPEA shift (default value of 0.25 au) for the zeroth order Hamiltonian was employed.<sup>33</sup> Additionally, an extra level shift<sup>34</sup> of 0.3 au was used to prevent weakly coupling intruder states interference, mainly with the high-lying states. Similar values of ca. 0.25 au have been used elsewhere to compute excited

states of TM complexes.<sup>8</sup> The spin-orbit (SO) UV-Vis spectra has been also computed with the CAS(14,13) wavefunction. The SO couplings have been evaluated with the SO-RASSI approach,<sup>35</sup> (further details can be found in the Supplementary Material).

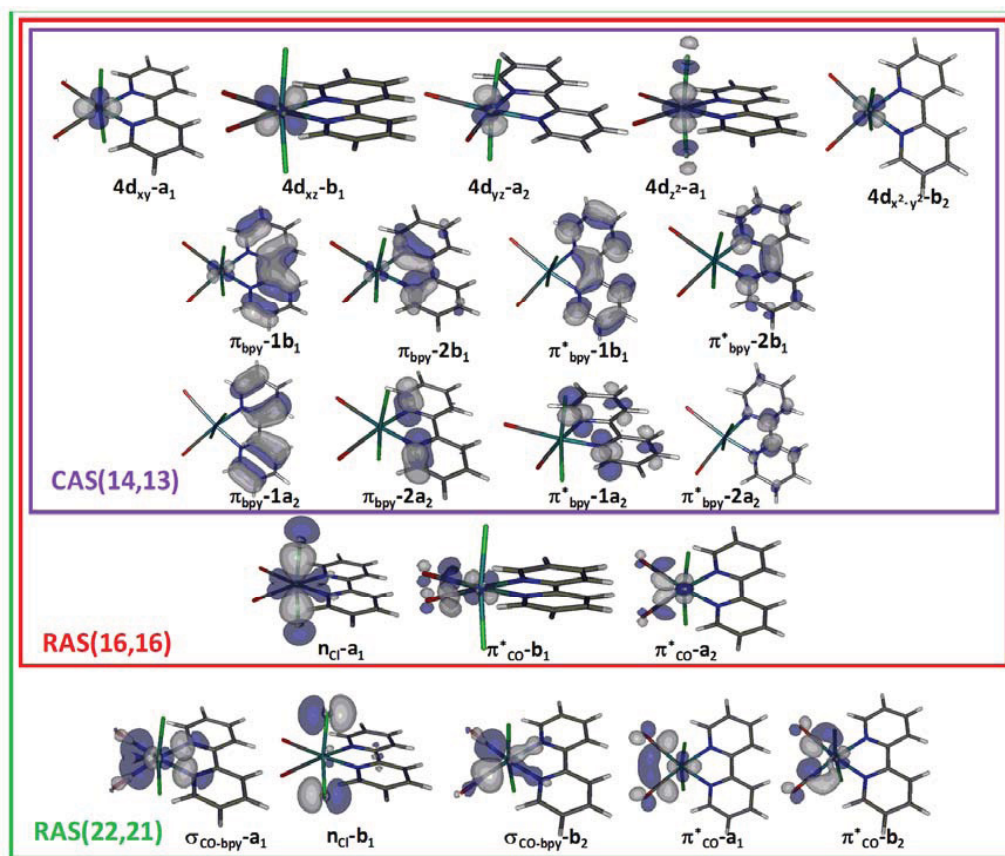


**Figure 2.** CASSCF and RASSCF active spaces employed.

The TD-DFT calculations were performed at the  $C_{2v}$  geometry with a 6-311G\* basis set (ECP-28-mwb pseudopotential for Ru). The different functionals employed are: i) several hybrid functionals with an increasing amount of exact exchange in the following order: B3LYP<sup>36</sup> (20% of exact exchange), PBE0<sup>16</sup> (25%) and B3LYP-35<sup>37</sup> (35%), ii) the meta-hybrid M06<sup>38</sup> and M06-2X<sup>38</sup> functionals (with 27% and 54% of exact exchange, respectively), iii) the pure functional PBE,<sup>39</sup> and iv) the long-range corrected CAM-B3LYP and LC- $\omega$ PBE functionals. Additionally, TD-DFT calculations were also

1  
2  
3 performed in solution using CH<sub>3</sub>CN as solvent with the polarization continuum model,<sup>40</sup> i.e PCM-TD-  
4 DFT calculations, with the same basis set.  
5

6  
7 The ground state optimization and TD-DFT calculations have been performed with the Gaussian09<sup>41</sup>  
8 program package whilst CASSCF/CASPT2 and RASSCF/RASPT2 calculations have been performed  
9 with the MOLCAS7.2<sup>42</sup> software.  
10  
11  
12  
13

### 14 15 16 17 **3. Results and discussion**

18 First of all, we report here the experimental values known for the complex **1**. Its UV/Vis spectrum  
19 recorded in CH<sub>3</sub>CN is characterized by a small band peaking at 352 nm or 3.52 eV (3.62 eV in CH<sub>2</sub>Cl<sub>2</sub>)  
20 showing an intensity of 1550 M<sup>-1</sup>cm<sup>-1</sup> and by a higher broader band centered at ca. 300 nm or 4.14 eV,  
21 with a higher relative intensity of 14100 M<sup>-1</sup>cm<sup>-1</sup>.<sup>22,23</sup> The peaks of this main band with their associated  
22 intensities are the following: 3.96 eV (14100 M<sup>-1</sup>cm<sup>-1</sup>), 4.13 eV (11300 M<sup>-1</sup>cm<sup>-1</sup>) and 4.34 (10000 M<sup>-1</sup>  
23 cm<sup>-1</sup>) Taking these values as a reference, hereafter we shall discuss the values obtained theoretically  
24 with the methods described above.  
25  
26  
27  
28  
29  
30  
31  
32  
33  
34  
35  
36

37 **3.1. CASPT2/CASSCF calculations.** Table 1 shows the CASPT2/CASSCF(14,13) results for the  
38 excited states of complex **1**. The CASSCF(14,13) calculations indicate that the low-lying singlet  
39 electronic excitations are mainly weakly absorbing <sup>1</sup>MC states of different symmetries, see S<sub>1</sub>-S<sub>5</sub> and S<sub>7</sub>  
40 states at the CASSCF level of theory. We note that among them there are states of A<sub>2</sub> symmetry that,  
41 although strictly forbidden by symmetry, might be populated e.g. in the course of photochemical  
42 deactivation channels. The <sup>1</sup>MLCT and <sup>1</sup>IL states showing substantial oscillator strengths are the S<sub>8</sub>, S<sub>9</sub>,  
43 S<sub>10</sub> and S<sub>11</sub> states at the CASSCF level of theory. The <sup>1</sup>MLCT states consist of transitions from the 4d  
44 orbitals of the Ru atom to the π\*<sub>bpy</sub> orbitals. The <sup>1</sup>IL states are transitions within the π<sub>bpy</sub>/π\*<sub>bpy</sub> orbitals  
45 and thus excitations retaining certain local character. To describe them all simultaneously at the  
46 CASSCF level of theory we need to compute at least six states of B<sub>2</sub> symmetry and 3/3/2 states of  
47 A<sub>1</sub>/B<sub>1</sub>/A<sub>2</sub> symmetry, respectively. The chosen number of states corresponds to the minimum amount of  
48  
49  
50  
51  
52  
53  
54  
55  
56  
57  
58  
59  
60

1  
2  
3 roots necessary to describe the spectrum below ca 5 eV in a balance manner, taking into account that  
4  
5 some spectroscopic states do not appear as low-energy roots at the CASSCF level of theory and that  
6  
7 some transitions are mixed through several roots (see e.g.  $S_8$  and  $S_{11}$  in Table 1). Table 1 also contains  
8  
9 the SS-CASPT2 and MS-CASPT2 values. Similar energies are obtained with both procedures, being the  
10  
11 roots of the  $B_2$  irreducible representation the ones most affected by the MS procedure, due to the larger  
12  
13 mixing present at the SA-CASSCF level of theory. The inclusion of dynamical correlation via CASPT2  
14  
15 leads to a large stabilization of some  $^1\text{MLCT}$  and  $^1\text{IL}$  states and thus to state reordering. As a  
16  
17 consequence, the  $S_9$  state ( $3^1A_1$ ) at the CASSCF level of theory for example becomes the first excited  
18  
19 state with MS-CASPT2 (or SS-CASPT2). On the contrary, dynamical correlation does not severely  
20  
21 affect the relative energies of the  $^1\text{MC}$  states, which remain almost unaffected (e.g.  $S_2$  and  $S_4$ ) or are  
22  
23 slightly blue/red-shifted ( $S_1$  and  $S_3$ , respectively). Returning our attention to the  $3^1A_1$  state, this is  
24  
25 predicted at 3.35 eV at CASPT2 level of theory and hence in reasonable agreement with the weak band  
26  
27 peaking experimentally at ca. 3.52 eV. Note that this state is the lowest at CASPT2 level of theory,  
28  
29 while it was the  $S_9$  with CASSCF. This demonstrates the importance of dynamical correlation on the  
30  
31 different type of states, as explained above. For simplicity, and although the order of states is altered in  
32  
33 many cases with the addition of the PT2 correction, in the following discussion we keep the state  
34  
35 numbers as provided by the CASSCF method. In view of the high oscillator strengths obtained with  
36  
37 CASSCF for the  $S_{11}$  ( $5^1B_2$ ) and  $S_{10}$  ( $4^1B_2$ ) states, theoretically predicted at 4.49 and 4.75 eV at the MS-  
38  
39 CASPT2 level of theory, these states can be then considered responsible of the strong band peaking at  
40  
41 3.96 and 4.13-4.34 eV. These states are ca. 0.5 eV blue-shifted with respect to the experiment, but one  
42  
43 should keep in mind that the experimental data are obtained in the presence of solvent, not included in  
44  
45 the present calculations.  
46  
47  
48  
49  
50  
51

52  
53 Regarding the intensities of the calculated states, as it can be seen in Table 1, all the  $^1\text{MC}$  states  
54  
55 as well as the  $S_6$  ( $^1\text{MLCT}$ ) state are almost dark at both the CASSCF and CASPT2 levels of theory. The  
56  
57 intensities of the bright  $S_{11}$  and  $S_{10}$  states are consistent at both the CASSCF and CASPT2 levels of  
58  
59 theory. Accordingly, the oscillator strength of the  $^1\text{IL}$  ( $S_{11}$ ) state is higher than the one of the  $^1\text{MLCT}$  ( $S_6$ )  
60

<sup>1</sup>B<sub>2</sub>) state. This is in agreement with the experimental evidence, since higher intensities are obtained for the band at 3.96 than for the one peaking at ca. 4.13-4.34 eV.

The previous analysis serves to focus on some relevant states (the <sup>4</sup><sup>1</sup>B<sub>2</sub> and <sup>3</sup><sup>1</sup>A<sub>1</sub> MLCT states, the <sup>5</sup><sup>1</sup>B<sub>2</sub> IL state, and exemplarily one MC state (<sup>1</sup><sup>1</sup>B<sub>1</sub>)) for which the CASPT2/CASSCF results will be compared with different TD-DFT and RASPT2/RASSCF protocols in the coming subsections. However, before proceeding to discuss such calculations, we have considered of interest to analyze the SO effects on the spectroscopic properties of complex 1. The SO-MS-CASPT2(14,13) values are also tabulated in Table 1 and illustrate that energetic shifts are present in all the low-lying excited states of complex 1. The biggest shift is found in the case of the <sup>2</sup><sup>1</sup>B<sub>1</sub> state (<sup>1</sup>MC state), amounting up to 0.04 eV as compared to the spin-free MS-CASPT2(14,13) value. The resulting SO-state is mixed with a close-lying triplet excited state (the spin-free contributions of the resultant SO-state are 72% of <sup>2</sup><sup>1</sup>B<sub>1</sub> and 25% of <sup>2</sup><sup>3</sup>A<sub>2</sub>; the lowest lying triplet excited states are summarized in Table S1 of the Supplementary Information). Such strong mixing is expected in states with participation of the ruthenium center, such as the <sup>1</sup>MC states. The SO shifts obtained here are comparable to those obtained in other TM complexes, e.g. Os complexes.<sup>43</sup> In summary, the SO effects modify the spectroscopic properties of complex 1 but not significantly. SO effects are on the other hand indispensable to the interpretation of many other photophysical phenomena, such as intersystem crossing (ISC) rates. We note that very efficient SO couplings (ca 280 cm<sup>-1</sup>) are found between the <sup>3</sup><sup>1</sup>A<sub>1</sub> and T<sub>1</sub> (<sup>1</sup><sup>3</sup>A<sub>2</sub>) states, which lie almost degenerate in energy favouring the ISC.

**3.2. TD-DFT calculations.** The results obtained with different functionals for the excited states specified above are collected in Table 2. The values including CH<sub>3</sub>CN are given in italics. The <sup>1</sup>MC state (<sup>1</sup><sup>1</sup>B<sub>1</sub> state, following the CASSCF label of Table 1) is predicted within all the employed functionals in a range of ca. 0.4 eV, being rather immune to solvent effects. It has been previously seen that TD-DFT can succeed to describe d-d transitions of closed-shell TM carbonyl complexes,<sup>44</sup> such as Cr(CO)<sub>6</sub>.<sup>45</sup> On the other hand, as pointed by Neese et al., TD-DFT has drawbacks when describing d-d

1  
2  
3 transitions in problematic configurations like  $d^5$  situations; for example, errors exceeding 0.6 eV were  
4 found in the TD-DFT energies of the  $[\text{Ni}(\text{H}_2\text{O})_6]^{2+}$  complex ( $d^8$  configuration) with the B3LYP  
5 functional.<sup>15</sup> TD-B3LYP was even not capable to reproduce the correct number of d-d excitations in this  
6 complex because some of them contained substantial double excitation character that TD-DFT cannot  
7 handle within the constraint of the adiabatic approximation. In our closed-shell complex **1**, meta-hybrids  
8 (namely the M06 and M06-2X) tend to slightly underestimate the d-d transition energy, especially M06,  
9 which yields the highest deviation (ca. 0.3-0.4 eV) in comparison to the rest of TD-DFT values and the  
10 MS-CASPT2(14,13) results. The range-separated functionals yield the larger values for the  $^1\text{MC}$  state,  
11 specially the LC- $\omega$ PBE functional which predicts 3.50 eV in good agreement with the CASPT2 value.  
12 Both hybrid and pure functionals predict the energy of the  $^1\text{B}_1$  state in a small range. We note that the  
13 larger the percentage of exact HF-exchange is contained in the hybrid functionals the higher are the  
14 excitation energies corresponding to the d-d transition; thus, B3LYP-35 (35% of exact exchange),  
15 PBE0 (25%) and B3LYP (20%) yield values of 3.34, 3.31 and 3.25 eV, in the gas phase, respectively.  
16 From all these values, we conclude that overall a reasonable description of the  $^1\text{MC}$  states can be  
17 obtained for complex **1** with TD-DFT, and therefore we expect a similar success for  $^1\text{MC}$  states in other  
18 related closed-shell Ru(II) polypyridyl complexes.

19  
20  
21  
22  
23  
24  
25  
26  
27  
28  
29  
30  
31  
32  
33  
34  
35  
36  
37  
38  
39 Regarding the  $^1\text{MLCT}$  states of complex **1**, namely the  $3^1\text{A}_1$  and  $4^1\text{B}_2$  states, one can clearly see at  
40 first sight the failure of some functionals –behaviour which is well known in CT states of organic  
41 dyes.<sup>46</sup> These states are specially subject of changing in the presence of a polar solvent. Indeed, both  
42  $^1\text{MLCT}$  states are blue-shifted by ca. 1 eV as compared to the gas phase values. It is worth noting that  
43 this effect manifests regardless the employed functional. Therefore, only the PCM-TD-DFT data will be  
44 compared with the experiment. The pure PBE functional leads to underestimations exceeding 1 eV for  
45 both  $^1\text{MLCT}$  states. An adequate description of  $^1\text{MLCT}$  states relies heavily on the choice of the  
46 functional. Conventional hybrid functionals have a clear tendency to increase the excitation energy of  
47 the  $^1\text{MLCT}$  states with increasing exact exchange. For instance, we see that the  $3^1\text{A}_1$  state is predicted  
48 at 3.42, 3.51, and 4.03 eV with B3LYP, PBE0 and B3LYP-35, respectively. These excitation energies  
49  
50  
51  
52  
53  
54  
55  
56  
57  
58  
59  
60



1  
2  
3 are in good agreement with the experimental evidence, especially the B3LYP and PBE0 values. The  
4  
5 best result for the  $^1\text{MLCT}$  states is obtained with the functional bearing an intermediate amount of  
6  
7 exact exchange, i.e. PBE0, which delivers an deviation from the experiment of only 0.01 eV for  $3^1\text{A}_1$   
8  
9 state. The trend of larger errors with increasing amount of exact exchange is also observed in the meta-  
10  
11 hybrid functional M06 and M06-2X. The  $3^1\text{A}_1$  state is best described with the M06 functional (27% of  
12  
13 exact exchange) which delivers a value of 3.47 eV (error 0.05 eV). The recently developed range-  
14  
15 separated functionals employed here perform differently for describing the  $^1\text{MLCT}$  states of complex **1**.  
16  
17 LC- $\omega$ PBE hugely overestimates the excitation energies of the  $^1\text{MLCT}$  states (e.g. the  $4^1\text{B}_2$  state is  
18  
19 overestimated by more than 2 eV). Interestingly, we note that CAM-B3LYP performs worse than the  
20  
21 hybrid functionals B3LYP-35, PBE0, B3LYP and M06. The  $3^1\text{A}_1$  state is theoretically predicted at 4.41  
22  
23 eV and hence the error with respect to the experiment amounts almost to 1 eV. The  $4^1\text{B}_2$  state is also  
24  
25 overestimated by 1 eV (see Table 3). These evidences are contrary to the good performance of CAM-  
26  
27 B3LYP in the treatment of CT states of organic dyes.<sup>47</sup> But indeed, the agreement of CAM-B3LYP to  
28  
29 describe MLCT states of other TM complexes<sup>19d,48</sup> is not better.

30  
31 The energies of the  $^1\text{IL}$  state are not as strongly dependent on the functional as the  $^1\text{MLCT}$  states,  
32  
33 yielding values in the gas phase for the  $3^1\text{B}_2$  state that range from 4.82 eV with the LC- $\omega$ PBE functional  
34  
35 to 4.02 eV with the pure PBE functional. We note that, oppositely to the  $^1\text{MLCT}$  states, inclusion of  
36  
37 solvent effects leads only to red-shifts of ca. 0.1 eV with (in all the functionals, see Table 2). Among the  
38  
39 hybrid functionals, the excitation energies are lower the smaller the amount of HF exchange, as it  
40  
41 happened with the  $^1\text{MC}$  and  $^1\text{MLCT}$  states. Interestingly, and in concordance with the  $^1\text{MLCT}$  states,  
42  
43 the agreement with the experiment is obtained with PBE, B3LYP, M06 or PBE0 (with errors for all the  
44  
45 functionals well below 0.30 eV), rather than with functionals containing high percentage of exact  
46  
47 exchange (as B3LYP-35 or M06-2X) or the range-separated functional CAM-B3LYP, even though the  
48  
49 errors for the latter functional are in the acceptable range of accuracy of TD-DFT (ca. 0.57 eV). A  
50  
51 similar behavior has been also observed for conjugated organic compounds, where the small maximum  
52  
53 average errors in the description of local  $\pi\pi^*$  excitations are obtained with the PBE0 functional.<sup>19</sup>  
54  
55  
56  
57  
58  
59  
60

1  
2  
3 Since the PCM-TD-DFT values look trustworthy, as long as a proper functional is chosen, we assign  
4 the UV-Vis spectra of complex 1 in the following way. The weak band peaking at ca. 3.52 eV is due to  
5 the  $3^1A_1$   $^1MLCT$  state. The strong band peaking at 3.96 and 4.13-4.34 eV, with absorption intensities of  
6  $14100 M^{-1}cm^{-1}$  and  $11300-10000 M^{-1}cm^{-1}$ , respectively, can be attributed to the  $5^1B_2$  ( $^1IL$ ) and the  $4^1B_2$   
7 ( $^1MLCT$ ) states, respectively. Such assignment is done in view of the energetic order the last two states,  
8 which is reproduced with most of the TD-DFT flavours (in the presence of solvent) and the MS-  
9 CASPT2(14,13) calculations. The oscillator strengths of both states are also in accordance to this  
10 assignment. Thus, the  $^1IL$  state possesses higher oscillator strength than the  $^1MLCT$  state, in accordance  
11 to the experimental absorption intensities.  
12  
13

14 A comment on the performance of the different TD-DFT flavors to predict oscillator strengths is in  
15 order here. As expected and in agreement with the experiment, the intensity of the  $^1MC$  state is very  
16 low, no matter which functional is used or whether solvation is included. Noteworthy, the oscillator  
17 strengths of the  $^1MLCT$  states computed in the gas phase are underestimated with all the functionals in  
18 comparison to the PCM-TD-DFT values; very likely, this error is connected to the underestimation of  
19 the excitation energies, among other effects. The least robust excitation is the one corresponding to the  
20 intense  $^1IL$  state, whose results are dependent of the functional employed. In gas phase, PBE and  
21 B3LYP predict oscillator strengths thrice smaller than the rest of functionals. The reason behind this  
22 fact might be the mixing of the intense  $^1IL$  state with an  $n\pi^*$  excitation –as reflected on the wavefunction  
23 coefficients. See for example that the  $\pi\pi^*/n\pi^*$  excitation wavefunction coefficients in the  $^1IL$  state with  
24 the B3LYP functional are 0.52/0.46, respectively, whilst with the PBE0 functional such values are  
25 0.65/0.20, respectively. A more uniform picture is obtained by comparing the PCM-TD-DFT oscillator  
26 strengths since all the functionals predict similar values for the  $^1IL$  state.  
27  
28  
29  
30  
31  
32  
33  
34  
35  
36  
37  
38  
39  
40  
41  
42  
43  
44  
45  
46  
47  
48  
49  
50  
51  
52

53 In summary it can be seen that the different functionals examined here show a different performance  
54 on the calculations of the low-lying excited states of complex 1. Figure 3 displays the errors in the  
55 energy of the PCM-TD-DFT values of the  $^1IL$  and the  $^1MLCT$  states, taking as a reference the  
56 experimental values. A direct comparison between the oscillator strengths and the absorption intensities  
57  
58  
59  
60

1  
2  
3 is not possible since some of the experimental bands overlap. As discussed before, acute problems are  
4 found in the description of  $^1\text{MLCT}$  states. These are only accurately calculated by hybrid functionals  
5 with intermediate percentages of exact exchange; the functionals M06, PBE0 and B3LYP, in this order,  
6 give the best accuracy when solvent effects are considered. This three functional plus the pure  
7 functional PBE seem to be the only ones which are able to get a reasonable value of the local  $^1\text{IL}$   
8 excitation of **1**. Based on these results the best balanced description of all kind of excited states of  
9 Ru(II)-polypyridyl complexes can be best obtained with M06 in first place and B3LYP and PBE0 in  
10 second and third places, respectively, even though slight underestimations of the d-d transition are  
11 found for the M06 functionals. The inclusion of solvent effects is mandatory, especially for the  $^1\text{MLCT}$   
12 states. Indeed, this combination (an hybrid functional with intermediate amount of exact exchange and  
13 the consideration of solvent effects via the PCM method) has been successfully used in other Ru(II)  
14 polypyridyl complexes.<sup>20b,c</sup> In this sense, it is surprising that the CAM-B3LYP functional, designed *a*  
15 *priori* to deal with CT states does not improve the conventional hybrid functionals when describing both  
16 the  $^1\text{MLCT}$  and  $^1\text{IL}$  states. Very likely, the bad performance of CAM-B3LYP for describing  $^1\text{MLCT}$   
17 states is due to the short distance between the donor and acceptor moieties. In contrast to these  
18 conclusions, the pure PBE functional (also in combination with solvent effects) has been found to  
19 outperform the B3LYP functional in the description of the excited states of  $\text{Fe}(\text{phen})_2(\text{CN})_2$ .<sup>49</sup> The  
20 reason behind the good performance of the pure functional PBE in this particular situation is probably  
21 the mixing of the d-based orbitals with the ligand-based orbitals, leading to an overlap of the orbitals  
22 involved in the state and hence to a loose CT character of these states. Whether this situation takes place  
23 in others TM-complexes needs to be evaluated for each particular case.  
24  
25  
26  
27  
28  
29  
30  
31  
32  
33  
34  
35  
36  
37  
38  
39  
40  
41  
42  
43  
44  
45  
46  
47  
48  
49  
50  
51  
52  
53  
54  
55  
56  
57  
58  
59  
60

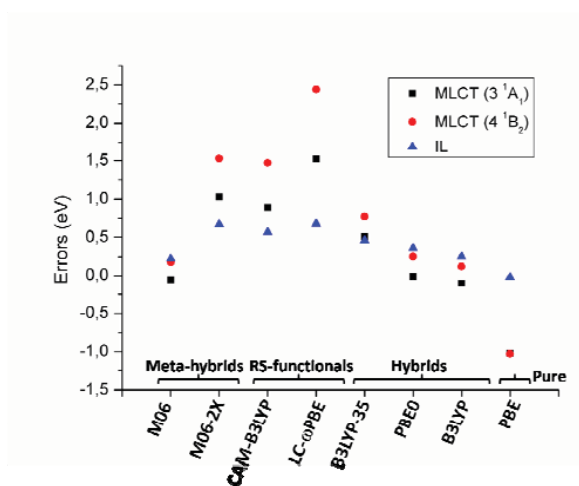


**Figure 3.** a) PCM-TD-DFT errors (eV) in the electronic excitation energies of complex **1** for different types of excited states.

**3.3. RASPT2/RASSCF calculations.** The energies and oscillator strengths obtained with the different RASPT2/RASSCF protocols are compiled in Table 3. The computational strategies that we will discuss below have been chosen following two intentions. The first is to improve the quality of the previous CASPT2/CASSCF using an affordable configuration space. The second is to find general hints about how to face the treatment of excited states of related TM complexes at the RASPT2/RASSCF level of theory.

As a first step with respect the CAS(14,13) calculations, we include the  $n_{\text{Cl-a}_1}$  orbital and two  $\pi^*_{\text{CO}}$  orbitals ( $\pi^*_{\text{CO-b}_1}$  and  $\pi^*_{\text{CO-a}_2}$ ) in the active space. The simplest approach is to distribute all the orbitals within RAS1 and RAS3 subspaces and leave the RAS2 empty while allowing SDTQ excitations within the RAS1/RAS3 subspaces. This is denoted as RASSCF(16,4,4;8,0,8). As it can be seen in Table 3 the number of CSFs is heavily reduced in comparison to the CASSCF(14,13) calculations –by almost a factor of 3. Unfortunately, while cheap and easy, this procedure leads to poor results for both the low- and high-lying excited states. The  $3^1A_1$  state, calculated at 3.35 eV with CASPT2(14,13), is now predicted at 4.32 eV with RASPT2(16,4,4;8,0,8), and hence deviating 1 eV from the CASPT2 value. The RASPT2(16,4,4;8,0,8) relative energies of the high-lying  $5^1B_2$  and  $4^1B_2$  bright states are only about

1  
2  
3 0.3-0.2 eV different from the CASPT2(14,13) values, but with shifts in different directions. An  
4  
5 important difference between both methodologies is that, as a consequence of this reverse shift, the  
6  
7  $^1\text{MLCT}$  ( $4^1\text{B}_2$ ) state is below the  $^1\text{IL}$  state ( $5^1\text{B}_2$ ) at the RASPT2(16,4,4;8,0,8) level of theory. The latter  
8  
9 result is suspicious in view of the previous CASPT2 and TD-DFT results. In principle, the solvent  
10  
11 effects could reverse the order of the states, since the  $^1\text{MLCT}$  state is more sensible than the  $^1\text{IL}$  state to  
12  
13 solvatochromic effects, as reflected with the PCM-TD-DFT calculations. Unfortunately, RASPT2  
14  
15 calculations in the present of solvent effects are computationally too demanding to be investigated, so  
16  
17 that no further conclusions can be reached. We note however that leaving the RAS2 empty has also  
18  
19 given poor results in describing the singlet-triplet splitting of copper complexes.<sup>11</sup> Even though this  
20  
21 strategy had resulted useful in describing ionization and low-lying excited states of simple systems,  
22  
23 such as organic  $\pi$  conjugated compounds,<sup>9</sup> the results obtained in this work also seem to confirm that in  
24  
25 TM complexes better results are obtained if the RAS2 subspace is not empty.  
26  
27  
28

29  
30 Therefore, in the following we focus on finding the optimal composition of the RAS2 subspace,  
31  
32 which as we will show, it is indeed the crucial step to obtain a balanced and accurate description of the  
33  
34 relevant excited states of **1**. Moving the  $n_{\text{Cl-a}_1}$ , the  $\pi_{\text{bpy-2a}_2}/\pi_{\text{bpy-2a}_2}^*$  pair and the two  $\pi_{\text{CO}}^*$  orbitals to the  
35  
36 RAS1/RAS3 subspaces leads to the RASSCF(16, $l,m$ ;2,11,3) calculations, which will allow up to D, T,  
37  
38 or Q excitations, depending on the  $l$  and  $m$  indexes. As we see in Table 2, the introduction of these  
39  
40 orbitals and therefore further correlation in the zeroth-order wavefunction implies a slightly better  
41  
42 description of some states. Exemplarily, the  $3^1\text{A}_1$  states goes from 5.61 eV at CASSCF(14,13) to 5.18  
43  
44 eV at RASSCF(16,2,2;2,11,3) level. The perturbative treatment leads to very similar results: the  $3^1\text{A}_1$   
45  
46 state is predicted at 3.36 eV with RASPT2(16,2,2;2,11,3) level of theory and the  $5^1\text{B}_2$  and  $4^1\text{B}_2$  are now  
47  
48 located at 4.83 and 4.58 eV, respectively. The results are hardly improved with respect to the  
49  
50 CASPT2(14,13) results since the transition responsible for the lowest energy band is located at the same  
51  
52 position and the error with respect to the peaks higher in energy ( $5^1\text{B}_2$  and  $4^1\text{B}_2$ ) is now ca. 0.9 and 0.4  
53  
54 eV, respectively (obviating solvatochromic effects) at the RASPT2(16,2,2;2,11,3) level of theory. An  
55  
56  
57  
58  
59  
60

1  
2  
3 improvement of these results can be attempted following two strategies: either i) increasing the allowed  
4 excitations within the RAS1/3 subspaces or ii) changing the current RAS partition.  
5  
6

7  
8 First, we shall discuss the former strategy. Allowing up to triple excitations is labeled by  
9 RASSCF(16,3,3;2,11,3), whilst up to triples-quadruples ( $l=3$  and  $m=4$ ) is denoted by  
10 RASSCF(16,3,4;2,11,3). As it can be seen the number of CSFs for such approaches is over 5 and 7  
11 million, respectively –on the limit of computational feasibility. Disappointingly, as it can be seen in  
12 Table 3, the relative energies of all the states show negligible changes regardless the level of excitation,  
13 at both RASSCF and RASPT2 levels of theory. These calculations do highlight that an enormous  
14 number of CSFs does not guarantee the quality of the results. If the orbitals composing RAS2 subspace  
15 are not properly selected and a reasonable reference space is achieved, perturbation theory will not be  
16 able to get accurate results.  
17  
18

19  
20 Therefore, we turn our attention to redefine the RAS partition. An additional pair of  $\pi_{\text{bpy}}/\pi_{\text{bpy}}^*$   
21 orbitals ( $\pi_{\text{bpy}}-1b_1/\pi_{\text{bpy}}^*-1a_2$ ) with high and low occupation numbers, respectively, is moved from the  
22 RAS2 to the RAS1/3 subspaces. This strategy has the additional advantage that, in principle, it allows to  
23 include additional orbitals in the RAS1/3 subspaces because now the number of CSFs is considerably  
24 reduced. By allowing SD excitations we get RASSCF(16,2,2;3,9,4) calculations. As it can be seen in  
25 Table 2 the number of CSF's is reduced by a factor of 10 in comparison to the RASSCF(16,2,2;2,11,3)  
26 calculations. Very interestingly, we note that the results obtained with the economic  
27 RASPT2(16,2,2;3,9,4) level of theory seem to be more balanced than the previous ones. The low-lying  
28  $3^1A_1$  state is now predicted at 3.92 eV. If we consider the solvatochromic blue shift calculated with the  
29 PCM-TD-DFT model, this state deviates even more from the experiment than the previous RASPT2  
30 schemes. On the other hand side we believe that the  $5^1B_2$  and  $4^1B_2$  states, located now at 4.19 and 3.96  
31 eV, are in closer agreement with the experimental evidence. Thus, the  $^1IL$  state is only accurately  
32 described within this latter procedure (recall that solvatochromic effects are not so important for this  
33 state, as reflected by the PCM-TD-DFT calculations). Additionally, the  $4^1B_2$   $^1MLCT$  state is also best  
34 predicted at this level of theory, assuming also a solvatochromic blue-shift. The  $^1MC$  ( $1^1B_1$ ) state seems  
35  
36  
37  
38  
39  
40  
41  
42  
43  
44  
45  
46  
47  
48  
49  
50  
51  
52  
53  
54  
55  
56  
57  
58  
59  
60

1  
2  
3 to be rather immune to electronic correlation and it is located at 3.23 eV –a very similar value as that  
4  
5 obtained with the other RAS calculations. In view of the satisfactory RASPT2(16,2,2;3,9,4) energies we  
6  
7 report oscillator strengths at this level of theory. The results can be found in parenthesis in Table 1. In  
8  
9 most of the cases, the oscillator strengths are in agreement with the MS-CASPT2(14,13) ones. The main  
10  
11 discrepancy is found in the  $S_{10}(4\ ^1B_2)$  state, where RASPT2(16,2,2;3,9,4) predicts more than one order of  
12  
13 magnitude smaller oscillator strength. Since the gas phase TD-DFT results also point to a weak  $4\ ^1B_2$   
14  
15 state we are confident that the RASPT2(16,2,2;3,9,4) oscillator strengths are trustable.  
16  
17

18  
19 Inclusion of further correlation orbitals leads to the RASPT2/RASSCF(22,2,2;6,9,6) calculations.  
20  
21 With a few millions of CSF's, these calculations are on the computational limit and would be  
22  
23 prohibitive at the CASPT2/CASSCF level of theory. They are probably an illustration of the size of  
24  
25 TM-polypyridyl complexes that can be nowadays calculated at the RASPT2/RASSCF level of theory.  
26  
27 Moreover, and more interestingly, they allow evaluating whether all the correlation orbitals are  
28  
29 necessary to get accurate results for complex **1**. As it can be seen in Table 3, the low-lying  $3\ ^1A_1$  state is  
30  
31 slightly better described than at the RASPT2(16,2,2;3,9,4) level of theory. The  $^1IL$  state is also  
32  
33 accurately predicted at the RASPT2(22,2,2;6,9,6) level of theory and the  $^1MC$  ( $1\ ^1B_1$ ) state seems to be  
34  
35 (again) unaffected by the inclusion of further correlation effects. On the other hand the  $^1MLCT$  ( $4\ ^1B_2$ )  
36  
37 state is blue-shifted as compared to the RASPT2(16,2,2;3,9,4) calculations, exhibiting similar values to  
38  
39 the rest of CASPT2 and RASPT2 values. We note however that at this level of theory the intense  $^1IL$   
40  
41 ( $5\ ^1B_2$ ) and the  $^1MLCT$  ( $4\ ^1B_2$ ) states are strongly mixed. For example, the wavefunction coefficients of  
42  
43 the  $4d_{yz}-a_2 \rightarrow \pi_{bpy}^*-1b_1/\pi_{bpy}-1a_2 \rightarrow \pi_{bpy}^*-2b_1$  excitations are 0.38/0.38, in the case of the latter state. As a  
44  
45 consequence of this (what we consider spurious) mixing, the oscillator strengths computed at the  
46  
47 alternative RASPT2(16,2,2;3,9,4) level of theory can be considered more accurate. Probably, a higher  
48  
49 number of average states is necessary to describe correctly the  $B_2$  states with this active space, but due  
50  
51 to the expensive cost of these calculations, no further trials have been done. We conclude therefore that  
52  
53 when going from the RASPT2(16,2,2;3,9,4) to the RASPT2(22,2,2;6,9,6) calculations almost no  
54  
55 improvement in the relative energies is achieved. The more economic RASPT2(16,2,2;3,9,4) partition is  
56  
57  
58  
59  
60

1  
2  
3 more valuable here, giving intensities in closer agreement with the experiment and the PCM-TD-DFT  
4  
5 values.  
6

#### 7 **4. Concluding remarks.**

8  
9  
10 TM-complexes are prototypes of systems where transitions of very different character, i.e., IL, MC,  
11 MLCT, LMCT states, can be found. This makes them specially complicated to handle computationally  
12 so that balanced results are obtained for all the excited states simultaneously. As an example of such a  
13 situation, we have calculated the excited states of the *trans(Cl)*-Ru(bpy)Cl<sub>2</sub>(CO)<sub>2</sub> complex with  
14 CASPT2/CASSCF and RASPT2/RASSCF protocols, allowing different partitions of the active space  
15 and different excitation levels. As found in the case of some organic systems,<sup>10</sup> in order to get accurate  
16 results the inclusion of correlation orbitals in the active space is important, however much more  
17 significant seems to be the choice of the partition of the RAS subspaces, especially the RAS2. From the  
18 results obtained here, we conclude that when treating TM-complexes, the RAS2 subspace should not be  
19 empty but it must contain the orbitals involved in the main electronic excitations to be described and  
20 only those. Other orbitals, relevant, but showing very high and very low occupation numbers should be  
21 better allocated to the RAS1 and RAS3 subspaces, respectively. Once an optimal partition is achieved,  
22 SD excitations within the RAS1/3 subspaces are sufficient to handle the additional dynamical  
23 correlation and thus obtain the right order of the states with accurate energies and intensities. These  
24 hints should be transferable to compute excited states of related TM-complexes, like the [Ru(bpy)<sub>3</sub>]<sup>2+</sup>  
25 complex, at RASPT2/RASSCF level of theory. Nonetheless, in general, it appears particularly difficult  
26 to obtain an accurate and balance description of all types of excited states of TM-polypyridyl complexes  
27 simultaneously and, therefore, the effect of different partitions within the RASPT2/RASSCF method  
28 should be considered.  
29  
30  
31  
32  
33  
34  
35  
36  
37  
38  
39  
40  
41  
42  
43  
44  
45  
46  
47  
48  
49  
50  
51  
52  
53  
54  
55  
56  
57  
58  
59  
60

The performance of several TD-DFT flavors is herein also assessed. Desirable is a general method which allows describing the different transitions contributing to the UV-Vis spectrum. Solvent effects



1  
2  
3 are found to be mandatory to obtain spectroscopic accuracy, especially in the case of MLCT states. We  
4  
5 find that whilst MC transitions are rather robust to any of the functionals tested. MLCT states are only  
6  
7 well described with functionals bearing intermediate amounts of exact exchange, such as M06, PBE0  
8  
9 and B3LYP, in combination with solvent effects. IL states are also best described with these functionals.  
10  
11 In view of these conclusions, here we find that the best compromise to treat all the excited states of  
12  
13 Ru(II)-polypyridyl complexes in a balanced manner is first then M06 and then the B3LYP and PBE0  
14  
15 functionals.  
16  
17

18  
19  
20 This study clearly shows that the rationalization of the UV/Vis spectra of TM-complexes exclusively  
21  
22 based on the matching of experimental and theoretical TD-DFT bands might be dangerous without an  
23  
24 initial exploration of the performance of different hybrid or range-separated functionals because some  
25  
26 <sup>1</sup>MLCT states might be theoretically underestimated (by more than 1 eV in some cases) but match  
27  
28 accidentally a different band of the experimental spectrum.  
29  
30

### 31 32 33 **Acknowledgements.**

34  
35  
36 This work has been funded by the Carl-Zeiss foundation (D.E.). Computer time in the  
37  
38 Rechenzentrum of the Friedrich-Schiller-Universität Jena is gratefully acknowledged. We are grateful  
39  
40 to one of the referees for pointing to the solvatochromic shifts, which turned to be rather crucial to  
41  
42 interpret the spectrum of *trans(Cl)-Ru(bpy)Cl<sub>2</sub>(CO)<sub>2</sub>*.  
43  
44  
45  
46  
47  
48  
49  
50  
51  
52  
53  
54  
55  
56  
57  
58  
59  
60

**Table 1.** Relative SA-CASSCF(14,13), SS- and MS-CASPT2(14,13) as well as SO-MS-CASPT2(14,13) electronic transitions energies,  $\Delta E$  (in eV), with oscillator strengths  $f$ , and main assignment for complex **1**. The square of the configuration interaction coefficient,  $c^2$ , indicates the weight of a particular transition to the corresponding state.

SA-CASSCF(14,13) <sup>a</sup>				SS-CASPT2 (14,13)	MS-CASPT2(14,13) <sup>b</sup>		SO-MS- CASPT2(14,13) <sup>b</sup>	
State	Assignment / Weight ( $c^2$ )	$f$	$\Delta E$ (eV)	$\Delta E$ (eV)	$\Delta E$ (eV) / $c^2$	$f^c$	$\Delta E$ (eV)	$f$
S <sub>0</sub> (1 <sup>1</sup> A <sub>1</sub> )	<sup>1</sup> GS / 0.86			0.0	0.0 / 0.86		0.0	
S <sub>1</sub> (1 <sup>1</sup> A <sub>2</sub> )	<sup>1</sup> MC (4d <sub>yz</sub> -a <sub>2</sub> → 4d <sub>z<sup>2</sup></sub> -a <sub>1</sub> ) / 0.71	0.000	3.15	3.76	3.76 / 0.72	0.000 (0.000)	3.78	0.000
S <sub>2</sub> (1 <sup>1</sup> B <sub>1</sub> )	<sup>1</sup> MC (4d <sub>xz</sub> -b <sub>1</sub> → 4d <sub>z<sup>2</sup></sub> -a <sub>1</sub> ) / 0.79	0.009	3.59	3.49	3.49 / 0.77	0.009 (0.007)	3.52	0.009
S <sub>3</sub> (2 <sup>1</sup> B <sub>1</sub> )	<sup>1</sup> MC (4d <sub>yz</sub> -a <sub>2</sub> → 4d <sub>x<sup>2</sup>-y<sup>2</sup></sub> -b <sub>2</sub> ) / 0.78	0.006	4.77	4.19	4.19 / 0.76	0.004 (0.004)	4.23	0.003
S <sub>4</sub> (2 <sup>1</sup> A <sub>2</sub> )	<sup>1</sup> MC (4d <sub>xz</sub> -b <sub>1</sub> → 4d <sub>x<sup>2</sup>-y<sup>2</sup></sub> -b <sub>2</sub> ) / 0.75	0.000	4.82	4.81	4.82 / 0.77	0.000 (0.000)	4.82	0.000
S <sub>5</sub> (2 <sup>1</sup> A <sub>1</sub> )	<sup>1</sup> MC (4d <sub>xy</sub> -a <sub>1</sub> → 4d <sub>z<sup>2</sup></sub> -a <sub>1</sub> ) / 0.84	0.007	5.13	5.57	5.57 / 0.85	0.006 (0.007)	5.59	0.006
S <sub>6</sub> (1 <sup>1</sup> B <sub>2</sub> )	<sup>1</sup> MLCT (4d <sub>yz</sub> -a <sub>2</sub> → π <sup>*</sup> <sub>bnv</sub> -2b <sub>1</sub> ) / 0.76	0.000	5.19	3.81	3.73 / 0.74	0.000 (0.000)	3.74	0.000
S <sub>7</sub> (2 <sup>1</sup> B <sub>2</sub> )	<sup>1</sup> MC (4d <sub>xy</sub> -a <sub>1</sub> → 4d <sub>x<sup>2</sup>-y<sup>2</sup></sub> -b <sub>2</sub> ) / 0.82	0.001	5.32	5.49	5.55 / 0.62	0.070 (0.018)	5.57	0.068
S <sub>8</sub> (3 <sup>1</sup> B <sub>2</sub> )	<sup>1</sup> IL (π <sub>bnv</sub> -1a <sub>2</sub> → π <sup>*</sup> <sub>bnv</sub> -1b <sub>1</sub> ) / 0.28	0.195	5.44	5.40	5.49 / 0.30	0.049 (-) <sup>d</sup>	5.51	0.051
	<sup>1</sup> IL (π <sub>bnv</sub> -1a <sub>2</sub> → π <sup>*</sup> <sub>bnv</sub> -2b <sub>1</sub> ) / 0.22							
S <sub>9</sub> (3 <sup>1</sup> A <sub>1</sub> )	<sup>1</sup> MLCT (4d <sub>xz</sub> -b <sub>1</sub> → π <sup>*</sup> <sub>bnv</sub> -2b <sub>1</sub> ) / 0.85	0.045	5.61	3.35	3.35 / 0.85	0.025 (0.059)	3.36	0.025
S <sub>10</sub> (4 <sup>1</sup> B <sub>2</sub> )	<sup>1</sup> MLCT (4d <sub>yz</sub> -a <sub>2</sub> → π <sup>*</sup> <sub>bnv</sub> -1b <sub>1</sub> ) / 0.69	0.162	6.34	4.74	4.75 / 0.60	0.199 (0.012)	4.77	0.198
S <sub>11</sub> (5 <sup>1</sup> B <sub>2</sub> )	<sup>1</sup> IL (π <sub>bnv</sub> -1a <sub>2</sub> → π <sup>*</sup> <sub>bnv</sub> -2b <sub>1</sub> ) / 0.52	0.405	6.64	4.65	4.49 / 0.40	0.306 (0.309)	4.50	0.306

<sup>a</sup>SA-(3,3,2,6)-CASSCF(14,13) calculations for A<sub>1</sub>, B<sub>1</sub>, A<sub>2</sub> and B<sub>2</sub> symmetries, respectively. <sup>b</sup>MS-SO/MS-(3,3,2,6)-CASPT2(14,13) calculations for A<sub>1</sub>, B<sub>1</sub>, A<sub>2</sub> and B<sub>2</sub> symmetries, respectively. <sup>c</sup>In parenthesis, oscillator strengths obtained with MS-RASPT2(16,2,2;3,9,4). <sup>d</sup>This state was not computed at the MS-RASPT2(16,2,2;3,9,4) level of theory.

**Table 2.** Selected TD-DFT electronic transitions energies,  $\Delta E$  (in eV), with oscillator strengths  $f$  against experimental values. Numbers in italics are calculated in solution ( $\text{CH}_3\text{CN}$ ) with the PCM model.

State	Meta-hybrid func(% HF exchange).				Range-sepatated func.				Hybrid functionals (% HF exchange)						Pure func.		Exptl
	M06 (27%)		M06-2X (54%)		CAM-B3LYP		LC- $\omega$ PBE		B3LYP-35 (35%)		PBE0 (25%)		B3LYP (20%)		PBE		
	$\Delta E$	$f$	$\Delta E$	$f$	$\Delta E$	$f$	$\Delta E$	$f$	$\Delta E$	$f$	$\Delta E$	$f$	$\Delta E$	$f$	$\Delta E$	$f$	$\Delta E$
$1^1\text{B}_1$ ( $^1\text{MC}$ )	2.99 <i>3.00</i>	0.001 <i>0.002</i>	3.06 <i>3.02</i>	0.003 <i>0.003</i>	3.39 <i>3.38</i>	0.003 <i>0.004</i>	3.50 <i>3.46</i>	0.003 <i>0.004</i>	3.34 <i>3.33</i>	0.003 <i>0.004</i>	3.31 <i>3.34</i>	0.002 <i>0.004</i>	3.25 <i>3.30</i>	0.001 <i>0.003</i>	3.09 <i>3.19</i>	0.002 <i>0.003</i>	
$3^1\text{A}_1$ ( $^1\text{MLCT}$ )	2.48 <i>3.47</i>	0.011 <i>0.023</i>	3.64 <i>4.55</i>	0.009 <i>0.019</i>	3.43 <i>4.41</i>	0.014 <i>0.031</i>	4.19 <i>5.05</i>	0.022 <i>0.047</i>	3.10 <i>4.03</i>	0.010 <i>0.021</i>	2.60 <i>3.51</i>	0.010 <i>0.019</i>	2.41 <i>3.42</i>	0.009 <i>0.019</i>	1.56 <i>2.50</i>	0.008 <i>0.016</i>	3.52 <sup>a</sup> 3.62 <sup>b</sup>
$5^1\text{B}_2$ ( $^1\text{IL}$ )	4.29 <i>4.18</i>	0.142 <i>0.315</i>	4.76 <i>4.63</i>	0.246 <i>0.358</i>	4.67 <i>4.53</i>	0.258 <i>0.386</i>	4.82 <i>4.64</i>	0.289 <i>0.353</i>	4.56 <i>4.42</i>	0.304 <i>0.392</i>	4.44 <i>4.32</i>	0.199 <i>0.280</i>	4.29 <i>4.21</i>	0.064 <i>0.247</i>	4.02 <i>3.94</i>	0.064 <i>0.287</i>	3.96 <sup>c</sup>
$4^1\text{B}_2$ ( $^1\text{MLCT}$ )	3.35 <i>4.42</i>	0.002 <i>0.071</i>	4.66 <i>5.77</i>	0.067 <i>0.022</i>	4.51 <i>5.71</i>	0.016 <i>0.034</i>	5.65 <i>6.68</i>	0.014 <i>0.139</i>	4.08 <i>5.01</i>	0.001 <i>0.029</i>	3.49 <i>4.49</i>	0.002 <i>0.107</i>	3.25 <i>4.36</i>	0.001 <i>0.123</i>	2.19 <i>3.21</i>	0.002 <i>0.002</i>	4.13- 4.34 <sup>a</sup>

<sup>a</sup>In  $\text{CH}_3\text{CN}$ , from Ref. 22. <sup>b</sup>In  $\text{CH}_2\text{Cl}_2$ , from Ref. 23.

**Table 3.** Relative RASSCF( $n,l,m;i,j,k$ ) and RASPT2( $n,l,m;i,j,k$ ) electronic transitions energies,  $\Delta E$  (in eV), of the main electronic excitations of complex **1**, at different levels of theory, compared to the SA-CASSCF, MS-CASPT2 and available experimental data.

States	SA-CASSCF (14,13)	MS-CASPT2 (14,13)	SA-RASSCF (16,4,4; 8,0,8) <sup>a</sup>	MS-RASPT2 (16,4,4; 8,0,8) <sup>b</sup>	SA-RASSCF <sup>a</sup> (16, $l,m$ ; 2,11,3)			MS-RASPT2 <sup>b</sup> (16, $l,m$ ; 2,11,3)			SA-RASSCF (16,2,2; 3,9,4) <sup>a</sup>	MS-RASPT2 (16,2,2; 3,9,4) <sup>b</sup>	SA-RASSCF (22,2,2; 6,9,6) <sup>a</sup>	MS-RASPT2 (22,2,2; 6,9,6) <sup>b</sup>	Exptl
					$l,m$ =2	$l,m$ =3	$l=3$ , $m=4$	$l,m$ =2	$l,m$ =3	$l=3$ , $m=4$					
1 <sup>1</sup> B <sub>1</sub> ( <sup>1</sup> MC)	3.59	3.49	4.50	3.36	3.99	4.03	4.04	3.31	3.31	3.31	4.20	3.23	4.53	3.55	-
3 <sup>1</sup> A <sub>1</sub> ( <sup>1</sup> MLCT)	5.61	3.35	5.70	4.32	5.18	5.22	5.22	3.36	3.35	3.35	5.51	3.92	5.33	3.83	3.52 <sup>c</sup> 3.62 <sup>d</sup>
5 <sup>1</sup> B <sub>2</sub> ( <sup>1</sup> IL)	6.64	4.49	6.41	4.83	6.08	6.07	6.07	4.83	4.85	4.87	6.83	4.19	6.62	4.30 <sup>e</sup>	3.96 <sup>e</sup>
4 <sup>1</sup> B <sub>2</sub> ( <sup>1</sup> MLCT)	6.34	4.75	6.92	4.57	6.58	6.57	6.58	4.58	4.61	4.62	6.35	3.96	6.17	4.61 <sup>e</sup>	4.13 <sup>e</sup>
Number of CSF's	183150		73108		2230837( $l,m=2$ ); 5495197 ( $l,m=3$ ); 7399206 ( $l=3, m=4$ )						557036		3890064		

<sup>a</sup>SA-(3,3,4)-RASSCF( $n,l,m;i,j,k$ ) calculations for A<sub>1</sub>, B<sub>1</sub> and B<sub>2</sub> symmetries, respectively. <sup>b</sup>MS-(3,3,4)-RASPT2( $n,l,m;i,j,k$ ) calculations for A<sub>1</sub>, B<sub>1</sub> and B<sub>2</sub> symmetries, respectively. <sup>c</sup>In CH<sub>3</sub>CN, from Ref. 22. <sup>d</sup>In CH<sub>2</sub>Cl<sub>2</sub>, from Ref. 23. <sup>e</sup>These states are strongly mixed at the MS(4)-RASPT2(22,2,2;6,9,6) level of theory.

## References:

1. a) Gust, D.; Moore, T. A.; Moore, A. L. *Acc. Chem. Res.* **2009**, *42*, 1890-1898. b) Rau, S.; Schäfer, B.; Gleich, D.; Anders, E.; Rudolph, M.; Friedrich, M.; Görls, H.; Henry, W.; Vos, J. G. *Angew. Chem. Int. Ed.* **2006**, *45*, 6215-6218. c) Tschierlei, S.; Karnahl, M.; Presselt, M.; Dietzek, B.; Guthmuller, J.; González, L.; Schmitt, M.; Rau, S.; Popp, J. *Angew. Chem. Int. Ed.* **2010**, *122*, 4073-4076.
2. a) Concepcion, J. J.; Jurss, J. W.; Brennaman, M. K.; Hoertz, P. G.; Patrocinio, A. O. T.; Iha, N. Y. M.; Templeton, J. L.; Meyer, T. J. *Acc. Chem. Res.* **2009**, *42*, 1945-1955. b) Romain, S.; Vigara, L.; Llobet, A. *Acc. Chem. Res.* **2009**, *42*, 1944-1953.
3. a) O'Regan B.; Grätzel, M. *Nature*, **1991**, *353*, 737. b) Hagfeldt, A.; Grätzel, M. *Acc. Chem. Res.* **2000**, *33*, 269. c) Grätzel, M. *Nature*. **2001**, *414*, 338. d) Grätzel, M. *Pure Appl. Chem.*, **2001**, *73*, 459. e) Benkő, G.; Kallioinen, J.; Korppi-Tommola, J. E. Y.; Yartsev, A. P.; Sundström, V. *J. Am. Chem. Soc.* **2002**, *124*, 489-493. f) Kallioinen, J.; Benkő, G.; Myllyperkiö, P.; Khriachtchev, L.; Skårman, B.; Wallenberg, R.; Tuomikoski, M.; Korppi-Tommola, J.; Sundström, V.; Yartsev, A. P. *J. Phys. Chem. B*, **2004**, *108*, 6365-6373. g) Grätzel, M. *Inorg. Chem.* **2005**, *44*, 6841.
4. Andersson, K.; Malmqvist, P.-A.; Roos, B. O. *J. Chem. Phys.* **1992**, *96*, 1218.
5. Pierloot, K.; Vancoillie, S. *J. Chem. Phys.* **2006**, *125*, 124303.
6. Gindensperger, E.; Köppel, H.; Daniel, C. *Chem. Comm.* **2010**, *46*, 8225-8227.
7. a) Olsen, J.; Roos, B. O.; Jorgensen, P.; Jensen, H. J. A. *J. Chem. Phys.* **1988**, *89*, 2185. b) Malmqvist, P.-A.; Rendell, A.; Roos, B. O. *J. Chem. Phys.* **1990**, *94*, 5477.
8. Malmqvist, P. -Å.; Pierloot, K.; Shahi, A. R. M.; Cramer, J. C.; Gagliardi, L. *J. Chem. Phys.* **2008**, *128*, 204109.
9. Shahi, A. R. M.; Cramer, C. J.; Gagliardi, L. *Phys. Chem. Chem. Phys.* **2009**, *11*, 10964-10972.

- 1  
2  
3  
4  
5 10. Sauri, V.; Serrano-Andrés, L.; Shahi, A. R. M.; Gagliardi, L.; Vancoillie, S.; Pierloot, K. *J. Chem.*  
6  
7 *Theory Comp.* **2011**, *7*, 153-168.  
8  
9  
10 11. Huber, S. M.; Shahi, A. R. M.; Aquilante, F.; Cramer, C. J.; Gagliardi, L. *J. Chem. Theory Comp.*  
11  
12 **2009**, *5*, 2967-2976.  
13  
14  
15 12. Casida, M. E. *Recent advances in Density Functional Methods. Part I*, World Scientific,  
16  
17 Singapore, **1995**.  
18  
19  
20 21 13. Cramer, C. J.; Truhlar, D. G. *Phys. Chem. Chem. Phys.* **2009**, *11*, 10757-10816.  
22  
23 24 14. a) Dreuw, A.; Weisman, J. L.; Head-Gordon, M. *J. Chem. Phys.* **2003**, *119*, 2943-2946. b) Dreuw,  
25  
26 A.; Head-Gordon, M. *Chem. Rev.* **2005**, *105*, 4009-4037.  
27  
28 29 15. Neese, F.; Petrenko, T.; Ganyushin, D.; Olbrich, G. *Coord. Chem. Rev.* **2007**, *251*, 288-327.  
30  
31 32 16. a) Ernzerhof, M.; Scuseria, G. E. *J. Chem. Phys.* **1999**, *110*, 5029-5036. b) Adamo, C.; Barone, V.  
33  
34 *J. Chem. Phys.* **1999**, *110*, 6158-6170.  
35  
36 37 17. Vydrov, O. A.; Scuseria, G. E. *J. Chem. Phys.* **2006**, *125*, 234109.  
38  
39 40 18. a) Yanai, T.; Tew, D. P.; Handy, N. C. *Chem. Phys. Lett.* **2004**, *393*, 51-56. b) Peach, M. J. G.;  
41  
42 Benfield, P.; Helgaker, T.; Tozer, D. J. *J. Chem. Phys.* **2008**, *128*, 044118.  
43  
44 45 19. a) Jacquemin, D.; Perpète, E. A.; Scuseria, G. E.; Ciofini, I.; Adamo, C. *J. Chem. Theory Comp.*  
46  
47 **2008**, *4*, 123-135. b) Escudero, D.; Trupp, S.; Bussemer, B.; Mohr, G.; González, L. *J. Chem. Theory*  
48  
49 *Comp.* **2011**, *7*, 1062. c) Jacquemin, D.; Preat, P.; Wathélet, V.; Fontaine, M.; Perpète, E. A. *J. Am.*  
50  
51 *Chem. Soc.* **2006**, *128*, 2072.  
52  
53 54 20. a) Bossert, J.; Daniel, C. *Coord. Chem. Rev.* **2008**, *23-24*, 2493-2503. b) Happ, B.; Escudero, D.;  
55  
56 Hager, M. D.; Friebe, C.; Winter, A.; Görls, H.; Altuntas, E.; González, L.; Schubert, U. S. *J. Org.*  
57  
58 *Chem.* **2010**, *75*, 4025-4038. c) Schulze, B.; Escudero, D.; Friebe, C.; Siebert, R.; Görls, H.; Köhn, U.;

- 1  
2  
3  
4  
5 Altuntas, E.; Baumgärtel, A.; Hager, M. D.; Winter, A.; Dietzek, B.; Popp, J.; González, L.; Schubert,  
6 U. S. *Chem. Eur. J.* **2011**, DOI:10.1002/chem.201100045 d) Guthmuller, J.; González, L. *Phys. Chem.*  
7 *Chem. Phys.* **2010**, *12*, 14812-14821. e) Vlcek, A., Jr.; Zalis, S.; *Coord. Chem. Rev.* **2007**, *251*, 258-287.  
8  
9  
10  
11  
12  
13 21. a) Petit, L.; Maldivi, P.; Adamo, C. *J. Chem. Theory Comp.* **2005**, *1*, 953-962. b) Holland, J. P.;  
14 Green, J. C. *J. Comp. Chem.* **2010**, *31*, 1008-1014.  
15  
16  
17  
18 22. Chardon-Noblat, S.; Deronzier, A.; Ziessel, R.; Zsoldos, D. *Inorg. Chem.* **1997**, *36*, 5384-5389.  
19  
20  
21 23. Eskelinen, E.; Haukka, M.; Venäläinen, T.; Pakkanen, T. A.; Wasberg, M.; Chardon-Noblat, S.;  
22 Deronzier, A. *Organometallics*. **2000**, *19*, 163-169.  
23  
24  
25  
26 24. Andrae, D.; Häusermann, U.; Dolg, M.; Stoll, H.; Preuss, H. *Theor. Chim. Acta* **1990**, *77*, 123-  
27 141.  
28  
29  
30  
31  
32 25. a) Pierloot, K.; Dumez, B.; Widmark, P. -O.; Roos, B. O. *Theor. Chim. Acta* **1995**, *90*, 87. b) Roos  
33 B. O.; Lindh, R.; Malmqvist, P. -Å.; Veryazov, A.; Widmark, P. -O. *J. Phys. Chem. A* **2005**, *109*,  
34 6575-6579.  
35  
36  
37  
38  
39 26. a) Hess, B. A. *Phys. Rev. A* **1985**, *32*, 756. b) Hess, B. A. *Phys. Rev. A* **1986**, *33*, 3742. c) Jansen,  
40 G.; Hess, B. A. *Phys. Rev. A* **1989**, *39*, 6016.  
41  
42  
43  
44 27. a) Aquilante, F.; Pedersen, T. B.; Lindh, R.; Roos, B. O.; De Meras, A. S.; Koch, H. *J. Chem.*  
45 *Phys.* **2008**, *129*, 8. b) Aquilante, F.; Malmqvist, P. A.; Pedersen, T. B.; Ghosh, A.; Roos, B. O. *J.*  
46 *Chem. Theory Comp.* **2008**, *4*, 694.  
47  
48  
49  
50  
51  
52 28. Roos, B. O.; Andersson, K.; Fülcher, M. P.; Malmqvist, P. - Å.; Serrano-Andrés, L.; Pierloot, K.;  
53 Merchán, M. Multiconfigurational Perturbation Theory: Applications in 35 Electronic Spectroscopy. In  
54 *Advances in Chemical Physics: New Methods in Computational Quantum Mechanics*; Prigogine, I.,  
55 Rice, S. A., Eds., John Wiley & Sons: New York, 1996; Vol. *XCIII*; pp 219-332.  
56  
57  
58  
59  
60

- 1  
2  
3  
4  
5 29. Pierloot, K. *Molec. Phys.* **2003**, *101*, 2083-2094.  
6  
7  
8 30. Pierloot, K. Calculations of electronic spectra of transition metal complexes. In *Computational*  
9 *Photochemistry*; Olivucci, M., Eds., Elsevier B. V.: Amsterdam 2005; pp 279-315.  
10  
11 31. Finley, J.; Malmqvist, P. -Å.; Roos, B. O.; Serrano-Andrés, L. *Chem. Phys. Lett.* **1998**, *288*, 299.  
12  
13 32. Malmqvist, P. -Å.; Roos, B. O. *Chem. Phys. Lett.* **1995**, *245*, 215.  
14  
15 33. Ghigo, G.; Roos, B. O.; Malmqvist, P. -Å. *Chem. Phys. Lett.* **2004**, *396*, 142.  
16  
17 34. Roos, B. O.; Andersson, K. *Chem. Phys. Lett.* **1995**, *245*, 215.  
18  
19 35. Roos, B. O.; Malmqvist, P. -Å. *Phys. Chem. Chem. Phys.* **2004**, *6*, 2919.  
20  
21 36. a) Becke, A. D. *J. Chem. Phys.* **1993**, *98*, 5648-5652. b) Lee, C. T.; Yang, W. T.; Parr, R. G. *Phys.*  
22 *Rev. B* **1988**, *37*, 785-789.  
23  
24 37. Menucci, B.; Cappelli, C.; Guido, C. A.; Cammi, R.; Tomasi, J. *J. Chem. Phys. A* **2009**, *113*,  
25 3009-3020.  
26  
27 38. Zhao, Y.; Truhlar, D. G. *Theor. Chem. Acc.* **2008**, *215*, 241.  
28  
29 39. Perdew, J. P.; Burke, K.; Ernzerhof, M. *Phys. Rev. Lett.* **1996**, *77*, 3865-3868.  
30  
31 40. a) Cossi, M.; Barone, V.; Menucci, B.; Tomasi, J. *Chem. Phys. Lett.* **1998**, *286*, 253. b) Menucci,  
32 B.; Tomasi, J. *J. Chem. Phys.* **1997**, *106*, 5151.  
33  
34 41 Gaussian 09, Revision **A.1**, Frisch, M. J.; Trucks, G. W.; Schlegel, H. B.; Scuseria, G. E.; Robb,  
35 M. A.; Cheeseman, J. R.; Scalmani, G.; Barone, V.; Mennucci, B.; Petersson, G. A.; Nakatsuji, H.;  
36 Caricato, M.; Li, X.; Hratchian, H. P.; Izmaylov, A. F.; Bloino, J.; Zheng, G.; Sonnenberg, J. L.; Hada,  
37 M.; Ehara, M.; Toyota, K.; Fukuda, R.; Hasegawa, J.; Ishida, M.; Nakajima, T.; Honda, Y.; Kitao, O.;  
38 Nakai, H.; Vreven, T.; Montgomery, Jr., J. A.; Peralta, J. E.; Ogliaro, F.; Bearpark, M.; Heyd, J. J.;



1  
2  
3  
4  
5 Brothers, E.; Kudin, K. N.; Staroverov, V. N.; Kobayashi, R.; Normand, J.; Raghavachari, K.; Rendell,  
6  
7 A.; Burant, J. C.; Iyengar, S. S.; Tomasi, J.; Cossi, M.; Rega, N.; Millam, N. J.; Klene, M.; Knox, J. E.;  
8  
9 Cross, J. B.; Bakken, V.; Adamo, C.; Jaramillo, J.; Gomperts, R.; Stratmann, R. E.; Yazyev, O.; Austin,  
10  
11 A. J.; Cammi, R.; Pomelli, C.; Ochterski, J. W.; Martin, R. L.; Morokuma, K.; Zakrzewski, V. G.; Voth,  
12  
13 G. A.; Salvador, P.; Dannenberg, J. J.; Dapprich, S.; Daniels, A. D.; Farkas, Ö.; Foresman, J. B.; Ortiz,  
14  
15 J. V.; Cioslowski, J.; Fox, D. J. Gaussian, Inc., Wallingford CT, **2009**.

16  
17  
18 42. a) Karlström, G.; Lindh, R.; Malmqvist, P. –Å.; Roos, B. O.; Ryde, U.; Veryazov, V.; Widmark, P.  
19  
20 –O.; Cossi, M.; Schimmelpfennig, P.; Neogrady, P.; Seijo, L. *Computational Material Science*, **2003**,  
21  
22 28, 222. b) Aquilante, F.; De Vico, L.; Ferré, N.; Ghigo, G.; Malmqvist, P. –Å.; Neogrady, P.; Pedersen,  
23  
24 T. B.; Pitonak, M.; Reiher, M.; Roos, B. O.; Serrano-Andrés, L.; Urban, M.; Veryazov, V.; Lindh, R. *J.*  
25  
26 *Comput. Chem.* **2010**, *31*, 224.

27  
28  
29 43 Vallet, V.; Strich, A.; Daniel, D. *Chem. Phys.* **2005**, *311*, 13.

30  
31  
32 44. Daniel, C. *Coord. Chem. Rev.* **2003**, *238-239*, 143-146.

33  
34  
35 45. Rosa, A.; Baerends, E. J.; Gisbergen, S. J. A.; Lenthe, E. V.; Groeneveld, J. A.; Snijders, J. G. *J.*  
36  
37 *Am. Chem. Soc.* **1999**, *121*, 10356.

38  
39  
40 46. a) Serrano-Andrés, L.; Fülcher, M. P. *J. Am. Chem. Soc.* **1998**, *120*, 10912. b) Peach, M. J. G.;  
41  
42 Benfield, P.; Helgaker, T.; Tozer, D. J. *J. Chem. Phys.* **2008**, *128*, 044118.

43  
44  
45 47. a) Peach, M. J. G.; Ruth Le Sueur, C.; Ruud, K.; Guillaume, M.; Tozer, D. J. *Phys. Chem. Chem.*  
46  
47 *Phys.* **2009**, *11*, 4465. b) Plötner, J.; Tozer, D. J.; Dreuw, A. *J. Chem. Theory Comp.* **2010**, *6*, 2315-  
48  
49 2324. c) Jacquemin, D.; Perpète, A.; Scuseria, G. E.; Ciofini, I.; Adamo, A. *Chem. Phys. Lett.* **2008**,  
50  
51 465, 226.

52  
53  
54 48. Fraser, M. G.; Blackman, A. G.; Irwin, G. I. S.; Easton, C. P.; Gordon, K. C. *Inorg. Chem.* **2010**,  
55  
56 49, 5180.

- 
- 1  
2  
3  
4  
5 49. Georgieva, I.; Aquino, A. J. A.; Trendafilova, N.; Santos, P. S.; Lischka, H. *Inorg. Chem.* **2010**,  
6  
7 49, 1634-1646.  
8  
9  
10  
11  
12  
13  
14  
15  
16  
17  
18  
19  
20  
21  
22  
23  
24  
25  
26  
27  
28  
29  
30  
31  
32  
33  
34  
35  
36  
37  
38  
39  
40  
41  
42  
43  
44  
45  
46  
47  
48  
49  
50  
51  
52  
53  
54  
55  
56  
57  
58  
59  
60

5.2 Spectroscopic properties of azobenzene-based pH indicator dyes: a quantum chemical and experimental study

---

**5.2 Spectroscopic properties of azobenzene-based pH indicator dyes: a quantum chemical and experimental study**

Reprinted with permission from Escudero et al. *J. Chem. Theory and Comp.* **2011**, 7, 1062. Copyright 2011 American Chemical Society.

# Spectroscopic Properties of Azobenzene-Based pH Indicator Dyes: A Quantum Chemical and Experimental Study

Daniel Escudero,<sup>†</sup> Sabine Trupp,<sup>‡</sup> Beate Bussemer,<sup>§</sup> Gerhard J. Mohr,<sup>‡</sup> and Leticia González<sup>\*,†</sup>

<sup>†</sup>Institute of Physical Chemistry, Theoretical Chemistry, Friedrich-Schiller University Jena, Helmholtzweg 4, D-07743 Jena, Germany

<sup>‡</sup>Department of Polytronic Systems, Workgroup Sensor Materials, Fraunhofer Research Institution for Modular Solid State Technologies (EMFT), Josef-Engert Strasse 9, D-93053 Regensburg, Germany

<sup>§</sup>Institute of Physical Chemistry, Friedrich-Schiller University Jena, Lessingstrasse 10, D-07743 Jena, Germany

**ABSTRACT:** The UV–visible absorption spectra of six new optical sensors based on acidochromic azobenzenes have been measured and assigned with the help of quantum chemical calculations. The investigated compounds are able to monitor the pH in the range from pH 3–10. Using the hybrid density functional PBE0 and including solvent effects with a polarized continuum model, the agreement between the experimental and theoretical UV/vis spectra of the dyes in their neutral and anionic forms is very good. The spectroscopic  $\pi\pi^*$  states, responsible for the optical properties of the sensors, are described within an accuracy of 0.1 eV. Similar accuracy is demonstrated in the  $n\pi^*$  states. The  $\pi\pi^*$  states can be assigned as a charge transfer from the aromatic  $\pi$  orbital localized in the azo-phenol moiety to the antibonding  $\pi^*$  of the azo group. Under basic conditions, the spectrum is bathochromically shifted and more intense than in acid media. Upon substitution in the phenyl moiety, red- or blue-shifts of the UV–visible bands are observed depending on whether the substituent is electron-donor or -withdrawing, respectively. These effects are stronger at high pH values and can be rationalized in terms of the stabilization and/or destabilization of the involved frontier orbitals.

## 1. INTRODUCTION

The development of pH sensors is a continuous challenge in chemistry.<sup>1</sup> Although the determination of pH with traditional electrochemical sensors is well-established, optical sensors are a valuable alternative where glass electrodes are impractical or impossible to use.<sup>2</sup> Moreover, optical sensors can be more versatile than electrodes, as they are easy and inexpensive to fabricate,<sup>3</sup> and profit from the current advances of optical spectroscopy.

Azobenzene and derivatives have attracted a considerable amount of attention due to their capability to reversibly switch between the cis and trans conformers using two different wavelengths,<sup>4</sup> and therefore their large applicability as molecular devices.<sup>5</sup> They are used as light-driven membranes,<sup>6</sup> as single-molecule optomechanical machines,<sup>7</sup> as media storage,<sup>8</sup> or to control peptide folding.<sup>9</sup> Moreover, because they allow for facile and multiple functionalizations, a wide range of azobenzene-based indicator dyes have been synthesized, initially for detecting alkali, earth alkali, and heavy metal ions,<sup>10</sup> but later also for monitoring electrically neutral and anionic analytes such as alcohols,<sup>11</sup> amines,<sup>12</sup> aldehydes,<sup>13</sup> saccharides,<sup>14</sup> and bisulfite.<sup>15</sup>

Recently, some of us have synthesized new derivatives of 2-hydroxyethylsulfonyl azobenzene (HESAB) indicator dyes with emphasis on measuring the pH in range between 3 and 10.<sup>16</sup> These indicators can be covalently linked to polymers containing hydroxyl functions such as cellulose, polyurethane hydrogel, and hydroxyalkyl methacrylate. Because one of our aims is to design indicator dyes, which exhibit strong color changes in this pH range, the goal of this Article is to present a comprehensive study of the substitution effects on the spectral properties of the corresponding protonated and deprotonated forms of HESAB. In particular, we want to predict whether or not

the absorbance spectra of the phenolic dyes in going from acid to base form (i.e., protonated to deprotonated form) are well separated, thus providing indicator materials whose color changes can be easily distinguished and quantified by optical sensor modules.

To shed some light into the photophysics of the HESAB compounds, which can in turn help to predict the potential use of these dyes as pH indicators, the experimental spectra have been characterized with the help of quantum chemical calculations. While recording absorption spectra can be close to routine, the computation of electronically excited states of large organic dyes with chemical accuracy (less than 0.1 eV) is still a challenging problem in modern quantum chemistry. Currently, time-dependent density functional theory (TD-DFT) is the most extended theoretical tool to compute transition energies and oscillator strengths in organic and inorganic compounds.<sup>17</sup> Although the performance of different functionals may vary depending on the treated systems,<sup>18</sup> it seems that corrected hybrid functionals are best suited to describe the excited states of delocalized aromatic dye systems,<sup>19</sup> and this approach is used here.

## 2. EXPERIMENTAL SECTION

**Sample Preparation.** The six azobenzene dyes (1–6) with their deprotonated forms ( $1^-$ – $6^-$ ) shown in Figure 1 were investigated. The azo function is in para position to the phenol hydroxyl group. Substitution effects are studied by substituting H by two electron donors ( $\text{CH}_3$ ,  $\text{OCH}_3$ ) and/or two electron-withdrawing (F, Br) substituents on the phenyl moiety.

**Received:** December 16, 2010

**Published:** March 09, 2011

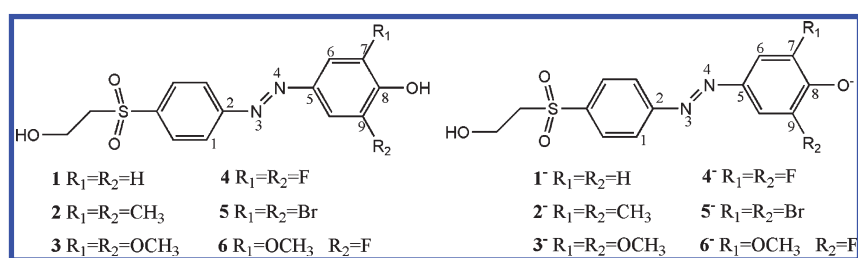


Figure 1. Chemical structure of the 2-hydroxyethylsulfonyl azobenzene dyes here investigated.

Table 1. Main Geometrical Parameters of Gas-Phase-Optimized Compounds 1–6 and 1<sup>-</sup>–6<sup>-</sup><sup>a</sup>

compound	$d_{3-4}^b$	$d_{2-3}^b$	$d_{4-5}^b$	$d_{6-7}^b$	$d_{8-9}^b$	$\alpha_{2-3-4}^c$	$\alpha_{3-4-5}^c$	$\tau_{1-3-4-6}^c$
azobenzene								
RI-BP86/TZVP <sup>d</sup>	1.267	1.417	1.417			114.8	114.8	180
PBE0/TZVP	1.243	1.413	1.413	1.386	1.393	115.1	115.1	180
X-ray <sup>e</sup>	1.247	1.428	1.428	1.384	1.391	114.1	114.1	178.1
1 (PCM-PBE0/TZVP)	1.248	1.413	1.399	1.380	1.401	114.7	116.2	170.5
1 (PBE0/TZVP)	1.271	1.418	1.408	1.390	1.410	114.2	115.4	167.5
2	1.246	1.412	1.402	1.384	1.405	114.5	115.7	163.2
3	1.247	1.410	1.400	1.388	1.404	114.3	115.8	162.3
4	1.244	1.412	1.405	1.377	1.397	114.6	115.2	165.7
5	1.244	1.412	1.405	1.377	1.397	114.6	115.2	165.7
6	1.245	1.412	1.403	1.386	1.392	114.4	115.6	166.2
1 <sup>-</sup> (PCM-PBE0/TZVP)	1.276	1.395	1.361	1.368	1.448	114.0	117.2	178.8
1 <sup>-</sup> (PBE0/TZVP)	1.288	1.377	1.344	1.359	1.459	113.7	117.4	173.1
2 <sup>-</sup> (PCM-PBE0/TZVP)	1.282	1.390	1.357	1.369	1.457	114.0	117.2	178.6
2 <sup>-</sup> (PBE0/TZVP)	1.289	1.376	1.344	1.361	1.465	113.7	117.5	172.9
3 <sup>-</sup>	1.295	1.370	1.339	1.361	1.471	113.8	117.1	172.6
4 <sup>-</sup>	1.283	1.380	1.347	1.355	1.459	113.8	117.1	171.4
5 <sup>-</sup>	1.277	1.386	1.354	1.359	1.466	113.9	117.2	170.9
6 <sup>-</sup>	1.289	1.375	1.343	1.363	1.456	113.9	117.2	171.8

<sup>a</sup>Theoretical and experimental values of *trans*-azobenzene are given for comparison. The corresponding chemical structures with the atom numbering can be found in Figure 1. <sup>b</sup>Distances in angstroms. <sup>c</sup>Angles in degrees. <sup>d</sup>Values obtained under  $C_{2h}$  symmetry constraint from ref 29. <sup>e</sup>Experimental values from ref 28.

The synthesis of the 2-hydroxyethylsulfonyl azo dye **1** was accomplished by diazotation of 2-(4-aminobenzenesulfonyl)-ethanol to phenol in acetic acid. The product was precipitated as fine yellow-orange powder. Yield: 28%. Anal. Calcd for C<sub>14</sub>H<sub>14</sub>N<sub>2</sub>O<sub>4</sub>S (306.34 g/mol): C, 54.89%; H, 4.61%; N, 9.14%; S, 10.47%. Found: C, 54.89%; H, 4.53%; N, 9.10%; S, 10.72%. <sup>1</sup>H NMR (DMSO):  $\delta$  (ppm) 7.85–8.07 (m, 6H, =CH–), 6.98 (m, 2H, =CH–), 3.74 (t, 2H, –CH<sub>2</sub>–), 3.51 (t, 2H, –CH<sub>2</sub>–). Mass spectrometry data (EI):  $m/e$  (%), 306 (38). The synthesis of the 2-hydroxyethylsulfonyl azo dyes **2–6** has been described in detail elsewhere.<sup>13</sup>

**Spectroscopic Measurements.** The absorbance spectra of the dissolved dyes **1–6** were recorded on a Lambda 16 UV–vis spectrometer (Perkin-Elmer) at 20 ± 2 °C. The dyes were dissolved in methanol and mixed with the aqueous buffered solutions in a 1:1 ratio because of the low solubility of the dyes in pure aqueous solution. A wide pH range buffer was used, which was 0.04 M in sodium acetate, 0.04 M in boric acid, 0.04 M in sodium dihydrogen phosphate, and 0.1 M in sodium sulfate. The pH was adjusted in a way that exclusively the neutral or the anionic form of the dyes was observed.

### 3. COMPUTATIONAL DETAILS

For the sake of computational ease, the 2-hydroxyethyl function was replaced by a methyl group in all of the calculations (see Figure 1). The resulting geometries were optimized in the *trans* configuration using the global hybrid functional PBE0<sup>20</sup> in combination with a polarized valence triple- $\zeta$  basis set (TZVP) for all atoms. The nature of the stationary points was confirmed by calculating the Hessian at the same level of theory. The calculation of the transition energies and oscillator strengths was done with the same functional. With 25% of exact Hartree–Fock exchange, PBE0 was chosen because it delivers excitation energies with mean absolute errors of 0.14 eV for organic dyes.<sup>19b</sup> The effect of the methanol environment on the excitations energies was modeled with the polarized continuum model (PCM)<sup>21</sup> and  $\epsilon = 32.6$ . For reference, the UV spectrum of the unsubstituted compounds **1/1<sup>-</sup>** is also calculated using correlated ab initio second-order approximated coupled-cluster theory<sup>22</sup> in the resolution of the identity approximation (RI-CC2)<sup>23</sup> and the pure functional BP86<sup>24,25</sup> also within RI approximation. The effect of the solvent on the geometries was also investigated at the PBE0 level of theory. RI-BP86 and

**Table 2.** UV/Vis Experimental Data of HESAB Compounds 1–6 under Acid and Basic Conditions (pH Is Also Given) Measured in Buffered Methanol ( $v/v = 1:1$ )<sup>a</sup>

	1 $\lambda_{\max}$	2 $\lambda_{\max}$	3 $\lambda_{\max}$	4 $\lambda_{\max}$	5 $\lambda_{\max}$	6 $\lambda_{\max}$
acid	pH = 3.52 456, 361 (2.72, 3.44)	pH = 3.17 373 sh, 427 (3.32 sh, 2.91)	pH = 4.16 460 sh, 395 (2.70 sh, 3.14)	pH = 3.19 355 (3.49)	pH = 3.19 354 (3.50)	pH = 3.16 374 (3.32)
basic	pH = 11.08 460 (2.70)	pH = 11.28 499 (2.49)	pH = 10.83 525 (2.36)	pH = 11.44 444 (2.79)	pH = 11.54 460, 292 (2.70, 4.25)	pH = 11.28 487(2.55)

<sup>a</sup> Maximum absorption peaks and most relevant shoulders (sh) in nm and in eV in parentheses.

**Table 3.** Molar Extinction Coefficients of the Dyes in Pure Methanol<sup>a</sup>

	$\epsilon$ [L mol <sup>-1</sup> cm <sup>-1</sup> ]		$\lambda_{\max}$ neutral form [nm]	$\lambda_{\max}$ anionic form [nm]
	neutral form	anionic form		
1/1 <sup>-</sup>	27 300	27 700	364	441
2/2 <sup>-</sup>	24 190	29 240	373	498
3/3 <sup>-</sup>	18 890	36 090	396	522
4/4 <sup>-</sup>	25 200	30 000	354	440
5/5 <sup>-</sup>	14 430	21 740	354	452
6/6 <sup>-</sup>	19 740	30 730	375	485

<sup>a</sup> The neutral form was obtained by addition of 100  $\mu$ L of 0.1 M hydrochloric acid, while the anionic form was obtained by addition of 100  $\mu$ L of triethylamine.

RI-CC2 calculations were performed with the TURBOMOLE.5.10 program package,<sup>26</sup> while the rest of calculations were performed with Gaussian 03.<sup>27</sup>

## 4. RESULTS AND DISCUSSION

**Structure of Azo-vinyl Sulfonyl Dyes.** The most relevant geometrical parameters of the studied compounds 1–6 and corresponding anions are collected in Table 1. For the sake of comparison, azobenzene in the *trans*-conformation is also included. The low-lying excited states of azobenzene (and derivatives) involve the antibonding orbital located in the N=N bond; therefore, it is important to describe this bond length properly. Experimentally, the N=N distance of azobenzene is 1.247 Å.<sup>28</sup> Hättig et al. showed that triple- $\zeta$  basis sets are indispensable for an accurate description of this bond.<sup>29</sup> It has been estimated that RI-BP86/TZVP level of theory delivers bond distances in azobenzene ca. 0.001 Å larger than MP2 but very similar to the crystal structure.<sup>29</sup> As we see in Table 1, RI-BP86/TZVP overestimates the N=N bond ( $d_{3-4}$ ) by ca. 0.02 Å. Interestingly, the result of the hybrid functional PBE0 (1.243 Å) is in much better agreement with the X-ray distance. The adjacent N–C bonds ( $d_{2-3}$  and  $d_{4-5}$ ) are underestimated by both BP86 and PBE0 by ca. 0.01 Å. Despite being noticeable, these discrepancies are within the error bar of the experiment.<sup>28</sup>

In view of the previous results and because no X-ray structures are available for HESAB derivatives to compare, we shall consider 0.01 Å as the error bar for the geometries of the HESAB compounds obtained with PBE0/TZVP. The N=N bond in the unsubstituted HESAB compound 1 is larger than in azobenzene and further destabilized upon deprotonation. Interestingly, when the solvent is included in the optimization (PCM-PBE0 values), the azo bond ( $d_{3-4}$ ) is compressed in the neutral and anionic forms, while the bonds nearby ( $d_{2-3}$  and  $d_{4-5}$ ) are

almost unaffected in the neutral form but stretched by ca. 0.02 Å in the anion.

The changes in the bond angles are negligible in both neutral and ionic forms (see  $\alpha$  values in Table 1). In contrast, the planarity of these compounds deserves some attention. Despite some controversy,<sup>30</sup> nowadays it seems well-accepted that azobenzene is planar in the gas phase, as suggested by early X-ray experiments<sup>28</sup> and confirmed by accurate MP2 calculations.<sup>29,31</sup> Simple substituted 4,4'-azobenzene derivatives are also planar at both MP2 and DFT levels of theory if the basis set is sufficiently large. On the contrary, if a smaller basis set, that is, MP2/6-31+G(d) level of theory is used, significantly twisted geometries, with a dihedral angle of ca. 20°, are predicted.<sup>30</sup> The dyes investigated here are twisted by ca. 15° (see dihedral  $\tau_{1-3-4-6}$  in Table 1). Because we employ the flexible TZ basis set, we are confident that the nonplanarity of HESAB systems in vacuum is physical and due to the bulky nature of the substituents. We note that the frequencies corresponding to the out-of-plane motion of the rings are very small (e.g., 62 and 105 cm<sup>-1</sup> in compound 1 and of similar magnitude or even smaller in the other neutral species), increasing the possibility that nonplanar geometries contribute to the experimental absorption spectrum (see below). Worth mentioning is that a certain degree of planarity is recovered upon deprotonation and that the 1/1<sup>-</sup> and 2<sup>-</sup> optimized structures in the presence of solvent are slightly more planar than in the gas phase (see Table 1). These effects are especially important to address properly the  $n\pi^*$  excitations of HESAB compounds, as we shall discuss below.

The rest of the compounds have been optimized only at the PBE0/TZVP level of theory. In the neutral HESAB, the calculated values for N=N and adjacent C–N bonds (now asymmetric), as well as the angle between them, are very similar to those of azobenzene (see Table 1). Both the electron donor (2 and 3) and the electron acceptor (4 and 5) substituents have little effect on the geometry of the neutral (or the anionic) HESAB. However, there are interesting changes upon deprotonation. In the phenolate form, a strong resonance effect through the conjugated system can be observed, which strongly influences the geometry in two ways: On the one hand, the N=N bond is activated, see that the distance of the azo moiety is enlarged in comparison to the neutral forms by 0.03–0.05 Å, and, on the other hand, the aromaticity of the ring decreases, see the different alternate C–C distances of the phenyl group. Also significant is that the planarity of the HESAB increases in the anionic forms. For instance, in the neutral form 3 the dihedral angle  $\tau_{1-3-4-6}$  is 17.4°, while in 3<sup>-</sup> it decreases to 6.8°.

**UV–Visible Absorption Spectroscopy.** Experimentally, the UV/vis spectra of these compounds (with 2-hydroxyethyl moieties, vide supra) are recorded in methanol/buffer (1:1) of different pH values. The experimental maximum absorption peaks of compounds 1–6 at specific pH values measured in buffered aqueous methanol are collected in Table 2, and the molar extinction coefficients in pure methanol solutions are given in Table 3.

Before discussing the assignment of the different spectra based on quantum chemical calculations, it is worth reviewing the spectrum of azobenzene, which has been the subject of extensive studies.<sup>29–32</sup> In the gas phase, the absorption spectrum is characterized by a weak  $n\pi^*$  transition at 2.82 eV (440 nm) followed by a strong  $\pi\pi^*$  state peaking at 4.12 eV (301 nm).<sup>33</sup> CC2 calculations deliver values of 2.84 and 4.04 eV, respectively, in very good agreement with the experimental values.<sup>29</sup> The employment of TD-DFT in azobenzene and derivatives is, however, not straightforward. Charge transfer (CT) states are typically very much underestimated due to the wrong long-range behavior of the applied standard exchange-correlation functionals.<sup>34</sup> Several strategies have emerged to consider long-range effects. For instance, range-separated functionals where the total exchange energy is split into short- and long-range contributions have been developed; examples of these functionals are LC-wB97,<sup>35</sup> LC-wB97XD,<sup>36</sup> or CAM-B3LYP.<sup>37</sup> Another possibility is to use hybrid functionals where the exact Hartree–Fock exchange is modified; an illustration is the PBE0 functional, which contains 25% of exact HF exchange. As expected, pure functionals deliver rather poor values in azobenzene. RI-BP86/aug-TZVP predicts the two transitions of azobenzene at 2.19 and 3.35 eV; that is, both bands are underestimated by more than 0.5 eV.<sup>29</sup> The hybrid functional B3LYP red-shifts experimental values to a lesser extent, but it still accounts for errors of 0.3–0.4 eV.<sup>29,30</sup> The systematic study of Jacquemin and co-workers for solvated azobenzene shows that among a large amount of GGA, meta-GGA, conventional hybrids, and the recently developed range-separated hybrid functionals, the PBE0 and CAM-B3LYP functionals give a quantitative agreement on the spectroscopic state of some selected substituted azobenzenes.<sup>19b</sup> In combination with solvent via the PCM algorithm, mean absolute errors of 0.14 eV for CT in organic dyes, including azobenzene, have been obtained with the PBE0 functional.<sup>19b</sup> These results are even better than the ones obtained with range-separated hybrids. Recently, Tozer et al. have investigated the relationship between the excitation energy errors and the spatial overlap between the orbitals involved in the excitation, concluding that errors are large when the overlap is low.<sup>38</sup> In CT situations where no overlap between the involved orbitals in the CT state is observed, they strongly recommend the use of range-separated functionals, like the CAM-B3LYP functional.<sup>39</sup> In azobenzene and the herein studied HESAB dyes, the orbitals involved in the spectroscopic CT excitation should show a high-overlap due to conjugation over the rings (see Figure 2). In such cases, hybrid functionals with augmented amount of exact exchange, like PBE0, can deliver very accurate values because excitations with local character are also present, in agreement with ref 19b.

In the following, we shall investigate first the unsubstituted HESAB system using different protocols for reference. Table 4 collects the excitation energies, oscillator strengths, and the corresponding assignment of the most important peaks of the absorption spectra of the neutral and ionic HESAB model compounds ( $1/1^-$ ) using RI-CC2, BP86, and PBE0 using different geometries, as specified. Figure 3a shows the experimental spectrum of **1** at pH = 3.52 and at pH = 11.08. At these pH values, the neutral (**1**) or the anionic ( $1^-$ ) form is expected to be predominant, respectively, because the p*K* of **1** in methanol/buffer is 8.35 (in plain buffer, the p*K*<sub>a</sub> is 7.64). Figure 3b–f displays the spectrum of **1** and  $1^-$  at different levels of theory. In Figure 2, the corresponding frontier orbitals are displayed. As we can see, these are very similar for the neutral and ionic forms. The

HOMO–1 of both anionic and neutral compounds  $1/1^-$  corresponds to the  $n_N$ , the HOMO is a  $\pi$  orbital delocalized mainly in the azo moiety and the phenol moiety, and the LUMO orbital is the antibonding counterpart.

As in azobenzene, the lowest singlet excitation of **1** corresponds to a weak  $n\pi^*$  state, followed by a strong  $\pi\pi^*$  state. This is predicted by all of the computational approaches but the intensity of the  $n\pi^*$  state is underestimated by all theories. In the following and for the sake of clarity, theoretical predictions will be denoted by  $eV_t$  (or  $nm_t$ ) and experimental data by  $eV_e$  ( $nm_e$ ). The most accurate RI-CC2/TZVP method (Figure 3b) obtain excitations at 2.85  $eV_t$  (435  $nm_t$ ) and 3.82  $eV_t$  (325  $nm_t$ ) for the  $S_1$  ( $n\pi^*$ ) and  $S_2$  ( $\pi\pi^*$ ) states, respectively. The  $\pi\pi^*$  state involves an electronic transition from the HOMO to the LUMO, that is, a CT from the azo-phenol moiety to the azo function (see Figure 2). The  $S_2$   $\pi\pi^*$  state, measured at ca. 3.4  $eV_e$  (360  $nm_e$ ), is overestimated with RI-CC2 by 0.4 eV probably due to the exclusion of the solvent. The use of a pure functional leads to a similar but opposite error: RI-BP86 predicts the  $S_2$   $\pi\pi^*$  state at 3.07  $eV_t$ , that is, underestimated by 0.4 eV with respect to the experiment (Table 4 and Figure 3c). This shift is reversed with the hybrid functional PBE0 (see Figure 3d), hence predicting a blue-shifted peak with an error of ca. 0.15 eV. The inclusion of solvent effects, only in the calculation of the excitation energies (Figure 3e) or both in the geometry and in the energies (Figure 3f), leads to values around 3.3  $eV_t$ . The  $\pi\pi^*$  state is then only blue-shifted with respect to the experiment by 0.1 eV. Because the differences in both latter procedures are not significant, the prescription PCM-PBE0//PBE0, that is, including the solvent only in the calculation of the energies but on vacuum geometries, seems to be a reasonable one to calculate the spectra of the substituted compounds.

The spectrum of  $1^-$  is characterized by a strong band peaking at 2.7  $eV_e$  (460  $nm_e$ ). This band corresponds to the  $\pi\pi^*$  state, and depending on the computational approach, it is preceded, followed, or embedded into two low-lying very weak  $n\pi^*$  transitions. With RI-CC2, the  $S_1$  corresponds to the intense HOMO→LUMO  $\pi\pi^*$  transition, calculated at 2.59  $eV_t$  (479  $nm_t$ ) and therefore with an error of ca. 0.1 eV. The  $S_2$  and  $S_3$  are excitations from the  $n_O$  and  $n_N$ , respectively, to the LUMO, at 2.85  $eV_t$  (435  $nm_t$ ) and 2.99  $eV_t$  (415  $nm_t$ ). With RI-BP86, the  $S_3$  at 2.68  $eV_t$  (464  $nm_t$ ) is responsible for the intense  $\pi\pi^*$  band, and the two  $n\pi^*$  states are below, clearly underestimated with respect to the RI-CC2 values. Even if the RI-BP86 result for the  $\pi\pi^*$  peak is in very close agreement with the experiment, one should keep in mind that solvent effects are not included, and hence this agreement is fortuitous. The use of the hybrid PBE0 functional intercalates the  $\pi\pi^*$  state at 2.91  $eV_t$  (426  $nm_t$ ) between the  $n\pi^*$  states. When taking into account solvent effects without and with solvent during the optimizations (Figure 3e,f and Table 4), this transition is red-shifted, appearing at ca. 2.8  $eV_t$  (~440  $nm_t$ ), in reasonable agreement with the experimental absorption maximum.

The description of the  $n\pi^*$  states deserves additional attention. It has been previously observed that typical global hybrids such as B3LYP or PBE0 show mean absolute errors similar to those of range-separated functionals, like CAM-B3LYP, in small organic dyes.<sup>40</sup> In solvated substituted azobenzenes, it has been shown that CAM-B3LYP outperforms other functionals, delivering minimum absolute errors as small as 0.02 eV for excitation energy of the  $n\pi^*$  state.<sup>32</sup> Acceptable residual discrepancies (<0.2 eV) are obtained with the global hybrid PBE0 in the same

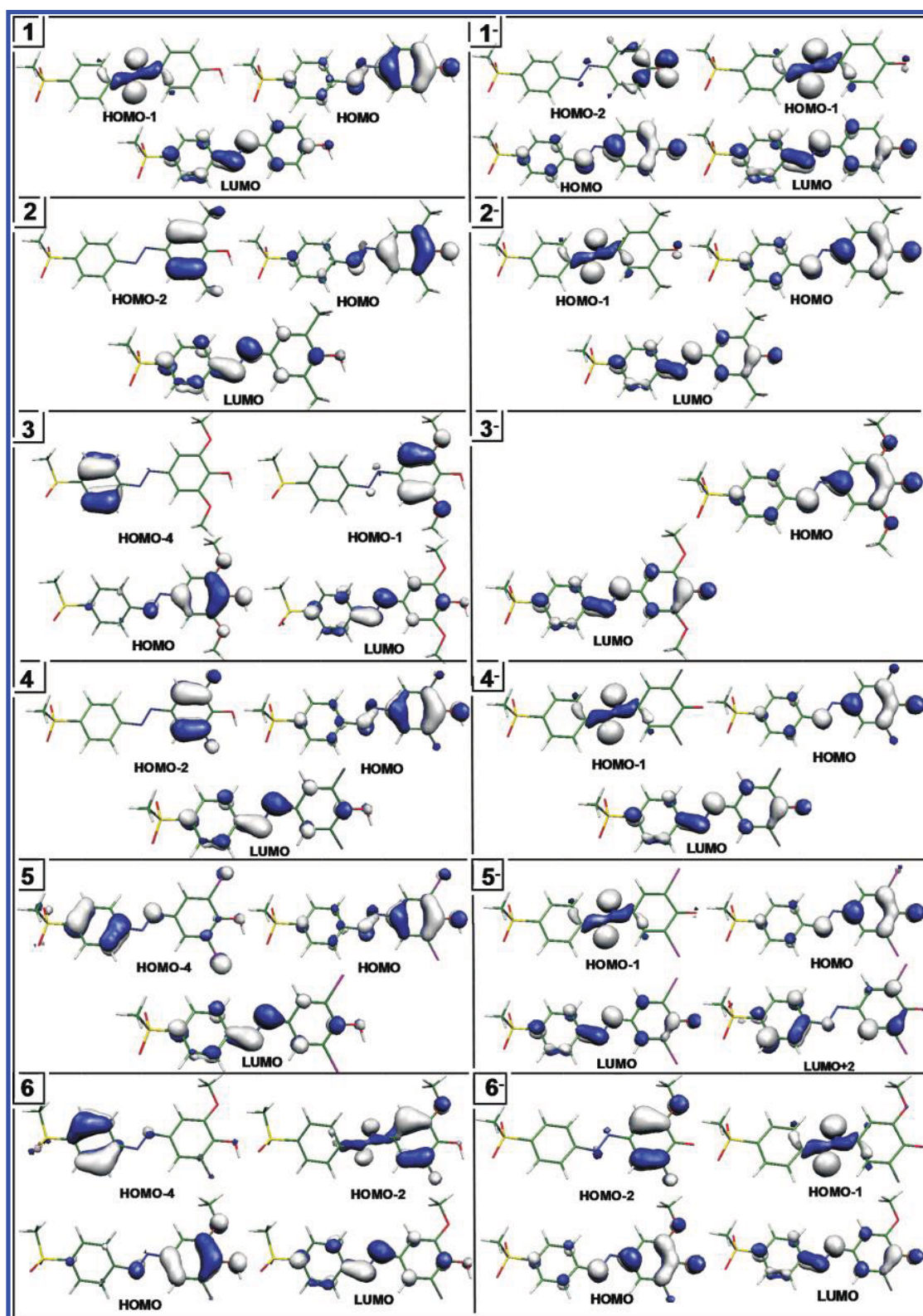


Figure 2. Kohn–Sham frontier orbitals involved in the main electronic transitions of  $1/1^-$  to  $6/6^-$  HESAB compounds.

compounds.<sup>32</sup> In our HESAB compound **1**, the  $n\pi^*$  state is responsible for the less intense band centered at 2.72 eV<sub>e</sub> (456 nm<sub>e</sub>); see Table 2. It is likely that the  $n\pi^*$  state in compound

$1^-$  is masked under the broad and intense  $\pi\pi^*$  band; therefore, we shall limit our discussion to the energies of compound **1**. The best agreement for the  $n\pi^*$  state is obtained with the accurate RI-



**Table 4.** Low-Lying Theoretical Electronic Transition Energies,  $\Delta E$  (in eV and nm), with Oscillator Strengths,  $f$ , and Main Assignment (Configuration Interaction Coefficient) for Compounds **1** and Its Corresponding Anion **1**<sup>−</sup>

<b>1</b>					<b>1</b> <sup>−</sup>				
state	$\Delta E$		$f$	assignment/ $c$	state	$\Delta E$		$f$	assignment
	eV	nm				eV	nm		
(RI-CC2//RI-BP86)					(RI-CC2//RI-BP86)				
S <sub>1</sub>	2.85	435	0.017	n <sub>N</sub> − $\pi^*$ (0.92)	S <sub>1</sub>	2.59	479	1.100	$\pi$ − $\pi^*$ (0.94)
S <sub>2</sub>	3.82	325	0.999	$\pi$ − $\pi^*$ (0.94)	S <sub>2</sub>	2.85	435	0.098	n <sub>O</sub> − $\pi^*$ (0.73)
S <sub>3</sub>					S <sub>3</sub>	2.99	415	0.059	n <sub>N</sub> − $\pi^*$ (0.79)
(RI-BP86//RI-BP86)					(RI-BP86//RI-BP86)				
S <sub>1</sub>	2.20	562	0.013	n <sub>N</sub> − $\pi^*$ (0.94)	S <sub>1</sub>	2.01	618	0.001	n <sub>O</sub> − $\pi^*$ (0.95)
S <sub>2</sub>	3.07	403	0.775	$\pi$ − $\pi^*$ (0.92)	S <sub>2</sub>	2.15	578	0.010	n <sub>N</sub> − $\pi^*$ (0.94)
S <sub>3</sub>					S <sub>3</sub>	2.68	464	1.100	$\pi$ − $\pi^*$ (0.92)
(PBE0//PBE0)					(PBE0//PBE0)				
S <sub>1</sub>	2.62	473	0.012	n <sub>N</sub> − $\pi^*$ (0.80)	S <sub>1</sub>	2.65	468	0.086	n <sub>N</sub> − $\pi^*$ (0.57)
S <sub>2</sub>	3.59	345	0.922	$\pi$ − $\pi^*$ (0.79)	S <sub>2</sub>	2.91	426	1.210	$\pi$ − $\pi^*$ (0.51)
S <sub>3</sub>					S <sub>3</sub>	3.05	406	0.008	n <sub>O</sub> − $\pi^*$ (0.68)
(PCM-PBE0//PBE0)					(PCM-PBE0//PBE0)				
S <sub>1</sub>	2.62	473	0.032	n <sub>N</sub> − $\pi^*$ (0.62)	S <sub>1</sub>	2.66	465	0.318	n <sub>N</sub> − $\pi^*$ (0.57)
S <sub>2</sub>	3.29	377	1.027	$\pi$ − $\pi^*$ (0.60)	S <sub>2</sub>	2.85	435	1.062	$\pi$ − $\pi^*$ (0.51)
S <sub>3</sub>					S <sub>3</sub>	3.59	345	0.000	n <sub>O</sub> − $\pi^*$ (0.68)
(PCM-PBE0//PCM-PBE0)					(PCM-PBE0//PCM-PBE0)				
S <sub>1</sub>	2.62	473	0.006	n <sub>N</sub> − $\pi^*$ (0.65)	S <sub>1</sub>	2.71	457	0.002	n <sub>N</sub> − $\pi^*$ (0.66)
S <sub>2</sub>	3.35	370	1.056	$\pi$ − $\pi^*$ (0.67)	S <sub>2</sub>	2.82	439	1.318	$\pi$ − $\pi^*$ (0.51)
S <sub>3</sub>					S <sub>3</sub>	3.58	346	0.000	n <sub>O</sub> − $\pi^*$ (0.68)

CC2 method (2.85 eV<sub>i</sub>) and with the global hybrid PBE0 functional (2.62 eV<sub>i</sub>). The inclusion of solvent effects on the calculation of the vertical excitations and on the optimized geometries has no effect on the energy of the n $\pi^*$  excitation (see Table 4). This negligible effect is in agreement with the small shifts that have been observed for other substituted azobenzene dyes when comparing gas-phase and solvated results.<sup>30</sup> The intensities of the n $\pi^*$  bands, however, are different depending on the protocol. The oscillator strengths of the n $\pi^*$  states of compounds **1** and **1**<sup>−</sup> are higher with PCM-PBE0//PBE0 than with the PBE0/PBE0 model or PCM-PBE0//PCM-PBE0 (see Table 4), and hence PCM-PBE0//PBE0 reproduces best the experimental evidence (see Figure 3e). As a consequence a broader  $\pi\pi^*$  band for compound **1**<sup>−</sup> is observed with the PCM-PBE0//PBE0 protocol than with the other approaches (compare Figure 3e with d and f). The increase of n $\pi^*$  intensity is due to electrostatic effects, because, for instance, the mixing of the n $\pi^*$  with the  $\pi\pi^*$  state for compound **1**<sup>−</sup> is the same with PCM-PBE0//PBE0 and PBE0//PBE0, and thus an increased absorption due to mixing with the strong  $\pi\pi^*$  excitation can be ruled out (see wave function coefficients of S<sub>1</sub> in Table 4). A more likely explanation roots to the geometry of the compounds. As we stated above, when considering bulk solvent effects on the optimization of the geometries, slightly more planar optimized structures are obtained. This planarization affects strongly the intensity of the n $\pi^*$  states of **1** and **1**<sup>−</sup> (compare exemplarily the S<sub>1</sub> oscillator strength values of **1**<sup>−</sup> with the PCM-PBE0//PBE0 and PCM-PBE0//PCM-PBE0 theoretical models). For the latter procedure, a purer n $\pi^*$  state is obtained, which might contribute to the enormous decreasing of the intensity. Focusing only on the intensities of the n $\pi^*$  state, it is surprising that the agreement with the experiment is better with PCM-PBE0//PBE0 rather than with the PCM-PBE0//PCM-PBE0 model. A plausible explanation for this fact might be the flat nature of the potential

energy surface in the vicinity of the planarization region, as suggested by the geometric controversy with the different theoretical approaches. To address this geometrical effect and its consequent effects on the intensities of the n $\pi^*$  state, molecular dynamic simulations evaluating the temperature effects on the UV/vis electronic spectrum might be appropriate, as has been done in *trans*-stilbene.<sup>41</sup>

Summarizing, the experimental spectra (Figure 3a) agree reasonably well with those obtained with PCM-PBE0//PBE0 (Figure 3e). The main band of **1** is theoretically blue-shifted by ca. 15 nm, and the one of **1**<sup>−</sup> is red-shifted by 25 nm (see Table 4). Yet, it is fair to mention that the theoretical peaks of **1** and **1**<sup>−</sup> at 377 and 435 nm<sub>t</sub> agree much better with the peaks obtained in pure methanol at 364 and 441 nm<sub>e</sub> (see Table 3). Therefore, we can infer that the differences between theory and experiment are mainly due to the fact that while the experimental data in Table 4 and Figure 3 are obtained in a buffered 1:1 water/methanol solutions, theory considers only pure methanol as a solvent.

As a general remark, we can conclude that in both the experimental and the theoretical spectra, a strong red (bathochromic) shift can be observed in the band of the anionic form of the dye with respect to the neutral form. This shift can be easily rationalized looking at the responsible transitions in both neutral and anionic forms (cf., Table 4). The involved orbitals, the HOMO/LUMO of the neutral and the anion, exhibit a similar conjugated  $\pi$  character but a different electronic redistribution (Figure 2). Thus, the bands in **1** and **1**<sup>−</sup> have origin in frontier orbitals of similar character but with different energies. Because of additional electrostatic repulsion with the negative charge in **1**<sup>−</sup>, all occupied orbitals are shifted to higher energies, leading to smaller occupied-virtual gaps with respect to **1**, and therefore red-shifted peaks are obtained for the HOMO→LUMO  $\pi\pi^*$  transitions. This is responsible for the

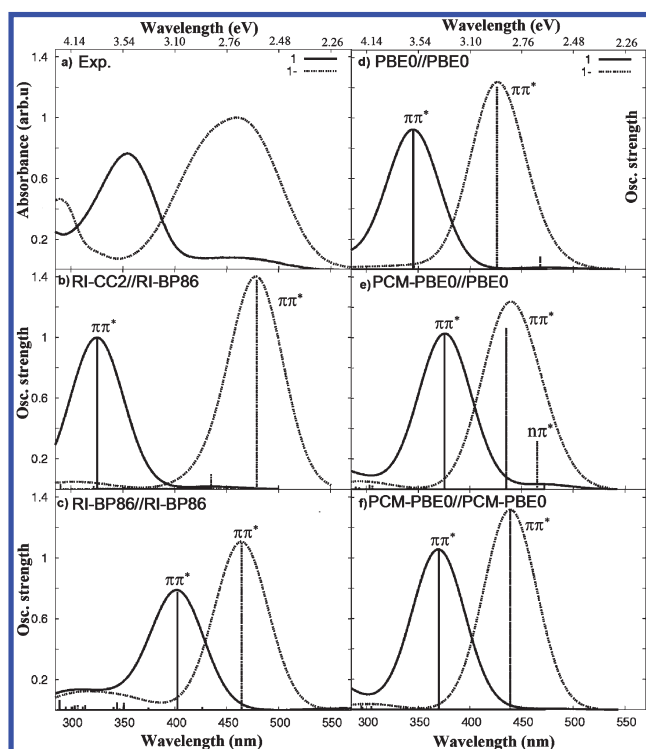


**Figure 3.** UV-vis absorption spectra of **1** (solid) and **1<sup>-</sup>** (dashed). (a) Experimental spectrum normalized to 1 in arbitrary units, (b) RI-CC2//RI-BP86, (c) RI-BP86//RI-BP86, (d) PBE0//PBE0, (e) PCM-PBE0//PBE0, and (f) PCM-PBE0//PCM-PBE0. The theoretical spectra are convoluted with a Lorentzian function with a full width at half-maximum (fwhm) of 60 nm; the corresponding transitions are marked with vertical lines.

different color of both forms (neutral and anionic) and consequently allows for this compound being used as an indicator (see Table 2).

To conclude, because the spectroscopic states ( $\pi\pi^*$ ), as well as the  $n\pi^*$  states of the pair **1/1<sup>-</sup>** are well described with the PCM-PBE0/PBE0 model, this level of theory will be employed to study the HESAB compounds **2/2<sup>-</sup>**–**6/6<sup>-</sup>**.

**Substitution Effects in the UV-Vis Spectra.** Having analyzed the basic spectral properties of the neutral and anionic forms of the reference compound **1** with respect to the bare azobenzene, we now proceed to evaluate how the electronic transitions are modulated by substitution on the phenol moiety. The corresponding spectra for the HESAB species with electron donor (**2/2<sup>-</sup>** and **3/3<sup>-</sup>**), electron acceptor (**4/4<sup>-</sup>** and **5/5<sup>-</sup>**), and both electron-donor and electron-acceptor (**6/6<sup>-</sup>**) substituents are shown in Figure 4. The main electronic transitions are collected in Table 5, and selected orbitals are found in Figure 2.

As stated above, the substituents influence not only the  $pK_a$  value<sup>16</sup> but also the spectral properties, altering the isosbestic point that appears between both anionic and neutral forms in the UV-vis spectrum, and in turn determining to which extent these compounds can be used as indicators. Even if both methyl and methoxy groups donate charge to the aromatic ring, the spectra of **2/2<sup>-</sup>** and **3/3<sup>-</sup>** are different (compare Figure 4a and b). The maximum absorption peaks of **2/2<sup>-</sup>** are separated by 126 nm<sub>e</sub>, while this gap is considerably reduced in the pair **3/3<sup>-</sup>**, showing partially overlapping bands and an isosbestic point less defined.

The main changes are in the spectra of **2** and **3**, while the spectra of **2<sup>-</sup>** and **3<sup>-</sup>** are only shifted by 26 nm<sub>e</sub>. In the dimethyl compound (**2**), the bright  $S_2$  state located at 374 nm<sub>e</sub> corresponds to an HOMO→LUMO  $\pi\pi^*$  excitation from the azo and phenol moieties to the  $\pi^*$  orbital, this transition being analogous to the one found in **1**. Additionally, a less intense  $\pi\pi^*$  transition contributes to the tail of the band at higher energies ( $S_3$  state, see Table 5). In the dimethoxy compound (**3**), on the other hand, at least two  $\pi\pi^*$  states ( $S_2$  and  $S_3$ ) contribute to the broad band peaking at 460 nm<sub>e</sub>. Presumably the wide profile of the band is due to the  $S_3$  state, which theoretically is determined at 362 nm<sub>e</sub>. An additional intense transition corresponding to the  $S_5$  contributes to the near-UV spectrum; this is an HOMO-4→LUMO excitation from a  $\pi$  orbital localized in the phenyl moiety to  $\pi^*_{\text{azo}}$  (see Figure 2). Note that in the case of **3** there is a stabilization of the  $n_N$  orbital (HOMO-2). This different behavior obeys the electronic effects: the methoxy group is more electron-donating than the methyl group and hence destabilizes to a major extent the localized and delocalized  $\pi$  orbitals, HOMO-1 and HOMO, respectively, of **3**. Accordingly, these orbitals correspond to HOMO-2 and HOMO, in compound **2**. Consequently, the HOMO→LUMO,  $\pi\pi^*_{\text{azo}}$  transition at 403 nm<sub>e</sub> is red-shifted with respect to **2** (compare with 374 nm<sub>e</sub> in **2**).

The agreement between the experimental and theoretical spectra for the pairs **2/2<sup>-</sup>** and **3/3<sup>-</sup>** is reasonable, with general blue-shifts from theory to experiment (Figure 4). The spectrum of **2** is simpler and similar to that of the unsubstituted compound **1**. Likewise, the spectra of the anionic compounds (**2<sup>-</sup>** and **3<sup>-</sup>**) resemble the spectra of **1<sup>-</sup>**. They are both characterized by a strong peak, experimentally located at 499 and 525 nm<sub>e</sub>, and theoretically blue-shifted at 456 nm<sub>e</sub> and 484 nm<sub>e</sub>, respectively. In **2<sup>-</sup>**, both  $S_1$  and  $S_2$  states contribute almost equally to the main band, which then can be assigned as a mixture of the  $\pi\pi^*_{\text{azo}}$  and  $n\pi^*_{\text{azo}}$  electronic excitations (Table 4). On the contrary, in compound **3<sup>-</sup>**, this peak is due to the  $S_1$  state, which is a HOMO→LUMO transition, localized in the  $\pi\pi^*_{\text{azo}}$  orbitals, as in **1<sup>-</sup>**.

The  $n\pi^*$  transitions in **2/2<sup>-</sup>** and **3/3<sup>-</sup>** are very similar to those encountered in the unsubstituted pair **1/1<sup>-</sup>** and show similar trends in terms of oscillator strengths (rather small in **2**, **3**, and **3<sup>-</sup>**). As in the pair **1/1<sup>-</sup>**, the  $n\pi^*$  transitions are red-shifted upon deprotonation. These effects will also appear in the electron-withdrawing substituted compounds (vide infra). Experimentally, the band of **2** shows a shoulder centered at 427 nm<sub>e</sub>, which is most likely due to the  $n\pi^*$  transition (466 nm<sub>e</sub>). The intensity of this transition is theoretically underestimated. Interestingly, in **2<sup>-</sup>**, where the  $n\pi^*$  transition is mixed with the  $\pi\pi^*$  transition (recall  $S_1$  and  $S_2$  in Table 5), higher oscillator strengths are obtained due to this mixing. To investigate whether this mixing changes when solvent effects are included in the optimization, which redounds in a more planar geometry (vide supra), and whether energies can be improved, test calculations in **2<sup>-</sup>** have been performed with the PCM-PBE0//PCM-PBE0 approach. The resulting energies and oscillator strengths are also included in Table 5 in brackets. As we can see, the mixing between the  $n\pi^*$  and  $\pi\pi^*$  transitions is slightly reduced (as we saw in the pair **1/1<sup>-</sup>**), rendering different oscillator strengths: a smaller/larger value for the  $S_1/S_2$  states, respectively. However, the solvent effect does not improve substantially the energies, although a slight shift toward the experimental values is obtained.

The neutral forms **4** and **5** show a broad band peaking at 355 and 354 nm<sub>e</sub>, respectively (cf., Table 2). As in the previous cases,

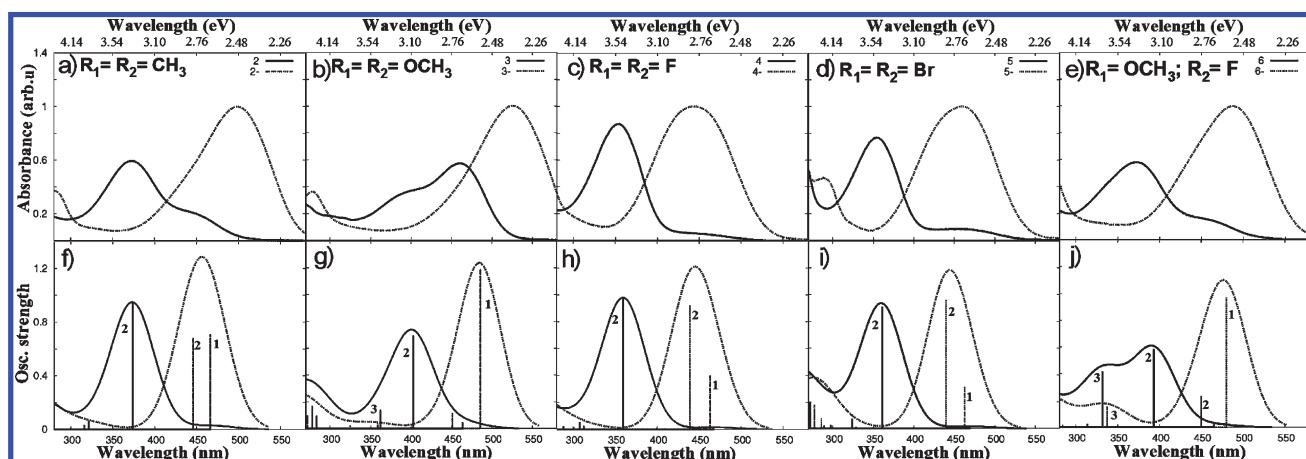


Figure 4. Experimental (top) and PCM-PBE0//PBE0 (bottom) spectra of neutral (solid) and anionic (dashed) compounds. The theoretical spectra are convoluted with a Lorentzian function with a full width at half-maximum (fwhm) of 60 nm; the transitions are marked with vertical lines indicating the corresponding singlet excited state.

Table 5. PCM-PBE0//PBE0 Calculated Electronic Excited States of Compounds 2–6 and Corresponding Anions<sup>a</sup>

state	$\Delta E$	$f$	assignment	state	$\Delta E$	$f$	assignment
2							
$S_1$	2.66(466)	0.029	H-1→L (0.62) $n_N-\pi^*$	$S_1$	2.66(466) [2.71(457)] <sup>b</sup>	0.709 [0.357]	H-1→L (-0.45) $n_N-\pi^*$ H→L (0.45) $\pi-\pi^*$ [H-1→L (0.57) $n_N-\pi^*$ ] [H→L (-0.31) $\pi-\pi^*$ ]
$S_2$	3.32(374)	0.940	H→L (0.61) $\pi-\pi^*$	$S_2$	2.78(446) [2.73(454)] <sup>b</sup>	0.684 [0.988]	H-1→L (0.49) $n_N-\pi^*$ H→L (0.41) $\pi-\pi^*$ [H-1→L (0.34) $n_N-\pi^*$ ] [H→L (0.52) $\pi-\pi^*$ ]
$S_3$	3.86(321)	0.063	H-2→L (0.68) $\pi-\pi^*$	$S_4$	3.86(321) [3.83(324)] <sup>b</sup>	0.023 [0.025]	H-3→L (0.68) $\pi-\pi^*$ [H-3→L (0.68) $\pi-\pi^*$ ]
3							
$S_1$	2.67(464)	0.048	H-2→L (0.61) $n_N-\pi^*$	$S_1$	2.55(486)	1.190	H→L (0.57) $\pi-\pi^*$
$S_2$	3.08(403)	0.694	H→L (0.61) $\pi-\pi^*$	$S_2$	2.75(451)	0.115	H-1→L (0.65) $n_N-\pi^*$
$S_3$	3.42(362)	0.138	H-1→L (0.64) $\pi-\pi^*$	$S_3$	3.46(359)	0.035	H-2→L (0.68) $\pi-\pi^*$
$S_5$	4.47(278)	0.168	H-4→L(0.48) $\pi-\pi^*$				
4							
$S_1$	2.65(467)	0.016	H-1→L (0.63) $n_N-\pi^*$	$S_1$	2.68(463)	0.404	H-1→L (0.54) $n_N-\pi^*$
$S_2$	3.45(360)	0.972	H→L (0.62) $\pi-\pi^*$	$S_2$	2.82(439)	0.921	H→L (0.49) $\pi-\pi^*$
$S_3$	4.03(308)	0.052	H-2→L (0.68) $\pi-\pi^*$	$S_4$	3.97(313)	0.024	H-2→L (0.68) $\pi-\pi^*$
5							
$S_1$	2.64(469)	0.016	H-1→L (0.62) $n_N-\pi^*$	$S_1$	2.68(463)	0.314	H-1→L (0.57) $n_N-\pi^*$
$S_2$	3.44(361)	0.909	H→L (0.62) $\pi-\pi^*$	$S_2$	2.82(440)	0.959	H→L (0.53) $\pi-\pi^*$
$S_3$	3.83(324)	0.072	H-2→L (0.67) $\pi-\pi^*$	$S_5$	4.17(297)	0.027	H→L+1 (0.63) $\pi-\pi^*$
$S_5$	4.57(271)	0.198	H-4→L (0.65) $\pi-\pi^*$	$S_6$	4.34(286)	0.075	H→L+2 (0.58) $\pi-\pi^*$
6							
$S_1$	2.67(465)	0.022	H-1→L (0.58) $n_N-\pi^*$	$S_1$	2.58(480)	0.973	H→L (0.55) $\pi-\pi^*$
$S_2$	3.15(393)	0.583	H→L(0.63) $\pi-\pi^*$	$S_2$	2.75(450)	0.232	H-1→L (0.61) $n_N-\pi^*$
$S_3$	3.73(332)	0.418	H-2→L (0.61) $\pi-\pi^*$	$S_3$	3.67(337)	0.154	H-2→L (0.67) $\pi-\pi^*$
$S_5$	4.56(271)	0.116	H-4→L (0.47) $\pi-\pi^*$	$S_5$	3.95(314)	0.028	H→L+1 (0.66) $\pi-\pi^*$

<sup>a</sup> The transition energies,  $\Delta E$ , for the most relevant transitions are given in eV (nm) with oscillator strengths,  $f$ , and main assignments (configuration interaction coefficient). <sup>b</sup> Values in brackets obtained at the PCM-PBE0//PCM-PBE0 level of theory.

the transitions underlying these bands are the HOMO→LUMO transitions of  $\pi\pi^*$  character. In **4**, this band is assigned to the bright  $S_2$  state, located at 360 nm, in excellent agreement with the experiment. In **5**, not only the  $S_2$  (361 nm), but to a minor extent the much weaker  $S_3$  (324 nm) state contributes to this

band. In both compounds, the  $S_2$  state is an HOMO→LUMO transition with  $\pi\pi^*_{azo}$  character. In **5**, the  $S_3$  state is an excitation from the HOMO-2, that is, a  $\pi$  orbital localized on the phenol moiety but not on the azo moiety. As it can be seen, the  $S_2$  transition in the electron-withdrawing compounds is blue-shifted

**Table 6.** Experimental and PCM-PBE0//PBE0 Calculated Ratios between the Heights of the Anion and Neutral Main Bands of Compounds 1–6 and 1<sup>−</sup>–6<sup>−</sup>, as well as the Ratio between the Calculated Oscillator Strengths *f* of the Main  $\pi\pi^*$  Transitions Underlying the Main Band of the Spectra

	1 <sup>−</sup> /1	2 <sup>−</sup> /2	3 <sup>−</sup> /3	4 <sup>−</sup> /4	5 <sup>−</sup> /5	6 <sup>−</sup> /6
experimental	1.30	1.68	1.74	1.14	1.30	1.72
theoretical	1.21	1.36	1.67	1.24	1.26	1.80
$f^-(\pi\pi^*)/f(\pi\pi^*)$	1.04	1.48 <sup>a</sup>	1.71	0.95	1.06	1.67 <sup>b</sup>

<sup>a</sup> Obtained considering the sum of the oscillator strengths of S<sub>1</sub> and S<sub>2</sub> of 2<sup>−</sup>, because the  $\pi\pi^*$  and  $n\pi^*$  are strongly mixed (see Table 5).

<sup>b</sup> Obtained considering only the oscillator strength of S<sub>2</sub> of 6.

both theoretically and experimentally in comparison to its analogous S<sub>2</sub> in the electron-donating compounds (2, 3) and the unsubstituted compound 1 (Table 5). This blue-shift can be attributed to the stabilization/destabilization of the HOMO/LUMO pair of orbitals due to electronic effects. Also well represented is the onset of the second band observed in the spectrum of 5 (Figure 4d), which can be assigned to the S<sub>5</sub> state, located at 271 nm<sub>e</sub>, and corresponds to an excitation from a  $\pi$  orbital localized on the phenyl ring (HOMO−4, in Figure 2) to the  $\pi^*_{\text{azo}}$  orbital.

As with the electron donor derivatives (2<sup>−</sup> and 3<sup>−</sup>) and the bare compound 1<sup>−</sup>, the HOMO→LUMO transition is responsible for the electronic properties of 4<sup>−</sup> and 5<sup>−</sup>. Small blue-shifts are observed with respect to 1<sup>−</sup>. As it was found in the other HESAB compounds, the red-shifted bands of 4<sup>−</sup> and 5<sup>−</sup> are more intense than the corresponding neutral ones. We note that the theoretical values are very close to the experimental ones: the theoretical absorption maxima in 5<sup>−</sup> are blue-shifted ca. 12 nm<sub>e</sub> and in 4<sup>−</sup> ca. 1 nm<sub>e</sub>, with respect to the experiment (cf., Table 3). The main band of 5<sup>−</sup>, peaking at 460 nm<sub>e</sub>, is explained by the S<sub>1</sub> and S<sub>2</sub> states, which correspond to the  $n\pi^*_{\text{azo}}$  and a  $\pi\pi^*$  transition, respectively (see Table 5). Additionally, compound 5<sup>−</sup> also shows a weaker band at higher energies (292 nm<sub>e</sub>), which is theoretically well described by the S<sub>5</sub> and S<sub>6</sub>  $\pi\pi^*$  states (297 and 286 nm<sub>e</sub>). It is gratifying to see that in most of the cases, the deviation from the experiment is below 0.1 eV. The maximum discrepancy between theory and experiment is found in the description of the main band of 3, with an error accounting to ca. 0.35 eV. These errors are in the upper limit of accuracy that can be expected for this methodology.

In summary, when comparing the spectroscopic properties of electron-donor and electron-withdrawing substituted HESABs with 1/1<sup>−</sup>, we can state the following: First, there is a significant red-shift of the main peaks of the anionic forms of the electron-donor compounds with respect to 1<sup>−</sup> (compare 460 nm<sub>e</sub> in 1<sup>−</sup> with 499 and 525 nm<sub>e</sub> in 2<sup>−</sup> and 3<sup>−</sup>, respectively, in Table 2) due to electronic effects, and although less striking, a small red-shift is present in the main peak of the acid forms (see 361 nm<sub>e</sub> in 1 versus 373 and 460 nm<sub>e</sub> in 2 and 3). In electron-withdrawing compounds, the trend is inverse; that is, the absorption of the basic forms is slightly blue-shifted in comparison to 1<sup>−</sup> (compare 460 nm<sub>e</sub> in 1<sup>−</sup> with 444 and 460 nm<sub>e</sub> in 4<sup>−</sup> and 5<sup>−</sup>). The main peaks of the acid forms are also slightly blue-shifted (see Table 2). Despite being small, these differences are recovered by the DFT calculations.

The spectra of the fluoromethoxy pair 6/6<sup>−</sup> (Figure 4e,j) resemble those of 1/1<sup>−</sup> due to compensating electronic effects.

The peak of 6 located at 374 nm<sub>e</sub> can be assigned to the S<sub>2</sub> and S<sub>3</sub> states, located at 393 and 332 nm<sub>e</sub>. The S<sub>2</sub> state corresponds to the usual HOMO→LUMO transition of  $\pi\pi^*_{\text{azo}}$  character. The S<sub>3</sub> is also a  $\pi\pi^*$  transition, but starts from the HOMO−2 orbital, which is mainly located in the phenol moiety (see Figure 2), as it has been found in 1, 2, and 4. The spectrum of 6<sup>−</sup> peaks at 487 nm<sub>e</sub> and it can be described by the S<sub>1</sub> (480 nm<sub>e</sub>), which is the  $\pi\pi^*_{\text{azo}}$  transition and a non-negligible contribution of the S<sub>2</sub>  $n\pi^*_{\text{azo}}$  state.

Finally, we have considered it of interest to analyze the effect of the pH and substitution pattern on the relative transition intensities. In Table 6, we have calculated the ratio between the heights of the anion and neutral main bands, using the experimental and computed PCM-PBE0//PBE0 spectra. The experimental values show that electron-donor species increases this ratio, while electron-withdrawing groups leave this value almost unchanged. It is gratifying to see that these trends are also theoretically reproduced. Additionally, we have calculated the ratio between the calculated oscillator strengths *f* of the strong  $\pi\pi^*$  transitions underlying the peaks of the anion and neutral spectra. The comparison of these ratios indicates the differences in intensity with respect to the reference pair 1/1<sup>−</sup>. As we can see, the trends for electron-donor (2/2<sup>−</sup> and 3/3<sup>−</sup>) and electron-withdrawing (4/4<sup>−</sup> and 5/5<sup>−</sup>) substitution are maintained. The value obtained for the compounds 6/6<sup>−</sup> is not really instructive because the spectrum is broad due to several transitions, but for the sake of uniformity only one transition (S<sub>2</sub>) has been taken into account.

## 5. CONCLUSIONS

In the present Article, the absorption spectra of substituted 2-hydroxyethylsulfonyl azobenzene (HESAB) pH indicator dyes are reported and theoretically assigned with the help of quantum chemical calculations. HESAB indicator dyes can be used for optically monitoring pH in the range from 3 to 10 and can be covalently linked to sensor layers exhibiting high chemical stability, as we have recently reported.<sup>16</sup> HESAB chemistry is not just limited to absorbance spectroscopy but could also be used to develop emission dyes. The absorbance spectra of all the neutral and anionic counterparts are well separated; accordingly, the color changes of HESAB dyes in going from acid to base form (i.e. protonated to deprotonated form) are from yellow to orange or red, hence making feasible its use as pH indicator dyes. Substitution of HESAB complexes by electron-donor and electron-withdrawing moieties biases not only the pK<sub>a</sub> values but also the spectroscopic properties of HESAB complexes. The differences of the spectroscopic features upon substitution as well as between the anionic and neutral forms (measured under different pH conditions) have been theoretically elucidated. The good agreement between theory and experiment has been achieved using the density functional protocol PCM-PBE0/PBE0, which includes the solvent effect in the energies with a continuum model but geometries optimized in gas phase. With this theoretical model, deviation from the experiment in the description of the  $n\pi^*$  and  $\pi\pi^*$  states is below 0.1 eV. Inclusion of additional solvent effects in the optimization of the geometries leads to minor improvements on the transition energies. However, because the geometries optimized in the presence of solvent are more planar than those in gas phase, the intensities of the  $n\pi^*$  transitions decrease substantially in comparison to that obtained in gas phase. In the species studied here, this effect leads to a

worse agreement with the weak experimental  $n\pi^*$  bands, very likely because temperature effects prevent the molecule from remaining planar, as indicated by the low frequency modes corresponding to the out-of-plane motion of the rings. Whether inclusion of solvent effects in the geometries is necessary in other cases needs to be cautiously evaluated for each particular case.

In general, from this study, the following conclusions are extracted for the HESAB dyes:

- (i) The spectroscopic state of all of the neutral and anionic HESAB dyes here investigated is the  $\pi\pi^*$  transition. This is then the state that determines the functionality of these complexes as pH indicators, while the  $n\pi^*$  transitions are much weaker or even dark.
- (ii) In all of the HESAB dyes, a red-shift is observed upon deprotonation. This effect can be trivially explained in terms of the additional electrostatic repulsion between the negative charge and the occupied orbitals, which are then shifted to higher energies, thus leading to smaller occupied-virtual gaps.
- (iii) In the electron-donor compounds, both the neutral and the anionic forms show peaks red-shifted with respect to the unsubstituted compound. An inverse trend is observed in the studied electron-withdrawing derivatives; peaks are blue-shifted with respect to the unsubstituted compound. These effects have been rationalized theoretically in terms of the stabilization/destabilization of the orbital levels due to electronic effects upon substitution. The consequences of substitution on the optical properties of the pH indicators are translated in a change of the color pattern between the pair of complexes, for instance, going from pale yellow to orange in  $1/1^-$  and from yellow/orange to red in  $3/3^-$ .
- (iv) In the compound where both electron-donor and -withdrawing substituents are present, the spectrum resembles very much that of the unsubstituted HESAB, due to compensating electronic effects.

When planning the synthesis of new indicator dyes, one important issue is the possible prediction of their future optical properties. This is important when sensor dyes have to be made spectrally compatible with cheap light sources (e.g., light emitting diodes or laser diodes). Furthermore, well-separated absorbance spectra between acid and base form simplify the setup of the optical sensor device and enhance the signal-to-noise ratio. In the present work, a good correlation between calculated and experimental absorbance spectra has been achieved, thus paving the way for the dedicated design of new sensor dyes and sensor devices.

## AUTHOR INFORMATION

### Corresponding Author

\*Fax: +49 3641 948302. E-mail: leticia.gonzalez@uni-jena.de.

## ACKNOWLEDGMENT

This work has been funded by the Carl-Zeiss foundation (D.E.), the BMBF project "Aquaoptrode" (no. 13N9535), the projects MO 1062/5-1 and MO 1062/6-1 of the Deutsche Forschungsgemeinschaft, and the project AZ-Nr.: 20.10-3410-2 (Projekt Sensormaterialien) of the Bayerische Staatsministerium für Wirtschaft, Infrastruktur, Verkehr und Technologie.

Computer time in the Rechenzentrum of the Friedrich-Schiller-Universität Jena is gratefully acknowledged.

## REFERENCES

- (1) McMillan, G. K.; Cameron, R. A. *Advanced pH Measurement and Control*, 3rd ed.; ISA: Research Triangle Park, NC, 2004.
- (2) See, for example: (a) Orellana, G., Moreno-Bondí, M. C., Eds. *Springer Series on Chemical Sensors and Biosensors*; Springer-Verlag: Berlin, Germany, 2004; Vol. 1. (b) Narayanaswamy, R., Wolfbeis, O. S., Eds. *Optical Sensors: Industrial, Environmental and Diagnostic Applications*; Springer: Berlin, Heidelberg, 2004. (c) Wolfbeis, O. S. *Anal. Chem.* **2006**, *78*, 3859.
- (3) Trupp, S.; Alberti, M.; Carofiglio, T.; Lubian, E.; Lehmann, H.; Heuermann, R.; Yacoub-George, E.; Bock, K.; Mohr, G. J. *Sens. Actuators, B* **2010**, *150*, 206.
- (4) (a) Durr, H.; Bouas-Laurent, H. *Photochromism, Molecules and Systems*; Elsevier: Amsterdam, 1990. (b) Barrett, C. J.; Mamiya, J.; Yager, K. G.; Ikeda, T. *Soft Matter* **2007**, *3*, 1249.
- (5) See, for example: Feringa, B. L. *Molecular Switches*; Wiley-VCH: Germany, 2003.
- (6) Shinkai, S.; Manabe, O. *Top. Curr. Chem.* **1984**, *121*, 76.
- (7) Hugel, T.; Holland, N. B.; Cattani, A.; Moroder, L.; Seitz, M.; Gaub, H. E. *Science* **2002**, *296*, 1103.
- (8) Natansohn, A.; Rochon, P. *Chem. Rev.* **2002**, *102*, 4139.
- (9) Spörlein, S.; Carstens, H.; Satzger, H.; Renner, C.; Behrendt, R.; Moroder, L.; Tavan, P.; Zinth, W.; Wachtveitl, J. *Proc. Natl. Acad. Sci. U.S.A.* **2002**, *99*, 7998.
- (10) Carofiglio, T.; Fregonese, C.; Mohr, G. J.; Rastrelli, F.; Tonellato, U. *Tetrahedron* **2006**, *62*, 1502.
- (11) Mohr, G. J. *Anal. Chim. Acta* **2004**, *508*, 233.
- (12) Mohr, G. J. *Dyes Pigm.* **2004**, *62*, 77.
- (13) Mohr, G. J. *Sens. Actuators, B* **2003**, *90*, 31.
- (14) Ward, C. J.; Patel, P.; James, T. D. *J. Chem. Soc., Perkin Trans.* **2002**, *1*, 462.
- (15) Mohr, G. J. *Chem. Commun.* **2002**, *22*, 2646.
- (16) Mohr, G. J.; Müller, H.; Bussemer, B.; Stark, A.; Carofiglio, T.; Trupp, S.; Heuermann, R.; Henkel, T.; Escudero, D.; González, L. *Anal. Bioanal. Chem.* **2008**, *392*, 1411.
- (17) (a) Runge, E.; Gross, E. K. U. *Phys. Rev. Lett.* **1984**, *52*, 997. (b) Stratmann, R. E.; Scuseria, G. E.; Frisch, M. J. *J. Chem. Phys.* **1998**, *109*, 8218. (c) Casida, M. E. In *Time-Dependent Density-Functional Response Theory for Molecules*; Chong, D. P., Ed.; World Scientific: Singapore, 1995; Vol. 1, pp 155–192. (d) Koch, W.; Holthausen, M. C. *A Chemist's Guide to Density Functional Theory*; Wiley-VCH: Germany, 2000. (e) Barone, V.; Polimeno, A. *Chem. Soc. Rev.* **2007**, *36*, 1724. (f) Jacquemin, D.; Perpète, E. A.; Ciofini, I.; Adamo, C. *Acc. Chem. Res.* **2009**, *42*, 326.
- (18) See, for example: (a) Goerigk, L.; Moellmann, J.; Grimme, S. *Phys. Chem. Chem. Phys.* **2009**, *11*, 4611. (b) Goerigk, L.; Grimme, S. *J. Chem. Phys.* **2010**, *132*, 1841103. (c) Jacquemin, D.; Perpète, E. A.; Ciofini, I.; Adamo, C. *J. Chem. Theory Comput.* **2010**, *6*, 1532.
- (19) (a) Jacquemin, D.; Preat, P.; Wathélet, V.; Fontaine, M.; Perpète, E. A. *J. Am. Chem. Soc.* **2006**, *128*, 2072. (b) Jacquemin, D.; Perpète, E. A.; Scuseria, G. E.; Ciofini, I.; Adamo, C. *J. Chem. Theory Comput.* **2008**, *4*, 123.
- (20) Adamo, C.; Barone, V. *J. Chem. Phys.* **1999**, *110*, 6158.
- (21) (a) Cossi, M.; Barone, V.; Mennucci, B.; Tomasi, J. *Chem. Phys. Lett.* **1998**, *286*, 253. (b) Mennucci, B.; Tomasi, J. *J. Chem. Phys.* **1997**, *106*, 5151.
- (22) Christiansen, O.; Koch, H.; Jørgensen, P. *Chem. Phys. Lett.* **1995**, *243*, 409.
- (23) Hättig, C.; Weigend, F. *J. Chem. Phys.* **1995**, *243*, 409.
- (24) Becke, A. D. *Phys. Rev. A* **1998**, *38*, 3098.
- (25) Perdew, J. P. *Phys. Rev. B* **1986**, *33*, 8822.
- (26) Ahlrichs, R.; Bär, M.; Häser, M.; Horn, H.; Kölmel, C. *Chem. Phys. Lett.* **1989**, *162*, 165.

(27) Frisch, M. J.; Trucks, G. W.; Schlegel, H. B.; Scuseria, G. E.; Robb, M. A.; Cheeseman, J. R.; Montgomery, J. A., Jr.; Vreven, T.; Kudin, K. N.; Burant, J. C.; Millam, J. M.; Iyengar, S. S.; Tomasi, J.; Barone, V.; Mennucci, B.; Cossi, M.; Scalmani, G.; Rega, N.; Petersson, G. A.; Nakatsuji, H.; Hada, M.; Ehara, M.; Toyota, K.; Fukuda, R.; Hasegawa, J.; Ishida, M.; Nakajima, T.; Honda, Y.; Kitao, O.; Nakai, H.; Klene, M.; Li, X.; Knox, J. E.; Hratchian, H. P.; Cross, J. B.; Bakken, V.; Adamo, C.; Jaramillo, J.; Gomperts, R.; Stratmann, R. E.; Yazyev, O.; Austin, A. J.; Cammi, R.; Pomelli, C.; Ochterski, J. W.; Ayala, P. Y.; Morokuma, K.; Voth, G. A.; Salvador, P.; Dannenberg, J. J.; Zakrzewski, V. G.; Dapprich, S.; Daniels, A. D.; Strain, M. C.; Farkas, O.; Malick, D. K.; Rabuck, A. D.; Raghavachari, K.; Foresman, J. B.; Ortiz, J. V.; Cui, Q.; Baboul, A. G.; Clifford, S.; Cioslowski, J.; Stefanov, B. B.; Liu, G.; Liashenko, A.; Piskorz, P.; Komaromi, I.; Martin, R. L.; Fox, D. J.; Keith, T.; Al-Laham, M. A.; Peng, C. Y.; Nanayakkara, A.; Challacombe, M.; Gill, P. M. W.; Johnson, B.; Chen, W.; Wong, M. W.; Gonzalez, C.; Pople, J. A. *Gaussian 03*, revision C.02; Gaussian, Inc.: Wallingford, CT, 2004.

(28) Bouwstra, J. A.; Schouten, A.; Kroon, J. *Acta Crystallogr., Sect. C* **1983**, *25*, 3561.

(29) Fliegler, H.; Köhn, A.; Hättig, C.; Ahlrichs, R. *J. Am. Chem. Soc.* **2003**, *125*, 9821.

(30) Briquet, A.; Vercauteren, D. P.; André, J.-M.; Perpète, E. A.; Jacquemin, D. *Chem. Phys. Lett.* **2007**, *435*, 257.

(31) Briquet, A.; Vercauteren, D. P.; Perpète, E. A.; Jacquemin, D. *Chem. Phys. Lett.* **2006**, *417*, 190.

(32) Jacquemin, D.; Perpète, A.; Scuseria, G. E.; Ciofini, I.; Adamo, A. *Chem. Phys. Lett.* **2008**, *465*, 226.

(33) Andersson, J.-A.; Petterson, R.; Tegner, L. *J. Photochem.* **1982**, *20*, 17.

(34) Dreuw, A.; Head-Gordon, M. *Chem. Rev.* **2005**, *105*, 4009.

(35) Chai, J.-D.; Head-Gordon, M. *J. Chem. Phys.* **2008**, *128*, 084106.

(36) Chai, J.-D.; Head-Gordon, M. *Phys. Chem. Chem. Phys.* **2008**, *10*, 6615.

(37) Yanai, T.; Tew, D.; Handy, H. *Chem. Phys. Lett.* **2004**, *393*, 51.

(38) Peach, M. J. G.; Benfield, P.; Helgaker, T.; Tozer, D. J. *Chem. Phys.* **2008**, *128*, 044118.

(39) Peach, M. J. G.; Ruth Le Sueur, C.; Ruud, K.; Guillaume, M.; Tozer, D. J. *Phys. Chem. Chem. Phys.* **2009**, *11*, 4465.

(40) Jacquemin, D.; Perpète, E. A.; Vydrov, O. A.; Scuseria, G. E.; Adamo, A. J. *Chem. Phys.* **2007**, *127*, 094102.

(41) Kwasniewski, S. P.; François, J. P.; Deleuze, M. S. *Int. J. Quantum Chem.* **2001**, *85*, 557.

**5.3 A heteroleptic bis(tridentate) ruthenium(II) complex of a click-derived abnormal carbene pincer ligand with potential for photosensitizer application**

---

**5.3 A heteroleptic bis(tridentate) ruthenium(II) complex of a click-derived abnormal carbene pincer ligand with potential for photosensitizer application**

Reprinted with permission from Schulze et al. *Chem. Eur. J.*, **2011**, *17*, 5494. Copyright 2011 John Wiley and Sons.

# A Heteroleptic Bis(tridentate) Ruthenium(II) Complex of a Click-Derived Abnormal Carbene Pincer Ligand with Potential for Photosensitizer Application

**Benjamin Schulze,<sup>[a]</sup> Daniel Escudero,<sup>[b]</sup> Christian Friebe,<sup>[a]</sup> Ronald Siebert,<sup>[c]</sup> Helmar Görls,<sup>[d]</sup> Uwe Köhn,<sup>[a]</sup> Esra Altuntas,<sup>[a]</sup> Anja Baumgaertel,<sup>[a]</sup> Martin D. Hager,<sup>[a]</sup> Andreas Winter,<sup>[a]</sup> Benjamin Dietzek,<sup>[c]</sup> Jürgen Popp,<sup>[c]</sup> Leticia González,<sup>\*,[b]</sup> and Ulrich S. Schubert<sup>\*,[a]</sup>**

Ruthenium(II) polypyridyl complexes have received particular interest with respect to photosensitizer applications, because they are stable and inert complexes that show a defined metal-to-ligand charge transfer (MLCT).<sup>[1]</sup> A central dilemma is that trisbidentate complexes (e.g., of 2,2'-bipyridine, bpy) show long excited-state lifetimes, whereas bis(tridentate) complexes (e.g., of 2,2':6',2''-terpyridine, tpy) allow the isomer-free construction of linear assemblies for vectorial electron-transfer processes.<sup>[2]</sup> The quest of diminishing the fast radiationless deactivation of the <sup>3</sup>MLCT state through the triplet metal-centered state (<sup>3</sup>MC) of bis(tridentate) ruthenium(II) polypyridyl complexes<sup>[3]</sup> has motivated numerous approaches<sup>[4-6]</sup> that aim at <sup>3</sup>MLCT lowering or <sup>3</sup>MC raising or both. Ideally, electronic manipulations are realized

by direct incorporation of stronger donors, that is, by cyclometalation<sup>[7]</sup> or coordination through anionic N-heterocycles<sup>[8]</sup> and N-heterocyclic carbenes (NHCs).<sup>[9]</sup> Thereby, strong  $\sigma$  and  $\pi$  donation by coordination through anionic carbon or nitrogen donors lead to a destabilized ground state and, thus, a lowered <sup>3</sup>MLCT, resulting in a radiationless deactivation governed by the energy-gap law<sup>[10]</sup> and a low driving force for the potential electron-transfer processes. In contrast, classical NHC ligands are strong, charge-neutral  $\sigma$  donors and  $\pi$  acceptors, thus causing a favorable <sup>3</sup>MC destabilization, but also undesirably blue-shifted MLCT transitions. Alternatively, the expansion to six-membered ring chelators<sup>[6]</sup> leads to excellent excited-state lifetimes by a more favorable bite angle, but can also cause the formation of isomers (*fac*, *mer*) that show very different properties and that are hard to separate.

In this regard, abnormal or mesoionic carbene ligands<sup>[11]</sup> provide superior  $\sigma$ -donating and only moderate  $\pi$ -accepting properties that ideally would lead to strongly destabilized <sup>3</sup>MC states and a maintained <sup>3</sup>MLCT energy. 1,2,3-Triazolylidenes match these demands and are readily accessible by modular click chemistry. Herein we present a heteroleptic bis(tridentate) ruthenium(II) complex (RuCNC) of the new 2',6'-bis(1-mesityl-3-methyl-1,2,3-triazol-4-yl-5-idene)pyridine (CNC) ligand and the parent tpy. A heteroleptic complex with tpy is particularly interesting, because it preserves the elaborated terpyridine chemistry, including a variety of ruthenium precursors, allows for asymmetric functionalization, and includes a reference ligand. The electronic and optical properties of RuCNC were investigated by experimental and theoretical studies.

The synthesis of RuCNC was achieved under mild reaction conditions with a high selectivity and reasonable yield (Scheme 1). For the preparation of 2',6'-bis(1-mesityl-3-methyl-1,2,3-triazolium-4-yl)pyridine tetrafluoroborate (H<sub>2</sub>CNC), the parent click-derived 2',6'-bis(1-mesityl-1,2,3-triazol-4-yl)pyridine (tripy)<sup>[12]</sup> could be methylated selectively with Meerwein's salt<sup>[13]</sup> as evidenced by single-crystal X-ray diffraction (Figure 1), spectroscopic, and spectrometric methods. Because free 1,2,3-triazolylidenes undergo a 5–3-methyl shift,<sup>[11]</sup> a stable silver(I)-precursor (AgCNC) was

[a] Dipl.-Chem. B. Schulze, Dipl.-Chem. C. Friebe, Dr. U. Köhn, E. Altuntas, Dipl.-Chem. A. Baumgaertel, Dr. M. D. Hager, Dr. A. Winter, Prof. Dr. U. S. Schubert  
Laboratory of Organic and Macromolecular Chemistry (IOMC)  
Jena Center for Soft Matter (JCSM)  
Friedrich-Schiller-University Jena  
Humboldtstr. 10, 07743 Jena (Germany)  
Fax: (+49) 3641948202  
E-mail: ulrich.schubert@uni-jena.de

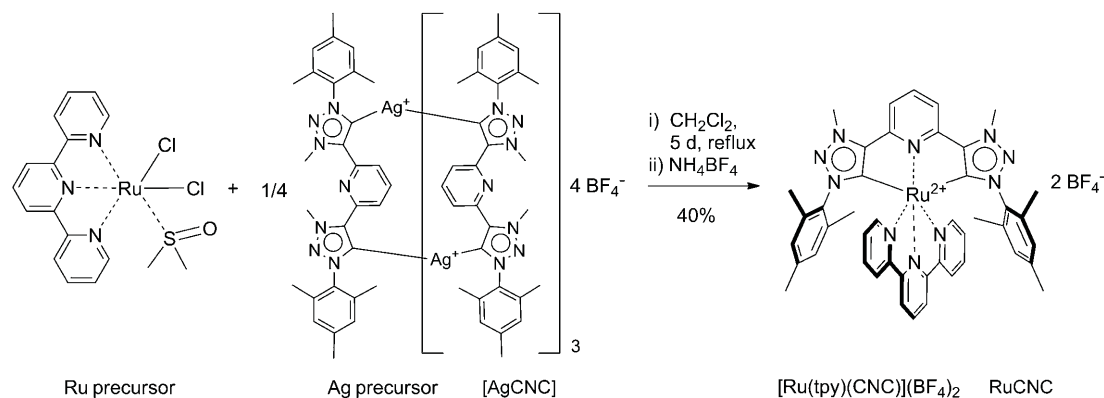
[b] D. Escudero, Prof. Dr. L. González  
Laboratory of Theoretical Chemistry  
Jena Center for Soft Matter (JCSM)  
Friedrich-Schiller-University Jena  
Helmholtzweg 4, 07743 Jena (Germany)  
Fax: (+49) 3641948302  
E-mail: leticia.gonzalez@uni-jena.de

[c] Dipl.-Chem. R. Siebert, Dr. B. Dietzek, Prof. Dr. J. Popp  
Institute of Physical Chemistry and Abbe Center of Photonics  
Jena Center for Soft Matter (JCSM)  
Friedrich-Schiller-University Jena  
Helmholtzweg 4, 07743 Jena (Germany)  
and  
Institute of Photonic Technology Jena  
Albert-Einstein-Straße 9, 07745 Jena (Germany)

[d] Dr. H. Görls  
Laboratory of Inorganic and Analytic Chemistry  
Friedrich-Schiller-University Jena  
Lessingstr. 8, 07743 Jena (Germany)

Supporting information for this article is available on the WWW under <http://dx.doi.org/10.1002/chem.201100045>.





Scheme 1. Schematic representation of the synthesis RuCNC.

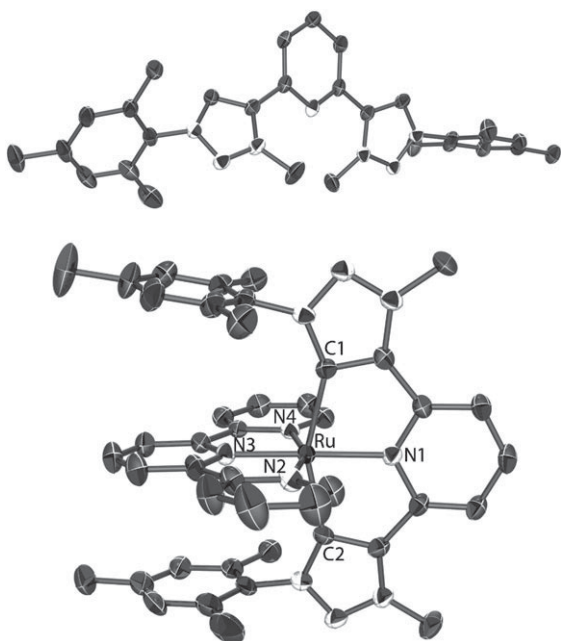


Figure 1. Solid-state structures of  $\text{H}_2\text{CNC}$  (top) and RuCNC (bottom, ellipsoids at 50% probability level; hydrogen atoms, solvents molecules, and tetrafluoroborate anions are omitted for clarity). Selected bond lengths ( $\text{\AA}$ ) and angles ( $^\circ$ ) of RuCNC: Ru–C1, 2.058(4); Ru–C2, 2.051(4); Ru–N1, 2.083(4); Ru–N2, 2.068(4); Ru–N3, 1.962(4); Ru–N4, 2.052(4); C1–Ru–C2, 154.34(17); N2–Ru–N4, 158.25(15); N1–Ru–N3, 178.48(15).

prepared by utilizing silver(I) oxide. ESI-ToF MS, MALDI-ToF MS, and MS/MS measurements revealed isotopically resolved peaks of up to tetrameric cycles (see Figure S36 in the Supporting Information for an optimized structure of the tetrameric complex).<sup>[14]</sup> In the milder ESI MS, mainly the 4:4 complex, beside 3:3 and 1:1 fragments, were observed. Diffusion-ordered NMR-spectroscopy (DOSY) measurements proved the uniformity of the proton signals and the formation of a higher aggregate. In the  $^{13}\text{C}$  NMR spectra, the abnormal carbene signals appeared with a typical  $^{107/109}\text{Ag}$  coupling at around 170 ppm that was shifted to higher field by 10 ppm compared with a silver complex of a normal imidazolylidene carbene with a carbon sextet.<sup>[14]</sup> For

the subsequent transmetalation, common ruthenium(II) and ruthenium(III) monocomplexes of tpy were tested, but only *cis*- $[\text{Ru}(\text{tpy})(\text{DMSO})\text{Cl}_2]$ <sup>[15]</sup> proved to be a sufficiently selective and reactive precursor. Single crystals of RuCNC suitable for X-ray diffraction were grown by vapor diffusion of diethyl ether into a methanolic solution (Figure 1). The C,N,C-pincer coordination as well as an intramolecular tweezer-like  $\pi$  stacking was clearly confirmed. The ruthenium–carbon bond lengths are identical to those reported for a related heteroleptic ruthenium(II) complex of the classical 2',6'-bis(3-methylimidazol-1-yl-2-ylidene)pyridine and terpyridine, other bond lengths are comparable and the bite angles are slightly larger.<sup>[9]</sup> The identity and purity of the complex were proven by MS and various NMR techniques. The triazolium protons vanished and characteristic high-field shifts due to the  $\pi$  stacking were visible in the  $^1\text{H}$  NMR spectrum. Furthermore, a strong low-field shift to around 185 ppm can be observed for the coordinating carbons in the  $^{13}\text{C}$  NMR spectrum, but again less pronounced than for classical NHC ligands.<sup>[9]</sup>

The UV/Vis absorption spectrum of RuCNC shows a typical MLCT transition, but, due to the reduced symmetry of the heteroleptic complex, it exhibits a comparatively low extinction coefficient and a band splitting. The absorption profile is similar to the related heteroleptic complex with *N,N,N*-bound tripy.<sup>[12]</sup> Noteworthy, the MLCT absorption is only marginally blue-shifted in comparison to the parent  $[\text{Ru}(\text{tpy})_2](\text{PF}_6)_2$  (see above and Table 1). The room-temperature emission measurement revealed an intense red and unstructured emission with quantum yields close to the  $[\text{Ru}(\text{bpy})_3](\text{PF}_6)_2$  reference value (Table 1). Furthermore, the emission showed a slow and monoexponential decay, thus arising from a single phosphorescent triplet state (Figure 2). The excited-state lifetime of 633 ns can almost compete with  $[\text{Ru}(\text{bpy})_3](\text{PF}_6)_2$  and is 2500 times longer than for  $[\text{Ru}(\text{tpy})_2](\text{PF}_6)_2$ .

In comparison to ruthenium(II) complexes of charge-neutral polypyridyl ligands, the redox potentials show a cathodic shift, most likely due to the anionic carbon of the mesoionic carbene, but a similar energy gap. The HOMO and LUMO energies calculated from the cyclovoltammetry results

Table 1. Selected photophysical and electrochemical data.

	[Ru(tpy) <sub>2</sub> ](PF <sub>6</sub> ) <sub>2</sub>	[Ru(bpy) <sub>3</sub> ](PF <sub>6</sub> ) <sub>2</sub>	RuCNC
$\lambda_{\text{max}}^{\text{Abs}}$ [nm] <sup>[a]</sup>	474	450	463
$\epsilon$ [10 <sup>4</sup> M <sup>-1</sup> cm <sup>-1</sup> ] <sup>[a]</sup>	1.8	1.4	1.0
$\lambda_{\text{ma}}^{\text{Em}}$ [nm]	–	597	643 (634) <sup>[b]</sup>
$\tau$ [ns]	0.21 <sup>[c]</sup>	860; <sup>[d]</sup> 680 <sup>[d,e]</sup>	633; 615 <sup>[e]</sup>
$\Phi_{\text{PL}}$ [%]	–	6.2 <sup>[f]</sup>	4.4; <sup>[g]</sup> 5.5 <sup>[e,g]</sup>
$E_{1/2}^{\text{Ox}}$ [V] <sup>[h]</sup>	0.90	0.90	0.60
$E_{1/2}^{\text{Red}}$ [V] <sup>[h]</sup>	–1.64	–1.71	–1.95
$E_{\text{LUMO}}$ [eV] <sup>[i]</sup>	–3.20	–3.28	–2.70
$E_{\text{HOMO}}$ [eV] <sup>[i]</sup>	–5.71	–5.70	–5.38

Measured in deaerated acetonitrile at 298 K, unless stated otherwise. [a] Maximum of the MLCT band. [b] Theoretical predicted AEE value (PCM-B3LYP/6-31G\*). [c] Measured in butyronitrile at 290 K; from ref. [3a]. [d] From ref. [16]. [e] Measured in deaerated CH<sub>2</sub>Cl<sub>2</sub>. [f] From ref. [17a]. [g] Against [Ru(bpy)<sub>3</sub>](PF<sub>6</sub>)<sub>2</sub> as standard. [h] Measured in CH<sub>3</sub>CN containing 0.1 M NBu<sub>4</sub>PF<sub>6</sub> and with Fc/Fc<sup>+</sup> as a reference. [i] Calculated by using  $E_{\text{LUMO/HOMO}} = [-(E_{\text{onset}}^{\text{Red/Ox}} - E_{\text{onset}}^{\text{Fc/Fc}^+}) - 4.8]$  eV.

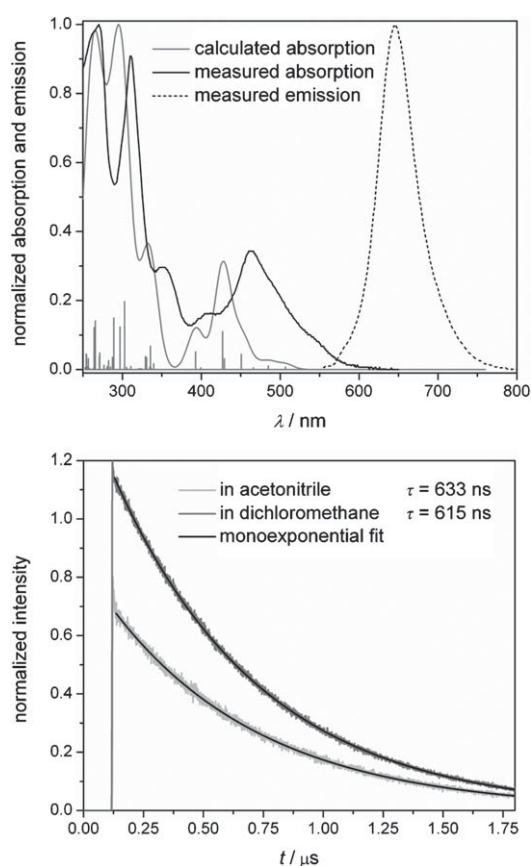


Figure 2. Calculated and measured UV/Vis absorption and measured emission spectra (top). Emission decay (bottom).

(Table 1) are raised in energy and, additionally, the oxidation appears to be reversible. To obtain a more detailed insight into the oxidation process, UV/Vis spectroelectrochemical experiments were executed (see Figure S31 in the Supporting Information). Several isosbestic points suggest the presence of only two species and, thus, a well-defined oxidation process. The most obvious spectral change is the strong decrease of the MLCT bands at 463, 410, and 352 nm, con-

sistent with the assignment of the oxidation process as a ruthenium(II)/ruthenium(III) transition. Additionally, a weak and broad band at around 600 to 800 nm appears, most likely due to ligand-to-metal charge transfer (LMCT,  $\pi \rightarrow d$ ) transitions, whereas the bands below 330 nm, in the region dominated by ligand-centered (LC) transitions, appear essentially unchanged. Remarkably, the reduction of the oxidized species regenerates the parent complex quantitatively. This highlights the potential of RuCNC to act as an electron donor.

To understand the electronic properties and the bonding of the abnormal carbene ligand to the ruthenium center, energy-decomposition analysis (EDA)<sup>[18]</sup> was performed (see computational details in the Supporting Information). The EDA (BP86-ZORA/TZP) calculation revealed that the interaction energy between the carbene and the ruthenium(II)-tpy fragment is  $-256$  kcal mol<sup>-1</sup>. Former EDA calculations on ruthenium complexes of normal (C2-bound) and abnormal (C4-bound) imidazolylidenes revealed interaction energies of  $-60$  to  $-70$  kcal mol<sup>-1</sup> for a single ruthenium-carbene bond.<sup>[19]</sup> Assuming these values for a tridentate system still leaves a significant energy difference, this means that CNC enables very strong ruthenium-abnormal carbene bonds. The global interaction energy stems roughly 1:1 from covalent and ionic interactions due to the mesoionic character of the carbene donor ligand. Concerning the covalency of the bond, strong  $\sigma$ -donating as well as  $\pi$ -accepting interactions contribute to the global energy (see Figure S37 and Table S3 in the Supporting Information). Furthermore, time-dependent DFT (TD-DFT) calculations in the presence of acetonitrile (PCM-TD-B3LYP/6-31G\*) were performed to rationalize the absorption and emission spectra. The geometry-optimization calculations show that the HOMOs are centered on the ruthenium, whereas the LUMOs are localized on both ligands (Figure 3b). Thus, several transitions, mainly of MLCT character and directed towards both ligands, are observable in the visible region of the absorption spectrum (see Figure 3a and Table S4 in the Supporting In-

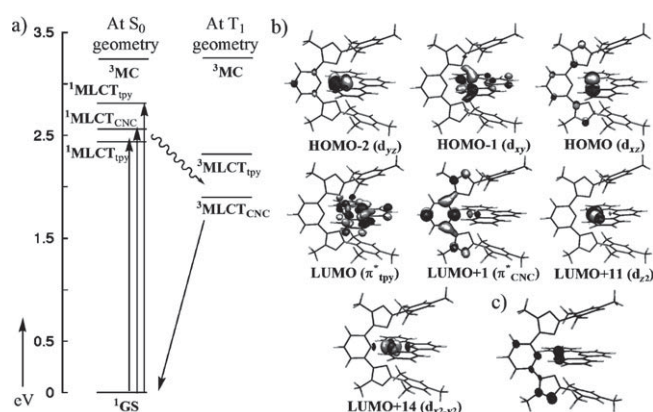


Figure 3. a) Energy-level scheme of the lowest excited states of RuCNC at both the S<sub>0</sub>- and T<sub>1</sub>-optimized geometries (GS = ground state). b) Most relevant Kohn-Sham orbitals computed at the PCM-B3LYP/6-31G\* level of theory. c) Spin-density plot of the T<sub>1</sub> state.

formation). The calculated UV/Vis spectrum is slightly blue-shifted in comparison with the measured spectrum, but both are consistent in shape (see Figure 2). Also, the computed emission maximum is in good agreement with the experiment (see the value of the theoretical predicted adiabatic electronic emission, AEE, in Table 1). Thereby, the longest-wavelength <sup>1</sup>MLCT absorption involves the tpy ligand, whereas, the <sup>3</sup>MLCT emission originates from the carbene ligand after redistribution of electron density in the course of vibrational relaxation and intersystem crossing. The MLCT nature of the T<sub>1</sub> state was confirmed by spin-density analysis (see Figure 3c). Remarkably, due to the strong  $\sigma$  donation, the <sup>3</sup>MC states are of very high energies, 32 kcal mol<sup>-1</sup> above the <sup>3</sup>MLCT, thus hardly populated thermally and therefore, the radiationless deactivation is suppressed efficiently (see Figure 3a and Table S5). Oppositely, for the parent compound [Ru(tpy)<sub>2</sub>]<sup>2+</sup>, it was found, with the help of  $\Delta$ DFT calculations, that the <sup>3</sup>MC state is even 4 kcal mol<sup>-1</sup> lower in energy than the <sup>3</sup>MLCT.<sup>[6f]</sup>

In conclusion, click chemistry and subsequent methylation was employed to introduce tridentate 2',6'-bis(1,2,3-triazolylidene)pyridine ligands with mesoionic carbene donors. Ruthenium(II) complexation was achieved by transmetalation from a tetrameric silver(I) cycle. Due to the superior  $\sigma$  donation of the mesoionic carbene, the heteroleptic ruthenium(II) complex of the new ligand and the parent terpyridine possesses promising photophysical and electrochemical properties with respect to photosensitizer applications. As a bis(tridentate), heteroleptic system, the complex allows for the construction of isomer-free, linear, and asymmetric substituted assemblies.

## Experimental Section

Experimental and computational details are provided in the Supporting Information. CCDC-787332 (H<sub>2</sub>CNC) and -787333 (RuCNC) contain the supplementary crystallographic data for this paper. These data can be obtained free of charge from The Cambridge Crystallographic Data Centre via [www.ccdc.cam.ac.uk/data\\_request/cif](http://www.ccdc.cam.ac.uk/data_request/cif).

## Acknowledgements

B.S., C.F., and R.S. are grateful to the Fonds der Chemischen Industrie for PhD scholarships. D.E. is grateful to the Carl-Zeiss-Stiftung for a PhD scholarship. B.D. thanks the Fonds der Chemischen Industrie. We also thank M. Jäger, W. Günther, and G. Sentis for discussions and performing experiments.

**Keywords:** carbenes • click chemistry • computational chemistry • photosensitizer • ruthenium

- [1] a) A. Juris, V. Balzani, F. Barigelletti, S. Campagna, P. Belser, A. von Zelewsky, *Coord. Chem. Rev.* **1988**, *84*, 85–277; b) J.-P. Sauvage, J.-P. Collin, J.-C. Chambron, S. Guillerez, C. Coudret, V. Balzani, F. Barigelletti, L. De Cola, L. Flamigni, *Chem. Rev.* **1994**, *94*, 993–1019.

- [2] a) E. A. Medlycott, G. S. Hanan, *Chem. Soc. Rev.* **2005**, *34*, 133–142; b) E. A. Medlycott, G. S. Hanan, *Coord. Chem. Rev.* **2006**, *250*, 1763–1782.
- [3] a) D. W. Fink, W. E. Ohnesorge, *J. Am. Chem. Soc.* **1969**, *91*, 4995–4998; b) A. Amini, A. Harriman, A. Mayeux, *Phys. Chem. Chem. Phys.* **2004**, *6*, 1157–1164.
- [4] For the multichromophore approach, see: a) J. Wang, G. S. Hanan, F. Loiseau, S. Campagna, *Chem. Commun.* **2004**, 2068–2069; b) J. H. Wang, Y. Q. Fang, L. Bourget-Merie, M. I. J. Poisson, G. S. Hanan, A. Juris, F. Loiseau, S. Campagna, *Chem. Eur. J.* **2006**, *12*, 8539–8548.
- [5] For electronic manipulations, see: a) M. Maestri, N. Armaroli, V. Balzani, E. C. Constable, A. M. W. Cargill Thompson, *Inorg. Chem.* **1995**, *34*, 2759–2767; b) Y.-Q. Fang, N. J. Taylor, G. S. Hanan, F. Loiseau, R. Passalacqua, S. Campagna, H. Nierengarten, A. V. Dorsse-laer, *J. Am. Chem. Soc.* **2002**, *124*, 7912–7913; c) R. Siebert, A. Winter, B. Dietzek, U. S. Schubert, J. Popp, *Macromol. Rapid Commun.* **2010**, *31*, 883–888.
- [6] For structural manipulations, see: a) L. Hammarström, O. Johansson, *Coord. Chem. Rev.* **2010**, *254*, 2546–2559; b) M. Abrahamsson, M. Jäger, T. Österman, L. Eriksson, P. Persson, H.-C. Becker, O. Johansson, L. Hammarström, *J. Am. Chem. Soc.* **2006**, *128*, 12616–12617; c) M. Abrahamsson, M. Jäger, R. J. Kumar, T. Österman, P. Persson, H.-C. Becker, O. Johansson, L. Hammarström, *J. Am. Chem. Soc.* **2008**, *130*, 15533–15542; d) F. Schramm, V. Meded, H. Fliegl, K. Fink, O. Fuhr, Z. Qu, W. Klopfer, S. Finn, T. E. Keyes, M. Ruben, *Inorg. Chem.* **2009**, *48*, 5677–5684; e) A. Breivogel, C. Förster, K. Heinze, *Inorg. Chem.* **2010**, *49*, 7052–7056; f) O. Anders Borg, S. S. M. C. Godinho, M. J. Lundqvist, S. Lunell, P. Persson, *J. Phys. Chem. A* **2008**, *112*, 4470–4476; as apparent from the last reference, an ideal octahedral symmetry avoids admixing of ruthenium(II) d orbitals to the LUMO; this lowers the probability of the <sup>3</sup>MLCT-to-<sup>3</sup>MC transition and, consequently, the energy of the MC state becomes less crucial.
- [7] a) J.-P. Collin, M. Beley, J.-P. Sauvage, F. Barigelletti, *Inorg. Chim. Acta* **1991**, *186*, 91–93; b) S. H. Wadman, M. Lutz, D. M. Tooke, A. L. Spek, F. Hartl, R. W. A. Havenith, G. P. M. van Klink, G. van Koten, *Inorg. Chem.* **2009**, *48*, 1887–1900; c) M. Jäger, A. Smeigh, F. Lombeck, H. Görls, J.-P. Collin, J.-P. Sauvage, L. Hammarström, O. Johansson, *Inorg. Chem.* **2010**, *49*, 374–376; d) P. G. Bomben, K. C. D. Robson, P. A. Sedach, C. P. Berlinguette, *Inorg. Chem.* **2009**, *48*, 9631–9643.
- [8] a) M. Duati, S. Fanni, J. G. Vos, *Inorg. Chem. Commun.* **2000**, *3*, 68–70; b) M. Duati, S. Tasca, F. C. Lynch, H. Bohlen, J. G. Vos, *Inorg. Chem.* **2003**, *42*, 8377–8384.
- [9] a) S. U. Son, K. H. Park, Y.-S. Lee, B. Y. Kim, C. H. Choi, M. S. Lah, Y. H. Jang, D.-J. Jang, Y. K. Chung, *Inorg. Chem.* **2004**, *43*, 6896–6898; b) H.-J. Park, K. H. Kim, S. Y. Choi, H.-M. Kim, W. I. Lee, Y. K. Kang, Y. K. Chung, *Inorg. Chem.* **2010**, *49*, 7340–7352.
- [10] a) R. Englman, J. Jortner, *Mol. Phys.* **1970**, *18*, 145–164; b) J. V. Caspar, B. P. Sullivan, E. M. Kober, T. J. Meyer, *Chem. Phys. Lett.* **1982**, *91*, 91–95.
- [11] a) P. Mathew, A. Neels, M. Albrecht, *J. Am. Chem. Soc.* **2008**, *130*, 13534–13535; b) G. Guisado-Barrios, J. Bouffard, B. Donnadieu, G. Bertrand, *Angew. Chem.* **2010**, *122*, 4869–4872; *Angew. Chem. Int. Ed.* **2010**, *49*, 4759–4762; c) O. Schuster, L. Yang, H. G. Raubenheimer, M. Albrecht, *Chem. Rev.* **2009**, *109*, 3445–3478; d) R. Lalrempuia, N. D. McDaniel, H. Müller-Bunz, S. Bernhard, M. Albrecht, *Angew. Chem.* **2010**, *122*, 9959–9962; *Angew. Chem. Int. Ed.* **2010**, *49*, 9765–9768.
- [12] a) Y. Li, J. C. Huffman, A. H. Flood, *Chem. Commun.* **2007**, 2692–2694; b) R. M. Meudtner, M. Ostermeier, R. Goddard, C. Limberg, S. Hecht, *Chem. Eur. J.* **2007**, *13*, 9834–9840; c) B. Schulze, C. Friebe, M. D. Hager, A. Winter, R. Hoogenboom, H. Görls, U. S. Schubert, *Dalton Trans.* **2009**, 787–794; d) M. Ostermeier, M.-A. Berlin, R. M. Meudtner, S. Demeshko, F. Meyer, C. Limberg, S. Hecht, *Chem. Eur. J.* **2010**, *16*, 10202–10213.
- [13] a) B. Schulze, C. Friebe, M. D. Hager, W. Günther, U. Köhn, B. O. Jahn, H. Görls, U. S. Schubert, *Org. Lett.* **2010**, *12*, 2710–2713;

- b) K. J. Kilpin, U. S. D. Paul, A.-L. Lee, J. D. Crowley, *Chem. Commun.* **2011**, 47, 328–330; c) K. M. Mullen, J. Mercurio, C. J. Serpell, P. D. Beer, *Angew. Chem.* **2009**, *121*, 4875–4878; *Angew. Chem. Int. Ed.* **2009**, *48*, 4781–4784; d) T. Karthikeyan, S. Sankararaman, *Tetrahedron Lett.* **2009**, *50*, 5834–5837.
- [14] a) M. L. Gower, J. D. Crowley, *Dalton Trans.* **2010**, 39, 2371–2378; b) C. Radloff, H.-Y. Gong, C. Schulte to Brinke, T. Pape, V. M. Lynch, J. L. Sessler, F. E. Hahn, *Chem. Eur. J.* **2010**, *16*, 13077–13081.
- [15] R. Ziessel, V. Grossshenny, M. Hissler, C. Stroh, *Inorg. Chem.* **2004**, *43*, 4262–4271.
- [16] B. Durham, J. V. Caspar, J. K. Nagle, T. J. Meyer, *J. Am. Chem. Soc.* **1982**, *104*, 4803–4810.
- [17] a) J. M. Calvert, J. V. Caspar, R. A. Binstead, T. D. Westmoreland, T. J. Meyer, *J. Am. Chem. Soc.* **1982**, *104*, 6620–6627; b) K. Suzuki, A. Kobayashi, S. Kaneko, K. Takehira, T. Yoshihara, H. Ishida, Y. Shiina, S. Oishic, S. Tobita, *Phys. Chem. Chem. Phys.* **2009**, *11*, 9850–9860. The second reference reported the photoluminescence quantum yield of [Ru(bpy)<sub>3</sub>](PF<sub>6</sub>)<sub>2</sub> to be 9.2%. According to that, the quantum yields of RuCNC would be 6.5 and 8.2%, respectively.
- [18] a) F. M. Bickelhaupt, E. J. Baerends, *Kohn–Sham Density Functional Theory: Predicting and Understanding Chemistry in Reviews in Computational Chemistry, Vol. 15* (Eds.: K. B. Lipkowitz, D. B. Boyd), Wiley-VCH, Weinheim, **2000**, pp. 1–86; b) M. Lein, G. Frenking in *Theory and Applications of Computational Chemistry: The First 40 Years* (Eds.: C. E. Dykstra, G. Frenking, K. S. Kim, G. E. Scuseria), Elsevier, Amsterdam, **2005**, pp. 291–367.
- [19] a) R. Tonner, G. Heydenrych, G. Frenking, *Chem. Asian J.* **2007**, *2*, 1555–1567; b) N. S. Antonova, J. J. Carbó, J. M. Poblet, *Organometallics* **2009**, *28*, 4283–4287.

Received: January 5, 2011  
Published online: April 12, 2011

5.4 N-Heterocyclic donor- and acceptor-type ligands based on  
2-(1H-[1,2,3]triazol-4-yl)pyridines and their ruthenium(II) complexes

---

**5.4 N-Heterocyclic donor- and acceptor-type ligands based  
on 2-(1H-[1,2,3]triazol-4-yl)pyridines and their ruthe-  
nium(II) complexes**

Reprinted with permission from Happ et al. *J. Org. Chem.*, **2010**, *75*, 4025. Copyright  
2010 American Chemical Society.

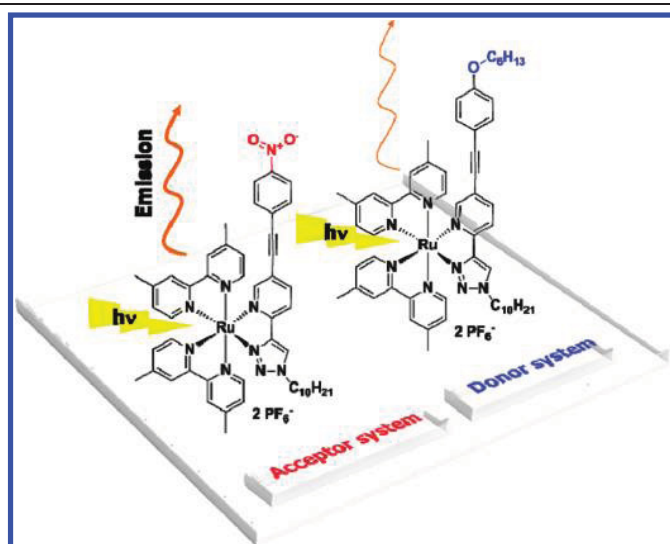
## *N*-Heterocyclic Donor- and Acceptor-Type Ligands Based on 2-(1*H*-[1,2,3]Triazol-4-yl)pyridines and Their Ruthenium(II) Complexes

Bobby Happ,<sup>†,‡</sup> Daniel Escudero,<sup>§</sup> Martin D. Hager,<sup>†,‡</sup> Christian Friebe,<sup>†</sup>  
Andreas Winter,<sup>†,‡,⊥</sup> Helmar Görls,<sup>¶</sup> Esra Altuntaş,<sup>†</sup> Leticia González,<sup>\*,§</sup> and  
Ulrich S. Schubert<sup>\*,†,‡,⊥</sup>

<sup>†</sup>Laboratory of Organic and Macromolecular Chemistry, Friedrich-Schiller-University Jena, Humboldtstrasse 10, 07743 Jena, Germany, <sup>‡</sup>Dutch Polymer Institute (DPI), P.O. Box 902, 5600 AX Eindhoven, The Netherlands, <sup>§</sup>Laboratory of Physical Chemistry, Friedrich-Schiller-University Jena, Helmholtzweg 4, 07743 Jena, Germany, <sup>⊥</sup>Laboratory of Macromolecular Chemistry and Nanoscience, Eindhoven University of Technology, P.O. Box 513, 5600 MB Eindhoven, The Netherlands, and <sup>¶</sup>Laboratory of Inorganic and Analytical Chemistry, Friedrich-Schiller-University Jena, Lessingstrasse 8, 07743 Jena, Germany

\*To whom correspondence should be addressed. L.G.: fax +49 (0)3641 948302 and e-mail leticia.gonzalez@uni-jena.de. U.S.S.: fax: +49 (0)3641 948202, e-mail ulrich.schubert@uni-jena.de, and internet www.schubert-group.com.

Received February 19, 2010



New 2-(1*H*-[1,2,3]triazol-4-yl)pyridine bidentate ligands were synthesized as bipyridine analogs, whereas different phenylacetylene moieties of donor and acceptor nature were attached at the 5-position of the pyridine unit. The latter moieties featured a crucial influence on the electronic properties of those ligands. The *N*-heterocyclic ligands were coordinated to ruthenium(II) metal ions by using a bis(4,4'-dimethyl-2,2'-bipyridine)ruthenium(II) precursor. The donor or acceptor capability of the 2-(1*H*-[1,2,3]triazol-4-yl)pyridine ligands determined the quantum yield of the resulting ruthenium(II) complexes remarkably. Separately, 2-([1,2,3]triazol-4-yl)pyridine ligands are known to be potential quenchers, but using these new ligand systems led to room temperature emission of the corresponding ruthenium(II) complexes. The compounds have been fully characterized by elemental analysis, high-resolution ESI mass spectrometry, <sup>1</sup>H and <sup>13</sup>C NMR spectroscopy, and X-ray crystallography. Theoretical calculations for two ruthenium(II) complexes bearing a donor and acceptor unit, respectively, were performed to gain a deeper understanding of the photophysical behavior.

### Introduction

The well-known *N*-heterocycles 2,2'-bipyridine (bpy) and 2,2':6',2''-terpyridine (tpy) have been widely studied owing to their predictable coordination behavior and the interesting

photophysical and electrochemical properties that can result from their corresponding metal complexes. Such distinctiveness can be utilized for supramolecular self-assembly, molecular electronics, and catalysis applications.<sup>1</sup> Because functionalization

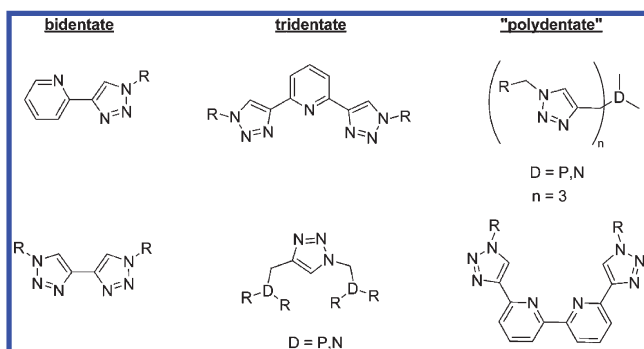


**FIGURE 1.** Schematic representation of 1*H*-[1,2,3]triazole-containing ligand architectures.

of polypyridine-based chelators can be synthetically troublesome,<sup>2</sup> it remains important to search for new approaches in the preparation of analogous bidentate chelating ligands that also possess well-defined coordination properties and can be prepared and modified with high effectiveness. In this respect the Cu<sup>I</sup>-catalyzed 1,3-cycloaddition of organic azides with terminal alkynes (the CuAAC reaction) has a great potential due to its mild reaction conditions and wide range of usable substrates.<sup>3</sup> The latter features have directed its application in the synthesis of functional molecules for biological and material sciences.<sup>4</sup> Furthermore, the development of the CuAAC reaction resulted in an increased interest toward the coordination chemistry of 1,4-functionalized 1*H*-[1,2,3]triazoles due to their potential as *N*-donor ligands. A variety of new bi-,<sup>5,6</sup> tri-,<sup>7</sup> and polydentate<sup>6</sup> 1*H*-[1,2,3]triazole-containing ligands have been synthesized and their coordination properties were investigated (Figure 1).

(1) (a) Balzani, V.; Juris, A.; Venturi, M.; Campagna, S.; Serroni, S. *Chem. Rev.* **1996**, *96*, 759–833. (b) Schubert, U. S.; Eschbaumer, C. *Angew. Chem., Int. Ed.* **2002**, *41*, 2892–2926. (c) Hofmeier, H.; Schubert, U. S. *Chem. Soc. Rev.* **2004**, *33*, 373–399. (d) Sauvage, J.-P.; Collin, J.-P.; Chambrion, J.-C.; Guillerez, S.; Coudret, C. *Chem. Rev.* **1994**, *94*, 993–1019. (e) Amabilino, D. B.; Stoddart, J. F. *Chem. Rev.* **1995**, *95*, 2725–2828.

(2) (a) Newkome, G. R.; Patri, A. K.; Holder, E.; Schubert, U. S. *Eur. J. Org. Chem.* **2004**, 235–254. (b) Heller, M.; Schubert, U. S. *Eur. J. Org. Chem.* **2003**, 947–961. (c) Marin, V.; Holder, E.; Schubert, U. S. *J. Polym. Sci., Part A: Polym. Chem.* **2004**, *42*, 374–385.

(3) (a) Kolb, H. C.; Finn, M. G.; Sharpless, K. B. *Angew. Chem., Int. Ed.* **2001**, *40*, 2004–2021. (b) Tornøe, C. W.; Christensen, C.; Meldal, M. *J. Org. Chem.* **2002**, *67*, 3057–3064. (c) Rostovtsev, V. V.; Green, L. G.; Fokin, V. V.; Sharpless, K. B. *Angew. Chem., Int. Ed.* **2002**, *41*, 2596–2599.

(4) (a) Lutz, J.-F. *Angew. Chem., Int. Ed.* **2007**, *46*, 1018–1025. (b) Bock, V. D.; Hiemstra, H.; van Maarseveen, J. H. *Eur. J. Org. Chem.* **2005**, 51–68. (c) Meldal, M.; Tornøe, C. W. *Chem. Rev.* **2008**, *108*, 2952–3015. (d) Kolb, H. C.; Sharpless, K. B. *Drug Discovery Today* **2003**, *8*, 1128–1137. (e) Angell, Y. L.; Burgess, K. *Chem. Soc. Rev.* **2007**, *36*, 1674–1689. (f) Becer, C. R.; Hoogenboom, R.; Schubert, U. S. *Angew. Chem., Int. Ed.* **2009**, *48*, 4900–4908.

(5) (a) Schweinfurth, D.; Hardcastle, K. I.; Bunz, U. H. F. *Chem. Commun.* **2008**, 2203–2205. (b) Monkowius, U.; Ritter, S.; Koenig, B.; Zabel, M.; Yersin, H. *Eur. J. Inorg. Chem.* **2007**, 4597–4606. (c) Richardson, C.; Fitchett, C. M.; Keene, F. R.; Steel, P. J. *Dalton Trans.* **2008**, 2534–2537.

(6) (a) Rodionov, V. O.; Fokin, V. V.; Finn, M. G. *Angew. Chem., Int. Ed.* **2005**, *44*, 2210–2215. (b) Huang, S.; Clark, R. J.; Zhu, L. *Org. Lett.* **2007**, *9*, 4999–5002. (c) Donnelly, P. S.; Zanatta, S. D.; Zammit, S. C.; White, J. M.; Williams, S. J. *Chem. Commun.* **2008**, 2459–2461.

(7) (a) Li, Y.; Huffman, J. C.; Flood, A. H. *Chem. Commun.* **2007**, 2692–2694. (b) Meudtner, R. M.; Ostermeier, M.; Goddard, R.; Limberg, C.; Hecht, S. *Chem.—Eur. J.* **2007**, *13*, 9834–9840. (c) Schuster, E. M.; Botoshansky, M.; Gandelman, M. *Angew. Chem., Int. Ed.* **2008**, *47*, 4555–4558. (d) Fletcher, J. T.; Bumgarner, B. J.; Engels, N. D.; Skoglund, D. A. *Organometallics* **2008**, *27*, 5430–5433. (e) Schulze, B.; Friebe, C.; Hager, M. D.; Winter, A.; Hoogenboom, R.; Goerls, H.; Schubert, U. S. *Dalton Trans.* **2009**, 787–794.

Our interest was to tune in particular the electronic properties of the bidentate 2-(1*H*-[1,2,3]triazol-4-yl)pyridine ligands. This was accomplished by introducing electron-donating and electron-withdrawing units on the 5-position of the pyridine ring with a 2-(1*H*-[1,2,3]triazol-4-yl)pyridine system (trzpy) as central structural motive (Scheme 1). In the present study the synthesis and the characterization of new 2-(1*H*-[1,2,3]triazol-4-yl)pyridine ligand systems with donor and acceptor nature are described by using the efficient Sonogashira coupling and the versatile copper(I)-catalyzed azide–alkyne 1,3-cycloaddition intended for the ligand synthesis as well as the subsequent coordination onto a bis-(4,4'-dimethyl-2,2'-bipyridine)ruthenium(II) precursor complex. The photophysical properties were studied by UV-vis and emission spectroscopy, cyclic voltammetry and analyzed in detail by theoretical calculations.

The coordination to the ruthenium(II) metal ion by using bis(4,4'-dimethyl-2,2'-bipyridine) as ancillary ligand revealed two interesting features. First, 2-(1*H*-[1,2,3]triazol-4-yl)pyridine systems are known to be potential luminescence quenchers at room temperature as soon as they are attached to a ruthenium(II) metal ion<sup>8</sup> and, unexpectedly, the herein described heteroleptic ruthenium(II) complexes bearing a 2-(1*H*-[1,2,3]triazol-4-yl)pyridine ligand furnished with an acceptor unit overcame this luminescence quenching and yielded in room temperature emission. Second, by replacing the latter acceptor system with a donor structure the luminescence at room temperature decreased considerably. Therefore, time-dependent density functional theory calculations (TD-DFT) were done to gain a deeper insight into the photophysical processes.

## Results and Discussion

**Synthesis.** The general procedure for the synthesis of donor-type 2-(1*H*-[1,2,3]triazol-4-yl)pyridine **5** is outlined in Scheme 2. The Sonogashira cross-coupling<sup>9</sup> and the CuAAC<sup>3b,c</sup> reaction were the key reaction types for the construction of the targeted ligand. Consecutive Sonogashira reactions with 2 mol % of Pd<sup>0</sup> catalyst were carried out to synthesize intermediate **3**. Subsequently, deprotection of the trimethylsilyl group (TMS) utilizing fluoride ions afforded **4** in good yield (75%). The subsequent CuAAC reaction provided the final product **5** (67% yield) by using 5 mol % CuSO<sub>4</sub> and 25 mol % sodium ascorbate as the catalytic system. The purity of **5** was proven by NMR spectroscopy, mass spectrometry, and elemental analysis.

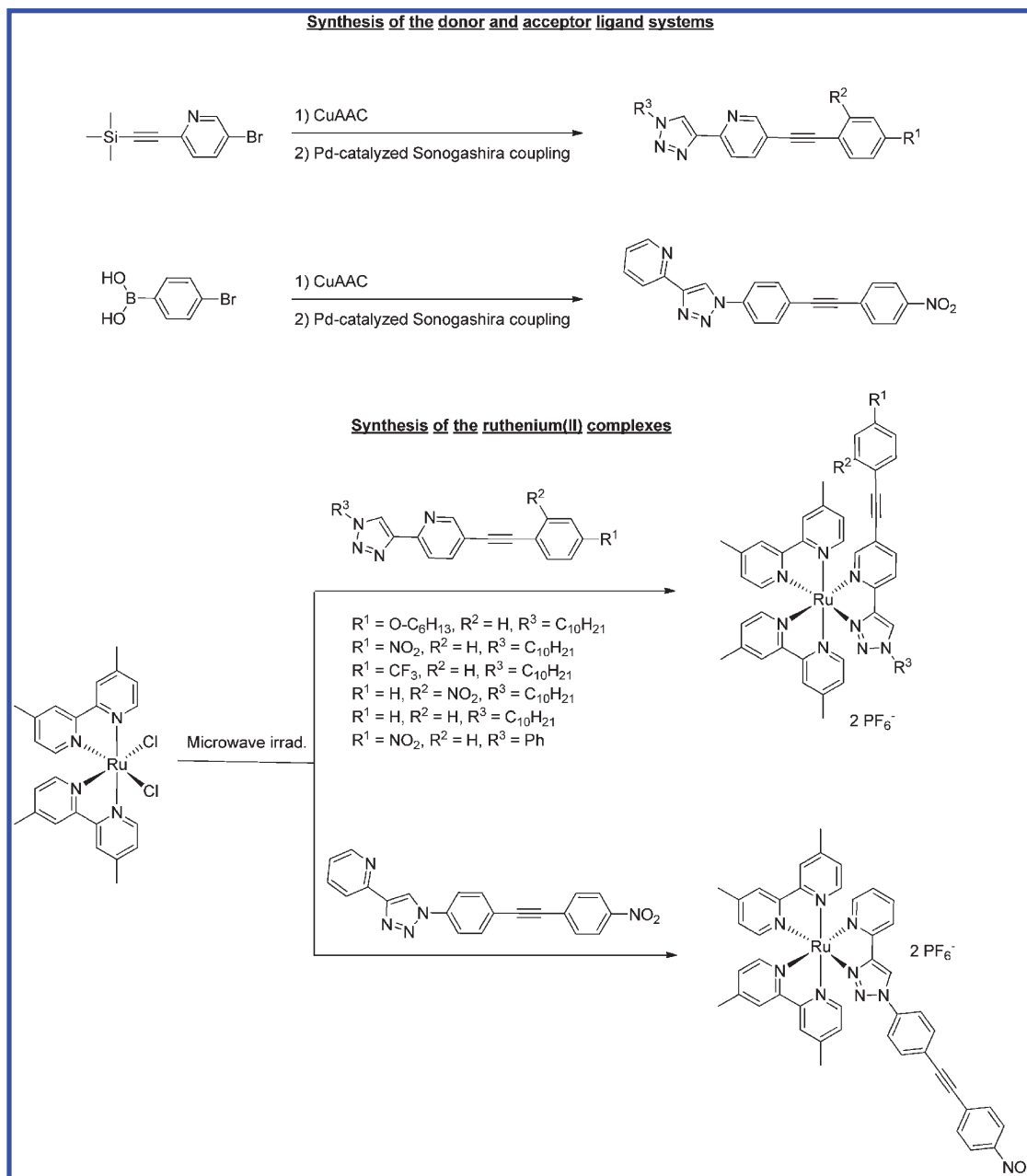
The synthesis of the acceptor systems **10a–d** also involved the Sonogashira cross-coupling and the CuAAC reaction as synthetic tools; however, a different synthetic approach had to be used. The synthesis of a precursor compound similar to **3** with electron-withdrawing substituents could not be performed. As a result, two alternative routes were applied to synthesize precursor compound **9** (Scheme 3). Though the first route consisted of one step less, both routes gave comparable overall yields (route 1: 61%; route 2: 51%). The reason for this observation might be the efficient cleavage of the TMS group<sup>10</sup> affording **6**

(8) Happ, B.; Friebe, C.; Winter, A.; Hager, M. D.; Hoogenboom, R.; Schubert, U. S. *Chem.—Asian J.* **2009**, *4*, 154–163.

(9) Analogue procedure: Bianchini, C.; Giambastiani, G.; Rios, I. G.; Meli, A.; Oberhauser, W.; Sorace, L.; Toti, A. *Organometallics* **2007**, *26*, 5066–5078.

(10) Nakano, Y.; Ishizuka, K.; Muraoka, K.; Ohtani, H.; Takayama, Y.; Sato, F. *Org. Lett.* **2004**, *6*, 2373–2376.

**SCHEME 1. Schematic Representation of the Synthesis of the *N*-Heterocyclic Ligands and Their Corresponding Heteroleptic Ruthenium(II) Complexes**



in quantitative yield. Subsequently, the ligands **10a–d** were obtained in good to high yields (70–93%) utilizing the straightforward Sonogashira cross-coupling with 2–4 mol % of the palladium(0) catalyst. All final products were purified by column chromatography on silica and the purity was confirmed by elemental analysis, high-resolution mass spectrometry (HR-ESI-MS), as well as  $^1\text{H}$  and  $^{13}\text{C}$  NMR spectroscopy.

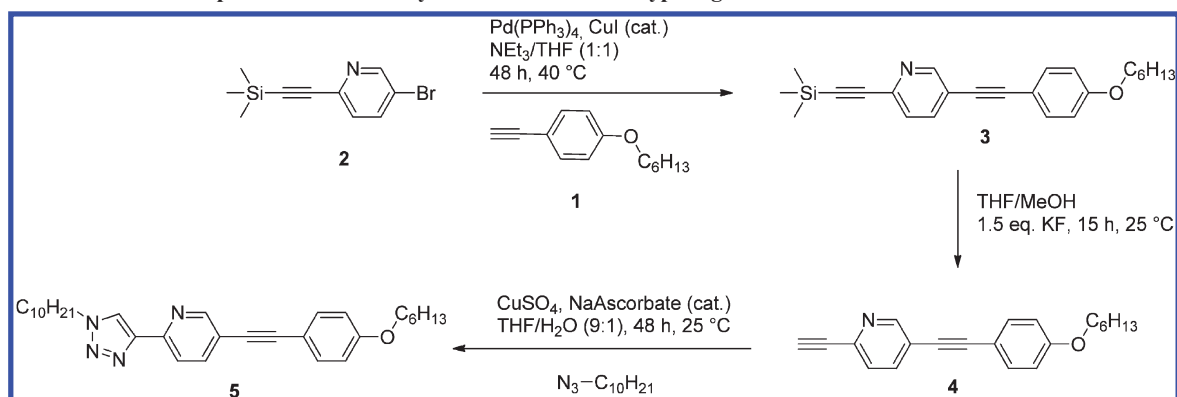
The second route turned out to be also a versatile way to introduce an aromatic substituent in the  $N^1$ -position of the triazole as an alternative to the decyl-moiety in **10** (Scheme 4). Substitution of the flexible alkyl-chain by a more rigid phenyl ring should enhance the growth of single crystals, in particular of the targeted heteroleptic  $\text{Ru}^{\text{II}}$  complexes. For this purpose, **6** was allowed to react with phenylazide<sup>8</sup> using the CuAAC reaction

yielding compound **11** (45%) after cleavage of the isopropanol protection group (Scheme 4). Finally, the  $N^1$ -phenyl-substituted compound **12** was obtained by Sonogashira cross-coupling reaction in good yield (77%).

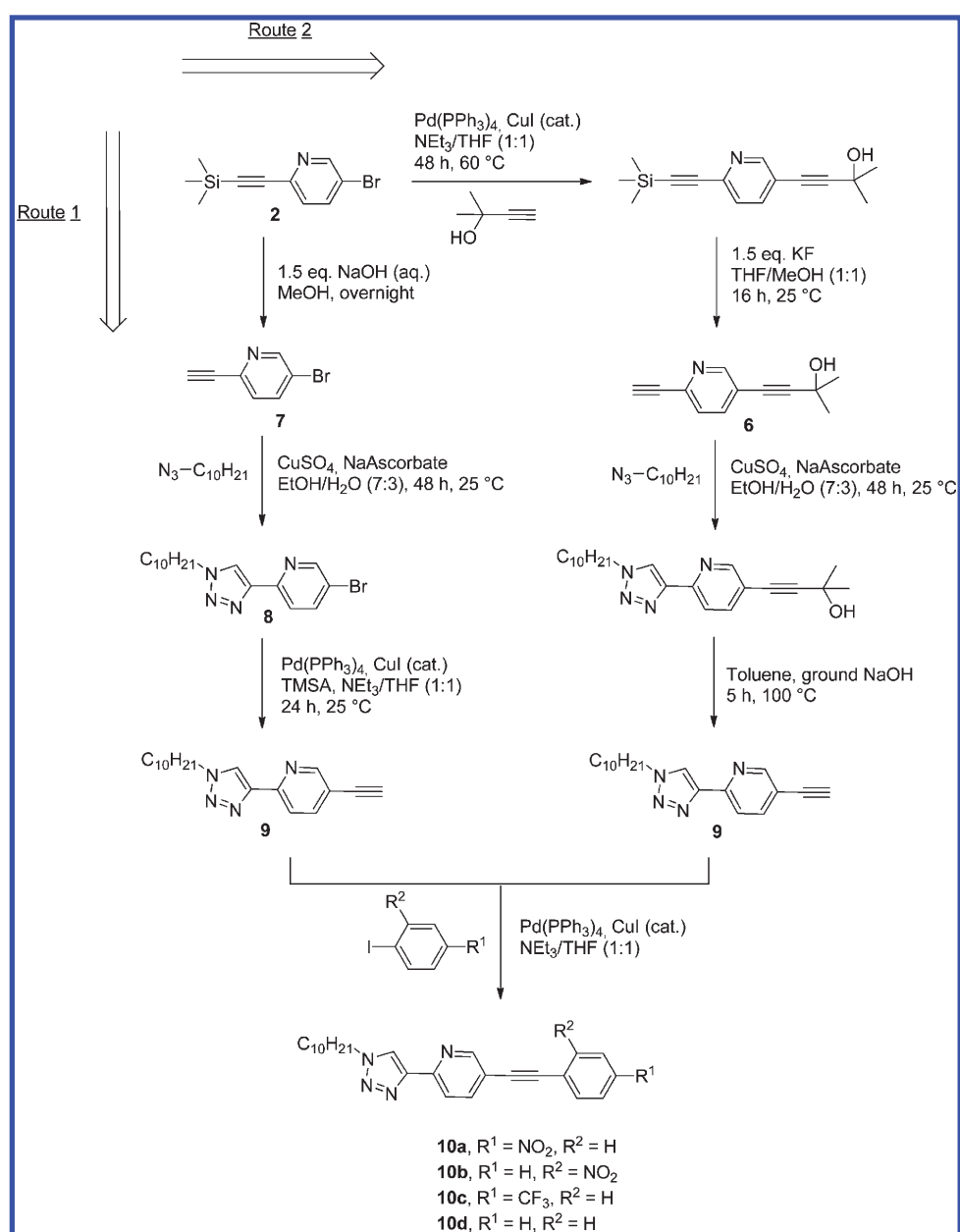
Besides the systems featuring donor or acceptor units attached to the pyridine ring (**5**, **10**, and **12**), also derivatives with similar substituents in the  $N^1$ -position of the 1*H*-[1,2,3]triazole subunit were in the focus (Scheme 5). For this purpose, (1-azidophenyl)boronic acid<sup>8</sup> and 2-ethynylpyridine were conjugated by using the CuAAC reaction yielding **13**. The purification steps, i.e. simple filtration and recrystallization from ethanol, fully met the criteria of a “click reaction” as defined by Sharpless et al.<sup>3a</sup> Following two times the standard protocol for the Sonogashira cross-coupling reaction, the final

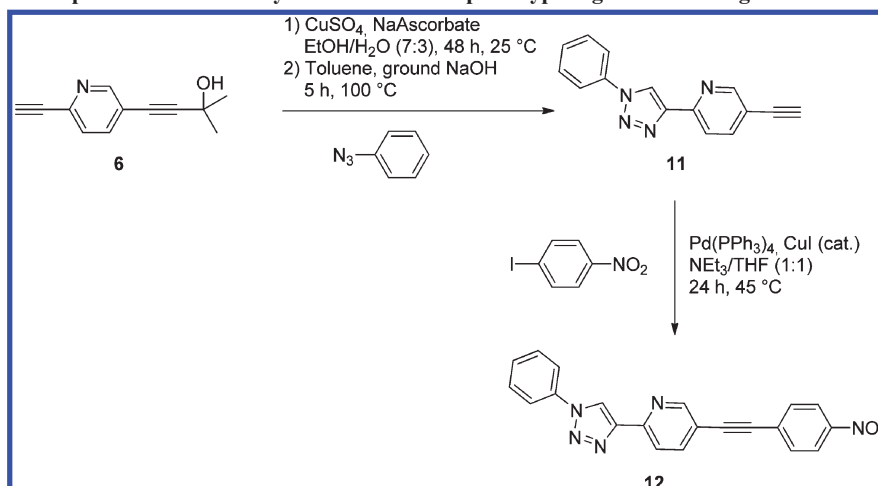
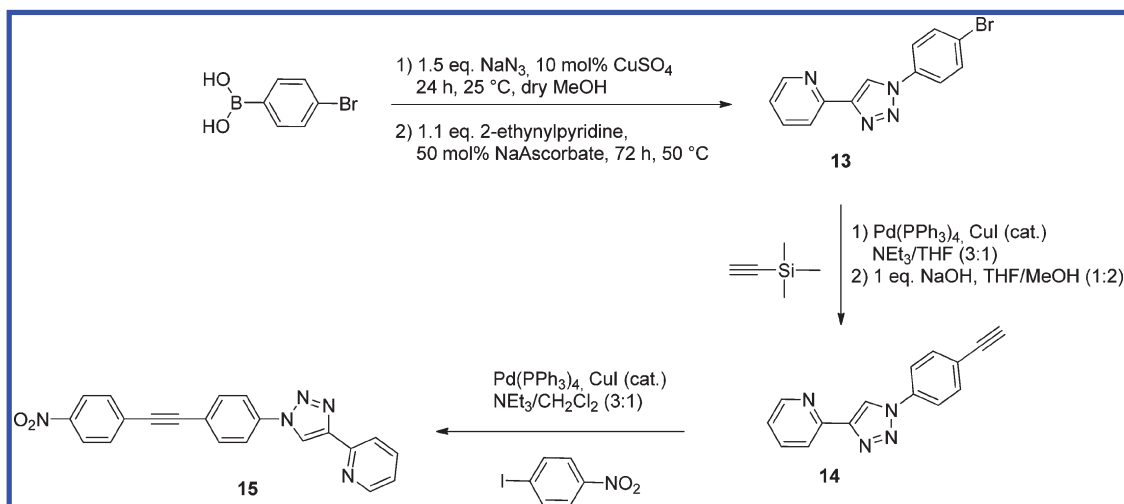


SCHEME 2. Schematic Representation of the Synthesis of the Donor-Type Ligand 5



SCHEME 3. Schematic Representation of the Synthesis of the Acceptor-Type Ligands 10



SCHEME 4. Schematic Representation of the Synthesis of the Acceptor-Type Ligand **12** Bearing an Aromatic MoietySCHEME 5. Schematic Representation of the Synthesis of a 2-(1*H*-[1,2,3]Triazol-4-yl)pyridyl Ligand with an Acceptor-Unit Attached on the Triazole Ring

acceptor-functionalized compound **15** was synthesized in moderate yield (50%). However, the implementation of the *O*-alkyl donor system in analogy to **5** was not yet successful.

The heteroleptic ruthenium(II) complexes **16** to **18** of the general structure  $[(\text{dmbpy})_2\text{RuL}](\text{PF}_6)_2$  ( $\text{dmbpy}$  = 4,4'-dimethyl-2,2'-bipyridine) were synthesized by heating  $\text{Ru}(\text{dmbpy})_2\text{Cl}_2$ <sup>8,11</sup> and the appropriate ligands ( $\text{L}$  = **5**, **10**, **12**, **15**) under microwave irradiation (Table 1). After 2 h the reactions were completed and a 10-fold excess of  $\text{NH}_4\text{PF}_6$  was added to precipitate the products. In most cases, precipitation occurred after 15 min and the pure complex was isolated after washing with ethanol and diethyl ether in moderate to very good yields (Table 1). Only **16c** and **17** had to be recrystallized from ethanol/water. The latter fact may explain the moderate yields obtained for these complexes. The verification of the structures of **16**–**18** was carried out by <sup>1</sup>H and <sup>13</sup>C NMR spectroscopy as well as HR-ESI mass spectrometry.

**Crystallographic Analysis.** For the heteroleptic  $\text{Ru}^{\text{II}}$  complex **17** single crystals suitable for X-ray crystallographic analysis were obtained by slow diethyl ether diffusion revealing the coordination of the two 4,4'-dimethyl-2,2'-bipyridine and the 2-(1*H*-[1,2,3]triazol-4-yl)pyridine ligand **12** to the  $\text{Ru}^{\text{II}}$  core. The molecule crystallizes in a triclinic system with  $P\bar{1}$  symmetry (for ORTEP see the Supporting Information). The structural parameters observed from **17** were compared to the corresponding structurally related homoleptic complex  $[\text{Ru}(\text{bpy})_3](\text{PF}_6)_2$ <sup>12</sup> (Figure 2).

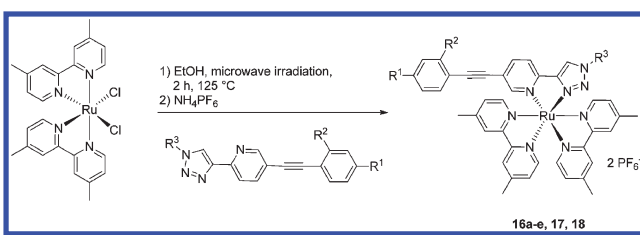
It is noteworthy that the interligand angle of the nitrogen atoms in the square plane were similar for both complexes (**17**: 170.40° and 174.40°;  $[\text{Ru}(\text{bpy})_3](\text{PF}_6)_2$ : 172.3°; see Figure 2) resulting in a comparable distortion of the ideal octahedral geometry. The bond length from ruthenium to the coordinating nitrogen atom of the triazole ring ( $\text{N}^7$ : 2.028(2), Figure 2) was shortened significantly compared

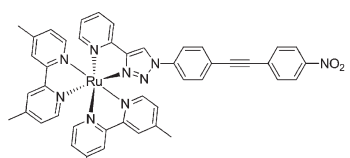
(11) Rau, S.; Ruben, M.; Büttner, T.; Temme, C.; Dautz, S.; Görls, H.; Rudolph, M.; Walther, D.; Vos, J. G. *J. Chem. Soc., Dalton Trans.* **2000**, 3649–3657.

(12) Biner, M.; Büergi, H. B.; Ludi, A.; Roehr, C. *J. Am. Chem. Soc.* **1992**, *114*, 5197–5203.

(13) Egbe, D. A. M.; Bader, C.; Nowotny, J.; Günther, W.; Klemm, E. *Macromolecules* **2003**, *36*, 5459–5469.

TABLE 1. Synthesis of the Heteroleptic Ruthenium(II) Complexes



Entry	Compound	Product	Yield (%)
1	16a	R <sup>1</sup> = OC <sub>6</sub> H <sub>13</sub> R <sup>2</sup> = H R <sup>3</sup> = <i>n</i> -C <sub>10</sub> H <sub>21</sub>	81
2	16b	R <sup>1</sup> = NO <sub>2</sub> R <sup>2</sup> = H R <sup>3</sup> = <i>n</i> -C <sub>10</sub> H <sub>21</sub>	88
3	16c	R <sup>1</sup> = CF <sub>3</sub> R <sup>2</sup> = H R <sup>3</sup> = <i>n</i> -C <sub>10</sub> H <sub>21</sub>	48
4	16d	R <sup>1</sup> = H R <sup>2</sup> = NO <sub>2</sub> R <sup>3</sup> = <i>n</i> -C <sub>10</sub> H <sub>21</sub>	90
5	16e	R <sup>1</sup> = H R <sup>2</sup> = H R <sup>3</sup> = C <sub>10</sub> H <sub>21</sub>	75
6	17	R <sup>1</sup> = NO <sub>2</sub> R <sup>2</sup> = H R <sup>3</sup> = phenyl	63
7	18		77

to that of the adjacent coordinating nitrogen atom of the bipyridine ring (N: 2.052(1), Figure 2). In contrast, the bond length of the opposed coordinating nitrogen to the triazole nitrogen was not reduced but comparable to that of bipyridine. This observation could be rationalized by the expected higher  $\pi$ -acceptor strength of the triazole ring and, consequently, the increased  $\pi$ -back-bonding resulting in a reduced bond length. Additionally, the distance between the ruthenium center and the nitrogen atom of the pyridine moiety of **12** was elongated considerably (N: 2.102(1), Figure 2). This fact derives from a reduction of electron density of this bond in concert with an increased  $\pi$ -back-bonding toward the triazole ring.

**Electrochemical Properties.** The complexes **16a–e** were subsequently characterized by cyclic voltammetry (CV). The

TABLE 2. Electrochemical Data of Selected Ru<sup>II</sup> Complexes

complex	$E_{1/2,ox}$ [V] <sup>a</sup>	$E_{1/2,red}$ [V] <sup>a</sup>	$E_g^{opt}$ [eV] <sup>b</sup>	$E^{HOMO}$ [eV] <sup>c</sup>	$E^{LUMO}$ [eV] <sup>c</sup>
16a	0.82, 1.28	-1.85, -2.06, -2.23	2.48	-5.62	-3.18
16b	0.88	-1.34, -1.97, -2.18	2.43	-5.67	-3.70
16c	0.84	-1.89, -2.13	2.44	-5.69	-3.21
16d	0.88	-1.36, -1.98, -2.11	2.43	-5.64	-3.62
16e	0.84	-1.85, -2.03, -2.18	2.49	-5.64	-3.17

<sup>a</sup>Measurements were performed in CH<sub>3</sub>CN containing 0.1 M TBAPF<sub>6</sub>. The potentials are given vs ferrocene/ferricenium (Fc/Fc<sup>+</sup>) couple. <sup>b</sup>Estimated from the UV-vis spectra at 10% of the maximum of the longest-wavelength absorption band on the low-energy side. <sup>c</sup>Determined using  $E^{HOMO} = -[(E_{onset,ox} - E_{onset,Fc/Fc^+}) - 4.8]eV$  and  $E^{LUMO} = -[(E_{onset,red} - E_{onset,Fc/Fc^+}) - 4.8]eV$ , respectively.<sup>13</sup>

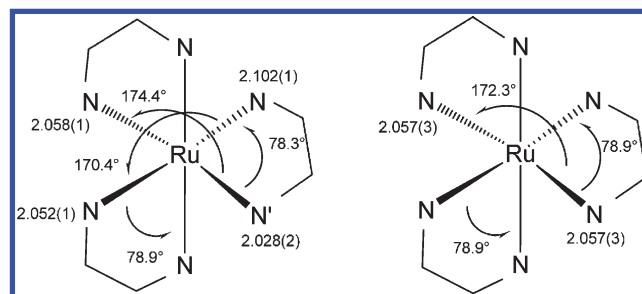


FIGURE 2. A comparison of bond angles and bond lengths derived from the crystallographic analysis. Left: Ru<sup>II</sup> complex **17**. Right: Ru(bpy)<sub>3</sub>(PF<sub>6</sub>)<sub>2</sub>.<sup>12</sup>

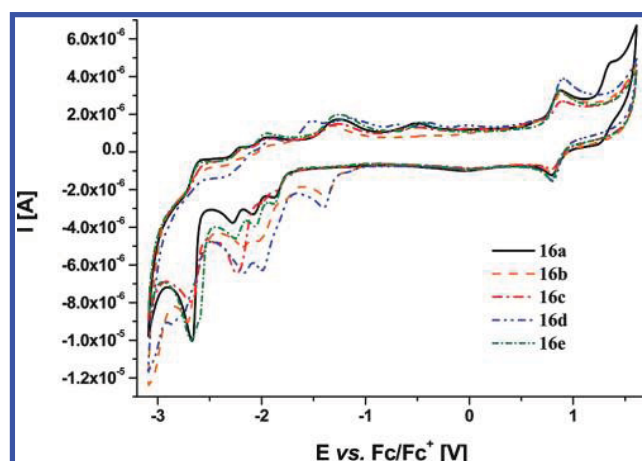


FIGURE 3. Cyclic voltammograms of ruthenium(II) complexes **16a** to **16e** (10<sup>-4</sup> M, CH<sub>3</sub>CN containing 0.1 M TBAPF<sub>6</sub>).

electrochemical properties are presented in Table 2 and Figure 3.

In all cases a first reversible oxidation wave occurred at around 0.85 V (vs Fc/Fc<sup>+</sup>) that can be assigned to a Ru<sup>II</sup>/Ru<sup>III</sup> oxidation process. Furthermore, compound **16a** showed a second oxidation process at 1.28 V, probably originating from an oxidation process of the triazole ligand. Due to the absence of electron-donating substituents at the triazole ligand, the respective ligand-centered  $\pi$ -orbitals are more stabilized for complexes **16b–e** and, therefore, no such oxidation processes were visible in the CV spectrum.

In contrast to the other systems, the nitro-containing complexes **16b** and **16d** featured a single reversible reduction wave at around -1.35 V vs Fc/Fc<sup>+</sup> that could be assigned to a triazole ligand-based reduction process. Both complexes provided a strongly electron-withdrawing substituent causing a stabilization of the triazole-ligand-located antibonding

**TABLE 3. Photophysical Data of the Donor- and Acceptor-Type Ligands**

compound	$\lambda_{\text{abs}}$ [nm] ( $\epsilon$ [ $10^3 \text{ L} \cdot \text{mol}^{-1} \cdot \text{cm}^{-1}$ ]) <sup>a</sup>	$\lambda_{\text{em}}$ [nm] <sup>a</sup>
<b>5</b>	250 (2), 323 (32), 338 (30)	378
<b>10a</b>	273 (26), 343 (47)	— <sup>b</sup>
<b>10b</b>	271 (30), 315 (33), 338 (21)	— <sup>b</sup>
<b>10c</b>	297 (24), 315 (32), 329 (26)	363
<b>10d</b>	297 (24), 315 (29), 329 (25)	358
<b>12</b>	270 (18), 342 (25)	— <sup>b</sup>

<sup>a</sup>For all measurements:  $10^{-6}$  M solution ( $\text{CH}_2\text{Cl}_2$ ). For emission measurements: excitation at longest absorption wavelength. <sup>b</sup>No emission detectable at room temperature.

$\pi^*$ -orbitals (*q.v.* results of the DFT calculations). Starting at  $-1.8$  V all five complexes showed additional reduction waves deriving from ligand-based (dmbpy and triazole ligand)  $\pi^*$ -orbitals.

**Photophysical Properties.** The UV–vis absorption and emission data of the donor- and acceptor-type systems are depicted in Table 3. As expected, ligand **10a** (nitro-moiety in the para-position) revealed the largest bathochromic shift in the absorption spectrum, but did not show fluorescence at room temperature. In contrast to **10a**, the donor-system **5** as well as the acceptor ligands without nitro groups (**10c/d**) revealed room temperature emission. Compound **5** showed the largest Stokes shift of  $3130 \text{ cm}^{-1}$  whereas **10c** and **10d** featured remarkably small Stokes shifts (**10c**:  $1220 \text{ cm}^{-1}$ ; **10d**:  $1240 \text{ cm}^{-1}$ ). The reason for the large Stokes shift of **5** was probably caused by the charge transfer nature of the electronic transition.

The optical properties of the heteroleptic ruthenium(II) complexes are summarized in Table 4. A common feature of all complexes was a broad absorption band at around 400 to 500 nm, which could be assigned mainly to various metal-to-ligand charge-transfer (MLCT) transitions between the ruthenium metal center and either the 4,4'-dimethyl-2,2'-bipyridine or the triazole ligand (see DFT calculations). All complexes possessed extinction coefficients of about  $20\,000 \text{ M}^{-1} \cdot \text{cm}^{-1}$ , whereas the alkoxy and the unsubstituted systems showed slightly higher values ( $24\,000$  and  $21\,000 \text{ M}^{-1} \cdot \text{cm}^{-1}$ ) than their trifluoromethyl ( $18\,000 \text{ M}^{-1} \cdot \text{cm}^{-1}$ ) or even nitro counterparts ( $12\,000$  and  $13\,000 \text{ M}^{-1} \cdot \text{cm}^{-1}$ ). Between 300 and 400 nm, the complexes investigated herein exhibited different absorption behavior concerning their wavelength maxima and band shape. Therefore, this region seemed to be dominated by intraligand (IL) transitions, namely located at the triazole ligand. A comparison with the respective absorption spectra of triazole ligands (Table 3) supported this assumption. At 286 nm a strong absorption ( $65\,000$  to  $135\,000 \text{ M}^{-1} \cdot \text{cm}^{-1}$ ) could be observed for all complexes, most likely originating from a dmbpy-located IL

transition. More bands were present below 280 nm that arose from further MLCT, ligand-to-ligand charge transfer (LLCT) and metal-centered (MC) d–d transitions, respectively.

The observed emission energies (Table 4) showed a clear dependency on the used substituent. Starting at 602 nm in the case of the alkoxy-containing system, the emission was strongly red-shifted to 621 nm for the unsubstituted triazole ligand and to 640 and even 674 nm in the case of the complexes possessing an *o*- and *p*-nitrophenyl moiety, respectively. This trend was most likely caused by the stabilization of the  $\pi^*$ -orbitals located at the triazole ligand via introduction of electron-withdrawing groups. These orbitals are, at least in case of electron-acceptor substituents, supposed to be involved in the emissive  $^3\text{MLCT}$  state, so that a lower energy level led to decreased emission energy.

Also depicted in Table 4 are the photoluminescence quantum yields ( $\Phi_{\text{PL}}$ ) of the ruthenium(II) systems. At least in aerated acetonitrile, the  $\Phi_{\text{PL}}$  values were rather low (around 0.1% for **16a–e**, nearly no emission in the case of phenyl-substituted **17** and about 0.3% for the “inverse” system **18**). When changing to dichloromethane as solvent, the emission efficiencies rose and a significant difference between the donor- (**16a**) and the acceptor-substituted complex (**16b**) became obvious (0.5% and 2.2%, respectively).

**DFT Calculations.** To gain a more detailed insight into the photophysical properties of the acceptor- and donor-based complexes, density functional theory (DFT) and time-dependent (TD) DFT (B3LYP/6-31G\*) calculations were performed. DFT/TD-DFT studies on Ru(II) polypyridyl complexes have been successfully used to understand and rationalize the experimental photophysical features of these complexes.<sup>15</sup> Figure 4 shows the obtained Kohn–Sham frontier orbitals and energy level schemes of the ground state optimized geometries of complexes **16a** and **16b**. In complex **16b** the highest occupied molecular orbitals (HOMOs) were the set  $t_{2g}$  of the central Ru<sup>II</sup> atom. A  $\pi$ -orbital localized in the 2-(1*H*-[1,2,3]triazol-4-yl)pyridine ligand ( $\pi_{\text{L}}$ ) was lower in energy corresponding to the HOMO-3. These orbitals were in different order in the complex **16a**: The  $\pi_{\text{L}}$  corresponded to the HOMO orbital and the set  $t_{2g}$  of orbitals was found lower in energy. Both complexes **16a** and **16b** also differed in the order of the lowest unoccupied molecular orbitals (LUMO). In the case of the acceptor-type compound the LUMO orbital corresponded to a  $\pi$ -antibonding orbital located in the 2-(1*H*-[1,2,3]triazol-4-yl)pyridine ligand ( $\pi^*_{\text{L}}$ ), while this orbital was shifted to the LUMO+2 in complex **16a**. In **16a** the LUMO possessed  $\pi$ -antibonding character and was located on the dmbpy ligand ( $\pi^*_{\text{dmbpy}}$ ). Substitution of the 2-(1*H*-[1,2,3]triazol-4-yl)pyridine ligand with an electron-donating or -withdrawing group,

**TABLE 4. Photophysical Data Recorded for the Ru<sup>II</sup> Complexes**

complex	$\lambda_{\text{abs}}$ [nm] ( $\epsilon$ [ $10^3 \text{ L} \cdot \text{mol}^{-1} \cdot \text{cm}^{-1}$ ]) <sup>a,b</sup>	$\lambda_{\text{em}}$ [nm] <sup>a</sup>	$\Phi_{\text{PL}}$ <sup>a,c</sup>
<b>16a</b>	206 (145.6), 286 (133.1), 333 (59.8), 435 (23.6)	602	0.001 [0.005 <sup>d</sup> ]
<b>16b</b>	209 (58.4), 286 (63.4), 328 (38.6), 441 (11.6)	674	0.001 [0.022 <sup>d</sup> ]
<b>16c</b>	209 (88.1), 286 (103.9), 312s (51.6), 440 (18.3)	620	0.002
<b>16d</b>	208 (66.6), 286 (74.7), 341s (22.6), 442 (12.4)	640	0.001
<b>16e</b>	205 (131.1), 286 (125.6), 315s (60.9), 438 (20.6)	621	0.001
<b>17</b>	206 (83.7), 286 (76.9), 326 (52.5), 440 (12.8)	642	< 0.001
<b>18</b>	195 (102.9), 286 (83.1), 316s (40.5), 442s (12.5)	610	0.003

<sup>a</sup>For all measurements:  $10^{-6}$  M solution in aerated  $\text{CH}_3\text{CN}$  at room temperature. For emission measurements: excitation at longest absorption wavelength. <sup>b</sup>“s” signifies absorption shoulder. <sup>c</sup>Photoluminescence quantum yields determined with  $[\text{Ru}(\text{bpy})_3](\text{PF}_6)_2$  ( $\Phi_{\text{PL}} = 0.062$ ) as standard.<sup>14</sup> <sup>d</sup>Measured in aerated  $\text{CH}_2\text{Cl}_2$  solution at room temperature ( $10^{-6}$  M).

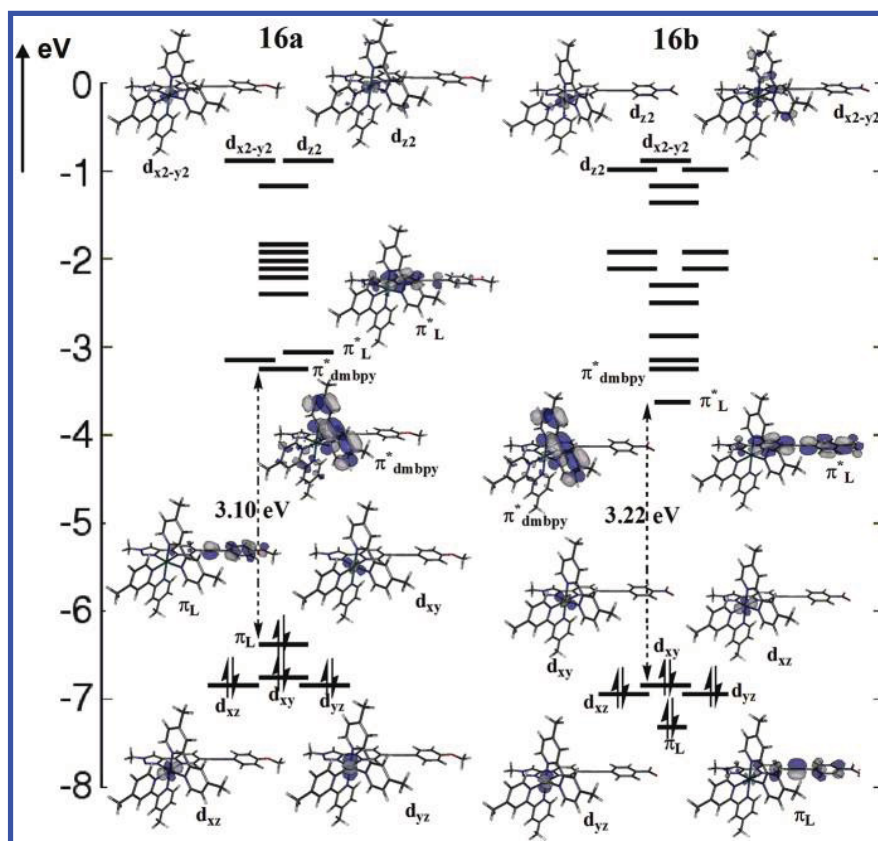


**FIGURE 4.** Energy level scheme for the Kohn–Sham orbitals of complexes **16a** and **16b**, including the most relevant Kohn–Sham orbitals and the HOMO–LUMO gaps calculated with B3LYP/6-31G\*.

respectively, had therefore an important influence on the energy level and ordering of the molecular orbitals.

The set  $e_g$  of Ru<sup>II</sup> orbitals was, as shown in Figure 4, strongly destabilized. Thus, the  $d_{z^2}$  and  $d_{x^2-y^2}$  orbitals corresponded to LUMO+10 and LUMO+11 in complex **16a**, respectively, while in complex **16b** they related to the orbitals LUMO+12 and LUMO+14. The energetic gaps between the HOMO and LUMO levels are also shown in Figure 4. We obtained theoretical HOMO–LUMO gaps of 3.10 and 3.22 eV for **16a** and **16b**, respectively.

Figure 5 shows the theoretical UV–vis spectra of complexes **16a** and **16b** vs the experimental ones. Table 5 collects the main TD-DFT electronic excitations recorded in the presence of solvent (i.e., CH<sub>2</sub>Cl<sub>2</sub>). A fairly good agreement between experiment and theory was observed, notwithstanding that TD-DFT generally tends to underestimate the energy of the charge-transfer states,<sup>16</sup> even if it is well-established that hybrid functionals, such as B3LYP, are less affected by this problem.<sup>17</sup> However, the combination of a

hybrid functional and the consideration of solvent effects on the electronic excitations seemed to be a reasonable approach to reproduce the photophysical properties of the ruthenium(II) complexes (with errors amounting to approximately 0.3 eV). The main features of the experimental spectra were reproduced. Three main bands were obtained for both complexes **16a** and **16b**. As seen in Figure 5, no absorption for both compounds was theoretically predicted beyond 470 nm. Experimentally, absorption was recorded up to 500 nm. The tail between 470 and 520 nm, where singlet–singlet excitations are dark or do not exist, should then be attributed to singlet–triplet excitations (due to non-negligible spin–orbit coupling for the ruthenium atom).

The effect of substitution with an acceptor or a donor unit attached in the 5-position of the pyridine ring had a significant influence on the nature as well as on the position of the UV–vis bands. Thus, in the case of **16a**, the low-energy broad band centered around 440 nm could be assigned to different singlet–singlet electronic excitations of MLCT character (see S<sub>4</sub>, S<sub>8</sub>, and S<sub>9</sub> in Table 5) as well as LLCT character (see S<sub>3</sub> and S<sub>7</sub> in Table 5). Although a very similar broad band was obtained in the case of compound **16b**, the character of the underlying transitions was different. In complex **16b** this band was mainly composed of MLCT states (see S<sub>4</sub>, S<sub>5</sub>, S<sub>6</sub>, and S<sub>8</sub> in Table 5).

The explanation of the different character of the low-energy bands of **16a** and **16b** could be found by analyzing the orbitals involved in these transitions. For instance, the LLCT states (S<sub>3</sub> and S<sub>7</sub>) of compound **16b**, which involved

(14) (a) Demas, J. N.; Crosby, G. A. *J. Phys. Chem.* **1971**, *75*, 991–1024. (b) Juris, A.; Balzani, V.; Barigelletti, F.; Campagna, S.; Belsler, B.; von Zelewsky, A. *Coord. Chem. Rev.* **1988**, *84*, 85–277.

(15) (a) Vlcek, A., Jr.; Zalis, S. *Coord. Chem. Rev.* **2007**, *251*, 258–287. (b) Charlot, M.-F.; Aukauloo, A. *J. Phys. Chem. A* **2007**, *111*, 11661–11672. (c) Abbotto, A.; Barolo, C.; Bellotto, L.; De Angelis, F.; Grätzel, M.; Manfredi, N.; Marini, C.; Fantacci, S.; Yum, J.-H.; Nazeeruddin, M. K. *Chem. Commun.* **2008**, 5318–5320.

(16) Dreuw, A.; Head-Gordon, M. *Chem. Rev.* **2005**, *105*, 4009–4037.

(17) Dreuw, A.; Weisman, J. L.; Head-Gordon, M. *J. Chem. Phys.* **2003**, *119*, 2943–2946.

TABLE 5. Main Theoretical Electronic Transition Energies ( $\Delta E$ ) with Corresponding Oscillator Strengths ( $f$ ) and Assignment for Complexes **16a** and **16b**

16a				16b			
state	$\Delta E$ (nm)	$f$	assignment	state	$\Delta E$ (nm)	$f$	assignment
S <sub>1</sub>	477	0.003	$d_{xy} \rightarrow \pi^*_{\text{dmbpy}}$ (0.53) MLCT	S <sub>1</sub>	479	0.010	$d_{xy} \rightarrow \pi^*_L$ (0.66) MLCT
S <sub>2</sub>	462	0.003	$d_{xy} \rightarrow \pi^*_{\text{dmbpy}}$ (0.59) MLCT	S <sub>2</sub>	466	0.011	$d_{xy} \rightarrow \pi^*_{\text{dmbpy}}$ (0.65) MLCT
S <sub>3</sub>	453	0.056	$\pi_L \rightarrow \pi^*_{\text{dmbpy}}$ (0.53) LLCT	S <sub>4</sub>	448	0.023	$d_{xz} \rightarrow \pi^*_L$ (0.66) MLCT
S <sub>4</sub>	441	0.162	$d_{xy} \rightarrow \pi^*_L$ (0.51) MLCT	S <sub>5</sub>	439	0.065	$d_{yz} \rightarrow \pi^*_L$ (0.54) MLCT
S <sub>7</sub>	430	0.180	$\pi_L \rightarrow \pi^*_{\text{dmbpy}}$ (0.54) LLCT	S <sub>6</sub>	433	0.030	$d_{xz} \rightarrow \pi^*_{\text{dmbpy}}$ (0.49) MLCT
S <sub>8</sub>	425	0.191	$d_{xy} \rightarrow \pi^*_{\text{dmbpy}}$ (-0.35) MLCT	S <sub>8</sub>	414	0.136	$d_{yz} \rightarrow \pi^*_{\text{dmbpy}}$ (0.40) MLCT
			$\pi_L \rightarrow \pi^*_L$ (0.35) IL				$d_{xz} \rightarrow \pi^*_{\text{dmbpy}}$ (0.43) MLCT
S <sub>9</sub>	420	0.313	$d_{xz} \rightarrow \pi^*_{\text{dmbpy}}$ (0.44) MLCT	S <sub>9</sub>	395	0.124	$d_{xz} \rightarrow \pi^*_{\text{dmbpy}}$ (0.54) MLCT
S <sub>10</sub>	407	0.104	$d_{xz} \rightarrow \pi^*_L$ (0.63) MLCT	S <sub>11</sub>	371	1.262	$\pi_L \rightarrow \pi^*_L$ (0.63) IL
S <sub>11</sub>	401	0.243	$d_{xz} \rightarrow \pi^*_{\text{dmbpy}}$ (0.45) MLCT	S <sub>13</sub>	348	0.039	$d_{yz} \rightarrow \pi^*_L$ (0.54) MLCT
S <sub>13</sub>	360	0.192	$\pi_L \rightarrow \pi^*_L$ (0.61) IL	S <sub>27</sub>	312	0.071	$d_{yz} \rightarrow \pi^*_{\text{dmbpy}}$ (-0.29) MLCT
							$d_{xz} \rightarrow \pi^*_{\text{dmbpy}}$ (0.30) MLCT
S <sub>30</sub>	307	0.094	$d_{yz} \rightarrow \pi^*_{\text{dmbpy}}$ (0.51) MLCT	S <sub>32</sub>	305	0.116	$d_{yz} \rightarrow \pi^*_{\text{dmbpy}}$ (0.32) MLCT
							$d_{yz} \rightarrow \pi^*_{\text{dmbpy}}$ (0.44) MLCT
S <sub>32</sub>	306	0.034	$d_{xy} \rightarrow \pi^*_{\text{dmbpy}}$ (0.37) MLCT	S <sub>42</sub>	294	0.066	$d_{xy} \rightarrow \pi^*_{\text{dmbpy}}$ (-0.38) MLCT
S <sub>47</sub>	282	0.234	$\pi_L \rightarrow \pi^*_L$ (0.52) IL	S <sub>49</sub>	276	0.284	$\pi_{\text{dmbpy}} \rightarrow \pi^*_{\text{dmbpy}}$ (0.41) IL
S <sub>52</sub>	276	0.177	$\pi_{\text{dmbpy}} \rightarrow \pi^*_L$ (0.54) LLCT	S <sub>50</sub>	274	0.419	$\pi_{\text{dmbpy}} \rightarrow \pi^*_{\text{dmbpy}}$ (0.33) IL
S <sub>54</sub>	273	0.286	$\pi_{\text{dmbpy}} \rightarrow \pi^*_{\text{dmbpy}}$ (0.25) LLCT	S <sub>51</sub>	273	0.286	$\pi_{\text{dmbpy}} \rightarrow \pi^*_{\text{dmbpy}}$ (0.23) IL
			$d_{xz} \rightarrow d_{xz}-y^2$ (0.24) MC				$\pi_{\text{dmbpy}} \rightarrow \pi^*_{\text{dmbpy}}$ (-0.22) IL
S <sub>55</sub>	273	0.509	$\pi_{\text{dmbpy}} \rightarrow \pi^*_L$ (0.27) LLCT	S <sub>54</sub>	265	0.146	$\pi_L \rightarrow \pi^*_L$ (0.54) IL
			$\pi_{\text{dmbpy}} \rightarrow \pi^*_{\text{dmbpy}}$ (-0.23) IL				
			$\pi_{\text{dmbpy}} \rightarrow \pi^*_{\text{dmbpy}}$ (0.23) IL				

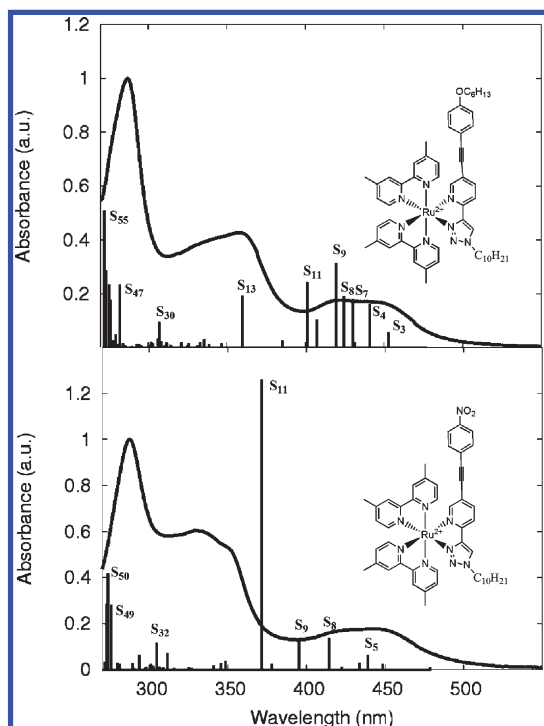


FIGURE 5. Experimental spectra of complexes **16a** (top) and **16b** (bottom) in solid lines superimposed to the TD-DFT (B3LYP/6-31G\* in  $\text{CH}_2\text{Cl}_2$ ) vertical excitations. The main electronic states are highlighted (see Table 5 for assignments).

electronic transitions from the same  $\pi$ -orbital localized in the 2-(1*H*-[1,2,3]triazol-4-yl)pyridine ligand ( $\pi_L$ ) to different  $\pi$ -antibonding orbitals located on the dmbpy ligands ( $\pi^*_{\text{dmbpy}}$ ), appeared lower in energy in **16a**. This fact was due to the destabilization of the  $\pi_L$  orbital in the donor-based compound as compared to the same orbital in the acceptor-based compound (recall that the  $\pi_L$  orbital is the HOMO in compound **16a** but the HOMO-3 in **16b**, see Figure 4). The

second band, located experimentally around 360 and 340 nm in complexes **16a** and **16b**, respectively, was characterized by the same electronic excitations (S<sub>13</sub> and S<sub>11</sub> for compounds **16a** and **16b**, respectively). These corresponded to intraligand (IL) states, which involved local  $\pi_L \rightarrow \pi^*_L$  electronic excitations within the 2-(1*H*-[1,2,3]triazol-4-yl)pyridine ligand. Finally, the most intense peak centered at 286 nm in both complexes was mainly due to IL states in **16b** and states of IL and LLCT character in the case of **16a** (see Table 5). In the case of **16a**, one of these states (S<sub>54</sub>) was mixed with a MC transition, involving an electronic excitation from the  $d_{xz}$  orbital to the unoccupied  $d_{xz}-y^2$  orbital.

Concerning the emission behavior, the trzpy-type ligand systems are known to be potential luminescence quenchers and the ruthenium(II) complexes reported previously did not show any luminescence at room temperature.<sup>7e,8</sup> Also the complexes presented in this contribution showed only very weak emission intensities (see Table 4). For excited Ru<sup>II</sup> polypyridyl complexes it is well-known that the triplet excited states are populated rapidly via efficient intersystem crossings (ISC) from the singlet photoexcited states<sup>18</sup> (due to the strong spin-orbit coupling of the ruthenium center). Afterward, relaxation to the lowest triplet excited state ( $T_1$ ) follows. Obviously, the nature of the low-lying singlets and triplets excited states should determine the effectiveness of the ISC. As revealed, different singlet excited states were obtained for complexes **16a** and **16b** and, consequently, a different emission behavior was expected. We are currently developing a methodology to estimate the phosphorescence rates and the quantum yields, based on accurate estimation of the spin-orbit couplings between the singlet and triplet manifolds which, in turn, determine the ISC rates.

## Conclusions

New 2-(1*H*-[1,2,3]triazol-4-yl)pyridine bidentate ligands were synthesized as bipyridine analogs, whereas different

(18) Bhasikuttan, A. C.; Suzuki, M.; Nakashima, S.; Okada, T. *J. Am. Chem. Soc.* **2002**, *124*, 8398–8345.

phenylacetylene moieties of donor and acceptor nature, respectively, were attached at the 5-position of the pyridine unit. The moieties featured a crucial influence on the electronic properties of these ligands. In addition, the *N*-heterocyclic ligands were coordinated to the ruthenium(II) metal ion by using the bis(4,4'-dimethyl-2,2'-bipyridine)-ruthenium(II) precursor. The Ru<sup>II</sup> complex with electron-donor nature revealed considerable weaker luminescence intensity at room temperature in contrast to the one with acceptor capability revealing remarkable luminescence at room temperature in CH<sub>2</sub>Cl<sub>2</sub>. Furthermore, 2-(1*H*-[1,2,3]triazol-4-yl)pyridine systems are known to be potential luminescence quenchers at room temperature as soon as they are attached to a ruthenium(II) metal ion. All herein described heteroleptic ruthenium(II) complexes overcame this luminescence quenching and led to room temperature emission in acetonitrile. The highest quantum yield could be found for the Ru<sup>II</sup> complex **16b** ( $\Phi = 0.02$ ) bearing a nitro group in the para-position of the phenylacetylene subunit.

### Experimental Section

**Materials and Instrumentation.** Unless noted otherwise, all reagents were acquired from commercial sources and used without further purification. Solvents were dried and distilled according to standard procedures and stored under argon. If not specified otherwise solvents were degassed by bubbling with argon 1 h before use. All reactions were performed in air-dried flasks under an argon atmosphere unless stated otherwise. Purification of reaction products was carried out by column chromatography with 40–63  $\mu\text{m}$  silica gel. Analytical thin layer chromatography (TLC) was performed on silica sheets pre-coated with silica gel 60 F254 and visualization was accomplished with UV light (254 nm). The heteroleptic ruthenium(II) complexes were synthesized by microwave-assisted reactions, using a Biotage Initiator ExpEU (maximum power: 400 W; working frequency: 2450 MHz) with closed reaction vials. During the experiments the temperature and the pressure profiles were detected. 1D-(<sup>1</sup>H and <sup>13</sup>C) and 2D-(<sup>1</sup>H–<sup>1</sup>H gCOSY) nuclear magnetic resonance spectra were recorded at 298 K. Chemical shifts are reported in parts per million (ppm,  $\delta$  scale) relative to the signal of the applied solvent. Coupling constants are given in hertz. Data are reported as follows: multiplicity (ap = apparent, br = broad, s = singlet, d = doublet, t = triplet, q = quartet, m = multiplet).

**Computational Details.** The geometries of **16a** and **16b** were optimized in the electronic singlet ground state using density functional theory (DFT) with the hybrid functional B3LYP<sup>19,20</sup> and the 6-31G\* basis set for all atoms. Relativistic effects were included in the Ru atom, using the ECP-28-mwb Stuttgart/Dresden pseudopotential.<sup>21</sup> For computational ease the structures were reduced by substitution of the decyl chain attached to the triazole ring by a methyl group and in the case of compound **16b**, additionally the hexyloxy group of **16a** was replaced by a methoxy group. The lowest-lying 55 vertical singlet electronic excitation energies were obtained by using TD-DFT at the S<sub>0</sub> optimized geometries. This calculation was performed in solution with CH<sub>2</sub>Cl<sub>2</sub> as solvent with the polarization continuum

model,<sup>22,23</sup> ( $\epsilon = 8.93$ ). All the calculations were performed with the Gaussian03 program package.<sup>24</sup>

**1-Ethynyl-4-(hexyloxy)benzene (1).**<sup>25</sup> 1-Iodo-4-(hexyloxy)benzene (1.5 g, 4.93 mmol), tetrakis(triphenylphosphine)-palladium(0) (114 mg, 0.1 mmol), and CuI (20 mg, 0.1 mmol) were dissolved in a degassed NET<sub>3</sub>/THF mixture (3:7 ratio, 35 mL) at room temperature. After trimethylsilylacetylene (0.7 mL, 4.93 mmol) was added quickly through a syringe, the solution was stirred for 24 h at room temperature. The salts formed were filtered off, and the solution was evaporated under reduced pressure. The yellow oil was purified by a chromatographic filtration over a silica gel pad (toluene as eluent) yielding pure 1-(trimethylsilyl)ethynyl-4-(hexyloxy)benzene. Subsequently, the silylated compound was dissolved in a mixture of THF and methanol and aq NaOH (5 M, 1 mL) was added. The reaction mixture was stirred overnight at room temperature and then extracted with dichloromethane after adding brine (50 mL). The organic extract was dried over anhydrous MgSO<sub>4</sub> and subsequent gel filtration (silica, toluene) afforded the pure, colorless product (0.91 g, 91%).

**5-Bromo-2-((trimethylsilyl)ethynyl)pyridine (2).**<sup>26</sup> 2,5-Dibromopyridine (3.5 g, 14.8 mmol), tetrakis(triphenylphosphine)-palladium(0) (347 mg, 0.3 mmol), and CuI (57 mg, 0.3 mmol) were dissolved in a degassed NET<sub>3</sub>/THF mixture (3:7 ratio, 50 mL) at 0 °C. After trimethylsilylacetylene (2.09 mL, 14.8 mmol) was added quickly through a syringe, the solution was stirred for 2 h at 0 °C and was then allowed to stir at room temperature overnight. The salts formed were filtered off, and the solution was evaporated under reduced pressure. The dark orange oil was purified by a chromatographic filtration over a silica gel pad (toluene as eluent) providing the product as yellow oil, which solidifies upon standing at room temperature after one week. Finally, purification by gentle sublimation ( $3.3 \times 10^{-2}$  mbar, 60 °C) afforded the pure product as a white powder (3.25 g, 86%).

**2-Ethynyl-5-((4-(hexyloxy)phenyl)ethynyl)pyridine (4).** 5-Bromo-2-((trimethylsilyl)ethynyl)pyridine (**2**, 1.0 g, 4 mmol), 1-ethynyl-4-(hexyloxy)benzene (**1**, 0.8 g, 4 mmol), tetrakis(triphenylphosphine)palladium(0) (90 mg, 0.08 mmol), and CuI (16 mg, 0.08 mmol) were dissolved in a degassed NET<sub>3</sub>/THF mixture (3:7 ratio, 35 mL) at room temperature and the solution was stirred for 48 h at room temperature. The salts formed were filtered off, and the solution was evaporated under reduced pressure. The dark red oil was purified by a gel filtration over silica (toluene as eluent). The obtained 2-((trimethylsilyl)ethynyl-5-((4-(hexyloxy)phenyl)ethynyl)pyridine was desilylated by dissolving in THF/MeOH (1:2 ratio, 30 mL) and treating with an equimolar amount of potassium fluoride. The red solution was stirred overnight under an argon atmosphere. After that the reaction mixture was concentrated under vacuum and

(24) Frisch, M. J.; Trucks, G. W.; Schlegel, H. B.; Scuseria, G. E.; Robb, M. A.; Cheeseman, J. R.; Montgomery, J. A., Jr.; Vreven, T.; Kudin, K. N.; Burant, J. C.; Millam, J. M.; Iyengar, S. S.; Tomasi, J.; Barone, V.; Mennucci, B.; Cossi, M.; Scalmani, G.; Rega, N.; Petersson, G. A.; Nakatsuji, H.; Hada, M.; Ehara, M.; Toyota, K.; Fukuda, R.; Hasegawa, J.; Ishida, M.; Nakajima, T.; Honda, Y.; Kitao, O.; Nakai, H.; Klene, M.; Li, X.; Knox, J. E.; Hratchian, H. P.; Cross, J. B.; Bakken, V.; Adamo, C.; Jaramillo, J.; Gomperts, R.; Stratmann, R. E.; Yazyev, O.; Austin, A. J.; Cammi, R.; Pomelli, C.; Ochterski, J. W.; Ayala, P. Y.; Morokuma, K.; Voth, G. A.; Salvador, P.; Dannenberg, J. J.; Zakrzewski, V. G.; Dapprich, S.; Daniels, A. D.; Strain, M. C.; Farkas, O.; Malick, D. K.; Rabuck, A. D.; Raghavachari, K.; Foresman, J. B.; Ortiz, J. V.; Cui, Q.; Baboul, A. G.; Clifford, S.; Cioslowski, J.; Stefanov, B. B.; Liu, G.; Liashenko, A.; Piskorz, P.; Komaromi, I.; Martin, R. L.; Fox, D. J.; Keith, T.; Al-Laham, M. A.; Peng, C. Y.; Nanayakkara, A.; Challacombe, M.; Gill, P. M. W.; Johnson, B.; Chen, W.; Wong, M. W.; Gonzalez, C.; Pople, J. A. *Gaussian-03*, Revision C.02; Gaussian, Inc., Wallingford, CT, 2004.

(25) Chang, J. Y.; Yeon, J. R.; Shru, Y. S.; Han, M. J.; Hong, S.-K. *Chem. Mater.* **2000**, *12*, 1076–1082.

(26) Bianchini, C.; Giambastiani, G.; Rios, I. G.; Meli, A.; Oberhauser, W.; Sorace, L.; Toti, A. *Organometallics* **2007**, *26*, 5066–5078.

(19) Becke, A. D. *J. Chem. Phys.* **1993**, *98*, 5648–5652.

(20) Lee, C. T.; Yang, W. T.; Parr, R. G. *Phys. Rev. B* **1988**, *37*, 785–789.

(21) Andrae, D.; Häusermann, U.; Dolg, M.; Stoll, H.; Preuss, H. *Theor. Chim. Acta* **1990**, *77*, 123–141.

(22) Cossi, M.; Barone, V.; Mennucci, B.; Tomasi, J. *Chem. Phys. Lett.* **1998**, *286*, 253–260.

(23) Mennucci, B.; Tomasi, J. *J. Chem. Phys.* **1997**, *106*, 5151–5158.

purified by means of gel filtration on silica gel yielding the desired product as a slight yellow powder (1.06 g, 87%). <sup>1</sup>H NMR (CDCl<sub>3</sub>, 300 MHz) δ 8.62 (d, *J* = 1.3 Hz, 1H), 7.73 (dd, *J* = 8.1 Hz, *J* = 2.1 Hz, 1H), 7.49–7.42 (m, 3H), 6.91–6.85 (m, 2H), 3.97 (t, <sup>3</sup>*J* = 6.6 Hz, 2H), 3.25 (s, 1H), 1.79–1.74 (m, 2H), 1.49–1.30 (m, 6H), 0.91 (t, *J* = 6.8 Hz, 3H). <sup>13</sup>C NMR (CDCl<sub>3</sub>, 75 MHz) δ 159.8, 152.2, 140.3, 138.1, 133.2, 126.71, 120.7, 114.7, 114.0, 94.9, 84.5, 82.6, 78.6, 68.1, 31.5, 29.1, 25.7, 22.6, 14.0. Anal. Calcd for C<sub>21</sub>H<sub>21</sub>NO: C 83.13, H 6.98, N 4.62. Found: C 82.78, H 7.08, N 4.92.

**2-(1-Decyl-1*H*-[1,2,3]triazol-4-yl)-5-((4-(hexyloxy)phenyl)ethynyl)pyridine (5).** A sealed microwave vial with 1-bromodecane (91 mg, 0.41 mmol) and 1.5 equiv of sodium azide (40 mg) in DMSO (5 mL) was heated under microwave irradiation for 1 h at 100 °C. Water was then added to quench the reaction and the product was extracted into diethyl ether, washed with brine, and dried over Na<sub>2</sub>SO<sub>4</sub>. The solution was subsequently reduced in vacuo to yield 1-azidodecane (95%). The organic azide, 2-ethynyl-5-((4-(hexyloxy)phenyl)ethynyl)pyridine (**4**, 127 mg, 0.42 mmol), CuSO<sub>4</sub> (7 mg, 0.042 mmol, dissolved in 0.5 mL water), and sodium ascorbate (42 mg, 0.21 mmol, dissolved in 1 mL water) were dissolved in THF (15 mL) and the reaction mixture was stirred for 24 h at room temperature. Subsequently, ethylenediaminetetraacetic acid-containing water (60 mL) was added to the reaction mixture and the product was extracted with CH<sub>2</sub>Cl<sub>2</sub>. Gel filtration on silica (CHCl<sub>3</sub>/EtOAc 1:1 ratio) and subsequent column chromatography (silica, CHCl<sub>3</sub>/EtOAc 20:1 ratio) provided the pure product as white powder (134 mg, 67%). <sup>1</sup>H NMR (CDCl<sub>3</sub>, 300 MHz) δ 8.68 (s, 1H), 8.13–8.11 (m, 2H), 7.86 (dd, *J* = 8.2 Hz, *J* = 2.1 Hz, 1H), 7.46–7.42 (m, 2H), 6.86–6.82 (m, 2H), 4.4 (t, *J* = 7.2 Hz, 2H), 3.97 (t, *J* = 6.5 Hz, 2H), 1.94–1.88 (m, 2H), 1.79–1.76 (m, 2H), 1.48–1.22 (m, 20H), 0.87–0.81 (m, 6H). <sup>13</sup>C NMR (CDCl<sub>3</sub>, 75 MHz) δ 159.5, 151.6, 148.7, 147.8, 139.0, 133.0, 122.0, 119.6, 119.3, 114.5, 114.3, 93.1, 84.8, 68.0, 50.4, 31.7, 31.5, 30.1, 29.3, 29.2, 29.1, 29.0, 28.9, 26.3, 25.6, 22.5, 14.0, 13.9. Anal. Calcd for C<sub>31</sub>H<sub>42</sub>N<sub>4</sub>O: C 76.50, H 8.70, N 11.51. Found: C 76.52, H 8.79, N 11.71.

**4-(6-Ethynylpyridin-3-yl)-2-methylbut-3-yn-2-ol (6).**<sup>27</sup> To a degassed solution of 5-bromo-2-[(trimethylsilyl)ethynyl]pyridine (**2**, 1.5 g, 5.9 mmol), CuI (23 mg, 0.12 mmol), and Pd(PPh<sub>3</sub>)<sub>4</sub> (140 mg, 0.12 mmol) in triethylamine (50 mL) was added 2-methyl-3-butyn-2-ol (0.58 mL, 5.9 mmol) and the reaction mixture was stirred for 24 h at 55 °C. The mixture was diluted with diethyl ether, washed once with brine, and dried over MgSO<sub>4</sub>. Concentration in vacuo yielded the crude product, which was purified by chromatography on silica gel (chloroform/ethyl acetate 4:1) to afford 5-(3-hydroxy-3-methyl-1-butynyl)-2-[(triisopropylsilyl)ethynyl]pyridine. To a stirred solution of the latter product in methanol (50 mL) was added solid potassium fluoride (1.5 equiv), and the mixture was stirred at room temperature overnight under an argon atmosphere. Subsequently, the reaction mixture was filtered by means of gel filtration on silica gel (chloroform/ethyl acetate 4:1) and concentrated in vacuo yielding the desired product as an orange powder (670 mg, 61%).

**5-Bromo-2-ethynylpyridine (7).**<sup>28</sup> To a solution of 2,5-dibromopyridine (7 g, 30 mmol), CuI (70 mg, 0.37 mmol), and Pd(PPh<sub>3</sub>)<sub>4</sub> (260 mg, 0.37 mmol) in degassed NEt<sub>3</sub>/THF (1:1 ratio, 100 mL) was added trimethylsilylacetylene (4.2 mL, 30 mmol). The mixture was stirred at room temperature overnight under argon atmosphere. After removal of the solvent under reduced pressure, the residue was purified by gel filtration (CHCl<sub>3</sub>) to yield 2-(trimethylsilyl)ethynyl-5-bromopyridine as off-white powder (6.95 g, 92%). Subsequently, the compound was dissolved in

methanol (80 mL) and treated with aq NaOH (5 M, 12 mL). The yellow solution was stirred overnight, whereupon the solution turned black. Subsequent gel filtration on silica (CHCl<sub>3</sub>) yielded the product as white powder (3.79 g, 69%).

**5-Bromo-2-(1-decyl-1*H*-[1,2,3]triazol-4-yl)pyridine (8).** 5-Bromo-2-ethynylpyridine (**7**, 1.04 g, 5.45 mmol) and 1-azidodecane (see synthesis of **5**, 1.0 g, 5.45 mmol) were dissolved in an ethanol/water mixture (7:1 ratio, 70 mL), using a round-bottomed flask (100 mL). Then copper(II) sulfate (80 mg, 0.5 mmol, dissolved in 3 mL of water) and sodium ascorbate (490 mg, 2.5 mmol, dissolved in 4 mL of water) were added. The reaction mixture turned yellow after a while and was stirred for 72 h at 25 °C. The yellow precipitate was filtered and washed with ethanol. After recrystallization from ethanol the pure product was obtained as colorless crystals (1.35 g, 67%). <sup>1</sup>H NMR (CDCl<sub>3</sub>, 300 MHz) δ 8.61 (s, 1H), 8.09–8.07 (m, 2H), 7.89–7.86 (m, 1H), 4.40 (t, *J* = 7.2 Hz, 2H), 1.94–1.89 (m, 2H), 1.34–1.24 (m, 14H), 0.87–0.81 (m, 3H). <sup>13</sup>C NMR (CDCl<sub>3</sub>, 75 MHz) δ 150.3, 148.9, 147.4, 139.4, 121.9, 121.3, 119.3, 50.5, 31.8, 30.2, 29.4, 29.3, 29.2, 28.9, 26.4, 22.6, 14.0. Anal. Calcd for C<sub>17</sub>H<sub>25</sub>BrN<sub>4</sub>: C 55.89, H 6.90, N 15.34. Found: C 56.22, H 7.23, N 14.98.

**2-(1-Decyl-1*H*-[1,2,3]triazol-4-yl)-5-ethynylpyridine (9, Route 1).** 4-(6-Ethynylpyridin-3-yl)-2-methylbut-3-yn-2-ol (**6**, 300 mg, 1.58 mmol) and 1-azidodecane (see synthesis of **5**, 275 mg, 1.5 mmol) were dissolved in an ethanol/water mixture (7:3 ratio, 30 mL), using a round-bottomed flask (100 mL). Then copper(II) sulfate (24 mg, 0.15 mmol, dissolved in 1 mL of water) and sodium ascorbate (150 mg, 0.75 mmol, dissolved in 1 mL of water) were added. The reaction mixture turned green after a while and was stirred for 72 h at 50 °C. Subsequently, an excess of water was poured into the reaction mixture (100 mL) and the crude product precipitated and was filtered off. Gel filtration on silica (CHCl<sub>3</sub>/EtOAc 1:1) provided 4-(6-(1-decyl-1*H*-[1,2,3]triazol-4-yl)pyridin-3-yl)-2-methylbut-3-yn-2-ol as white powder (490 mg, 85%). This intermediate was dissolved in dry toluene (30 mL). After adding ground NaOH (200 mg, 5 mmol) and KOH (150 mg, 2.6 mmol) the reaction mixture was refluxed for 5 h. Subsequent column chromatography on silica (CHCl<sub>3</sub>/EtOAc 2:1 ratio) yielded 2-(1-decyl-1*H*-[1,2,3]triazol-4-yl)-5-ethynylpyridine as transparent crystals (303 mg, 74%). <sup>1</sup>H NMR (CDCl<sub>3</sub>, 300 MHz) δ 8.67 (d, *J* = 1.6 Hz, 1H), 8.20–8.14 (m, 2H), 7.89–7.83 (m, 1H), 4.41 (t, *J* = 7.2 Hz, 2H), 3.25 (s, 1H), 1.95–1.89 (m, 2H), 1.34–1.25 (m, 14H), 0.87 (t, *J* = 6.5 Hz, 3H). <sup>13</sup>C NMR (CDCl<sub>3</sub>, 75 MHz) δ 152.4, 149.7, 147.7, 139.9, 122.2, 119.3, 118.0, 80.8, 80.5, 50.5, 31.8, 30.2, 29.4, 29.3, 29.2, 28.9, 26.4, 22.6, 14.0. Anal. Calcd for C<sub>19</sub>H<sub>26</sub>N<sub>4</sub>: C 73.51, H 8.44, N 18.05. Found: C 73.50, H 8.24, N 18.38.

**2-(1-Decyl-1*H*-[1,2,3]triazol-4-yl)-5-ethynylpyridine (9, Route 2).** To a solution of 5-bromo-2-(1-decyl-1*H*-[1,2,3]triazol-4-yl)pyridine (**8**, 1.0 g, 2.74 mmol), CuI (13 mg, 0.07 mmol), and Pd(PPh<sub>3</sub>)<sub>4</sub> (80 mg, 0.07 mmol) in degassed NEt<sub>3</sub>/CH<sub>2</sub>Cl<sub>2</sub> (3:1 ratio, 500 mL) was added trimethylsilylacetylene (280 mg, 2.8 mmol). The mixture was stirred 48 h at room temperature under argon atmosphere. After removal of the solvent under reduced pressure, the residue was purified by gel filtration on silica (chloroform). Afterward, the trimethylsilyl-protected product was dissolved in methanol (40 mL) and treated with aq NaOH (5 M, 1 mL). After 5 h the solvent was removed and the crude product was finally purified by gradient column chromatography on silica (CHCl<sub>3</sub>, CHCl<sub>3</sub>/EtOAc 3:1 ratio) yielding the product as white powder (470 mg, 55%).

**General Procedure of the Sonogashira Reaction.** 2-(1-Decyl-1*H*-[1,2,3]triazol-4-yl)-5-ethynylpyridine (0.32 mmol), nitro-substituted 1-iodobenzene (0.32 mmol), tetrakis(triphenylphosphine)palladium(0) (16 mg, 0.012 mmol), and CuI (8 mg, 0.012 mmol) were dissolved in a degassed NEt<sub>3</sub>/THF mixture (1:1, 10 mL). The solution was stirred for 48 h at 40 °C under argon atmosphere. The salts formed were filtered off, and the solution

(27) Nakano, Y.; Ishizuka, K.; Muraoka, K.; Ohtani, H.; Takayama, Y.; Sato, F. *Org. Lett.* **2004**, *6*, 2373–2376.

(28) Tilley, J. W.; Zawoiski, S. *J. Org. Chem.* **1988**, *53*, 386–390.



was evaporated under reduced pressure. The pure product was isolated by column chromatography over silica.

**2-(1-Decyl-1*H*-[1,2,3]triazol-4-yl)-5-((4-nitrophenyl)ethynyl)pyridine (10a).** According to the general procedure the product was synthesized and purified by column chromatography over silica (CHCl<sub>3</sub>, *R<sub>f</sub>* 0.6) yielding **10a** as a slight yellow powder (128 mg, 93%). <sup>1</sup>H NMR (CDCl<sub>3</sub>, 300 MHz) δ 8.76 (s, 1H), 8.26–8.16 (m, 4H), 7.94–7.90 (m, 1H), 7.71–7.68 (m, 2H), 4.4 (t, *J* = 7.2 Hz, 2H), 1.99–1.91 (m, 2H), 1.35–1.25 (m, 14H), 0.87–0.81 (m, 3H). <sup>13</sup>C NMR (CDCl<sub>3</sub>, 75 MHz) δ 152.1, 150.0, 147.6, 147.3, 139.5, 132.4, 129.5, 123.7, 122.4, 119.6, 118.1, 91.3, 90.9, 50.6, 31.8, 30.2, 29.4, 29.3, 29.2, 29.0, 26.5, 22.6, 14.1. ESI-TOF MS: *m/z* 432.24 ([M + H]<sup>+</sup>). Anal. Calcd for C<sub>25</sub>H<sub>29</sub>N<sub>5</sub>O<sub>2</sub>: C 69.58, H 6.77, N 16.23. Found: C 69.21, H 6.72, N 16.58.

**2-(1-Decyl-1*H*-[1,2,3]triazol-4-yl)-5-((2-nitrophenyl)ethynyl)pyridine (10b).** According to the general procedure the product was synthesized and purified by column chromatography over silica (CHCl<sub>3</sub>/EtOAc, 5:1 ratio) yielding **10b** as off-white powder (63 mg, 69%). <sup>1</sup>H NMR (CDCl<sub>3</sub>, 300 MHz) δ 8.76 (s, 1H), 8.21–8.10 (m, 3H), 7.97–7.91 (m, 1H), 7.73–7.69 (m, 1H), 7.63–7.60 (m, 1H), 7.53–7.49 (m, 1H), 4.42 (t, *J* = 7.2 Hz, 2H), 1.99–1.91 (m, 2H), 1.34–1.24 (m, 14H), 0.88 (t, *J* = 6.7 Hz, 3H). <sup>13</sup>C NMR (CDCl<sub>3</sub>, 75 MHz) δ 152.2, 150.0, 149.5, 147.7, 139.7, 134.6, 132.9, 129.0, 124.8, 122.4, 119.5, 118.1, 93.8, 88.2, 50.6, 31.8, 30.2, 29.4, 29.3, 29.2, 29.0, 26.4, 22.6, 14.1. ESI-HRMS calcd for C<sub>25</sub>H<sub>30</sub>N<sub>5</sub>O<sub>2</sub> ([M + H]<sup>+</sup>) 432.2394, found 432.2390.

**2-(1-Decyl-1*H*-[1,2,3]triazol-4-yl)-5-((4-(trifluoromethyl)phenyl)ethynyl)pyridine (10c).** According to the general procedure, the product was synthesized and purified by column chromatography over silica (CHCl<sub>3</sub>, *R<sub>f</sub>* 0.5) yielding **10c** as white powder (81 mg, 94%). <sup>1</sup>H NMR (CDCl<sub>3</sub>, 300 MHz) δ 8.72 (s, 1H), 8.21–8.17 (m, 2H), 7.92–7.88 (m, 1H), 7.68–7.61 (m, 4H), 4.42 (t, *J* = 7.2 Hz, 2H), 1.96–1.90 (m, 2H), 1.34–1.24 (m, 14H), 0.88 (t, *J* = 6.7 Hz, 3H). <sup>13</sup>C NMR (CDCl<sub>3</sub>, 75 MHz) δ 152.0, 139.5, 131.9, 126.4, 125.6, 125.5, 125.4, 125.4, 125.3, 122.4, 119.5, 118.5, 91.4, 88.5, 50.6, 31.8, 30.2, 29.5, 29.4, 29.2, 29.0, 26.5, 22.7, 14.1. ESI-HRMS calcd for C<sub>26</sub>H<sub>30</sub>F<sub>3</sub>N<sub>4</sub> ([M + H]<sup>+</sup>) 455.2417, found 455.2408.

**5-((4-Phenyl)ethynyl)-2-(1-phenyl-1*H*-[1,2,3]triazol-4-yl)pyridine (10d).** According to the general procedure the product was synthesized and purified by column chromatography over silica (CHCl<sub>3</sub>/EtOAc, 5:1 ratio) yielding **10d** as off-white powder (44 mg, 61%). <sup>1</sup>H NMR (CDCl<sub>3</sub>, 300 MHz) δ 8.74 (s, 1H), 8.16–8.11 (m, 2H), 7.90–7.84 (m, 1H), 7.58–7.54 (m, 2H), 7.39–7.35 (m, 3H), 4.42 (t, *J* = 7.2 Hz, 2H), 1.96–1.89 (m, 2H), 1.34–1.24 (m, 14H), 0.88 (t, *J* = 6.7 Hz, 3H). <sup>13</sup>C NMR (CDCl<sub>3</sub>, 75 MHz) δ 151.8, 139.3, 131.7, 128.8, 128.4, 122.6, 122.2, 119.5, 119.4, 93.1, 86.1, 50.6, 31.8, 30.2, 29.4, 29.3, 29.2, 29.0, 26.4, 22.6, 14.1. ESI-HRMS calcd for C<sub>25</sub>H<sub>30</sub>N<sub>4</sub>Na ([M + Na]<sup>+</sup>) 409.2363, found 409.2334.

**5-Ethynyl-2-(1-phenyl-1*H*-[1,2,3]triazol-4-yl)pyridine (11).** Sodium azide (330 mg, 5.1 mmol) and anhydrous CuSO<sub>4</sub> (54 mg, 0.34 mmol) were dissolved in abs methanol (30 mL). Phenylboronic acid (414 mg, 3.4 mmol) was added to the brown solution and the reaction mixture was stirred for 48 h at room temperature. The conversion was controlled by TLC on silica (CHCl<sub>3</sub>). The slightly green solution was concentrated to 10 mL in vacuum and, subsequently, THF (20 mL), sodium ascorbate (336 mg, 1.7 mmol, in 1 mL of water), 4-(6-ethynylpyridin-3-yl)-2-methylbut-3-yn-2-ol (600 mg, 3.24 mmol), and water (4 mL) were added. The reaction was stirred for 72 h at 50 °C. After that, an excess of water was added to the reaction mixture and the precipitate was filtered off. The filtrate was cautiously extracted with CHCl<sub>3</sub> and the organic extract was combined with the precipitate. The CHCl<sub>3</sub> solution was dried over NaSO<sub>4</sub> and filtered. Column chromatography on silica (CHCl<sub>3</sub>/EtOAc, 2:1 ratio) provided the (2-methylbut-3-yn-2-ol)-protected product as a white powder. The deprotection was accomplished by refluxing overnight in toluene with ground NaOH

(1.5 equiv). The toluene solution was washed with water and subsequent gel filtration on silica provided the pure desired product (360 mg, 45%). <sup>1</sup>H NMR (CDCl<sub>3</sub>, 300 MHz) δ 8.71 (s, 1H), 8.61 (s, 1H), 8.23 (d, *J* = 8.2 Hz, 1H), 7.90 (dd, *J* = 8.2 Hz, *J* = 2.0 Hz, 1H), 7.83–7.80 (m, 2H), 7.59–7.44 (m, 3H), 3.28 (s, 1H, CH). <sup>13</sup>C NMR (CDCl<sub>3</sub>, 75 MHz) δ 152.5, 149.2, 148.3, 140.0, 136.8, 129.9, 128.9, 120.4, 119.6, 118.3, 81.0, 80.5. Anal. Calcd for C<sub>15</sub>H<sub>10</sub>N<sub>4</sub>: C 73.16, H 4.09, N 22.75. Found: C 73.49, H 3.78, N 22.50.

**5-((4-Nitrophenyl)ethynyl)-2-(1-phenyl-1*H*-[1,2,3]triazol-4-yl)pyridine (12).** 5-Ethynyl-2-(1-phenyl-1*H*-[1,2,3]triazol-4-yl)pyridine (**11**, 75 mg, 0.3 mmol), 1-iodo-4-nitrobenzene (76 mg, 0.3 mmol), tetrakis(triphenylphosphine)palladium(0) (8 mg, 0.006 mmol), and CuI (2 mg, 0.006 mmol) were dissolved in a degassed NEt<sub>3</sub>/THF mixture (3:1 ratio, 10 mL) and the solution was stirred for 48 h at 40 °C under argon atmosphere. The solvent was evaporated under reduced pressure. The pure product was isolated by column chromatography over silica (CHCl<sub>3</sub>) as slightly yellow powder (85 mg, 77%). <sup>1</sup>H NMR (CDCl<sub>3</sub>, 300 MHz) δ 8.80 (s, 1H), 8.65 (s, 1H), 8.32–8.25 (m, 3H), 7.98–7.96 (m, 1H), 7.85–7.82 (m, 2H), 7.74–7.71 (m, 2H), 7.61–7.47 (m, 3H). <sup>13</sup>C NMR (CDCl<sub>3</sub>, 75 MHz) δ 147.3, 143.3, 139.6, 136.9, 132.4, 129.9, 129.1, 123.7, 120.5, 91.2, 91.1 (some carbon signals are missing due to the low solubility of the compound). ESI-HRMS calcd for C<sub>21</sub>H<sub>13</sub>N<sub>5</sub>O<sub>2</sub>Na ([M + Na]<sup>+</sup>) 390.0961, found 390.0940.

**2-(1-(4-Bromophenyl)-1*H*-[1,2,3]triazol-4-yl)pyridine (13).** Sodium azide (480 mg, 7.5 mmol) and anhydrous CuSO<sub>4</sub> (80 mg, 0.5 mmol) were dissolved in abs methanol (40 mL). (4-Bromophenyl)boronic acid (1 g, 5 mmol) was added to the brown solution and the reaction mixture was stirred for 48 h at room temperature. The conversion was controlled by TLC on silica (ethyl acetate). Sodium ascorbate (400 mg, 2 mmol, in 1 mL of water), 2-ethynylpyridine (515 mg, 5 mmol), and water (5 mL) were added. The reaction was stirred for 5 days at 40 °C. After that, an excess of water was added to the reaction mixture and the precipitate was filtered off. The filtrate was cautiously extracted with CHCl<sub>3</sub> and the organic extract was combined with the precipitate. The CHCl<sub>3</sub> solution was dried over NaSO<sub>4</sub> and filtered and the solvent was evaporated. Subsequent recrystallization from ethanol provided the pure product as colorless crystals (905 mg, 61%). <sup>1</sup>H NMR (CDCl<sub>3</sub>, 300 MHz) δ 8.62–8.60 (m, 1H), 8.59 (s, 1H), 8.24–8.21 (m, 1H), 7.83–7.80 (m, 1H), 7.75–7.67 (m, 4H), 7.29–7.26 (m, 1H). <sup>13</sup>C NMR (CDCl<sub>3</sub>, 75 MHz) δ 149.5, 137.0, 133.0, 123.2, 121.8, 120.5, 119.8. Anal. Calcd for C<sub>13</sub>H<sub>9</sub>BrN<sub>4</sub>: C 51.85, H 3.01, N 18.60. Found: C 51.76, H 3.09, N 18.69.

**2-(1-(4-Ethynylphenyl)-1*H*-[1,2,3]triazol-4-yl)pyridine (14).** 2-(1-(4-Bromophenyl)-1*H*-[1,2,3]triazol-4-yl)pyridine (**13**, 600 mg, 2 mmol), trimethylsilylacetylene (0.3 mL, 2.05 mmol), tetrakis(triphenylphosphine)palladium(0) (95 mg, 0.08 mmol) and CuI (18 mg, 0.08 mmol) were dissolved in a degassed NEt<sub>3</sub>/THF mixture (2:1 ratio, 10 mL) and the reaction mixture was stirred for 24 h at 40 °C under argon atmosphere. The solution was evaporated under reduced pressure. The trimethylsilyl-protected product was isolated by column chromatography over silica (CHCl<sub>3</sub>). The product was dissolved in a MeOH/THF solvent mixture (2:1 ratio, 30 mL) and treated with aq NaOH (200 mg of NaOH in 3 mL of water). After stirring overnight under an argon atmosphere the final product was purified by column chromatography over silica (CHCl<sub>3</sub>) and obtained as white powder (340 mg, 69%). <sup>1</sup>H NMR (CDCl<sub>3</sub>, 300 MHz) δ 8.63–8.60 (m, 2H), 8.23–8.20 (m, 1H), 7.84–7.78 (m, 3H), 7.67–7.63 (m, 2H), 7.26–7.21 (m, 1H), 3.19 (s, 1H). <sup>13</sup>C NMR (CDCl<sub>3</sub>, 75 MHz) δ 149.7, 149.5, 136.9, 133.5, 123.1, 122.8, 120.4, 120.0, 119.6, 82.2, 79.0. Anal. Calcd for C<sub>15</sub>H<sub>10</sub>N<sub>4</sub>: C 73.16, H 4.09, N 22.75. Found: C 73.34, H 4.12, N 23.04.

**2-(1-(4-((4-Nitrophenyl)ethynyl)phenyl)-1*H*-[1,2,3]triazol-4-yl)pyridine (15).** 2-(1-(4-Ethynylphenyl)-1*H*-[1,2,3]triazol-4-yl)pyridine (**14**, 65 mg, 0.26 mmol), 1-iodo-4-nitrobenzene (68 mg,

0.27 mmol), tetrakis(triphenylphosphine)palladium(0) (16 mg, 0.006 mmol), and CuI (3 mg, 0.006 mmol) were dissolved in a degassed  $\text{NEt}_3$ /THF mixture (10:1 ratio, 25 mL) and the solution was stirred for 24 h at 50 °C under argon atmosphere. The solvents were evaporated under reduced pressure and the pure product was obtained by crystallization from chloroform at 5 °C (48 mg, 50%).  $^1\text{H}$  NMR ( $\text{CDCl}_3$ , 300 MHz)  $\delta$  8.66–8.62 (m, 2H), 8.25–8.22 (m, 3H), 7.88–7.70 (m, 7H), 7.30–7.26 (m, 1H).  $^{13}\text{C}$  NMR ( $\text{CDCl}_3$ , 75 MHz)  $\delta$  147.3, 133.4, 132.4, 129.6, 123.7, 122.8, 120.2, 119.6, 93.1 (some carbon signals are missing due to the low solubility of the compound). ESI-TOF MS:  $m/z$  368.12 ( $[\text{M} + \text{H}]^+$ ). Anal. Calcd for  $\text{C}_{21}\text{H}_{13}\text{N}_5\text{O}_2$ : C 68.66, H 3.57, N 19.06. Found: C 68.32, H 3.74, N 19.31.

**General Procedure for Complexing the (1*H*-1,2,3-Triazole)-pyridine Ligand to  $\text{Ru}(\text{dmbpy})_2\text{Cl}_2$ .** *cis*-Dichlorobis(4,4'-dimethyl-2,2'-bipyridine)ruthenium(II)<sup>11</sup> (43 mg, 0.08 mmol) and the respective 1*H*-[1,2,3]triazole ligand (0.08 mmol) were suspended in degassed ethanol (8 mL). After heating under microwave irradiation at 125 °C for 2 h, the red solution was treated with a 10-fold excess of  $\text{NH}_4\text{PF}_6$  and subsequently stirred until precipitation occurred (10 min to 2 h). The colored precipitate was filtered off and purified by washing twice with ethanol and diethyl ether providing the pure product. In the cases where the  $^1\text{H}$  NMR spectrum indicated any impurities, the compound was further purified by recrystallization from ethanol.

**Bis(4,4'-dimethyl-2,2'-bipyridine)-{2-(1-decyl-1*H*-[1,2,3]triazol-4-yl)-5-((4-hexyloxy)phenyl)ethynyl}pyridine}ruthenium(II) Hexafluorophosphate (16a).** According to the above standing general procedure *cis*-dichlorobis(4,4'-dimethyl-2,2'-bipyridine)ruthenium(II) (30 mg, 0.056 mmol) and 2-(1-decyl-1*H*-[1,2,3]triazol-4-yl)-5-((4-hexyloxy)phenyl)ethynylpyridine (**5**, 27 mg, 0.056 mmol) were reacted to yield the complex as an orange powder after washing twice with ethanol and diethyl ether (55 mg, 81%).  $^1\text{H}$  NMR ( $\text{CD}_3\text{CN}$ , 300 MHz)  $\delta$  8.68 (s, 1H), 8.38 (s, 2H), 8.31 (s, 1H), 8.28 (s, 1H), 8.10–8.00 (m, 2H), 7.73–7.61 (m, 4H), 7.50 (d,  $J = 5.8$  Hz, 1H), 7.43–7.38 (m, 2H), 7.28–7.22 (m, 3H), 7.17–7.14 (m, 1H), 6.94–6.87 (m, 2H), 4.34 (t,  $J = 7.0$  Hz, 2H), 4.0 (t,  $J = 6.5$  Hz, 2H), 2.56–2.52 (m, 12H), 1.95–1.92 (m, 4H), 1.83–1.69 (m, 4H), 1.47–1.08 (m, 20H), 0.93–0.86 (m, 6H).  $^{13}\text{C}$  NMR ( $\text{CD}_3\text{CN}$ , 75 MHz)  $\delta$  161.3, 158.1, 157.8, 157.7, 157.5, 153.8, 152.2, 152.1, 152.0, 151.9, 151.21, 151.2, 151.1, 150.9, 150.6, 148.1, 140.5, 134.2, 129.2, 129.0, 128.4, 126.6, 125.9, 125.8, 125.4, 125.0, 123.3, 122.9, 115.8, 113.9, 96.6, 83.8, 69.1, 53.0, 32.6, 32.2, 30.1, 30.0, 29.9, 29.7, 29.3, 26.6, 26.3, 23.3, 23.2, 21.22, 21.2, 21.1, 14.3, 14.2. ESI-TOF MS  $m/z$  1101.40 ( $[\text{M} - \text{PF}_6]^{2+}$ ), 478.22 ( $[\text{M} - 2\text{PF}_6]^{2+}$ ). ESI-HRMS calcd for  $\text{C}_{55}\text{H}_{66}\text{N}_8\text{O}_2\text{Ru}$  [ $\text{M} - 2\text{PF}_6]^{2+}$  478.2203, found 478.2199.

**Bis(4,4'-dimethyl-2,2'-bipyridine)-{2-(1-decyl-1*H*-[1,2,3]triazol-4-yl)-5-((4-nitrophenyl)ethynyl)pyridine}ruthenium(II) Hexafluorophosphate (16b).** According to the above standing general procedure *cis*-dichlorobis(4,4'-dimethyl-2,2'-bipyridine)ruthenium(II) (35 mg, 0.065 mmol) and 2-(1-decyl-1*H*-[1,2,3]triazol-4-yl)-5-((4-nitrophenyl)ethynyl)pyridine (**10a**, 28 mg, 0.065 mmol) were reacted to yield the pure complex as an orange powder after washing twice with ethanol and diethyl ether (68 mg, 88%).  $^1\text{H}$  NMR ( $(\text{CD}_3)_2\text{CO}$ , 300 MHz)  $\delta$  9.23 (s, 1H), 8.67–8.60 (m, 4H), 8.42–8.39 (m, 1H), 8.30–8.25 (m, 3H), 8.12–8.08 (m, 2H), 7.96 (d, 1H), 7.87 (d, 1H), 7.78–7.70 (m, 3H), 7.44–7.32 (m, 4H), 4.52 (t,  $J = 7.1$  Hz, 2H), 2.58–2.52 (m, 12H), 2.05–2.01 (m, 2H), 1.89–1.79 (m, 2H), 1.25–1.07 (m, 12H), 0.87–0.81 (m, 3H).  $^{13}\text{C}$  NMR ( $(\text{CD}_3)_2\text{CO}$ , 75 MHz)  $\delta$  158.1, 158.0, 157.8, 154.5, 152.4, 152.21, 152.2, 151.2, 151.1, 148.9, 148.2, 141.4, 133.6, 129.4, 129.0, 128.7, 126.0, 125.5, 125.2, 124.7, 123.1, 121.9, 95.6, 89.3, 52.1, 32.6, 26.7, 23.3, 21.2, 14.3. ESI-TOF MS  $m/z$  1046.3 ( $[\text{M} - \text{PF}_6]^{2+}$ ), 450.67 ( $[\text{M} - 2\text{PF}_6]^{2+}$ ). ESI-HRMS calcd for  $\text{C}_{49}\text{H}_{53}\text{N}_9\text{O}_2\text{Ru}$  [ $\text{M} - 2\text{PF}_6]^{2+}$ ]: 450.6684, found 450.6685.

**Bis(4,4'-dimethyl-2,2'-bipyridine)-{2-(1-decyl-1*H*-[1,2,3]triazol-4-yl)-5-((4-(trifluoromethyl)phenyl)ethynyl)pyridine}ruthenium(II) Hexafluorophosphate (16c).** According to the above standing general procedure *cis*-dichlorobis(4,4'-dimethyl-2,2'-bipyridine)ruthenium(II) (30 mg, 0.056 mmol) and 2-(1-decyl-1*H*-[1,2,3]triazol-4-yl)-5-((4-(trifluoromethyl)phenyl)ethynyl)pyridine (**10c**, 25 mg, 0.056 mmol) were reacted to yield the pure complex as red powder after recrystallization from ethanol (32 mg, 48%).  $^1\text{H}$  NMR ( $\text{CD}_3\text{CN}$ , 300 MHz)  $\delta$  8.71 (s, 1H), 8.38 (s, 2H), 8.31–8.27 (m, 2H), 8.11–8.08 (m, 2H), 7.79–7.60 (m, 8H), 7.49–7.46 (m, 1H), 7.28–7.23 (m, 3H), 7.18–7.16 (m, 1H), 4.35 (t,  $J = 7.0$  Hz, 2H), 2.56–2.51 (m, 12H), 1.80–1.72 (m, 2H), 1.37–1.07 (m, 14H), 0.89 (t,  $J = 6.7$  Hz, 3H).  $^{13}\text{C}$  NMR ( $\text{CD}_3\text{CN}$ , 75 MHz)  $\delta$  157.2, 156.9, 156.7, 156.6, 153.4, 151.3, 151.2, 151.1, 151.0, 150.7, 150.3, 150.2, 150.0, 147.1, 140.1, 132.2, 128.2, 128.0, 127.5, 126.0, 125.7, 125.6, 125.0, 124.9, 124.5, 124.1, 122.1, 121.3, 93.2, 86.1, 52.1, 31.6, 29.2, 29.2, 29.1, 29.0, 28.4, 25.6, 22.4, 20.4, 20.3, 20.2, 13.4. ESI-TOF MS  $m/z$  1069.30 ( $[\text{M} - \text{PF}_6]^{2+}$ ), 462.17 ( $[\text{M} - 2\text{PF}_6]^{2+}$ ). ESI-HRMS calcd for  $\text{C}_{50}\text{H}_{53}\text{F}_9\text{N}_8\text{PRu}$  [ $\text{M} - \text{PF}_6]^{2+}$ ] 1069.3025, found 1069.2993.

**Bis(4,4'-dimethyl-2,2'-bipyridine)-{2-(1-decyl-1*H*-[1,2,3]triazol-4-yl)-5-((2-nitrophenyl)ethynyl)pyridine}ruthenium(II) Hexafluorophosphate (16d).** According to the above standing general procedure *cis*-dichlorobis(4,4'-dimethyl-2,2'-bipyridine)ruthenium(II) (30 mg, 0.056 mmol) and 2-(1-decyl-1*H*-[1,2,3]triazol-4-yl)-5-((2-nitrophenyl)ethynyl)pyridine (**10b**, 24 mg, 0.056 mmol) were reacted to yield the pure complex as red powder after washing twice with ethanol and diethyl ether (59 mg, 90%).  $^1\text{H}$  NMR ( $\text{CD}_3\text{CN}$ , 300 MHz)  $\delta$  8.71 (s, 1H), 8.38–8.29 (m, 4H), 8.13–8.09 (m, 3H), 7.74–7.53 (m, 8H), 7.27–7.23 (m, 3H), 7.17–7.15 (m, 1H), 4.35 (t,  $J = 7.0$  Hz, 2H), 2.58–2.52 (m, 12H), 1.80–1.72 (m, 2H), 1.37–1.07 (m, 14H), 0.89 (t,  $J = 6.7$  Hz, 3H).  $^{13}\text{C}$  NMR ( $\text{CD}_3\text{CN}$ , 75 MHz)  $\delta$  158.1, 157.8, 157.7, 157.5, 154.5, 152.2, 152.2, 152.0, 151.8, 151.6, 151.3, 151.2, 150.9, 147.9, 140.5, 135.5, 134.6, 131.5, 129.2, 129.0, 128.4, 127.0, 126.0, 125.9, 125.8, 125.4, 125.1, 123.0, 122.1, 91.4, 91.2, 53.1, 32.6, 30.1, 30.1, 30.0, 29.9, 29.3, 26.6, 23.3, 21.3, 21.2, 21.1, 14.3. ESI-TOF MS  $m/z$  1046.30 ( $[\text{M} - \text{PF}_6]^{2+}$ ), 450.67 ( $[\text{M} - 2\text{PF}_6]^{2+}$ ). ESI-HRMS calcd for  $\text{C}_{49}\text{H}_{53}\text{F}_6\text{N}_9\text{O}_2\text{PRu}$  [ $\text{M} - \text{PF}_6]^{2+}$ ] 1046.3002, found 1046.2997.

**Bis(4,4'-dimethyl-2,2'-bipyridine)-{5-((4-phenyl)ethynyl)-2-(1-phenyl-1*H*-[1,2,3]triazol-4-yl)pyridine}ruthenium(II) Hexafluorophosphate (16e).** According to the above-mentioned general procedure *cis*-dichlorobis(4,4'-dimethyl-2,2'-bipyridine)ruthenium(II) (30 mg, 0.056 mmol) and 5-((4-phenyl)ethynyl)-2-(1-phenyl-1*H*-[1,2,3]triazol-4-yl)pyridine (**10d**, 23 mg, 0.056 mmol) were reacted to yield the pure complex as red powder after washing twice with ethanol and diethyl ether (48 mg, 75%).  $^1\text{H}$  NMR ( $\text{CD}_3\text{CN}$ , 300 MHz)  $\delta$  8.69 (s, 1H), 8.37–8.27 (m, 4H), 8.11–8.05 (m, 2H), 7.75–7.72 (m, 2H), 7.66–7.62 (m, 2H), 7.50–7.39 (m, 6H), 7.27–7.24 (m, 3H), 7.18–7.16 (m, 1H), 4.34 (t,  $J = 7.0$  Hz, 2H), 2.56–2.51 (m, 12H), 1.79–1.71 (m, 2H), 1.37–1.06 (m, 14H), 0.89 (t,  $J = 6.7$  Hz, 3H).  $^{13}\text{C}$  NMR ( $\text{CD}_3\text{CN}$ , 75 MHz)  $\delta$  157.2, 156.9, 156.7, 156.6, 153.2, 151.3, 151.2, 151.1, 151.0, 150.3, 150.3, 150.2, 150.2, 150.0, 147.1, 139.9, 131.6, 129.7, 128.8, 128.2, 128.0, 127.5, 125.8, 125.0, 124.9, 124.5, 124.1, 122.0, 121.9, 121.4, 95.0, 83.9, 52.1, 31.6, 29.2, 29.1, 29.0, 28.4, 25.6, 22.4, 20.3, 20.2, 13.4. ESI-TOF MS  $m/z$  1001.32 ( $[\text{M} - \text{PF}_6]^{2+}$ ), 428.18 ( $[\text{M} - 2\text{PF}_6]^{2+}$ ). ESI-HRMS calcd for  $\text{C}_{49}\text{H}_{54}\text{F}_6\text{N}_8\text{PRu}$  [ $\text{M} - \text{PF}_6]^{2+}$ ] 1001.3151, found 1001.3168.

**Bis(4,4'-dimethyl-2,2'-bipyridine)-{5-((4-nitrophenyl)ethynyl)-2-(1-phenyl-1*H*-[1,2,3]triazol-4-yl)pyridine}ruthenium(II) Hexafluorophosphate (17).** According to the above standing general procedure  $\text{Ru}(\text{dmbpy})_2\text{Cl}_2$  (35 mg, 0.065 mmol) and 5-((4-nitrophenyl)ethynyl)-2-(1-phenyl-1*H*-[1,2,3]triazol-4-yl)pyridine (**12**, 24 mg, 0.065 mmol) were reacted to yield the pure complex as red powder after washing twice with ethanol and diethyl ether (45 mg, 63%).  $^1\text{H}$  NMR ( $\text{CD}_3\text{CN}$ , 300 MHz)  $\delta$  9.24 (s, 1H), 8.39 (s, 2H), 8.33–8.18 (m, 6H), 7.86 (s, 1H), 7.79–7.76 (m, 2H),

7.71–7.53 (m, 9H), 7.29–7.25 (m, 3H), 7.17 (m, 1H), 2.56–2.53 (m, 12H).  $^{13}\text{C}$  NMR ( $\text{CD}_3\text{CN}$ , 75 MHz)  $\delta$  157.1, 156.8, 156.7, 156.5, 153.7, 151.5, 151.4, 151.0, 150.9, 150.5, 150.5, 150.4, 150.4, 150.2, 148.0, 140.4, 136.1, 132.7, 130.3, 130.1, 128.3, 128.2, 128.0, 127.5, 125.0, 124.9, 124.6, 124.2, 123.9, 122.2, 121.4, 120.7, 92.9, 88.2, 20.3, 20.3, 20.2. ESI-TOF MS  $m/z$  982.17 ( $[\text{M} - \text{PF}_6]^+$ ). ESI-HRMS calcd for  $\text{C}_{45}\text{H}_{37}\text{F}_6\text{N}_9\text{O}_2\text{PRu}$  ( $[\text{M} - \text{PF}_6]^+$ ) 982.1750, found 982.1776.

**Bis(4,4'-dimethyl-2,2'-bipyridine)-{2-(1-(4-(4-nitrophenyl)ethynyl)phenyl)-1*H*-[1,2,3]triazol-4-yl)pyridine}ruthenium(II) Hexafluorophosphate (18).** According to the above standing general procedure  $\text{Ru}(\text{dmbpy})_2\text{Cl}_2$  (25 mg, 0.046 mmol) and 2-(1-(4-(4-nitrophenyl)ethynyl)phenyl)-1*H*-[1,2,3]triazol-4-yl)pyridine (**15**, 17 mg, 0.046 mmol) were reacted 2.5 h to yield the pure complex as red powder after washing twice with ethanol and diethyl ether (40 mg, 77%).  $^1\text{H}$  NMR ( $\text{CD}_3\text{CN}$ , 300 MHz)  $\delta$  9.25 (s, 1H), 8.38–8.32 (m, 4H), 8.25–8.21 (m, 2H), 8.17–8.15 (m, 1H), 8.03–8.0 (m, 1H), 7.83–7.73 (m, 7H), 7.71–7.58 (m, 4H), 7.36–7.19 (m, 5H), 2.55–2.51 (m, 12H).  $^{13}\text{C}$  NMR ( $\text{CD}_3\text{CN}$ , 75 MHz)  $\delta$  157.2, 156.8, 156.8, 156.5, 151.7, 151.3, 151.1, 151.1, 150.8, 150.6, 150.4,

150.3, 150.1, 148.7, 147.6, 138.1, 136.1, 133.4, 132.5, 129.0, 128.3, 128.2, 127.5, 126.2, 124.9, 124.8, 124.6, 124.2, 123.9, 123.8, 123.4, 122.7, 120.8, 92.1, 89.4, 20.3, 20.3. ESI-TOF MS  $m/z$  982.17 ( $[\text{M} - \text{PF}_6]^+$ ). ESI-HRMS calcd for  $\text{C}_{45}\text{H}_{37}\text{F}_6\text{N}_9\text{O}_2\text{PRu}$  ( $[\text{M} - \text{PF}_6]^+$ ) 982.1750, found 982.1759.

**Acknowledgment.** Financial support of this work by the Dutch Polymer Institute (DPI), the Nederlandse Organisatie voor Wetenschappelijk Onderzoek (NWO, VICI award to U.S.S.), the Fonds der Chemischen Industrie (C.F.), and the Carl-Zeiss Stiftung (D.E.) is kindly acknowledged.

**Supporting Information Available:** UV–vis absorption and emission spectra for the ligands and corresponding ruthenium complexes, crystallographic data for **17**, computational details of **16a** and **16b** (Cartesian coordinates and total energies), and  $^1\text{H}$  and  $^{13}\text{C}$  NMR spectra of all new compounds. This material is available free of charge via the Internet at <http://pubs.acs.org>.

## 5.5 Phenyl-1H-[1,2,3]triazoles as new cyclometalating ligands for Ir(III) complexes

Reprinted with permission from Beyer et al. *Organometallics*, **2009**, *28*, 5478. Copyright 2009 American Chemical Society.

## Phenyl-1*H*-[1,2,3]triazoles as New Cyclometalating Ligands for Iridium(III) Complexes

Beatrice Beyer,<sup>†</sup> Christoph Ulbricht,<sup>‡</sup> Daniel Escudero,<sup>§</sup> Christian Friebe,<sup>†</sup>  
Andreas Winter,<sup>‡</sup> Leticia González,<sup>\*,§</sup> and Ulrich S. Schubert<sup>\*,†,‡</sup>

<sup>†</sup>Laboratory of Organic and Macromolecular Chemistry, Friedrich-Schiller-Universität Jena, Humboldtstrasse 10, 07743 Jena, Germany, <sup>‡</sup>Laboratory of Macromolecular Chemistry and Nanoscience, Eindhoven University of Technology, P.O. Box 513, 5600 MB Eindhoven, The Netherlands, and <sup>§</sup>Laboratory of Theoretical Chemistry, Friedrich-Schiller-Universität Jena, Helmholtzweg 4, 07743 Jena, Germany

Received May 11, 2009

We report on the synthesis and characterization of bis-cyclometalated iridium(III) complexes with 4-phenyl-1*H*-[1,2,3]triazole, synthesized via a “click”-chemistry approach, as a new type of cyclometalating ligand. The photophysical and electrochemical properties of these complexes are investigated experimentally as well as theoretically by using density functional theory. The properties of these new complexes are compared to their known 2-phenylpyridinato analogues. The emission of the herein described complexes is clearly influenced by the applied ancillary ligand and can be adjusted over a broad range of frequencies. The results indicate that the phenyl-1*H*-[1,2,3]triazole ligands in general cause a spectral blue shift.

### Introduction

Organic light-emitting diodes (OLEDs) have received considerable attention during recent years in the academic world and in industry for display and lighting applications.<sup>1–6</sup> For the fabrication of high-efficiency OLEDs, the development of high-performance materials plays an important role. Iridium(III) complexes show, in contrast to complexes based on other heavy-metal atoms (e.g., Ru<sup>II</sup>, Rh<sup>I</sup>, Os<sup>II</sup>), an intense phosphorescence at room temperature.<sup>7</sup> This emission originates from a triplet metal-to-ligand charge transfer (MLCT) or in some cases from a triplet ligand-centered (LC) state. Due to the strong spin–orbit coupling, the phosphorescent lifetimes are in the microsecond regime. Besides the advantage of obtaining an internal quantum efficiency of theoretically up to 100% in electroluminescent devices,<sup>8</sup> the emission color of iridium(III) complexes can easily be varied from blue to red by adapting the coordinated ligand system. Several strategies have been reported in order to tune the photophysical properties of these complexes and to achieve blue emission, e.g., employing electron-withdrawing

substituents in the cyclometalating ligand<sup>9</sup> and using cationic<sup>10</sup> as well as anionic Ir<sup>III</sup> complexes.<sup>11</sup> In recent years many different ligand systems were investigated in order to obtain phosphors with high quantum yields and color purity. In particular bis- and tris-cyclometalated iridium(III) complexes exhibit a high potential for applications in OLEDs. To form bis-cyclometalated species chloro-bridged dimeric iridium(III) precursors can be reacted with a broad variety of coordination motifs, e.g. bipyridine, picolinate, acetylacetonate, and their derivatives.<sup>12–17</sup> Besides the straightforward synthesis, the utilization of ancillary ligands provides further options to introduce functionalities and to tune the optical and electrical properties. For the understanding of the photophysical behavior of such Ir<sup>III</sup> complexes, theoretical investigations have proven to be very useful.<sup>11,18</sup>

\*Corresponding author. Fax: +49 3641 948302. E-mail: leticia.gonzalez@uni-jena.de. Fax: +49 3641 948202. E-mail: ulrich.schubert@uni-jena.de.

- (1) Lowry, M. S.; Bernhard, S. *Chem.—Eur. J.* **2006**, *12*, 7970–7977.
- (2) D’Andrade, B. W.; Forrest, S. R. *Adv. Mater.* **2004**, *16*, 1585–1595.
- (3) Holder, E.; Langeveld, B. M. W.; Schubert, U. S. *Adv. Mater.* **2005**, *17*, 1109–1121.
- (4) Forrest, S. R.; Thompson, M. E. *Chem. Rev.* **2007**, *107*, 923–925.
- (5) Müllen, K.; Scherf, U. *Organic Light-Emitting Devices*; Wiley-VCH: Weinheim, Germany, 2006.
- (6) Ulbricht, C.; Beyer, B.; Friebe, C.; Winter, A.; Schubert, U. S. *Adv. Mater.* **2009**, DOI: 10.1002/adma.200803537.
- (7) Yersin, H. *Highly Efficient OLEDs with Phosphorescent Materials*; Wiley-VCH: Weinheim, Germany, 2008.
- (8) Baldo, M. A.; Lamansky, S.; Burrows, P. E.; Thompson, M. E.; Forrest, S. R. *Appl. Phys. Lett.* **1999**, *75*, 4–6.

(9) Gu, X.; Fei, T.; Zhang, H.; Xu, H.; Yang, B.; Ma, Y.; Liu, X. *J. Phys. Chem. A* **2008**, *112*, 8387–8393.

(10) Zeng, X.; Tavasli, M.; Perepichka, I. F.; Batsanov, A. S.; Bryce, M. R.; Chiang, C.-J.; Rothe, C.; Monkman, A. P. *Chem.—Eur. J.* **2008**, *14*, 933–943.

(11) Di Censo, D.; Fantacci, S.; De Angelis, F.; Klein, C.; Evans, N.; Kalyanasundaram, K.; Bolink, H. J.; Grätzel, M.; Nazeeruddin, M. K. *Inorg. Chem.* **2008**, *47*, 980–989.

(12) Lamansky, S.; Djurovich, P.; Murphy, D.; Abdel-Razzaq, F.; Lee, H.-E.; Adachi, C.; Burrows, P. E.; Forrest, S. R.; Thompson, M. E. *J. Am. Chem. Soc.* **2001**, *123*, 4304–4312.

(13) You, Y. M.; Park, S. Y. *J. Am. Chem. Soc.* **2005**, *127*, 12438–12439.

(14) Kwon, T.-H.; Kim, M. K.; Kwon, J.; Shin, D.-Y.; Park, S.-J.; Lee, C.-L.; Kim, J.-J.; Hong, J. I. *Chem. Mater.* **2007**, *19*, 3673–3680.

(15) Tsuzuki, T.; Shirasawa, N.; Suzuki, T.; Tokito, S. *Adv. Mater.* **2003**, *15*, 1455–1458.

(16) Zhen, H.; Luo, J.; Yang, W.; Chen, Q.; Ying, L.; Jianhua, Z.; Wu, H.; Cao, Y. *J. Mater. Chem.* **2007**, *17*, 2824–2831.

(17) Li, J.; Djurovich, P. I.; Alleyne, B. D.; Yousufuddin, M.; Ho, N. N.; Thomas, J. C.; Peters, J. C.; Bau, R.; Thompson, M. E. *Inorg. Chem.* **2005**, *44*, 1713–1727.

(18) Tamayo, A. B.; Alleyne, B. D.; Djurovich, P. I.; Lamansky, S.; Tsyba, I.; Ho, N. N.; Bau, R.; Thompson, M. E. *J. Am. Chem. Soc.* **2003**, *125*, 7377–7387.

In the past decade, the synthesis of 1*H*-[1,2,3]triazoles experienced a great revival in the form of the copper(I)-catalyzed Huisgen cycloaddition. This procedure was introduced independently by the groups of K. B. Sharpless and M. Meldal.<sup>19–21</sup> The addition of a Cu<sup>I</sup> catalyst leads to the exclusive formation of the 1,4-regioisomer, increases the reaction rate by a factor of 10<sup>7</sup>, and enables the performance of the reaction under mild conditions.<sup>22</sup> With this so-called “click” reaction it is possible to introduce different functionalities via the acetylene and the organic azide. Weck and co-workers used the efficient cycloaddition reaction to attach alkyne-functionalized tris-cyclometalated iridium(III) complexes to azide-bearing polymeric backbones, yielding phosphorescent polymers.<sup>23</sup> Performing the “click” reaction with alkyne-functionalized terpyridine moieties at an azide-terminated monolayer Haensch et al. anchored coordination sites to a surface. After the reaction with a dimeric precursor surface-tethered bis-cyclometalated iridium(III) complexes were obtained.<sup>24</sup> Besides the utilization of the “click” reaction as a linking tool [1,2,3]triazoles can be applied as coordination motifs. “Clicked” terpyridine<sup>25,26</sup> and bipyridine<sup>27</sup> analogues were recently introduced and applied in the formation of the respective ruthenium(II) complexes. While 1,2,4-triazoles are established moieties in ancillary ligands applied to synthesize neutral iridium(III) complexes<sup>28–33</sup> and even appear in bpy analogues<sup>34</sup> and cyclometalating<sup>35</sup> systems, the potential of [1,2,3]triazoles as coordination site for iridium(III) species is investigated only marginally. In an early work by Nonoyama et al. 2-aryl-4,5-dimethyl-[1,2,3]-triazoles were used as cyclometalating ligands in the formation of dimeric iridium(III) precursor complexes.<sup>36</sup> A similar dimer with 2-phenyl-2*H*-[1,2,3]triazolo[4,5-*f*]quinoline as

cyclometalating ligands was synthesized by Tomkutė-Lukšienė et al. and was further reacted with acetoacetone to yield the respective bis-cyclometalated iridium(III) complex.<sup>37</sup> Orselli et al. applied 2-(1*H*-[1,2,3]triazol-5-yl)pyridine and 2-[4-(aryl)-1*H*-[1,2,3]triazol-5-yl]pyridines as ancillary ligands in the formation of neutral bis-cyclometalated iridium(III) complexes.<sup>38</sup> Phenyl-1*H*-[1,2,3]triazoles with variable substituents in 1- and 4-position, easily accessible by “clicking” the respective azides and acetylenes moieties, have not been investigated regarding potential applications as cyclometalating ligands in the coordination of iridium(III) species, so far.

Here, we report on the synthesis and characterization of new heteroleptic iridium(III) complexes using phenyl-1*H*-[1,2,3]triazoles as cyclometalating ligands. “Click” chemistry was used for the straightforward synthesis of two different types of potential ligand systems. The properties of the new phosphors were analyzed and compared to classical complexes based on 2-phenylpyridine (Hppy). In addition, a DFT and time-dependent DFT (TD-DFT) study of the ground and excited states of selected Ir<sup>III</sup> complexes has been performed in order to interpret the experimental photophysical data. This study provides valuable information regarding the excited states involved in the absorption and emission processes.

## Results and Discussion

**Synthesis and Characterization.** The synthesis of the new cyclometalating ligands was carried out in a highly efficient one-pot consecutive procedure. Following literature descriptions, the respective acetylene derivative was reacted with the organic azide, formed *in situ* from the corresponding bromo compound.<sup>39,40</sup> It is noteworthy that no further copper(I) catalyst had to be added after the formation of the arylazide in order to perform the “click” reaction. The so-called “click” rules, as specified by Sharpless,<sup>20</sup> were completely fulfilled. After reacting the organic azides and acetylene compounds in an environmentally friendly solvent mixture (i.e., ethanol/water, 7:3 ratio) at room temperature, the potential ligands 1-decyl-4-phenyl-1*H*-[1,2,3]triazole (**H-a**) and 4-decyl-1-phenyl-1*H*-[1,2,3]triazole (**H-b**) could be obtained in high yields by simple purification procedures (Scheme 1). The formation of only one triazole regioisomer was verified by <sup>1</sup>H NMR spectroscopy. The signal originating from the *ortho*-protons of the phenyl ring (asterisk in Figure 1) is significantly high-field shifted for **H-a** (7.84 ppm) and **H-b** (7.75 ppm) in comparison to 2-phenylpyridine (Hppy, 8.04 ppm). This can be explained by the higher electron density in the phenyl ring due to mesomerism of the lone electron pairs of the triazole nitrogen atoms to the attached phenyl ring. Furthermore, the ligands were characterized by <sup>13</sup>C NMR and UV–vis absorption spectroscopy as well as MALDI-TOF mass spectrometry and elemental analysis.

(19) Tornø, C. W.; Christensen, C.; Meldal, M. *J. Org. Chem.* **2002**, *67*, 3057–3064.

(20) Kolb, H. C.; Finn, M. G.; Sharpless, K. B. *Angew. Chem., Int. Ed.* **2001**, *40*, 2004–2021.

(21) Rostovtsev, V. V.; Green, L. G.; Fokin, V. V.; Sharpless, K. B. *Angew. Chem., Int. Ed.* **2002**, *41*, 2596–2599.

(22) Bock, V. D.; Hiemstra, H.; Maarseveen, J. H. *Eur. J. Org. Chem.* **2006**, *1*, 51–68.

(23) Wang, X.-Y.; Kimyonok, A.; Weck, M. *Chem. Commun.* **2006**, 3933–3935.

(24) Haensch, C.; Chiper, M.; Ulbricht, C.; Winter, A.; Hoepfner, S.; Schubert, U. S. *Langmuir* **2008**, *24*, 12981–12985.

(25) Li, Y. J.; Huffman, J. C.; Flood, A. H. *Chem. Commun.* **2007**, 2692–2694.

(26) Schulze, B.; Friebe, C.; Hager, M. D.; Winter, A.; Hoogenboom, R.; Görls, H.; Schubert, U. S. *Dalton* **2009**, 787–794.

(27) Happ, B.; Friebe, C.; Winter, A.; Hager, M. D.; Hoogenboom, R.; Schubert, U. S. *Chem. Asian. J.* **2009**, *4*, 154–163.

(28) Yang, C.-H.; Li, S.-W.; Chi, Y.; Cheng, Y.-M.; Yeh, Y.-S.; Chou, P.-T.; Lee, G.-H.; Wang, C.-H.; Shu, C.-F. *Inorg. Chem.* **2005**, *44*, 7770–7780.

(29) Liang, B.; Jiang, C.; Chen, Z.; Zhang, X.; Shi, H.; Cao, Y. *J. Mater. Chem.* **2006**, *16*, 1281–1286.

(30) Takizawa, S.-y.; Nishida, J.-i.; Tsuzuki, T.; Tokito, S.; Yamashita, Y. *Inorg. Chem.* **2007**, *46*, 4308–4319.

(31) Liang, B.; Wang, L.; Xu, Y.; Shi, H.; Cao, Y. *Adv. Funct. Mater.* **2007**, *17*, 3580–3589.

(32) Chang, C.-F.; Cheng, Y.-M.; Chi, Y.; Chiu, Y.-C.; Lin, C.-C.; Lee, G.-H.; Chou, P.-T.; Chen, C.-C.; Chang, C.-H.; Wu, C.-C. *Angew. Chem., Int. Ed.* **2008**, *47*, 4542–4545.

(33) Song, Y.-H.; Chiu, Y.-C.; Chi, Y.; Cheng, Y.-M.; Lai, C.-H.; Chou, P.-T.; Wong, K.-T.; Tsai, M.-H.; Wu, C.-C. *Chem.—Eur. J.* **2008**, *14*, 5423–5434.

(34) van Diemen, J. H.; Haasnoot, J. G.; Hage, R.; Müller, E.; Reedijk, J. *Inorg. Chim. Acta* **1991**, *181*, 245–251.

(35) Lo, S.-C.; Shipley, C. P.; Bera, R. N.; Harding, R. E.; Cowley, A. R.; Burn, P. L.; Samuel, I. D. W. *Chem. Mater.* **2006**, *18*, 5119–5129.

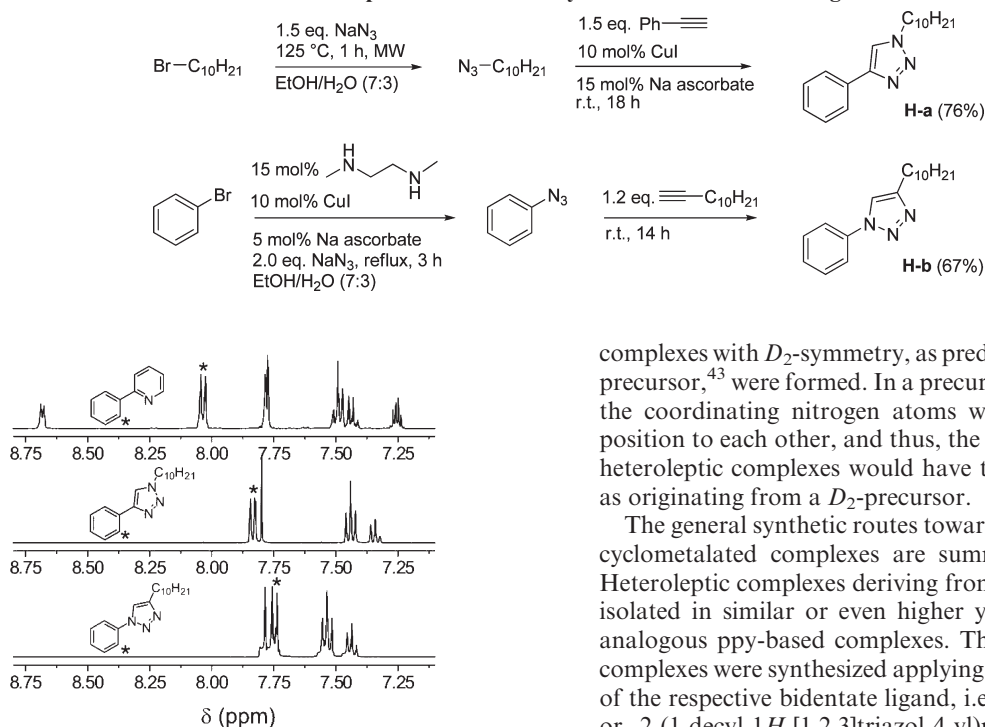
(36) Nonoyama, M.; Hayata, C. *Transition Met. Chem.* **1978**, *3*, 366–369.

(37) Tomkutė-Lukšienė, D.; Malinauskas, T.; Stanišauskaitė, A.; Getautis, V.; Kazlauskas, K.; Vitta, P.; Žukauskas, A.; Juršėnas, S. *J. Photochem. Photobiol. A: Chem.* **2008**, *198*, 106–110.

(38) Orselli, E.; Albuquerque, R. Q.; Fransen, P. M.; Fröhlich, R.; Janssen, H. M.; De Cola, L. *J. Mater. Chem.* **2008**, *18*, 4579–4590.

(39) Ju, Y.; Kumar, D.; Varma, R. S. *J. Org. Chem.* **2006**, *71*, 6697–6700.

(40) Anderson, J.; Madsen, U.; Björkling, F.; Liang, X. *Synlett* **2005**, 2209–2213.

Scheme 1. Schematic Representation of the Synthesis of the Potential Ligands **H-a** and **H-b**

**Figure 1.** <sup>1</sup>H NMR spectra (aromatic region) of Hppy (top), **H-a** (middle), and **H-b** (bottom). For all spectra: 400 MHz, room temperature, CD<sub>2</sub>Cl<sub>2</sub>.

Although the “click” reaction offers many advantages to easily engineer heterocycles, it has one inherent drawback. The handling of organic azides is connected with certain safety considerations.<sup>41</sup> Therefore, it was not advisable to synthesize 4-phenyl-[1,2,3]triazoles with short alkyl chains. For comparison, the same alkyl chain length was used for ligands **H-a** and **H-b**. However, the presence of the required alkyl chains dramatically reduced the probability of obtaining single crystals suitable for X-ray analysis.

The synthesized phenyl-triazole derivatives **H-a** and **H-b** as well as the commercially available 2-phenylpyridine were reacted with IrCl<sub>3</sub> × 3H<sub>2</sub>O to form the respective dimeric chloro-bridged iridium(III) precursor complexes following literature procedures (Scheme 2).<sup>42</sup> The isolated yields of the new dimeric precursors **A** and **B** were good (76% and 53%, respectively), but lower than that of [(Ir(ppy)<sub>2</sub>-μ-Cl)<sub>2</sub>] (**C**, 90% yield). This might be attributed to the circumstance that column chromatography was necessary as an additional purification step (**A**, **B** vs **C**) and the slightly lower ability of the phenyl-1*H*-[1,2,3]triazoles to form stable carbanions for the cyclometalation due to the increased electron density in the C<sup>2'</sup>-position, as already observed by <sup>1</sup>H NMR spectroscopy. Despite thorough purification, the NMR spectra recorded from precursors **A** and **B** appeared rather undefined. However, elemental analyses showed good compositional consistency with the expected molecular formula of a dimeric precursor complex. Since the desired bis-cyclometalated Ir<sup>III</sup> complexes could be synthesized in the following with precursor **A**, it is assumed that not only dimeric

complexes with *D*<sub>2</sub>-symmetry, as predicted for the ppy-based precursor,<sup>43</sup> were formed. In a precursor with *C*<sub>2*v*</sub>-symmetry the coordinating nitrogen atoms would still be in *trans*-position to each other, and thus, the ligands in the resulting heteroleptic complexes would have the same configuration as originating from a *D*<sub>2</sub>-precursor.

The general synthetic routes toward different types of bis-cyclometalated complexes are summarized in Scheme 3. Heteroleptic complexes deriving from precursor **A** could be isolated in similar or even higher yields compared to the analogous ppy-based complexes. The charged iridium(III) complexes were synthesized applying an excess (5 to 9 equiv) of the respective bidentate ligand, i.e., 2,2'-bipyridine (bpy) or 2-(1-decyl-1*H*-[1,2,3]triazol-4-yl)pyridine (trpy). After 14 h refluxing in a solvent mixture of CH<sub>2</sub>Cl<sub>2</sub>/CH<sub>3</sub>OH (4:5), an anion exchange with NH<sub>4</sub>PF<sub>6</sub> was performed. The neutral complexes were obtained from the reaction with either acetylacetonate (Hacac, 10 equiv) or picolinic acid (Hpic, 5 equiv) in the presence of equimolar amounts of Na<sub>2</sub>CO<sub>3</sub> by refluxing for 14 h in C<sub>2</sub>H<sub>5</sub>OH and CH<sub>2</sub>Cl<sub>2</sub>, respectively.

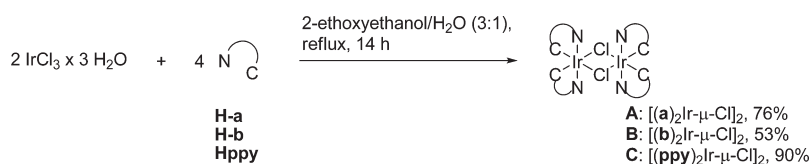
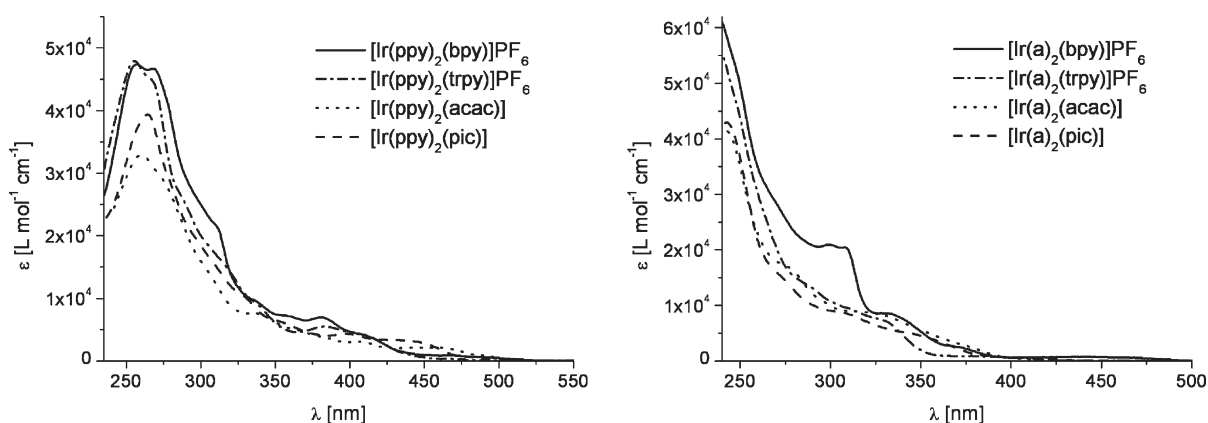
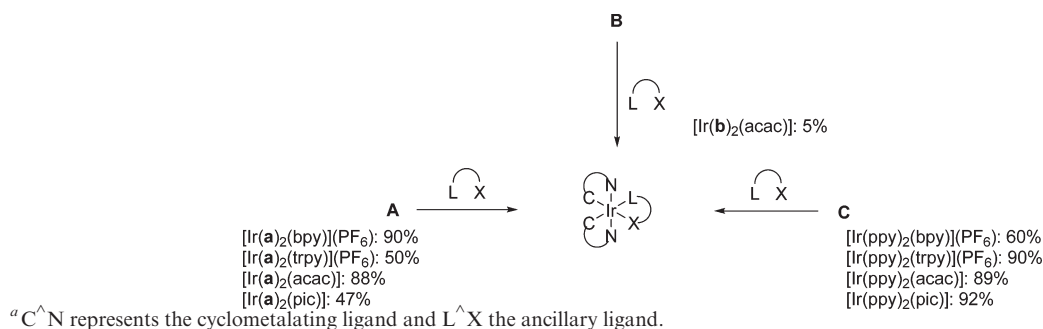
Starting from precursor **B**, the expected heteroleptic complexes could not be isolated, with exception of complex [Ir(**b**)<sub>2</sub>(acac)]. Due to the poor yield of approximately 5% a full characterization of this complex could not be carried out. In all other cases, either many byproducts were formed, in particular for the charged systems (i.e., bpy and trpy) or the attempts to cleave the chloro bridge to form neutral complexes failed. The instability of the crude products on the column material prevented any purification by column chromatography. In addition, the release of the cyclometalating ligand (i.e., **H-b**) during the synthetic attempts with precursor **B** could be observed as well. It is supposed that the thermodynamic stability of complexes originating from **H-b** is remarkably lower than for complexes synthesized from **H-a**. Thus, the position of the cyclometalating phenyl ring seems to be important for the σ-donor and π-acceptor strength of the new ligands. As already concluded from the <sup>1</sup>H NMR spectra of these two types of ligands, **H-b** features a higher electron density than **H-a** in the phenyl ring. Apparently, the π-back-donation from the Ir<sup>III</sup> center to the ligand **b** is also less pronounced.

**Electro-optical Properties.** The experimental UV–vis absorption spectra of both 2-phenylpyridine-(Ir(ppy)<sub>2</sub>L<sup>Δ</sup>X) and phenyl-1*H*-[1,2,3]triazole-containing complexes (Ir(**a**)<sub>2</sub>-L<sup>Δ</sup>X), are depicted in Figure 2. The corresponding photoluminescence (PL) spectra are shown in Figure 3. The

(41) Bräse, S.; Gil, C.; Knepper, K.; Zimmermann, V. *Angew. Chem., Int. Ed.* **2005**, *44*, 5188–5240.

(42) Winter, A.; Ulbricht, C.; Holder, E.; Risch, N.; Schubert, U. S. *Aust. J. Chem.* **2006**, *59*, 773–782.

(43) Sprouse, S.; King, K. A.; Spellane, P. J.; Watts, R. J. *J. Am. Chem. Soc.* **1984**, *106*, 6647–6653.

**Scheme 2. Schematic Representation of the Synthesis of the Dimeric Iridium(III) Precursor Complexes  $[\text{Ir}(\text{C}^{\wedge}\text{N})_2\text{-}\mu\text{-Cl}]_2$** 

**Scheme 3. Schematic Representation of the Synthesis of Heteroleptic Iridium(III) Complexes<sup>a</sup>**


**Figure 2.** Experimental UV-vis absorption spectra of the  $\text{Ir}^{\text{III}}$  complexes containing ppy (left) and **a** (right) as cyclometalating ligand. For all spectra:  $10^{-6}$  M in  $\text{CH}_2\text{Cl}_2$ , room temperature.

photophysical and electrochemical characteristics of the complexes are summarized in Tables 1 and 2.

It is noteworthy that in the case of the complexes based on 2-phenylpyridine (i.e.,  $[\text{Ir}(\text{ppy})_2(\text{acac})]$ ,  $[\text{Ir}(\text{ppy})_2(\text{bpy})](\text{PF}_6)$ , and  $[\text{Ir}(\text{ppy})_2(\text{pic})]$ ) the observed data (Table 1) are in accordance with the values reported in the literature.<sup>12,44,46</sup> Furthermore the experimental spectra reveal the expected absorption blue-shifts for the [1,2,3]triazole-derived complexes in comparison to their 2-phenylpyridine counterparts, while the shape of the absorption bands exhibits a high resemblance.

In order to gain a more detailed insight into the photophysical properties of the (phenyl-1*H*-[1,2,3]triazole)-based  $\text{Ir}^{\text{III}}$  complexes, theoretical  $\Delta$ -DFT and TD-DFT (B3LYP/TZVP) calculations have been performed for  $[\text{Ir}(\mathbf{a})_2(\text{bpy})]^+$ ,  $[\text{Ir}(\mathbf{a})_2(\text{acac})]$ , and  $[\text{Ir}(\mathbf{a})_2(\text{pic})]$ . Figure 4 shows the obtained

Kohn-Sham frontier orbitals and the energy level schemes of the three complexes.

In the neutral complexes the highest occupied molecular orbitals (HOMOs) are the  $t_{2g}$ -orbital set of the central  $\text{Ir}^{\text{III}}$  ion. In the case of  $[\text{Ir}(\mathbf{a})_2(\text{bpy})]^+$ , however, a  $\pi$ -orbital of the cyclometalating ligand is intercalated within the occupied 5*d*-orbitals. For all complexes the HOMO corresponds to the 5*d*<sub>xy</sub>-orbital, while the LUMO is a  $\pi^*$ -orbital. Interestingly, this antibonding orbital is located on the ancillary ligand in the case of  $[\text{Ir}(\mathbf{a})_2(\text{bpy})]^+$  and  $[\text{Ir}(\mathbf{a})_2(\text{pic})]$  but on the cyclometalating ligand in the case of  $[\text{Ir}(\mathbf{a})_2(\text{acac})]$ . The following unoccupied orbitals are mostly of  $\pi^*$ -antibonding character (not specified in Figure 4). The  $e_g$ -orbitals of  $\text{Ir}^{\text{III}}$  are, as seen in Figure 4, strongly destabilized in these complexes. This is a common feature for cyclometalated  $\text{Ir}^{\text{III}}$  complexes, since the strong ligand field effect of the phenyl anion ligand increases the gap between the  $t_{2g}$ - and  $e_g$ -orbitals. Thus, 5*d*<sub>z<sup>2</sup></sub> and 5*d*<sub>x<sup>2</sup>-y<sup>2</sup></sub> correspond to LUMO+11 and LUMO+13 in  $[\text{Ir}(\mathbf{a})_2(\text{bpy})]^+$ , respectively, while in  $[\text{Ir}(\mathbf{a})_2(\text{pic})]$  and  $[\text{Ir}(\mathbf{a})_2(\text{acac})]$  they relate to LUMO+10 and LUMO+12. The energetic gaps between the HOMO and LUMO levels are also noted in Figure 4. As stated in the introduction, a blue-shifted emission in  $\text{Ir}^{\text{III}}$  systems can be achieved by properly choosing the substituents on the

(44) Lo, K. K.-W.; Chan, J. S.-W.; Lui, L.-H.; Chung, C.-K. *Organometallics* **2004**, *23*, 3108–3116.

(45) Nastasi, F.; Puntoriero, F.; Campagna, S.; Schergna, S.; Maggini, M.; Cardinali, F.; Delavaux-Nicot, B.; Nierengarten, J.-F. *Chem. Commun.* **2007**, 3556–3558.

(46) Gupta, D.; Katiyar, M.; Deepak; Hazra, T.; Verma, A.; Manoharan, S. S.; Biswas, A. *Opt. Mater.* **2006**, *28*, 1355–1361.



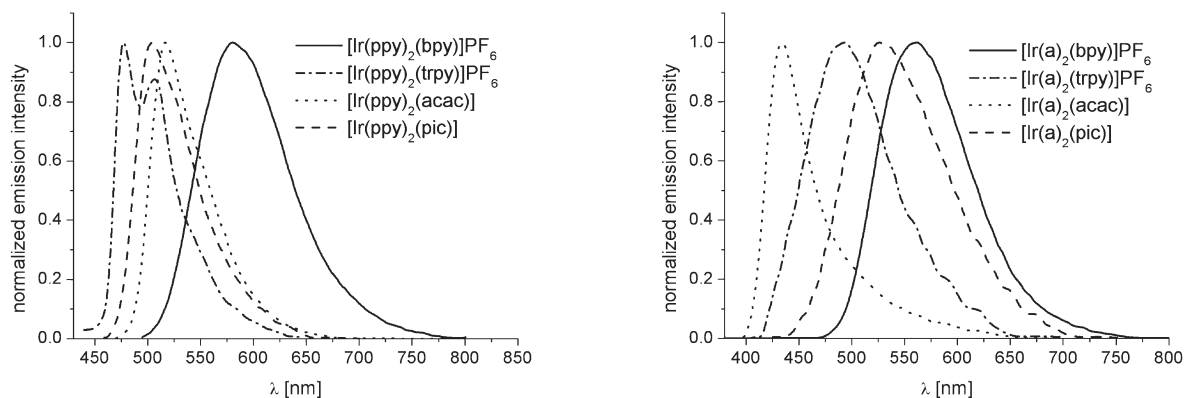


**Figure 3.** Photoluminescence spectra of the Ir<sup>III</sup> complexes containing ppy (left) and **a** (right) as cyclometalating ligand. For all spectra: 10<sup>-7</sup> M in degassed CH<sub>2</sub>Cl<sub>2</sub>, room temperature, excitation at longest absorption wavelength.

**Table 1.** Selected Photophysical Properties of the Investigated Ir<sup>III</sup> Complexes

complex	$\lambda_{\text{abs}}$ [nm] (log $\epsilon$ ) <sup>a</sup>	$\lambda_{\text{PL}}$ [nm] <sup>b</sup>	$E_{0-0}$ [nm] <sup>c</sup>	$\Phi_{\text{PL}}$ <sup>b,d</sup>
[Ir( <b>a</b> ) <sub>2</sub> (bpy)](PF <sub>6</sub> )	240 (4.79), 299 (4.32), 330 (3.93), 441 (2.88), 470 (2.74)	560	474	0.45
[Ir( <b>a</b> ) <sub>2</sub> (trpy)](PF <sub>6</sub> )	240 (4.74), 329 (3.87), 378 (2.92)	495	415	0.29
[Ir( <b>a</b> ) <sub>2</sub> (acac)]	241 (4.62), 276 (4.23), 318 (3.95)	435	400	0.02
[Ir( <b>a</b> ) <sub>2</sub> (pic)]	243 (4.63), 303 (3.95), 347 (3.68), 399 (2.82)	527	440	0.11
[Ir(ppy) <sub>2</sub> (bpy)](PF <sub>6</sub> )	257 (4.68), 269 (4.67), 381 (3.85), 466 (2.94), 492 (2.74)	580	498	0.29
[Ir(ppy) <sub>2</sub> (trpy)](PF <sub>6</sub> )	256 (4.68), 266 (4.65), 382 (3.74), 408 (3.63)	477, 507	451	0.21
[Ir(ppy) <sub>2</sub> (acac)]	260 (4.52), 337 (3.88), 405 (3.49), 456 (3.32), 489 (2.94)	517	481	0.53
[Ir(ppy) <sub>2</sub> (pic)]	264 (4.60), 398 (3.64), 429 (3.53), 477 (2.83)	505	467	0.29

<sup>a</sup> Measured in CH<sub>2</sub>Cl<sub>2</sub>, 10<sup>-6</sup> M, room temperature. <sup>b</sup> Measured in degassed CH<sub>2</sub>Cl<sub>2</sub>, 10<sup>-7</sup> M, room temperature. <sup>c</sup> The 0–0 vibration gap is estimated by the intersection of absorption and emission spectra. <sup>d</sup> Absolute quantum yields.

cyclometalating ligands as well as on the ancillary ligand, which stabilizes the HOMO and/or destabilizes the LUMO and, thus, increases the HOMO–LUMO energy gap.<sup>13,47</sup> For the complexes studied herein we have obtained decreasing theoretical energy gaps of 4.31, 3.68, and 3.21 eV for [Ir(**a**)<sub>2</sub>(acac)], [Ir(**a**)<sub>2</sub>(pic)], and [Ir(**a**)<sub>2</sub>(bpy)]<sup>+</sup>, respectively. This trend has been confirmed by electrochemical data derived from cyclic voltammetry investigations (Table 2). There, the HOMO energy levels, which were calculated from the oxidation potentials (assigned to a reversible Ir<sup>III</sup>/Ir<sup>IV</sup> oxidation), show good agreement with the calculated values. Since, except for the case of the bpy systems, the reduction potentials appear out of the accessible range of the cyclic voltammetry measurements, the LUMO energies were determined by using the optical band gaps estimated from the absorption spectra. In comparison to the experimentally derived data, values obtained by the theoretical calculations show particularly an overestimation regarding the LUMO levels and, therefore, also for the theoretical band gaps  $E_g$ . However the relative change within the complex series is consistent for both the LUMO energies and the HOMO–LUMO energy gaps ( $E_g^{\text{acac}} > E_g^{\text{pic}} > E_g^{\text{bpy}}$ ), see Table 2.

Previous theoretical studies have dealt with the well-known [Ir(ppy)<sub>2</sub>(L<sup>^</sup>X)]-type derivatives.<sup>49,50</sup> For instance, for [Ir(ppy)<sub>2</sub>(acac)] an energetic gap of 3.46 eV was obtained also using the B3LYP functional. On the basis of these data

we can evaluate the influence of the cyclometalating ligand (i.e., **a** vs ppy) on the HOMO–LUMO gap. Apparently, ligand **a** increases the energy gap (4.31 eV) as compared to the ppy ligand-based complex (3.46 eV).<sup>50</sup> This difference stems from both the stabilization of the HOMO and the destabilization of the LUMO, which can both be caused by the increased  $\pi$ -acceptor ability of the [1,2,3]triazole moiety. The enhanced possibility to receive electron density in the  $\pi^*$ -orbitals of the ligand-centered  $\pi$ -system via back-bonding stabilizes the occupied  $t_{2g}$ -orbitals of the iridium. On the other hand it also destabilizes the unoccupied  $\pi^*$ -orbitals of the ligands including the LUMO level.

By analyzing the effect of the ancillary ligand (i.e., bpy, acac, pic) on the energetic ordering of the frontier orbitals, several points arise. First, a larger band gap is observed for the neutral compounds in comparison to the cationic [Ir(**a**)<sub>2</sub>(bpy)]<sup>+</sup> complex. It has been reported previously that by using cationic Ir<sup>III</sup> complexes the HOMO energies are stabilized, and, thus, larger energy gaps can be achieved.<sup>11,50</sup> Indeed, the HOMO orbital is stabilized in the cationic compound studied here, namely, [Ir(**a**)<sub>2</sub>(bpy)]<sup>+</sup>, in comparison to the neutral complexes. However, the LUMO is more stabilized to a major extent than the HOMO, and as a consequence, the HOMO–LUMO energy gap is reduced. Second, a comparison between the neutral compounds (i.e., [Ir(**a**)<sub>2</sub>(acac)] and [Ir(**a**)<sub>2</sub>(pic)]) shows that the major differences between them originate from the LUMO energies rather than the HOMO energies. As stated above, both LUMOs show  $\pi^*$ -character, but are located on the cyclometalating and on the ancillary ligand, respectively. In [Ir(**a**)<sub>2</sub>(pic)] the LUMO located on the ancillary ligand ( $\pi^*_{\text{anc}}$ ) is stabilized with respect to the  $\pi^*_{\text{anc}}$ -orbital in [Ir(**a**)<sub>2</sub>(acac)], which lies higher in energy than the  $\pi^*$ -orbital of the cyclometalating ligands. This fact can be attributed to the higher conjugation of

(47) Sajoto, T.; Djurovich, P. I.; Tamayo, A.; Yousufuddin, M.; Bau, R.; Thompson, M. E.; Holmes, R. J.; Forrest, S. R. *Inorg. Chem.* **2005**, *44*, 7992–8003.

(48) Egbe, D. A. M.; Bader, C.; Nowotny, J.; Günther, W.; Klemm, E. *Macromolecules* **2003**, *36*, 5459–5469.

(49) Hay, P. J. *J. Phys. Chem. A* **2002**, *106*, 1634–1641.

(50) Liu, T.; Xia, B.-H.; Zhou, X.; Zheng, Q.-C.; Pan, Q.-J.; Zhang, H.-X. *Theor. Chem. Acc.* **2008**, *121*, 155–164.

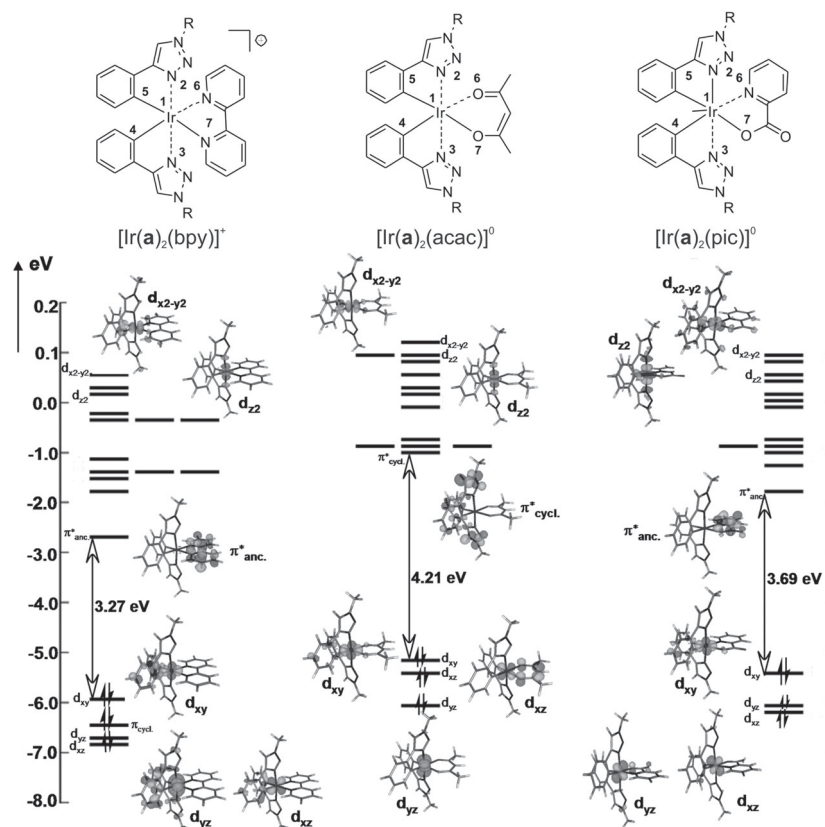


**Figure 4.** (Top) Schematic representation of the heteroleptic bis-cyclometalated Ir<sup>III</sup> complexes investigated theoretically herein (R = CH<sub>3</sub>, the atom labeling denotes the main geometrical parameters of the gas phase optimized complexes as summarized in Table 5). (Bottom) Energy level schemes for the Kohn–Sham orbitals of the Ir<sup>III</sup> complexes, including the most relevant Kohn–Sham orbitals and the HOMO–LUMO gaps calculated with B3LYP/TZVP.

**Table 2. Electrochemical Data of the Synthesized Ir<sup>III</sup> Complexes**

complex	$E_{1/2,ox}$ [V] <sup>a</sup>	$E_g^{opt}$ [eV] <sup>b</sup>	$E_g^{theo}$ [eV]	$E_c^{HOMO}$ [eV] <sup>c</sup>	$E^{LUMO}$ [eV] <sup>d</sup>
[Ir(a) <sub>2</sub> (bpy)](PF <sub>6</sub> )	1.23	2.49	3.21	-5.63 (-6.22) <sup>e</sup>	-3.14 (-3.01) <sup>e</sup>
[Ir(a) <sub>2</sub> (trpy)](PF <sub>6</sub> )	1.20	2.88		-5.59	-2.71
[Ir(a) <sub>2</sub> (acac)]	0.71	3.15	4.31	-5.11 (-5.25) <sup>e</sup>	-1.96 (-0.94) <sup>e</sup>
[Ir(a) <sub>2</sub> (pic)]	0.90	2.82	3.68	-5.29 (-5.54) <sup>e</sup>	-2.47 (-1.86) <sup>e</sup>
[Ir(ppy) <sub>2</sub> (bpy)](PF <sub>6</sub> )	1.27	2.37		-5.68	-3.31
[Ir(ppy) <sub>2</sub> (trpy)](PF <sub>6</sub> )	1.23	2.76		-5.66	-2.90
[Ir(ppy) <sub>2</sub> (acac)]	0.76	2.41		-5.18	-2.77
[Ir(ppy) <sub>2</sub> (pic)]	0.94	2.46		-5.32	-2.86

<sup>a</sup>Measurements were performed in CH<sub>2</sub>Cl<sub>2</sub> containing 0.1 M TBAPF<sub>6</sub>. The potentials are given vs standard hydrogen electrode (SHE). <sup>b</sup>Estimated from the UV–vis spectra at 10% absorption on the longer wavelength side. <sup>c</sup> $E_c^{HOMO}$  calculated from  $E_{1/2,ox}$ . <sup>d</sup>Determined from  $E_g^{opt}$  and  $E_c^{HOMO}$ . <sup>e</sup>Values obtained at the B3LYP/TZVP level of theory in parentheses.

the  $\pi^*$ -orbital in case of the aromatic picolate ligand. As a consequence, a smaller band gap is obtained for [Ir(a)<sub>2</sub>(pic)].

A comparison of the calculated and experimental absorption spectra for the complexes [Ir(a)<sub>2</sub>(bpy)]<sup>+</sup>, [Ir(a)<sub>2</sub>(acac)], and [Ir(a)<sub>2</sub>(pic)] is presented in Figure 5. In Table 3 the main electronic singlet–singlet vertical excitations, their oscillator strengths, and their corresponding assignments are summarized. The agreement between the calculated and experimental values is good, notwithstanding that TD-DFT tends to overestimate the charge-transfer (CT) states.<sup>51</sup>

On the other hand it is well established that hybrid functionals, such as B3LYP, are less affected by this problem.<sup>52</sup> The experimental spectra show weak absorption bands from 350 to 425 nm (up to 500 nm for the charged bpy complex) with extinction coefficients ( $\epsilon$ ) in the range 1000 to 5000 L·mol<sup>-1</sup>·cm<sup>-1</sup>. These bands can be assigned to singlet metal-to-ligand charge-transfer (MLCT) transitions from metal-centered d-orbitals to  $\pi^*$ -orbitals localized on either the ancillary or the cyclometalating ligand. The presence of ligand-centered (LC) transitions leads to strong absorption transitions (10 000 to 60 000 L·mol<sup>-1</sup>·cm<sup>-1</sup>) in the short-wavelength region below 300 nm. The involved molecular orbitals of these transitions are localized either on one ligand (ancillary or cyclometalating) or between different ones.

As shown in Figure 2, no absorption is found above 500 nm. The long tail between 360 and 500 nm, in particular for [Ir(a)<sub>2</sub>(pic)], where singlet–singlet excitations are dark or do not exist, should be then attributed to singlet–triplet excitations (see Table 4). Note that within the computational approach used herein, singlet–triplet excitation energies have no intensity because spin–orbit coupling is neglected in the TD-DFT calculations.

From Table 3 we can conclude that all compounds show common features in their UV–vis absorption spectra. The low-energy range up to 4.50 eV (273 nm) is characterized by MLCT transitions between an orbital of the  $t_{2g}$ -set and a  $\pi^*$ -antibonding orbital of either the cyclometalating or ancillary

(51) Dreuw, A.; Head-Gordon, M. *Chem. Rev.* **2005**, *105*, 4009–4037.

(52) Dreuw, A.; Weisman, J. L.; Head-Gordon, M. *J. Chem. Phys.* **2003**, *119*, 2943–2946.

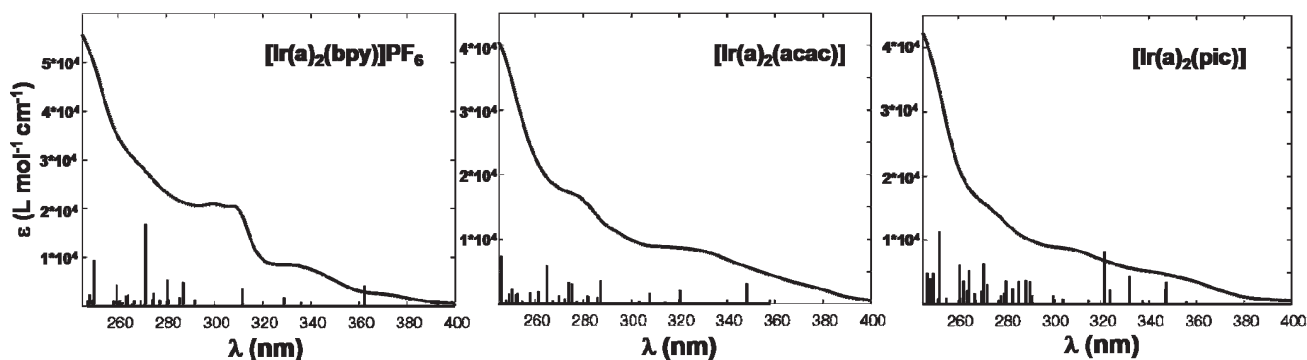


**Figure 5.** Experimental spectra of Ir<sup>III</sup> complexes with **a** as cyclometalating ligand (solid line) and TD-DFT (B3LYP/TZVP in CH<sub>2</sub>Cl<sub>2</sub>) vertical excitations. The oscillator strengths of the vertical excitations have been scaled to the experimental spectra.

ligand. Only for [Ir(**a**)<sub>2</sub>(bpy)]<sup>+</sup> is a LC transition, namely, a transition from a  $\pi$ -orbital localized on the cyclometalating ligand ( $\pi_{\text{cycl}}$ ) to a  $\pi^*$ -orbital localized on the ancillary ligand ( $\pi^*_{\text{anc}}$ ), found at low energies (see  $S_2$  in Table 3). In particular, for this compound a shoulder of the peak that dominates the UV–vis spectrum can be observed around 300 nm; this peak can be attributed presumably to  $S_{11}$  and  $S_{17}$ , but is underestimated in terms of oscillator strength. Beyond 4.50 eV, the shape of the spectra of [Ir(**a**)<sub>2</sub>(bpy)]<sup>+</sup> is dominated by both LC and MLCT transitions, but mainly by LC transitions in the case of [Ir(**a**)<sub>2</sub>(acac)] and [Ir(**a**)<sub>2</sub>(pic)]. Additionally, for [Ir(**a**)<sub>2</sub>(pic)] a metal-centered (MC) transition that corresponds to  $S_{38}$  is found.

In the following we turn our attention to the nature of the excited states involved in the emission process, for which both theoretical calculations and experimental photoluminescence measurements were carried out. The PL spectra of all discussed complexes have been depicted in Figure 3. One can clearly see the change of character of the lowest excited state from a <sup>3</sup>LC dominated one in the case of [Ir(ppy)<sub>2</sub>(trpy)](PF<sub>6</sub>)—identifiable through a blue-shifted, narrow, and structured band—to a more <sup>3</sup>MLCT dominated state for the 2,2′-bipyridine-substituted complex (i.e., red-shifted, broad, and unstructured band). In contrast, the [Ir(**a**)<sub>2</sub>(L<sup>^</sup>X)](PF<sub>6</sub>)<sub>n</sub>-type complexes (Figure 3, right) feature only emission bands without any structuring, suggesting a <sup>3</sup>MLCT character of the emission transitions. This assumption is supported by the obtained calculation results collected in Table 4. It might be caused by the higher HOMO–LUMO energy gaps that are present in the 4-phenyl-1*H*-[1,2,3]triazole moiety compared to the 2-phenylpyridine unit, which lead to a decreased possibility of interaction between the LC transitions and the lower energy MLCT states. Consequently this fact would cause a decreased contribution of LC states to the photoluminescence process in the case of the [1,2,3]triazole-type complexes. The related photoluminescence quantum yields differ significantly (Table 1). They range from nearly no emission in the case of [Ir(**a**)<sub>2</sub>(acac)] ( $\Phi_{\text{PL}} = 0.02$ ) to notable values, as for its bpy-match [Ir(**a**)<sub>2</sub>(bpy)](PF<sub>6</sub>) ( $\Phi_{\text{PL}} = 0.45$ ). Further investigations of the photoluminescence properties, such as PL lifetime measurements, are currently ongoing. In addition, the incorporation of the new bis-cyclometalated Ir<sup>III</sup> complexes into OLED devices in order to gain more insight into the electro-optical behavior of the emitters and to study the derived device characteristics represents future targets.

For excited Ir<sup>III</sup> complexes it is well known that the triplet excited states are populated rapidly via efficient intersystem

crossing (ISC) between the singlet and triplet photoexcited states (due to the strong spin–orbit coupling induced by the Ir<sup>III</sup> center). Afterward, internal conversion (IC) and vibrational relaxation (i.e., solvent deactivation) to the lowest triplet excited state ( $T_1$ ) follow. The theoretical emission energies cannot be directly derived from the calculation of the singlet–triplet excitation transitions. For a given couple of electronic states, the emission intensities are determined by the vibrational wave function overlaps (the Franck–Condon factors) between the lowest vibrational level of the excited state and various vibrational levels of the electronic ground state. Recently, simulations of emission spectra have been achieved for large organic molecules<sup>53</sup> and organometallic complexes.<sup>54</sup>

Here, we restrict ourselves to calculate the emission spectral maxima for [Ir(**a**)<sub>2</sub>(bpy)]<sup>+</sup>, [Ir(**a**)<sub>2</sub>(acac)], and [Ir(**a**)<sub>2</sub>(pic)]; see Table 4. A two-step approach is followed. As a first step, the five lowest lying singlet–triplet excitations were obtained at the TD-B3LYP/TZVP level of theory in the presence of solvent (CH<sub>2</sub>Cl<sub>2</sub>). Interestingly, in all cases the emissive state ( $T_1$ ) is of MLCT character. The following triplet excited states are also mainly of <sup>3</sup>MLCT character, with the exception of  $T_3$  in [Ir(**a**)<sub>2</sub>(bpy)]<sup>+</sup>, for which a <sup>3</sup>LC state is found. The comparison of the so-obtained excitation energies for  $T_1$  in [Ir(**a**)<sub>2</sub>(bpy)]<sup>+</sup> (505 nm), [Ir(**a**)<sub>2</sub>(acac)] (413 nm), and [Ir(**a**)<sub>2</sub>(pic)] (422 nm) with the experimental photoluminescence maxima (560, 435, and 527 nm, respectively, from Table 1) shows a hypsochromic shift for the theoretical values, in particular for the picolinate derivative. Since these complexes possess excited state lifetimes in the microsecond regime, allowing for relaxation to the lowest triplet excited state, and these TD-DFT excitations are vertical transitions from the electronic ground state  $S_0$ , blue-shifted peaks are inherent. Therefore, as a second step, triplet state optimizations have been carried out to yield adiabatic emission energies. The  $T_1$  minima of the three compounds are <sup>3</sup>MLCT states, with one electron of the HOMO ( $5d_{xy}$ ) promoted to a  $\pi^*$ -orbital. As stated in the computational details, the main geometrical differences with respect to  $S_0$  refer to the shortening of some of the Ir–C<sup>^</sup>N bond distances in the  $T_1$  minima, which has been already discussed for related iridium(III) complexes.<sup>55</sup> As

(53) Santoro, F.; Improta, R.; Lami, A.; Bloino, J.; Barone, V. *J. Chem. Phys.* **2007**, *126*, 084509/1–084509/13.

(54) De Angelis, F.; Santoro, F.; Nazeeruddin, M. K.; Barone, V. *J. Phys. Chem. B* **2008**, *112*, 13181–13183.

(55) De Angelis, F.; Fantacci, S.; Evans, N.; Klein, C.; Zakeeruddin, S. M.; Moser, J.-E.; Kalyanasundaram, K.; Bolink, H. J.; Grätzel, M.; Nazeeruddin, M. K. *Inorg. Chem.* **2007**, *46*, 5989–6001.

**Table 3. Main Theoretical Electronic Transitions Energies ( $\Delta E$ ), with Corresponding Oscillator Strengths ( $f$ ) and Assignment for Cyclometalated Complexes  $[\text{Ir}(\mathbf{a})_2(\text{L}^\wedge\text{X})]$** 

state	$\Delta E$ [eV (nm)]	$f$	assignment	state	$\Delta E$ [eV (nm)]	$f$	assignment
$[\text{Ir}(\mathbf{a})_2(\text{bpy})]^+$							
S <sub>1</sub>	2.48(500)	0.000	$d_{xy} \rightarrow \pi^*_{\text{anc}}$ (70%) MLCT	S <sub>23</sub>	4.51(275)	0.042	$\pi_{\text{cycl}} \rightarrow \pi^*_{\text{cycl}}$ (59%) LC
S <sub>2</sub>	3.16(393)	0.017	$\pi_{\text{cycl}} \rightarrow \pi^*_{\text{anc}}$ (70%) LC	S <sub>25</sub>	4.57(271)	0.262	$d_{xz} \rightarrow \pi^*_{\text{anc}}$ (49%) MLCT
S <sub>5</sub>	3.42(362)	0.066	$d_{xz} \rightarrow \pi^*_{\text{anc}}$ (64%) MLCT	S <sub>31</sub>	4.69(264)	0.036	$\pi_{\text{anc}} \rightarrow \pi^*_{\text{anc}}$ (33%) LC
S <sub>9</sub>	3.77(329)	0.027	$d_{xy} \rightarrow \pi^*_{\text{cycl}}$ (68%) MLCT	S <sub>32</sub>	4.71(263)	0.034	$d_{yz} \rightarrow \pi^*_{\text{cycl}}$ (53%) MLCT
S <sub>11</sub>	3.98(312)	0.057	$d_{xy} \rightarrow \pi^*_{\text{cycl}}$ (68%) MLCT	S <sub>35</sub>	4.78(259)	0.068	$\pi_{\text{cycl}} \rightarrow \pi^*_{\text{cycl}}$ (53%) LC
S <sub>17</sub>	4.32(287)	0.077	$d_{xy} \rightarrow \pi^*_{\text{anc}}$ (43%) MLCT	S <sub>41</sub>	4.96(250)	0.146	$d_{xz} \rightarrow \pi^*_{\text{cycl}}$ (40%) MLCT
S <sub>20</sub>	4.42(281)	0.083	$\pi_{\text{anc}} \rightarrow \pi^*_{\text{anc}}$ (37%) LC				$d_{xy} \rightarrow \pi^*_{\text{cycl}}$ (32%) MLCT
			$d_{xy} \rightarrow \pi^*_{\text{anc}}$ (41%) MLCT				$d_{xz} \rightarrow \pi^*_{\text{cycl}}$ (39%) MLCT
			$d_{xz} \rightarrow \pi^*_{\text{anc}}$ (34%) MLCT				
$[\text{Ir}(\mathbf{a})_2(\text{acac})]$							
S <sub>1</sub>	3.47(358)	0.011	$d_{xy} \rightarrow \pi^*_{\text{cycl}}$ (66%) MLCT	S <sub>24</sub>	4.68(265)	0.108	$\pi_{\text{anc}} \rightarrow \pi^*_{\text{cycl}}$ (62%) LC
S <sub>3</sub>	3.56(348)	0.058	$d_{xy} \rightarrow \pi^*_{\text{cycl}}$ (67%) MLCT	S <sub>25</sub>	4.74(261)	0.034	$\pi_{\text{anc}} \rightarrow \pi^*_{\text{anc}}$ (59%) LC
S <sub>6</sub>	3.87(320)	0.040	$d_{xz} \rightarrow \pi^*_{\text{cycl}}$ (61%) MLCT	S <sub>27</sub>	4.80(258)	0.032	$\sigma_{\text{Ir-C/O}} \rightarrow \pi^*_{\text{cycl}}$ (49%) LC
S <sub>11</sub>	4.31(288)	0.066	$d_{yz} \rightarrow \pi^*_{\text{cycl}}$ (65%) MLCT	S <sub>34</sub>	4.95(250)	0.041	$\sigma_{\text{Ir-C/O}} \rightarrow \pi^*_{\text{anc}}$ (37%) LC
S <sub>16</sub>	4.50(275)	0.057	$d_{yz} \rightarrow \pi^*_{\text{cycl}}$ (47%) MLCT	S <sub>39</sub>	5.04(246)	0.135	$\sigma_{\text{Ir-C/O}} \rightarrow \pi^*_{\text{cycl}}$ (33%) LC
S <sub>18</sub>	4.53(274)	0.061	$d_{xy} \rightarrow \pi^*_{\text{cycl}}$ (59%) MLCT	S <sub>43</sub>	5.13(242)	0.037	$\pi_{\text{cycl}} \rightarrow \pi^*_{\text{cycl}}$ (38%) LC
							$n_{\text{O}} \rightarrow \pi^*_{\text{cycl}}$ (30%) LC
							$n_{\text{O}} \rightarrow \pi^*_{\text{cycl}}$ (36%) LC
							$n_{\text{O}} \rightarrow \pi^*_{\text{cycl}}$ (37%) LC
$[\text{Ir}(\mathbf{a})_2(\text{pic})]$							
S <sub>1</sub>	2.97(417)	0.001	$d_{xy} \rightarrow \pi^*_{\text{anc}}$ (70%) MLCT	S <sub>30</sub>	4.73(262)	0.029	$\pi_{\text{cycl}} \rightarrow \pi^*_{\text{anc}}$ (48%) LC
S <sub>3</sub>	3.57(347)	0.027	$d_{xy} \rightarrow \pi^*_{\text{cycl}}$ (77%) MLCT	S <sub>32</sub>	4.76(261)	0.047	$d_{xz} \rightarrow \pi^*_{\text{cycl}}$ (32%) MLCT
S <sub>8</sub>	3.86(322)	0.063	$d_{xy} \rightarrow \pi^*_{\text{anc}}$ (44%) MLCT	S <sub>35</sub>	4.92(252)	0.088	$\pi_{\text{cycl}} \rightarrow \pi^*_{\text{anc}}$ (30%) LC
S <sub>14</sub>	4.27(290)	0.028	$d_{xz} \rightarrow \pi^*_{\text{anc}}$ (39%) MLCT	S <sub>37</sub>	4.97(250)	0.038	$\pi_{\text{cycl}} \rightarrow \pi^*_{\text{cycl}}$ (53%) LC
S <sub>15</sub>	4.30(288)	0.029	$d_{yz} \rightarrow \pi^*_{\text{cycl}}$ (38%) MLCT				
S <sub>15</sub>	4.30(288)	0.029	$d_{yz} \rightarrow \pi^*_{\text{cycl}}$ (30%) MLCT	S <sub>38</sub>	4.97(249)	0.031	$\pi_{\text{cycl}} \rightarrow \pi^*_{\text{cycl}}$ (42%) LC
S <sub>15</sub>	4.30(288)	0.029	$d_{xy} \rightarrow \pi^*_{\text{anc}}$ (44%) MLCT				
S <sub>23</sub>	4.58(271)	0.049	$d_{xy} \rightarrow \pi^*_{\text{cycl}}$ (40%) MLCT	S <sub>38</sub>	4.97(249)	0.031	$\pi_{\text{cycl}} \rightarrow \pi^*_{\text{cycl}}$ (36%) LC
S <sub>27</sub>	4.68(265)	0.041	$d_{xy} \rightarrow \pi^*_{\text{cycl}}$ (39%) MLCT	S <sub>44</sub>	5.14(241)	0.047	$d_{xy} \rightarrow d_{z^2}$ (26%) MC
							$\pi_{\text{cycl}} \rightarrow \pi^*_{\text{cycl}}$ (24%) LC
							$\pi_{\text{cycl}} \rightarrow \pi^*_{\text{cycl}}$ (38%) LC

**Table 4. Lowest Singlet–Triplet Theoretical Emission Energies by Means of TD-DFT and  $\Delta$ -DFT Approaches<sup>a</sup>**

	$[\text{Ir}(\mathbf{a})_2(\text{bpy})]^+$	$[\text{Ir}(\mathbf{a})_2(\text{acac})]$	$[\text{Ir}(\mathbf{a})_2(\text{pic})]$
TD-DFT Vertical Singlet–Triplet Excitations; $\Delta E$ [eV (nm)] and Assignment			
T <sub>1</sub>	2.46 (505) <sup>3</sup> MLCT	3.00 (413) <sup>3</sup> MLCT	2.94 (422) <sup>3</sup> MLCT
T <sub>2</sub>	2.96 (419) <sup>3</sup> MLCT/ <sup>3</sup> LC	3.11 (399) <sup>3</sup> MLCT	3.15 (394) <sup>3</sup> MLCT
T <sub>3</sub>	3.09 (401) <sup>3</sup> LC	3.15 (394) <sup>3</sup> MLCT	3.21 (386) <sup>3</sup> MLCT
T <sub>4</sub>	3.22 (384) <sup>3</sup> MLCT	3.30 (376) <sup>3</sup> MLCT	3.34 (371) <sup>3</sup> MLCT
T <sub>5</sub>	3.27 (379) <sup>3</sup> MLCT/ <sup>3</sup> LC	3.36 (369) <sup>3</sup> MLCT	3.36 (369) <sup>3</sup> MLCT
Theoretical $E_{e-e}$ ; $\Delta E$ [eV (nm)]			
	436	421	417
Theoretical AEE; $\Delta E$ [eV (nm)]			
	581	476	472

<sup>a</sup>The values are obtained in the presence of solvent.

shown in Table 4, the theoretical values of the adiabatic electronic emission (AEE; 581, 476, and 472 nm) obtained as the energy difference between T<sub>1</sub> and S<sub>0</sub> at the optimized T<sub>1</sub> geometry correlate much better to the experimental spectral PL maxima (560, 435, and 527 nm). Additional information is obtained through the  $E_{e-e}$  energies (i.e., the energy differences between T<sub>1</sub> and S<sub>0</sub> minima on each potential energy surface), which can be approximated to the  $E_{0-0}$  experimental values,

which can be estimated experimentally as the intersection point between the emission and absorption spectra. The theoretical values of 436, 421, and 417 nm, obtained for  $[\text{Ir}(\mathbf{a})_2(\text{bpy})]^+$ ,  $[\text{Ir}(\mathbf{a})_2(\text{acac})]$ , and  $[\text{Ir}(\mathbf{a})_2(\text{pic})]$ , respectively, agree well with the experimental ones (474, 400, and 440 nm, compare Table 1).

## Conclusion

A series of heteroleptic iridium(III) complexes coordinating new cyclometalating ligands, prepared via “click” chemistry approaches, were synthesized and characterized. The electro-optical properties were discussed in comparison to their corresponding literature-known 2-phenylpyridine-based counterparts. The experimental data were supported by extensive DFT calculations. The spectroscopic results as well as the theoretical studies reveal an increased possibility of color-tuning through changing the ancillary ligand for the new cyclometalated systems associated with the expected blue-shift of the spectral characteristics. Cyclic voltammetry investigations supported by theoretical calculations indicated the destabilization of the LUMOs to be the main reason for this hypsochromicity.

## Experimental Section

**Materials and General Experimental Details.** The solvents were purchased from Biosolve. All chemicals were of reagent grade, obtained from commercial suppliers, and used as received

unless specified otherwise. The ancillary ligand 2-(1-decyl-1*H*-[1,2,3]-triazol-4-yl)pyridine (trpy) was synthesized according to the literature.<sup>27</sup> Modified literature procedures were used for the synthesis of the heteroleptic complexes [Ir(ppy)<sub>2</sub>(acac)],<sup>15</sup> [Ir(ppy)<sub>2</sub>(pic)],<sup>16</sup> and [Ir(ppy)<sub>2</sub>(bpy)].<sup>56,57</sup> Column chromatography was carried out on standardized aluminum oxide 90 (0.063–0.200 mm) or silica gel 60 (0.040–0.063 mm) purchased from Merck. Column chromatographic separations were monitored using Merck 60 F254 precoated silica gel and aluminum oxide sheets and visualized under UV light at  $\lambda_{\text{exc}} = 254$  and 365 nm, respectively.

**Instrumentation.** For the microwave experiments a single mode Initiator 8 microwave from Biotage was used. The electromagnetic field had a frequency of 2.45 GHz. For all experiments a fixed temperature was applied, the prestirring time constituted 10 s, and the stirrer rate was set to 600 rpm. 1D (<sup>1</sup>H and <sup>13</sup>C) and 2D (<sup>1</sup>H–<sup>1</sup>H gCOSY) nuclear magnetic resonance spectra were recorded on a Varian Mercury 400 MHz instrument at 298 K in deuterated solvents. Chemical shifts are reported in parts per million ( $\delta$  in ppm) referenced to TMS; coupling constants are given in hertz (Hz). UV–vis absorption spectra were recorded at sample concentrations of  $10^{-5}$  to  $10^{-6}$  mol·L<sup>-1</sup> on a Perkin-Elmer Lambda 45 UV/vis spectrometer (1 cm cuvettes). Emission spectra and absolute quantum yields were measured on a Perkin-Elmer LS50B luminescence spectrometer and a module system of the C9920 series from Hamamatsu Photonics, respectively. Samples with a concentration of about  $10^{-6}$  to  $10^{-7}$  mol·L<sup>-1</sup> were investigated. The absorption maxima at the longest wavelengths were chosen for excitation. Cyclic voltammetry (CV) measurements were conducted with an Autolab PGSTAT30 model potentiostat with a standard three-electrode configuration, using a platinum-disk working electrode, a platinum-rod auxiliary electrode, and a Ag/AgCl reference electrode. The experiments were carried out in CH<sub>2</sub>Cl<sub>2</sub> containing tetrabutylammonium hexafluorophosphate salt (0.1 mol·L<sup>-1</sup>) using a scan rate of 100 mV·s<sup>-1</sup>. Ferrocene was used as internal standard for the determination of the potentials vs SHE and the corresponding HOMO/LUMO levels. Matrix-assisted laser desorption-ionization time-of-flight (MALDI-TOF) mass spectrometry was performed on a Voyager-DE PRO Biospectrometry Workstation (Applied Biosystems) time-of-flight mass spectrometer, using dithranol as matrix. Electrospray ionization (ESI) mass spectrometry was conducted on a Finnigan MAT 95XL. Elemental analyses were carried out on a EuroVector EuroEA3000 elemental analyzer for CHNS-O.

**Safety Comment.** Sodium azide is a very toxic salt, personal protection precautions had to be taken. As, in particular, low-molar-mass organic azides are potentially explosive, attention had to be taken during their handling. Generally, when the total number of carbon ( $N_C$ ) plus oxygen ( $N_O$ ) atoms is less than the total numbers of nitrogen atoms ( $N_N$ ) by a ratio of 3, the compound is considered to be an explosive hazard. Therefore, the compounds were directly prepared prior to use if possible.

**1-Decyl-4-phenyl-1*H*-[1,2,3]triazole (H-a).** 1-Bromodecane (662 mg, 2.99 mmol) and sodium azide (295 mg, 4.54 mmol, 1.5 equiv) were reacted in ethanol/water (7:3 ratio, 15 mL) at 125 °C under microwave irradiation for 1 h. Afterward, CuI (56.6 mg, 10 mol%) and sodium L-ascorbate (30.4 mg, 5 mol%) as catalyst system as well as phenylacetylene (496 mg, 4.50 mmol, 1.5 equiv) were added, and the reaction mixture was stirred at room temperature for 18 h. The mixture was poured into water (200 mL), and the precipitate was filtered off. The precipitate was dissolved in CH<sub>2</sub>Cl<sub>2</sub> (150 mL) and filtered. After washing with water (3 × 80 mL) and drying over MgSO<sub>4</sub>,

the solution was concentrated under reduced pressure and dropped into *n*-pentane. **H-a** was isolated as colorless needles after storing the solution for 3 days in the freezer (652 mg, 76%). <sup>1</sup>H NMR (CD<sub>2</sub>Cl<sub>2</sub>, 400 MHz):  $\delta$  7.84 (d, <sup>3</sup> $J_{H,H} = 7.2$  Hz, 2H, *H*<sup>2</sup>), 7.80 (s, 1H, triazole-*H*), 7.44 (m<sub>c</sub>, 2H, *H*<sup>3</sup>), 7.34 (t, <sup>3</sup> $J_{H,H} = 7.4$  Hz, 1H, *H*<sup>4</sup>), 4.39 (t, <sup>3</sup> $J_{H,H} = 7.2$  Hz, 2H, N-CH<sub>2</sub>), 1.95 (m<sub>c</sub>, 2H, N-CH<sub>2</sub>-CH<sub>2</sub>), 1.37–1.29 (m, 14H, (CH<sub>2</sub>)<sub>7</sub>), 0.89 (t, <sup>3</sup> $J_{H,H} = 7.0$  Hz, 3H, CH<sub>3</sub>) ppm. <sup>13</sup>C NMR (CD<sub>2</sub>Cl<sub>2</sub>, 100 MHz):  $\delta$  147.3, 131.0, 128.8, 127.9, 125.5, 119.6, 50.4, 31.9, 30.3, 29.5, 29.4, 29.3, 29.0, 26.5, 22.7, 13.9 ppm. MALDI-TOF MS (dithranol):  $m/z = 286.22$  ([M + H]<sup>+</sup>). Anal. Calcd (%) for C<sub>18</sub>H<sub>27</sub>N<sub>3</sub> (285.43): C, 75.74; H, 9.83; N, 14.54. Found: C, 75.69; H, 9.83; N, 14.54. UV/vis (CH<sub>2</sub>Cl<sub>2</sub>):  $\lambda_{\text{abs}}$  ( $\epsilon/L \cdot \text{mol}^{-1} \cdot \text{cm}^{-1}$ ) = 252 (20 100) nm.

**4-Decyl-1-phenyl-1*H*-[1,2,3]triazole (H-b).** Bromobenzene (631 mg, 4.02 mmol), *N,N'*-dimethylethylenediamine (51.7 mg, 15 mol%), CuI (76.3 mg, 10 mol%), and sodium L-ascorbate (41.4 mg, 5 mol%) were suspended in an ethanol/water mixture (20 mL, 7:3 ratio). The flask was flushed with argon, and NaN<sub>3</sub> (521 mg, 8.01 mmol, 2.0 equiv) was added, a color change to blue could be observed. The reaction mixture was heated to reflux for 3 h. After cooling to room temperature, 1-dodecyne (781 mg, 4.70 mmol, 1.17 equiv) was dropped into the now slightly yellow mixture. The reaction mixture was stirred for 14 h, and the solid was subsequently filtered off, washed with water (3 × 100 mL), and dried. The crude product was dissolved in dichloromethane (200 mL), and the solution was filtered. The organic solution was washed with water (3 × 80 mL) and dried over MgSO<sub>4</sub>. After gel filtration (silica, CH<sub>2</sub>Cl<sub>2</sub> as eluent), the concentrated CH<sub>2</sub>Cl<sub>2</sub> phase was dropped into *n*-pentane to precipitate **H-b** as white solid (769 mg, 67%). <sup>1</sup>H NMR (CD<sub>2</sub>Cl<sub>2</sub>, 400 MHz):  $\delta$  7.81 (s, 1H, triazole-*H*), 7.75 (d, <sup>3</sup> $J_{H,H} = 7.6$  Hz, 2H, *H*<sup>2</sup>), 7.54 (m<sub>c</sub>, 2H, *H*<sup>3</sup>), 7.44 (m<sub>c</sub>, 1H, *H*<sup>4</sup>), 2.78 (t, <sup>3</sup> $J_{H,H} = 7.8$  Hz, 2H, N-CH<sub>2</sub>), 1.74 (m<sub>c</sub>, 2H, N-CH<sub>2</sub>-CH<sub>2</sub>), 1.46–1.23 (m, 14H, (CH<sub>2</sub>)<sub>7</sub>), 0.90 (t, <sup>3</sup> $J_{H,H} = 7.2$  Hz, 3H, CH<sub>3</sub>) ppm. <sup>13</sup>C NMR (CD<sub>2</sub>Cl<sub>2</sub>, 100 MHz):  $\delta$  149.1, 137.4, 129.6, 128.2, 120.2, 118.8, 31.9, 29.6, 29.4, 29.3, 25.6, 22.7, 13.9 ppm. MALDI-TOF MS (dithranol):  $m/z = 286.23$  ([M + H]<sup>+</sup>). Anal. Calcd (%) for C<sub>18</sub>H<sub>27</sub>N<sub>3</sub> (285.43): C, 75.74; H, 9.83; N, 14.54. Found: C, 75.89; H, 9.64; N, 14.71. UV/vis (CH<sub>2</sub>Cl<sub>2</sub>):  $\lambda_{\text{abs}}$  ( $\epsilon/L \cdot \text{mol}^{-1} \cdot \text{cm}^{-1}$ ) = 252 (9300) nm.

**Tetrakis(1-decyl-4-phenyl-1*H*-[1,2,3]triazolato-*C*<sup>2</sup>,*N*<sup>3</sup>)-(μ-dichloro)diiridium(III) (A).** 1-Decyl-4-phenyl-1*H*-[1,2,3]triazole (**H-a**, 158 mg, 0.56 mmol, 2.0 equiv) and IrCl<sub>3</sub> × 3H<sub>2</sub>O (98 mg, 0.28 mmol) were reacted for 14 h in degassed 2-ethoxyethanol/water (12 mL, 3:1 ratio) under reflux excluding light. After cooling to room temperature, water was added and the yellow suspension was extracted with CH<sub>2</sub>Cl<sub>2</sub> (150 mL). The organic phase was washed with water (3 × 50 mL) and dried over MgSO<sub>4</sub>. The concentrated CH<sub>2</sub>Cl<sub>2</sub> phase was dropped into *n*-pentane. This procedure was repeated twice to remove unreacted ligand. After gel filtration (Al<sub>2</sub>O<sub>3</sub>, CH<sub>3</sub>CN → CH<sub>3</sub>CN/H<sub>2</sub>O (8:2 ratio) saturated with KNO<sub>3</sub>) the precursor complex **A** was obtained as a bright yellow powder (169 mg, 76%). ESI-MS (CH<sub>2</sub>Cl<sub>2</sub>/CH<sub>3</sub>OH):  $m/z = 1557.5$  ([M - Cl]<sup>+</sup>). Anal. Calcd (%) for C<sub>72</sub>H<sub>104</sub>Cl<sub>2</sub>Ir<sub>2</sub>N<sub>12</sub> (1593.02): C, 54.29; H, 6.58; N, 10.55. Found: C, 54.27; H, 6.65; N, 10.78.

**Tetrakis(4-decyl-1-phenyl-1*H*-[1,2,3]triazolato-*C*<sup>2</sup>,*N*<sup>3</sup>)-(μ-dichloro)diiridium(III) (B).** IrCl<sub>3</sub> × 3H<sub>2</sub>O (314 mg, 0.89 mmol) and 4-decyl-1-phenyl-1*H*-[1,2,3]triazole (**H-b**, 515 mg, 1.81 mmol, 2.0 equiv) were reacted in 52 mL of solvent as described above. After purification, **B** was obtained as a slightly orange powder (375.5 mg, 53%). MALDI-TOF MS (dithranol):  $m/z = 1557.7$  ([M - Cl]<sup>+</sup>). Anal. Calcd (%) for C<sub>72</sub>H<sub>104</sub>Cl<sub>2</sub>Ir<sub>2</sub>N<sub>12</sub> (1593.02): C, 54.29; H, 6.58; N, 10.55. Found: C, 54.18; H, 6.91; N, 10.50.

**General Procedure for the Synthesis of Charged Ir<sup>III</sup> Complexes.** A mixture of dichloromethane and methanol (9 mL per 0.05 mmol of precursor, 4:5 ratio) was refluxed for 1 h under argon atmosphere. The precursor complex (1.0 equiv) and

(56) Neve, F.; Crispini, A.; Campagna, S.; Serroni, S. *Inorg. Chem.* **1999**, *38*, 2250–2258.

(57) Marin, V.; Holder, E.; Schubert, U. S. *J. Polym. Sci., Part A: Polym. Chem.* **2004**, *42*, 374–385.

2,2'-bipyridine (bpy, 6.0 equiv) or 2-(1-decyl-1*H*-[1,2,3]-triazol-4-yl)pyridine (trpy, 6.0 equiv), respectively, were added. The reaction mixture was stirred for 14 h under reflux excluding light. After cooling to room temperature  $\text{NH}_4\text{PF}_6$  (5–9 equiv) was added, and the mixture was stirred for 1 h. The solvents were removed under reduced pressure, and the residue was dissolved in  $\text{CH}_2\text{Cl}_2$  (15 mL). The solution was washed with water ( $3 \times 8$  mL) and dried over  $\text{MgSO}_4$ . The concentrated  $\text{CH}_2\text{Cl}_2$  solution was added dropwise to diethyl ether, and the precipitating solid was filtered off using a glass filter frit and washed with diethyl ether. This precipitation procedure was repeated two times to obtain the charged  $\text{Ir}^{\text{III}}$  complex. When required, further purification was achieved by column chromatography ( $\text{Al}_2\text{O}_3$ ,  $\text{CH}_2\text{Cl}_2 \rightarrow \text{CH}_2\text{Cl}_2/\text{CH}_3\text{OH}$  (95:5 ratio)).

**Bis(1-decyl-4-phenyl-1*H*-[1,2,3]-triazolato- $N^3, C^2$ )(2,2'-bipyridine)iridium(III) hexafluorophosphate,  $[\text{Ir}(\text{a})_2(\text{bpy})](\text{PF}_6)$ .** Precursor complex A (29 mg, 0.02 mmol) and 2,2'-bipyridine (18.0 mg, 0.12 mmol, 6.0 equiv) were reacted according to the general protocol to yield  $[\text{Ir}(\text{a})_2(\text{bpy})](\text{PF}_6)$  as a yellow powder (37 mg, 90%).  $^1\text{H}$  NMR ( $\text{CD}_2\text{Cl}_2$ , 400 MHz):  $\delta$  8.36 (d,  $^3J_{\text{H,H}} = 7.6$  Hz, 2H, bpy- $H^6$ ), 8.20 (d,  $^3J_{\text{H,H}} = 5.2$  Hz, 2H, bpy- $H^3$ ), 8.06 (m<sub>c</sub>, 2H, bpy- $H^5$ ), 7.81 (s, 2H, triazole- $H$ ), 7.49 (d,  $^3J_{\text{H,H}} = 7.6$  Hz, 2H,  $H^6$  (a)), 7.40 (m<sub>c</sub>, 2H, bpy- $H^4$ ), 7.03 (m<sub>c</sub>, 2H,  $H^2$  (a)), 6.89 (m<sub>c</sub>, 2H,  $H^4$  (a)), 6.26 (d,  $^3J_{\text{H,H}} = 7.6$  Hz, 2H,  $H^3$  (a)), 4.26 (m<sub>c</sub>, 4H, N- $\text{CH}_2$ ), 1.85 (m<sub>c</sub>, 4H, N- $\text{CH}_2$ - $\text{CH}_2$ ), 1.52–1.18 (m, 28H,  $(\text{CH}_2)_7$ ), 0.89 (t,  $^3J_{\text{H,H}} = 6.2$  Hz, 6H,  $\text{CH}_3$ ) ppm.  $^{13}\text{C}$  NMR ( $\text{CD}_2\text{Cl}_2$ , 100 MHz):  $\delta$  157.1, 156.6, 151.6, 145.9, 138.5, 135.5, 132.4, 128.5, 127.0, 123.2, 122.7, 122.3, 118.3, 52.1, 31.8, 29.7, 29.4, 29.2, 28.8, 26.2, 22.6, 13.8 ppm. MALDI-TOF MS (dithranol):  $m/z = 917.46$  ( $[\text{M} - \text{PF}_6]^+$ ). Anal. Calcd (%) for  $\text{C}_{46}\text{H}_{60}\text{F}_6\text{IrN}_8\text{P}$  (1062.2): C, 52.01; H, 5.69; N, 10.55. Found: C, 52.25; H, 5.65; N, 10.62. UV/vis ( $\text{CH}_2\text{Cl}_2$ ):  $\lambda_{\text{abs}}$  ( $\epsilon/\text{L} \cdot \text{mol}^{-1} \cdot \text{cm}^{-1}$ ) = 441 (760), 330 (8600), 299 (21000), 240 (61200) nm. Emission ( $\text{CH}_2\text{Cl}_2$ ,  $\lambda_{\text{exc}} = 470$  nm):  $\lambda_{\text{max}} = 550$  nm. Quantum yield ( $\text{CH}_2\text{Cl}_2$ ,  $\lambda_{\text{exc}} = 470$  nm):  $\Phi_{\text{PL}} = 0.45$ .

**Bis(1-decyl-4-phenyl-1*H*-[1,2,3]-triazolato- $N^3, C^2$ )(2-(1-decyl-1*H*-[1,2,3]-triazol-4-yl)pyridine- $N^3, N$ )iridium(III) Hexafluorophosphate,  $[\text{Ir}(\text{a})_2(\text{trpy})](\text{PF}_6)$ .** Precursor complex A (20 mg, 0.01 mmol) and 2-(1-decyl-1*H*-[1,2,3]-triazol-4-yl)pyridine (trpy, 20 mg, 0.07 mmol, 7.0 equiv) were reacted according to the general protocol to yield  $[\text{Ir}(\text{a})_2(\text{trpy})](\text{PF}_6)$  as a slightly yellow powder after precipitation into *n*-pentane (17 mg, 50%).  $^1\text{H}$  NMR ( $\text{CD}_2\text{Cl}_2$ , 400 MHz):  $\delta$  8.60 (s, 1H, triazole- $H$  (trpy)), 8.10 (m<sub>c</sub>, 1H,  $H^6$  (trpy)), 8.02–8.00 (m, 1H,  $H^3$  (trpy)), 7.96 (m<sub>c</sub>, 1H,  $H^5$  (trpy)), 7.78 (2  $\times$  s, 2H, triazole- $H$  (a)), 7.45 (m<sub>c</sub>, 2H,  $H^6$  (a)), 7.23 (m<sub>c</sub>, 1H,  $H^4$  (trpy)), 7.04–6.95 (m, 2H,  $H^3$  (a)), 6.85 (m<sub>c</sub>, 2H,  $H^4$  (a)), 6.27–6.22 (m, 2H,  $H^2$  (a)), 4.51 (m, 2H, N- $\text{CH}_2$  (trpy)), 4.36–4.23 (m, 4H, N- $\text{CH}_2$  (a)), 1.99–1.87 (m, 6H, N- $\text{CH}_2$ - $\text{CH}_2$ ), 1.48–1.23 (m, 42H,  $(\text{CH}_2)_7$ ), 0.90 (m<sub>c</sub>, 9H,  $\text{CH}_3$ ) ppm. MALDI-TOF MS (dithranol):  $m/z = 1047.89$  ( $[\text{M} - \text{PF}_6]^+$ ). Anal. Calcd (%) for  $\text{C}_{53}\text{H}_{78}\text{F}_6\text{IrN}_{10}\text{P}$  (1192.43): C, 53.38; H, 6.59; N, 11.75. Found: C, 53.54; H, 6.88; N, 11.90. UV/vis ( $\text{CH}_2\text{Cl}_2$ ):  $\lambda_{\text{abs}}$  ( $\epsilon/\text{L} \cdot \text{mol}^{-1} \cdot \text{cm}^{-1}$ ) = 378 (830), 329 (7400), 240 (55300) nm. Emission ( $\text{CH}_2\text{Cl}_2$ ,  $\lambda_{\text{exc}} = 378$  nm):  $\lambda_{\text{max}} = 495$  nm. Quantum yield ( $\text{CH}_2\text{Cl}_2$ ,  $\lambda_{\text{exc}} = 378$  nm):  $\Phi_{\text{PL}} = 0.29$ .

**Bis(2-phenylpyridinato- $N, C^2$ )(2-(1-decyl-1*H*-[1,2,3]-triazole-4-yl)pyridine- $N^3, N$ ) iridium(III) hexafluorophosphate,  $[\text{Ir}(\text{ppy})_2(\text{trpy})](\text{PF}_6)$ .** Precursor complex C (56 mg, 0.05 mmol) and trpy (30 mg, 0.105 mmol, 2.1 equiv) were reacted according to the general protocol to yield  $[\text{Ir}(\text{ppy})_2(\text{trpy})](\text{PF}_6)$  as a yellow powder after additional washing with *n*-pentane (85 mg, 90%).  $^1\text{H}$  NMR ( $\text{CD}_2\text{Cl}_2$ , 400 MHz):  $\delta$  8.76 (s, 1 H, triazole- $H$ ), 8.23 (d,  $^3J_{\text{H,H}} = 7.9$  Hz, 1H, trpy- $H^3$ ), 8.04 (m, trpy- $H^4$ ), 7.96 (d,  $^3J_{\text{H,H}} = 8.2$  Hz, 2H, py- $H^3$ ), 7.85 (m<sub>c</sub>, 1H, trpy- $H^6$ ), 7.77–7.83 (m, 2H, py- $H^4$ ), 7.74 (m<sub>c</sub>, 1H, ph- $H^3$ ), 7.70 (m<sub>c</sub>, 2H, py- $H^6$ , ph- $H^3$ ), 7.52 (d,  $^3J_{\text{H,H}} = 5.1$  Hz, 1H, py- $H^5$ ), 7.31 (m<sub>c</sub>, 1H, trpy- $H^5$ ), 7.00–7.10 (m, 4H, 2  $\times$  py- $H^5$  and ph- $H^4$ ), 6.94 (m<sub>c</sub>, 1 H, ph- $H^5$ ), 6.88 (m<sub>c</sub>, 1 H, ph- $H^5$ ), 6.32 (m<sub>c</sub>, 2H, ph- $H^6$ ), 4.46 (t,  $^3J_{\text{H,H}} = 6.8$  Hz, 2H, N- $\text{CH}_2$ ), 1.93 (m<sub>c</sub>, 2H, N- $\text{CH}_2$ - $\text{CH}_2$ ), 1.16–1.37

(m, 14H,  $(\text{CH}_2)_7$ ), 0.89 (t,  $^3J_{\text{H,H}} = 6.8$  Hz, 3H,  $\text{CH}_3$ ).  $^{13}\text{C}$  NMR ( $\text{CD}_2\text{Cl}_2$ , 100 MHz):  $\delta$  168.0, 167.4, 150.3, 149.5, 149.3, 148.5, 148.5, 144.0, 139.6, 138.1, 138.0, 131.9, 131.6, 130.5, 129.8, 126.4, 125.7, 124.8, 124.3, 123.3, 123.0, 122.7, 122.2, 119.6, 119.5, 52.5, 31.8, 29.8, 29.4, 29.4, 29.2, 28.8, 26.2, 22.6, 13.9 ppm. Anal. Calcd (%) for  $\text{C}_{39}\text{H}_{42}\text{F}_6\text{IrN}_6\text{P}$  (931.97): C, 50.26; H, 4.54; N, 9.02. Found: C, 50.26; H, 4.48; N, 8.88. UV/vis ( $\text{CH}_2\text{Cl}_2$ ):  $\lambda_{\text{abs}}$  ( $\epsilon/\text{L} \cdot \text{mol}^{-1} \cdot \text{cm}^{-1}$ ) = 412 (4400), 384 (5850), 254 (50500). Emission ( $\text{CH}_2\text{Cl}_2$ ,  $\lambda_{\text{exc}} = 408$  nm):  $\lambda_{\text{max}} = 477$  nm. Quantum yield ( $\text{CH}_2\text{Cl}_2$ ,  $\lambda_{\text{exc}} = 408$  nm):  $\Phi_{\text{PL}} = 0.21$ .

**Bis(1-decyl-4-phenyl-1*H*-[1,2,3]-triazolato- $N^3, C^2$ )acetylacetonatoiridium(III),  $[\text{Ir}(\text{a})_2(\text{acac})]$ .** The precursor complex A (60 mg, 0.04 mmol) was dissolved in degassed ethanol (10 mL), and acetylacetonone (Hacac, 40 mg, 0.4 mmol, 10.0 equiv) and sodium carbonate (42.4 mg, 0.4 mmol, 10.0 equiv) were added. The reaction mixture was stirred for 14 h under reflux and exclusion of light. The crude product was purified by column chromatography ( $\text{Al}_2\text{O}_3$ ,  $\text{CH}_2\text{Cl}_2$ ) to yield  $[\text{Ir}(\text{a})_2(\text{acac})]$  as slightly yellow powder (61 mg, 88%).  $^1\text{H}$  NMR ( $\text{CD}_2\text{Cl}_2$ , 400 MHz):  $\delta$  7.76 (s, 2H, triazole- $H$ ), 7.33 (d,  $^3J_{\text{H,H}} = 7.4$  Hz, 2H,  $H^3$ ), 6.81 (m<sub>c</sub>, 2H,  $H^4$ ), 6.65 (m<sub>c</sub>, 2H,  $H^5$ ), 6.17 (d,  $^3J_{\text{H,H}} = 7.6$  Hz, 2H,  $H^6$ ), 5.21 (s, 1H, acac- $\text{CH}$ ), 4.56–4.44 (m, 4H, N- $\text{CH}_2$ ), 2.06–2.00 (m, 4H, N- $\text{CH}_2$ - $\text{CH}_2$ ), 1.78 (s, 6H, acac- $\text{CH}_3$ ), 1.41–1.32 (m, 28H,  $(\text{CH}_2)_7$ ), 0.91 (t,  $^3J_{\text{H,H}} = 6.8$  Hz, 6H,  $\text{CH}_3$ ) ppm.  $^{13}\text{C}$  NMR ( $\text{CD}_2\text{Cl}_2$ , 100 MHz):  $\delta$  184.8, 157.3, 142.1, 137.0, 134.0, 126.7, 121.1, 120.9, 117.4, 99.8, 52.1, 31.9, 30.1, 29.5, 29.5, 29.3, 29.0, 27.8, 26.3, 22.7, 13.9 ppm. Anal. Calcd (%) for  $\text{C}_{41}\text{H}_{59}\text{F}_6\text{IrN}_6\text{O}_2\text{P}$  (860.16): C, 57.25; H, 6.91; N, 9.77. Found: C, 57.60; H, 7.12; N, 9.38. MALDI-TOF MS (dithranol):  $m/z = 860.65$  ( $[\text{M}]^+$ ), 761.62 ( $[\text{M} - \text{acac}]^+$ ). UV/vis ( $\text{CH}_2\text{Cl}_2$ ):  $\lambda_{\text{abs}}$  ( $\epsilon/\text{L} \cdot \text{mol}^{-1} \cdot \text{cm}^{-1}$ ) = 312 (9000), 276 (17000), 241 (41900) nm. Emission ( $\text{CH}_2\text{Cl}_2$ ,  $\lambda_{\text{exc}} = 318$  nm):  $\lambda_{\text{max}} = 435$  nm. Quantum yield ( $\text{CH}_2\text{Cl}_2$ ,  $\lambda_{\text{exc}} = 318$  nm):  $\Phi_{\text{PL}} = 0.02$ .

**Bis(4-decyl-1-phenyl-1*H*-[1,2,3]-triazolato- $N^3, C^2$ )acetylacetonatoiridium(III),  $[\text{Ir}(\text{b})_2(\text{acac})]$ .** The precursor complex B (59 mg, 0.04 mmol) was dissolved in ethanol (12 mL) and degassed for 1 h under argon. Afterwards, Hacac (100 mg, 1.0 mmol, 25 equiv) and  $\text{Na}_2\text{CO}_3$  (42 mg, 0.4 mmol, 10 equiv) were added. The reaction mixture was refluxed for 2 days. After cooling to room temperature the solvent was evaporated. The solid was dissolved in  $\text{CH}_2\text{Cl}_2$  (40 mL), washed with water ( $3 \times 20$  mL), and dried over  $\text{MgSO}_4$ . The concentrated solution was dropped into *n*-pentane for precipitation. The crude product was purified further via column chromatography ( $\text{Al}_2\text{O}_3$ ,  $\text{CH}_2\text{Cl}_2$ ) to yield  $[\text{Ir}(\text{b})_2(\text{acac})]$  as a light yellow powder (3 mg, 5%).  $^1\text{H}$  NMR ( $\text{CD}_2\text{Cl}_2$ , 400 MHz):  $\delta$  8.03 (s, 2H, triazole- $H$ ), 7.28 (d,  $^3J_{\text{H,H}} = 8.0$  Hz, 2H,  $H^6$ ), 6.96 (m<sub>c</sub>, 2H,  $H^5$ ), 6.76 (m<sub>c</sub>, 2H,  $H^4$ ), 6.74 (d,  $^3J_{\text{H,H}} = 7.4$  Hz, 2H,  $H^3$ ), 5.31 (s, 1H, acac- $\text{CH}$ ), 2.91 (t,  $^3J_{\text{H,H}} = 7.4$  Hz, 4H, N- $\text{CH}_2$ ), 1.99 (m<sub>c</sub>, 4H, N- $\text{CH}_2$ - $\text{CH}_2$ ), 1.83 (s, 6H, acac- $\text{CH}_3$ ), 1.32–1.28 (m, 28H,  $(\text{CH}_2)_7$ ), 0.90 (t,  $^3J_{\text{H,H}} = 7.0$  Hz, 6H,  $\text{CH}_3$ ) ppm. MALDI-TOF MS (dithranol):  $m/z = 861.69$  ( $[\text{M} + \text{H}]^+$ ), 761.63 ( $[\text{M} - \text{acac}]^+$ ).

**Bis(1-decyl-4-phenyl-1*H*-[1,2,3]-triazolato- $N^3, C^2$ )(picolinato- $N, O$ )iridium(III),  $[\text{Ir}(\text{a})_2(\text{pic})]$ .** A solution of precursor complex A (24 mg, 0.015 mmol) in  $\text{CH}_2\text{Cl}_2$  (10 mL) was degassed for 1 h. Afterwards, picolinic acid (Hpic, 10 mg, 0.08 mmol, 5.3 equiv) and sodium carbonate (8 mg, 0.08 mmol, 5.3 equiv) were added, and the mixture was refluxed for 14 h. After cooling to room temperature, the organic phase was washed with water ( $3 \times 5$  mL) and dried over  $\text{MgSO}_4$ . After column chromatography ( $\text{Al}_2\text{O}_3$ ,  $\text{CH}_2\text{Cl}_2/\text{CH}_3\text{OH}$  (98:2 ratio) as eluent),  $[\text{Ir}(\text{a})_2(\text{pic})]$  was yielded as a yellow powder (13 mg, 47%).  $^1\text{H}$  NMR ( $\text{CD}_2\text{Cl}_2$ , 400 MHz):  $\delta$  8.17 (d,  $^3J_{\text{H,H}} = 7.6$  Hz, 1H, pic- $H$ ), 7.88–7.82 (m, 2H, pic- $H$ ), 7.78, 7.77 (2  $\times$  s, 2H, triazole- $H$ ), 7.40 (m<sub>c</sub>, 2H,  $H^6$ ), 7.26 (m<sub>c</sub>, 1H, pic- $H$ ), 6.88 (m<sub>c</sub>, 2H,  $H^5$ ), 6.74 (m<sub>c</sub>, 2H,  $H^4$ ), 6.28, 6.20 (2  $\times$  d,  $^3J_{\text{H,H}} = 8.8$  Hz,  $^3J_{\text{H,H}} = 9.2$  Hz, 2H,  $H^3$ ), 4.45, 4.26 (2  $\times$  m<sub>c</sub>, 4H, N- $\text{CH}_2$ ), 1.98, 1.89 (2  $\times$  m<sub>c</sub>, 4H, N- $\text{CH}_2$ - $\text{CH}_2$ ), 1.33–1.28 (m, 28H,  $(\text{CH}_2)_7$ ), 0.90 (t,  $^3J_{\text{H,H}} = 6.8$  Hz, 6H,  $\text{CH}_3$ ) ppm.  $^{13}\text{C}$  NMR ( $\text{CD}_2\text{Cl}_2$ , 100 MHz):  $\delta$  172.8, 157.6, 156.8,

153.1, 149.0, 145.1, 142.6, 137.0, 136.4, 136.1, 133.4, 133.1, 127.6, 127.3, 126.9, 126.6, 121.7, 121.5, 121.1, 117.7, 117.5, 52.3, 51.8, 31.8, 30.0, 29.9, 29.4, 29.2, 29.2, 29.0, 28.9, 26.3, 22.7, 13.8 ppm. MALDI-TOF MS (dithranol):  $m/z = 844.25$  ( $[M + H]^+$ ), 761.40 ( $[M - \text{pic}]^+$ ). Anal. Calcd (%) for  $\text{C}_{42}\text{H}_{56}\text{IrN}_7\text{O}_2$  (883.41): C, 57.12; H, 6.39; N, 11.10. Found: C, 56.90; H, 6.56; N, 10.80. UV/vis ( $\text{CH}_2\text{Cl}_2$ ):  $\lambda_{\text{abs}}$  ( $\epsilon/\text{L}\cdot\text{mol}^{-1}\cdot\text{cm}^{-1}$ ) = 399 (660), 347 (4800), 303 (8900), 243 (43 000) nm. Emission ( $\text{CH}_2\text{Cl}_2$ ,  $\lambda_{\text{exc}} = 399$  nm):  $\lambda_{\text{max}} = 527$  nm. Quantum yield ( $\text{CH}_2\text{Cl}_2$ ,  $\lambda_{\text{exc}} = 399$  nm):  $\Phi_{\text{PL}} = 0.11$ .

**Computational Details.** The geometries of  $[\text{Ir}(\mathbf{a})_2(\text{bpy})]^+$ ,  $[\text{Ir}(\mathbf{a})_2(\text{acac})]$ , and  $[\text{Ir}(\mathbf{a})_2(\text{pic})]$  (see Figure 4 for schematic representations) in the electronic singlet ground state and in the lowest triplet excited state were optimized using density functional theory (DFT), as implemented in Gaussian03.<sup>58</sup> The  $\text{C}_{10}$ -alkyl chain of the 4-phenyl-1*H*-[1,2,3]triazole cyclometalating ligand was replaced by a methyl group for computational ease. The geometries were fully optimized without any symmetry constraints. The hybrid functional B3LYP<sup>59,60</sup> has been combined with a polarized valence triple- $\zeta$  basis set (TZVP) for all atoms. Relativistic effects for the iridium atom have been considered using the ECP-60-mwb Stuttgart/Dresden pseudo-potential.<sup>61</sup>

**Table 5. Main Geometrical Parameters of the Gas Phase Optimized Complexes  $[\text{Ir}(\mathbf{a})_2(\text{bpy})]^+$ ,  $[\text{Ir}(\mathbf{a})_2(\text{acac})]$ , and  $[\text{Ir}(\mathbf{a})_2(\text{pic})]$  in the Ground ( $S_0$ ) and Lowest Triplet State ( $T_1$ )<sup>a</sup>**

	$[\text{Ir}(\mathbf{a})_2(\text{bpy})]^+$		$[\text{Ir}(\mathbf{a})_2(\text{acac})]$		$[\text{Ir}(\mathbf{a})_2(\text{pic})]$	
	$S_0$	$T_1$	$S_0$	$T_1$	$S_0$	$T_1$
$d_{1-2}$ [Å]	2.056	2.059	2.050	2.060	2.047	2.047
$d_{1-3}$ [Å]	2.057	2.059	2.050	2.042	2.051	2.056
$d_{1-4}$ [Å]	2.057	2.034	2.038	2.038	2.045	2.043
$d_{1-5}$ [Å]	2.058	2.034	2.038	1.995	2.051	2.001
$d_{1-6}$ [Å]	2.197	2.175	2.186	2.194	2.196	2.228
$d_{1-7}$ [Å]	2.198	2.175	2.186	2.193	2.178	2.175
$\alpha_{3-1-2}$ [°]	171.6	175.3	174.7	175.4	173.9	174.9

<sup>a</sup> The corresponding chemical structures with the atom labeling can be found in Figure 4.

The most relevant calculated geometrical parameters for the complexes  $[\text{Ir}(\mathbf{a})_2(\text{bpy})]^+$ ,  $[\text{Ir}(\mathbf{a})_2(\text{acac})]$ , and  $[\text{Ir}(\mathbf{a})_2(\text{pic})]$  in the electronic singlet ground state ( $S_0$ ) and in the lowest triplet excited state ( $T_1$ ) are summarized in Table 5. In general, the bond lengths and angles fit well with those reported experimentally and theoretically for other related heteroleptic  $\text{Ir}^{\text{III}}$  com-

plexes.<sup>62,63</sup> No significant differences have been found among the three complexes, in which the  $\text{Ir}-\text{C}^{\wedge}\text{N}$  bond distances (2.04 to 2.06 Å) and  $\text{Ir}-\text{L}^{\wedge}\text{X}$  bond distances (around 2.18–2.19 Å) are concerned. A slight variation is found in the different angles between the coordinated nitrogen atoms of the cyclometalating ligand and the  $\text{Ir}^{\text{III}}$  center ( $\alpha_{3-1-2}$ ), which is close to 175° in the case of  $[\text{Ir}(\mathbf{a})_2(\text{acac})]$  in comparison to 174° for  $[\text{Ir}(\mathbf{a})_2(\text{pic})]$  and 172° for  $[\text{Ir}(\mathbf{a})_2(\text{bpy})]^+$ , respectively. Regarding the triplet optimized geometries, a shortening of some of the  $\text{Ir}-\text{C}^{\wedge}\text{N}$  bond distances with respect to the ground state is found, in particular in the  $d_{1-5}$  distance. The angle  $\alpha_{3-1-2}$  is larger in all the triplet optimized geometries in comparison to that of the  $S_0$  geometries.

The vertical transition energies have been obtained using TD-DFT<sup>64</sup> at the  $S_0$  optimized geometries. In order to reproduce the measured absorption UV-vis spectra, the first 45 singlet excitations were calculated, with the same functional and basis set as in the optimizations. Since the experimental UV-vis spectra were recorded in solution using  $\text{CH}_2\text{Cl}_2$  as solvent, the polarization continuum model (PCM;  $\text{CH}_2\text{Cl}_2$ ;  $\epsilon = 8.93$ ) was used. For simulating the phosphorescence emission spectra two types of calculation were performed: (i) TD-DFT singlet-triplet calculations, performed at the ground-state geometry, which provide the vertical absorption energies. Here, the first five vertical low-lying triplet states were obtained, also in the presence of  $\text{CH}_2\text{Cl}_2$ . (ii)  $\Delta$ -DFT calculations yielding the energy difference between the first triplet excited state at its optimized geometry and the closed-shell ground state at the same geometry in the gas phase, i.e., the adiabatic electronic emission (AEE). This is a simple and reliable way to determine emission energies. Additionally, the theoretical  $E_{e-e}$ , which is the energy difference between  $T_1$  and  $S_0$  minima on their corresponding potential energy surface, has been calculated. It is expected that  $E_{e-e}$  energies are close to the  $E_{0-0}$  values, i.e., the energy difference between the ground vibrational state of  $S_0$  and  $T_1$ , assuming that the zero-point energy of both states does not greatly differ. More accurate energetic values of AEE and  $E_{e-e}$  were obtained through single-point calculations in the presence of solvent ( $\text{CH}_2\text{Cl}_2$ ,  $\epsilon = 8.93$ ) using the PCM algorithm<sup>65,66</sup> as implemented in Gaussian-03 software.

**Acknowledgment.** The authors acknowledge financial support from the Dutch Polymer Institute (C.U., C.F., A. W.), the Nederlandse Organisatie voor Wetenschappelijk Onderzoek (VICI award for U.S.S.), the Fonds der Chemischen Industrie, and the Carl-Zeiss Stiftung (D.E.). We also thank Rebecca Eckardt (elemental analysis), as well as Tina Erdmenger and Nicole Herzer (MALDI-TOF MS), for help with the respective measurements, and Martin Richter and Jörg Hildebrand for preliminary theoretical calculations. We are grateful to Prof. Dr. Rene Jansen (Eindhoven University of Technology, The Netherlands) for granting access to the analytical setups.

(58) Frisch, M. J.; Trucks, G. W.; Schlegel, H. B.; Scuseria, G. E.; Robb, M. A.; Cheeseman, J. R.; Montgomery, J. A., Jr.; Vreven, T.; Kudin, K. N.; Burant, J. C.; Millam, J. M.; Iyengar, S. S.; Tomasi, J.; Barone, V.; Mennucci, B.; Cossi, M.; Scalmani, G.; Rega, N.; Petersson, G. A.; Nakatsuji, H.; Hada, M.; Ehara, M.; Toyota, K.; Fukuda, R.; Hasegawa, J.; Ishida, M.; Nakajima, T.; Honda, Y.; Kitao, O.; Nakai, H.; Klene, M.; Li, X.; Knox, J. E.; Hratchian, H. P.; Cross, J. B.; Bakken, V.; Adamo, C.; Jaramillo, J.; Gomperts, R.; Stratmann, R. E.; Yazyev, O.; Austin, A. J.; Cammi, R.; Pomelli, C.; Ochterski, J. W.; Ayala, P. Y.; Morokuma, K.; Voth, G. A.; Salvador, P.; Dannenberg, J. J.; Zakrzewski, V. G.; Dapprich, S.; Daniels, A. D.; Strain, M. C.; Farkas, O.; Malick, D. K.; Rabuck, A. D.; Raghavachari, K.; Foresman, J. B.; Ortiz, J. V.; Cui, Q.; Baboul, A. G.; Clifford, S.; Cioslowski, J.; Stefanov, B. B.; Liu, G.; Liashenko, A.; Piskorz, P.; Komaromi, I.; Martin, R. L.; Fox, D. J.; Keith, T.; Al-Laham, M. A.; Peng, C. Y.; Nanayakkara, A.; Challacombe, M.; Gill, P. M. W.; Johnson, B.; Chen, W.; Wong, M. W.; Gonzalez, C.; Pople, J. A.; *Gaussian-03, Revision C.02*; Gaussian, Inc., Wallingford, CT, 2004.

(59) Becke, A. D. *J. Chem. Phys.* **1993**, *98*, 5648–5652.

(60) Lee, C. T.; Yang, W. T.; Parr, R. G. *Phys. Rev. B* **1988**, *37*, 785–789.

(61) Andrae, D.; Häusermann, U.; Dolg, M.; Stoll, H.; Preuss, H. *Theor. Chim. Acta* **1990**, *77*, 123–141.

(62) Lamansky, S.; Djurovich, P.; Murphy, D.; Abdel-Razzaq, F.; Kwong, R.; Tsyba, I.; Bortz, M.; Mui, B.; Bau, R.; Thompson, M. E. *Inorg. Chem.* **2001**, *40*, 1704–1711.

(63) Cheng-Hsien, Y.; Wei-Lin, S.; Kai-Hung, F.; Shao-Pin, W.; I-Wen, S. *Organometallics* **2006**, *25*, 4514–4519.

(64) Casida, M. E. Time-Dependent Density Functional Response Theory for Molecules. In *Recent Advances in Density Functional Methods*; Chong, D. P., Ed.; World Scientific Publishing Company: Singapore 1995; Part I, pp 155–192.

(65) Cossi, M.; Barone, V.; Mennucci, B.; Tomasi, J. *Chem. Phys. Lett.* **1998**, *286*, 253–260.

(66) Mennucci, B.; Tomasi, J. *J. Chem. Phys.* **1997**, *106*, 5151–5158.

**5.6 Structure-property relationship of red- and green-emitting iridium(III) complexes with respect to their temperature and oxygen sensitivity**

Reprinted with permission from Tian et al. *Eur. J. Inorg. Chem.*, **2010**, 4875. Copyright 2010 John Wiley and Sons.



## Structure–Property Relationship of Red- and Green-Emitting Iridium(III) Complexes with Respect to Their Temperature and Oxygen Sensitivity

Nan Tian,<sup>[a,b]</sup> Daniel Lenkeit,<sup>[a]</sup> Simon Pelz,<sup>[a]</sup> Lorenz H. Fischer,<sup>[c]</sup> Daniel Escudero,<sup>\*,[d]</sup>  
Ralf Schiewek,<sup>[e]</sup> Dennis Klink,<sup>[e]</sup> Oliver J. Schmitz,<sup>[e]</sup> Leticia González,<sup>[d]</sup>  
Michael Schäferling,<sup>\*,[c]</sup> and Elisabeth Holder<sup>\*,[a,b]</sup>

**Keywords:** Iridium / Phosphorescence / Temperature sensitivity / Oxygen sensitivity / Density functional calculations

We report on the structural design and characterization of a series of neutral heteroleptic iridium(III) complexes equipped with 2-phenylpyridine, 2-(naphthalen-1-yl)pyridine, and 1-phenylisoquinoline as cyclometalating ligands. To gradually increase the unsymmetrical architecture of the heteroleptic iridium(III) complexes, they have been furnished with 2,2,6,6-tetramethylheptane-3,5-dione, 1-(9*H*-carbazol-9-yl)-5,5-dimethylhexane-2,4-dione, and 1-[3,6-bis(4-hexylphenyl)-9*H*-carbazol-9-yl]-5,5-dimethylhexane-2,4-dione as ancillary ligands. The photophysical and electrochemical properties of these asymmetric Ir<sup>III</sup> complexes have been investi-

gated experimentally as well as theoretically by using density functional theory (DFT) calculations. The properties of these new neutral heteroleptic iridium(III) complexes have been experimentally compared to homoleptic Ir<sup>III</sup> complex structures that reveal symmetrical architectures due to three similar cyclometalating ligands. The emission intensity of the herein described two classes of Ir<sup>III</sup> complexes is clearly influenced by applying changes to temperature and air pressure. The emphasis is on general design rules for oxygen-sensitive Ir<sup>III</sup> emitters due to the correlation of the structure-dependent oxygen sensitivity to their phosphorescence lifetimes.

### Introduction

Neutral iridium(III) complexes received much attention due to their outstanding optical properties,<sup>[1–6]</sup> which make them highly valuable in light-emitting diodes<sup>[7]</sup> or sensor systems<sup>[8]</sup> as well as in biomedical imaging.<sup>[9]</sup> On account of the extraordinary possibility to intermix excited states, they usually reveal intensive and, due to spin–orbit coupling, spin-allowed phosphorescence in both solution and bulk.<sup>[1,4]</sup> The intermixed states, namely, singlet and triplet metal-to-ligand charge-transfer (MLCT) states as well as singlet and triplet ligand-centered (LC) states<sup>[10]</sup> allow the variation of the phosphorescence emission<sup>[11,12]</sup> from

blue<sup>[13]</sup> to near-infrared<sup>[14]</sup> by the structural design of Ir<sup>III</sup> complexes. Besides the color variation on demand, neutral cyclometalated Ir<sup>III</sup> complexes are furnished with high photostability and quantum yields<sup>[3,4]</sup> as well as lifetimes of usually several microseconds.<sup>[10]</sup> The lowest triplet MLCT states<sup>[15]</sup> have to be controlled to tailor the phosphorescence of iridium(III) complexes.<sup>[11,12]</sup> All phosphorescent light emission occurs from these states. A series of design rules have to be obeyed to obtain Ir<sup>III</sup> complexes that can be easily pumped and show efficient emission, microsecond lifetimes, high complex stability, and sensitivity to their environment:<sup>[11,12]</sup> (1) The lowest excited state must be of charge-transfer (CT) or of intraligand (IL)  $\pi$ – $\pi^*$  character to prevent photochemical instability. (2) Metal-centered (MC) d–d excited states must be above the emitting level; this helps to prevent thermal excitation that leads to efficient excited state decay and thus to photochemical instability. (3) Spin–orbit coupling should be high to enhance radiative decay ( $S_n$  and  $T_n$ ), thereby competing with radiationless decay ( $T_1$  and  $S_0$ ). (4) Pure  $\pi$ – $\pi^*$  phosphorescence has a tendency to be long-lived, hence preventing efficient emission; thus, either spin–orbit coupling or mixing with CT states is required to effectively increase  $\pi$ – $\pi^*$  phosphorescence. (5) The emitting state should not be too low in energy, because low-lying emitting states enhance radiationless processes.

In addition to the above-mentioned precious optical properties and general design rules,<sup>[11,12]</sup> the phosphorescence of different neutral Ir<sup>III</sup> complexes is sensitive

[a] Functional Polymers Group and Institute of Polymer Technology, University of Wuppertal, Gaußstr. 20, 42097 Wuppertal, Germany  
Fax: +49-202-439-3880  
E-mail: holder@uni-wuppertal.de

[b] Dutch Polymer Institute (DPI),  
P. O. Box 513, 5600 AX Eindhoven, The Netherlands

[c] Institute of Analytical Chemistry, Chemo- and Biosensors, University of Regensburg, 93040 Regensburg, Germany  
Fax: +49-941-943-4064  
E-mail: michael.schaeferling@chemie.uni-regensburg.de

[d] Institute of Physical Chemistry, Friedrich Schiller University Jena, Helmholtzweg 4, 07743 Jena, Germany  
Fax: +49-3641-948302  
E-mail: daniel.escudero@uni-jena.de

[e] Analytical Chemistry, University of Wuppertal, Gaußstr. 20, 42097 Wuppertal, Germany

Supporting information for this article is available on the WWW under <http://dx.doi.org/10.1002/ejic.201000610>.

towards oxygen (and therefore to barometric pressure) and temperature.<sup>[8,16,17]</sup> Luminescent oxygen- and temperature-sensitive probes have found numerous applications in optical sensors, biomedical imaging, and pressure- or temperature-sensitive paints for fluid mechanics. Neutral iridium(III) complexes can be commonly divided into structures of homoleptic and heteroleptic architecture.<sup>[7,12]</sup> Generally, unsymmetrical structures (in the case of Ir<sup>III</sup> emitters, heteroleptic architectures) induce high environmental sensitivity.

Temperature sensitivity can be achieved by having two states of different nature within an energy gap of  $kT$  of each other. Applying temperature will then change the population of the quasidegenerate states and thus influence the decay rates, emission intensities, and lifetimes. One option is the thermal activation of an MC state; conversely, care must be taken to not induce permanent decomposition.<sup>[11]</sup>

To achieve oxygen sensitivity based on phosphorescence quenching, one has to focus on structures with high quantum yields and long lifetimes.<sup>[16,18]</sup> However, within a given class of complexes the bimolecular rate constants are insensitive to the specific structure.<sup>[11]</sup> This rule also applies to pressure sensitivity, as shown in the present investigation.

In this study, we report on the synthesis and characterization of a series of heteroleptic green, orange-red, and red Ir<sup>III</sup> complexes that were carefully designed by applying the above-mentioned rules. DFT and time-dependent DFT (TD-DFT) studies of the ground and excited states of selected Ir<sup>III</sup> complexes have been performed to help interpret the experimental photophysical data. Moreover, the characteristics of these novel heteroleptic complexes have been compared to a selection of already known homoleptic Ir<sup>III</sup> complexes based on cyclometalating C<sup>^</sup>N-type ligands of blue, green, and red emission color. It was attempted to reveal a general synthetic design concept to obtain iridium(III) complexes with a pronounced sensitivity to oxygen (and likewise air pressure) or temperature.

## Results and Discussion

### Synthesis and Characterization

To study the oxygen (in terms of barometric pressure) and temperature sensitivity of a selection of blue-, green-, and red-emitting homoleptic and heteroleptic iridium(III) complexes, a series of unsymmetrical heteroleptic phosphorescent green, orange-red, and red iridium(III) complexes were synthesized and characterized. For this purpose, a set of C<sup>^</sup>N and ancillary ligands were prepared.<sup>[7]</sup> 1-Phenylisoquinoline (**1**)<sup>[7]</sup> (see Supporting Information) was obtained by an optimized and simplified Suzuki protocol<sup>[19]</sup> in 92% yield by using tetrakis(triphenylphosphane)palladium(0) as cross-coupling catalyst.

The same (but intensively optimized) reaction pathway was used to couple (4-hexylphenyl)boronic acid (**2**) (see Figure S1) with 3,6-diiodo-9*H*-carbazole<sup>[20,21]</sup> to yield novel 3,6-bis(4-hexylphenyl)-9*H*-carbazole (**3**) (see Figure S1) in

58% yield. Tetrakis(triphenylphosphane)palladium(0) was yet again utilized as cross-coupling catalyst (Figure S1 in the Supporting Information). Several attempts of using modified Suzuki C–C coupling protocols were carried out to obtain compound **3**. However, reactions performed by using other cross-coupling functionalities like bromo functions, that were combined with a series of boronic acid esters, ended only in no or low conversion with unsatisfactory yields of **3**. This finding goes hand-in-hand with rarely described reactions of the same type in the literature.<sup>[22]</sup> Only a few examples can be found of coupling bare phenyl substituents onto carbazoles in their 3,6-position.<sup>[22,23]</sup> Ethyl 2-[3,6-bis(4-hexylphenyl)-9*H*-carbazol-9-yl]acetate (**4**) (see Figure S1) was obtained in a yield of 62% by treating **3** with ethyl 2-bromoacetate under K<sub>2</sub>CO<sub>3</sub> basic conditions.<sup>[8,24]</sup> Subsequently, 1-[3,6-bis(4-hexylphenyl)-9*H*-carbazol-9-yl]-5,5-dimethylhexane-2,4-dione (**5**) (see Figure S1) was obtained in a yield of 80% by treating **4** with 3,3-dimethyl-2-oxobutan-1-ide, which was obtained by using potassium hexamethyldisilazane (KHMDs), in a Claisen-type reaction.<sup>[8,24]</sup> The  $\mu$ -chlorido-bridged dimers **6a–c** (see Supporting Information) were synthesized in yields of 70–78% according to the well-known Nonoyama method,<sup>[25]</sup> but treating IrCl<sub>3</sub>·*n*H<sub>2</sub>O with **1** (1-phenylisoquinoline, piq), 2-(naphthalen-1-yl)pyridine (npy), and 2-phenylpyridine (ppy), respectively. Heteroleptic iridium(III) complexes **7a–c** were prepared in yields of 66–71% by combining **6a–c** with commercially available 2,2,6,6-tetramethylheptane-3,5-dione (denoted as acac) according to a bridge-splitting method using K<sub>2</sub>CO<sub>3</sub> as base (Figure 1). Iridium(III) complexes **8a–c** (Figure 1) were obtained in yields of 61–67% according to the same reaction conditions but by treating **6a–c** with 1-(9*H*-carbazol-9-yl)-5,5-dimethylhexane-2,4-dione (denoted as carbazole-acac).<sup>[8]</sup> Finally, the iridium(III) complexes **9a–c** (yield: 65–72%) were obtained by adding 1-[3,6-bis(4-hexylphenyl)-9*H*-carbazol-9-yl]-5,5-dimethylhexane-2,4-dione (denoted as phenyl-carbazole-acac) to **6a–c** (Figure 1). The complexes in the series **7a–c** to **9a–c** were easily soluble in solvents of medium polarity.

<sup>1</sup>H NMR spectra were obtained from solutions of the compounds in deuterated chloroform. The structures of **7a–c** to **9a–c** were confirmed by applying 2D <sup>1</sup>H–<sup>1</sup>H COSY NMR spectroscopic experiments. Atmospheric-pressure laser-ionization mass-spectrometry (APLI-MS) techniques were additionally utilized to identify the molecular weight and the purity of the heteroleptic Ir<sup>III</sup> complexes **7a–c** to **9a–c**. For all heteroleptic complexes **7a–c** to **9a–c** the molecular peak could be detected according to the calculated values and, moreover, the molecular-peak pattern could be exactly simulated. In addition, correct elemental analyses proved the purity of compounds **7a–c** to **9a–c**, correspondingly. All of the heteroleptic Ir<sup>III</sup> complexes **7a–c** to **9a–c** were subjected to thermal gravimetric analysis (TGA) to verify that their thermal stability was higher than 280 °C at 5% weight loss, thus qualifying the novel compounds **7a–c** to **9a–c** as probes with excellent temperature stabilities (Table 1).

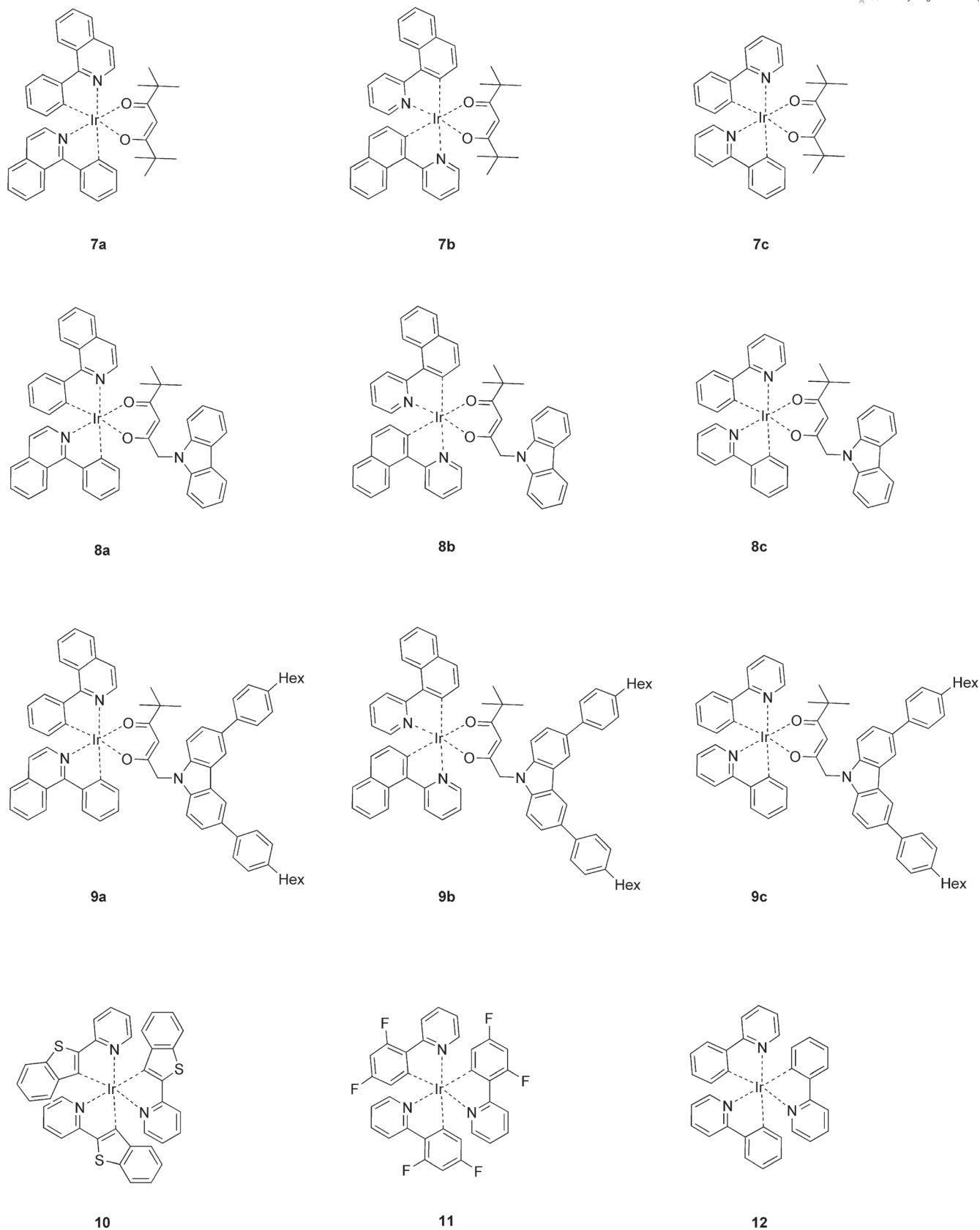


Figure 1. Schematic representation of the structures of the analyzed heteroleptic complexes **7a–c** to **9a–c** and homoleptic Ir<sup>III</sup> complexes **10–12**.

Table 1. Data of absorption, emission, quantum yields, and decomposition temperature ( $T_d$ ) for iridium(III) complexes.

Material	Absorbance [nm] ( $\log \epsilon$ [ $L \text{ mol}^{-1} \text{ cm}^{-1}$ ])	Maximum emission [nm]	Quantum yield <sup>[a]</sup> [%]	$T_d$ <sup>[b]</sup> [°C]
<b>7a</b>	293 (4.98), 344 (3.73) 419 (3.28), 484 (3.20)	630	35	284.3
<b>7b</b>	240 (4.03), 300 (4.04) 458 (3.11), 497 (3.14)	600	37	281.2
<b>7c</b>	260 (5.29), 341 (3.62) 412 (3.25), 468 (3.14)	522	43	302.3
<b>8a</b>	247 (5.33), 291 (5.20) 341 (3.93), 478 (3.29)	624	31	356.0
<b>8b</b>	242 (3.99), 296 (3.87) 346 (3.54), 490 (2.83)	597	34	336.0
<b>8c</b>	240 (4.02), 262 (3.99) 345 (3.37), 462 (2.70)	521	37	337.3
<b>9a</b>	264 (3.97), 299 (3.98) 359 (3.40), 481 (2.79)	625	30	340.0
<b>9b</b>	262 (5.06), 296 (5.02) 356 (3.66), 490 (3.18)	595	32	315.6
<b>9c</b>	235 (3.86), 262 (5.08) 291 (3.98), 466 (2.49)	522	44	324.6

[a] Determined according to the method of Demas and Crosby.<sup>[28]</sup> [b] At 5% weight loss.

### Optical Properties

The experimental UV/Vis absorption and emission spectra of complexes **7a–c** to **9a–c** recorded in  $\text{CHCl}_3$  are depicted in Figure 2. Table 1 collects their photophysical characteristics. To gain insight into the excited states that are responsible for the photophysical properties of these  $\text{Ir}^{\text{III}}$

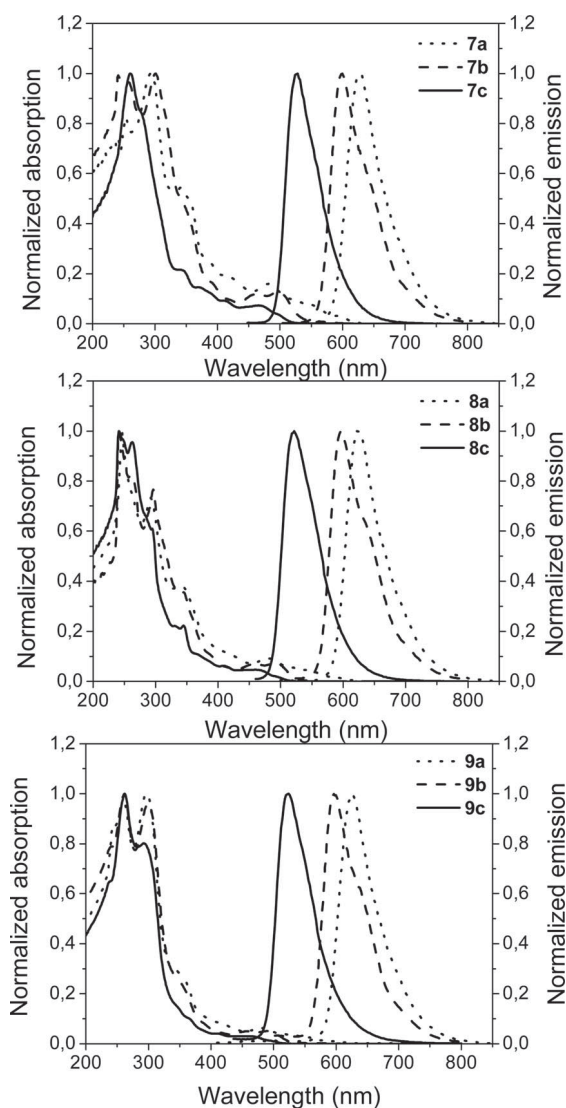


Figure 2. Absorption and emission properties of the iridium(III) complex series **7a–c** to **9a–c** ( $10^{-5}$  M in  $\text{CHCl}_3$ ).

complexes, theoretical  $\Delta$ -DFT and TD-DFT (B3LYP/6-31G\*) calculations have been performed, by way of example, for complexes **7a,c** and **8a,c** (see Figure 1). Figures 3 and 4 show their corresponding Kohn–Sham orbitals and the energy-level schemes. In all the complexes the HOMO orbital is the  $5d_{xy}$  orbital of the  $\text{Ir}^{\text{III}}$  center. The rest of the orbitals of the set  $t_{2g}$  ( $5d_{xz}$  and  $5d_{yz}$  orbitals) are found to occupy lower-lying energy levels. In the case of complexes **7a** (Figure 3) and **8c** (Figure 4), some  $\pi$  orbitals localized in the ancillary ligand ( $\pi_{\text{anc}}$ ) are intercalated within the set  $t_{2g}$  of orbitals. Interestingly, for all the complexes the LUMO orbital is a  $\pi$ -antibonding orbital localized on the cyclometalating ligand ( $\pi^*_{\text{cycl}}$ ).

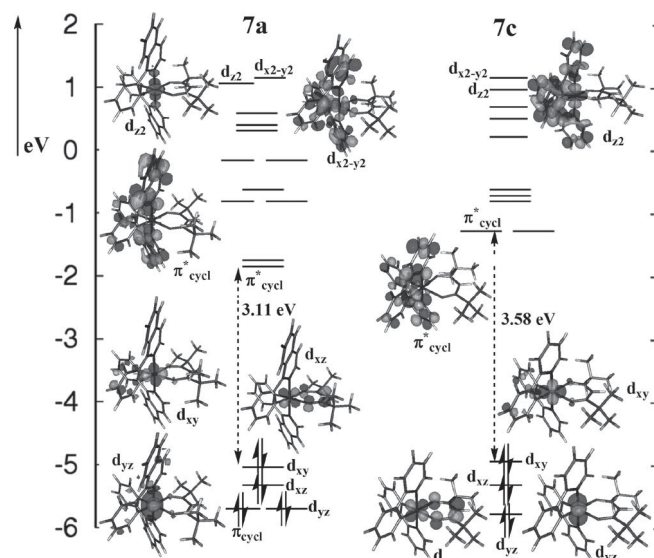


Figure 3. Energy-level scheme of complexes **7a,c**, including the most relevant Kohn–Sham orbitals and the HOMO–LUMO gaps calculated with B3LYP/6-31G\*.

In the cyclometalating piq-based complexes **7a** and **8a**, the LUMO orbital is stabilized relative to the LUMO orbital of the ppy-based complexes **7c** and **8c**. This stabilization is due to the delocalization of this orbital in the piq cyclometalating ligand relative to the ppy ligand. Since the HOMO energies are very close within the piq/ppy series, larger HOMO–LUMO gaps are obtained for the ppy series (compare 3.58–3.61 eV to 3.11–3.09 eV, in Figures 3 and 4). The  $e_g$  orbitals of the  $\text{Ir}^{\text{III}}$  center are, as seen in Figures 3 and 4, strongly destabilized for all the complexes. This is a

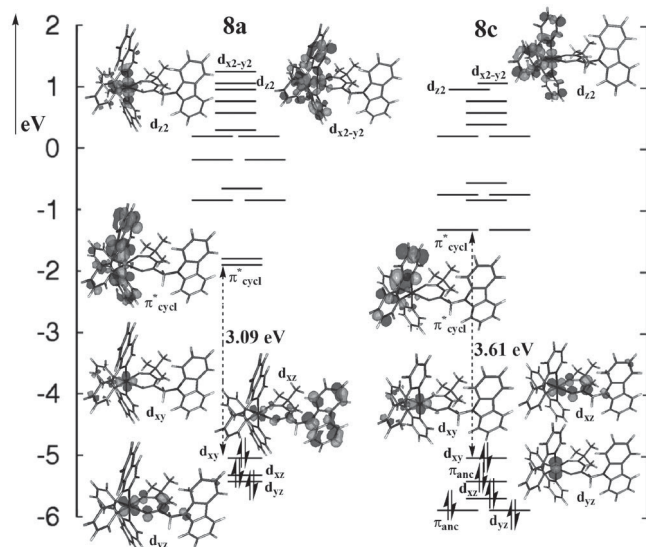


Figure 4. Energy-level scheme of complexes **8a,c**, including the most relevant Kohn–Sham orbitals and the HOMO–LUMO gaps calculated with B3LYP/6-31G\*.

common feature for cyclometalated Ir<sup>III</sup> complexes, since the strong ligand-field effect of the phenyl anion ( $C^-$ ) ligand increases the gap between the sets of  $t_{2g}$  and  $e_g$  orbitals.

In the following, we turn our attention to the interpretation of the UV/Vis data. The UV/Vis spectra of complexes **7a–c** to **9a–c** show some general features. The photophysical properties are more robust within the same cyclometalating ligand series rather than with the same ancillary ligand (compare the UV/Vis spectra of complexes with the same ancillary ligand, e.g., **7a** vs. **7c** with respect to complexes with the same cyclometalating ligand, e.g., **7c** vs. **8c**). In the complexes that bear the piq and npy cyclometalating ligands, more common features are obtained than with the ppy cyclometalating ligands. The UV/Vis spectra of all the complexes are dominated by some intense absorption bands located in the far-UV region (below 300 nm). In the piq- and npy-based complexes, these bands are split into two main peaks at 300 and 250 nm. In the ppy-based compounds, a single band peaks at about 260 nm. Some shoulders of the aforementioned intense bands higher in energy (around 350 nm) can be seen in all complexes. Between 450 and 550 nm, low-lying weak absorption bands follow.

A comparison of the calculated and experimental absorption spectra for complexes **7a,c** and **8a,c** is presented in Figure 5. The associated most relevant electronic singlet–singlet vertical excitations, their oscillator strengths, and their correspondent assignments are summarized in Table 2. Among them, we find <sup>1</sup>MLCT states, IL excitations as well as ligand-to-ligand CT excitations (<sup>1</sup>LLCT). The simulated convoluted UV/Vis spectra are shown in Figure 5 with dashed lines. As can be seen, the agreement between the calculated and experimental spectra is very good, notwithstanding that TD-DFT tends to underestimate CT states.<sup>[26]</sup> The weak experimental absorption bands located between

450 and 550 nm are theoretically assigned as spin-allowed <sup>1</sup>MLCT transitions (see, for example,  $S_1$ ,  $S_2$ ,  $S_3$ , and  $S_6$  in complex **7a** in Table 2). These electronic excitations are red-shifted for the piq-based complexes, as stated both theoretically and experimentally (see Figure 5). This fact can be explained through the above-mentioned stabilization of the cyclometalating-based antibonding orbitals of the piq-related compounds. As shown in Figure 5, no absorption is predicted beyond 550 nm in complexes **7a,c** and beyond 480 nm for complexes **8a,c**. The long tails of, for instance, **8a** up to 600 nm, at which point singlet–singlet excitations are dark or do not exist, should then be attributed to <sup>3</sup>MLCT excited states.<sup>[10,24,27]</sup> The very intense bands that peak in the region of 300 nm for complexes **7a** and **8a** and approximately 260 nm for complexes **7c** and **8c** are of very different character. They correspond to high-energy <sup>1</sup>MLCT transitions in case of **7a,c** (see  $S_{25}$  and  $S_{35}$  for complexes **7a** and **8a** in Table 2), whereas in **7c** and **8c** they are due to mainly IL  $\pi \rightarrow \pi^*$  transitions within the cyclometalating ligands (see  $S_{36}$  and  $S_{50}$  for complexes **7c** and **8c**, respectively). These ligand-based bands are also present but slightly blueshifted in the npy and piq series (peaking at around 250 nm; see Figure 2). As expected, these bands are also present in the UV/Vis spectra of the isolated cyclometalating ligands 2-phenylpyridine, **1**, and 2-(naphthalen-1-yl)pyridine, respectively.<sup>[10,24]</sup> The  $\beta$ -diketonato-based transitions also contribute to these bands at about 270 nm (see  $S_{46}$  and  $S_{42}$  for complexes **8a** and **8c**, respectively, in Table 2), which is analogous to the absorptions of the free  $\beta$ -diketone. The shoulders of the intense band located in the visible region at around 300–350 nm in complexes **7c** and **8c** and at approximately 350–400 nm in complexes **7a** and **8a** are due to electronic transitions of a very diverse nature. Among them, <sup>1</sup>IL as well as <sup>1</sup>MLCT transitions dominate this region.

Next, we shall discuss the nature of the excited states involved in the emission process. The experimental phosphorescence spectra can also be found in Figure 2. Complexes **7a–9a** present maximum emission wavelengths ( $\lambda_{\max}$ ) that are higher than 624 nm as intense red light with quantum yields of more than 30%. The complexes **7b–9b** show orange-red phosphorescence ( $\lambda_{\max} \approx 595$ –600 nm) with quantum yields higher than 32%. Typically, the series of green-emitting ( $\lambda_{\max} \approx 521$ –522 nm) complexes **7c–9c** reveal the uppermost quantum yield of 44% (see Table 1). Since the lowest triplet excited states involve a  $\pi^*$  orbital located on the cyclometalating ligand (vide infra), this ligand should play the most important role in the emission spectra, as experimentally confirmed within the series **7a–9a**, **7b–9b** and **7c–9c**.

For Ir<sup>III</sup> complexes it is well known that the lowest triplet excited state ( $T_1$ ) is populated rapidly through an efficient intersystem crossing between the manifolds of singlets and triplets (due to strong spin–orbit coupling for the Ir<sup>III</sup> atom). To reproduce the emission-spectral maxima of **7a,c** and **8a,c** theoretically, a two-step approach has been considered. First, the five lowest-lying triplet excitations at the Franck–Condon geometry have been obtained at the TD-

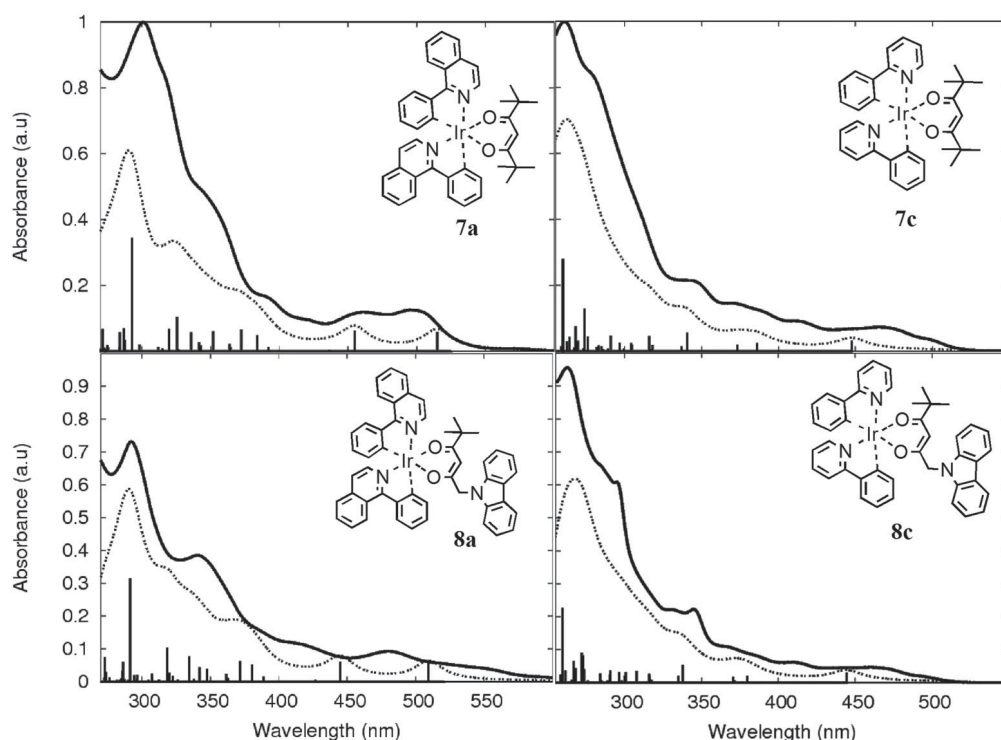


Figure 5. Experimental UV/Vis spectra (solid lines) of complexes **7a,c** and **8a,c** with TD-DFT (B3LYP/6-31G\*) vertical excitations. The simulated UV/Vis spectra with a Lorentzian broadening of 25 nm of band width on half-height are presented with dashed lines.

Table 2. Main theoretical electronic-transition energies ( $\Delta E$ ), with corresponding oscillator strengths ( $f$ ) and assignments of complexes **7a,c** and **8a,c**.

State	$\Delta E$ [nm]	$f$	Assignment	State	$\Delta E$ [nm]	$f$	Assignment
<b>7a</b>				<b>7c</b>			
S <sub>1</sub>	525	0.001	5d <sub>xy</sub> →π* <sub>cycl</sub> (0.68) MLCT	S <sub>1</sub>	448	0.032	5d <sub>xy</sub> →π* <sub>cycl</sub> (0.68) MLCT
S <sub>2</sub>	515	0.059	5d <sub>xy</sub> →π* <sub>cycl</sub> (0.68) MLCT	S <sub>3</sub>	386	0.025	5d <sub>xz</sub> →π* <sub>cycl</sub> (0.68) MLCT
S <sub>3</sub>	455	0.063	5d <sub>xz</sub> →π* <sub>cycl</sub> (0.69) MLCT	S <sub>8</sub>	341	0.056	5d <sub>yz</sub> →π* <sub>cycl</sub> (0.66) MLCT
S <sub>6</sub>	384	0.049	5d <sub>yz</sub> →π* <sub>cycl</sub> (0.61) MLCT	S <sub>14</sub>	316	0.047	π <sub>cycl</sub> →π* <sub>cycl</sub> (0.48) IL
S <sub>7</sub>	372	0.066	π <sub>cycl</sub> →π* <sub>cycl</sub> (0.63) IL	S <sub>19</sub>	291	0.048	π <sub>cycl</sub> →π* <sub>cycl</sub> (0.51) IL
S <sub>12</sub>	352	0.060	π <sub>cycl</sub> →π* <sub>cycl</sub> (0.68) IL	S <sub>27</sub>	276	0.045	π <sub>anc</sub> →π* <sub>cycl</sub> (0.47) LLCT
S <sub>18</sub>	326	0.105	d <sub>xz</sub> →π* <sub>cycl</sub> (0.53) MLCT	S <sub>28</sub>	274	0.130	π <sub>anc</sub> →π* <sub>cycl</sub> (0.48) LLCT
S <sub>19</sub>	320	0.068	4d <sub>xz</sub> →π* <sub>cycl</sub> (0.53) MLCT	S <sub>31</sub>	268	0.076	π <sub>anc</sub> →π* <sub>cycl</sub> (0.38) LLCT
S <sub>25</sub>	293	0.344	5d <sub>xz</sub> →π* <sub>cycl</sub> (0.61) MLCT	S <sub>34</sub>	264	0.044	π <sub>cycl</sub> →π* <sub>cycl</sub> (0.52) IL
S <sub>28</sub>	287	0.070	π <sub>cycl</sub> →π* <sub>cycl</sub> (0.54) IL	S <sub>36</sub>	260	0.275	π <sub>cycl</sub> →π* <sub>cycl</sub> (0.39) IL
<b>8a</b>				<b>8c</b>			
S <sub>1</sub>	521	0.001	5d <sub>xy</sub> →π* <sub>cycl</sub> (0.68) MLCT	S <sub>1</sub>	444	0.030	5d <sub>xy</sub> →π* <sub>cycl</sub> (0.68) MLCT
S <sub>2</sub>	509	0.056	5d <sub>xy</sub> →π* <sub>cycl</sub> (0.68) MLCT	S <sub>3</sub>	380	0.022	5d <sub>xz</sub> →π* <sub>cycl</sub> (0.57) MLCT
S <sub>3</sub>	445	0.062	5d <sub>yz</sub> →π* <sub>cycl</sub> (0.62) MLCT	S <sub>10</sub>	338	0.055	5d <sub>yz</sub> →π* <sub>cycl</sub> (0.58) MLCT
S <sub>8</sub>	381	0.053	4d <sub>xz</sub> →π* <sub>cycl</sub> (0.59) MLCT	S <sub>22</sub>	308	0.035	π <sub>anc</sub> →π* <sub>anc</sub> (0.60) IL
S <sub>9</sub>	372	0.062	π <sub>cycl</sub> →π* <sub>cycl</sub> (0.57) IL	S <sub>28</sub>	291	0.037	π <sub>cycl</sub> →π* <sub>cycl</sub> (0.43) IL
S <sub>17</sub>	342	0.043	4d <sub>yz</sub> →π* <sub>cycl</sub> (0.60) MLCT	S <sub>40</sub>	274	0.042	π <sub>anc</sub> →π* <sub>cycl</sub> (0.37) LLCT
S <sub>19</sub>	334	0.077	π <sub>cycl</sub> →π* <sub>cycl</sub> (0.57) IL	S <sub>42</sub>	273	0.082	π <sub>anc</sub> →π* <sub>anc</sub> (0.37) IL; π <sub>cycl</sub> →π* <sub>cycl</sub> (-0.38) IL
S <sub>24</sub>	319	0.105	π <sub>cycl</sub> →π* <sub>cycl</sub> (0.42) IL	S <sub>44</sub>	272	0.090	π <sub>cycl</sub> →π* <sub>cycl</sub> (0.31) IL
S <sub>35</sub>	291	0.315	4d <sub>xz</sub> →π* <sub>cycl</sub> (0.59) MLCT	S <sub>46</sub>	267	0.065	5d <sub>yz</sub> →π* <sub>cycl</sub> (0.32) MLCT
S <sub>46</sub>	274	0.075	π <sub>anc</sub> →π* <sub>anc</sub> (0.54) IL	S <sub>50</sub>	260	0.227	π <sub>cycl</sub> →π* <sub>cycl</sub> (0.31) IL

B3LYP/6-31G\* level of theory (see Table 3). All of them are of <sup>3</sup>MLCT character. The so-obtained S<sub>0</sub>-T<sub>1</sub> gaps are clearly blueshifted with respect to the experimental emission maxima. This is expected since the triplet states have not been allowed to relax. Therefore, as a second step, trip-

let-state optimizations were carried out to yield adiabatic emission energies (*AEE*; see Table 3). We note that relaxation along the triplet potential-energy surfaces leads to the same triplet excited state regardless of substitution of the ancillary or cyclometalating ligands. Thus, the T<sub>1</sub> minima

Table 3. Lowest singlet–triplet theoretical emission energies by means of TD-DFT and  $\Delta$ -DFT approaches.

	<b>7a</b>	<b>7c</b>	<b>8a</b>	<b>8c</b>
	TD-DFT vertical singlet–triplet excitations; $\Delta E$ [nm] and resulting $^3$ MLCT assignment			
T <sub>1</sub>	592	490	592	486
T <sub>2</sub>	585	478	581	480
T <sub>3</sub>	512	427	504	430
T <sub>4</sub>	506	416	501	414
T <sub>5</sub>	452	413	445	412
	Theoretical $E_{e-e}$ ; $\Delta E$ [nm] (experimental $E_{0-0}$ [nm])			
	615 (545)	500 (489)	610 (572)	499 (479)
	Theoretical $AEE$ ; $\Delta E$ [nm] (experimental emission maxima [nm])			
	701 (630)	550 (522)	698 (624)	548 (521)

of all the complexes are of  $^3$ MLCT character, as reflected through the analysis of spin densities and in accordance to the TD-DFT data. They are all transitions going from a d orbital of the Ir<sup>III</sup> atom to a  $\pi^*_{\text{cycl}}$  orbital. As it can be seen in Table 3, the  $AEE$  values (obtained as the energy difference between T<sub>1</sub> and S<sub>0</sub> at the optimized T<sub>1</sub> geometry) are then in more reasonable agreement with the experimental emission maxima (errors amount to 0.2 eV, which is the accepted error inherent to the functional). The theoretical values of 701, 550, 698, and 548 nm, obtained for **7a**, **7c**, **8a**, and **8c**, respectively, correlate well with the experimental ones of 630, 522, 624, and 521 nm (Table 3). The electronic ZPE  $E_{e-e}$  energies (i.e., the energy difference between T<sub>1</sub> and S<sub>0</sub> minima on each potential-energy surface) also show a fair agreement with the  $E_{0-0}$  experimental values (estimated experimentally as the intersection point between the emission and absorption spectra).

### Pressure and Temperature Sensitivity

The pressure ( $pO_2$ ) and temperature dependency of the phosphorescence lifetimes of compounds **7a–c**, **8b–c**, **9b–c**, and of three commercially available homoleptic iridium(III) complexes {tris[2-(benzo[*b*]thiophen-2-yl)pyridinato- $C^3,N$ ]-iridium(III), [Ir(btpy)<sub>3</sub>] (**10**); tris[2-(4,6-difluorophenyl)pyridinato- $C^2,N$ ]-iridium(III), [Ir(Fppy)<sub>3</sub>] (**11**); and tris(2-phenylpyridinato- $C^2,N$ )-iridium(III), [Ir(ppy)<sub>3</sub>] (**12**)} representing red-, blue-, and green-emitting reference compounds, were characterized. The dyes were incorporated into standardized polystyrene films of 6  $\mu\text{m}$  thickness. These were fabricated with a knife-coating device on a solid poly(ethylene terephthalate) (PET) support. The backside of the PET foil was coated with a highly reflective silicone/TiO<sub>2</sub> screen layer. The luminescence lifetimes were obtained according to the rapid lifetime determination (RLD) method.<sup>[29,30]</sup> This ratiometric method provides intrinsic referenced signals and can be used to calculate the average luminescence lifetimes. For this purpose, the sensor films were photoexcited by means of a pulsed 405 nm LED with an internal frequency of 125 kHz and 5  $\mu\text{s}$  pulse lengths. The luminescence intensity was integrated by a triggered CCD camera within two precisely timed gates ( $A_1$  and  $A_2$ )

of 1.4  $\mu\text{s}$  with delay times of 0  $\mu\text{s}$  ( $t_1$ ) and 0.7  $\mu\text{s}$  ( $t_2$ ) after the LED pulse, respectively. This was followed by the acquisition of the corresponding dark images for background subtraction. The whole imaging process has been described in previous work.<sup>[31]</sup>

The luminescence lifetimes ( $\tau$ ) can be calculated according to Equation (1),<sup>[32]</sup> when one assumes a monoexponential decay of luminescence emission, and with the two gates  $t_1$  and  $t_2$  being of the same width.

$$\tau = \frac{t_2 - t_1}{\ln \frac{A_1}{A_2}} \quad (1)$$

The intrinsic referencing reduces the signal noise. It provides a highly reproducible signal, which is unsusceptible to the common interferences in luminescence measurements. It has to be emphasized that luminescence decays of metal–ligand complexes are not monoexponential, and the lifetimes determined by this simple ratiometric method do not represent exact values as obtained with single-photon counting measurements. However, the values acquired at identical experimental settings reflect changes of luminescence lifetimes within a series of measurements. For comparison, Baranoff et al. reported a lifetime  $\tau_0$  of the triplet emission of [Ir(btpy)<sub>3</sub>] at 596 nm of 4.0  $\mu\text{s}$  in toluene at 298 K<sup>[33]</sup> (see Table 4). Furthermore, the oxidation potential of the complexes was measured by means of cyclic voltammetry against ferrocene (Fc/Fc<sup>+</sup>) in dried tetrahydrofuran. All determined parameters are summarized in Tables 4 and 5.

Table 4. Reversible oxidation potentials, phosphorescence emission maxima, and lifetimes of cyclometalated iridium(III) complexes and their pressure and temperature sensitivities.

	<b>8b</b>	<b>8c</b>	<b>10</b>	<b>11</b>	<b>12</b>
$E_{\text{ox}}$ vs. Fc/Fc <sup>+</sup> [V]	0.27	0.28	0.25	0.64	0.31
Emission max. [nm]	590	521	596, (645)	470	512
$\tau$ [ $\mu\text{s}$ ] <sup>[a]</sup>	3.4	1.3	6.6	1.0	1.2
$T$ coeff. [%/(t)/°C]	0.43	0.48	0.35	0.31	0.19
$K_{\text{sv}}$ [ $10^{-4}$ mbar <sup>-1</sup> ] <sup>[b]</sup>	1.49	0.65	2.17	0.40	0.47

[a] At 50 mbar air pressure and 30 °C. [b] Stern–Volmer constant in 6  $\mu\text{m}$  polystyrene (PS) film.

Table 5. Characterization of heteroleptic (phenylpyridine)-, (naphthylpyridine)-, and (phenylisoquinoline)iridium complexes with different ancillary ligands.

	7a	7b	7c	8b	8c	9b	9c
$E_{\text{ox}}$ vs. $\text{Fc}/\text{Fc}^+$ [V]	0.26	0.27	0.25	0.27	0.28	0.27	0.27
Emission max. [nm]	625	600	526	590	521	595	522
$\tau$ [ $\mu\text{s}$ ] <sup>[a]</sup>	1.1	3.6	1.2	3.4	1.3	3.3	1.1
$T$ coeff. [%/( $t$ )/ $^{\circ}\text{C}$ ]	0.21	0.40	0.37	0.43	0.48	0.40	0.43
$K_{\text{SV}}$ [ $10^{-4}$ mbar $^{-1}$ ] <sup>[b]</sup>	0.61	1.33	0.732	1.49	0.65	1.26	0.63

[a] At 50 mbar air pressure and 30  $^{\circ}\text{C}$ . [b] In 6  $\mu\text{m}$  PS film.

In this study, the pressure and temperature calibration of the iridium(III) phosphors was performed with square samples of  $3 \times 3$  cm size of the dyed PS films. These were placed in a calibration chamber, in which the air pressure can be adjusted from 50 to 2000 mbar and the temperature from 1 to 60  $^{\circ}\text{C}$ . The assembly of the calibration chamber and of the imaging set up has been outlined in a recent publication.<sup>[8]</sup> The results of the temperature calibrations are shown in Figure 6. The resulting lifetimes were normalized to the first value (1  $^{\circ}\text{C}$  at 1000 mbar) of the series of measurements to display the graphs in one plot. The results of the pressure calibrations are shown in Figure 7 in the form of Stern–Volmer plots. From the obtained data the Stern–Volmer ( $K_{\text{SV}}$ ) constants and the temperature coefficients were calculated according to linear fits. The fits are very consistent in case of pressure dependency with correlation coefficients  $R^2$  larger than 0.99. Although the temperature plots are apparently not linear, the calculated linear temperature coefficients are a suitable quantity for the temperature sensitivity.

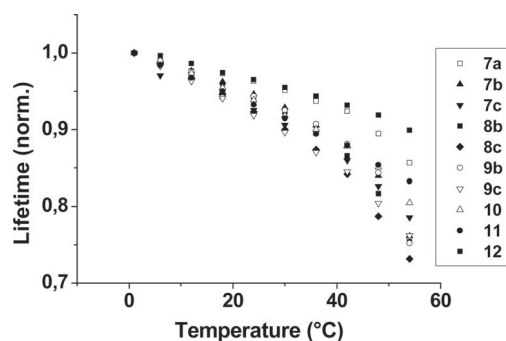


Figure 6. Temperature dependence of the normalized luminescence lifetimes of cyclometalated iridium(III) complexes 7–12 in 6  $\mu\text{m}$  PS films at 1000 mbar.

Generally, in the cases of metal–ligand complexes, the emission maximum is determined by the energy gap between the excited triplet state and the ground state, which can be correlated with the energy difference of the frontier molecular orbitals (HOMO–LUMO gap). It is clear that increased HOMO–LUMO gaps result in emission maxima of higher energy. The oxidation potential, which depends on the energy level of the HOMO, decreases with lower energy gaps (see Table 4). Unfortunately, reduction potentials could not be measured with our setup. They occur at potentials lower than  $-2.0$  V.<sup>[32]</sup>

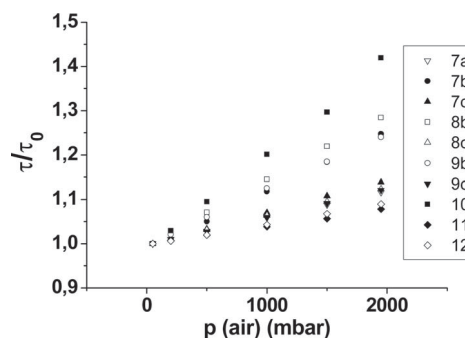


Figure 7. Air-pressure dependence of the luminescence lifetimes of cyclometalated iridium(III) complexes in 6  $\mu\text{m}$  PS films at  $T = 30$   $^{\circ}\text{C}$ . All plots are referenced to the according lifetime values at 50 mbar air pressure and 1  $^{\circ}\text{C}$ .

The influence of the ancillary ligand on the temperature and oxygen sensitivity is very small. Within a series of complexes that bear the same cyclometalating ligand (7b–9b or 7c–9c, respectively)  $K_{\text{SV}}$  and temperature coefficients show only negligible deviations. In contrast, the cyclometalating ligands have a high impact on the sensing properties, as expected from their very different photophysical properties.

#### Calibration of Pressure Sensitivity

The series of homoleptic and heteroleptic  $\text{Ir}^{\text{III}}$  complexes that emit from blue to red also showed an increase in oxygen (and pressure) sensitivity with increasing lifetimes of the excited triplet state. This can be expected as a consequence of the Stern–Volmer equation [Equation (2)], which describes the dependency of the luminescence lifetime from partial oxygen pressure:

$$\frac{I_0}{I} = \frac{\tau_0}{\tau} = 1 + K_{\text{SV}}[Q] \quad (2)$$

in which  $I_0$  is the luminescence intensity and  $\tau_0$  the lifetime in absence of quencher (oxygen) under standard conditions.  $I$  and  $\tau$  are intensity and lifetime in the presence of oxygen with concentration  $[Q]$ . The presence of oxygen quenches the luminescence lifetime and intensity likewise.

$K_{\text{SV}}$  is the Stern–Volmer constant defined in Equation (3), with  $K_{\text{q}}$  being the bimolecular dynamic quenching constant.

$$K_{\text{SV}} = \tau_0 \cdot K_{\text{q}} \quad (3)$$

The red-emitting series with the npy ligand (7b–9b) shows much higher oxygen sensitivity relative to the green-emitting series with the ppy cyclometalating ligand (7c–9c). With respect to Equation (3), this is due to the longer lifetimes of the complexes with the npy ligand. The highest oxygen-quenching efficiency is observed for  $[\text{Ir}(\text{btpy})_3]$  (10) with a  $K_{\text{SV}}$  of  $2.17 [10^{-4} \text{ mbar}^{-1}]$  relative to air pressure. Stern–Volmer constants of several cyclometalated iridium(III) complexes have been reported, but they can be hardly compared, because they have been determined under different experimental conditions and with various polymer



matrices.<sup>[16,34–39]</sup> Generally, with the exception of **10** and the npy complexes, the iridium(III) complexes are not very efficiently quenched by oxygen.

A general influence of the emission wavelength on the sensitivity to oxygen cannot be deduced as the deep red-emitting complex **7a** shows only slight oxygen sensitivity. It is apparent that the luminescence quenching by oxygen is a bimolecular process and is affected by many factors.

Another very important aspect that determines the response is the oxygen permeability of the matrix polymer. In this study, all complexes were calibrated in PS, which possesses an oxygen permeability  $P$  of  $1.9 \times 10^{-13} \text{ cm}^3 \text{ (STP) cm (cm}^2 \text{ s Pa)}^{-1}$  {the permeability coefficient  $P$  is defined by:  $P = [(\text{quantity of oxygen}) \times (\text{film thickness})] / [(\text{area}) \times (\text{time}) \times (\text{pressure drop across film})]$  (STP = standard temperature and pressure).<sup>[40]</sup> Because of this moderate permeability, PS is an appropriate polymer binder to compare the luminescence responses to temperature and oxygen of a series of dyes under standard conditions. If polymers with higher oxygen permeabilities are applied, the oxygen sensitivity and  $K_{SV}$  values increase, and also the differences between the single complexes are more pronounced. Figure 8 compares the response to oxygen of complex **10** in PS and ethyl cellulose (EC). The latter provides a very high oxygen permeability with  $P = 11 \times 10^{-13} \text{ cm}^3 \text{ (STP) cm (cm}^2 \text{ s Pa)}^{-1}$ .<sup>[40]</sup> This results in an increased  $K_{SV}$  of 40 [ $10^{-4} \text{ mbar}^{-1}$ ], which is a very high sensitivity compared to other luminescent probes used in optical oxygen sensors. A comparison of the performance of  $[\text{Ir}(\text{btpy})_3]$  as indicator for oxygen (or barometric pressure) with established oxygen-sensitive probes can be found in previous work.<sup>[16]</sup>

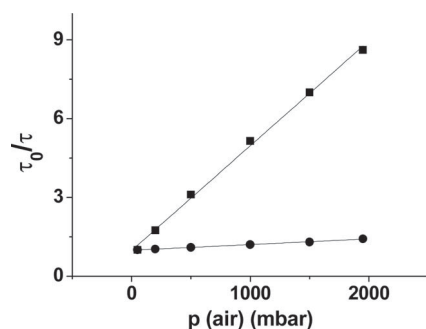


Figure 8. Stern–Volmer plots for **10** in PS (●) and EC 49 (■) (EC with 49% ethoxy grade) at 30 °C.

### Calibration of Temperature Sensitivity

Nearly all luminescent dyes display a strong sensitivity towards temperature. The Boltzmann distribution is one factor for this phenomenon, because it governs the populations of the different vibrational levels of the electronic states involved. The matrix polymer also influences the temperature dependency of the luminescence intensity. Generally, thermal quenching can be observed. This implies decreasing photoluminescence intensities and lifetimes with increasing temperature. Besides the factors discussed above,

nonradiative relaxation mechanisms become dominant at higher temperatures, because deactivating states are thermally activated. For example, the decreasing energy difference between the electronic states can be converted more easily to vibrational energy in the complex ligand or in the polymer matrix. Furthermore, the energy of the excited electronic state can be transferred to appropriate electronic states of the environment. Finally, the oxygen permeability of the matrix polymer increases with temperature. This results in a higher concentration of quenching oxygen molecules in the polymer binder at increased temperatures. Among the studied iridium(III) complexes, the green-emitting series that bears ppy ligands (**7c–9c**) show the highest temperature sensitivity. The calibration plots for the temperature response are nonlinear and can be fitted by an Arrhenius-type equation [Equation (4)]:<sup>[11]</sup>

$$\frac{1}{\tau} = k_0 + k_1 \cdot \exp\left(-\frac{\Delta E}{RT}\right) \quad (4)$$

in which  $\tau$  is the lifetime,  $k_0$  the temperature-independent decay rate for the deactivation of the excited state,  $k_1$  the pre-exponential factor,  $\Delta E$  the energy gap between the emitting level and an upper deactivating excited state,  $R$  the gas constant, and  $T$  the temperature in Kelvin. Figure 9 shows exemplary the Arrhenius fit of the thermal quenching of **8c** in PS at 1000 mbar air pressure with the fitting parameters:  $k_0 = 0.76 \mu\text{s}^{-1}$ ,  $k_1 = 19.5 \times 10^4 \mu\text{s}^{-1}$ , and  $\Delta E = 36.5 \text{ kJ mol}^{-1}$ . The correlation coefficient  $R^2$  for the fit is 0.994.

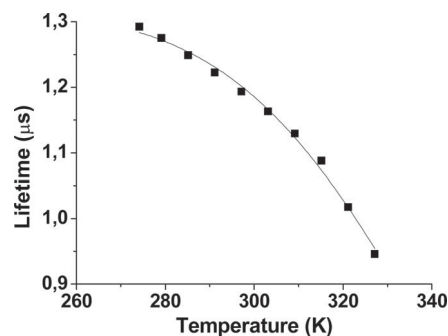


Figure 9. Temperature dependence of the luminescence lifetime of **8c** in PS at 1000 mbar and Arrhenius fit according to Equation (4) (straight line).

Generally, the temperature sensitivity of cyclometalated iridium(III) complexes is very low relative to other luminescent metal–ligand complexes. Hence, the temperature coefficients of typical luminescent indicators for  $T$  such as ruthenium and europium complexes<sup>[29,41,42]</sup> are up to two times higher than those of the green-emitting iridium(III) complexes described here. The exceptional property of the green emitters, particularly of **8c**, is their shortwave-emission wavelengths, which make them easy to combine with the numerous available red-emitting oxygen indicators for dual sensors. The high reproducibility and the very low standard deviations of the calibration plots and the broad dynamic range of the response are also advantageous.

## Conclusion

The design of a full series of neutral heteroleptic iridium(III) complexes equipped with 2-phenylpyridine, 2-(naphthalen-1-yl)pyridine, and 1-phenylisoquinoline as cyclometalating ligands was presented. To obtain unsymmetrical iridium(III) complexes, 2,2,6,6-tetramethylheptane-3,5-dione, 1-(9*H*-carbazol-9-yl)-5,5-dimethylhexane-2,4-dione, and 1-[3,6-bis(4-hexylphenyl)-9*H*-carbazol-9-yl]-5,5-dimethylhexane-2,4-dione were utilized as ancillary ligands. These serve to gradually increase the unsymmetrical architecture of the Ir<sup>III</sup> complexes. The photophysical and electrochemical properties of the Ir<sup>III</sup> complexes were investigated experimentally as well as theoretically by extensive  $\Delta$ -DFT and TD-DFT calculations on a selected set of Ir<sup>III</sup> structures. Moreover, the properties of the carefully designed heteroleptic iridium(III) complexes were compared to homoleptic Ir<sup>III</sup> complex structures that reveal symmetrical architectures. These consist of three equal cyclometalating ligands. The emission intensities of the two classes of heteroleptic Ir<sup>III</sup> complexes respond to changes of partial oxygen pressure and, to a lesser extent, to temperature changes. Notably, oxygen-sensitive Ir<sup>III</sup> emitters can be targeted due to the clear correlation of superior oxygen sensitivities with enhanced phosphorescence lifetimes.

**Supporting Information** (see footnote on the first page of this article): Experimental section of materials, instrumentation, calibration of pressure and temperature sensitivity, computational details, synthetic procedures, scheme for the synthesis of 2–5 (Figure S1), APLI-MS spectra, and references.

## Acknowledgments

E. H., M. S., and O. S. acknowledge the Deutsche Forschungsgemeinschaft (DFG) for financial support. This research forms part of the research program of the Dutch Polymer Institute (DPI) (project no. 629). D. E. acknowledges the Carl-Zeiss Stiftung for financial support. We thank Dr. Ulrich Henne and Dr. Christian Klein from the German Aerospace Center (DLR) in Göttingen for providing the calibration unit and Ulrich Lange for his assistance in the electrochemical measurements. E. H. acknowledges Professor Ullrich Scherf for granting access to the tools of the Macromolecular Chemistry at the University of Wuppertal (BUW) and Anke Helfer for TGA analysis; Melanie Dausend and Jürgen Dönecke (Organic Chemistry, BUW) for performing routine mass spectrometry as well as Ralf Radon (Analytical Chemistry, BUW) for elemental analysis. Professor Otto S. Wolfbeis is acknowledged for helpful comments.

- [1] K. Kalyanasundaram, M. Grätzel, *Coord. Chem. Rev.* **1977**, *77*, 347–414.
- [2] A. J. Lees, *Chem. Rev.* **1987**, *87*, 711–743.
- [3] S. Lamansky, P. Djurovich, D. Murphy, F. Abdel-Razzaq, R. Kwong, I. Tsyba, M. Bortz, B. Mui, R. Bau, M. E. Thompson, *Inorg. Chem.* **2001**, *40*, 1704–1711.
- [4] S. Lamansky, P. Djurovich, D. Murphy, F. Abdel-Razzaq, H.-E. Lee, C. Adachi, P. E. Burrows, S. R. Forrest, M. E. Thompson, *J. Am. Chem. Soc.* **2001**, *123*, 4304–4312.
- [5] H. Z. Xie, M. W. Liu, O. Y. Wang, X. H. Zhang, C. S. Lee, L. S. Hung, S. T. Lee, P. F. Teng, H. L. Kwong, H. Zheng, C. M. Che, *Adv. Mater.* **2001**, *13*, 1245–1248.
- [6] C. Adachi, M. A. Baldo, M. E. Thompson, S. R. Forrest, *J. Appl. Phys.* **2001**, *90*, 5048–5051.
- [7] E. Holder, B. M. W. Langeveld, U. S. Schubert, *Adv. Mater.* **2005**, *17*, 1109–1121.
- [8] L. H. Fischer, M. I. J. Stich, O. S. Wolfbeis, N. Tian, E. Holder, M. Schäferling, *Chem. Eur. J.* **2009**, *15*, 10857–10863.
- [9] Q. Zhao, M. Yu, L. Shi, S. Liu, C. Li, M. Shi, Z. Zhou, C. Huang, F. Li, *Organometallics* **2010**, *29*, 1085–1091.
- [10] K.-C. Tang, K. L. Liu, I.-C. Chen, *Chem. Phys. Lett.* **2004**, *386*, 437–441.
- [11] J. N. Demas, B. A. DeGraff, *Anal. Chem.* **1991**, *63*, 829A–837A.
- [12] Y. You, S. Y. Park, *Dalton Trans.* **2009**, 1267–1282.
- [13] T. Sajoto, P. I. Djurovich, A. Tamayo, M. Yousufuddin, R. Bau, M. E. Thompson, R. J. Holmes, S. R. Forrest, *Inorg. Chem.* **2005**, *44*, 7992–8003.
- [14] J. Qiao, L. Duan, L. Tang, L. He, L. Wang, Y. Qiu, *J. Mater. Chem.* **2009**, *19*, 6573–6580.
- [15] H.-S. Duan, P.-T. Chou, C.-C. Hsu, J.-Y. Hung, Y. Chi, *Inorg. Chem.* **2009**, *48*, 6501–6508.
- [16] C. S. K. Mak, D. Pentlehner, M. Stich, O. S. Wolfbeis, W. K. Chan, H. Yersin, *Chem. Mater.* **2009**, *21*, 2173–2175.
- [17] M. C. DeRosa, D. J. Hodgson, G. D. Enright, B. Dawson, C. E. B. Evans, R. J. Crutchley, *J. Am. Chem. Soc.* **2004**, *126*, 7619–7626.
- [18] L. Huynh, Z. Wang, J. Yang, V. Stoeva, A. Lough, I. Manners, M. A. Winnik, *Chem. Mater.* **2005**, *17*, 4765–4773.
- [19] S.-J. Liu, Q. Zhao, Q.-L. Fan, W. Huang, *Eur. J. Inorg. Chem.* **2008**, 2177–2185.
- [20] Y. Maegawa, Y. Goto, S. Inagaki, T. Shimada, *Tetrahedron Lett.* **2006**, *47*, 6957–6960.
- [21] Y. Morisaki, J. A. Fernandes, N. Wada, Y. Chujo, *J. Polym. Sci., Part A: Polym. Chem.* **2009**, *47*, 4279–4288.
- [22] M. Inoue, T. Suzuki, M. Nakada, *J. Am. Chem. Soc.* **2003**, *125*, 1140–1141.
- [23] U. Jacquemard, S. Routier, A. Tatibouet, J. Kluza, W. Laine, C. Bal, C. Bailly, J.-Y. Merour, *Org. Biomol. Chem.* **2004**, *2*, 1476–1483.
- [24] N. Tian, A. Thiessen, R. Schiewek, O. J. Schmitz, D. Hertel, K. Meerholz, E. Holder, *J. Org. Chem.* **2009**, *74*, 2718–2725.
- [25] M. Nonoyama, *Bull. Chem. Soc. Jpn.* **1974**, *47*, 767–768.
- [26] A. Dreuw, M. Head-Gordon, *Chem. Rev.* **2005**, *105*, 4009–4037.
- [27] B. Beyer, C. Ulbricht, D. Escudero, C. Friebe, A. Winter, L. González, U. S. Schubert, *Organometallics* **2009**, *28*, 5478–5488.
- [28] J. N. Demas, G. A. Crosby, *J. Phys. Chem.* **1971**, *75*, 991–1024.
- [29] M. I. Stich, O. S. Wolfbeis, “Fluorescence Sensing and Imaging Using Pressure-Sensitive Paints and Temperature-Sensitive Paints” in *Standardization and Quality Assurance in Fluorescence Measurements I* (Ed.: U. Resch-Genger), Springer Ser. Fluoresc., Springer Verlag Berlin Heidelberg, **2008**, vol 5, part E, 429–461.
- [30] C. Moore, S. P. Chan, J. N. Demas, B. A. DeGraff, *Appl. Spectrosc.* **2004**, *58*, 603–607.
- [31] G. Liebsch, I. Klimant, B. Frank, G. Holst, O. S. Wolfbeis, *Appl. Spectrosc.* **2000**, *54*, 548–559.
- [32] J. H. Bell, E. T. Schairer, L. A. Hand, R. D. Mehta, *Annu. Rev. Fluid Mech.* **2001**, *33*, 155–206.
- [33] E. Baranoff, J.-H. Yum, M. Graetzel, M. K. Nazeeruddin, *J. Organomet. Chem.* **2009**, *694*, 2661–2670.
- [34] Y. Amaoa, Y. Ishikawa, I. Okura, *Anal. Chim. Acta* **2001**, *445*, 177–182.
- [35] A. Medina-Castillo, J. Fernandez-Sanchez, C. Klein, M. K. Nazeeruddin, A. Segura-Carretero, A. Fernandez-Gutierrez, M. Graetzel, U. E. Spiqhiger-Keller, *Analyst* **2007**, *132*, 929–936.
- [36] S. M. Borisov, I. Klimant, *Anal. Chem.* **2007**, *79*, 7501–7590.
- [37] G. Di Marco, M. Lanza, M. Pieruccini, S. Campagna, *Adv. Mater.* **1996**, *8*, 576–580.

- [38] G. Di Marco, M. Lanza, A. Mamo, I. Stefio, C. Di Pietro, G. Romero, S. Campagna, *Anal. Chem.* **1998**, *70*, 5019–5023.
- [39] L. Huynh, J. Wang, V. Stoeva, A. Lough, I. Manners, M. A. Winnik, *Chem. Mater.* **2005**, *17*, 4765–4773.
- [40] J. Brandrup, E. H. Immergut, E. A. Grulke, *Polymer Handbook*, Wiley-VCH, **1999**.
- [41] M. E. Köse, B. F. Carroll, K. S. Schanze, *Langmuir* **2005**, *21*, 9121–9129.
- [42] B. Zelelow, G. E. Kahlil, G. Phelan, B. Carlson, M. Gouterman, J. B. Callis, L. R. Dalton, *Sens. Actuators B* **2003**, *96*, 304–314.

Received: June 1, 2010  
Published Online: August 26, 2010

**5.7 Selective carbon-carbon bond cleavage of 2,2'-dibromotolane  
via photolysis of its appropriate (diphosphine) $Pt^0$  com-  
plex in the solid state**

Petzold et al. *Dalton Trans.*, **2008**, 1979. Reproduced by permission of The Royal Society of Chemistry (RSC)

<http://pubs.rsc.org/en/content/articlepdf/2008/dt/b801230j?page=search>

# Selective carbon–carbon bond cleavage of 2,2′-dibromotolane *via* photolysis of its appropriate (diphosphine)Pt<sup>0</sup> complex in the solid state†

Holm Petzold,<sup>a</sup> Thomas Weisheit,<sup>a</sup> Helmar Görls,<sup>a</sup> Hergen Breitzke,<sup>b</sup> Gerd Buntkowsky,<sup>b</sup> Daniel Escudero,<sup>b</sup> Leticia González<sup>b</sup> and Wolfgang Weigand\*<sup>a</sup>

Received 22nd January 2008, Accepted 28th January 2008

First published as an Advance Article on the web 20th February 2008

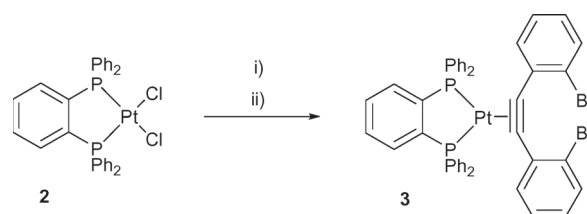
DOI: 10.1039/b801230j

By irradiating crystals of a (diphosphine)Pt<sup>0</sup> complex containing 2,2′-dibromotolane as ligand with sunlight, a rare example of selective carbon–carbon bond cleavage in the solid state could be observed.

In several homogeneous catalytic processes,<sup>1</sup> binding of a C,C bond (C,C = alkenes as well as alkynes) and oxidative addition of a substrate to a (diphosphine)M<sup>0</sup> (M = Ni, Pd, Pt) complex fragment are competitive key steps. In most instances oxidative addition of a low valent metal complex fragment into an aryl–halide bond is energetically favoured, but whether binding to a C,C bond or oxidative addition is kinetically favoured depends on the substrate and the complex fragment used. Whereas in the case of M = Pt the complex fragment binds strongly to C,C bonds,<sup>2</sup> similar palladium complexes are less stable. If olefin and aryl–halide functions are connected by a  $\pi$ -system, oxidative addition of the aryl–halide bond can follow binding of the complex fragment to the olefin, and “walking” along the  $\pi$ -system. Intermediates of these reactions have been isolated.<sup>3</sup> The reactivity of those complex fragments can be tuned by fixing the P–Pt–P angle. Whereas the linear complexes [Pt<sup>0</sup>(PR<sub>3</sub>)<sub>2</sub>] with bulky phosphine ligands have been isolated,<sup>4</sup> complex fragments with bidentate phosphino ligands are highly reactive and cannot be isolated.<sup>5</sup> However, their corresponding C,C adducts are very stable. Interestingly, theoretical investigations revealed that the strength of the metal–C,C bond itself is only slightly influenced by the P–Pt–P angle.<sup>6</sup> In contrast to the olefin complexes, in the corresponding alkyne complexes the (diphosphine)Pt<sup>0</sup> complex fragment can undergo insertion reactions into the aryl–alkynyl carbon–carbon bond caused by irradiation with UV-light, as reported for (diphosphine)( $\eta^2$ -tolane)Pt<sup>0</sup> complexes.<sup>7–9</sup> Very recently, this type of reaction has been used to investigate aryl–alkynyl bond formation and bond cleavage in tolane derivatives having fluoro and methyl substituted aryl groups bonded to the (dtbpe)Pt<sup>0</sup> complex fragment (dtbpe = bis(di-*tert*-butylphosphino)ethane).<sup>9</sup> So far, all these reactions have been carried out in solution.

To the best of our knowledge, here we report on the first example of a light induced highly selective insertion of a (diphosphine)Pt<sup>0</sup>

complex fragment into a carbon–carbon bond of a coordinated bromo substituted substrate in the solid state. In an extension of our recently published improved syntheses of Pt<sup>0</sup> complexes,<sup>10</sup> we have synthesized the complex [(dppbe)( $\eta^2$ -2,2′-dibromotolane)Pt<sup>0</sup>] (**3**) (dppbe = 1,2-bis(diphenylphosphino)benzene) in high yield by reaction of 2,2′-dibromotolane (**1**) with *in situ* generated Pt<sup>II</sup> hydrido species (Scheme 1).



Scheme 1 Synthesis of complex **3**; (i) NaBH<sub>4</sub> in CH<sub>2</sub>Cl<sub>2</sub>–EtOH; (ii) **1**.

The <sup>31</sup>P{<sup>1</sup>H} NMR spectrum of **3** shows a singlet at  $\delta = 51.3$  with <sup>195</sup>Pt-satellites (<sup>1</sup>J(P,Pt) = 3184 Hz). In the appropriate <sup>195</sup>Pt NMR spectrum a typical triplet at  $\delta = -4747$  appears (<sup>1</sup>J(Pt,P) = 3175 Hz). Solid state <sup>31</sup>P NMR-MAS spectra reveal that the P1 and P2 atoms are chemically and magnetically non-equivalent in the solid state. The spectra show two signals at  $\delta 47.8$  and  $38.2$  with <sup>195</sup>Pt-satellites (<sup>1</sup>J(P,Pt) = 3173(30) Hz). The IR absorption at  $\nu = 1780$  cm<sup>-1</sup> underlines the  $\eta^2$ -coordination of the tolane ligand to the platinum centre.<sup>11</sup>

The surprisingly stable complex **3** was crystallized from boiling toluene without any decomposition yielding yellow crystals suitable for X-ray analysis.‡ Interestingly, **3** proved to be remarkably stable under prolonged heating (200 h, 105 °C). The expected oxidative addition of one of the two carbon–bromine bonds was not observed. The X-ray structure of complex **3** is presented in Fig. 1. The bond lengths and angles accord with reported structures of similar tolane complexes.<sup>7,9–11</sup> The angle P1–Pt–P2 (84.90(7)°) is predetermined by the rigid bridged diphosphine ligand. Due to the  $\pi$ -back donation ( $d_{Pt} \rightarrow \pi^*_{alkyne}$ ) the bond C1–C2 is typically significantly longer (1.303(10) Å) than those in free tolane derivatives.<sup>2</sup> Bending of angles C1–C2–C3 and C2–C1–C9 about 35° aligns with the more alkene character of the C1–C2 bond. Repulsion of the two bromine atoms of the coordinated tolane ligand forces both phenyl groups to twist by approximately 70°.

By chance, we observed 25% conversion of **3** to a new complex (**4**) in the <sup>31</sup>P{<sup>1</sup>H} NMR spectrum of crystals of **3**, stored for several days in a Schlenk flask. The coupling constants of the new complex **4** (AB-spin system with <sup>2</sup>J(P,P) = 5.5 Hz and

<sup>a</sup>Institut für Anorganische und Analytische Chemie, Friedrich-Schiller-Universität, 07743, Jena, Germany. E-mail: c8wewo@uni-jena.de; Fax: +49-3641-948102; Tel: +49-3641-948160

<sup>b</sup>Institut für Physikalische Chemie, Friedrich-Schiller-Universität, 07743, Jena, Germany

† CCDC reference numbers 6660013, 660014 and 662326. For crystallographic data in CIF or other electronic format see DOI: 10.1039/b801230j Electronic supplementary information (ESI) available: Complete experimental procedures, spectroscopic and crystallographic data, and computational details. See DOI: 10.1039/b801230j

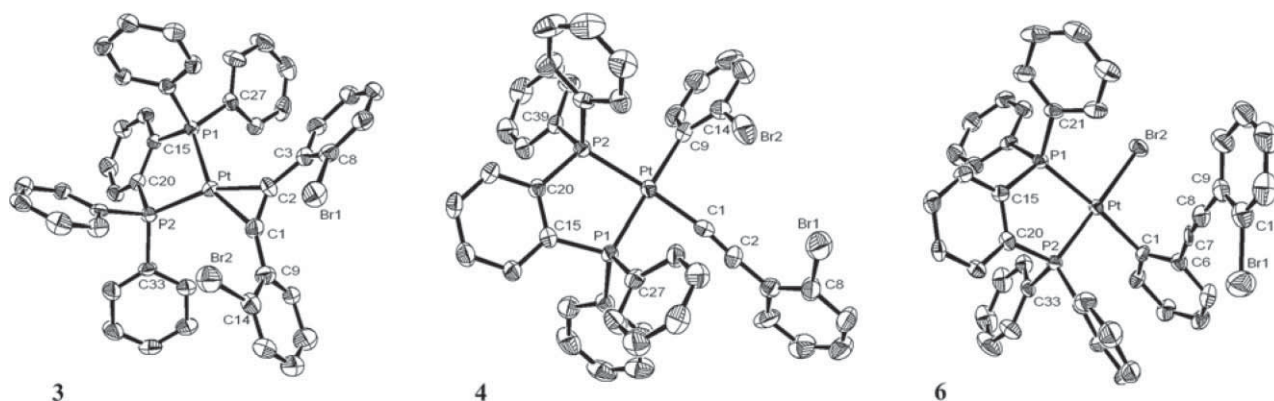
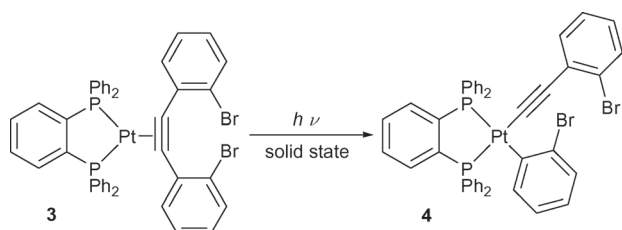


Fig. 1 Structures of complexes **3**, **4** and **6** with thermal ellipsoids at 50% probability level. Hydrogen atoms have been omitted for clarity.

$^1J(\text{P,Pt}) = 2473$  Hz and  $1767$  Hz, respectively) were in good agreement with those reported for alkynyl phenyl complexes synthesized by irradiating solutions of similar complexes containing the non-substituted tolane ligand with UV-light.<sup>7,8</sup>

Prolonged irradiation of compound **3** with sunlight afforded full conversion to complex **4**. It turned out that the exclusive reaction of **3** to **4** is only observed by irradiation of **3** in the solid state. In sunlight complex **3** is quantitatively converted to complex **4** obtained as a pale yellow powder within a few hours (Scheme 2).



Scheme 2 Selective formation of **4** via irradiation of crystals of **3** with sunlight.

The solution state  $^{195}\text{Pt}$  NMR spectrum shows a doublet of doublets at  $\delta -4703$  ( $^1J(\text{Pt,P}) = 2454$  Hz and  $1778$  Hz, respectively) according to an AB-spin system. In the IR spectrum of complex **4** an absorption at  $\nu = 2115$   $\text{cm}^{-1}$  is observed assigned to the presence of an end-on coordinated alkyne ligand. X-Ray single crystal analysis unambiguously confirmed the structure of **4** (Fig. 1). The arrangement of the ligands around the platinum centre is distorted square planar. The angle C1–Pt–C9 of  $89.7(3)^\circ$  is almost equal to the theoretical value of  $90^\circ$ , whereas the angle P1–Pt–P2 of  $86.41(7)^\circ$  is predetermined by the dppbe ligand. The length of the bond C1–C2 ( $1.203(10)$  Å) is in the typical range of a carbon–carbon triple bond.

Attempts to react the known complex  $[(\text{dppbe})(\eta^2\text{-tolane})\text{Pt}^0]$  (**5**)<sup>10</sup> under similar conditions revealed no reaction. No signals assignable to the insertion product were found in the NMR spectra.

A closer look at the molecular structures of **3** (Fig. 1) and **5** in the solid state reveals that the spatial orientation of the phenyl rings of the tolane ligands is the most obvious difference. The dihedral angles C1–C2–C3–C8 and C2–C1–C9–C14 are  $47.4(8)^\circ$  and  $111.4(8)^\circ$  respectively in complex **3** compared to  $9.6(3)^\circ$  and  $30.4(3)^\circ$  in **5**.<sup>10</sup>

The different photochemistry of complexes **3** and **5** can be rationalized in terms of the surprisingly very different UV/Vis absorption spectra. Time-dependent density functional theory (TD-DFT) simulated absorption spectra (computational details in ESI†) show a very different distribution of the main peaks as well as different electronic transitions (Fig. 2). Whereas in complex **5** the main electronic transitions correspond to  $\pi_{\text{alkyne}} \rightarrow \pi_{\text{phenyl}}^*$  transitions, in complex **3** the peaks are of  $d_{\text{Pt}} \rightarrow \pi_{\text{alkyne}}^*$  character. Depopulation of the  $d_{\text{Pt}}$  orbitals and concomitant population of the antibonding  $\pi_{\text{alkyne}}^*$  leads to a destabilization of the alkyne group via  $\pi$ -back donation, which promotes carbon–carbon bond cleavage and the consequential further rearrangement of **3** into **4**.

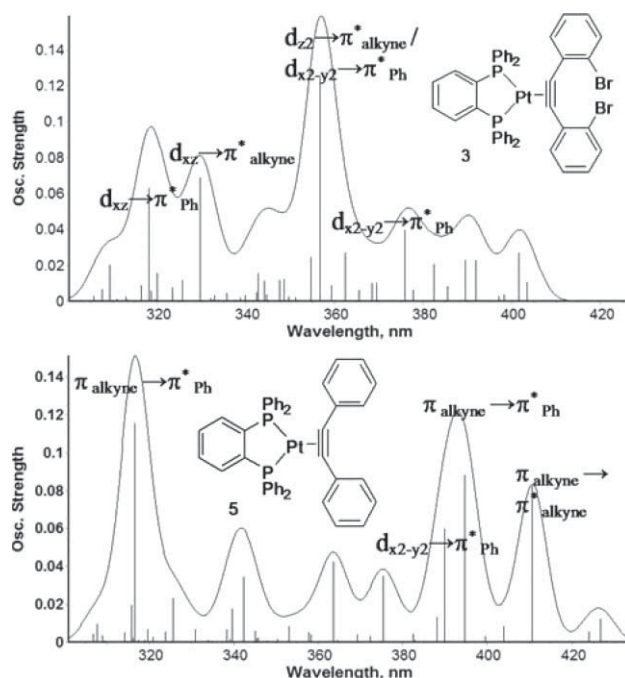
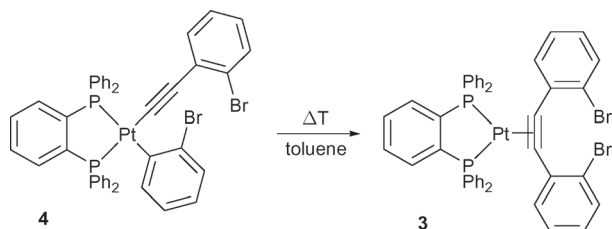


Fig. 2 TD-DFT theoretical absorption spectra of complexes **3** and **5** simulated with a Lorentzian band shape with a width at half height of 8 nm. Only the most intense transitions are assigned.

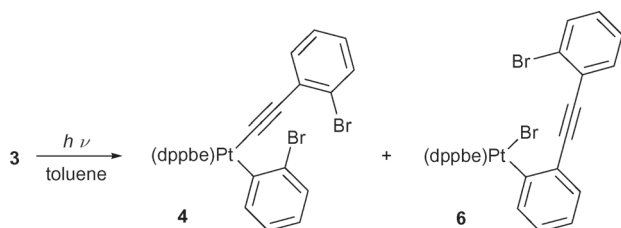
We also investigated whether this reaction is reversible under thermal conditions. As previously reported similar reactions are

uphill reactions,<sup>7,9</sup> hence they are reversible by prolonged heating of **4**. The activation energy is typically high in Pt<sup>II</sup> complexes, so that after 40 h heating at 105 °C only 30% of **4** has reverted to **3**. However, after 8 d 60% of **4** has reverted to **3** (Scheme 3). In order to prove if **3** and **4** are in thermal equilibrium a sample of **3** was heated under similar conditions, though no signals assignable to **4** have been observed in the <sup>31</sup>P{<sup>1</sup>H} NMR spectrum.



**Scheme 3** Thermal induced back reaction of complex **4** yielding **3**.

The high selectivity of the carbon–carbon bond cleavage is lost during irradiation in solution (Scheme 4). If **3** was dissolved in CH<sub>2</sub>Cl<sub>2</sub> and irradiated with sunlight for about 5 h the <sup>31</sup>P{<sup>1</sup>H} NMR spectrum of the crude product exhibited full conversion of complex **3**, however only a 1 : 1 mixture of **4** and a new complex (**6**) (AB-spin system with <sup>2</sup>J(P,P) = 4.7 Hz and <sup>1</sup>J(Pt,P) = 4064 Hz and 1749 Hz, respectively) was yielded.



**Scheme 4** Photolysis of **3** in solution leads to a 1 : 1 mixture of **4** and **6**.

Adjacent to the signal of **4**, a second signal ( $\delta = -4703$  (<sup>1</sup>J(Pt,P) = 3961 Hz and 1703 Hz, respectively) assigned to **6** was found in the <sup>195</sup>Pt NMR spectrum of this sample. Complex **6** was isolated by column chromatography and fully characterized. X-Ray single crystal analysis confirms the proposed structure of **6** (Fig. 1). The arrangement of the ligands around the platinum centre is distorted square planar. Due to the strong *trans*-influence of the phenyl ligand the Pt–P1 bond is significantly longer than Pt–P2.

Reduced time of irradiation of **3** in solution led to an incomplete conversion but still the described 1 : 1 mixture of **4** and **6** was yielded. Also the irradiation at lower temperatures (–78 °C) for about 3 h led to an incomplete conversion of **3** and the <sup>31</sup>P{<sup>1</sup>H} NMR spectrum did not reveal a preference for one of the products. Additionally, the thermal induced back reaction after irradiation of complex **3** in solution was investigated. In the <sup>31</sup>P{<sup>1</sup>H} NMR spectrum of this sample the signals of **4** disappeared and the singlet of **3** was observed again, whereas the signals of **6** still remained unchanged. This underlines the irreversible formation of **6** *via* photolysis of **3** in solution.

In conclusion, carbon–carbon bond cleavage in complex **3** occurs astonishingly fast and is highly selective during irradiation with sunlight in the solid state. Our current investigations show that these reactions are not restricted to bromine substituted substrates and the application of the dppbe ligand. The increased selectivity of this reaction in the solid state together with the improved and versatile synthesis may open many opportunities to investigate carbon–carbon bond cleavage, carbon–carbon bond formation on (diphosphine)Pt<sup>0</sup> complex fragments as well as the influence of different substitution patterns on activation energies and entropies.

## Acknowledgements

The Friedrich-Schiller-Universität Jena and the “Fundació Sa Nostra” is acknowledged for financial support (D.E.).

## Notes and references

‡ Crystal data for **3**: C<sub>44</sub>H<sub>32</sub>Br<sub>2</sub>P<sub>2</sub>Pt, *M* = 977.55 g mol<sup>-1</sup>, monoclinic, space group *P*2<sub>1</sub>/*n*, *a* = 11.1456(4), *b* = 22.1637(7), *c* = 15.3986(4) Å,  $\beta$  = 106.710(2)°, *V* = 3643.3(2) Å<sup>3</sup>, *T* = –90 °C, *Z* = 4, *R*<sub>int</sub> = 0.0899, *R*<sub>1</sub><sub>obs</sub> = 0.0544, *wR*<sub>2</sub><sub>obs</sub> = 0.1328, *R*<sub>1</sub><sub>all</sub> = 0.0800, *wR*<sub>2</sub><sub>all</sub> = 0.1463. Crystal data for **4**: C<sub>44</sub>H<sub>32</sub>Br<sub>2</sub>P<sub>2</sub>Pt, *M* = 977.55 g mol<sup>-1</sup>, triclinic, space group *P* $\bar{1}$ , *a* = 8.8929(3), *b* = 10.7362(4), *c* = 21.0258(7) Å,  $\alpha$  = 80.862(2)°,  $\beta$  = 88.179(2)°,  $\gamma$  = 68.483(2)°, *V* = 1843.09(11) Å<sup>3</sup>, *T* = –90 °C, *Z* = 2, *R*<sub>int</sub> = 0.0376, *R*<sub>1</sub><sub>obs</sub> = 0.0560, *wR*<sub>2</sub><sub>obs</sub> = 0.1408, *R*<sub>1</sub><sub>all</sub> = 0.0762, *wR*<sub>2</sub><sub>all</sub> = 0.1501. Crystal data for **6**: C<sub>44</sub>H<sub>32</sub>Br<sub>2</sub>P<sub>2</sub>Pt·1.5(C<sub>4</sub>H<sub>8</sub>O), *M* = 1085.70 g mol<sup>-1</sup>, monoclinic, space group *P*2<sub>1</sub>/*c*, *a* = 21.3703(6), *b* = 13.6258(3), *c* = 15.6040(3) Å,  $\beta$  = 93.290(1)°, *V* = 4536.20(18) Å<sup>3</sup>, *T* = –90 °C, *Z* = 4, *R*<sub>int</sub> = 0.0757, *R*<sub>1</sub><sub>obs</sub> = 0.0488, *wR*<sub>2</sub><sub>obs</sub> = 0.1059, *R*<sub>1</sub><sub>all</sub> = 0.0819, *wR*<sub>2</sub><sub>all</sub> = 0.1194.

- (a) For reviews, see: A. Zapf and M. Beller, *Chem. Commun.*, 2005, **4**, 431–440; P. Espinet and M. Echavarren, *Angew. Chem., Int. Ed.*, 2004, **43**, 4704–4734; M. E. van der Boom and D. Milstein, *Chem. Rev.*, 2003, **103**, 1759–1792; C. J. Elsevier, *Coord. Chem. Rev.*, 1999, **185**, 809–822; E. I. Negishi, *Handbook of Organopalladium Chemistry for Organic Synthesis* Wiley, New York, 2002; F. Diederich and P. J. Stang, *Metalcatalyzed Cross-Coupling Reactions*, Wiley-VCH, New York, 1998; L. S. Hegedus, *Transition Metals in the Synthesis of Complex Organic Molecules*, University Science Books, Mill Valley, CA, 1st edn, 1994.
- A. Fürstner and P. W. Davies, *Angew. Chem.*, 2007, **119**, 3478–3519, (*Angew. Chem., Int. Ed.*, 2007, **46**, 3410–3449).
- A. Lucassen, L. J. W. Shimon and M. E. van der Boom, *Organometallics*, 2006, **25**, 3308–3310; D. Strawser, A. Karton, O. V. Zenkina, M. A. Iron, L. J. W. Shimon, J. M. L. Martin and M. E. van der Boom, *J. Am. Chem. Soc.*, 2005, **127**, 9322–9323.
- S. Otsuka, T. Yoshida, M. Matsumoto and K. Nakatsu, *J. Am. Chem. Soc.*, 1976, **98**, 5850–5858.
- M. Hackett and G. M. Whitesides, *J. Am. Chem. Soc.*, 1988, **110**, 1449–1462; P. Hofmann, H. HeiB and G. Z. Müller, *Z. Naturforsch., B: Chem. Sci.*, 1987, **42**, 395–409; P. Hofmann, H. HeiB, P. Neiteler, G. Müller and J. Lachmann, *Angew. Chem.*, 1990, **102**, 935–938, (*Angew. Chem., Int. Ed.*, 1990, **29**, 880–882); P. Hofmann, L. A. Perez-Moya, M. E. Krause, O. Kumberger and G. Müller, *Z. Naturforsch., B: Chem. Sci.*, 1990, **45**, 898–908; M. Hackett, J. A. Ibers and G. M. Whitesides, *J. Am. Chem. Soc.*, 1988, **110**, 1436–1448.
- C. Massera and G. Frenking, *Organometallics*, 2003, **22**, 2758–2765.
- C. Müller, C. N. Iverson, R. J. Lachicotte and W. D. Jones, *J. Am. Chem. Soc.*, 2001, **123**, 9718–9719.
- G. K. Anderson, G. J. Lumetta and J. W. Siria, *J. Organomet. Chem.*, 1992, **434**, 253–259.
- A. Gunay and W. D. Jones, *J. Am. Chem. Soc.*, 2007, **129**, 8729–8735.
- H. Petzold, H. Görls and W. Weigand, *J. Organomet. Chem.*, 2007, **692**, 2736–2742.
- K. Zhang, J. Hu, K. C. Chan, K. Y. Wong and J. H. K. Yip, *Eur. J. Inorg. Chem.*, 384–393.

**5.8 Substituent effects on the light-induced C-C and C-Br bond activation in (bisphosphine)( $\eta^2$ -tolane)Pt<sup>0</sup> complexes. A TD-DFT study**

Escudero et al. *Phys. Chem. Chem. Phys.*, **2009**, *11*, 4593. Reproduced by permission of the PCCP Owner Societies.

<http://pubs.rsc.org/en/content/articlepdf/2009/cp/b903603b?page=search>



# Substituent effects on the light-induced C–C and C–Br bond activation in (bisphosphine)( $\eta^2$ -tolane)Pt<sup>0</sup> complexes. A TD-DFT study

Daniel Escudero,<sup>a</sup> Mariana Assmann,<sup>a</sup> Anne Pospiech,<sup>a</sup> Wolfgang Weigand<sup>b</sup> and Leticia González\*<sup>a</sup>

Received 20th February 2009, Accepted 14th April 2009

First published as an Advance Article on the web 5th May 2009

DOI: 10.1039/b903603b

A theoretical study of the steric and electronic effects of different substituents on the electronic ground and excited states of (bisphosphine)( $\eta^2$ -tolane)Pt<sup>0</sup> complexes is presented. A natural-bond-order (NBO) analysis has been performed to describe the bonding nature of the “hapto-like” coordination of the Pt atom to the alkyne bond of the tolane group. The results show an important contribution of the  $\pi$ -back donation in all complexes, amounting to half of the energy associated to the  $\sigma$ -bonding interaction. A TD-DFT study of the absorption spectra helps rationalizing the photochemistry of the complexes. Metal–ligand charge transfer (MLCT) transitions from the Pt atom to the alkyne are assigned as the photochemical “active” states responsible for C–C bond cleavage. Electronic excitations to the  $\sigma^*$  orbital of the C–Br bond are involved in C–Br bond activation. It is shown that both steric and electronic effects play an important role in determining the presence of these electronic excitations.

## 1. Introduction

Recently, we reported a rare example of selective carbon–carbon bond cleavage in the solid state induced by light.<sup>1</sup> A highly selective insertion of a (bisphosphine)Pt<sup>0</sup> complex fragment in a C–C bond of a coordinated bromo-substituted substrate was observed for the first time in the solid state under sunlight irradiation. In solution, C–Br and C–C insertion products were observed (see Scheme 1).<sup>1</sup>

Other similar photochemical reactions, like the insertion of the (bisphosphine)Pt<sup>0</sup> complex fragment into the aryl-ethynyl carbon–carbon bond with UV-light have only been observed in solution.<sup>2–4</sup> While in the case of Pt compounds the fragments bind strongly to C,C bonds,<sup>5</sup> similar palladium complexes are less stable. It has been stated that the reactivity of the Pt complexes can be tuned by fixing the P–Pt–P angle. However, previous theoretical studies of the equilibrium ground state geometries revealed that the strength of the metal–C,C bond is only slightly influenced by this P–Pt–P angle.<sup>6</sup> Interestingly, not all (bisphosphine)Pt<sup>0</sup> complexes show the same photochemistry. For instance, the unsubstituted (bisphosphine)( $\eta^2$ -tolane)Pt<sup>0</sup> complex **1** undergoes no photoreaction, either in solution or in the solid state, as compared with **2** (see Fig. 1). In our recent report<sup>1</sup> we ascribed the different photochemistry of complexes **1** and **2** to their very different UV–Vis absorption spectra: whilst in complex **1** the main electronic transitions correspond to excitations from the alkyne (alk) to the phenyl (ph) group ( $\pi_{\text{alk}} \rightarrow \pi_{\text{ph}}^*$ ) in complex **2** the bright states present metal-to-ligand charge transfer (MLCT) character from the 5d orbitals

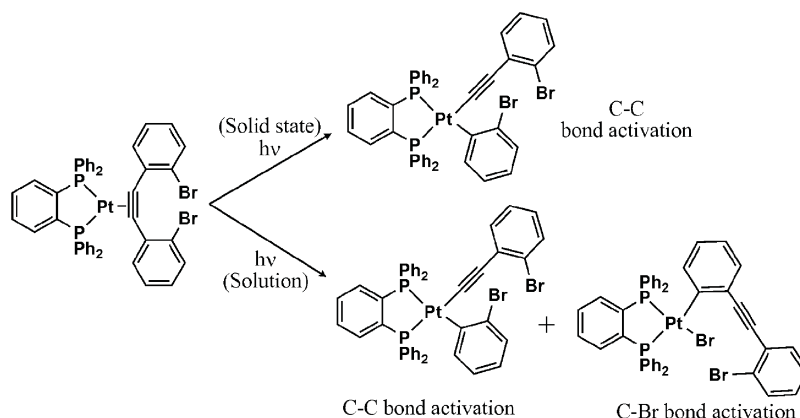
of the Pt to the alkyne group ( $d_{\text{Pt}} \rightarrow \pi_{\text{alk}}^*$ ). Depopulation of the  $d_{\text{Pt}}$  orbitals and concomitant population of the anti-bonding  $\pi_{\text{alk}}^*$  orbital leads to destabilization of the alkyne group, which by enhancing the  $\pi$ -back donation promotes the carbon–carbon bond cleavage and consequently the further rearrangement shown in Scheme 1. Whether this is only an electronic effect or a consequence of the steric constraints imposed by the substituent, is not clear. Thus, in this paper, we deal with the influence of substituting the tolane moiety with several ligands of different electronic nature (electron-donor/withdrawing) in several positions (*ortho/meta/para*). The different substituents serve to discern electronic from steric effects between the phenyl rings of the tolane moiety which can influence the photophysical properties of (bisphosphine)Pt<sup>0</sup> complexes and their photochemical reactivity.

Taking complex **1** [(dppbe)Pt( $\eta^2$ -tolane)] (dppbe = 1,2-bis(diphenylphosphino)benzene) as a reference, we consider complexes **2**, **3** and **4** by substituting some positions of the tolane group with an electron-withdrawing group (bromine), in *ortho* (2,2'-), *meta* (3,3'-) and *para* (4,4'-), see Scheme 2. Likewise, an analogous series of complexes **6**, **7** and **8** is obtained with an electron-donor group (hydroxyl) in the corresponding positions. In addition, the complex **5**, with Br in both *ortho*- and *para*-positions, [(dppbe)( $\eta^2$ -2,2',4,4'-tetra-bromotolane)Pt<sup>0</sup>] is also under study.

The rest of the paper is organized as follows. Section 2 gives details on the employed methods. Density functional theory (DFT) and its time-dependent version (TD-DFT) calculations provide helpful information on the structure and excited states involved in the UV–Vis absorption spectrum of the chosen complexes, respectively. Furthermore, natural-bond-order (NBO) analyses are performed to characterize the bonding nature of the complexes in the ground state geometries. Results and discussion are presented in section 3.

<sup>a</sup> Institut für Physikalische Chemie, Friedrich-Schiller-Universität, 07743 Jena, Germany. E-mail: leticia.gonzalez@uni-jena.de; Fax: +49-3641-948302; Tel: +49-3641-948300

<sup>b</sup> Institut für Anorganische und Analytische Chemie, Friedrich-Schiller-Universität, 07743 Jena, Germany



**Scheme 1** Selective C–C and C–Br activation in a (bisphosphine)( $\eta^2$ -tolane)Pt<sup>0</sup> complex upon light irradiation.

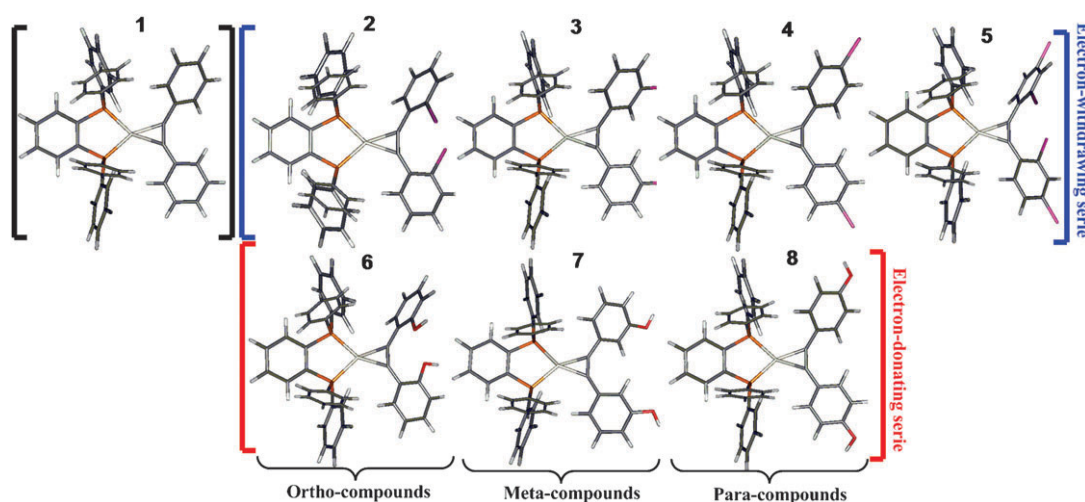
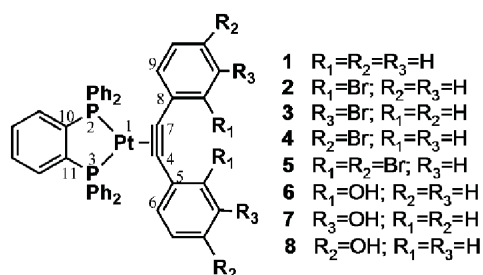


**Fig. 1** (Bisphosphine)( $\eta^2$ -tolane)Pt<sup>0</sup> complexes 1–8 defined in Scheme 2.



**Scheme 2** Systems studied in this work.

## 2. Theoretical methods

All the complexes have been optimized in the electronic ground state using DFT in its resolution of the identity (RI) version, *i.e.* RI-DFT.<sup>7</sup> The Becke exchange<sup>8</sup> and Perdew functional<sup>9</sup> have been combined with a polarized triple zeta basis set (TZVP) for all atoms. Relativistic effects have been considered for the Pt atom using the ECP-60-mwb Stuttgart/Dresden pseudopotential.<sup>10</sup> The UV–Vis absorption spectrum is calculated using TD-DFT<sup>11</sup> spanned over 85 states with the same functional and basis sets as mentioned above. These calculations were performed with the TURBOMOLE(V.5.10)<sup>12</sup> program package.

In order to estimate the energetic stabilization associated with the back-bonding interaction present in the complexes in the electronic ground state a second-order perturbative NBO<sup>13</sup> analysis has been carried out. The NBO analysis is based on a method which optimally expresses a given wavefunction into a localized one. The density matrix is first used to define a minimum basis of atomic orbitals in which the natural atomic orbitals (or NAOs) are expanded. These serve to expand natural hybrid orbitals (NHOs) which finally compose the orthonormal set of natural bond orbitals. The resulting orbitals are centered on one atom (“core” or “lone pair” orbitals), two atoms (“bond” orbitals), or three atoms (“delocalized bond over three centers” or “3C-bond” orbitals). The NBO orbitals are chosen such that the occupancy is maximized giving the most accurate possible Lewis-like picture, in which all orbitals have occupancies of exactly 2, 1, or 0. Deviations from the idealized localized Lewis structures indicate delocalization effects and back-bonding interactions. Such interactions can be measured with the stabilization energy  $E(2)$  computed by means of second-order perturbation theory,

$$E(2) = q_i \frac{F(i,j)^2}{\epsilon_i - \epsilon_j} \quad (1)$$

where  $q_i$  is the occupancy of the donor orbital,  $\varepsilon_i$ ,  $\varepsilon_j$  are the energies of the donor and acceptor orbitals and  $F(i,j)$  is the off-diagonal NBO Fock matrix element that measures how much energy is gained by sharing electrons between orbitals  $i$  and  $j$ . The NBO calculations were performed with the Gaussian03<sup>14</sup> program package using the B3LYP<sup>15,16</sup> functional and the same basis set as in the optimizations.

### 3. Results and discussion

#### 3.1 Equilibrium ground state properties

Fig. 1 shows the (biphosphine)( $\eta^2$ -tolane)Pt<sup>0</sup> complexes included in this study and Table 1 summarizes their more characteristic geometrical parameters. In general, the bond lengths and angles fit well with those of other tolane derivatives.<sup>4,17</sup> In the two compounds (**1** and **2**) for which experimental X-ray structures are available,<sup>1</sup> we observe good agreement with the predicted theoretical values. The employed functional overestimates in a small extent the bond distances related to the Pt coordination in comparison with the X-ray data. The largest deviations between theory and experiment are observed for the Pt<sub>1</sub>–P<sub>2</sub> and Pt<sub>1</sub>–P<sub>3</sub> bond distances, which are theoretically overestimated *ca.* 0.07–0.08 Å. The hapticity of Pt to the alkyne takes place with bond distances around 2.05 Å. The  $d_{4-7}$  bond lengths of all the complexes, ranging from 1.303 to 1.314 Å (see Table 1), are longer than the typical alkyne bond distances. Such distances are yet longer than those found in free tolane derivatives. This effect can be explained *via*  $\pi$ -back donation from the  $d_{Pt}$  to  $\pi^*_{alk}$  orbital upon coordinating to the Pt atom. As a consequence, the angles  $\alpha_{8-7-4}$  and  $\alpha_{7-4-5}$  deviate from the ideal angle of 180°, being constrained to values ranging from 140 to 153°, and thus tending to typical values for double bonds. The bending angle  $\alpha_{2-1-3}$  is predicted in all complexes, both experimentally and theoretically, close to the ideal angle of 90° that corresponds to a square planar coordination of the Pt

atom. The deviation from 90° is due to the intrinsic rigidity of the bridged biphosphine ligand, which is supposed to be responsible for the reactivity of this fragment in the electronic ground state (*vide supra*).<sup>6</sup>

The substituent effects of the electron-donor or electron-withdrawing groups are reflected in an elongation of the corresponding alkyne bond distances, regardless of the electronic nature of the substituent. As expected, however, the effects of substitution in different position (*ortho*-, *meta*- and *para*-), strongly affect the spatial orientation of the phenyl rings of the tolane ligand. For *ortho*-derivatives larger dihedral angles are obtained ( $\tau_{4-7-8-9}/\tau_{7-4-5-6}$ ) due to steric hindrance between both *ortho* substituents (compare structures **2**, **5**, and **6** with the rest of the compounds). Another steric consequence is that the two angles defining the  $\eta$ -coordination of the Pt to the tolane ligand ( $\alpha_{8-7-4}/\alpha_{7-4-5}$ ) are distinct in the *ortho*-derivatives but similar in the *meta*- and *para*-complexes. Consequently, the latter complexes and the unsubstituted (**1**) one are more symmetric than the *ortho*-derivatives (**2** and **6**).

The  $\pi$ -back donation interactions from the  $d_{Pt}$  to  $\pi^*_{alk}$  and the  $\sigma$ -bonding interactions in the electronic ground state can be quantified in terms of a NBO second-order perturbative energy analysis. Table 2 collects the stabilization energies  $E(2)$  for the main  $\sigma$ -bonding and  $\pi$ -back bonding interactions, as well as the occupancies of the  $\pi$ -orbitals involved in the alkyne triple bond. These values demonstrate the importance of these interactions in rationalizing the nature of the bonding in these complexes.

Due to the presence of occupied 5d orbitals with appropriate symmetry, a  $\pi$ -back donation from the  $d_{x^2-y^2}$  to the  $\pi^*_{alk}(3)$  orbital is possible (see NBO orbitals in Fig. 2). Such interactions have been also found for similar Pt complexes, both experimentally and theoretically.<sup>18</sup> As seen in Table 2, the corresponding NBO interaction energies range from 260 to 290 kJ/mol, indicating that this  $\pi$ -back donation is very effective in all studied complexes. For reference, these values

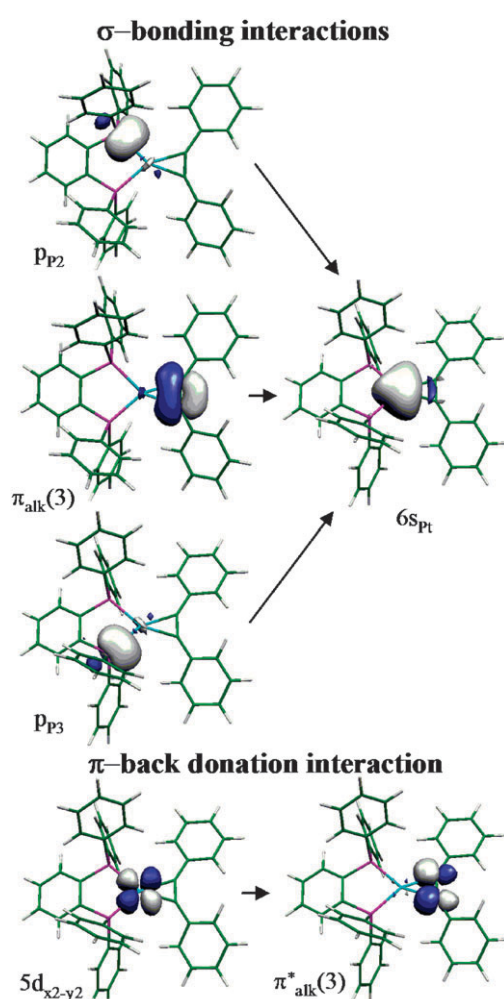
**Table 1** Main geometrical parameters of complexes **1–8**. Distances in ångströms and angles in degrees. See atom numbering in Scheme 2

Compound	$d_{1-2}/d_{1-3}$	$d_{1-7}/d_{1-4}$	$d_{2-10}/d_{3-11}$	$d_{4-7}$	$\alpha_{2-1-3}$	$\alpha_{8-7-4}/\alpha_{7-4-5}$	$\alpha_{10-2-1}/\alpha_{11-3-1}$	$\tau_{4-7-8-9}/\tau_{7-4-5-6}$
<b>1</b> (X-ray <sup>a</sup> )	2.260	2.038	1.827	1.300	86.6	146.4	109.1	30.5
	2.266	2.041	1.832			145.4	108.7	9.4
<b>1</b> (DFT)	2.332	2.096	1.870	1.303	85.5	150.7	108.1	29.4
	2.325	2.090	1.869			147.4	108.3	7.2
<b>2</b> (X-ray <sup>a</sup> )	2.247	2.034	1.839	1.303	84.9	146.3	108.5	47.2
	2.269	2.067	1.841			147.0	107.4	111.4
<b>2</b> (DFT)	2.323	2.075	1.861	1.314	84.9	151.2	110.1	57.2
	2.322	2.079	1.862			148.8	110.0	16.0
<b>3</b> (DFT)	2.335	2.083	1.869	1.311	84.9	147.5	108.4	33.2
	2.333	2.083	1.868			146.2	108.4	11.7
<b>4</b> (DFT)	2.333	2.082	1.869	1.312	85.0	147.5	108.5	29.6
	2.335	2.084	1.869			146.7	108.3	12.3
<b>5</b> (DFT)	2.333	2.096	1.871	1.304	85.5	150.4	108.1	83.6
	2.324	2.088	1.867			147.1	108.4	26.9
<b>6</b> (DFT)	2.327	2.095	1.873	1.303	85.7	149.1	108.3	75.3
	2.324	2.085	1.871			145.6	108.3	14.2
<b>7</b> (DFT)	2.334	2.082	1.869	1.310	84.6	147.5	108.3	25.9
	2.335	2.084	1.870			146.6	108.2	4.1
<b>8</b> (DFT)	2.333	2.083	1.869	1.311	84.6	147.7	108.4	25.2
	2.334	2.086	1.870			146.6	108.2	4.6

<sup>a</sup> Ref. 1.

**Table 2** NBO Analysis: total second-order perturbative interaction between the metal and alkyne/biphosphine ligands ( $E(2)$ ) in  $\text{kJ mol}^{-1}$ . Bond order occupancies of the  $\pi$  and  $\pi^*$  bonds of the alkyne moiety are also presented. The corresponding orbitals are shown in Fig. 2

Compound	$E(2)$ $d_{x^2-y^2} \rightarrow \pi^*_{\text{alk}}(3)$	$E(2)$ $\pi_{\text{alk}}(3) \rightarrow d/p_{\text{PT}}$	$E(2)$ $p_{\text{P}2} \rightarrow d/p_{\text{PT}}$	$E(2)$ $p_{\text{P}3} \rightarrow d/p_{\text{PT}}$	Occup. $\pi_{\text{alk}}(2)$	Occup. $\pi_{\text{alk}}(3)$	Occup. $\pi^*_{\text{alk}}(2)$	Occup. $\pi^*_{\text{alk}}(3)$
<b>1</b>	264	567	868	882	1.841	1.744	0.146	0.617
<b>2</b>	290	624	822	823	1.859	1.737	0.109	0.638
<b>3</b>	283	561	862	865	1.836	1.737	0.146	0.648
<b>4</b>	274	589	897	889	1.840	1.737	0.153	0.641
<b>5</b>	261	621	943	936	1.891	1.733	0.096	0.657
<b>6</b>	280	596	882	857	1.874	1.728	0.102	0.650
<b>7</b>	283	579	868	866	1.834	1.742	0.146	0.644
<b>8</b>	273	607	881	882	1.845	1.739	0.161	0.629

**Fig. 2** NBO orbitals of complex **1** involved in the main  $\sigma$ -bonding and  $\pi$ -back bonding interactions.

can be compared to the value of *ca.* 400  $\text{kJ/mol}$  obtained in ferrocene complexes for a similar  $\pi$ -back interaction.<sup>19</sup> The strength of this interaction is also reflected in the high occupancy of the  $\pi^*_{\text{alk}}(3)$  orbital. In contrast, the perpendicular antibonding  $\pi$  orbital,  $\pi^*_{\text{alk}}(2)$ , is barely occupied since it is much less involved in  $\pi$ -back bonding donation. As can be seen in Table 2, electron-donor or electron-withdrawing groups and its substitution pattern have little influence on this interaction.

Strong  $\sigma$ -bonding interactions up to *ca.* 620  $\text{kJ mol}^{-1}$  have been found from the  $\pi_{\text{alk}}(3)$  bond to the 6s orbital of the Pt atom. This strong interaction is also reflected in the depopulation of the  $\pi_{\text{alk}}(3)$  orbital as compared with that of  $\pi_{\text{alk}}(2)$ , see Table 2 and Fig. 2. As can be seen, this interaction in the *ortho*- and *para*-derivatives is similar and stronger than in the unsubstituted and *meta*-compounds. Other important  $\sigma$ -bonding interactions contributing to the overall stabilization of these complexes have been found between the phosphorus and Pt atoms ( $p_{\text{P}} \rightarrow 6s_{\text{Pt}}$ ). They amount up to 940  $\text{kJ mol}^{-1}$ , in the case of **5**, and *ca.* 60–120  $\text{kJ mol}^{-1}$  less for the other compounds (see Fig. 2 and Table 2). In view of the calculated  $\pi$ - and  $\sigma$ -interaction energies, it can be stated that in the hapto-like coordination of the Pt atom with the triple bond, globally, the latter acts as a two electron donor, but with an important contribution of the  $\pi$ -back bonding. Both  $\sigma$ -bonding and  $\pi$ -back donation interactions have an overall effect of weakening the triple bond, as reflected by the  $\pi_{\text{alk}}$  bond occupancies (see Table 2).

### 3.2 Excited state properties

The UV–Vis spectra of complexes **1** to **8** predicted with TD-DFT are shown in Fig. 3. In a previous study<sup>1</sup> we have reported a good correlation between the experimental and theoretical spectra of complexes **1** and **2**; therefore, we expect the same degree of accuracy in the rest of the studied compounds (**3–8**), for which no experimental data is available. Table 3 collects the most important electronic transitions contributing to the absorption spectra, selected according to their oscillator strength. The transitions are classified as MLCT, ligand–ligand charge transfer (LLCT), and intra-ligand (IL), which are the transitions dominating the spectra of all considered compounds. The orbitals involved in the Franck–Condon transitions—exemplarily for compound **1**—are shown in Fig. 4.

Analyzing the Kohn–Sham orbitals one can see that the HOMO is in all cases of  $\pi$  character and is mainly localized in the alkyne moiety (see exemplarily  $\pi_{\text{alk}}$  of complex **1** in Fig. 4). The 5d occupied orbitals of the Pt atom are deeper in energy, being the  $e_{\text{g}}$  set of orbitals located in the HOMO – 1 and HOMO – 2.

Also common to all complexes is that the LUMO is a  $\pi^*$  orbital localized in the dppbe ligand (see Fig. 4). The  $\pi^*_{\text{alk}}$  orbital, which is important for understanding the photochemistry of these compounds, is energetically shifted upon

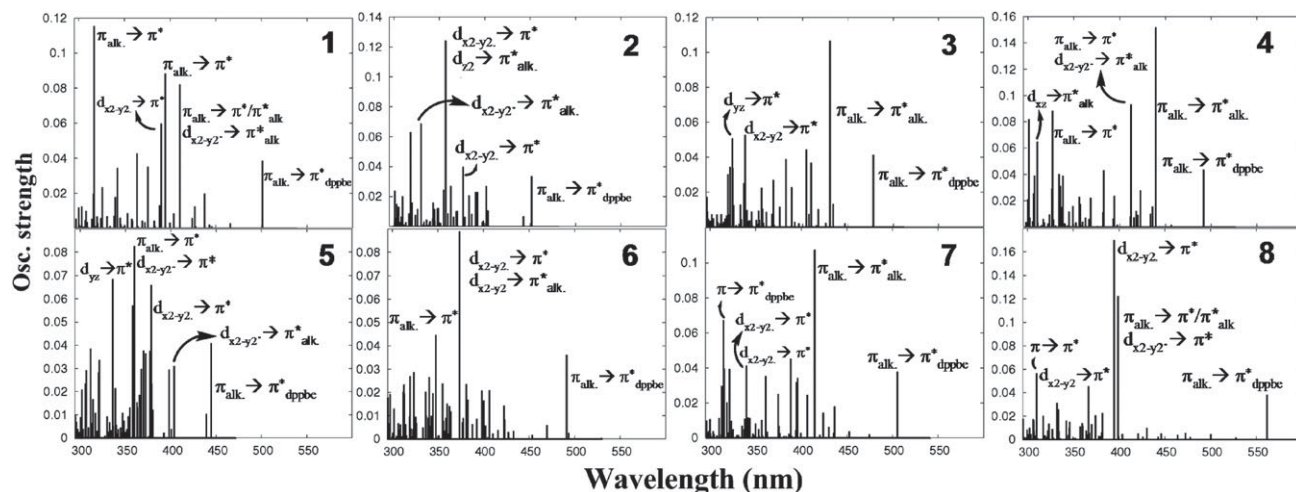


Fig. 3 TD-DFT UV-Vis spectra of complexes 1–8. The main electronic transitions are highlighted.

substituent effects. In the case of compound **1** it corresponds to the LUMO + 2, for it is somewhat stabilized due to conjugation through the phenyl rings of the tolane moiety (see Fig. 4). The same conjugation effect applies for the *meta*- and *para*-derivatives. In contrast, in the *ortho*-derivatives less conjugation is observed through the tolane moiety due to the twisting of the phenyl rings. Such effects shall influence the energy and oscillator strength of the MLCT  $d \rightarrow \pi^*_{\text{alk}}$  transitions of the different compounds. Indeed, the UV-Vis spectra of the compounds are more robust with respect to the substitution pattern than to the electronic nature of the substituent. As seen in Fig. 3, the spectra of the *ortho*-related compounds **2** and **6**, the *meta*-related compounds **3** and **7** and the *para*-related compounds **4** and **8** globally resemble one another in greater extent than within the electron-donating/withdrawing series (compare also **2**, **3**, **4**, and **6**, **7**, **8**, respectively).

Analyzing Table 3, it can be observed that the lowest-lying bright state is in all cases of LLCT character, corresponding to a transition from the alkyne moiety ( $\pi_{\text{alk}}$ ) to the dppbe ligand ( $\pi^*_{\text{dppbe}}$ ). Compared to the unsubstituted compound **1**, where this transition appears at 501 nm, this state is blue-shifted in the electron-withdrawing series **2**–**5**, predicted at 452, 478, and 492, and 444 nm, respectively. If we just focus on the substitution pattern, this transition appears in increasing energetic order for *ortho* > *meta* > *para*, both in the electron-withdrawing and electron-donating series.

In what the photochemical “active” states responsible for the photochemical reactivity are concerned, *i.e.* the MLCT transitions of  $d \rightarrow \pi^*_{\text{alk}}$  character, several interesting points arise. Such MLCT transitions are not found in the unsubstituted compound **1** (or are mainly dark states)<sup>1</sup> but they are in complex **2**, and also in the other derivatives. In particular, the  $d_{x2-y2} \rightarrow \pi^*_{\text{alk}}$  excitation, responsible for efficient  $\pi$ -back donation (see section 3.1), is present in all complexes. For complex **1**, it is predicted at 404 nm with a very small oscillator strength. For the electron-donating series this transition appears blue-shifted at 374, 396 and 374 nm, in complexes **6**, **7**, and **8**, respectively (see Table 3). Modest oscillator strengths are observed in all complexes,

except in the *ortho* derivative (**6**), where the wavefunction is mixed.

For the electron-withdrawing series a red-shift of this peak is observed in **3** and **4** with excitations at 417 and 423 nm, while in complexes **2** and **5** the excitations are slightly blue-shifted or unaffected, respectively. It should be noted that this transition is also mixed in the *para*-compound (see S<sub>7</sub> and S<sub>11</sub>).

Other strong MLCT transitions of  $d \rightarrow \pi^*_{\text{alk}}$  character are found in the electron-withdrawing series which are absent in the electron-donor and the unsubstituted compounds. Thus, for complexes **2** and **5** there are at least another two very intense  $d \rightarrow \pi^*_{\text{alk}}$  excitations (S<sub>24</sub> and S<sub>45</sub> for complex **2** and S<sub>43</sub> and S<sub>63</sub> for complex **5**, see Table 3). Interestingly, it seems that intense  $d \rightarrow \pi^*_{\text{alk}}$  transitions (as in **2** and **5**) are a consequence of both—steric hindrance between the phenyl rings due to *ortho*-substitution and electron-withdrawing groups. Therefore, we predict these two complexes should be most efficient in showing C–C activation. In complexes **3** and **4** there are another one (S<sub>38</sub>) and two (S<sub>36</sub> and S<sub>54</sub>)  $d \rightarrow \pi^*_{\text{alk}}$  transitions, respectively. In contrast, in the electron-rich compounds there are only few additional  $d \rightarrow \pi^*_{\text{alk}}$  transitions (see S<sub>56</sub> in **7** and S<sub>57</sub> in **8**). This indicates that complexes **6**–**8** should also be subject to C–C activation, albeit be less efficient than their electron-withdrawing counterparts. We note that MLCT transitions from the Pt to the bis-phosphine are very weak and thus they are not listed in Table 3.

In summary, both the pattern substitution and the electronic nature of the substituent play an important role in determining the presence or absence of the photochemical active MLCT states of  $d \rightarrow \pi^*_{\text{alk}}$  character. Obviously, upon sunlight irradiation depopulation of the  $d_{\text{Pt}}$  orbitals and concomitant population of the  $\pi^*_{\text{alk}}$  are the more efficient the more and brighter states are available. Such states promote an additional  $\pi$ -back bonding, hence weakening the haptic-coordination of the metal to the tolane group and then favoring the C–C insertion rearrangement products. Therefore, the electron-acceptor derivatives and the *ortho*-derivative **6**, due to the major number of  $d \rightarrow \pi^*_{\text{alk}}$  excitations

**Table 3** Main singlet excitations contributing to the absorption spectra of compounds **1–8** with excitation energies ( $\Delta E$ ) in nm and oscillator strengths  $f$ 

State	$\Delta E/\text{nm}$	$f$	Assignment	State	$\Delta E/\text{nm}$	$f$	Assignment
<b>1</b>							
S <sub>2</sub>	501	0.039	$\pi_{\text{alk}} \rightarrow \pi_{\text{dppbe}}^*$ (98%) LLCT	S <sub>15</sub>	390	0.060	$d_{x^2-y^2} \rightarrow \pi^*$ (95%) MLCT
S <sub>11</sub>	411	0.082	$\pi_{\text{alk}} \rightarrow \pi_{\text{alk}}^*$ (34%) IL $\pi_{\text{alk}} \rightarrow \pi^*$ (18%) LLCT $d_{x^2-y^2} \rightarrow \pi_{\text{alk}}^*$ (18%) MLCT	S <sub>23</sub>	364	0.043	$d_{x^2-y^2} \rightarrow \pi^*$ (92%) MLCT
S <sub>12</sub>	404	0.009	$d_{x^2-y^2} \rightarrow \pi_{\text{alk}}^*$ (63%) MLCT	S <sub>45</sub>	317	0.116	$\pi_{\text{alk}} \rightarrow \pi^*$ (58%) LLCT
S <sub>14</sub>	395	0.088	$\pi_{\text{alk}} \rightarrow \pi^*$ (65%) LLCT				
<b>2</b>							
S <sub>3</sub>	452	0.034	$\pi_{\text{alk}} \rightarrow \pi_{\text{dppbe}}^*$ (86%) LLCT	S <sub>45</sub>	330	0.069	$d_{xz} \rightarrow \pi_{\text{alk}}^*$ (69%) MLCT
S <sub>11</sub>	392	0.023	$d_{x^2-y^2} \rightarrow \pi_{\text{alk}}^*$ (65%) MLCT	S <sub>51</sub>	318	0.063	$d_{xz} \rightarrow \pi^*$ (34%) MLCT $d_{x^2-y^2} \rightarrow \pi^*$ (29%) MLCT
S <sub>18</sub>	376	0.040	$d_{x^2-y^2} \rightarrow \pi^*$ (88%) MLCT	S <sub>61</sub>	305	0.013	$\pi_{\text{alk}} \rightarrow \sigma_{\text{C-Br}}^*$ (43%) LLCT
S <sub>24</sub>	357	0.124	$d_{x^2-y^2} \rightarrow \pi^*$ (35%) MLCT $d_{z^2} \rightarrow \pi_{\text{alk}}^*$ (26%) MLCT				
<b>3</b>							
S <sub>2</sub>	478	0.041	$\pi_{\text{alk}} \rightarrow \pi_{\text{dppbe}}^*$ (81%) LLCT	S <sub>37</sub>	336	0.053	$d_{x^2-y^2} \rightarrow \pi^*$ (43%) MLCT
S <sub>5</sub>	430	0.107	$\pi_{\text{alk}} \rightarrow \pi_{\text{alk}}^*$ (50%) IL	S <sub>38</sub>	335	0.025	$d_{xz} \rightarrow \pi_{\text{alk}}^*$ (33%) MLCT
S <sub>7</sub>	417	0.010	$d_{x^2-y^2} \rightarrow \pi_{\text{alk}}^*$ (74%) MLCT	S <sub>48</sub>	322	0.051	$d_{yz} \rightarrow \pi^*$ (22%) LLCT $\pi_{\text{alk}} \rightarrow \pi^*$ (17%) MLCT
S <sub>12</sub>	404	0.044	$\pi_{\text{alk}} \rightarrow \pi^*$ (73%) LLCT	S <sub>61</sub>	291	0.035	$d_{yz} \rightarrow \pi^*$ (32%) MLCT $d_{x^2-y^2} \rightarrow \sigma_{\text{C-Br}}^*$ (30%) MLCT
<b>4</b>							
S <sub>2</sub>	492	0.041	$\pi_{\text{alk}} \rightarrow \pi_{\text{dppbe}}^*$ (81%) LLCT	S <sub>36</sub>	337	0.015	$d_{yz} \rightarrow \pi_{\text{alk}}^*$ (84%) MLCT
S <sub>4</sub>	439	0.152	$\pi_{\text{alk}} \rightarrow \pi_{\text{alk}}^*$ (50%) IL	S <sub>42</sub>	327	0.088	$\pi_{\text{alk}} \rightarrow \pi^*$ (38%) LLCT $d_{yz} \rightarrow \pi^*$ (22%) MLCT
S <sub>7</sub>	423	0.028	$\pi_{\text{alk}} \rightarrow \pi^*$ (53%) LLCT $d_{x^2-y^2} \rightarrow \pi_{\text{alk}}^*$ (41%) MLCT	S <sub>54</sub>	310	0.065	$d_{xz} \rightarrow \pi_{\text{alk}}^*$ (47%) MLCT
S <sub>11</sub>	412	0.093	$\pi_{\text{alk}} \rightarrow \pi^*$ (40%) LLCT $d_{x^2-y^2} \rightarrow \pi_{\text{alk}}^*$ (16%) MLCT	S <sub>61</sub>	305	0.082	$d_{x^2-y^2} \rightarrow \pi^*$ (54%) MLCT $d_{x^2-y^2} \rightarrow \sigma_{\text{C-Br}}^*$ (19%) MLCT
S <sub>16</sub>	383	0.043	$d_{x^2-y^2} \rightarrow \pi^*$ (98%) MLCT				
<b>5</b>							
S <sub>3</sub>	444	0.041	$\pi_{\text{alk}} \rightarrow \pi_{\text{dppbe}}^*$ (86%) LLCT	S <sub>26</sub>	355	0.013	$\pi_{\text{alk}} \rightarrow \sigma_{\text{C-Br}}^*$ (49%) LLCT
S <sub>7</sub>	404	0.031	$d_{x^2-y^2} \rightarrow \pi_{\text{alk}}^*$ (63%) MLCT	S <sub>41</sub>	339	0.022	$d_{yz} \rightarrow \pi_{\text{alk}}^*$ (63%) MLCT
S <sub>15</sub>	378	0.066	$d_{x^2-y^2} \rightarrow \pi^*$ (44%) MLCT	S <sub>43</sub>	336	0.069	$d_{yz} \rightarrow \pi^*$ (50%) MLCT $d_{yz} \rightarrow \pi_{\text{alk}}^*$ (17%) MLCT
S <sub>16</sub>	377	0.038	$\pi_{\text{alk}} \rightarrow \pi^*$ (47%) LLCT	S <sub>59</sub>	314	0.017	$d_{xz} \rightarrow \pi_{\text{alk}}^*$ (60%) MLCT
S <sub>19</sub>	370	0.038	$\pi_{\text{alk}} \rightarrow \pi^*$ (45%) LLCT	S <sub>63</sub>	311	0.039	$d_{xz} \rightarrow \pi^*$ (36%) MLCT $d_{xz} \rightarrow \pi_{\text{alk}}^*$ (22%) MLCT
S <sub>24</sub>	360	0.083	$\pi_{\text{alk}} \rightarrow \pi^*$ (32%) LLCT $d_{x^2-y^2} \rightarrow \pi^*$ (26%) MLCT				
<b>6</b>							
S <sub>3</sub>	491	0.036	$\pi_{\text{alk}} \rightarrow \pi_{\text{dppbe}}^*$ (87%) LLCT	S <sub>48</sub>	348	0.045	$\pi_{\text{alk}} \rightarrow \pi^*$ (53%) LLCT
S <sub>25</sub>	374	0.089	$d_{x^2-y^2} \rightarrow \pi^*$ (43%) MLCT $d_{x^2-y^2} \rightarrow \pi_{\text{alk}}^*$ (38%) MLCT				
<b>7</b>							
S <sub>2</sub>	505	0.038	$\pi_{\text{alk}} \rightarrow \pi_{\text{dppbe}}^*$ (99%) LLCT	S <sub>41</sub>	340	0.041	$d_{x^2-y^2} \rightarrow \pi^*$ (80%) MLCT
S <sub>11</sub>	415	0.107	$\pi_{\text{alk}} \rightarrow \pi_{\text{alk}}^*$ (45%) IL	S <sub>56</sub>	321	0.039	$d_{xz} \rightarrow \pi_{\text{alk}}^*$ (41%) MLCT
S <sub>14</sub>	396	0.034	$d_{x^2-y^2} \rightarrow \pi_{\text{alk}}^*$ (46%) MLCT $\pi_{\text{alk}} \rightarrow \pi^*$ (38%) LLCT	S <sub>60</sub>	315	0.040	$\pi \rightarrow \pi_{\text{dppbe}}^*$ (76%) LLCT
S <sub>18</sub>	388	0.045	$d_{x^2-y^2} \rightarrow \pi^*$ (93%) MLCT	S <sub>62</sub>	314	0.067	$\pi \rightarrow \pi_{\text{dppbe}}^*$ (96%) LLCT
<b>8</b>							
S <sub>2</sub>	562	0.038	$\pi_{\text{alk}} \rightarrow \pi_{\text{dppbe}}^*$ (99%) LLCT	S <sub>24</sub>	367	0.045	$d_{x^2-y^2} \rightarrow \pi^*$ (56%) MLCT
S <sub>15</sub>	399	0.122	$\pi_{\text{alk}} \rightarrow \pi_{\text{alk}}^*$ (26%) IL $d_{x^2-y^2} \rightarrow \pi^*$ (25%) MLCT $\pi_{\text{alk}} \rightarrow \pi^*$ (18%) LLCT	S <sub>56</sub>	310	0.057	$\pi \rightarrow \pi^*$ (69%) LLCT
S <sub>16</sub>	394	0.170	$d_{x^2-y^2} \rightarrow \pi^*$ (72%) MLCT	S <sub>57</sub>	310	0.038	$d_{xz} \rightarrow \pi_{\text{alk}}^*$ (77%) MLCT
S <sub>21</sub>	374	0.021	$d_{x^2-y^2} \rightarrow \pi_{\text{alk}}^*$ (92%) MLCT				

and the very strong  $d_{x^2-y^2} \rightarrow \pi_{\text{alk}}^*$  transition, respectively, should yield more efficiently C–C rearrangement products than complexes **1**, **7** and **8**, which might not react or present less C–C bond cleavage.

Besides C–C bond activation, C–Br bond cleavage has been observed experimentally in solution in compound **2** while in the solid state only the C–C insertion product was achieved (recall Scheme 1).<sup>1</sup> A plausible reason why

C–Br activation does not occur in the solid state can be derived by analyzing the crystal structure<sup>1</sup> of complex **2**. In view of the large distances found in the crystal between the Br and the Pt atoms it is highly unlikely that the products resulting from C–Br insertion are achieved either *via* unimolecular or bimolecular processes. In solution, however, mobility allows for a bimolecular approach. From the electronic point of view, this activation requires

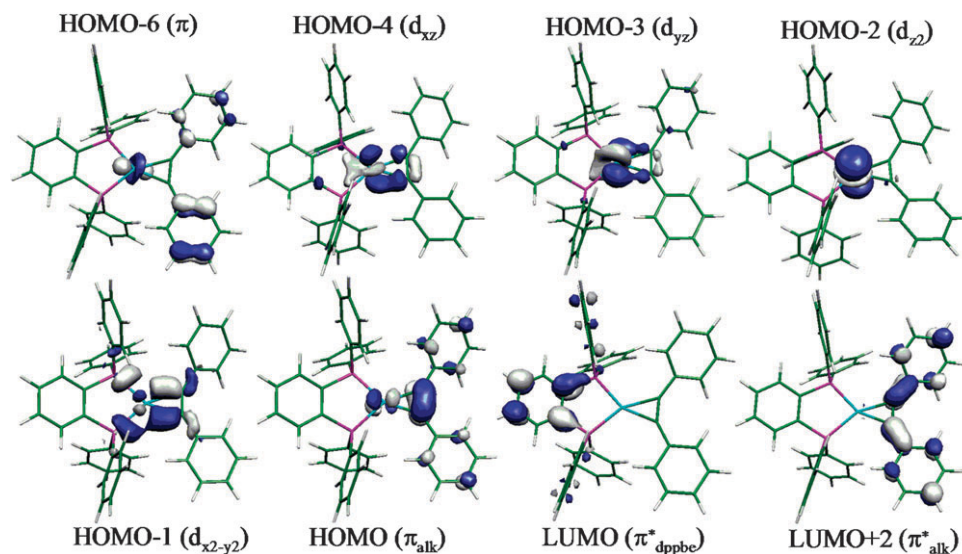


Fig. 4 Selected Kohn–Sham orbitals of complex **1**.

C–C activation, plus a weakening of the C–Br bond after light irradiation, and this can be rationalized looking for excitations to the  $\sigma^*_{\text{C-Br}}$  orbital. As can be seen in Table 3, LLCT and MLCT transitions with  $\pi_{\text{alk}} \rightarrow \sigma^*_{\text{C-Br}}$  and  $d_{x^2-y^2} \rightarrow \sigma^*_{\text{C-Br}}$  character are present in complexes **2** and **5** and **3** and **4**, respectively. Especially, in complex **4**, this transition is rather strong. Therefore, we predict that this complex is prone to efficient C–Br activation.

### 3. Conclusions

In this paper, the influence of electron-donor and electron-withdrawing substituents as well as the *ortho*, *meta*, and *para*-substitution pattern have been analysed on the electronic ground and excited states of (bisphosphine)Pt<sup>0</sup> complexes. The nature of the bonding interactions in the different derivatives has been described with the help of the NBO method. Based on the second-order perturbative stabilization energies, it can be concluded that the  $\pi$ -back bonding interactions are very important for describing the haptic-like coordination of the Pt atom to the alkyne, amounting to half of the energy associated with the  $\sigma$ -bonding interactions. No remarkable substitution effects have been found in the bonding of the herein studied complexes.

The UV/Vis absorption spectra predicted with TD-DFT are mainly characterized by MLCT, LLCT and IL transitions. The  $d \rightarrow \pi^*_{\text{alk}}$  and  $d/\pi_{\text{alk}} \rightarrow \sigma^*_{\text{C-Br}}$  transitions have been assigned to be responsible for C–C and C–Br activation, respectively. Our study shows that for the chosen complexes, both the electronic nature of the substituent as well as the steric effects between the phenyl rings of the tolane moiety contribute to the appearance of the  $d \rightarrow \pi^*_{\text{alk}}$  bands, and the consequent tuning of the photochemical reactivity. Since the  $d \rightarrow \pi^*_{\text{alk}}$  bands are predominant and stronger in complexes with electron-withdrawing substituents at *ortho*-positions, it is expected that such complexes should undergo a C–C bond cleavage to a major extent.

### Acknowledgements

The authors acknowledge fruitful discussions with Thomas Weisheit and financial support from the Carl-Zeiss Stiftung (D.E) and the Friedrich-Schiller-Universität Jena.

### References

- H. Petzold, T. Weisheit, H. Görls, H. Breitzke, G. Buntkowsky, D. Escudero, L. González and W. Weigand, *Dalton Trans.*, 2008, 1979–1981.
- C. Müller, C. N. Iverson, R. J. Lachicotte and W. D. Jones, *J. Am. Chem. Soc.*, 2001, **123**, 9718–9719.
- G. K. Anderson, G. J. Lumetta and J. W. Siria, *J. Organomet. Chem.*, 1992, **434**, 253–259.
- A. Gunay and W. D. Jones, *J. Am. Chem. Soc.*, 2007, **129**, 8729–8735.
- A. Fürstner and P. W. Davies, *Angew. Chem.*, 2007, **119**, 3478–3519; A. Fürstner and P. W. Davies, *Angew. Chem., Int. Ed.*, 2007, **46**, 3410–3449.
- C. Massera and G. Frenking, *Organometallics*, 2003, **22**, 2758–2765.
- K. Eichkorn, O. Treutler, H. Öhm, M. Häser and R. Ahlrichs, *Chem. Phys. Lett.*, 1995, **240**, 283.
- A. D. Becke, *Phys. Rev. A*, 1998, **38**, 3098.
- J. P. Perdew, *Phys. Rev. B*, 1986, **33**, 8822.
- D. Andrae, U. Häussermann, M. Dolg, H. Stoll and H. Preuss, *Theor. Chim. Acta*, 1990, **77**, 123.
- M. E. Casida, *Recent Advances in Density Functional Methods. Part I*, World Scientific, Singapore, 1995.
- R. Ahlrichs, M. Bär, M. Häser, H. Horn and C. Kölmel, *Chem. Phys. Lett.*, 1989, **162**, 165.
- F. Weinhold and C. R. Landis, *Valence and Bonding: A Natural Bond Orbital Donor–Acceptor Perspective*, Cambridge University Press, 2005.
- M. J. Frisch, G. W. Trucks, H. B. Schlegel, G. E. Scuseria, M. A. Robb, J. R. Cheeseman, J. A. Montgomery, Jr., T. Vreven, K. N. Kudin, J. C. Burant, J. M. Millam, S. S. Iyengar, J. Tomasi, V. Barone, B. Mennucci, M. Cossi, G. Scalmani, N. Rega, G. A. Petersson, H. Nakatsuji, M. Hada, M. Ehara, K. Toyota, R. Fukuda, J. Hasegawa, M. Ishida, T. Nakajima, Y. Honda, O. Kitao, H. Nakai, M. Klene, X. Li, J. E. Knox, H. P. Hratchian, J. B. Cross, V. Bakken, C. Adamo, J. Jaramillo, R. Gomperts, R. E. Stratmann, O. Yazyev, A. J. Austin, R. Cammi, C. Pomelli, J. Ochterski, P. Y. Ayala, K. Morokuma, G. A. Voth, P. Salvador, J. J. Dannenberg,

- 
- V. G. Zakrzewski, S. Dapprich, A. D. Daniels, M. C. Strain, O. Farkas, D. K. Malick, A. D. Rabuck, K. Raghavachari, J. B. Foresman, J. V. Ortiz, Q. Cui, A. G. Baboul, S. Clifford, J. Cioslowski, B. B. Stefanov, G. Liu, A. Liashenko, P. Piskorz, I. Komaromi, R. L. Martin, D. J. Fox, T. Keith, M. A. Al-Laham, C. Y. Peng, A. Nanayakkara, M. Challacombe, P. M. W. Gill, B. G. Johnson, W. Chen, M. W. Wong, C. Gonzalez and J. A. Pople, *GAUSSIAN 03 (Revision C.02)*, Gaussian, Inc., Wallingford, CT, 2004.
- 15 A. D. Becke, *J. Chem. Phys.*, 1993, **98**, 5648–5652.  
16 C. Lee, W. Yang and R. G. Parr, *Phys. Rev. B*, 1988, **37**, 785–789.  
17 H. Petzold, H. Görls and W. Weigand, *J. Organomet. Chem.*, 2007, **692**, 2736–2742.  
18 L. Cavalla, A. Macchioni, C. Zuccaccia, D. Zuccaccia, I. Orabona and F. Ruffo, *Organometallics*, 2004, **23**, 2137–2145.  
19 G. Zhang, H. Zhang, M. Sun, Y. Liu, X. Pang, X. Yu, B. Liu and Z. Li, *J. Comput. Chem.*, 2007, **28**, 2260–2274.



**5.9 Photochemical behavior of (diphosphine)( $\eta^2$ -tolane)Pt<sup>0</sup> complexes.  
Part A: Experimental considerations in solution and in the solid state**

---

**5.9 Photochemical behavior of (diphosphine)( $\eta^2$ -tolane)Pt<sup>0</sup>  
complexes. Part A: Experimental considerations in  
solution and in the solid state**

Weisheit et al. *Dalton Trans.*, **2010**, *39*, 9493. Reproduced by permission of The Royal Society of Chemistry (RSC)

<http://pubs.rsc.org/en/content/articlepdf/2010/dt/b925562a?page=search>

# Photochemical behavior of (diphosphine)( $\eta^2$ -tolane)Pt<sup>0</sup> complexes. Part A: Experimental considerations in solution and in the solid state†

Thomas Weisheit,<sup>a</sup> Daniel Escudero,<sup>b</sup> Holm Petzold,<sup>c</sup> Helmar Görls,<sup>a</sup> Leticia González<sup>b</sup> and Wolfgang Weigand<sup>\*a</sup>

Received 9th December 2009, Accepted 13th August 2010

DOI: 10.1039/b925562a

A series of various (diphosphine)( $\eta^2$ -tolane)Pt<sup>0</sup> complexes exhibiting manifold substitution pattern of the tolane ligand (**5a–g**) and different rigid diphosphines defining various bite angles at the Pt center (**9a–b**) have been synthesized. All compounds were isolated and characterized by means of spectroscopic methods and additionally by X-ray structure determination (**5a–e**, **9a–b**). In view of potential C<sub>aryl</sub>–C<sub>ethynyl</sub> bond activation, we investigated their photochemical behavior in the solid state as well as in solution by irradiating with sunlight. The reactivity towards C<sub>aryl</sub>–C<sub>ethynyl</sub> bond activation in the crystalline state and in solution is discussed in relation to substituents attached to the tolane ligand and on the extent of the torsion of its phenyl rings. Complexes **5a–c** and **9a** either bearing electron withdrawing bromides or possessing a large dihedral angle of the phenyl rings, showed selective oxidative addition of the C<sub>aryl</sub>–C<sub>ethynyl</sub> bond to the Pt center in the solid state, yielding complexes **6a–c** and **10a**, respectively. In contrast, **5d–f** and **9b** proved to be unreactive under similar conditions because of their electron donating methoxy groups as well as the reduced twisting of their phenyl or pyridyl moieties of the tolane ligands. Irradiation of complexes **5a** and **5b** with sunlight in solution revealed the formation of the appropriate C–Br activated compounds **7a** and **7b** along with **6a** and **6b** in a 1 : 1 mixture. The observed photochemical C<sub>aryl</sub>–C<sub>ethynyl</sub> bond activation is reversible under thermal conditions, regaining the appropriate Pt<sup>0</sup> complexes by reductive elimination.

## Introduction

The activation of carbon–carbon bonds by using metal complexes in a homogeneous medium has attracted much interest particular in view of applications in petroleum chemistry.<sup>1–3</sup> During the last decades some examples for C–C bond activation by means of oxidative addition on a metal complex have been reported. Most of them are driven by relief of ring strain<sup>2–4</sup> in the corresponding insertion products or the fact that the C–C bond is forced to react with the metal center by proximity.<sup>3,5,6</sup> On the other hand, only a few examples for the activation of unstrained C–C bonds are known so far.<sup>6,7</sup> The principal reasons for this scarcity of examples might be the more favorable C–H bond activation due to the higher activation barrier of C–C bonds<sup>8</sup> and the considerably increased stability of the resulting metal–hydrogen bond in comparison with the corresponding metal–carbon bond.<sup>9</sup> However, C–C bond cleavage also depends on the nature of the respective C–C bond. Although C<sub>aryl</sub>–C<sub>aryl</sub> or C<sub>aryl</sub>–C<sub>alkyl</sub> bonds are generally stronger than C<sub>alkyl</sub>–C<sub>alkyl</sub> bonds their activation by rhodium or iridium complexes

has been reported.<sup>9,10</sup> The determined metal–C<sub>aryl</sub> bond strength of the resulting product, which is significantly higher than that of a metal–C<sub>alkyl</sub> bond, was supposed to be the driving force of these reactions.

However, beside the thermal activation of inactivated C–C bonds, Jones *et al.* reported on the oxidative addition of Pt<sup>0</sup> complex fragments to the C<sub>aryl</sub>–C<sub>ethynyl</sub> bond of coordinated diphenylacetylene derivatives (tolanes) *via* irradiating solutions of these complexes with UV light.<sup>11,12</sup> Interestingly, C–C bond cleavage in this system is only observed under photochemical conditions and not *via* thermal treatment of the Pt<sup>0</sup> complexes.

Therefore, the framework of a tolane ligand coordinated to a (diphosphine)Pt<sup>0</sup> complex fragment is estimated to be an efficient system for studying the driving force of this type of photochemical C–C bond activation. In this context, Jones *et al.* investigated the influence of the substitution pattern of the tolane ligand on the photochemical reactivity of its appropriate platinum complex.<sup>12</sup> It was shown that stabilization of the addition products is achieved when electron withdrawing groups were introduced and therefore, the activation energy of the bond cleavage can be tuned by the choice of the acetylenic ligand.

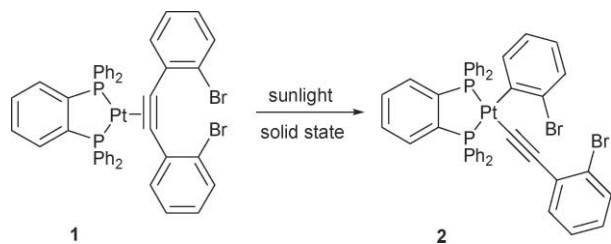
Recently we could show that the aforementioned C–C bond activation is not restricted to the solution state. By irradiating crystals of (dppbe)( $\eta^2$ -2,2'-dibromotolane)Pt<sup>0</sup> (**1**) with sunlight a highly selective insertion of the (dppbe)Pt moiety into the C<sub>aryl</sub>–C<sub>ethynyl</sub> bond was observed (Scheme 1).<sup>13</sup> The different photochemistry of this complex compared to that of (dppbe)( $\eta^2$ -tolane)Pt<sup>0</sup> was explained by remarkable differences in their calculated UV/Vis spectra and electronic transitions included therein.<sup>13</sup> A conspicuous feature of **1** in the solid state is the twisting of

<sup>a</sup>Institut für Anorganische und Analytische Chemie, Friedrich-Schiller-Universität Jena, August-Bebel-Str. 2, 07743, Jena, Germany. E-mail: wolfgang.weigand@uni-jena.de; Fax: +49-3641-948102; Tel: +49-3641-948160

<sup>b</sup>Institut für Physikalische Chemie, Friedrich-Schiller-Universität Jena, Helmholzweg 4, 807743, Jena, Germany

<sup>c</sup>TU Chemnitz, Institut für Chemie, Straße der Nationen 62, 09111, Chemnitz, Germany

† CCDC reference numbers 743160 (for **5a**), 743161 (for **5b**), 743162 (for **5c**), 743163 (for **5d**), 743164 (for **5e**), 743165 (for **6b**), 743166 (for **7b**), 743167 (for **9a**) and 743269 (for **9b**). For crystallographic data in CIF or other electronic format see DOI: 10.1039/b925562a



**Scheme 1** Selective C–C bond cleavage in the solid state *via* irradiation of crystals of (dppbe)( $\eta^2$ -2,2'-dibromotolane)Pt<sup>0</sup> with sunlight.

either phenyl groups of the tolane ligand against each other. Their spatial orientation is caused by the repulsion of both *ortho*-bonded bromine atoms.<sup>13</sup> Additionally, the reported solid-state reaction of **1** might be explained by the electron-withdrawing nature of the bromine atoms as well.

In order to study the effect of the spatial orientation of the phenyl groups as well as the influence of attached electron donating groups (EDGs) and electron withdrawing groups (EWGs), we synthesized a series of novel (diphosphine)Pt<sup>0</sup> complexes with different tolane ligands. Hence, their photochemical behavior in the solid state as well as in solution was paid main attention to. A detailed discussion supported by density functional theory (DFT) and time-dependent density functional theory (TD-DFT) methods of the different reactivity will be given in part B.‡

## Results and discussion

According to our previously reported synthesis of (diphosphine)(nbe)Pt<sup>0</sup> [nbe = norbornene] complexes,<sup>14</sup> the required (dppbe)Pt( $\eta^2$ -tolane) complexes **5a–g** were prepared by reaction of (dppbe)PtCl<sub>2</sub> (**3**) with sodium borohydride in dichloromethane–ethanol and subsequent treatment with the appropriate tolane derivative **4a–g** (Scheme 2). Complexes **5a–g** were obtained analytically pure as yellow to orange solids *via* crystallization by diffusion of pentane into concentrated toluene or benzene solutions of the appropriate crude products. The <sup>31</sup>P{<sup>1</sup>H} NMR spectra of **5a–c** and **5e–g** revealed a singlet along with the appropriate <sup>195</sup>Pt satellites, pointing to their symmetrical conformation. In contrast, the unsymmetrical complex **5d** shows an AB spin-system pattern in the <sup>31</sup>P{<sup>1</sup>H} NMR spectrum, consisting of two coinciding doublets together with <sup>195</sup>Pt satellites.

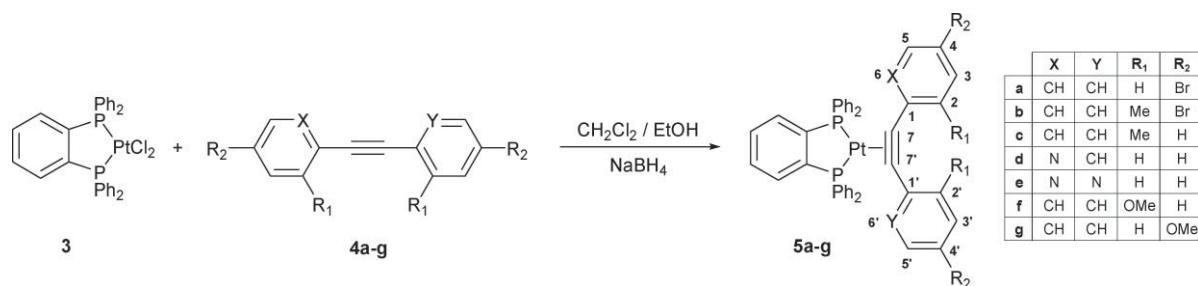
‡ D. Escudero, T. Weisheit, W. Weigand and L. González, Photochemical behavior of (diphosphine)( $\eta^2$ -tolane)Pt<sup>0</sup> complexes in solution and in the solid state; Part B: Theoretical part, *Dalton Trans.*, 2010, **39**, DOI: 10.1039/B925928G.

The chemical shifts (51.3–52.6 ppm) as well as the <sup>1</sup>J<sub>Pt</sub> coupling constants (3063–3143 Hz) of **5a–g** are in a narrow range, suggesting only minor influence of the acetylene ligand on the electronic nature of the Pt complex fragment. The purity and constitution of **5a–g** were confirmed by satisfying elemental analysis as well as mass spectrometry. Additionally, the results of the X-ray structure determination of **5a–e** (Fig. 1) prove the proposed structures of these complexes. Selected bond lengths and angles are summarized in Table 1 and are comparable with those reported for related Pt<sup>0</sup>-tolane complexes.<sup>11–15</sup> The experimentally measured values are in good agreement with the theoretically calculated ones (Table 1). Noteworthy differences are only observed for torsion angles C(8)–C(3)–C(9)–C(14), which are more sensitive to packing effects. The arrangement of the ligands around the platinum center is distorted square-planar for each complex. Due to the  $\pi$  back donation ( $d_{Pt} \rightarrow \pi^*_{alkyne}$ ) the bond lengths C(1)–C(2) are significantly longer than those reported for uncoordinated alkynes.<sup>16</sup> Furthermore, the decline of the angles C(1)–C(2)–C(3) and C(2)–C(1)–C(9), compared to uncoordinated tolanes (180°), is in good accordance with the increased alkene character of the formerly alkynes. The importance of the  $\pi$  back donation in these complexes was also verified by means of natural-bond-order (NBO) calculations.<sup>17</sup>

As a consequence of the  $\pi$  back donation, the wave numbers of the  $\nu(C\equiv C)$  are perspicuously shifted to smaller values for coordinated alkynes.<sup>16</sup>

In continuation of the results achieved with **1**, we first focused on the photoreactions of **5a** in the solid state and in solution. This complex shows a torsion angle C(8)–C(3)–C(9)–C(14) (see Table 1) of 30.7°, which is remarkably smaller than that of **1**, promising decreased steric influence compared to **1**. Nevertheless, both bromine atoms in *para*-position should provide a comparable electronic contribution to the reactivity as observed for **1**. Indeed, the irradiation of crystalline **5a** with sunlight for 12 days resulted in the selective conversion into a new unsymmetrical complex in 90% yield based on the <sup>31</sup>P{<sup>1</sup>H} NMR data. Its <sup>31</sup>P{<sup>1</sup>H} NMR spectrum shows two doublets at 50.6 and 49.2 ppm along with <sup>195</sup>Pt satellites. The observed <sup>1</sup>J<sub>Pt</sub> coupling constants (2467/1575 Hz) agree with the formation of the corresponding C–C activated counterpart **6a** (Scheme 3). Complex **6a** was isolated by column chromatography and obtained as pale yellow powder. Strong absorption at  $\nu = 2112\text{ cm}^{-1}$  in the IR spectrum verifies the end-on coordination of the alkyne ligand. The constitution and purity of **6a** was unambiguously confirmed by mass spectrometry as well as elemental analysis.

As expected, this selectivity vanishes when **5a** is irradiated in toluene solution. The <sup>31</sup>P{<sup>1</sup>H} NMR spectrum of the reaction mixture shows two AB spin systems with corresponding <sup>195</sup>Pt



**Scheme 2** Synthesis of (dppbe)( $\eta^2$ -tolane)Pt<sup>0</sup> complexes **5a–g**.

**Table 1** Selected bond lengths [Å] and angles [°] of complexes **5a–e** and **9a–b**. The corresponding calculated values are given in italics<sup>a</sup>

	<b>5a</b>	<b>5b</b>	<b>5c</b>	<b>5d</b>	<b>5e</b>	<b>9a</b>	<b>9b</b>
P(1)–Pt	2.2569(14)	2.2499(11)	2.2498(14)	2.2650(13)	2.2508(14)	2.2541(14)	2.2658(14)
	2.333	2.333	2.324	2.335	2.333	2.319	2.344
P(2)–Pt	2.2583(14)	2.2463(11)	2.2686(13)	2.2566(13)	2.2453(14)	2.2507(14)	2.2707(16)
	2.335	2.325	2.331	2.333	2.328	2.315	2.348
C(1)–Pt	2.027(6)	2.049(4)	2.064(6)	2.030(5)	2.041(5)	2.047(6)	2.045(6)
	2.082	2.101	2.101	2.077	2.064	2.099	2.101
C(2)–Pt	2.039(6)	2.040(4)	2.042(5)	2.041(5)	2.027(6)	2.052(6)	2.059(6)
	2.084	2.089	2.090	2.081	2.079	2.102	2.103
C(1)–C(2)	1.295(8)	1.302(6)	1.300(7)	1.293(8)	1.299(9)	1.288(8)	1.295(8)
	1.312	1.305	1.304	1.312	1.314	1.305	1.306
P(1)–Pt–P(2)	85.00(5)	86.47(4)	86.25(5)	86.63(5)	87.28(5)	88.10(5)	102.79(5)
	85.0	85.7	85.7	84.8	85.3	91.8	102.1
C(1)–Pt–C(2)	37.1(2)	37.13(18)	36.9(2)	37.0(2)	37.3(2)	36.6(2)	36.8(2)
	36.7	36.3	36.3	36.8	37.0	36.2	36.2
C(1)–C(2)–C(3)	144.4(6)	153.2(4)	146.9(6)	144.3(5)	144.0(6)	149.1(6)	145.5(6)
	146.7	149.8	150.1	145.1	144.4	145.5	145.9
C(2)–C(1)–C(9)	145.9(6)	149.0(4)	141.2(5)	143.4(5)	144.6(6)	149.2(6)	146.8(6)
	147.5	146.6	146.9	144.7	144.9	148.4	146.0
C(8)–C(3)–C(9)–C(14) <sup>b</sup>	30.7(6)	63.4(4)	71.0(6)	6.4(7)	26.9(6)	121.9(6)	75.6(6)
	18.9	92.2	91.9	3.6	7.3	96.5	72.5

<sup>a</sup> Theoretical values were calculated using the BP86/TZVP(ecp-mwb-60 for Pt) level. <sup>b</sup> Torsion angle between both phenyl groups of the appropriate tolane ligand; for **5d** this angle is defined as N(1)–C(3)–C(9)–C(10) and for **5e** C(4)–C(3)–C(9)–N(2), respectively.

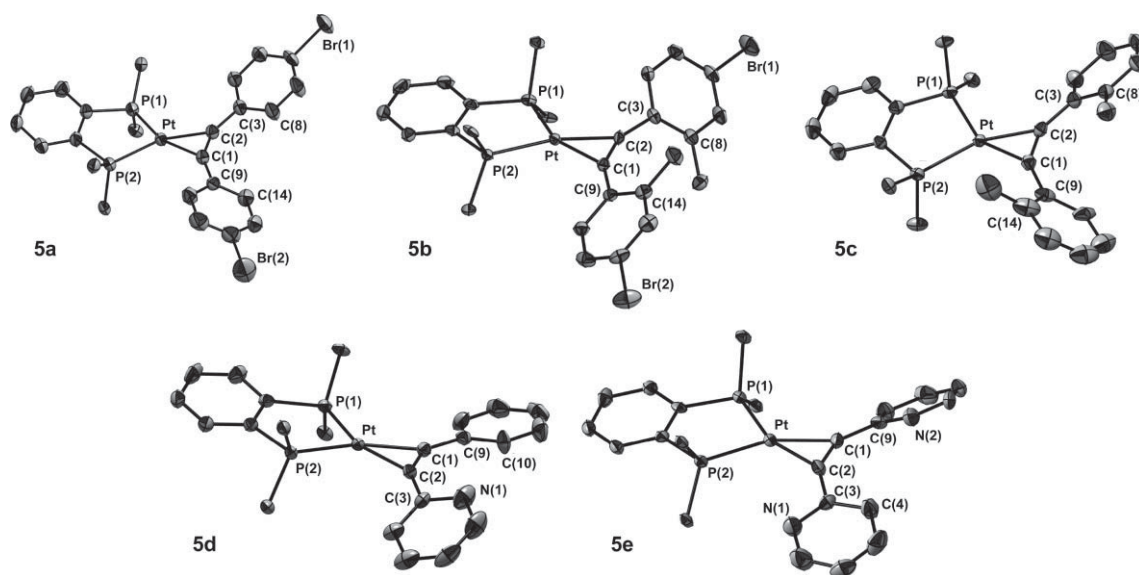
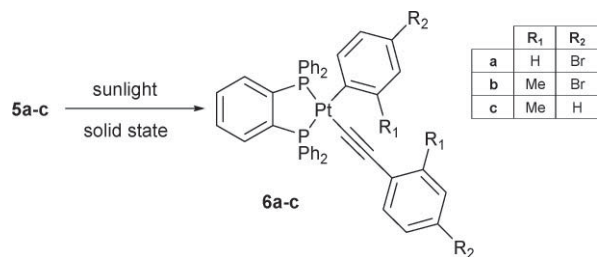


**Fig. 1** Molecular structures of complexes **5a–e** with thermal ellipsoids at 50% probability level. Hydrogen atoms and solvent molecules have been omitted for clarity. The phenyl groups of the dppbe ligand are represented by their *ipso*-carbon atoms. Selected bond lengths and angles are summarized in Table 1.

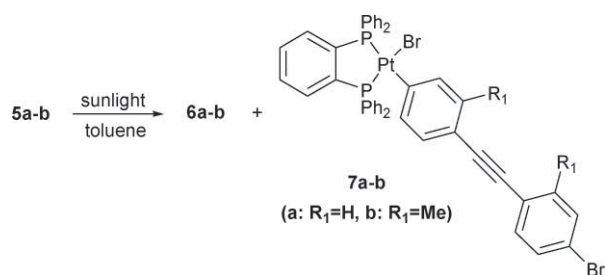
satellites, indicating the presence of two unsymmetrical complexes in a 1:1 ratio, whereas one of them was identified as **6a** and the second complex showed resonances at 49.3 and 43.2 ppm with appropriate  $^1J_{\text{P,Pt}}$  coupling constants of 1658 and 3988 Hz, respectively. The value of almost 4000 Hz points to the presence of a bromine ligand *trans* to a phosphorous atom, as observed for the C–Br activated counterpart of **1**,<sup>13</sup> hence the formation of complex **7a** is likely (Scheme 4), but nevertheless attempts to isolate **7a** by column chromatography failed.

These results show that the presence of the bromine moieties at the coordinated tolane ligand mainly increases the reactivity towards C–C bond activation. Indeed, the  $^{31}\text{P}\{^1\text{H}\}$  NMR spectra

of irradiated samples of **5b** and **5c** revealed the conversion of the starting materials to the appropriate C–C activated Pt<sup>II</sup> counterparts **6b** and **6c** (Scheme 3), indicated by two doublets along with  $^{195}\text{Pt}$  satellites, respectively (for **6b**: 50.1/48.9 ppm,  $^1J_{\text{P,Pt}} = 2474/1639$  Hz and for **6c**: 50.5/48.6 ppm,  $^1J_{\text{P,Pt}} = 2469/1561$  Hz). Interestingly, after similar reaction periods 45% of **5b** are converted to **6b**, but only 25% of **5c** have been reacted to **6c**. The torsion angles of **5b** and **5c** have approximately the same value due to the *ortho*-bonded methyl groups, which should provide a comparable steric contribution to the reactivity. However, methyl groups also possess a marginal electron donating character, countervailing the electron withdrawing properties of the bromine substituents in



**Scheme 3** Selective formation of the C–C activated compounds **6a–c** by irradiation of the appropriate (dppbe)( $\eta^2$ -tolane)Pt<sup>0</sup> complexes with sunlight.



**Scheme 4** Irradiation of the bromo-substituted complexes in solution results in the formation of the C–C activated compounds **6** and the C–Br activated ones **7** in a 1 : 1 ratio.

**5b**, which might explain the reduced conversion of **5b** and **5c** in comparison to **5a**.

The reaction of **5b** in toluene solution resulted in the formation of two complexes in a 1 : 1 ratio, which were found to be the C–C activated product **6b** and the C–Br activated compound **7b**, with respect to the <sup>31</sup>P{<sup>1</sup>H} NMR data of the crude product (Scheme 4). Column chromatography of the product mixture yielded both complexes in analytical purity, which was verified by spectroscopic methods and elemental analysis. The <sup>31</sup>P{<sup>1</sup>H} NMR spectra of **6b** and **7b** revealed two doublets as well as the corresponding <sup>195</sup>Pt satellites due to their unsymmetrical conformation (for **7b**: 49.6/43.0 ppm, <sup>1</sup>J<sub>P,Pt</sub> = 1684/4090 Hz). The <sup>1</sup>J<sub>P,Pt</sub> values of **7b** are comparable to that of **7a**, verifying the insertion of the (dppbe)Pt<sup>0</sup> complex fragment into one of the C–Br bonds. The proposed molecular structures of **6b** and **7b** are unambiguously confirmed by the results of the X-ray structure determination (Fig. 2 and 3).

The arrangement of the ligands around the metal center is slightly distorted from square planarity. The remarkably enlarged bond length Pt–P(1) in comparison to Pt–P(2) in complex **7b** can be plausibly explained by the greater extent of the *trans*-influence of the sp<sup>2</sup> hybridized carbon atom. In contrast to the appropriate (dppbe)( $\eta^2$ -tolane)Pt<sup>0</sup> complex, the bond lengths C(1)–C(2) and C(8)–C(9) in compounds **6b** and **7b**, respectively, are in the typical range of carbon–carbon triple bonds. Furthermore, the end-on coordination of the alkyne to the platinum atom in **6b** is underlined by the detected strong absorption at  $\nu = 2110\text{ cm}^{-1}$  in the corresponding IR spectrum.

Irradiation of a toluene solution of **5c** with sunlight for approximately 10 days, results in the selective formation of **6c**. No evidence for activation of the carbon–methyl bond was detected in the <sup>1</sup>H and the <sup>31</sup>P{<sup>1</sup>H} NMR spectra. The yield, calculated on the basis of the <sup>31</sup>P{<sup>1</sup>H} NMR spectrum, increases to approximately

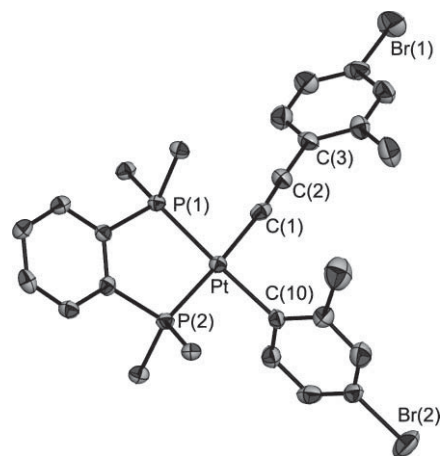


**Fig. 2** Molecular structure of **6b** with thermal ellipsoids at 50% probability level. Hydrogen atoms have been omitted for clarity. The phenyl groups of the dppbe ligand are represented by their *ipso*-carbon atoms. Selected bond lengths [Å] and angles [°]: P(1)–Pt 2.2761(14), P(2)–Pt 2.2709(14), C(1)–Pt 2.022(6), C(10)–Pt 2.093(5), C(1)–C(2) 1.193(8), P(1)–Pt–P(2) 86.64(5), P(1)–Pt–C(1) 90.63(15), P(2)–Pt–C(10) 94.23(15), C(1)–Pt–C(10) 88.6(2), Pt–C(1)–C(2) 173.5(5).

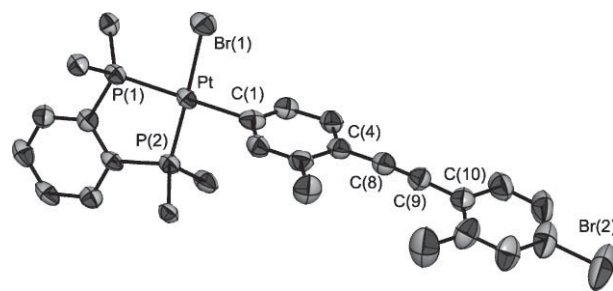


**Fig. 3** Molecular structure of **7b** with thermal ellipsoids at 50% probability level. Hydrogen atoms and solvent molecules have been omitted for clarity. The phenyl groups of the dppbe ligand are represented by their *ipso*-carbon atoms. Selected bond lengths [Å] and angles [°]: P(1)–Pt 2.2806(19), P(2)–Pt 2.2082(17), C(1)–Pt 2.099(8), Pt–Br(1) 2.4679(8), C(8)–C(9) 1.176(10), P(1)–Pt–P(2) 87.62(6), P(1)–Pt–Br(1) 90.35(5), P(2)–Pt–C(1) 93.02(19), C(1)–Pt–Br(1) 89.01(18), C(4)–C(8)–C(9) 175.9(8).

75% compared with 25% in the respective experiment in the solid state.

Considering these previous observations, the question arises whether the insertion of the Pt<sup>0</sup> complex fragment into the C<sub>aryl</sub>–C<sub>ethynyl</sub> bond occurs intramolecular or intermolecular in the crystalline state. Taking a closer look to the arrangement of the (diphosphine)( $\eta^2$ -tolane)Pt<sup>0</sup> complexes in the crystal ought to be a simplified estimation concerning this problem. Fig. 4 exemplarily shows the alignment of **5a** in the solid state. The shortest distance between two platinum atoms of neighbouring molecules of **5a** (labeled as **A** and **B**) was determined to be 7.45 Å. The toluene moiety of **B**, highlighted as purple triangle, is evidently not directed to the Pt center of **A**, suggesting that their distance is not significantly shorter than 7.45 Å. Indeed, approximated distances, calculated between the Pt atom of **A** and one of the C<sub>ethynyl</sub> atoms of **B**, were found to be 7.07 Å and 7.84 Å, respectively. Regarding that typically observed distances among reactive centers in the course of photochemical reactions in the

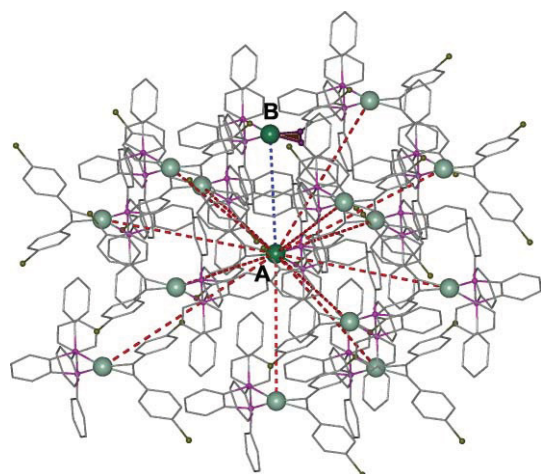


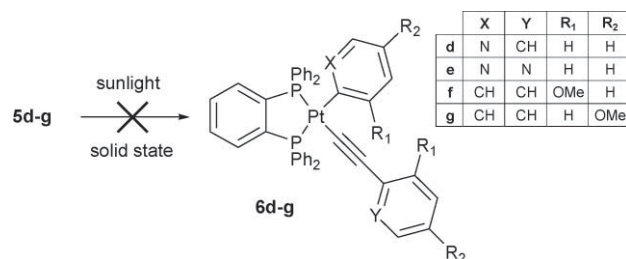
**Fig. 4** Section of the crystal-state arrangement of **5a**. Platinum atoms are depicted as green colored spheres. Intermetallic Pt...Pt distances are represented by dashed lines, whereas red lines exhibit a length of approximately 10–13 Å and the shortest contact (7.45 Å) is emphasized by a blue colored dashed line.

solid state are generally in the range of 4 Å,<sup>18</sup> a bimolecular reaction mechanism can be excluded. However, an intramolecular attack of the (diphosphine)Pt moiety on the C<sub>aryl</sub>–C<sub>ethynyl</sub> bond after a photo-excitation of **5a** (see Part B<sup>†</sup>) seems to be more plausible due to the close proximity of the Pt atom to the regarded bond. This might result in a reduced activation barrier for C–C bond activation and explains the high selectivity in the solid state. The determined intermolecular Pt...Pt distances of complexes **5b–5g** and **9a–b** are comparable to those of **5a**. Therefore, an expansion of the postulated mechanism of the solid state C–C bond activation to these complexes ought to be justified.

On the contrary, the formation of the C–Br activated compound **7a** via irradiating **5a** in solution can be reasonably explained by a “ring-walking” mechanism of the (diphosphine)Pt moiety along the  $\pi$ -system of the tolane ligand as similarly described for bromo substituted stilbene and azostilbene derivatives coordinated to a (PEt<sub>3</sub>)<sub>2</sub>Ni<sup>19</sup> as well as (PEt<sub>3</sub>)<sub>2</sub>Pt complex fragment.<sup>20</sup>

The photochemical conversions of **5a–c** to their C–C activated counterparts suggest that the reactivity towards C–C bond cleavage in the solid state obviously depends on the electronic nature of the used tolane ligand as well as on the spatial orientation of its phenyl groups (for a detailed explanation see Part B<sup>†</sup>). In view of a minimization of potential steric influences, complexes **5d** and **5e** have been synthesized. The decreased steric bulkiness of the pyridyl groups allows an almost coplanar arrangement in the corresponding complexes, as reflected by the torsion angles of 6.4° and 26.9° found for complexes **5d** and **5e**, respectively (Table 1). Therefore, crystalline samples of **5d** and **5e** were placed in the sunlight for approximately two weeks. After this period, no obvious alterations of these samples were observed. Their <sup>31</sup>P{<sup>1</sup>H} NMR spectra revealed the signals of the starting material unchanged, indicating that no photoreaction occurred (Scheme 5).

The photolysis of **5d** and **5e** in solution resulted in the formation of some unidentified side products. No signals assignable to the corresponding C–C activated products have been detected in the appropriate <sup>31</sup>P{<sup>1</sup>H} NMR spectra.

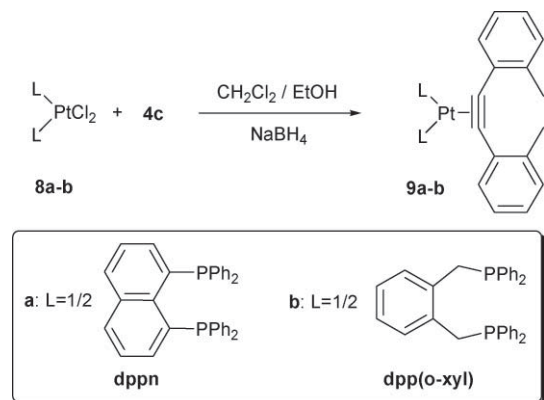


**Scheme 5** Complexes **5d–g** are non-reactive towards sunlight in the solid state.

In order to study the influence of EDGs attached to the tolane ligand, complexes **5f** and **5g** were placed in the sunlight for photoreactions. However, neither **5f** nor **5g** showed any rearrangement towards C–C or C–O bond activation with respect to the <sup>31</sup>P{<sup>1</sup>H} NMR spectroscopic data (Scheme 5). These results suggest an inhibition of C–C bond cleavage in the solid state by the presence of EDGs on the tolane moiety. Furthermore, in the case of **5f**, this inhibition-effect seems to be stronger than a potential C–C bond activation arising from the spatial orientation of the phenyl rings, because its dihedral angle ought to be in the same range as observed for the other complexes bearing *ortho*-substituted tolanes. Single crystals of **5f** and **5g** were of poor quality and not suitable for X-ray structure determination. Hence, no information of the alignment of the phenyl groups in the solid state is available. However, some information can be extracted from the theoretical optimized geometries of **5f** and **5g**, which predict C(8)–C(3)–C(9)–C(14) torsion angles of 72.2° and 20.1°, respectively. Due to its greater torsion angle, in comparison with **5g**, we expect complex **5f** to be prone in view of C–C bond activation. Accordingly, the photolysis of **5f** in toluene solution resulted in the predominant formation of **6f**, which was verified by the presence of an AB spin system pattern accompanied with <sup>195</sup>Pt satellites (49.5/47.6 ppm, <sup>1</sup>J<sub>P,Pt</sub> = 2473/1687 Hz) in the <sup>31</sup>P{<sup>1</sup>H} NMR spectrum. The reaction of **5g** under similar conditions revealed almost no conversion into the corresponding insertion product **6g**, based on the <sup>31</sup>P{<sup>1</sup>H} NMR spectroscopic data. However, attempts to isolate compounds **6f** and **6g** by means of column chromatography failed.

In order to investigate the influence of the bridging diphosphine ligand on the reactivity, we focused on one tolane ligand (**4c**) and synthesized two additional Pt<sup>0</sup> complexes (**9a–b**) with diphosphine ligands promising different bite angles P–Pt–P. Compounds **9a** and **9b** were prepared by reduction of the appropriate Pt<sup>II</sup> metal precursor (**8a–b**) with sodium borohydride in dichloromethane–ethanol solution and subsequent treatment with **4c** (Scheme 6). Diffusion of pentane into saturated benzene solutions of the crude products afforded orange (**9a**) and pale yellow (**9b**) crystals in analytical purity. The <sup>31</sup>P{<sup>1</sup>H} NMR spectra of **9a** and **9b** show a singlet with <sup>195</sup>Pt satellites at 17.4 and 13.6 ppm, respectively. Interestingly, the <sup>1</sup>J<sub>P,Pt</sub> values increase with the corresponding bite angles of the diphosphines. A similar correlation between these values was already observed in related systems.<sup>14,21,22</sup>

The molecular arrangements of **9a** and **9b** were unambiguously confirmed by the results of the X-ray structure determination (Fig. 5 and 6). Both complexes exhibit a distorted square-planar coordination geometry. Selected bond lengths and angles are summarized in Table 1 and comparable with those determined



**Scheme 6** Synthesis of (diphosphine)( $\eta^2$ -2,2'-dimethyltolene)Pt<sup>0</sup> complexes **9a–b**, bearing diphosphines with different bite angles.

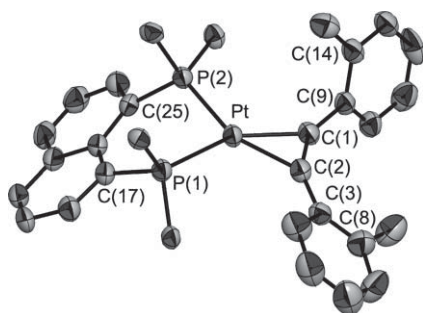


**Fig. 5** Molecular structure of **9a** with thermal ellipsoids at 50% probability level. Hydrogen atoms and solvent molecules have been omitted for clarity. The phenyl groups of the 1,8-bis(diphenylphosphanyl)naphthalene ligand (dppn) are represented by their *ipso*-carbon atoms. Selected bond lengths and angles are summarized in Table 1.

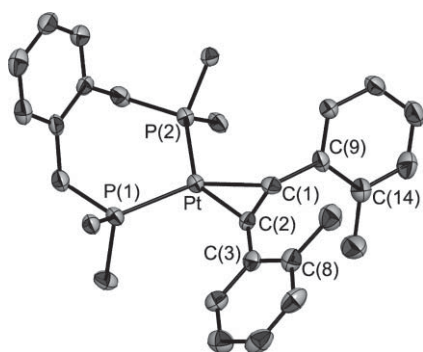
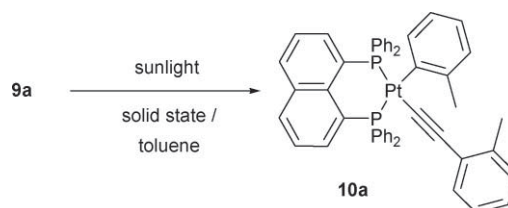


**Fig. 6** Molecular structure of **9b** with thermal ellipsoids at 50% probability level. Hydrogen atoms and solvent molecules have been omitted for clarity. The phenyl groups of the  $\alpha,\alpha'$ -bis(diphenylphosphanyl)-*o*-xylene [dpp(*o*-xy)] ligand are represented by their *ipso*-carbon atoms. Selected bond lengths and angles are summarized in Table 1.

for **5a–e**, except the angles P(1)–Pt–P(2) which are predetermined by the particular diphosphine. The torsion angle of the phenyl rings of the toluene ligand in **9b** was experimentally determined to be 75.6°, which is in good agreement with the theoretically calculated value of 72.5° (Table 1) and thus, is comparable to that in **5c**. In contrast, the appropriate angle in **9a** was found to be significantly enlarged to 121.9°.

If crystals of **9a** are irradiated with sunlight for two weeks, smooth fading of the orange color was observed pointing to

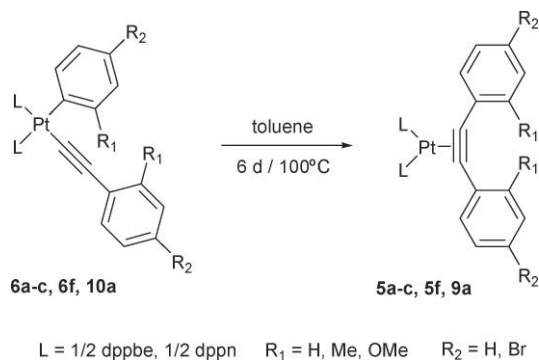
a photochemical induced reaction. Indeed, the  $^{31}\text{P}\{^1\text{H}\}$  NMR spectrum of this sample displayed full conversion of **9a** to an unsymmetrical complex characterized by two doublets at 11.9 and 9.0 ppm. The  $^1J_{\text{P,Pt}}$  values (2427/1499 Hz) are comparable to those determined for **6a–c**, pointing to the formation of **10a** (Scheme 7). The IR spectrum of **10a** shows strong absorption at  $\nu = 2112\text{ cm}^{-1}$ , typical for an end-on coordinated alkyne ligand. In contrast, a crystalline sample of **9b**, which was placed in sunlight for a similar period, did not show any visible alterations as confirmed by the unchanged  $^{31}\text{P}\{^1\text{H}\}$  NMR spectrum.



**Scheme 7** The dppn complex **9a** shows light induced selective C–C bond cleavage in the crystalline state as well as in solution.

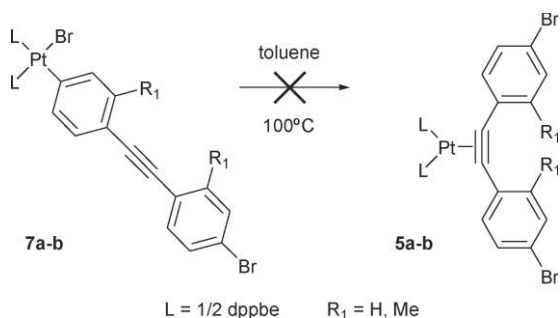
The exposure of a toluene solution of **9a** to the sunlight resulted in the exclusive formation of **10a**, as can be followed by  $^{31}\text{P}\{^1\text{H}\}$  NMR spectroscopy. On the contrary, the  $^{31}\text{P}\{^1\text{H}\}$  NMR spectrum of a solution of **9b**, irradiated with sunlight for several days, indicates almost no conversion of **9b** except for a small amount of the dioxidized phosphine ligand (33.0 ppm). On the one hand, the differences in the reactivity of **9a/9b** in solid state and solution might be explained by the remarkably different torsion angles of the phenyl rings of the coordinated **4c**. On the other hand, a clear trend in the relation between the phosphine chelate ring size (and hence the bite angle P–Pt–P) and the reactivity is evident. Whereas **5c** and **9a**, realizing 5- and 6-membered chelate rings, respectively, and exhibiting relatively small P–Pt–P angles (86–88°), are reactive towards sunlight in the solid state and in solution, **9b** proved to be unreactive under similar conditions, as mentioned above. This complex exhibits a 7-membered chelate ring with an appropriate P–Pt–P angle of almost 103°. These miscellaneous diphosphines are known to influence the electronic nature of the appropriate Pt<sup>0</sup> fragment,<sup>23</sup> what might explain the different reactivity of complexes **5c**, **9a** and **9b** in the solid state and in solution, respectively. A detailed discussion concerning the factors influencing the reactivity is given in Part B.‡

Generally, the described photochemically induced C–C bond activation is thermodynamically uphill, hence the reactivity is reversible under thermal conditions. In order to prove this assumption for the specified complexes **5a–c**, **5f** and **9a**, which show C–C bond activation, their thermal induced back reactions were investigated (for mechanistic DFT studies see Part B.‡). Therefore, toluene-*d*<sub>8</sub> solutions of **5a–c**, **5f** and **9a** were placed in NMR tubes and exposed to sunlight. After 10 days the formation of the corresponding Pt<sup>II</sup> counterparts was confirmed by  $^{31}\text{P}\{^1\text{H}\}$  NMR spectroscopy and thereupon the NMR tubes were sealed and placed in an oil bath at 100 °C. After 6 days a  $^{31}\text{P}\{^1\text{H}\}$  NMR spectrum of each sample was recorded. The  $^{31}\text{P}\{^1\text{H}\}$  NMR spectroscopic data of the experiments on **5c**, **5f** and **9a** revealed the quantitative re-conversion of the photochemically generated Pt<sup>II</sup> complexes **6c**, **6f** and **10a** into the appropriate Pt<sup>0</sup> complexes (Scheme 8).



**Scheme 8** Photochemical C–C bond cleavage in (diphosphine)( $\eta^2$ -tolane)Pt<sup>0</sup> complexes is reversible under thermal conditions.

If 1 : 1 mixtures of **6a** and **7a** as well as **6b** and **7b**, obtained by irradiating solutions of **5a** and **5b** with sunlight, respectively, are treated in a similar manner, the <sup>31</sup>P{<sup>1</sup>H} NMR spectra only revealed the re-conversion of **6a** and **6b** into **5a** and **5b** (Scheme 8), whereas the signals of **7a** and **7b** remained unchanged. This underlines the irreversible light induced oxidative addition of the C–Br bond to the (diphosphine)Pt<sup>0</sup> moiety in **5a** and **5b**, respectively (Scheme 9). The irreversibility of the C–Br bond activation reaction is addressed in Part B,<sup>‡</sup> where mechanistic DFT studies show that the appropriate backwards thermal reductive elimination is thermodynamically uphill.



**Scheme 9** Complexes **7a** and **7b** are stable towards higher temperatures and show no rearrangement to **5a** and **5b**, respectively.

## Conclusions

In summary, we were able to extend our previously reported simple and straightforward synthesis of (diphosphine)(tolane)Pt<sup>0</sup> complexes to a new series of complexes (**5a–g** and **9a–b**), bearing toluene ligands with manifold substituent patterns. Comparison of their reactivity towards C–C bond activation showed that on the one hand the spatial orientation of the phenyl rings of the toluene ligand and on the other hand the electronic properties of substituents attached to the toluene moiety influence the light induced intramolecular oxidative addition of the C<sub>aryl</sub>–C<sub>ethynyl</sub> bond to the Pt<sup>0</sup> moiety in the crystalline state as well as in solution. While compounds **5d–g**, exhibiting either a relatively small twisting of the phenyl or pyridyl rings of the toluene ligand or strong EDGs, are unreactive towards sunlight, complexes **5a–c** and **9a** could be selectively converted to the appropriate C–C activated counterparts. Additionally, solution state photolysis of **5a** and **5b**, bearing bromo substituted toluene ligands, leads to 1 : 1 mixtures of

the C–C activated as well as the C–Br activated complexes **7a** and **7b**. The formation of **7a** and **7b** can be reasonably explained by a “ring walking” mechanism of the Pt<sup>0</sup> complex fragment on the  $\pi$ -system of the ligand resulting in C–Br bond activation. However, the highly selective formation of the C–C activated complexes in the crystalline state might be caused by the close proximity of both reactive sites of the appropriate complex. The observed C–C bond cleavage proved to be reversible under thermal conditions, whereas the insertion of the Pt<sup>0</sup> complex fragment in the C–Br bonds turned out to be irreversible, pointing to the thermal stability of complexes **7a** and **7b**, respectively.

In order to render the mechanism of this bond cleavage in the crystalline state precisely, more information about the excited states in the course of the reactions are indispensable. Therefore, results of theoretical calculations on the UV-spectra of the (diphosphine)( $\eta^2$ -tolane)Pt<sup>0</sup> complexes are presented in Part B of this work,<sup>‡</sup> which should substantiate the factors influencing the different reactivity towards C–C bond cleavage.

## Experimental section

### General considerations

Unless otherwise stated, all reactions were carried out under an atmosphere of argon by using standard Schlenk techniques. All chemicals were purchased from commercial suppliers and used without further purification. The starting materials (dppbe)PtCl<sub>2</sub> (**3**),<sup>24</sup> (dppn)PtCl<sub>2</sub> (**8a**),<sup>25</sup> (dpp(o-xyl))PtCl<sub>2</sub> (**8b**)<sup>26</sup> as well as the toluene derivatives **4d**<sup>27</sup> and **4e**<sup>27</sup> were prepared according to literature procedures. Compounds **4a**,<sup>28</sup> **4c**,<sup>29</sup> **4f**<sup>30</sup> and **4g**<sup>30</sup> are known from literature and were synthesized in a similar manner as the synthesis of **4b** described below. The determined spectroscopic data are in good agreement with the reported ones. The NMR spectra were recorded either with BRUKER AVANCE 400 or BRUKER AVANCE 200 spectrometers at 27 °C. <sup>1</sup>H NMR spectra were calibrated using the signal of the residual non-deuterated solvent, while <sup>13</sup>C{<sup>1</sup>H} NMR spectra were measured using the signal of the solvent as internal standard. <sup>31</sup>P{<sup>1</sup>H} NMR spectra were determined using 85% H<sub>3</sub>PO<sub>4</sub> as external standard. The assignment of the signals in the <sup>1</sup>H and <sup>13</sup>C{<sup>1</sup>H} NMR spectra of compounds **5a–g** and **9a–b** was performed by means of two-dimensional NMR methods (<sup>1</sup>H,<sup>1</sup>H-COSY, <sup>1</sup>H,<sup>13</sup>C-HSQC and <sup>1</sup>H,<sup>13</sup>C-HMBC). The protons as well as carbon atoms of the appropriate toluene ligand are labeled according to Scheme 2, whereas the signals of the ethynyl carbon atoms could not be detected due to their low intensity. The complexity of the <sup>1</sup>H and <sup>13</sup>C{<sup>1</sup>H} NMR spectra of compounds **6a**, **7a**, **7b** and **10a** disabled an exact assignment for most of the signals, even by applying two-dimensional NMR methods. Mass spectra were taken with a FINNIGAN MAT SSQ 710 mass spectrometer. IR spectra were recorded with a PERKIN ELMER system 2000 FT-IR spectrometer. Elemental analyses were performed with a Vario EL III CHNS (Elementaranalysen GmbH Hanau) as single determinations. Melting points were determined using an AXIOLAB microscope with a THMS 600 heating plate and are uncorrected.

**2,2'-dimethyl-4,4'-dibromotoluene (4b).** To a solution of 2-iodo-5-bromotoluene (4.43 g, 14.9 mmol) in Et<sub>3</sub>N (40 mL) trimethylsilylacetylene (1.48 g, 15.1 mmol), copper(I)iodide (117 mg,



0.61 mmol) and  $(\text{PPh}_3)_2\text{PdCl}_2$  (126 mg, 0.18 mmol) were added, whereupon the color of the solution turned to black and triethylammoniumiodide began to precipitate. After stirring for 5 days the solid was filtered through Celite® and the residue was rinsed with diethyl ether. The combined solvents were removed under reduced pressure to give a dark oil which was distilled *in vacuo* to give 2-trimethylsilylethynyl-5-bromotoluene<sup>31</sup> as colorless oil. (3.42 g, 88%);  $\delta_{\text{H}}$ (200 MHz,  $\text{CDCl}_3$ ) 7.35–7.18 (m, 3 H), 2.37 (s, 3 H), 0.23 (s, 9 H);  $\delta_{\text{C}}$ (50 MHz,  $\text{CDCl}_3$ ) 142.6 (s), 133.3 (s), 132.3 (s), 128.6 (s), 122.5 (s), 122.0 (s), 102.9 (s), 99.6 (s), 20.4 (s), 0.0 (s).

A solution of 2-trimethylsilylethynyl-5-bromotoluene (2.50 g, 9.34 mmol) in thf (30 mL) was cooled to  $-78^\circ\text{C}$  and tetra-*n*-butylammoniumfluoride, dissolved in thf (20 mL), was added drop wise. After warming to room temperature the yellow solution was stirred over night. Then the solution was washed three times with water, the phases were separated and the organic layer was dried over  $\text{Na}_2\text{SO}_4$ . The solvent was removed under reduced pressure to yield 2-ethynyl-5-bromotoluene as pale yellow oil. (1.70 g, 93%);  $\delta_{\text{H}}$ (200 MHz,  $\text{CDCl}_3$ ) 7.34–7.21 (m, 3 H), 3.28 (s, 1 H), 2.37 (s, 3 H);  $\delta_{\text{C}}$ (50 MHz,  $\text{CDCl}_3$ ) 142.8 (s), 133.7 (s), 132.4 (s), 128.8 (s), 122.8 (s), 120.9 (s), 82.0 (s), 81.5 (s), 20.4 (s).

To a solution of 2-ethynyl-5-bromotoluene (1.70 g, 8.72 mmol) in  $\text{Et}_3\text{N}$  (40 mL) 2-iodo-5-bromotoluene (2.61 g, 8.80 mmol), copper(i)iodide (113 mg, 0.59 mmol) and  $(\text{PPh}_3)_2\text{PdCl}_2$  (104 mg, 0.15 mmol) were added, whereas the color of the solution turned black and triethylammoniumiodide began to precipitate. After stirring for 5 days the solvent was removed *in vacuo*. The residue was dissolved in  $\text{CH}_2\text{Cl}_2$  and washed with water, saturated  $\text{NH}_4\text{Cl}$  solution and again water and dried over  $\text{Na}_2\text{SO}_4$ . After removing the solvent the crude product was recrystallized from ethanol to yield **4b** as white solid (2.06 g, 65%). Mp: 119–120 °C;  $\delta_{\text{H}}$ (200 MHz,  $\text{CDCl}_3$ ) 7.41 (m, 2 H), 7.33–7.28 (m, 4 H), 2.48 (s, 6 H);  $\delta_{\text{C}}$ (50 MHz,  $\text{CDCl}_3$ ) 141.9 (s), 133.1 (s), 132.5 (s), 128.9 (s), 122.4 (s), 122.0 (s), 92.3 (s), 20.7 (s); Anal. calcd. for  $\text{C}_{16}\text{H}_{12}\text{Br}_2$ : C 52.78, H 3.32, Br 43.89; Found: C 53.14, H 3.30, Br 43.72.

#### General procedure for the syntheses of the (diphosphine)( $\eta^2$ -tolane) $\text{Pt}^0$ complexes

The appropriate (diphosphine) $\text{PtCl}_2$  was suspended in  $\text{CH}_2\text{Cl}_2$  (12 mL) and ethanol (3 mL) in a Schlenk flask. To this suspension  $\text{NaBH}_4$  (50 mg, 1.06 mmol) was added and stirred for 6 h at rt. During this period the mixture became yellow to orange in color and the (diphosphine) $\text{PtCl}_2$  dissolved. Water (5 mL) was added to the mixture and after diminishing of the hydrogen evolution the phases were separated using a pipette and the appropriate toluene ligand was added to the organic layer in equimolar ratio. This solution was stirred over night. After removing the solvent under reduced pressure, the residue was dissolved in a small amount of thf and this solution was filtered through a silica gel charged pipette. The solvent was evaporated and the yellow to orange colored crude product was dissolved in toluene or benzene (3 mL). Pure complexes were obtained by slow diffusion of pentane into these solutions.

**[(dppbe)( $\eta^2$ -4,4'-dibromotoluene) $\text{Pt}^0$ ] (5a).** Compound **3** (142 mg, 0.20 mmol) was reacted with **4a** (66 mg, 0.20 mmol) to yield **5a** (83 mg, 40%) as orange crystals.

Mp: 127 °C (dec.);  $\delta_{\text{H}}$ (400 MHz,  $\text{CD}_2\text{Cl}_2$ ) 7.77 (m, 2 H, *o*- $\text{C}_6\text{H}_4$  of dppbe), 7.59 (m, 8 H, *o*- $\text{C}_6\text{H}_5$  of dppbe), 7.48 (m, 2 H, *m*-

$\text{C}_6\text{H}_4$  of dppbe), 7.35 (m, 16 H, *m*- $\text{C}_6\text{H}_5$  and *p*- $\text{C}_6\text{H}_5$  of dppbe and *H*-2/*H*-2' and *H*-6/*H*-6'), 7.26 (m, 4 H, *H*-3/*H*-3' and *H*-5/*H*-5');  $\delta_{\text{C}}$ (100 MHz,  $\text{CD}_2\text{Cl}_2$ ) 146.4 (m, *ipso*- $\text{C}_6\text{H}_4$  of dppbe), 135.5 (m, *ipso*- $\text{C}_6\text{H}_5$  of dppbe), 134.4 (m, *C*-1/*C*-1'), 134.0 (m, *o*- $\text{C}_6\text{H}_4$  of dppbe), 133.3 (m, *o*- $\text{C}_6\text{H}_5$  of dppbe), 132.3 (m, *C*-2/*C*-2' and *C*-6/*C*-6'), 131.5 (s, *C*-3/*C*-3' and *C*-5/*C*-5'), 131.2 (s, *m*- $\text{C}_6\text{H}_4$  of dppbe), 130.3 (s, *p*- $\text{C}_6\text{H}_5$  of dppbe), 128.8 (m, *m*- $\text{C}_6\text{H}_5$  of dppbe), 120.1 (s, *C*-4/*C*-4');  $\delta_{\text{P}}$ (81 MHz,  $\text{CD}_2\text{Cl}_2$ ) 51.17 (s with  $^{195}\text{Pt}$  satellites,  $^1J_{\text{Pt}}$  = 3087 Hz);  $\nu(\text{KBr})/\text{cm}^{-1}$  3052 (s), 1736 (s,  $\nu(\text{C}\equiv\text{C})$ ), 1629 (s), 1482 (vs), 1434 (vs), 1389 (m), 1097 (vs) 1067 (s), 1008 (s), 826 (s), 745 (s), 694 (vs), 669 (s), 548 (vs), 527 (s); *m/z* (DEI) 976 (2%,  $[\text{M}]^+$ ), 896 (2,  $[\text{M} - \text{Br}]^+$ ), 721 (30,  $[(\text{dppbe})\text{PtBr}]^+$ ), 641 (10,  $[(\text{dppbe})\text{Pt}]^+$ ), 336 (23, **4a**<sup>+</sup>); Anal. calcd. for  $\text{C}_{44}\text{H}_{32}\text{Br}_2\text{P}_2$ : C 54.06, H 3.30, Br 16.35; Found C 54.30, H 3.51, Br 16.01.

**[(dppbe)( $\eta^2$ -2,2'-dimethyl-4,4'-dibromotoluene) $\text{Pt}^0$ ] (5b).** Compound **3** (175 mg, 0.25 mmol) was reacted with **4b** (89 mg, 0.24 mmol) to yield **5b** (111 mg, 45%) as yellow crystals.

Mp: >230 °C;  $\delta_{\text{H}}$ (400 MHz,  $\text{CD}_2\text{Cl}_2$ ) 7.81 (m, 2 H, *o*- $\text{C}_6\text{H}_4$  of dppbe), 7.50 (m, 10 H, *m*- $\text{C}_6\text{H}_4$  and *o*- $\text{C}_6\text{H}_5$  of dppbe), 7.36 (m, 4 H, *p*- $\text{C}_6\text{H}_5$  of dppbe), 7.29 (m, 8 H, *m*- $\text{C}_6\text{H}_5$  of dppbe), 7.22 (s, 2 H, *H*-3/*H*-3'), 7.00 (m, 4 H, *H*-5/*H*-5' and *H*-6/*H*-6'), 1.96 (s, 6 H,  $\text{CH}_3$ );  $\delta_{\text{C}}$ (100 MHz,  $\text{CD}_2\text{Cl}_2$ ) 146.4 (m, *ipso*- $\text{C}_6\text{H}_4$  of dppbe), 138.7 (m, *C*-2/*C*-2'), 137.0 (m, *C*-1/*C*-1'), 135.8 (m, *ipso*- $\text{C}_6\text{H}_5$  of dppbe), 134.1 (m, *o*- $\text{C}_6\text{H}_4$  of dppbe), 133.1 (m, *o*- $\text{C}_6\text{H}_5$  of dppbe), 132.6 (s, *C*-6/*C*-6'), 132.1 (s, *C*-3/*C*-3'), 131.2 (s, *m*- $\text{C}_6\text{H}_4$  of dppbe), 130.1 (s, *p*- $\text{C}_6\text{H}_5$  of dppbe), 128.7 (m, *m*- $\text{C}_6\text{H}_5$  of dppbe), 128.2 (s, *C*-5/*C*-5'), 119.3 (s, *C*-4/*C*-4'), 21.0 (s,  $\text{CH}_3$ );  $\delta_{\text{P}}$ (81 MHz,  $\text{CD}_2\text{Cl}_2$ ) 51.59 (s with  $^{195}\text{Pt}$  satellites,  $^1J_{\text{Pt}}$  = 3143 Hz);  $\nu(\text{KBr})/\text{cm}^{-1}$  3052 (m), 2930 (w), 1763 (m,  $\nu(\text{C}\equiv\text{C})$ ), 1625 (m), 1475 (s), 1434 (s), 1188 (m), 1097 (s), 891 (m), 745 (m), 694 (vs), 549 (vs), 527 (vs), 507 (s); *m/z*(DEI) 1006 (2%,  $[\text{M}]^+$ ), 923 (2,  $[\text{M} - \text{Br}]^+$ ), 721 (6,  $[(\text{dppbe})\text{PtBr}]^+$ ), 641 (2,  $[(\text{dppbe})\text{Pt}]^+$ ), 485 (1,  $[(\text{dppbe})\text{Pt} - 2\times\text{Ph}]^+$ ), 364 (3, **4b**<sup>+</sup>); Anal. calcd. for  $\text{C}_{46}\text{H}_{36}\text{Br}_2\text{P}_2$ : C 54.94, H 3.61, Br 15.89; Found C 55.16, H 3.69, Br 16.01.

**[(dppbe)( $\eta^2$ -2,2'-dimethyltoluene) $\text{Pt}^0$ ] (5c).** Compound **3** (129 mg, 0.18 mmol) was reacted with **4c** (37 mg, 0.18 mmol) to yield **5c** (113 mg, 74%) as orange crystals.

Mp: 132 °C (dec.);  $\delta_{\text{H}}$ (400 MHz,  $\text{CD}_2\text{Cl}_2$ ) 7.81 (m, 2 H, *o*- $\text{C}_6\text{H}_4$  of dppbe), 7.52 (m, 8 H, *o*- $\text{C}_6\text{H}_5$  of dppbe), 7.45 (m, 2 H, *m*- $\text{C}_6\text{H}_4$  of dppbe), 7.34 (m, 4 H, *p*- $\text{C}_6\text{H}_5$  of dppbe), 7.28 (m, 8 H, *m*- $\text{C}_6\text{H}_5$  of dppbe), 7.15 (d,  $^3J_{\text{H,H}} = 7.6$  Hz, 2 H, *H*-6/*H*-6'), 7.07 (d,  $^3J_{\text{H,H}} = 7.2$  Hz, 2 H, *H*-3/*H*-3'), 6.98 (t,  $^3J_{\text{H,H}} = 7.2$  Hz, 2 H, *H*-4/*H*-4' or *H*-5/*H*-5'), 6.91 (t,  $^3J_{\text{H,H}} = 7.2$  Hz, 2 H, *H*-4/*H*-4' or *H*-5/*H*-5'), 2.01 (s, 6 H,  $\text{CH}_3$ );  $\delta_{\text{C}}$ (100 MHz,  $\text{CD}_2\text{Cl}_2$ ) 146.7 (m, *ipso*- $\text{C}_6\text{H}_4$  of dppbe), 137.8 (m, *C*-2/*C*-2'), 136.6 (m, *C*-1/*C*-1'), 136.2 (m, *ipso*- $\text{C}_6\text{H}_5$  of dppbe), 134.1 (m, *o*- $\text{C}_6\text{H}_4$  of dppbe), 133.2 (m, *o*- $\text{C}_6\text{H}_5$  of dppbe), 131.3 (s, *C*-6/*C*-6'), 131.0 (s, *m*- $\text{C}_6\text{H}_4$  of dppbe), 129.9 (s, *p*- $\text{C}_6\text{H}_5$  of dppbe), 129.4 (s, *C*-3/*C*-3'), 128.6 (m, *m*- $\text{C}_6\text{H}_5$  of dppbe), 125.9 (s, *C*-4/*C*-4' or *C*-5/*C*-5'), 125.2 (s, *C*-4/*C*-4' or *C*-5/*C*-5'), 21.2 (s,  $\text{CH}_3$ );  $\delta_{\text{P}}$ (81 MHz,  $\text{CD}_2\text{Cl}_2$ ) 52.05 (s with  $^{195}\text{Pt}$  satellites,  $^1J_{\text{Pt}}$  = 3138 Hz);  $\nu(\text{KBr})/\text{cm}^{-1}$  3052 (s), 2922 (m), 1778 (m,  $\nu(\text{C}\equiv\text{C})$ ), 1753 (m), 1625 (s), 1481 (s), 1434 (vs), 1096 (s), 759 (s) 694 (vs), 547 (vs), 527 (vs); *m/z*(DEI) 847 (100%,  $[\text{M}]^+$ ), 641 (60,  $[(\text{dppbe})\text{Pt}]^+$ ), 486 (10,  $[(\text{dppbe})\text{Pt} - 2\times\text{Ph}]^+$ ), 205 (20, **4c**<sup>+</sup>); Anal. calcd. for  $\text{C}_{46}\text{H}_{38}\text{P}_2$ : C 65.17, H 4.52; Found C 64.88, H 4.46.

**[(dppbe)( $\eta^2$ -1-phenyl-2-(2-pyridyl)acetylene)Pt<sup>0</sup>] (5d).** Compound **3** (112 mg, 0.16 mmol) was reacted with **4d** (29 mg, 0.16 mmol) to yield **5d** (54 mg, 49%) as yellow crystals.

Mp: 138 °C (dec.);  $\delta_{\text{H}}$ (400 MHz, CD<sub>2</sub>Cl<sub>2</sub>) 8.61 (d,  $^3J_{\text{H,H}} = 4.2$  Hz, 1 H, *H*-5), 7.99 (d,  $^3J_{\text{H,H}} = 7.0$  Hz, 2 H, *H*-2'/*H*-6'), 7.79 (m, 2 H, *o*-C<sub>6</sub>H<sub>4</sub> of dppbe), 7.67 (m, 8 H, *o*-C<sub>6</sub>H<sub>5</sub> of dppbe), 7.48 (m, 2 H, *m*-C<sub>6</sub>H<sub>4</sub> of dppbe), 7.33 (m, 13 H, *m*-C<sub>6</sub>H<sub>5</sub> and *p*-C<sub>6</sub>H<sub>5</sub> of dppbe and *H*-3), 7.25 (d,  $^3J_{\text{H,H}} = 7.7$  Hz, 1 H, *H*-2), 7.16 (m, 3 H, *H*-3', *H*-4' and *H*-5'), 6.97 (m, 1 H, *H*-4);  $\delta_{\text{C}}$ (100 MHz, CD<sub>2</sub>Cl<sub>2</sub>) 154.6 (m, *C*-1), 149.8 (s, *C*-5), 146.4 (m, *ipso*-C<sub>6</sub>H<sub>4</sub> of dppbe), 136.2 (s, *C*-3), 135.5 (m, *ipso*-C<sub>6</sub>H<sub>5</sub> of dppbe), 134.0 (m, *o*-C<sub>6</sub>H<sub>4</sub> of dppbe and *C*-1'), 133.4 (m, *o*-C<sub>6</sub>H<sub>5</sub> of dppbe), 132.7 (m, *C*-2' and *C*-6'), 131.1 (s, *m*-C<sub>6</sub>H<sub>4</sub> of dppbe), 130.2 (s, *p*-C<sub>6</sub>H<sub>5</sub> of dppbe), 128.7 (m, *m*-C<sub>6</sub>H<sub>5</sub> of dppbe), 128.3 (s, *C*-3' and *C*-5'), 127.4 (s, *C*-2), 127.2 (s, *C*-4'), 120.4 (s, *C*-4);  $\delta_{\text{P}}$ (81 MHz, CD<sub>2</sub>Cl<sub>2</sub>) 51.28 (d with <sup>195</sup>Pt satellites,  $^1J_{\text{P,Pt}} = 3063$  Hz,  $^2J_{\text{P,P}} = 55.1$  Hz), 51.25 (d with <sup>195</sup>Pt satellites,  $^1J_{\text{P,Pt}} = 3079$  Hz,  $^2J_{\text{P,P}} = 55.1$  Hz);  $\nu(\text{KBr})/\text{cm}^{-1}$  3051 (s), 1736 (s,  $\nu(\text{C}\equiv\text{C})$ ), 1629 (s), 1579 (vs), 1555 (m), 1482 (s), 1435 (vs), 1424 (vs), 1097 (vs), 759 (s), 694 (vs), 669 (s), 548 (vs), 527 (vs);  $m/z(\text{FAB in nba})$  821 (80%, [M]<sup>+</sup>), 641 (65, [(dppbe)Pt]<sup>+</sup>), 561 (55, [(dppbe)Pt - Ph]<sup>+</sup>), 485 (75, [(dppbe)Pt - 2×Ph]<sup>+</sup>); Anal. calcd. for C<sub>43</sub>H<sub>33</sub>NP<sub>2</sub>Pt · C<sub>4</sub>H<sub>8</sub>O: C 63.22, H 4.63, N 1.57; Found C 63.26, H 4.67, N 1.56.

**[(dppbe)( $\eta^2$ -1,2-bis(2-pyridyl)acetylene)Pt<sup>0</sup>] (5e).** Compound **3** (133 mg, 0.19 mmol) was reacted with **4e** (34 mg, 0.19 mmol) to yield **5e** (75 mg, 49%) as yellow crystals.

Mp: 165 °C (dec.);  $\delta_{\text{H}}$ (400 MHz, CD<sub>2</sub>Cl<sub>2</sub>) 8.53 (m, 2 H, *H*-5/*H*-5'), 7.96 (d,  $^3J_{\text{H,H}} = 7.8$  Hz, 2 H, *H*-2/*H*-2'), 7.84 (m, 2 H, *o*-C<sub>6</sub>H<sub>4</sub> of dppbe), 7.74 (m, 8 H, *o*-C<sub>6</sub>H<sub>5</sub> of dppbe), 7.49 (m, 4 H, *m*-C<sub>6</sub>H<sub>4</sub> of dppbe and *H*-3/*H*-3'), 7.33 (m, 12 H, *m*-C<sub>6</sub>H<sub>5</sub> and *p*-C<sub>6</sub>H<sub>5</sub> of dppbe), 7.01 (m, 2 H, *H*-4/*H*-4');  $\delta_{\text{C}}$ (100 MHz, CD<sub>2</sub>Cl<sub>2</sub>) 153.5 (m, *C*-1/*C*-1'), 149.7 (s, *C*-5/*C*-5'), 146.5 (m, *ipso*-C<sub>6</sub>H<sub>4</sub> of dppbe), 136.1 (s, *C*-3/*C*-3'), 135.9 (m, *ipso*-C<sub>6</sub>H<sub>5</sub> of dppbe), 134.2 (m, *o*-C<sub>6</sub>H<sub>4</sub> of dppbe), 133.5 (m, *o*-C<sub>6</sub>H<sub>5</sub> of dppbe), 131.1 (s, *m*-C<sub>6</sub>H<sub>4</sub> of dppbe), 130.1 (s, *p*-C<sub>6</sub>H<sub>5</sub> of dppbe), 128.6 (m, *m*-C<sub>6</sub>H<sub>5</sub> of dppbe), 127.4 (m, *C*-2/*C*-2'), 121.0 (s, *C*-4/*C*-4');  $\delta_{\text{P}}$ (81 MHz, CD<sub>2</sub>Cl<sub>2</sub>) 52.60 (s with <sup>195</sup>Pt satellites,  $^1J_{\text{P,Pt}} = 3108$  Hz);  $\nu(\text{KBr})/\text{cm}^{-1}$  3049 (s), 1736 (s,  $\nu(\text{C}\equiv\text{C})$ ), 1628 (m), 1579 (vs), 1556 (s), 1481 (s), 1461 (vs), 1434 (vs), 1425 (vs), 1272 (m), 1097 (s), 781 (s), 744 (s), 694 (vs), 549 (vs), 527 (vs);  $m/z(\text{FAB in nba})$  822 (25%, [M]<sup>+</sup>), 641 (15, [(dppbe)Pt]<sup>+</sup>), 561 (15, [(dppbe)Pt - Ph]<sup>+</sup>), 485 (40, [(dppbe)Pt - 2×Ph]<sup>+</sup>), 408 (40, [(dppbe)Pt - 3×Ph]<sup>+</sup>); Anal. calcd. for C<sub>42</sub>H<sub>32</sub>N<sub>2</sub>P<sub>2</sub>Pt: C 61.39, H 3.93, N 3.41; Found C 61.54, H 3.81, N 3.35.

**[(dppbe)( $\eta^2$ -2,2'-dimethoxytolane)Pt<sup>0</sup>] (5f).** Compound **3** (129 mg, 0.18 mmol) was reacted with **4f** (43 mg, 0.18 mmol) to yield **5f** (54 mg, 34%) as yellow crystals.

Mp: 183 °C (dec.);  $\delta_{\text{H}}$ (400 MHz, CD<sub>2</sub>Cl<sub>2</sub>) 7.79 (m, 2 H, *o*-C<sub>6</sub>H<sub>4</sub> of dppbe), 7.60 (m, 8 H, *o*-C<sub>6</sub>H<sub>5</sub> of dppbe), 7.45 (m, 2 H, *m*-C<sub>6</sub>H<sub>4</sub> of dppbe), 7.29 (m, 12 H, *m*-C<sub>6</sub>H<sub>5</sub> and *p*-C<sub>6</sub>H<sub>5</sub> of dppbe), 7.11 (m, 2 H, *H*-6/*H*-6'), 7.07 (t,  $^3J_{\text{H,H}} = 7.2$  Hz, 2 H, *H*-4/*H*-4'), 6.77 (d,  $^3J_{\text{H,H}} = 8.4$  Hz, 2 H, *H*-3/*H*-3'), 6.67 (t,  $^3J_{\text{H,H}} = 7.2$  Hz, 2 H, *H*-5/*H*-5'), 3.43 (s, 6 H, OCH<sub>3</sub>);  $\delta_{\text{C}}$ (100 MHz, CD<sub>2</sub>Cl<sub>2</sub>) 157.6 (s, *C*-2/*C*-2'), 146.9 (m, *ipso*-C<sub>6</sub>H<sub>4</sub> of dppbe), 136.3 (m, *ipso*-C<sub>6</sub>H<sub>5</sub> of dppbe), 134.0 (m, *o*-C<sub>6</sub>H<sub>4</sub> of dppbe), 133.3 (m, *o*-C<sub>6</sub>H<sub>5</sub> of dppbe), 133.1 (s, *C*-6/*C*-6'), 130.9 (s, *m*-C<sub>6</sub>H<sub>4</sub> of dppbe), 129.9 (s, *p*-C<sub>6</sub>H<sub>5</sub> of dppbe), 128.6 (m, *m*-C<sub>6</sub>H<sub>5</sub> of dppbe), 127.1 (s, *C*-4/*C*-4'), 126.6 (m, *C*-1/*C*-1'), 119.8 (s, *C*-5/*C*-5'), 110.0 (s, *C*-3/*C*-3'), 55.0 (s,

OCH<sub>3</sub>);  $\delta_{\text{P}}$ (81 MHz, CD<sub>2</sub>Cl<sub>2</sub>) 51.68 (s with <sup>195</sup>Pt satellites,  $^1J_{\text{P,Pt}} = 3107$  Hz);  $\nu(\text{KBr})/\text{cm}^{-1}$  3052 (s), 2935 (m), 2830 (m), 1785 (m,  $\nu(\text{C}\equiv\text{C})$ ), 1625 (s), 1587 (s), 1571 (s), 1481 (vs), 1433 (vs), 1241 (vs), 1181 (s), 1096 (vs), 1027 (s), 747 (vs), 695 (vs), 548 (vs), 526 (vs), 507 (vs);  $m/z(\text{DEI})$  879 (1%, [M]<sup>+</sup>), 641 (3, [(dppbe)Pt]<sup>+</sup>), 485 (2, [(dppbe)Pt - 2×Ph]<sup>+</sup>), 238 (100, [4f]<sup>+</sup>); Anal. calcd. for C<sub>46</sub>H<sub>38</sub>O<sub>2</sub>P<sub>2</sub>Pt · 0.5 C<sub>7</sub>H<sub>8</sub>: C 64.21, H 4.57; Found C 63.98, H 4.81.

**[(dppbe)( $\eta^2$ -4,4'-dimethoxytolane)Pt<sup>0</sup>] (5g).** Compound **3** (140 mg, 0.20 mmol) was reacted with **4g** (46 mg, 0.20 mmol) to yield **5g** (68 mg, 39%) as orange crystals.

Mp: >230 °C;  $\delta_{\text{H}}$ (400 MHz, CD<sub>2</sub>Cl<sub>2</sub>) 7.79 (m, 2 H, *o*-C<sub>6</sub>H<sub>4</sub> of dppbe), 7.65 (m, 8 H, *o*-C<sub>6</sub>H<sub>5</sub> of dppbe), 7.48 (m, 6 H, *m*-C<sub>6</sub>H<sub>4</sub> of dppbe and *H*-2/*H*-2' and *H*-6/*H*-6'), 7.34 (m, 12 H, *m*-C<sub>6</sub>H<sub>5</sub> and *p*-C<sub>6</sub>H<sub>5</sub> of dppbe), 6.68 (m, 4 H, *H*-3/*H*-3' and *H*-5/*H*-5'), 3.76 (s, 6 H, OCH<sub>3</sub>);  $\delta_{\text{C}}$ (100 MHz, CD<sub>2</sub>Cl<sub>2</sub>) 158.5 (s, *C*-4/*C*-4'), 146.9 (m, *ipso*-C<sub>6</sub>H<sub>4</sub> of dppbe), 136.0 (m, *ipso*-C<sub>6</sub>H<sub>5</sub> of dppbe), 134.0 (m, *o*-C<sub>6</sub>H<sub>4</sub> of dppbe), 133.4 (m, *o*-C<sub>6</sub>H<sub>5</sub> of dppbe), 132.4 (s, *C*-2/*C*-2' and *C*-6/*C*-6'), 131.0 (s, *m*-C<sub>6</sub>H<sub>4</sub> of dppbe), 130.1 (s, *p*-C<sub>6</sub>H<sub>5</sub> of dppbe), 128.7 (m, *m*-C<sub>6</sub>H<sub>5</sub> of dppbe), 128.0 (m, *C*-1/*C*-1'), 113.8 (s, *C*-3/*C*-3' and *C*-5/*C*-5'), 55.6 (s, OCH<sub>3</sub>);  $\delta_{\text{P}}$ (81 MHz, CD<sub>2</sub>Cl<sub>2</sub>) 51.63 (s with <sup>195</sup>Pt satellites,  $^1J_{\text{P,Pt}} = 3065$  Hz);  $\nu(\text{KBr})/\text{cm}^{-1}$  3052 (s), 2954 (m), 2834 (m), 1743 (m,  $\nu(\text{C}\equiv\text{C})$ ), 1601 (s), 1506 (vs), 1481 (s), 1435 (vs), 1285 (s), 1242 (vs), 1180 (s), 1097 (s), 1028 (s), 831 (s), 747 (s), 694 (vs), 669 (s), 546 (vs), 526 (vs), 506 (s);  $m/z(\text{DEI})$  879 (1%, [M]<sup>+</sup>), 641 (3, [(dppbe)Pt]<sup>+</sup>), 486 (1, [(dppbe)Pt - 2×Ph]<sup>+</sup>), 238 (100, [4g]<sup>+</sup>); Anal. calcd. for C<sub>46</sub>H<sub>38</sub>O<sub>2</sub>P<sub>2</sub>Pt: C 62.80, H 4.35; Found C 62.46, H 4.36.

**[(dppn)( $\eta^2$ -2,2'-dimethyltolane)Pt<sup>0</sup>] (9a).** Compound **8a** (235 mg, 0.31 mmol) was reacted with **4c** (64 mg, 0.31 mmol) to yield **9a** (175 mg, 63%) as orange crystals.

Mp: 106 °C (dec.);  $\delta_{\text{H}}$ (400 MHz, CD<sub>2</sub>Cl<sub>2</sub>) 8.02 (dd,  $^3J_{\text{H,H}} = 8.0$  Hz,  $^4J_{\text{H,H}} = 1.2$  Hz, 2 H, *H*-4 and *H*-5 of dppn), 7.46 (m, 2 H, *H*-2 and *H*-7 of dppn), 7.39 (t,  $^3J_{\text{H,H}} = 7.5$  Hz, 2 H, *H*-3 and *H*-6 of dppn), 7.14 (m, 12 H, *o*-C<sub>6</sub>H<sub>5</sub> and *p*-C<sub>6</sub>H<sub>5</sub> of dppn), 7.02 (m, 8 H, *m*-C<sub>6</sub>H<sub>5</sub> of dppn), 6.94 (m, 2 H, *H*-6/*H*-6'), 6.88 (dt,  $^3J_{\text{H,H}} = 7.4$  Hz,  $^4J_{\text{H,H}} = 1.5$  Hz, 2 H, *H*-5/*H*-5'), 6.73 (m, 2 H, *H*-3/*H*-3'), 6.70 (m, 2 H, *H*-4/*H*-4'), 1.98 (s, 6 H, CH<sub>3</sub>);  $\delta_{\text{C}}$ (50 MHz, CD<sub>2</sub>Cl<sub>2</sub>) 139.1 (m, *C*-8a of dppn), 136.9 (m, *C*-2 and *C*-7 of dppn and *C*-2/*C*-2'), 136.2 (m, *ipso*-C<sub>6</sub>H<sub>5</sub> of dppn), 135.9 (m, *C*-1 and *C*-8 of dppn and *C*-1/*C*-1'), 133.6 (m, *o*-C<sub>6</sub>H<sub>5</sub> of dppn), 132.8 (s, *C*-4 and *C*-5 of dppn), 130.0 (s, *C*-3/*C*-3'), 129.3 (s, *p*-C<sub>6</sub>H<sub>5</sub> of dppn), 128.2 (m, *m*-C<sub>6</sub>H<sub>5</sub> of dppn), 127.8 (m, *C*-4a of dppn), 125.2 (m, *C*-3 and *C*-6 of dppn and *C*-4/*C*-4' and *C*-5/*C*-5'), 21.2 (s, CH<sub>3</sub>);  $\delta_{\text{P}}$ (81 MHz, CD<sub>2</sub>Cl<sub>2</sub>) 17.43 (s with <sup>195</sup>Pt satellites,  $^1J_{\text{P,Pt}} = 3049$  Hz);  $\nu(\text{KBr})/\text{cm}^{-1}$  3053 (s), 2952 (m), 2919 (m), 1775 (s,  $\nu(\text{C}\equiv\text{C})$ ), 1751 (s,  $\nu(\text{C}\equiv\text{C})$ ), 1595 (s), 1479 (vs), 1455 (s), 1434 (vs), 1313 (m), 1182 (m), 1093 (vs), 875 (m), 824 (m), 772 (vs), 744 (vs), 693 (vs), 587 (vs), 519 (vs), 495 (vs);  $m/z(\text{FAB in nba})$  898 (2%, [M]<sup>+</sup>), 691 (6, [(dppn)Pt]<sup>+</sup>), 535 (4, [(dppn)Pt - 2×Ph]<sup>+</sup>); Anal. calcd. for C<sub>50</sub>H<sub>40</sub>P<sub>2</sub>Pt · C<sub>5</sub>H<sub>12</sub>: C 68.10, H 5.40; Found C 67.91, H 5.25.

**[(dpp(o-xy))( $\eta^2$ -2,2'-dimethyltolane)Pt<sup>0</sup>] (9b).** Compound **8b** (140 mg, 0.19 mmol) was reacted with **4c** (40 mg, 0.19 mmol) to yield **9b** (63 mg, 38%) as pale yellow crystals.

Mp: 203 °C (dec.);  $\delta_{\text{H}}$ (400 MHz, CD<sub>2</sub>Cl<sub>2</sub>) 7.60 (m, 8 H, *o*-C<sub>6</sub>H<sub>5</sub> of dpp(o-xy)), 7.36 (m, 4 H, *p*-C<sub>6</sub>H<sub>5</sub> of dpp(o-xy)), 7.29 (m, 8 H, *m*-C<sub>6</sub>H<sub>5</sub> of dpp(o-xy)), 6.93 (d,  $^3J_{\text{H,H}} = 7.5$  Hz, 2 H, *H*-6/*H*-6'), 6.81 (dt,  $^3J_{\text{H,H}} = 7.3$  Hz,  $^4J_{\text{H,H}} = 1.7$  Hz, 2 H, *H*-5/*H*-5'), 6.74

(m, 2 H, *m*-C<sub>6</sub>H<sub>4</sub> of dpp(o-xyl)), 6.63 (m, 2 H, *H*-4/*H*-4'), 6.60 (m, 2 H, *H*-3/*H*-3'), 6.25 (m, 2 H, *o*-C<sub>6</sub>H<sub>4</sub> of dpp(o-xyl)), 4.13 (m, 4 H, PCH<sub>2</sub>), 1.82 (s, 6 H, CH<sub>3</sub>);  $\delta_{\text{C}}$ (100 MHz, CD<sub>2</sub>Cl<sub>2</sub>) 137.4 (m, *C*-2/*C*-2'), 136.8 (m, *ipso*-C<sub>6</sub>H<sub>5</sub> of dpp(o-xyl)), 135.9 (m, *C*-1/*C*-1'), 134.8 (s, *ipso*-C<sub>6</sub>H<sub>4</sub> of dpp(o-xyl)), 133.7 (m, *o*-C<sub>6</sub>H<sub>5</sub> of dpp(o-xyl)), 131.2 (s, *o*-C<sub>6</sub>H<sub>4</sub> of dpp(o-xyl)), 129.9 (s, *p*-C<sub>6</sub>H<sub>5</sub> of dpp(o-xyl)), 129.6 (s, *C*-3/*C*-3'), 129.1 (s, *C*-6/*C*-6'), 128.2 (m, *m*-C<sub>6</sub>H<sub>5</sub> of dpp(o-xyl)), 126.1 (s, *m*-C<sub>6</sub>H<sub>4</sub> of dpp(o-xyl)), 125.3 (s, *C*-5/*C*-5'), 124.8 (s, *C*-4/*C*-4'), 38.9 (m, PCH<sub>2</sub>), 21.0 (s, CH<sub>3</sub>);  $\delta_{\text{P}}$ (81 MHz, CD<sub>2</sub>Cl<sub>2</sub>) 13.58 (s with <sup>195</sup>Pt satellites, <sup>1</sup>*J*<sub>P,Pt</sub> = 3449 Hz);  $\nu(\text{KBr})/\text{cm}^{-1}$  3053 (s), 2943 (m), 2916 (m), 1779 (s,  $\nu(\text{C}\equiv\text{C})$ ), 1754 (m,  $\nu(\text{C}\equiv\text{C})$ ), 1595 (s), 1480 (vs), 1455 (s), 1435 (vs), 1183 (m), 1096 (vs), 1027 (m), 863 (s), 837 (s), 763 (vs), 742 (vs), 695 (vs), 503 (vs); *m/z*(FAB in nba) 876 (1%, [M]<sup>+</sup>), 669 (4, [(dpp(o-xyl))Pt]<sup>+</sup>); Anal. calcd. for C<sub>48</sub>H<sub>42</sub>P<sub>2</sub>Pt · C<sub>6</sub>H<sub>6</sub>: C 67.99, H 5.07; Found C 67.52, H 5.38.

### Irradiation experiments in the solid state

In a sample vial the appropriate (diphosphine)( $\eta^2$ -tolane)Pt<sup>0</sup> complex was placed in the sunlight for the stated periods. From time to time the vial was turned to ensure constant irradiation conditions. A portion of each sample was dissolved in benzene-d<sub>6</sub> and a <sup>31</sup>P{<sup>1</sup>H} NMR spectrum was recorded to survey the result of the experiment.

**5a.** Complex **5a** (11 mg, 0.011 mmol) was irradiated with sunlight for approximately 12 days. Integration of the signals in the corresponding <sup>31</sup>P{<sup>1</sup>H} NMR spectrum revealed nearly 90% conversion of **5a** to **6a**.

$\delta_{\text{P}}$ (81 MHz, C<sub>6</sub>D<sub>6</sub>) 51.17 (s with <sup>195</sup>Pt satellites, <sup>1</sup>*J*<sub>P,Pt</sub> = 3102 Hz, residual **5a**), 50.59 (d with <sup>195</sup>Pt satellites, <sup>1</sup>*J*<sub>P,Pt</sub> = 2467 Hz, <sup>2</sup>*J*<sub>P,P</sub> = 3.2 Hz, **6a**), 49.23 (d with <sup>195</sup>Pt satellites, <sup>1</sup>*J*<sub>P,Pt</sub> = 1575 Hz, <sup>2</sup>*J*<sub>P,P</sub> = 3.2 Hz, **6a**).

**5b.** Complex **5b** (16 mg, 0.016 mmol) was irradiated with sunlight for approximately 10 days. Integration of the signals in the corresponding <sup>31</sup>P{<sup>1</sup>H} NMR spectrum revealed 45% conversion of **5b** to **6b**.

$\delta_{\text{P}}$ (81 MHz, C<sub>6</sub>D<sub>6</sub>) 51.77 (s with <sup>195</sup>Pt satellites, <sup>1</sup>*J*<sub>P,Pt</sub> = 3132 Hz, residual **5b**), 50.22 (d with <sup>195</sup>Pt satellites, <sup>1</sup>*J*<sub>P,Pt</sub> = 2454 Hz, <sup>2</sup>*J*<sub>P,P</sub> = 3.0 Hz, **6b**), 48.89 (d with <sup>195</sup>Pt satellites, <sup>1</sup>*J*<sub>P,Pt</sub> = 1615 Hz, <sup>2</sup>*J*<sub>P,P</sub> = 3.0 Hz, **6b**).

**5c.** Complex **5c** (13 mg, 0.015 mmol) was irradiated with sunlight for approximately 11 days. Integration of the signals in the corresponding <sup>31</sup>P{<sup>1</sup>H} NMR spectrum revealed 25% conversion of **5c** to **6c**.

$\delta_{\text{P}}$ (81 MHz, C<sub>6</sub>D<sub>6</sub>) 52.38 (s with <sup>195</sup>Pt satellites, <sup>1</sup>*J*<sub>P,Pt</sub> = 3149 Hz, residual **5c**), 50.50 (d with <sup>195</sup>Pt satellites, <sup>1</sup>*J*<sub>P,Pt</sub> = 2469 Hz, <sup>2</sup>*J*<sub>P,P</sub> = 2.8 Hz, **6c**), 48.57 (d with <sup>195</sup>Pt satellites, <sup>1</sup>*J*<sub>P,Pt</sub> = 1561 Hz, <sup>2</sup>*J*<sub>P,P</sub> = 2.8 Hz, **6c**).

**5d–g and 9b.** The appropriate (diphosphine)( $\eta^2$ -tolane)Pt<sup>0</sup> complex (12 mg, 0.012–0.015 mmol) was irradiated with sunlight for approximately 14 days. The corresponding <sup>31</sup>P{<sup>1</sup>H} NMR spectrum showed only the resonances of the starting material. No evidence for C–C bond activation was observed in any case.

**9a.** Orange crystals of **9a** (98 mg, 0.110 mmol) were placed in a sample vial and irradiated as described above for 50 days to ensure full conversion into **10a**. The reaction progress was checked

by <sup>31</sup>P{<sup>1</sup>H} NMR spectroscopy. After completion of the reaction **10a** was obtained as yellow powder (88 mg, 90%).

Mp: 175 °C (dec.);  $\delta_{\text{H}}$ (400 MHz, CD<sub>2</sub>Cl<sub>2</sub>) 8.08 (d, <sup>3</sup>*J*<sub>H,H</sub> = 8.0 Hz, 2 H, *H*-4 and *H*-5 of dppn), 7.62–7.41 (m, 8 H, *H*-2, *H*-3, *H*-6 and *H*-7 of dppn), 7.37–7.16 (m, 10 H), 7.06 (m, 2 H), 7.01–6.79 (m, 6 H), 6.73 (m, 3 H), 6.60 (m, 2 H), 6.42 (m, 1 H), 2.40 (s, 3 H, CH<sub>3</sub>), 1.88 (s, 3 H, CH<sub>3</sub>);  $\delta_{\text{C}}$ (100 MHz, CD<sub>2</sub>Cl<sub>2</sub>) 159.7 (m), 143.1 (m), 138.9 (s), 138.5 (s), 136.4 (m including 2 different C-atoms), 135.1 (s), 134.7 (m including 2 different C-atoms), 134.2 (m including 2 different C-atoms), 133.7 (m including 2 different C-atoms), 131.5 (s), 130.7 (s), 130.2 (s), 128.9 (m), 128.5 (m including 3 different C-atoms), 127.8 (m), 125.7 (m), 124.9 (m including 2 different C-atoms), 123.8 (m), 121.3 (s), 26.9 (s, CH<sub>3</sub>), 20.1 (s, CH<sub>3</sub>);  $\delta_{\text{P}}$ (81 MHz, CD<sub>2</sub>Cl<sub>2</sub>) 11.92 (d with <sup>195</sup>Pt satellites, <sup>1</sup>*J*<sub>P,Pt</sub> = 2427 Hz, <sup>2</sup>*J*<sub>P,P</sub> = 34 Hz), 8.98 (d with <sup>195</sup>Pt satellites, <sup>1</sup>*J*<sub>P,Pt</sub> = 1499 Hz, <sup>2</sup>*J*<sub>P,P</sub> = 34 Hz);  $\nu(\text{KBr})/\text{cm}^{-1}$  3052 (s), 2982 (m), 2916 (m), 2112 (s,  $\nu(\text{C}\equiv\text{C})$ ), 1595 (s), 1573 (m), 1480 (vs), 1435 (vs), 1329 (s), 1314 (s), 1185 (s), 1158 (s), 1096 (vs), 878 (m), 824 (s), 771 (vs), 743 (vs), 693 (vs), 585 (vs), 524 (vs), 499 (vs); *m/z*(DEI) 897 (10%, [M]<sup>+</sup>), 691 (20, [(dppn)Pt]<sup>+</sup>), 206 (100, [4c]<sup>+</sup>); Anal. calcd. for C<sub>50</sub>H<sub>40</sub>P<sub>2</sub>Pt · 0.25 CH<sub>2</sub>Cl<sub>2</sub>: C 65.67, H 4.44; Found C 65.90, H 4.57.

### Irradiation experiments in solution

The appropriate (diphosphine)( $\eta^2$ -tolane)Pt<sup>0</sup> complex was dissolved in toluene and put in a round bottom flask. These solutions were irradiated with sunlight for the stated periods and the reaction progress was checked by TLC. After completion of the reactions the solvent was removed under reduced pressure and the residue was worked up by column chromatography to isolate the corresponding products. In the case of **5c**, **5g**, **5f** and **9a**, this work up procedure failed.

**5a.** A solution of **5a** (120 mg, 0.123 mmol) in toluene (60 mL) was irradiated with sunlight for approximately 30 days. After removing the solvent the residue was chromatographed on silica gel using dichloromethane–hexane (2/1) → dichloromethane as eluent to yield **6a** (45 mg, 37%) as pale yellow powder.

Mp: 158 °C (dec.);  $\delta_{\text{H}}$ (400 MHz, CD<sub>2</sub>Cl<sub>2</sub>) 7.75 (m, 5 H), 7.67 (m, 1 H), 7.54–7.42 (m, 11 H), 7.34 (m, 8 H), 7.20 (m, 2 H), 7.05 (m, 1 H), 6.97 (m, 2 H), 6.81 (m, 2 H);  $\delta_{\text{C}}$ (100 MHz, CD<sub>2</sub>Cl<sub>2</sub>) 155.2 (m), 139.8 (m), 134.4 (m), 134.1 (m, including 3 different C-atoms), 132.8 (s), 132.5 (m, including 2 different C-atoms), 131.9 (s), 131.2 (m, including 2 different C-atoms), 130.0 (m), 129.6 (s), 129.0 (m, including 2 different C-atoms), 119.0 (s), 116.8 (s);  $\delta_{\text{P}}$ (81 MHz, CD<sub>2</sub>Cl<sub>2</sub>) 50.33 (d with <sup>195</sup>Pt satellites, <sup>1</sup>*J*<sub>P,Pt</sub> = 2493 Hz, <sup>2</sup>*J*<sub>P,P</sub> = 4.0 Hz), 49.01 (d with <sup>195</sup>Pt satellites, <sup>1</sup>*J*<sub>P,Pt</sub> = 1603 Hz, <sup>2</sup>*J*<sub>P,P</sub> = 4.0 Hz);  $\nu(\text{KBr})/\text{cm}^{-1}$  3054 (m), 2112 (s,  $\nu(\text{C}\equiv\text{C})$ ), 1620 (w), 1581 (w), 1481 (vs), 1468 (s), 1435 (vs), 1210 (m), 1185 (m), 1114 (s), 1100 (vs), 1069 (s), 1003 (vs), 824 (s), 799 (s), 745 (s), 693 (vs), 670 (s), 551 (vs), 532 (vs), 506 (s); *m/z*(DEI) 977 (0.1%, [M]<sup>+</sup>), 897 (0.05, [M – Br]<sup>+</sup>), 721 (1, [(dppbe)PtBr]<sup>+</sup>); Anal. calcd. for C<sub>44</sub>H<sub>32</sub>Br<sub>2</sub>P<sub>2</sub>Pt: C 54.06, H 3.30, Br 16.35; Found C 54.27, H 3.38, Br 16.76.

**5b.** A solution of **5b** (237 mg, 0.236 mmol) in toluene (60 mL) was irradiated with sunlight for approximately 21 days. After removing the solvent the residue was chromatographed on silica gel using dichloromethane–hexane (2/1) → dichloromethane as

**Table 2** Crystal data and refinement details for the X-ray structure determinations

Compound	5a	5b	5c	5d	5e	6b	7b	9a	9b
Formula	C <sub>44</sub> H <sub>32</sub> Br <sub>2</sub> P <sub>2</sub> Pt	C <sub>46</sub> H <sub>36</sub> Br <sub>2</sub> P <sub>2</sub> Pt	C <sub>46</sub> H <sub>38</sub> P <sub>2</sub> Pt	C <sub>43</sub> H <sub>33</sub> NP <sub>2</sub> Pt	C <sub>42</sub> H <sub>32</sub> N <sub>2</sub> P <sub>2</sub> Pt	C <sub>46</sub> H <sub>36</sub> Br <sub>2</sub> P <sub>2</sub> Pt	C <sub>46</sub> H <sub>36</sub> Br <sub>2</sub> P <sub>2</sub> Pt, C <sub>4</sub> H <sub>8</sub> O	C <sub>50</sub> H <sub>40</sub> P <sub>2</sub> Pt, C <sub>6</sub> H <sub>6</sub>	C <sub>48</sub> H <sub>42</sub> P <sub>2</sub> Pt, C <sub>6</sub> H <sub>6</sub>
Fw/g mol <sup>-1</sup>	977.55	1005.60	847.79	820.73	821.73	1005.60	1077.70	975.96	953.95
<i>T</i> /°C	-90(2)	-90(2)	-90(2)	-90(2)	-90(2)	-90(2)	-90(2)	-90(2)	-90(2)
Crystal system	Triclinic	Orthorhombic	Triclinic	Triclinic	Triclinic	Triclinic	Monoclinic	Triclinic	Triclinic
Space group	<i>P</i> $\bar{1}$	<i>Pbca</i>	<i>P</i> $\bar{1}$	<i>P</i> $\bar{1}$	<i>P</i> $\bar{1}$	<i>P</i> $\bar{1}$	<i>P</i> 2 <sub>1</sub> / <i>n</i>	<i>P</i> $\bar{1}$	<i>P</i> $\bar{1}$
<i>a</i> /Å	10.7128(4)	20.5293(3)	11.1682(5)	11.3596(4)	8.9010(4)	8.9257(2)	15.3444(5)	11.8366(5)	11.6006(5)
<i>b</i> /Å	11.4086(4)	16.4027(2)	12.2745(5)	11.5124(3)	11.0800(6)	11.2405(4)	15.6009(3)	12.6126(5)	12.9579(5)
<i>c</i> /Å	16.6238(6)	23.2611(3)	15.0911(7)	14.0287(5)	19.0760(7)	20.9629(8)	21.3260(6)	15.7836(9)	15.4685(5)
$\alpha$ /°	100.791(2)	90	79.550(2)	71.401(2)	103.772(3)	78.7990(10)	90	102.484(2)	91.791(2)
$\beta$ /°	96.609(2)	90	69.759(2)	83.585(2)	96.509(2)	83.363(2)	111.085(2)	107.407(3)	107.389(2)
$\gamma$ /°	107.566(2)	90	69.043(2)	88.476(2)	107.308(2)	69.013(2)	90	95.895(3)	103.098(2)
<i>V</i> /Å <sup>3</sup>	1870.52(12)	7832.85(18)	1808.67(14)	1727.8(1)	1709.75(14)	1923.84(11)	4763.4(2)	2159.55(18)	2148.93(14)
<i>Z</i>	2	8	2	2	2	2	4	2	2
$\rho$ /g cm <sup>-3</sup>	1.736	1.705	1.557	1.578	1.596	1.736	1.503	1.501	1.474
$\mu$ /cm <sup>-1</sup>	60.03	57.37	40	41.85	42.3	58.4	47.24	33.61	33.76
Measured data	11771	48171	12759	12393	12065	13479	31984	15004	15688
Data with									
<i>I</i> > 2 $\sigma$ ( <i>I</i> )	6807	6750	6772	6421	6139	6971	7025	7358	7398
Unique data/ <i>R</i> <sub>int</sub>	7820/0.0485	8934/0.0822	8218/0.0447	7859/0.0494	7769/0.0502	8752/0.0332	10847/0.0669	9765/0.0365	9765/0.0470
<i>wR</i> <sub>2</sub> (all data, on <i>F</i> <sup>2</sup> ) <sup>a</sup>	0.1268	0.0775	0.0902	0.0912	0.0996	0.0962	0.1483	0.1090	0.1226
<i>R</i> <sub>1</sub> ( <i>I</i> > 2 $\sigma$ ( <i>I</i> )) <sup>a</sup>	0.0482	0.0349	0.0451	0.0420	0.0470	0.0426	0.0534	0.0469	0.0526
<i>s</i> <sup>b</sup>	1.048	1.036	1.020	1.018	1.060	1.008	1.004	1.023	1.011
Res. dens./e Å <sup>-3</sup>	1.396/-1.646	1.298/-1.458	1.471/-1.288	1.078/-1.469	1.094/-1.133	1.318/-1.457	1.476/-1.506	1.530/-1.432	1.657/-1.741
Absorpt. method	NONE	NONE	NONE	NONE	NONE	NONE	NONE	NONE	NONE
CCDC No.	743160	743161	743162	743163	743164	743165	743166	743167	743269

<sup>a</sup> Definition of the *R* indices:  $R_1 = (\sum ||F_o| - |F_c||) / \sum |F_o|$ ;  $wR_2 = \{\sum [w(F_o^2 - F_c^2)^2] / \sum [w(F_o^2)^2]\}^{1/2}$  with  $w^{-1} = \sigma^2(F_o^2) + (aP)^2 + bP$ ;  $P = [2F_c^2 + \text{Max}(F_o^2)]/3$ ; <sup>b</sup>  $s = \{\sum [w(F_o^2 - F_c^2)^2] / (N_o - N_p)\}^{1/2}$ .

eluent to yield **6b** (60 mg, 25%) as white powder and **7b** (57 mg, 24%) as yellow crystals.

**6b.** Mp: >230 °C;  $\delta_H$ (400 MHz, CD<sub>2</sub>Cl<sub>2</sub>) 7.84 (m, 2 H), 7.77 (m, 1 H), 7.66 (m, 5 H), 7.56–7.38 (m, 12 H), 7.24 (m, 2 H), 7.12 (s, 1 H), 7.02 (dd, <sup>3</sup>*J*<sub>H,H</sub> = 8.2 Hz, <sup>4</sup>*J*<sub>H,H</sub> = 1.9 Hz, 1 H), 6.92 (m, 4 H), 6.83 (m, 1 H), 6.73 (m, 1 H), 1.94 (s, 3 H, CH<sub>3</sub>), 1.93 (s, 3 H, CH<sub>3</sub>);  $\delta_C$ (100 MHz, CD<sub>2</sub>Cl<sub>2</sub>) 147.3 (m), 141.8 (m), 138.3 (m), 134.4 (m, including 3 different C-atoms), 133.8 (m), 132.7 (m, including 3 different C-atoms), 131.8 (m, including 2 different C-atoms), 131.1 (m), 129.1 (m, including 2 different C-atoms), 128.7 (m), 128.2 (s), 126.5 (m), 118.4 (s), 116.9 (s), 25.9 (s, CH<sub>3</sub>), 20.6 (s, CH<sub>3</sub>);  $\delta_P$ (81 MHz, CD<sub>2</sub>Cl<sub>2</sub>) 50.08 (d with <sup>195</sup>Pt satellites, <sup>1</sup>*J*<sub>Pt</sub> = 2474 Hz, <sup>2</sup>*J*<sub>Pt</sub> = 4.0 Hz), 48.86 (d with <sup>195</sup>Pt satellites, <sup>1</sup>*J*<sub>Pt</sub> = 1639 Hz, <sup>2</sup>*J*<sub>Pt</sub> = 4.0 Hz);  $\nu$ (KBr)/cm<sup>-1</sup> 3053 (s), 2950 (w), 2110 (s,  $\nu$ (C≡C)), 1619 (m), 1472 (vs), 1435 (vs), 1187 (s), 1100 (vs), 1028 (s), 865 (m), 839 (m), 815 (m), 745 (s), 693 (vs), 670 (s), 552 (vs), 532 (vs), 506 (vs); *m/z*(DEI) 1006 (2%, [M]<sup>+</sup>), 924 (4, [M – Br]<sup>+</sup>), 721 (35, [(dppbe)PtBr]<sup>+</sup>), 641 (12, [(dppbe)Pt]<sup>+</sup>), 487 (4, [(dppbe)Pt – 2xPh]<sup>+</sup>), 364 (4, [4b]<sup>+</sup>); Anal. calcd. for C<sub>46</sub>H<sub>36</sub>Br<sub>2</sub>P<sub>2</sub>Pt: C 54.94, H 3.61, Br 15.89; Found C 55.28, H 3.59, Br 15.31.

**7b.** Mp: 151 °C (dec.);  $\delta_H$ (400 MHz, CD<sub>2</sub>Cl<sub>2</sub>) 7.76 (m, 4 H), 7.63 (m, 1 H), 7.51 (m, 11 H), 7.38 (m, 10 H), 7.29 (m, 2 H), 6.98 (m, 2 H), 6.80 (d, <sup>3</sup>*J*<sub>H,H</sub> = 7.0 Hz, 1 H), 2.45 (s, 3 H, CH<sub>3</sub>), 2.13 (s, 3 H, CH<sub>3</sub>);  $\delta_C$ (100 MHz, CD<sub>2</sub>Cl<sub>2</sub>) 136.5 (m), 142.2 (m), 139.0 (m), 138.1 (m), 135.4 (m), 134.0 (m, including 5 different C-atoms), 133.1 (s), 132.6 (m), 131.6 (m), 131.3 (s), 130.1 (m), 128.9 (m, including 3 different C-atoms), 123.6 (s), 121.5 (s), 117.0 (m), 95.6 (s, C≡C), 89.5 (s, C≡C), 21.0 (s, CH<sub>3</sub>), 20.7 (s, CH<sub>3</sub>);  $\delta_P$ (81 MHz, CD<sub>2</sub>Cl<sub>2</sub>) 49.64 (d with <sup>195</sup>Pt satellites, <sup>1</sup>*J*<sub>Pt</sub> = 1684 Hz, <sup>2</sup>*J*<sub>Pt</sub> = 3.5 Hz), 43.01

(d with <sup>195</sup>Pt satellites, <sup>1</sup>*J*<sub>Pt</sub> = 4090 Hz, <sup>2</sup>*J*<sub>Pt</sub> = 3.5 Hz);  $\nu$ (KBr)/cm<sup>-1</sup> 3053 (m), 2973 (m), 2868 (m), 2205 (m,  $\nu$ (C≡C)), 1631 (m), 1573 (s), 1484 (vs), 1435 (vs), 1190 (s), 1100 (vs), 881 (s), 816 (s), 746 (s), 693 (vs), 671 (s), 560 (vs), 533 (vs), 505 (vs); *m/z*(DEI) 1006 (2%, [M]<sup>+</sup>), 924 (3, [M – Br]<sup>+</sup>), 721 (40, [(dppbe)PtBr]<sup>+</sup>), 641 (10, [(dppbe)Pt]<sup>+</sup>), 283 (80, [4b – Br]<sup>+</sup>); Anal. calcd. for C<sub>46</sub>H<sub>36</sub>Br<sub>2</sub>P<sub>2</sub>Pt · 2 C<sub>4</sub>H<sub>8</sub>O: C 56.41, H 4.56, Br 13.90; Found C 56.84, H 4.49, Br 14.03.

### Crystal structure determinations

The intensity data for the compounds were collected on a Nonius KappaCCD diffractometer using graphite-monochromated Mo-K $\alpha$  radiation. Data were corrected for Lorentz and polarization effects but not for absorption effects.<sup>32,33</sup> The structures were solved by direct methods (SHELXS)<sup>34</sup> and refined by full-matrix least squares techniques against *F*<sub>o</sub><sup>2</sup> (SHELXL-97) (Table 2).<sup>35</sup> All hydrogen atoms were included at calculated positions with fixed thermal parameters. All non-disordered non-hydrogen atoms were refined anisotropically.<sup>35</sup> Diamond 3.0b as well as POV-Ray 3.6.1c were used for structure representations. CCDC-743160 (for **5a**), -743161 (for **5b**), -743162 (for **5c**), -743163 (for **5d**), -743164 (for **5e**), -743165 (for **6b**), -743166 (for **7b**), -743167 (for **9a**) and -743269 (for **9b**) contain the supplementary crystallographic data for this paper.† These data can be obtained free of charge from the Cambridge Crystallographic Centre via www.ccdc.cam.ac.uk/data\_request/cif.

### Computational details

See part B.†

## Acknowledgements

The donation of  $K_2PtCl_4$  by the Heraeus GmbH is gratefully acknowledged by the authors. Additionally, we thank the students A. Pospiech and M. Assmann for preparing the phosphane ligands as well as some tolanes. Financial support from the Carl-Zeiss Stiftung (D.E.) is also acknowledged. Finally, we thank the reviewers for their valuable comments and suggestions.

## Notes and references

- M. Murakami and Y. Ito, in *Topics in Organometallic Chemistry*, ed. S. Murai, Springer, Berlin, 1999, vol. 3, pp. 97–129; K. C. Bishop III, *Chem. Rev.*, 1976, **76**, 461–486.
- P. W. Jennings and L. L. Johnson, *Chem. Rev.*, 1994, **94**, 2241–2290; R. H. Crabtree, *Chem. Rev.*, 1985, **85**, 245–269.
- B. Rybtchinski and D. Milstein, *Angew. Chem., Int. Ed.*, 1999, **38**, 870–883.
- C. Perthuisot and W. D. Jones, *J. Am. Chem. Soc.*, 1994, **116**, 3647–3648; C. Perthuisot, B. L. Edelbach, D. L. Zubris and W. D. Jones, *Organometallics*, 1997, **16**, 2016–2023; B. L. Edelbach, R. J. Lachicotte and W. D. Jones, *J. Am. Chem. Soc.*, 1998, **120**, 2843–2853; W. D. Jones, *Nature*, 1993, **364**, 676–677; D. D. Wick, T. O. Northcutt, R. J. Lachicotte and W. D. Jones, *Organometallics*, 1998, **17**, 4484–4492; T. Nishimura and K. Ohe, *J. Am. Chem. Soc.*, 1999, **121**, 2645–2646; T. Nishimura and S. Uemura, *J. Am. Chem. Soc.*, 1999, **121**, 11010–11011; Z. Lu, C.-H. Jun, S. R. de Gala, O. Eisenstein and R. H. Crabtree, *Organometallics*, 1995, **14**, 1168–1175; Z. Lu, C.-H. Jun, S. R. de Gala, M. Sigalas, O. Eisenstein and R. H. Crabtree, *J. Chem. Soc., Chem. Commun.*, 1993, 1877–1880; H. Schwager, S. Spyroudis and K. P. C. Vollhardt, *J. Organomet. Chem.*, 1990, **382**, 191–200; J. J. Eisch, A. M. Piotrowski, K. I. Han, C. Krüger and Y. H. Tsay, *Organometallics*, 1985, **4**, 224–231; T. C. Flood and J. A. Statler, *Organometallics*, 1984, **3**, 1795–1803.
- M. Gozin, A. Weisman, Y. Ben-David and D. Milstein, *Nature*, 1993, **364**, 699–701; M. Gozin, M. Aizenberg, S.-Y. Liou, A. Weisman, Y. Ben-David and D. Milstein, *Nature*, 1994, **370**, 42–44; R. H. Crabtree, R. P. Dion, D. J. Gibboni, D. V. McGrath and E. M. Holt, *J. Am. Chem. Soc.*, 1986, **108**, 7222–7227; A. Barretta, F. G. N. Cloke, A. Feigenbaum, M. L. H. Green, A. Gourdon and K. Prout, *J. Chem. Soc., Chem. Commun.*, 1981, 156–158; M. Gandelman, A. Vigalok, L. J. W. Shimon and D. Milstein, *Organometallics*, 1997, **16**, 3981–3986; S.-Y. Liou, M. Gozin and D. Milstein, *J. Am. Chem. Soc.*, 1995, **117**, 9774–9775; S.-Y. Liou, M. Gozin and D. Milstein, *J. Chem. Soc., Chem. Commun.*, 1995, 1965–1966.
- B. Rybtchinski, A. Vigalok, Y. Ben-David and D. Milstein, *J. Am. Chem. Soc.*, 1996, **118**, 12406–12415; M. E. van der Boom, H.-B. Kraatz, Y. Ben-David and D. Milstein, *Chem. Commun.*, 1996, 2167–2168.
- R. H. Crabtree and R. P. Dion, *J. Chem. Soc., Chem. Commun.*, 1984, 1260–1261; J. J. Garcia and W. D. Jones, *Organometallics*, 2000, **19**, 5544–5545; J. W. Suggs and S. D. Cox, *J. Organomet. Chem.*, 1981, **221**, 199–201; C.-H. Jun, C. W. Moon, H. Lee and D.-Y. Lee, *J. Mol. Catal. A: Chem.*, 2002, **189**, 145–156.
- J. J. Low and W. A. Goddard III, *J. Am. Chem. Soc.*, 1984, **106**, 8321–8322; P. E. M. Siegbahn and M. R. A. Blomberg, *J. Am. Chem. Soc.*, 1992, **114**, 10548–10556.
- J. A. Martinho, Simões and J. A. Beauchamp, *Chem. Rev.*, 1990, **90**, 629–688.
- S. P. Nolan, C. D. Hoff, P. O. Stoutland, L. J. Newman, J. M. Buchanan, R. G. Bergman, G. K. Young and K. S. Peters, *J. Am. Chem. Soc.*, 1987, **109**, 3143–3145; W. D. Jones and F. J. Feher, *J. Am. Chem. Soc.*, 1984, **106**, 1650–1663; P. O. Stoutland, R. G. Bergman, S. P. Nolan and C. D. Hoff, *Polyhedron*, 1988, **7**, 1429–1440.
- C. Müller, C. N. Iverson, R. J. Lachicotte and W. D. Jones, *J. Am. Chem. Soc.*, 2001, **123**, 9718–9719; A. Gunay, C. Müller, R. J. Lachicotte, W. W. Brennessel and W. D. Jones, *Organometallics*, 2009, **28**, 6524–6530.
- A. Gunay and W. D. Jones, *J. Am. Chem. Soc.*, 2007, **129**, 8729–8735.
- H. Petzold, T. Weisheit, H. Görls, H. Breitzke, G. Buntkowsky, D. Escudero, L. González and W. Weigand, *Dalton Trans.*, 2008, 1979–1981.
- H. Petzold, H. Görls and W. Weigand, *J. Organomet. Chem.*, 2007, **692**, 2736–2742.
- K. Zhang, J. Hu, K. C. Chan, K. Y. Wong and J. H. K. Yip, *Eur. J. Inorg. Chem.*, 2007, 384–393.
- A. Fürstner and P. W. Davies, *Angew. Chem.*, 2007, **119**, 3478–3519; A. Fürstner and P. W. Davies, *Angew. Chem., Int. Ed.*, 2007, **46**, 3410–3449.
- D. Escudero, M. Assmann, A. Pospiech, W. Weigand and L. González, *Chem. Phys. Phys. Chem.*, 2009, **11**, 4593–4600.
- K. Tanaka and F. Toda, *Chem. Rev.*, 2000, **100**, 1025–1074 and references therein.
- O. V. Zenkina, A. Karton, D. Freeman, L. J. W. Shimon, J. M. L. Martin and M. E. van der Boom, *Inorg. Chem.*, 2008, **47**, 5114–5121.
- O. Zenkina, M. Altman, G. Leitus, L. J. W. Shimon, R. Cohen and M. E. van der Boom, *Organometallics*, 2007, **26**, 4528–4534; D. Strawser, A. Karton, O. V. Zenkina, M. A. Iron, L. J. W. Shimon, J. M. L. Martin and M. E. van der Boom, *J. Am. Chem. Soc.*, 2005, **127**, 9322–9323; A. C. B. Lucassen, L. J. W. Shimon and M. E. van der Boom, *Organometallics*, 2006, **25**, 3308–3310.
- T. Weisheit, H. Petzold, H. Görls, G. Mloston and W. Weigand, *Eur. J. Inorg. Chem.*, 2009, 3545–3551.
- T. Niksch, H. Görls, M. Friedrich, R. Oilunkaniemi, R. Laitinen and W. Weigand, *Eur. J. Inorg. Chem.*, 2009, 74–94.
- P. Hofmann, H. Heiß and G. Müller, *Z. Naturforsch.*, 1987, **42b**, 395–409; C. Massera and G. Frenking, *Organometallics*, 2003, **22**, 2758–2765.
- I. M. Al-Najjar, *Inorg. Chim. Acta*, 1987, **128**, 93–104.
- J.-E. Song, B.-O. Kim and Y. Ha, *Mater. Sci. Eng., C*, 2004, **24**, 191–194.
- M. Camalli, F. Caruso, S. Chaloupka, E. M. Leber, H. Rimml and L. M. Venanzi, *Helv. Chim. Acta*, 1990, **73**, 2263–2274.
- J. Okubo, H. Shinozaki, T. Koitabashi and R. Yomura, *Bull. Chem. Soc. Jpn.*, 1998, **71**, 329–335.
- M. J. Mio, L. C. Kopel, J. B. Braun, T. L. Gadzikwa, K. L. Hull, R. G. Brisbois, C. J. Markworth and P. A. Criecco, *Org. Lett.*, 2002, **4**, 3199–3202.
- V. Mouriès, R. Waschbüsch, J. Carran and P. Savignac, *Synthesis*, 1998, 271–274.
- M.-J. Wu, L.-M. Wei, C.-F. Lin, S.-P. Leou and L.-L. Wei, *Tetrahedron*, 2001, **57**, 7839–7844.
- C. Y. Ju, Y. Chong, J. F. Kayyem and M. Gozin, *J. Org. Chem.*, 1999, **64**, 2070–2079.
- COLLECT, Data Collection Software; Nonius B.V., Netherlands, 1998.
- Z. Otwinowski and W. Minor, “Processing of X-Ray Diffraction Data Collected in Oscillation Mode” in *Methods in Enzymology: Macromolecular Crystallography, Part A*, ed. C. W. Carter, and R. M. Sweet, Academic Press, San Diego, 1997, Vol. 276, pp. 307–326.
- G. M. Sheldrick, *Acta Crystallogr., Sect. A: Found. Crystallogr.*, 1990, **46**, 467–473.
- G. M. Sheldrick *SHELXL-97* (Release 97-2), University of Göttingen, Germany, 1997.

**5.10 Photochemical behavior of (diphosphine)( $\eta^2$ -tolane)Pt<sup>0</sup> complexes. Part B: An insight from DFT calculations**

Escudero et al. *Dalton Trans.*, **2010**, *39*, 9505. Reproduced by permission of The Royal Society of Chemistry (RSC)

<http://pubs.rsc.org/en/content/articlepdf/2010/dt/b925928g?page=search>

# Photochemical behavior of (bisphosphane)( $\eta^2$ -tolane)Pt<sup>0</sup> complexes. Part B: An insight from DFT calculations

Daniel Escudero,<sup>a</sup> Thomas Weisheit,<sup>b</sup> Wolfgang Weigand<sup>b</sup> and Leticia González<sup>\*a</sup>

Received 9th December 2009, Accepted 13th August 2010

DOI: 10.1039/b925928g

A series of various (bisphosphane)( $\eta^2$ -tolane)Pt<sup>0</sup> complexes, exhibiting a manifold of substitution patterns of the tolane ligand (**5a–g**) and different rigid bisphosphanes defining various P–Pt–P bite angles at the Pt center (**9a–b**) have been theoretically investigated using time-dependent density functional theory (TD-DFT). UV/Vis absorption spectra have been calculated in order to rationalize the photochemistry of the complexes. Metal–ligand charge transfer (MLCT) transitions from the Pt atom to the alkyne are assigned as the photochemical “active” states responsible for promoting the C<sub>aryl</sub>–C<sub>ethynyl</sub> bond activation. The steric, the electronic effects, as well as the P–Pt–P bite angle play an important role in determining the presence/absence of photochemical “active” states of d →  $\pi^*_{alk}$  character. Thus, electron-withdrawing substituted series and *ortho*-substituted complexes are best candidates to achieve C<sub>aryl</sub>–C<sub>ethynyl</sub> bond activation. C–Br bond cleavage is also theoretically rationalized. The observed photochemical C<sub>aryl</sub>–C<sub>ethynyl</sub> bond cleavage is, oppositely to C–Br bond activation, reversible under thermal conditions regaining the appropriate Pt<sup>0</sup> complexes by reductive elimination (see T. Weisheit, D. Escudero, H. Petzold, H. Görls, L. González and W. Weigand, Photochemical behavior of (bisphosphane)( $\eta^2$ -tolane)Pt<sup>0</sup> complexes in solution and in the solid state. Part A: Experimental considerations, *Dalton Trans.*, 2010, **39**, DOI: 10.1039/B925562a). In this part, we rationalize and clarify the thermal reductive elimination reactions *via* mechanistic DFT studies on the ground state.

## 1. Introduction

Recently, we reported on a rare example of selective carbon–carbon bond cleavage in the solid state induced by light.<sup>1</sup> A highly selective insertion of a (bisphosphane)Pt<sup>0</sup> complex fragment in a C–C bond of a coordinated bromo substituted substrate was observed for the first time in the solid state under sunlight irradiation. In solution, both C–Br and C–C insertion products were observed.<sup>1</sup> In a previous theoretical report<sup>2</sup> we dealt with the influence of substituting the tolane moiety for the dpbbe(Pt) series (dpbbe = 1,2-bis(diphenylphosphanyl) benzene), with several ligands of different electronic nature (electron-donor/-withdrawing groups (EDG/EWG) in *ortho/meta/para* positions). TD-DFT absorption spectra helped us to rationalize the different photochemistry of the complexes. In Ref. 1 a hypothesis was put forward: the MLCT states from the Pt atom to the alkyne (d →  $\pi^*_{alk}$ ) are the photochemical “active” states since they are present and with high oscillator strength only in those complexes undergoing photochemical bond activation. Moreover, an analysis of the photochemical “active” MLCT states from the Pt atom to the alkyne (d →  $\pi^*_{alk}$ ) revealed that both the electronic nature of the substituents as well as the steric effects between the phenyl rings of the tolane moiety contribute to the appearance of bright d →  $\pi^*_{alk}$  states. Specifically, these states were predominant

and more intense in complexes with EWGs and *ortho*-position substituted compounds.<sup>2</sup>

In this paper we extend our study by analyzing all the complexes which have been synthesized and characterized by means of spectroscopic methods in Part A.<sup>†</sup> Thus, complexes of the dpbbe series (**5a–5g**) bearing different ligands in *ortho*- (**5b**, **5c** and **5f**) and *para*- positions (**5a**, **5b** and **5g**) as well as pyridine and bis-pyridine derivatives (**5d** and **5e**, respectively) are studied (see Scheme 1).

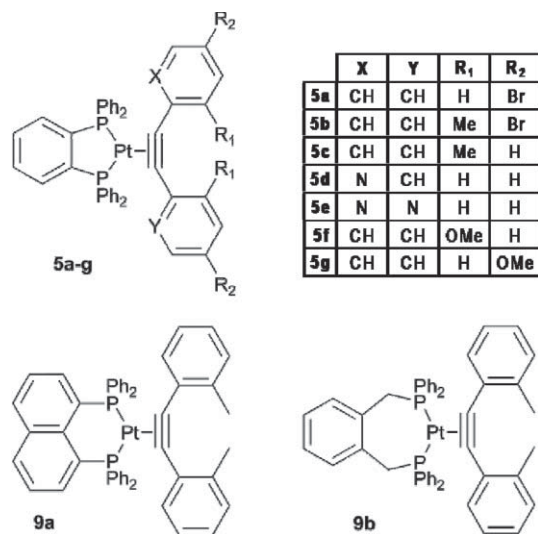
Additionally, the effect of EDGs (**5c**, **5f** and **5g**) as well as EWG (**5a**) on the photochemical properties is analyzed. *A priori*, complex **5b** is prone to achieve C<sub>aryl</sub>–C<sub>ethynyl</sub> bond-cleavage since exhibits steric hindrance between the phenyl groups of the tolane moiety and substitution by a strong electron-withdrawing group, namely bromine.

The effect of different bisphosphane ligands, which exhibit also different P–Pt–P bite angles, is also under consideration through complexes **9a** and **9b**, which bear 1,8-bis(diphenylphosphanyl)naphthalene (*i.e.* dpbn) and  $\alpha,\alpha'$ -bis(diphenylphosphanyl)-*o*-xylene (*i.e.* dpp(*o*-xyl)) ligands. Both complexes are *ortho*-methyl substituted compounds, and therefore they also exhibit steric hindrance between the phenyl groups of the tolane moiety.

<sup>a</sup>Institut für Physikalische Chemie, Friedrich-Schiller-Universität, 07743, Jena, Germany. E-mail: leticia.gonzalez@uni-jena.de; Fax: +49-3641-948302; Tel: +49-3641-948360

<sup>b</sup>Institut für Anorganische und Analytische Chemie, Friedrich-Schiller-Universität Jena, 07743, Jena, Germany

<sup>†</sup>T. Weisheit, D. Escudero, H. Petzold, H. Görls, L. González and W. Weigand, Photochemical behavior of (bisphosphane)( $\eta^2$ -tolane)Pt<sup>0</sup> complexes in solution and in the solid state. Part A: Experimental considerations, *Dalton Trans.*, 2010, **39**, DOI: 10.1039/B925562a.



Scheme 1 Complexes studied herein.

## 2. Theoretical methods

All the complexes, transition states and intermediates have been optimized in the electronic ground state using DFT in its Resolution of the Identity (RI) version, *i.e.* RI-DFT<sup>3</sup> and the BP86 protocol. The Becke exchange<sup>4</sup> and Perdew functional<sup>5</sup> have been combined with a polarized triple zeta basis set (TZVP) for all atoms. Relativistic effects have been considered for the Pt atom using the ECP-60-mwb Stuttgart/Dresden pseudopotential.<sup>6</sup> A vibrational analysis on all the stationary points has been done to confirm the character of the geometries, *i.e.* minima or transition states. The UV-Vis absorption spectrum is calculated using TD-DFT<sup>7</sup> spanned over 85 states at the same level of theory as the optimizations, *i.e.*, RI-BP86/TZVP. This protocol is used since it has already proven to give good agreement between theoretical and experimental results for ( $\eta^2$ -tolane)Pt<sup>0</sup> derivatives.<sup>2</sup> The optimizations and TD-DFT calculations were performed with the TURBOMOLE(V.5.10)<sup>8</sup> program package.

For the mechanistic studies, the relative stabilities are calculated as gas phase Gibbs free energies at 298 K. To this aim, single point energy calculations have been carried out with the popular hybrid B3LYP<sup>9,10</sup> and the double hybrid B2GP-PLYP<sup>11</sup> functional using a basis set of polarized triplet zeta quality, namely 6-311G\*. The B2GP-PLYP functional is known to describe very accurately thermochemical data of late transition metal reactions.<sup>11</sup> These single point energies have been carried out with the Gaussian 03 program package.<sup>12</sup>

## 3. Experimental methods

The experimental UV-Vis spectra were taken on a Specord S600 (Analytik Jena) device by measuring methylenechloride solutions of the appropriate complexes.

## 4. Results and discussion

### 4.1. Excited state properties

The UV-Vis spectra of complexes **5a–c**, **5d–e**, **5f–g** and **9a–b** are depicted in Fig. 1, Fig. 2, Fig. 3 and Fig. 4, respectively. The

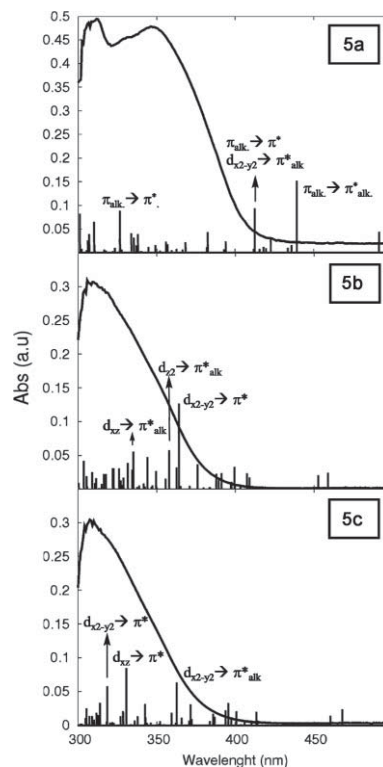


Fig. 1 Experimental UV-Vis absorption spectra and TD-DFT vertical excitations (as sticks) of complexes **5a–5c**. The main electronic excitations are labeled.

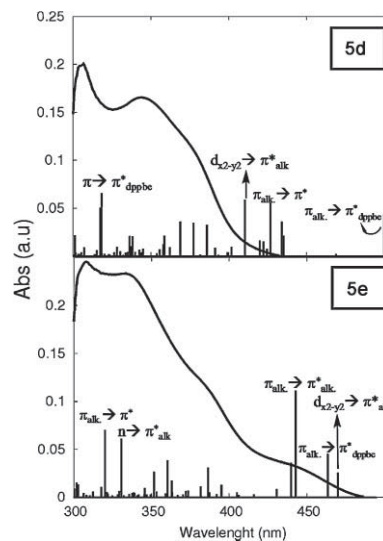
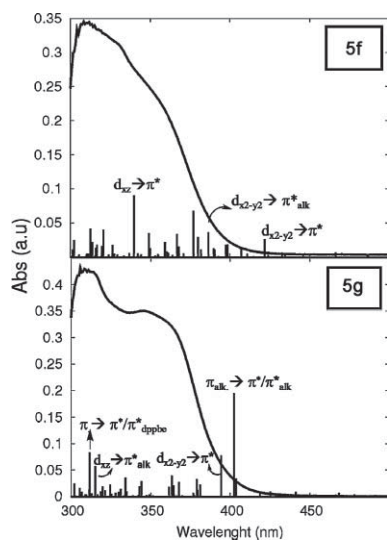


Fig. 2 Experimental UV-Vis absorption spectra and TD-DFT vertical excitations (as sticks) of complexes **5d–5e**. The main electronic excitations are labeled.

experimental UV-Vis spectra are superimposed to the predicted vertical TD-DFT (RI-BP86/TZVP) electronic excitations. The data for **5b** are taken from Ref. 2. As in Ref. 2, here we find that RI-BP86/TZVP performs reasonably well, with errors within the experimental accuracy. The maximum errors, amounting to *ca.* 0.7 eV, are found for some low-lying charge-transfer (CT) states; see *e.g.*, S<sub>4</sub> in the complex **5a**. This is not surprising, since it is well-known that pure CT states are particularly difficult to





**Fig. 3** Experimental UV-Vis absorption spectra and TD-DFT vertical excitations (as sticks) of complexes **5f–5g**. The main electronic excitations are labeled.

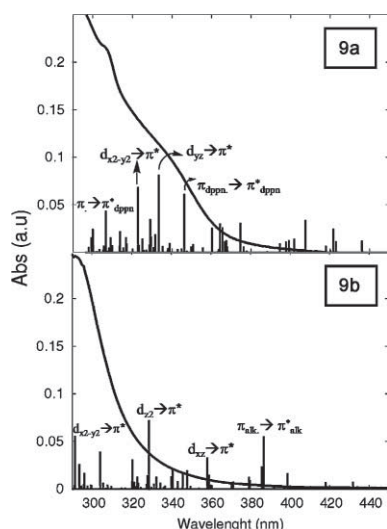


**Fig. 4** Experimental UV-Vis absorption spectra and TD-DFT vertical excitations (as sticks) of complexes **9a–9b**. The main electronic excitations are labeled.

be described with TD-DFT, resulting strongly underestimated.<sup>13</sup> Hybrid functionals, like PBE0, seem to be less affected by this problem.<sup>14</sup> Nevertheless, the MLCT states, which are the photochemical “active” states in our system, exhibit similar errors when using pure or hybrid functional.<sup>15</sup> Since the pure CT have no role in the photochemical C–C and C–Br bond activation of these complexes, the errors delivered by the TD-DFT calculations do not affect the conclusions reached in this paper. Table 1 collects the main electronic excitations contributing to the absorption spectra of complexes **5a–g** and **9a–b**. The most important electronic excitations for these complexes are intra-ligand (IL), MLCT, and ligand-ligand charge transfer (LLCT). In general, the low-lying energy absorption region is dominated by LLCT excitations of  $\pi_{\text{alk}} \rightarrow \pi^*_{\text{dppbe}}$  character, while the high-lying absorption region is characterized by MLCT and LLCT excitations, which are responsible for the experimental broad band peaking extending

from 310 nm to 340 nm in all the complexes. The small peaks at 310 nm superimposed to this broad band are an artifact of the instrument generating data at the short wavelength.

For illustration, the relevant Kohn–Sham orbitals contributing to the main vertical electronic excitations of compound **5e** are depicted in Fig. 5. In all the complexes the HOMO orbital is located in the alkyne moiety ( $\pi_{\text{alk}}$ ). In all the cases it is mixed with the unoccupied  $d_{xy}$  orbital of the Pt center. According to the  $d^8$  coordination for the Pt<sup>0</sup> center, four valence 5d orbitals are occupied ( $d_{x^2-y^2}$ ,  $d_{z^2}$ ,  $d_{yz}$  and  $d_{xz}$  in decreasing energetic order). In complex **5e** these orbitals correspond to HOMO-1, HOMO-2, HOMO-4 and HOMO-5, respectively (see Fig. 5). In complex **5e** the orbital HOMO-3 corresponds to a lone pair of the nitrogen atom of the pyridine moiety ( $n_{\text{N}}$ , not shown in Fig. 5). Depending on the substitution pattern of the tolane derivative (complexes **5a–g**) as well as on the nature of the bisphosphane ligand (complexes **9a–b**) the order of the highest occupied molecular orbitals changes, observing the following general trends: a) intercalation of  $n_{\text{N}}$  orbitals within the 5d orbitals of the Pt center for the pyridine derivatives (**5d–e**), b) intercalation of a  $\pi$  orbital of the tolane ligand within the 5d orbitals of the Pt center for the methoxy-derivatives (**5f–g**), and c) a change in the order of the 5d orbitals for complex **9b**. In this latter complex the P–Pt–P bite angle is increased and consequently the  $d_{x^2-y^2}$  orbital is stabilized, transforming into the HOMO-2.

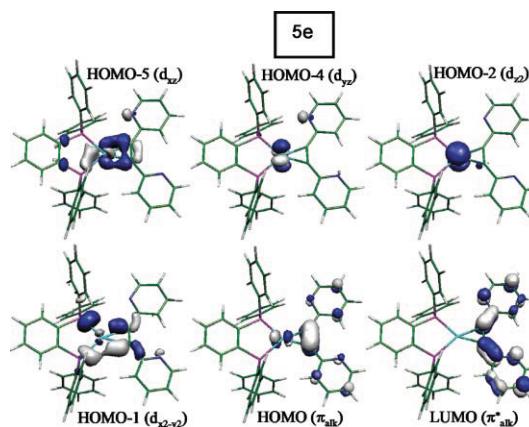


**Fig. 5** Selected Kohn–Sham orbitals of complex **5e**.

The photochemical active  $\pi^*_{\text{alk}}$  orbital corresponds to the LUMO orbital in the case of complex **5e** (see Fig. 5), while it is destabilized in the remaining complexes. Thus, in the dppbe series (complexes **5a–g**) the LUMO is an antibonding  $\pi$  orbital localized in the dppbe ligand ( $\pi^*_{\text{dppbe}}$ ). In general, the  $\pi^*_{\text{alk}}$  orbital is more destabilized in the case of the *ortho*-derivatives than in the remaining complexes (being LUMO+7, LUMO+8 and LUMO+7 for **5b**, **5c** and **5f**, respectively). In the *ortho*-substituted complexes conjugation through the tolane moiety is not possible due to the twisting of the phenyl rings. As we have previously seen<sup>2</sup> such effects influence the energy and oscillator strength of the MLCT  $d \rightarrow \pi^*_{\text{alk}}$  transitions. Indeed, the UV-Vis spectra are more robust with respect to the *ortho/para* substitution pattern than to the electronic nature of the substituent. Analyzing Table 1, it can be observed that the lowest-lying bright state for the dppbe series (apart from complex **5e**) is of LLCT character, corresponding to a transition from the alkyne moiety ( $\pi_{\text{alk}}$ ) to the dppbe ligand

**Table 1** Main singlet excitations contributing to the absorption spectra of compounds **5a–g** and **9a–b**. Excitation energies in nm and oscillator strengths *f*

<b>5a</b>							
State	$\Delta E/\text{nm}$	<i>f</i>	Assignment	State	$\Delta E/\text{nm}$	<i>f</i>	Assignment
S <sub>2</sub>	492	0.041	$\pi_{\text{alk}} \rightarrow \pi_{\text{dppbe}}^*$ (81%) LLCT	S <sub>36</sub>	337	0.015	$d_{\text{yz}} \rightarrow \pi_{\text{alk}}^*$ (84%) MLCT
S <sub>4</sub>	439	0.152	$\pi_{\text{alk}} \rightarrow \pi_{\text{alk}}^*$ (50%) IL	S <sub>42</sub>	327	0.088	$\pi_{\text{alk}} \rightarrow \pi^*$ (38%) LLCT
S <sub>7</sub>	423	0.028	$\pi_{\text{alk}} \rightarrow \pi^*$ (53%) LLCT	S <sub>54</sub>	310	0.065	$d_{\text{yz}} \rightarrow \pi^*$ (22%) MLCT
S <sub>11</sub>	412	0.093	$d_{\text{x2-y2}} \rightarrow \pi_{\text{alk}}^*$ (41%) MLCT	S <sub>61</sub>	305	0.082	$d_{\text{xy}} \rightarrow \pi_{\text{alk}}^*$ (47%) MLCT
			$\pi_{\text{alk}} \rightarrow \pi^*$ (40%) LLCT				$d_{\text{x2-y2}} \rightarrow \pi^*$ (54%) MLCT
			$d_{\text{x2-y2}} \rightarrow \pi_{\text{alk}}^*$ (16%) MLCT				$d_{\text{x2-y2}} \rightarrow \sigma_{\text{C-Br}}^*$ (19%) MLCT
<b>5b</b>							
S <sub>3</sub>	459	0.024	$\pi_{\text{alk}} \rightarrow \pi_{\text{dppbe}}^*$ (78%) LLCT	S <sub>38</sub>	335	0.056	$d_{\text{xz}} \rightarrow \pi^*$ (46%) MLCT
S <sub>10</sub>	399	0.033	$d_{\text{x2-y2}} \rightarrow \pi^*$ (71%) MLCT	S <sub>40</sub>	331	0.039	$d_{\text{z2}} \rightarrow \pi^*$ (63%) MLCT
S <sub>19</sub>	376	0.037	$d_{\text{x2-y2}} \rightarrow \pi_{\text{alk}}^*$ (71%) MLCT	S <sub>51</sub>	316	0.022	$d_{\text{xz}} \rightarrow \pi_{\text{alk}}^*$ (47%) MLCT
S <sub>24</sub>	358	0.058	$d_{\text{z2}} \rightarrow \pi^*$ (58%) MLCT	S <sub>58</sub>	312	0.001	$d_{\text{x2-y2}} \rightarrow \sigma_{\text{C-Br}}^*$ (64%) MLCT
S <sub>32</sub>	344	0.047	$\pi_{\text{alk}} \rightarrow \pi^*$ (51%) LLCT	S <sub>66</sub>	304	0.041	$d_{\text{yz}} \rightarrow \pi^*$ (48%) MLCT
<b>5c</b>							
S <sub>3</sub>	468	0.024	$\pi_{\text{alk}} \rightarrow \pi_{\text{dppbe}}^*$ (83%) LLCT	S <sub>40</sub>	331	0.085	$d_{\text{xz}} \rightarrow \pi^*$ (44%) MLCT
S <sub>14</sub>	396	0.033	$d_{\text{x2-y2}} \rightarrow \pi^*$ (56%) MLCT	S <sub>42</sub>	329	0.021	$d_{\text{z2}} \rightarrow \pi_{\text{alk}}^*$ (76%) MLCT
S <sub>20</sub>	371	0.031	$d_{\text{x2-y2}} \rightarrow \pi_{\text{d}}^*$ (74%) MLCT	S <sub>48</sub>	319	0.058	$d_{\text{xz}} \rightarrow \pi^*$ (45%) MLCT
S <sub>23</sub>	363	0.063	$d_{\text{x2-y2}} \rightarrow \pi_{\text{alk}}^*$ (74%) MLCT	S <sub>51</sub>	314	0.033	$d_{\text{x2-y2}} \rightarrow \pi^*$ (39%) MLCT
S <sub>2</sub>	500	0.043	$\pi_{\text{alk}} \rightarrow \pi_{\text{dppbe}}^*$ (71%) LLCT	S <sub>19</sub>	378	0.035	$\pi_{\text{alk}} \rightarrow \pi^*$ (86%) LLCT
			$\pi_{\text{alk}} \rightarrow \pi^*$ (34%) IL				S <sub>21</sub>
S <sub>6</sub>	434	0.036	$d_{\text{x2-y2}} \rightarrow \pi_{\text{dppbe}}^*$ (31%) MLCT	S <sub>37</sub>	336	0.021	$d_{\text{yz}} \rightarrow \pi_{\text{alk}}^*$ (61%) MLCT
			$\pi_{\text{alk}} \rightarrow \pi^*$ (45%) IL				S <sub>50</sub>
S <sub>7</sub>	427	0.056	$\pi_{\text{alk}} \rightarrow \pi^*$ (45%) IL	S <sub>51</sub>	317	0.050	$\pi_{\text{alk}} \rightarrow \pi^*$ (32%) LLCT
S <sub>12</sub>	410	0.059	$d_{\text{x2-y2}} \rightarrow \pi_{\text{alk}}^*$ (74%) MLCT				$\pi \rightarrow \pi_{\text{dppbe}}^*$ (55%) LLCT
S <sub>17</sub>	386	0.032	$d_{\text{x2-y2}} \rightarrow \pi^*$ (97%) MLCT	S <sub>24</sub>	360	0.038	$d_{\text{x2-y2}} \rightarrow \pi^*$ (88%) MLCT
<b>5e</b>							
S <sub>2</sub>	470	0.026	$d_{\text{x2-y2}} \rightarrow \pi_{\text{alk}}^*$ (63%) MLCT	S <sub>28</sub>	352	0.027	$d_{\text{x2-y2}} \rightarrow \pi^*$ (62%) MLCT
S <sub>3</sub>	463	0.045	$\pi_{\text{alk}} \rightarrow \pi_{\text{dppbe}}^*$ (92%) LLCT	S <sub>43</sub>	331	0.061	$n_{\text{N}} \rightarrow \pi_{\text{alk}}^*$ (65%) LLCT
S <sub>4</sub>	443	0.111	$\pi_{\text{alk}} \rightarrow \pi_{\text{alk}}^*$ (54%) IL	S <sub>52</sub>	320	0.070	$\pi_{\text{alk}} \rightarrow \pi^*$ (60%) LLCT
S <sub>5</sub>	440	0.036	$\pi_{\text{alk}} \rightarrow \pi^*$ (87%) LLCT	S <sub>39</sub>	349	0.035	$d_{\text{z2}} \rightarrow \pi^*$ (52%) MLCT
S <sub>15</sub>	387	0.031	$d_{\text{x2-y2}} \rightarrow \pi^*$ (93%) MLCT				S <sub>45</sub>
S <sub>2</sub>	506	0.037	$\pi_{\text{alk}} \rightarrow \pi_{\text{dppbe}}^*$ (97%) LLCT	S <sub>56</sub>	321	0.040	$d_{\text{yz}} \rightarrow \pi^*$ (58%) MLCT
S <sub>21</sub>	387	0.036	$\pi_{\text{alk}} \rightarrow \pi^*$ (53%) LLCT	S <sub>62</sub>	313	0.042	$\pi \rightarrow \pi^*$ (45%) LLCT
S <sub>25</sub>	377	0.068	$d_{\text{x2-y2}} \rightarrow \pi_{\text{alk}}^*$ (65%) MLCT	S <sub>28</sub>	363	0.040	$d_{\text{xz}} \rightarrow \pi_{\text{dppbe}}^*$ (56%) MLCT
S <sub>28</sub>	367	0.034	$d_{\text{x2-y2}} \rightarrow \pi_{\text{dppbe}}^*$ (28%) MLCT				S <sub>41</sub>
<b>5f</b>							
S <sub>2</sub>	560	0.042	$\pi_{\text{alk}} \rightarrow \pi_{\text{dppbe}}^*$ (98%) LLCT	S <sub>54</sub>	315	0.057	$d_{\text{xz}} \rightarrow \pi^*$ (45%) MLCT
S <sub>14</sub>	404	0.034	$d_{\text{xy}} \rightarrow \pi_{\text{dppbe}}^*$ (84%) MLCT	S <sub>56</sub>	312	0.083	$d_{\text{xz}} \rightarrow \pi_{\text{alk}}^*$ (38%) MLCT
S <sub>15</sub>	402	0.195	$\pi_{\text{alk}} \rightarrow \pi_{\text{alk}}^*$ (30%) IL				$\pi \rightarrow \pi^*$ (23%) LLCT
S <sub>19</sub>	379	0.033	$\pi_{\text{alk}} \rightarrow \pi^*$ (17%) LLCT	S <sub>51</sub>	329	0.035	$d_{\text{z2}} \rightarrow \pi^*$ (56%) MLCT
			$d_{\text{x2-y2}} \rightarrow \pi^*$ (86%) MLCT				S <sub>58</sub>
S <sub>24</sub>	375	0.031	$d_{\text{x2-y2}} \rightarrow \pi^*$ (60%) MLCT	S <sub>74</sub>	307	0.044	$\pi \rightarrow \pi_{\text{dppn}}^*$ (38%) LLCT
S <sub>30</sub>	364	0.030	$d_{\text{x2-y2}} \rightarrow \pi_{\text{alk}}^*$ (20%) MLCT				$d_{\text{z2}} \rightarrow \pi^*$ (20%) MLCT
S <sub>39</sub>	346	0.061	$d_{\text{z2}} \rightarrow \pi^*$ (20%) MLCT	S <sub>47</sub>	333	0.081	$\pi_{\text{dppn}} \rightarrow \pi_{\text{dppn}}^*$ (60%) IL
			$\pi_{\text{dppn}} \rightarrow \pi_{\text{dppn}}^*$ (60%) IL				$d_{\text{yz}} \rightarrow \pi^*$ (37%) MLCT
S <sub>47</sub>	333	0.081	$d_{\text{yz}} \rightarrow \pi^*$ (37%) MLCT	S <sub>56</sub>	304	0.039	$d_{\text{xz}} \rightarrow \pi^*$ (74%) MLCT
<b>9b</b>							
S <sub>11</sub>	387	0.055	$\pi_{\text{alk}} \rightarrow \pi_{\text{alk}}^*$ (60%) IL	S <sub>70</sub>	291	0.056	$d_{\text{x2-y2}} \rightarrow \pi^*$ (44%) MLCT
S <sub>21</sub>	358	0.033	$d_{\text{xz}} \rightarrow \pi^*$ (74%) MLCT	S <sub>39</sub>	349	0.035	$d_{\text{x2-y2}} \rightarrow \pi_{\text{dpp(oxyl)}}^*$ (80%) MLCT
S <sub>37</sub>	329	0.072	$d_{\text{z2}} \rightarrow \pi^*$ (24%) MLCT				$d_{\text{xz}} \rightarrow \pi^*$ (84%) MLCT
			$\pi_{\text{alk}} \rightarrow \pi^*$ (20%) LLCT				

( $\pi_{\text{dppbe}}^*$ ). For complex **5e** it corresponds to a  $d_{\text{x2-y2}} \rightarrow \pi_{\text{alk}}^*$  transition of MLCT character. This transition is red-shifted comparing to the rest of compounds due to the stabilization of the  $\pi_{\text{alk}}^*$  orbital, as stated above. For complexes **9a** and **9b** the first lowest-lying bright excitation correspond to a  $d_{\text{x2-y2}} \rightarrow \pi^*$  and a  $\pi_{\text{alk}} \rightarrow \pi_{\text{alk}}^*$  transitions, respectively.

MLCT transitions from the Pt atom to the alkyne are assigned as the photochemical “active” states responsible for the activation of C<sub>aryl</sub>–C<sub>ethynyl</sub> bonds. The influence of substituting the tolane

moiety in the dppbe series with several ligands of different electronic nature (electron-donor/withdrawing) in several positions (*ortho/meta/para*) has been stated in Ref. 2. Thus, an analysis of the photochemical “active” MLCT states revealed that both the electronic nature of the substituents as well as the steric effects between the phenyl rings of the tolane moiety contribute to the appearance of bright  $d \rightarrow \pi_{\text{alk}}^*$  bands. These bands were predominant and stronger in complexes with electron-withdrawing substituents or in compounds bearing *ortho*-substituted tolane ligands. The

$d_{x_2-y_2} \rightarrow \pi^*_{\text{alk}}$  transition of MLCT character is present and bright in most of the compounds (excluding **5g** and **9b**, where it is a dark state). For complexes **5a**, **5b** and **5c** this transition appears at 423, 376 and 363 nm, respectively (see Table 1). As it can be observed for the *ortho*-substituted compounds (**5b–c**) this transition is blue-shifted due to the destabilization of the  $\pi^*_{\text{alk}}$  in the *ortho*-series (*vide supra*). For the pyridine series (**5d–e**) this state appears at 410 and 470 nm, being red-shifted due to the stabilization of the  $\pi^*_{\text{alk}}$  orbital (especially for **5e**). Interestingly, the behavior for the electron-donor species (**5c**, **5f** and **5g**) depends more on the steric influences rather than on its electronic nature. Thus, for the *ortho*-substituted compounds (**5c** and **5f**), a very bright  $d_{x_2-y_2} \rightarrow \pi^*_{\text{alk}}$  transition is found, peaking at 377 nm for complex **5f** (see Table 1). Oppositely, for the *para*-methoxy substituted compound (**5g**) this transition is a dark state. Noteworthy, a change in the bisphosphane ligand, which in turn affects the P–Pt–P bite angle, also influences the presence/absence of  $d_{x_2-y_2} \rightarrow \pi^*_{\text{alk}}$  transitions. Complex **9a**, which shows a similar P–Pt–P bite angle compared to the dppbe series, also presents an intense  $d_{x_2-y_2} \rightarrow \pi^*_{\text{alk}}$  transition, peaking at 364 nm. This fact is in concordance with its dihedral angle (122°), similar to the remaining *ortho*-substituted complexes (**5b**, **5c** and **5f**). Oppositely, in complex **9b**, also exhibiting a similar dihedral angle (73°) but showing a dramatic change on the P–Pt–P angle, no bright  $d_{x_2-y_2} \rightarrow \pi^*_{\text{alk}}$  excitation is found.

Similar trends for other strong photochemical “active” states of  $d \rightarrow \pi^*_{\text{alk}}$  character are observed. They are predominant in most of the *ortho*-substituted series (**5b–c**) as well as in EWG complexes (**5a–b**). Hence, for complex **5a** two additional strong  $d \rightarrow \pi^*_{\text{alk}}$  excitations (see  $S_{36}$  and  $S_{54}$  in Table 1) are found. For complexes **5b** and **5c** there is at least an additional strong  $d \rightarrow \pi^*_{\text{alk}}$  excitation ( $S_{51}$  for **5b** and  $S_{42}$  for **5c**, see Table 1). Unexpectedly, there is another strong “active” state for complex **5d** ( $S_{37}$ ), which is in disagreement to the experimentally non-observed photochemical desired C–C bond cleavage products. As stated in Part A,† complexes **5d** and **5e** do react in solution upon sunlight irradiation, but the concomitant photoproducts could not be identified. Therefore, we ascribe this alternative photochemical reactivity to the presence of photochemical “active” states of  $d \rightarrow \pi^*_{\text{alk}}$  character.

In summary, both the substitution pattern and the electronic nature of the substituents play an important role in determining the presence or absence of the photochemical active MLCT states of  $d \rightarrow \pi^*_{\text{alk}}$  character. Obviously, upon sunlight irradiation depopulation of the  $d_{\text{Pt}}$  orbitals and concomitant population of the  $\pi^*_{\text{alk}}$  is more efficient the more and brighter states are available. Such states promote additional  $\pi$ -back bonding, hence weakening the  $\eta^2$ -coordination of the tolane to the Pt atom and then favoring the C–C activated products.<sup>2</sup> Therefore, the electron-withdrawing derivatives (complexes **5a** and **5b**) as well as the *ortho*-derivatives (**5c** and **5f**), should yield more efficiently C–C rearrangement products, due to the large number of  $d \rightarrow \pi^*_{\text{alk}}$  excitations and the very strong  $d_{x_2-y_2} \rightarrow \pi^*_{\text{alk}}$  transition, respectively. These results are in good agreement with the experimental facts (see Part A†). Interestingly, no photochemical product is observed in complex **5f** in the solid state, although it reacts in solution –according to the theoretical predictions.

Besides C–C bond activation, C–Br bond cleavage products have been obtained in solution after irradiation with sunlight on the bromine substituted complexes **5a–b** in a 1 : 1 ratio. Conspicuously, in the solid state only the C–C activation product was achieved

(see Part A†). A plausible explanation of why C–Br activation does not occur in the solid state can be obtained by analyzing the crystal structure of complexes **5a–b** (see exemplarily Fig. 4 in Part A†). The large distances found in the crystal between the Br and the Pt atoms make it highly unlikely that the products resulting from C–Br insertion are achieved either *via* unimolecular or bimolecular processes. In solution, however, mobility allows for a bimolecular or unimolecular approach. Van der Boom *et al.* have experimentally observed thermal aryl-halide bond activation in similar Pt<sup>0</sup> azobenzene derivatives in solution and justified it with a unimolecular approach.<sup>16</sup> Based on mechanistic DFT studies, they have proposed a plausible “ring-walking” mechanism of the Pt along the phenyl ring after rupture of the  $\eta^2$ -coordination to the azo moiety. Since here no activation products are observed under thermal conditions, we attribute C–Br activation in solution to be promoted photochemically, at least in the first stages of the reaction. Hence, from the electronic point of view, this activation requires an initial rupture of the  $\eta^2$ -coordination of the Pt to the alkyne, plus a weakening of the C–Br bond after light irradiation. This fact can be rationalized by excitations to the  $\sigma^*_{\text{C-Br}}$  orbital, in addition to the  $d \rightarrow \pi^*_{\text{alk}}$  excitations. As it can be seen in Table 1, MLCT transitions of  $d_{x_2-y_2} \rightarrow \sigma^*_{\text{C-Br}}$  character are present in complexes **5a** and **5b**.

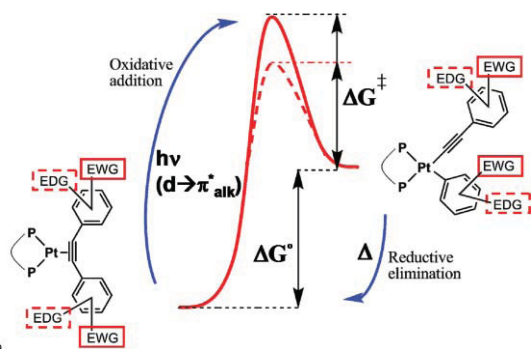
## 4.2. Mechanistic studies of the thermal reactions

The calculation of the mechanism of the C–C oxidative addition reaction (Pt<sup>0</sup> → Pt<sup>II</sup>) from the “photochemical active”  $d \rightarrow \pi^*_{\text{alk}}$  excited states is a challenging task due to the size of these complexes. Therefore, in this study we shall concentrate on the mechanistic study of the backwards thermal reaction which can be easily done using DFT ground state calculations. The insights obtained from the thermal reductive elimination will give hints to understand the photochemical reactions. The thermal reaction mechanisms beginning from the  $C_{\text{aryl}}-C_{\text{ethynyl}}$  as well as from the  $C_{\text{aryl}}-\text{Br}$  activated products are studied in this section.

### 4.2.1. Mechanistic study of the thermal reductive elimination beginning from the $C_{\text{aryl}}-C_{\text{ethynyl}}$ activated products.

As stated in Part A,† the observed photochemical  $C_{\text{aryl}}-C_{\text{ethynyl}}$  bond activation is reversible under thermal conditions, even though the forward reaction does not proceed thermally. This behavior has been also observed by Jones *et al.* in similar Pt<sup>0</sup> complexes.<sup>17</sup> They studied the influence of substituting the tolane ligand with EDGs/EWGs on the thermal reaction. It was shown that the energetic profile can be tuned by changing the electronic nature of the substituents of the tolane ring. As it can be seen in Scheme 2, lower activation barriers were obtained for the EDG-substituted compounds. Moreover, a further stabilization of the photolysis products was achieved by EWG-substituted complexes.

The aim of this subsection is to characterize the mechanism of the thermal reductive elimination (Pt<sup>II</sup> → Pt<sup>0</sup>) by means of ground state DFT calculations, analyzing the effects of substitution (EDGs/EWGs) on the energetic profile of the reaction. In this mechanistic study we have selected complexes **5a** (*para*-bromine substituted, an EWG compound) and **5g** (*para*-methoxy substituted, an EDG compound). Additionally, the energetic profile of **5f** has been also studied in order to analyze the effect of the substitution pattern on the thermal reaction.



**Scheme 2** Energetic profile of the photochemical oxidative addition leading to  $C_{\text{aryl}}-C_{\text{ethynyl}}$  bond activation and its thermal reductive elimination. Dashed line for EDG substituted compounds and solid line for EWG substituted compounds.

Gas phase Gibbs free energies of the reaction ( $\Delta G^\circ$ ) as well as activation barriers ( $\Delta G^\ddagger$ ) at the B3LYP/6-311G\*\*//RI-BP86/TZVP and B2GP-PLYP/6-311G\*\*//RI-BP86/TZVP levels of theory can be found in Table 2. As it can be seen,  $\Delta G^\circ$  and  $\Delta G^\ddagger$  values differ depending on the applied functional. The obtained  $\Delta G^\circ$  values range from  $-10$  to  $-16$  kcal mol $^{-1}$ , depending on the functional and the particular complex. The activation barriers  $\Delta G^\ddagger$  are predicted at *ca.* 25 kcal mol $^{-1}$  with the B3LYP functional and at *ca.* 36 kcal mol $^{-1}$  with B2GP-PLYP. We note that the substituent effect trends are conserved regardless of the applied functional. Since very accurate values were achieved with the double-hybrid functional B2GP-PLYP for activation barriers of prototype C–C bond activation reactions in Pd complexes,<sup>11</sup> here we also expect the results obtained with the B2GP-PLYP functional to be more accurate. Accordingly, the B3LYP  $\Delta G^\circ$  values are overestimated by *ca.* 4 kcal mol $^{-1}$  and the barrier heights are underestimated by *ca.* 10 kcal mol $^{-1}$ . Experimental activation barriers for C–C bond cleavage reactions in similar (bisphosphane)( $\eta^2$ -tolane)Pt $^0$  complexes<sup>17</sup> range between 31–33.5 kcal mol $^{-1}$  (measured at *ca.* 350 K), and consequently also in accordance to the B2GP-PLYP computed activation barriers.

In Fig. 6 we show the energetic profile, which is analogous in all the complexes. Between the reactant **R** (recall that this is the photochemical product) and **P**, which is the complex after reductive elimination, there is one transition state (**TS**). In Table 3 are collected the main geometrical parameters of the stationary points (**R**, **TS** and **P**) which change along the reaction coordinate of complexes **5a**, **5f** and **5g**. As experimentally observed (see Part A $\ddagger$ ) exothermic profiles are obtained for the thermal reductive elimination. Therefore, the Pt $^0$  products are more stable for all the

**Table 2** Gas phase Gibbs free energies and activation barriers for the thermal reductive elimination reaction beginning from the  $C_{\text{aryl}}-C_{\text{ethynyl}}$  activated products at the B3LYP/6-311G\*\*//RI-BP86/TZVP and the B2GP-PLYP/6-311G\*\*//RI-BP86/TZVP levels of theory. Values presented in kcal mol $^{-1}$

$\Delta G^\circ$ /kcal mol $^{-1}$	<b>5a</b>	<b>5f</b>	<b>5g</b>
B3LYP/6-311G*	-13.64	-12.96	-16.27
B2GP-PLYP/6-311G*	-10.28	-9.38	-12.79
$\Delta G^\ddagger$ (kcal mol $^{-1}$ )	<b>5a</b>	<b>5f</b>	<b>5g</b>
B3LYP/6-311G*	25.03	24.69	24.52
B2GP-PLYP/6-311G*	36.20	35.83	35.52

**Table 3** Main geometrical parameters of the stationary points (**R**, **TS** and **P**) along the reaction coordinate of complexes **5a**, **5f** and **5g**. Optimized geometries at the RI-BP86/TZVP level of theory. Distances are in Å. Experimental distances for which its X-ray structure is available are included between brackets

<b>5a</b>	$C_{\text{aryl}}-C_{\text{ethynyl}}$	$C_{\text{ethynyl}}-C_{\text{ethynyl}}$	Pt- $C_{\text{ethynyl}}$ (1)	Pt- $C_{\text{ethynyl}}$ (2)
<b>R</b>	2.82	1.23	2.00	3.24
<b>TS</b>	1.78	1.25	2.01	3.22
<b>P</b>	1.44 (1.45)	1.31 (1.30)	2.08 (2.03)	2.08 (2.04)
<b>5f</b>				
<b>R</b>	2.82	1.23	2.00	3.24
<b>TS</b>	1.78	1.25	2.02	3.22
<b>P</b>	1.45	1.30	2.09	2.08
<b>5g</b>				
<b>R</b>	2.82	1.23	2.00	3.24
<b>TS</b>	1.80	1.25	2.01	3.21
<b>P</b>	1.44	1.31	2.08	2.09

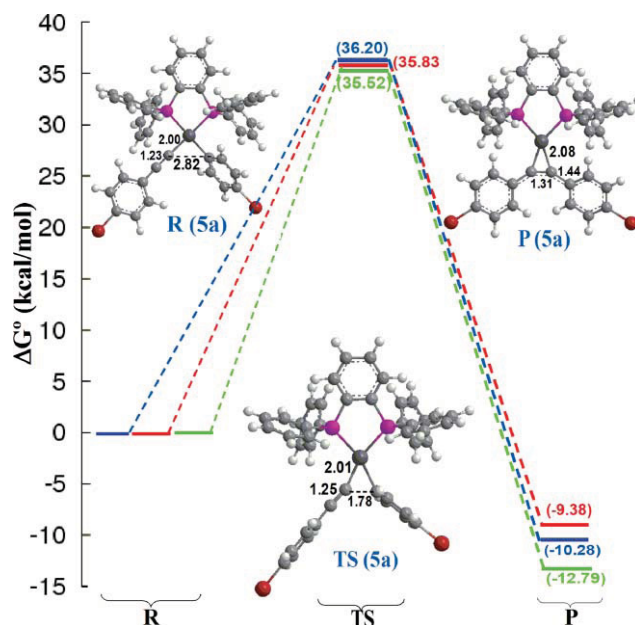


**Fig. 6** Energy diagram of the thermal reductive elimination beginning from the  $C_{\text{aryl}}-C_{\text{ethynyl}}$  activated products leading to complexes **5a** (blue), **5f** (red) and **5g** (green), calculated at the B2GP-PLYP/6-311G\*\*//RI-BP86/TZVP level of theory. Relative free energy Gibbs are given in kcal mol $^{-1}$  with respect to complexes **R**. Molecular structures are depicted exemplarily for complex **5a** (distances are in Å). Bromine atoms are in red, carbon atoms in grey, hydrogen atoms in white and phosphorus atoms in pink.

complexes, regardless of the electronic nature of the substituents. One first important conclusion that can be extracted from the thermochemical data of the *para*-substituted compounds (**5a** and **5g**) is that EDGs stabilize in a major extent the Pt $^0$  elimination products in comparison to the studied EWG-substituted complex (see values of  $\Delta G^\circ$  in Table 2). Controversially, it has been stated that the Pt- $C_{\text{aryl}}$  bond<sup>18</sup> is more stabilized with EWG, but these ligands might also be expected to stabilize the Pt $^0$ -(alkyne) complex, as it has been observed previously.<sup>19,20</sup> Thus, it seems that a further stabilization of the Pt $^0$ -(alkyne) complex is achieved for the EWG complex (**5a**). As expected, the substitution pattern also plays an important role in determining the relative stabilities of

the complexes. As it can be seen in Table 2, the *ortho*-substituted compound (**5f**) exhibits the lowest  $\Delta G^\circ$  value. This fact can be attributed to the steric hindrance of the phenyl rings of the product complex **P**, which is not present in the structure of the reactant **R**.

The **TS** determines the activation barrier of the reaction. In the **TS** structures, the distance between  $C_{\text{aryl}}$  and  $C_{\text{ethynyl}}$  atoms is considerably reduced compared to the initial structures **R** (compare *e.g.* 2.82 Å in **R** with 1.78 Å in **TS** for complex **5a**, see Table 3). Additionally, an enlargement of the alkyne bond distance of 0.02 Å is observed in the structures of **TS** for all the complexes. Another important change when going from **R** to **TS** is observed in the twisting of the phenyl ring with respect to the quasi-square planar coordination plane. One phenyl ring is almost coplanar in **R**, whilst both phenyl rings are twisted *ca.* 90° in the structure of **TS**. A relaxation along the reaction coordinate leads to the final products (**P**). The weakening of the Pt– $C_{\text{ethynyl}}$  bond allows the tolane moiety moving towards reaching the  $\eta^2$ -coordination of the alkyne to the Pt center. In addition to the movement of the tolane ring this reorganization implies a) an enlargement of the alkyne bond distance (due to the efficient  $\pi$ -back donation in the  $\eta^2$ -coordination, as reported recently<sup>2</sup>), b) a further strengthening of the  $C_{\text{aryl}}-C_{\text{ethynyl}}$  bond and c) a change of the twisting of the phenyl ring with respect to the quasi-square planar coordination plane, which returns to be almost coplanar in the case of **P** of **5a** and **5g**, as well as in their respective initial reactants **R**. In the case of **P** of **5f** this twisting angle is important due to the steric hindrance (see part A).

Concerning the effect of EWGs and EDGs on the modification of the activation barrier several interesting points arise. As has been experimentally observed,<sup>17</sup> EDGs on the tolane rings reduce the activation barrier of the thermal reductive elimination (see values of  $\Delta G^\ddagger$  in Table 2). Therefore, the Pt<sup>II</sup>-aryl products with EDGs are kinetically more labile than the ones substituted with EWGs. When comparing the substitution pattern in the EDG series (complexes **5f** and **5g**) it can be seen that, unlike the  $\Delta G^\circ$  values,  $\Delta G^\ddagger$  barriers are very similar regardless of the substitution pattern (see Table 2).

Analyzing the overall thermal reaction can help understanding better the mechanism of the photochemical reaction. As it can be seen from Fig. 6, the oxidative addition reaction (going from **P** to **R**) does neither proceed thermally nor under thermodynamical or kinetically controlled conditions. An endothermic reaction profile with large activation barriers of *ca.* 45 to 49 kcal mol<sup>-1</sup> is obtained, preventing the thermal oxidative additive reaction. However, this reaction takes place photochemically after populating the “active states” of  $d \rightarrow \pi^*_{\text{alk}}$  character. After irradiation, enough energy is available to overcome such barriers and allow the reaction to relax on the excited state potential to achieve the  $C_{\text{aryl}}-C_{\text{ethynyl}}$  bond activated products.

**4.2.2. Mechanistic study of the thermal reductive elimination beginning from the  $C_{\text{aryl}}-\text{Br}$  activated products.** As stated in Part A,<sup>†</sup> the observed photochemical promoted  $C_{\text{aryl}}-\text{Br}$  bond activation in solution, taking place in the same proportion as the  $C_{\text{aryl}}-C_{\text{ethynyl}}$  bond activation in complexes **5a** and **5b** is, oppositely to  $C_{\text{aryl}}-C_{\text{ethynyl}}$  bond activation, irreversible under thermal conditions. Exemplarily, DFT ground state calculations have been performed in complex **5a** to rationalize these facts. Table 4 summarizes gas phase Gibbs free energies of the reaction ( $\Delta G^\circ$ ) as well as activation

**Table 4** Gas phase Gibbs free energies and activation barriers for the thermal reductive elimination reaction beginning from the  $C_{\text{aryl}}-\text{Br}_1$  activated product at the B3LYP/6-311G\*\*//RI-BP86/TZVP and the B2GP-PLYP/6-311G\*\*//RI-BP86/TZVP levels of theory. Values presented in kcal mol<sup>-1</sup>

<b>5a</b>	$\Delta G^\circ$ /kcal mol <sup>-1</sup>	$\Delta G^\ddagger$ /kcal mol <sup>-1</sup>
B3LYP/6-311G*	16.51	53.64
B2GP-PLYP/6-311G*	21.74	69.44

barriers ( $\Delta G^\ddagger$ ) at the B3LYP/6-311G\*\*//RI-BP86/TZVP and B2GP-PLYP/6-311G\*\*//RI-BP86/TZVP levels of theory.

As in Section 4.2.1., both functionals predict similar Gibbs free energies but show disparities in the activation barriers, which are underestimated by *ca.* 15 kcal mol<sup>-1</sup> with the B3LYP functional. As stated above, the B2GP-PLYP values are more reliable for bond activation reactions with transition metal atoms. In Fig. 7 we show the energetic profile of the thermal reductive elimination beginning from the  $C_{\text{aryl}}-\text{Br}$  activated product for the complex **5a**.

The  $\Delta G^\circ$  values clearly indicate that the reaction profile is endothermic, amounting to *ca.* 22 kcal mol<sup>-1</sup> with the double hybrid functional. Since the thermal backward reductive elimination reaction leading to the initial products (**P**) is thermodynamically not favored, the experimentally observed photochemical C–Br bond activation reaction for complexes **5a** and **5b** is irreversible upon sunlight. We note that the  $C_{\text{aryl}}-\text{Br}$  bond activated product **R1** is the global minimum of all the complexes presented in Section 4.2.

As it can be seen in Fig. 7, between the reactant **R1** (the  $C_{\text{aryl}}-\text{Br}$  bond activated photochemical product) and the reductive elimination product **P** there are three intermediates (**I1**, **I2** and **I3**) as well as four transition states (**TS1**, **TS2**, **TS3** and **TS4**). We propose a “ring-walking” mechanism of the (bisphosphane)Pt along the tolane moiety. In **TS1** the Pt–Br bond is already broken (goes from 2.53 Å in **R1** to 3.62 Å in **TS1**) whilst the C–Br is being formed (see 3.23 Å in **R1** and 2.01 Å in **TS1**). In **TS1** the Pt atom coordinates to one of the carbons of the phenyl group (2.12 Å). Relaxation on the potential energy surface leads to the intermediate **I1**, where the Pt atom coordinates in a  $\eta^2$ -fashion to two carbons of the phenyl moiety (with bonding distances 2.14 and 2.21 Å). Furthermore a twisting of the (bisphosphane)Pt unit is produced to decrease steric hindrance with the tolane moiety. The “ring-walking” mechanism leads to the second transition state (**TS2**), where the bond with the first carbon atom is already broken. Moreover, in **TS2** the Pt atom interacts mainly with the second carbon atom of the phenyl ring (bearing a Pt–C distance of 2.27 Å) and it approaches the third carbon atom of the phenyl ring (2.56 Å). In the intermediate **I2**, the Pt  $\eta^2$ -coordinates to the second and third carbons of the phenyl ring (Pt–C bond distances of 2.18 and 2.19 Å, respectively); also it can be seen that the twisting of the (bisphosphane)Pt to the tolane moiety turns to be similar to the one achieved for **R1** and **TS1**. From here on, the (bisphosphane)Pt unit moves along the tolane moiety and again  $\eta^2$ -coordinates to the tolane moiety but in **TS3** and **I3** at the third and fourth carbon atoms of the phenyl ring. The main difference between this two stationary points is the twisting of the (bisphosphane)Pt unit with respect to the tolane moiety. The fourth transition state (**TS4**) is the rate limiting step of the reaction. With an activation barrier ( $\Delta G^\ddagger$ ) of *ca.* 70 kcal mol<sup>-1</sup> makes

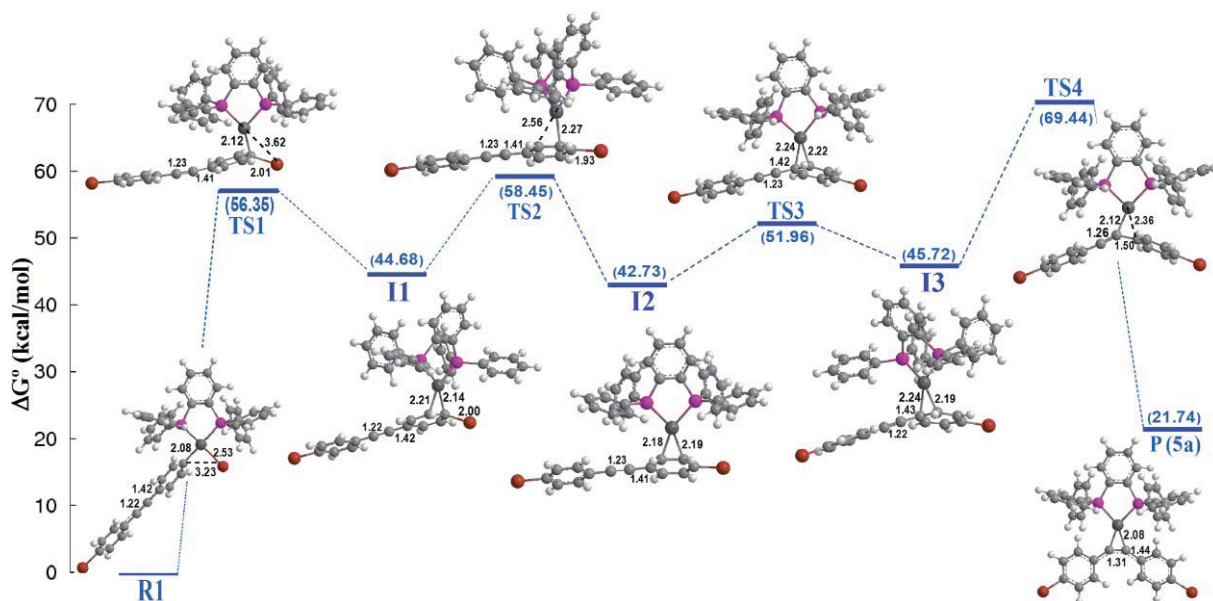


**Fig. 7** Energy diagram of the thermal reductive elimination beginning from the  $C_{\text{aryl}}\text{-Br}$  activate product leading to complex **5a** (blue), calculated at the B2GP-PLYP/6-311G\*\*/RI-BP86/TZVP level of theory. Relative free energy Gibbs are given in kcal mol<sup>-1</sup> with respect to complex R1. Main distances (in Å) along the reaction coordinate are indicated. Bromine atoms are in red, carbon atoms in grey, hydrogen atoms in white, and phosphorus atoms in pink.

this reaction not only thermodynamically but also kinetically unfeasible. In **TS4** the Pt atom coordinates in an *ipso* fashion to the alkyne (2.12 Å) and the phenyl (2.36 Å) moieties. Finally, the same product **P** as in the mechanism of  $C_{\text{aryl}}\text{-C}_{\text{ethynyl}}$  reductive elimination (see section 4.2.1) is achieved. The product **P** is characterized by a  $\eta^2$ -coordination of the Pt to the alkyne moiety (*vide supra*), thus enlarging the alkyne bond distance due to efficient  $\pi$ -back donation.

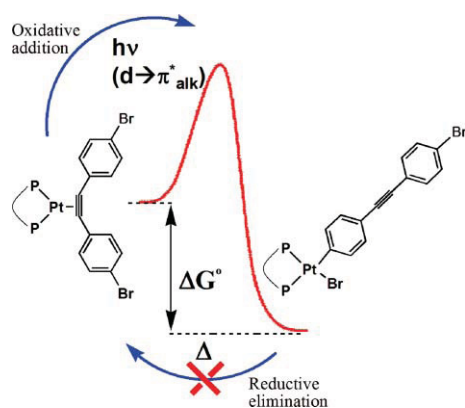
In Scheme 3 the energetic profile of the photochemical  $C_{\text{aryl}}\text{-Br}$  bond activation and its thermal reductive elimination is summarized. As in the case of the  $C_{\text{aryl}}\text{-C}_{\text{ethynyl}}$  bond activation, through the analysis of the backwards thermal reaction important facts of the photochemical mechanism can be deduced. As we stated above, in contrast to the  $C_{\text{aryl}}\text{-C}_{\text{ethynyl}}$  bond activation, the  $C_{\text{aryl}}\text{-Br}$  backwards thermal reductive elimination reaction does not take place due to the endothermic energetic profile with huge activation barriers of *ca.* 70 kcal mol<sup>-1</sup>. Furthermore, Fig. 7 helps

to understand why the oxidative addition reaction (going from **P** to **R1**) does not proceed thermally either. This is due to the big activation barrier (*ca.* 49 kcal mol<sup>-1</sup>) although the energetic profile is exothermic. As in the  $C_{\text{aryl}}\text{-C}_{\text{ethynyl}}$  bond activation, a photochemical pre-activation of complexes **P** is required. After irradiation, the “active states” of  $d \rightarrow \pi^*_{\text{alk}}$  character are populated and the energy excess allows the barrier of *ca.* 49 kcal mol<sup>-1</sup> to be overcome. Relaxation on the excited potential energy surfaces leads to the  $C_{\text{aryl}}\text{-Br}$  bond activated products.

## Conclusions

In summary, we have studied the first stages of the photochemical oxidative addition reaction ( $\text{Pt}^0 \rightarrow \text{Pt}^{\text{II}}$ ) using TD-DFT. Additionally, the backwards thermal reductive elimination reaction - *i.e.* ( $\text{Pt}^{\text{II}} \rightarrow \text{Pt}^0$ ) - in (bisphosphane)( $\eta^2$ -tolane) $\text{Pt}^0$  complexes from the  $C_{\text{aryl}}\text{-Br}$  as well as from the  $C_{\text{aryl}}\text{-C}_{\text{ethynyl}}$  bond activated products - have been studied with ground state DFT calculations.

The photochemical  $C_{\text{aryl}}\text{-C}_{\text{ethynyl}}$  bond activation is promoted *via* population of the “active” photochemical states, which are MLCT states of  $d \rightarrow \pi^*_{\text{alk}}$  character. An exhaustive analysis of the different (bisphosphane)( $\eta^2$ -tolane) $\text{Pt}^0$  complexes studied experimentally (see Part A†) and theoretically confirms that for the chosen complexes, both the electronic nature of the substituent as well as the steric effects between the phenyl rings of the tolane moiety contribute to the appearance of the  $d \rightarrow \pi^*_{\text{alk}}$  bands, and therefore responsible for tuning the photochemical reactivity. Since the  $d \rightarrow \pi^*_{\text{alk}}$  bands are predominant and stronger in complexes with electron-withdrawing substituents and in *ortho*-substituted compounds, it is expected that such complexes are prone to C-C bond activation; indeed, this has been seen experimentally (see Part A†). By changing the bisphosphane ligand, which in turns changes concomitantly the P-Pt-P bite angle, the photochemical reactivity



**Scheme 3** Energetic profile of the photochemical oxidative addition leading to  $C_{\text{aryl}}\text{-Br}$  bond activation and its thermal reductive elimination.

can also be tuned. Hence, a modification of the P–Pt–P bite angle determines the presence/absence of “active” photochemical states of  $d \rightarrow \pi^*_{\text{alk}}$  character. Furthermore, C–Br activation has been also theoretically rationalized as the debilitation of the  $\eta^2$ -coordination of the Pt center to the alkyne due to  $d \rightarrow \pi^*_{\text{alk}}$  excitations plus a weakening of the C–Br bond due to MLCT transitions of  $d \rightarrow \sigma^*_{\text{C-Br}}$  character.

The mechanisms of the reversible thermal reductive elimination reaction ( $\text{Pt}^{\text{II}} \rightarrow \text{Pt}^0$ ) from the  $\text{C}_{\text{aryl}}\text{--C}_{\text{ethynyl}}$  as well as from the  $\text{C}_{\text{aryl}}\text{--Br}$  bond activated products have been elucidated, and several stationary points have been located on the potential energy surfaces of the complexes. Concerning the thermal reductive elimination beginning from the  $\text{C}_{\text{aryl}}\text{--C}_{\text{ethynyl}}$  activated products, the exothermic energetic profile of the reaction is analogous for all the complexes herein studied. This fact is in accordance to the experimental results (see part A†). Both the electronic nature of the substituents as well as its substitution pattern biases the  $\Delta G^\circ$  values. The activation barriers are determined by the structure of the transition state, which is affected by the electronic nature of the substituent. Accordingly, the bromine substituted compound (EWG) has the highest activation barriers, while the EDG compounds show lower activation barriers.

Regarding the thermal reductive elimination reaction beginning from the  $\text{C}_{\text{aryl}}\text{--Br}$  activated product, we find an endothermic energetic profile, in accordance to the experimental evidence that in complexes **5a** and **5b** thermal reductive elimination reaction is not observed. The  $\text{C}_{\text{aryl}}\text{--Br}$  bond activated product is the global minimum of all the complexes presented herein.

## Acknowledgements

We thank financial support from the Carl-Zeiss Stiftung (D.E). Valuable comments and suggestions of the referees are also gratefully acknowledged.

## Notes and references

- H. Petzold, T. Weisheit, H. Görls, H. Breitzke, G. Buntkowsky, D. Escudero, L. González and W. Weigand, *Dalton Trans.*, 2008, 1979–1981.
- D. Escudero, M. Assmann, A. Pospiech, W. Weigand and L. González, *Phys. Chem. Chem. Phys.*, 2009, **11**, 4593–4600.
- K. Eichkorn, O. Treutler, H. Öhm, M. Häser and R. Ahlrichs, *Chem. Phys. Lett.*, 1995, **240**, 283–289.
- A. D. Becke, *Phys. Rev. A: At., Mol., Opt. Phys.*, 1988, **38**, 3098–3100.
- J. P. Perdew, *Phys. Rev. B: Condens. Matter*, 1986, **33**, 8822–8824.
- D. Andrae, U. Häussermann, M. Dolg, H. Stoll and H. Preuss, *Theor. Chim. Acta*, 1990, **77**, 123–141.
- M. E. Casida, *Recent advances in Density Functional Methods. Part I*. World Scientific, Singapore, 1995.
- R. Ahlrichs, M. Bär, M. Häser, H. Horn and C. Kölmel, *Chem. Phys. Lett.*, 1989, **162**, 165–169.
- A. D. Becke, *J. Chem. Phys.*, 1993, **98**, 5648–5652.
- C. T. Lee, W. T. Yang and R. G. Parr, *Phys. Rev. B: Condens. Matter*, 1988, **37**, 785–789.
- A. Karton, A. Tarnopolsky, J.-F. Lamère, G. C. Schatz and J. M. L. Martin, *J. Phys. Chem. A*, 2008, **112**, 12868–12886.
- M. J. Frisch, W. G. Trucks, H. B. Schlegel, G. E. Scuseria, M. A. Robb, J. R. Cheeseman, J. A. Jr. Montgomery, T. Vreven, K. N. Kudin, J. C. Burant, J. M. Millam, S. S. Iyengar, J. Tomassi, V. Barone, B. Menucci, M. Cossi, G. Scalmani, N. Rega, G. A. Petersson, H. Nakatsuji, M. Hada, M. Ehara, K. Toyota, R. Fukuda, J. Hasegawa, M. Ishida, T. Nakajima, Y. Honda, O. Kitao, H. Nakai, M. Klana, X. Li, J. E. Knox, H. P. Hratchian, J. B. Cross, V. Bakken, C. Adamo, J. Jaramillo, R. Gomperts, R. E. Stratmann, O. Yazyev, A. J. Austin, R. Cammi, C. Pomelli, J. W. Ochterski, P. Y. Ayala, K. Morokuma, G. A. Voth, P. Salvador, J. J. Dannenberg, V. G. Zakrzewski, S. Dapprich, A. D. Daniels, M. C. Strain, O. Farkas, D. K. Malick, A. D. Rabuck, K. Raghavachari, J. B. Foresman, J. V. Ortiz, Q. Cui, A. G. Baboul, S. Clifford, J. Cioslowski, B. B. Stefanov, G. Liu, A. Liashenko, P. Piskorz, I. Komaromi, R. L. Martin, D. J. Fox, T. Keith, M. A. Al-Laham, C. Y. Peng, A. Nanayakkara, M. Challacombe, P. M. W. Gill, B. Johnson, W. Chen, M. W. Wong, C. González, J. A. Pople, *Gaussian-03*, Revision C.02, 2004, Gaussian, Inc., Walingford CT.
- A. Drew and M. Head-Gordon, *Chem. Rev.*, 2005, **105**, 4009–4037.
- D. Jacquemin, E. A. Perpète, G. E. Scuseria, I. Ciofini and C. Adamo, *J. Chem. Theory Comput.*, 2008, **4**, 123–125.
- I. Georgieva, A. J. A. Aquino, N. Trendafilova, P. S. Santos and H. Lischka, *Inorg. Chem.*, 2010, **49**, 1634–1646.
- O. Zenkina, M. Altman, G. Leitus, L. J. W. Shimon, R. Cohen and M. E. Van Der Boom, *Organometallics*, 2007, **26**, 4528–4534.
- A. Gunay and W. D. Jones, *J. Am. Chem. Soc.*, 2007, **129**, 8729–8735.
- M. Murakami and Y. Ito, Cleavage of carbon–carbon single bonds by transition metals, in *Topics in Organometallic Chemistry*, Springer, Berlin, 1999, vol. 3, pp. 97–129.
- T. Oshiki, A. Yamada, K. Kawai, H. Arimitsu and K. Takai, *Organometallics*, 2007, **26**, 173–182.
- Y. Yu, J. M. Smith, C. J. Flaschenriem and P. L. Holland, *Inorg. Chem.*, 2006, **45**, 5742–5751.

## 5. APPENDED PUBLICATIONS

---



## 6

# Conclusions and Outlook

This thesis deals with the computation of photophysical and photochemical properties of transition metal complexes and organic compounds. Quantum chemical calculations for excited states are helpful tools to rationalize the processes occurring after light excitation. Indeed, they are sometimes indispensable to interpret the results of an enormous variety of experiments. Accordingly, there is a big demand to calibrate the theoretical methods available for the computation of the excited states. Whilst multiconfigurational strategies, such as the CASPT2/CASSCF method in its current version, can provide good accuracy (0.1 eV), there is an urgent need to go beyond the size that this method allows in order to treat larger molecules or systems which require larger active spaces. In this sense, the RASPT2/RASSCF procedure appears as a powerful alternative. In this thesis we have tested the viability of the RASPT2/RASSCF method to compute the excited states of Ru(II)polypyridyl complexes. Large systems are nowadays treated with TD-DFT, whose accuracy extremely depends on the chosen functional. Promising functionals have been developed in the last years to treat Rydberg and charge-transfer states, such as the long-range corrected CAM-B3LYP functional. Despite its success for describing long-range charge-transfer states of organic complexes, in this thesis we demonstrate that CAM-B3LYP fails to describe the metal-to-ligand charge-transfer states of Ru(II)polypyridyl complexes. Instead, metal-to-ligand charge-transfer states are found to be accurately predicted only with functionals possessing intermediate amounts of exact exchange, such as B3LYP. Indeed, as it has been illustrated throughout this thesis, a reasonable interpretation of photophysical and photochemical properties of transition metal complexes can be obtained from

## 6. CONCLUSIONS AND OUTLOOK

---

the TD-DFT calculations, when i) the solvent is included in the calculations and ii) a proper choice of the functional is done.

Solar energy conversion is going to be of vital importance in the near future. As we stated in the introduction, much effort has been then dedicated to develop technologies which harness solar energy in an efficient manner. In this sense, there is still some place left to increase these efficiencies *via* molecular design and concomitant tune of the photophysical properties of the dyes. This is very often done in a trial-and-error manner. Instead, predictive tools would be highly desirable. To this aim, the computation of excited states and photochemical properties can provide useful hints to guide molecular design strategies. Transition metal complexes are very often used as photoactive compounds in sunlight-based technologies. This is the case of the Ru(II) polypyridyl complexes 8, 9 and 10 studied in this thesis. We have rationalized with the help of TD-DFT and quantum chemical calculations the underlying reasons of their observed long-lived excited states. Such knowledge can be profited in the design of new ruthenium complexes with optimal photophysical properties.

Due to the striking competition of radiative and non-radiative deactivation processes in many of these transition metal complexes, it is clear that the near future should be devoted to perform reaction dynamics calculations in order to get information about excited state lifetimes and estimations of quantum yields. This is still a challenge for transition metal complexes, due to prohibitive size of the systems and the need of an accurate description of the excited states with multiconfigurational methods. Another challenge is the consideration of all type of coupling effects during the reaction dynamic simulations, since as we have seen along this thesis, spin-orbit effects and non-adiabatic coupling terms are indispensable for the correct interpretation of many spectroscopic phenomena.

# 7

## Zusammenfassung

Quantenchemische Rechnungen und molekulardynamische Simulationen sind wertvolle Werkzeuge, um die photophysikalischen und photochemischen Eigenschaften molekularer Systeme zu charakterisieren. Während die Beschreibung der Eigenschaften des elektronischen Grundzustandes inzwischen fast schon Routine ist, bleibt die Charakterisierung angeregter Zustände noch immer eine Herausforderung. Auch das Verständnis der Reaktivität im Grundzustand ist herausfordernd und in mancher Hinsicht kompliziert. Berechnungen angeregter Zustände sind jedoch fast immer deutlich komplizierter und zeitaufwändiger. Trotz aller damit eventuell verbundenen Rückschläge und Frustrationen gibt es ein wachsendes Interesse an der Berechnung angeregter Zustände und dem Aufdecken der Mechanismen photochemischer Reaktionen. In den letzten Jahrzehnten wurden die wesentlichen Entwicklungen im Bereich der theoretischen Spektroskopie und Photochemie bei organischen Verbindungen erzielt. Es gibt daneben jedoch auch einen wachsenden Fortschritt bei der Berechnung angeregter Zustände von Übergangsmetallkomplexen, ungeachtet aller dabei auftretenden Schwierigkeiten. Das 21. Jahrhundert schickt sich an, das Jahrhundert des Lichts zu werden. Verständnis und Kontrolle photochemischer Reaktionen werden für viele Bereiche der Optik und Photonik von entscheidender Bedeutung werden. In diesem Sinne könnte Sonnenlicht der Treibstoff der Zukunft werden. Die Entwicklung von Technologien, die Sonnenenergie effizient nutzen, wurde und wird mit großem Aufwand vorangetrieben. Häufig werden in derartigen Systemen Übergangsmetallkomplexe als Lichtsammleinheiten eingesetzt. So werden z.B. häufig Solarzellen mit Ru(II)polypyridil-Komplexen sensibilisiert. In dieser Arbeit wurden die Spektroskopie und die Photochemie aus-

## 7. ZUSAMENFASSUNG

---

gewählter Übergangsmetallkomplexe und organischer Verbindungen untersucht. Teile der Arbeit fanden in enger Kooperation mit experimentell arbeitenden Gruppen statt, die einige der Verbindungen synthetisierten und spektroskopisch charakterisierten. Die Ergebnisse der Arbeit können wie folgt zusammengefasst werden:

- i) Einschätzung der Eignung der zeitabhängigen Dichtefunktionaltheorie (TD-DFT) und anderer quantenchemischer Methoden für angeregte Zustände von Übergangsmetallkomplexen und organischen Farbstoffen. Eine ausgewogene Beschreibung angeregter Zustände von Übergangsmetallkomplexen oder organischen Farbstoffen zu erhalten erweist sich als ausgesprochen schwierig. Auf der einen Seite leiden die ökonomischen TD-DFT-Methoden an ihrem sprunghaften Verhalten, abhängig vom verwendeten Funktional. Dies ist insbesondere kritisch in der Beschreibung von Ladungstransferzuständen. In dieser Arbeit wurde gezeigt, dass Hybridfunktionale mit einem mittleren Anteil an exaktem Austausch den anderen Funktionalen überlegen ist. Dies gilt sowohl bei der Behandlung der Übergangsmetallkomplexe (Ru(II)polypyridil-Komplexe) als auch für die organischen Farbstoffe (so die Azobenzen-ähnlichen Verbindungen). Andererseits gibt es die auf der Störungstheorie 2. Ordnung und restricted active space basierenden Methode (RASPT2), die in der Lage ist sehr große active spaces zu behandeln. In der vorliegenden Arbeit wurden hiermit angeregte Zustände von Ru(II)polypyridil-Komplexen untersucht. Als hauptsächlicher Flaschenhals in der genauen Beschreibung der Spektroskopie dieser Komplexe erweist sich die optimale Aufteilung der Teilräume (RAS). Schliesslich haben wir gefunden, dass der Einfluss von Lösungsmittelleffekten von ausschlaggebender Bedeutung für die spektroskopische Genauigkeit ist. Dies bezieht sich nicht nur auf die exakten elektronischen Energien (einige Metall-Ligand-Ladungstransferzustände sind gegenüber der Gasphase um 1 eV verschoben), sondern auch auf die korrekte Beschreibung der Oszillatorstärken (wie es für die  $n^*$ -Zustände der Azobenzen-ähnlichen organischen Farbstoffe bestätigt werden konnte).
- ii) Anwendung auf Ru(II)polypyridil-Komplexe: Einblicke in deren Photochemie. Basierend auf den unter i) erhaltenen Vergleichswerten wurden die photophysikalischen Eigenschaften einiger Ru(II)polypyridin-Komplexe untersucht. Der Fokus lag dabei auf der Aufklärung der photochemischen Prozesse nach der Absorption

---

von Licht. Die Lebensdauer der angeregten Zustände sowie die Abklingraten der strahlenden und strahlungslosen Übergänge dieser Komplexe lassen sich z.B. durch Modifikation der Liganden verändern. Im Rahmen dieser Arbeit wurde die Veränderungen der Strahlungseigenschaften verschiedener Komplexe mittels TD-DFT- und CASSCF (complete active space self consistent field)-Rechnungen untersucht. So wurde z.B. nachgewiesen, dass die radikale Veränderung der photophysikalischen Eigenschaften der Komplexe 9 und 10 auf den deutlich unterschiedlichen berechneten Abklingraten basiert.

- iii) Anwendung auf Ir(III)-cyclometallierte Komplexe: Einblicke in deren Strahlungseigenschaften. In dieser Arbeit wurden verschiedene TD-DFT- und  $\Delta$ -SCF-Ansätze zur Berechnung des Strahlungsmaximums untersucht. Die Werte der adiabatischen Strahlungsenergie ( $\Delta$ -SCF) und die Singulett-Triplett-Anregungen (TD-DFT) der  $T_1$ -Geometrie sind die besten Ansätze, um das Strahlungsmaximum der Ir(III)-cyclometallierten Komplexe zu erhalten. Zusätzlich wurde die Blauverschiebung für eine Serie von Verbindungen in Termen der Orbitalenergie ausgedrückt.
- iv) Die photochemische Aktivierung der C-C-Bindung und deren thermische Umkehrung bei (Bisphosphan)( $\mu^2 - Tolan$ ) $Pt^0$ -Komplexen. Mittels DFT- und TD-DFT-Rechnungen konnte der Mechanismus der photochemischen C-C und C-Br Bindungsbruchreaktion, die bei diesen Komplexen nach der Bestrahlung mit Sonnenlicht auftritt, erklärt werden. Die C-C und/oder C-Br Bindungsaktivierung wird durch Anregung bestimmter Zustände mit  $d_{Pt}\pi_{alk}^*$  Charakter, befördert. Bei der Analyse einer Reihe von Verbindungen konnte gezeigt werden, dass sowohl elektronische als auch sterische Effekte das Vorhandensein dieser photochemisch "aktiven" Zustände bestimmen. DFT-Studien zeigen, in Übereinstimmung mit den experimentellen Befunden, einen exothermen Verlauf für die thermische Umkehrreaktion, beginnend beim C-C-bindungsaktivierten Produkt und einen endothermen Verlauf für den C-Br-Pfad.
- v) Quantenchemische Studien und ab-initio Moleküldynamik in 2H-Azirin. Diese Arbeit zielte auch darauf ab, die selektive C-C oder C-N Bindungsaktivierung in Abhängigkeit von der Anregungswellenlänge zu verstehen. Es wurden quantenchemische Rechnungen durchgeführt, um die Deaktivierungskanäle für beide

## 7. ZUSAMENFASSUNG

---

Reaktionspfade zu finden. Die zudem durchgeführten Moleküldynamiksimulationen haben das durch quantenchemische Rechnungen erhaltene "statische" Bild bestätigt. Zusätzlich wurden zeitaufgelöste Informationen (unter Beachtung der ultraschnellen Natur dieser Reaktionen) und erwartete Quantenausbeuten aus ab-initio-Moleküldynamikstudien erhalten.

# References

- [1] N. J. TURRO. University Science Books, California, 1991. 1
- [2] M. KLESSINGER AND J. MICHL. VCH., New York, 1995. 1, 8, 11
- [3] D. H. D. JOHN AND G. T. J. FIELD. Chapman and Hall, London, 1963. 1
- [4] F. BASOLO AND R. G. PEARSON. Wiley, New York, 1958. 2
- [5] C. J. BALLHAUSEN. McGraw-Hill, New York, 1962. 2
- [6] L. E. ORGEL. *Q. Rev. London*, **8**:422, 1954. 2
- [7] C. K. JORGENSEN. Pergamon, Oxford, 1962. 2
- [8] M. SCHLIWA. Wiley-VCH, Weinheim, Germany, 2003. 2
- [9] B. L. FERINGA. Wiley-VCH, Weinheim, Germany, 2003. 2
- [10] V. FERINGA, A. CREDI, AND M. VENTURI. Wiley-VCH, Weinheim, Germany, 2006. 2
- [11] V. BALZANI, A. CREDI, AND M. VENTURI. *Chem. Sus. Chem.*, **1**:26, 2008. 2, 9, 10
- [12] L. S. HUNG AND C. H. CHEN. *Mat. Sci. and Eng. R.*, **39**:143, 2002. 2
- [13] S. PROTTHI AND M. FAGNONI. *Photochem. Photobiol. Sci.*, **8**:1449, 2009. 2, 24
- [14] N. AMAROLI AND V. BALZANI. *Angew. Chem. Int. Ed.*, **46**:52, 2007. 2
- [15] N. S. LEWIS. *MRS Bull.*, **32**:808, 2007. 2
- [16] B. O'REAGAN AND M. GRAETZEL. *Nature*, **353**:737, 1991. 2, 18
- [17] V. BALZANI, L. MOGGI, M. F. MANFRIN, F. BOLLETA, AND M. GLERIA. *Science*, **189**:852, 1975. 2
- [18] M. GRAETZEL. Academic Press, New York, 1983. 2
- [19] W. DOMCKE, D. R. YARKONY, AND H. KOPPEL. World scientific, Singapore, 2004. 7
- [20] M. BAER. Wiley Interscience, New York, 2006. 7
- [21] M. OLIVUCCI. Elsevier, Amsterdam, 2005. 7, 8
- [22] H. M. DAMRAUER, G. CERULLO, A. YEH, T. R. BOUSSIE, C. V. SHANK, AND J. K. MCCUSKER. *Science*, **275**:54, 1997. 8, 9
- [23] G. J. ATCHITY, S. S. XANTHEAS, AND K. RUEDEBERG. *J. Chem. Phys.*, **95**:1862, 1991. 8
- [24] A. H. ZEVALI. World Scientific, Singapore, 1994. 8
- [25] K. PIERLOOT. Elsevier, Amsterdam, 2005. 8
- [26] V. BALZANI, A. JURIS, M. VENTURI, S. CAMPAGNA, AND S. SERRONI. *Chem. Rev.*, **96**:759, 1996. 9, 10
- [27] A. JURIS, V. BALZANI, F. BARIGELLETI, S. CAMPAGNA, P. BELSER, AND A. VON ZELEWSKY. *Coord. Chem. Rev.*, **84**:85, 1988. 9
- [28] A. T. YEH, C. V. SHANK, AND J. K. MCCUSKER. *Science*, **289**:935, 2000. 9
- [29] M. F. CHARLOT, Y. PELLEGRIN, A. QUARANTA, W. LEIBL, AND A. AUKAULO. *Chem. Eur. J.*, **12**:796, 2006. 9
- [30] V. BALZANI, S. CAMPAGNA, G. DENTI, A. JURIS, S. SERRONI, AND M. VENTURI. *Acc. Chem. Res.*, **31**:26, 1998. 10, 16
- [31] J. P. SAUVAGE, J. P. COLLIN, J. C. CHAMBRON, S. GUILLEREZ, C. COUDRET, V. BALZANI, F. BARIGELLETI, L. DE COLA, AND L. FLAMIGNI. *Chem. Rev.*, **94**:993, 1994. 10
- [32] E. A. MEDLYCOTT AND G. S. HANAN. *Chem. Soc. Rev.*, **34**:133, 2005. 10, 50
- [33] M. MAESTRI, A. ARMAROLI, V. BALZANI, E. C. CONSTABLE, AND A. THOMPSON. *Inorg. Chem.*, **34**:2759, 1995. 10, 12, 50
- [34] M. ABRAHAMSSON, M. JAEGER, R. J. KUMAR, T. OESTERMAN, P. PERSSON, H. C. BECKER, O. JOHANSSON, AND L. HAMMARSTROEM. *J. Am. Chem. Soc.*, **130**:15533, 2008. 10
- [35] I. M. DIXON, F. ALARY, AND J. H. HEULLY. *Dalton Trans.*, **39**:10959, 2010. 10
- [36] H. F. SUEN, S. W. WILSON, M. POMERANTZ, AND J. L. WALSH. *Inorg. Chem.*, **28**:786, 1989. 10
- [37] B. ELIAS AND A. KIRSCH-DE MESMAEKER. *Coord. Chem. Rev.*, **250**:1627, 2006. 10
- [38] J. H. HEULLY, F. ALARY, AND M. BOGGIO-PASQUA. *J. Chem. Phys.*, **131**:184308, 2009. 11
- [39] X. Y. WANG, A. DEL GUERZO, AND R. H. SCHMEHL. *J. Photochem. Photobiol. C*, **5**:55, 2004. 12
- [40] E. A. MEDLYCOTT AND G. S. HANAN. *Coord. Chem. Rev.*, **250**:1763, 2006. 12
- [41] M. DUATI, S. TASCA, F. C. LYNCH, H. BOHLEN, J. G. VOS, S. STAGNI, AND M. D. WARD. *Inorg. Chem.*, **42**:8377, 2003. 12

## REFERENCES

---

- [42] S. U. SON, K. H. PARK, Y. S. LEE, B. Y. KIM, C. H. CHOI, M. S. LAH, Y. H. JANG, D. J. JANG, AND Y. K. CHUNG. *Inorg. Chem.*, **43**:6896, 2004. 12
- [43] M. HISSLER, A. EL-GHAYOURY, A. HARRIMAN, AND R. ZIESSEL. *Angew. Chem. Int. Ed.*, **37**:1717, 1998. 12
- [44] M. I. J. POLSON, F. LOISEAU, S. CAMPAGNA, , AND G. S. HANAN. *Chem. Comm.*, page 1301, 2006. 12
- [45] Y. Q. FANG, N. J. TAYLOR, G. S. HANAN, F. LOISEAU, R. PASSALACQUA, S. CAMPAGNA, H. NIERENGARTEN, AND A. VAN DORSSELAER. *J. Am. Chem. Soc.*, **124**:7912, 2002. 12
- [46] J. H. WANG, Y. Q. FANG, G. S. HANAN, F. LOISEAU, AND S. CAMPAGNA. *Inorg. Chem.*, **44**:5, 2005. 12
- [47] R. ENGLMAN AND J. JORTNER. *Molec. Phys.*, **18**:145, 1970. 12, 20
- [48] J. V. CASPAR, E. M. KOBER, B. P. SULLIVAN, AND T. J. MEYER. *J. Am. Chem. Soc.*, **104**:632, 1982. 12, 13
- [49] J. A. TREADWAY, B. LOEB, R. LOPEZ, P. A. ANDERSON, F. R. KEENE, AND T. J. MEYER. *Inorg. Chem.*, **35**:2242, 1996. 12
- [50] E. M. KOBER, J. V. CASPAR, R. S. LUMPKIN, AND T. J. MEYER. *J. Phys. Chem.*, **90**:3722, 1986. 12
- [51] B. J. PANTUCH, D. E. LACKY, AND G. A. CROSBY. *J. Phys. Chem.*, **84**:2061, 1980. 13
- [52] P. A. MABROUK AND M. S. WRIGHTON. *Inorg. Chem.*, **25**:526, 1986. 13
- [53] G. D. DANZER, J. A. GOLUS, AND J. R. KINCAID. *J. Am. Chem. Soc.*, **115**:8643, 1993. 13
- [54] S. J. STRICKLER AND R. A. BERG. *J. Chem. Phys.*, **37**:814, 1962. 13
- [55] D. R. ORT AND C. F. YOCUM. Kluwer, Dordrecht, 1996. 15
- [56] K. N. FERREIRA, T. M. IVERSON, K. MAGHLAULI, J. BARBER, AND S. IWATA. *Science*, **303**:1831, 2004. 15
- [57] V. BALZANI AND F. SCANDOLA. Pergamon, Oxford, 1996. 16
- [58] V. BALZANI, A. CREDI, AND M. VENTURI. Wiley-VCH, Weinheim, Germany, 2006. 16
- [59] G. R. NEWKOME, C. N. MOOREFIELD, AND F. VOEGTLE. Wiley-VCH, Weinheim, Germany, 2001. 16
- [60] A. ADRONOV AND J. M. J. FRECHET. *Chem. Comm.*, page 1701, 2000. 16
- [61] V. BALZANI, P. CERONI, A. JURIS, M. VENTURI, S. CAMPAGNA, F. PUNTOTIERO, AND S. SERRONI. *Coord. Chem. Rev.*, **219**:545, 2001. 16
- [62] D. GUST, T. A. MOORE, AND A. L. MOORE. *Acc. Chem. Res.*, **34**:40, 2001. 16
- [63] D. M. GULDI. *Chem. Soc. Rev.*, **31**:22, 2002. 16
- [64] S. L. GILAT, A. ADRONOV, AND J. M. J. FRECHET. *Angew. Chem. Int. Ed.*, **38**:1422, 1999. 16
- [65] K. R. J. THOMAS, A. L. THOMPSON, A. V. SIVAKUMAR, C. J. BARDEEN, AND S. THAYUMANAVAN. *J. Am. Chem. Soc.*, **127**:373, 2005. 16
- [66] D. GUST, T. A. MOORE, AND A. L. MOORE. *Acc. Chem. Res.*, **26**:198, 1993. 17
- [67] V. BALZANI. Wiley-VCH, Weinheim, Germany, 2001. 17
- [68] L. FLAMIGNI, E. BARANOFF, J. P. COLLIN, AND J. P. SAUVAGE. *Chem. Eur. J.*, **12**:6592, 2006. 17
- [69] P. A. LIDDELL, D. KUCIAUSKAS, J. P. SUMIDA, B. NASH, D. NGUYEN, A. L. MOORE, T. A. MOORE, AND D. GUST. *J. Am. Chem. Soc.*, **119**:1400, 1997. 17
- [70] S. FUKUZUMI AND D. M. GULDI. Wiley-VCH, Weinheim, Germany, 2001. 17
- [71] W. RUETTINGER AND G. C. DISMUKES. *Chem. Rev.*, **97**:1, 1997. 18
- [72] X. SALA, I. ROMERO, M. RODRIGUEZ, L. ESCRICHE, AND A. LLOBET. *Angew. Chem. Int. Ed.*, **48**:2842, 2009. 18
- [73] J. J. CONCEPCION, J. H. JURSS, M. K. BRENNAMAN, P. G. HOERTZ, A. O. T. PATROCINIO, N. Y. M. IHA, J. L. TEMPLETON, AND T. J. MEYER. *Acc. Chem. Res.*, **42**:1954, 2009. 18
- [74] S. W. GESTERN, G. J. SAMUELS, AND T. J. MEYER. *J. Am. Chem. Soc.*, **104**:4029, 1982. 18
- [75] S. RAU, B. SCHAEFER, D. GLEICH, E. ANDERS, M. RUDOLPH, M. FRIEDRICH, H. GOERLS, W. HENRY, AND J. G. VOS. *Angew. Chem. Int. Ed.*, **45**:6215, 2006. 18
- [76] H. OZAWA, M. HAGA, AND K. SAKAI. *J. Am. Chem. Soc.*, **128**:4926, 2006. 18
- [77] G. AJAYAKUMAR, M. KOBAYASHI, S. MASAOKA, AND K. SAKAI. *Dalton Trans.*, page 3955, 2011. 18
- [78] T. W. HAMANN, R. A. JENSEN, A. B. F. MARTINSONAND H. VAN RYSWYK, AND J. T. HUPP. *Energy Environ. Sci.*, **1**:66, 2008. 18, 20, 21
- [79] J. N. CLIFFORD, E. MARTINEZ-FERRERO, A. VITERISI, AND E. PALOMARES. *Chem. Soc. Rev.*, **40**:1635, 2011. 18
- [80] M. GRAETZEL. *Inorg. Chem.*, **44**:6841, 2005. 18
- [81] M. GRAETZEL. *MRS Bull.*, **30**:23, 2005. 18
- [82] M. K. NAZEERUDDIN, F. DE ANGELIS, S. FANTACCI, A. SELLONI, G. VISCARDI, P. LISKA, S. ITO, B. TAKERU, AND M. GRAETZEL. *J. Am. Chem. Soc.*, **127**:16835, 2005. 19
- [83] Z. S. WANG, M. YANAGIDA, K. SAYAMA, AND H. SUGIHARA. *Chem. Mater.*, **18**:2912, 2006. 19



## REFERENCES

- [84] S. A. HAQUE, E. PALOMARES, B. M. CHO, A. N. M. GREEN, N. HIRATA, D. R. KLUG, AND J. R. DURRANT. *J. Am. Chem. Soc.*, **127**:3456, 2005. 20
- [85] K. ZHU, N. KOPIDAKIS, N. R. NEALE, J. VAN DE LAGE-MAAAT, AND A. J. FRANK. *J. Phys. Chem. B*, **110**:25174, 2006. 20
- [86] S. ITO, S. M. NAZEERUDDIN, R. HUMPHRY-BAKER, P. LISKA, R. CHARVET, P. COMTE, M. K. NAZEERUDDIN, P. PECHY, M. TAKATA, H. MIURA, S. UCHIDA, AND M. GRAETZEL. *Adv. Mater.*, **18**:1202, 2006. 21
- [87] Z. S. WANG, Y. CUI, K. HARA, Y. DAN-OH, C. KASADA, AND A. SHINPO. *Adv. Mater.*, **19**:1138, 2007. 21
- [88] S. YANAGIDA, Y. YU, AND K. MANSEKI. *Acc. Chem. Res.*, **42**:1827, 2009. 21
- [89] B. C. O'REAGAN, I. LOPEZ-DUARTE, M. V. MARTINEZ-DIAZ, A. FORNELI, J. ALBERO, A. MORANDEIRA, E. PALOMARES, T. TORRES, AND J. R. DURRANT. *J. Am. Chem. Soc.*, **130**:2906, 2008. 21
- [90] J. N. CLIFFORD, E. PALOMARES, M. K. NAZEERUDDINA, M. GRAETZEL, AND J. R. DURRANT. **111**:6561, 2007. 21
- [91] L. M. PETER. **111**:6601, 2007. 21
- [92] S. A. SAPP, C. M. ELLIOTT, C. CONTADO, S. CARAMORI, AND C. A. BIGNOZZI. *J. Am. Chem. Soc.*, **124**:11215, 2002. 21
- [93] H. NUSBAUMER, S. M. NAZEERUDDIN, J. E. MOSER, AND M. GRAETZEL. *Chem. Eur. J.*, **9**:3756, 2003. 21
- [94] S. HATTORI, Y. WADA, S. YANAGIDA, AND S. FUKUZUMI. *J. Am. Chem. Soc.*, **127**:9648, 2005. 21
- [95] G. OSKAM, B. V. BERGERON, G. J. MEYER, AND P. C. SEARSON. *J. Phys. Chem. B*, **105**:6867, 2001. 21
- [96] H. YERSIN. Wiley-VCH, Weinheim, Germany, 2008. 22, 23
- [97] E. HOLDER, B. M. W. LANGEVELD, AND U. S. SCHUBERT. *Adv. Mater.*, **17**:1109, 2005. 22
- [98] B. W. D'ANDRADE AND S. R. FORREST. *Adv. Mater.*, **16**:1585, 2004. 22
- [99] Y. SUN, N. C. GIEBINK, H. KANNO, B. MA, M. E. THOMPSON, AND S. R. FORREST. *Nature*, **400**:908, 2006. 22
- [100] B. D. CHIN, M. C. SUH, M. H. KIM, S. T. LEE, H. D. KIM, AND H. K. CHUNG. *Appl. Phys. Lett.*, **86**:133505, 2005. 22
- [101] S. LAMANSKY, P. DJUROVICH, D. MURPHY, F. ABDELRAZZAQ, H. E. LEE, C. ADACHI, P. E. BURROWS, S. R. FORREST, AND M. E. THOMPSON. *J. Am. Chem. Soc.*, **123**:4304, 2001. 22, 23
- [102] Y. YOU AND Y. PARK. *J. Am. Chem. Soc.*, **127**:12438, 2005. 22, 23
- [103] M. K. NAZEERUDDIN, R. HUMPHRY-BAKER, D. BERNER, S. RIVIER, L. ZUPPIROLI, AND M. GRAETZEL. *J. Am. Chem. Soc.*, **125**:8790, 2003. 23
- [104] Y. TAO, Q. WANG, C. YANG, Q. WANG, Z. ZHANG, T. ZOU, J. QIN, AND D. MA. *Angew. Chem. Int. Ed.*, **47**:8104, 2008. 23
- [105] E. BARANOFF, J. H. YUM, M. GRAETZEL, AND M. K. NAZEERUDDIN. *J. Org. Chem.*, **69**:2661, 2009. 23
- [106] Y. YOU AND S. Y. PARK. *Dalton Trans.*, page 1267, 2009. 23
- [107] P. T. CHOU AND Y. CHI. *Chem. Eur. J.*, **13**:380, 2007. 23
- [108] X. GU, T. FEI, H. ZHANG, H. XU, B. YANG, Y. MA, AND X. LIU. *J. Phys. Chem. A*, **112**:8387, 2008. 23
- [109] T. TSUZUKI, N. SHIRASAWA, T. SUZUKI, AND S. TOKITO. *Adv. Mater.*, **15**:1455, 2003. 23
- [110] B. LIANG, C. JIANG, Z. CHEN, X. ZHANG, H. SHI, AND Y. CAO. *J. Mater. Chem.*, **16**:1281, 2006. 23
- [111] C. L. HO, W. Y. WONG, Z. Q. GAO, C. H. CHEN, K. W. CHEAH, B. YAO, Z. YIE, Q. WANG, D. MA, L. WANG, X. M. YU, H. S. KWOK, AND Z. LIN. *Adv. Func. Mater.*, **18**:319, 2008. 23
- [112] C. H. YANG, S. W. LI, Y. CHI, Y. M. CHENG, Y. S. YEH, P. T. CHOU, G. H. LEE, C. H. WANG, AND C. F. SHU. *Inorg. Chem.*, **44**:7770, 2005. 23
- [113] Q. ZHAO, M. YU, L. SHI, S. LIU, C. LI, M. SHI, Z. ZHOU, C. HUANG, AND F. LI. *Organometallics*, **29**:1085, 2010. 23
- [114] L. H. FISCHER, M. I. J. STICH, O. S. WOLFBEIS, N. TIAN, E. HOLDER, AND M. SCHAEFERLING. *Chem. Eur. J.*, **15**:10857, 2009. 23
- [115] C. S. K. MAK, D. PENTLEHNER, M. STICH, O. S. WOLFBEIS, W. K. CHAN, AND H. YERSIN. *Chem. Mater.*, **21**:2173, 2009. 23
- [116] M. C. DEROSA, D. J. HODGSON, G. D. ENRIGHT, B. DAWSON, C. E. B. EVANS, AND R. J. CRUTCHLEY. *J. Am. Chem. Soc.*, **126**:7619, 2004. 23
- [117] P. ESSER, B. POHLMAN, AND H. D. SCHARF. *Angew. Chem. Int. Ed.*, **33**:2009, 1994. 24
- [118] M. OELGEMOELLER, C. JUNG, AND J. MATTAY. *Pure Appl. Chem.*, **79**:1939, 2007. 24
- [119] A. ALBINI AND M. FAGNONI. *Green Chem.*, **6**:1, 2004. 24
- [120] S. MALATO, J. BLANCO, A. VIDAL, AND C. RICHTER. *Appl. Catal. B*, **37**:1, 2002. 24
- [121] S. FLORIO, F. M. PERNA, R. LUISI, J. BARLUENGA, F. RODRIGUEZ, AND F. J. FAANS. *J. Org. Chem.*, **69**:5480, 2004. 24
- [122] J. BARLUENGA, M. A. FERNANDEZ-RODRIGUEZ, E. AGUILAR, F. FERNANDEZ-MARI, A. SALINAS, AND B. OLANO. *Chem. Eur. J.*, **7**:3533, 2001. 24
- [123] S. G. DAVIES, R. F. NEWTON, AND J. M. J. WILLIAMS. *Tetrahedron Lett.*, **30**:2967, 1989. 24

## REFERENCES

---

- [124] K. KAMIKAWA, A. TACHIBANA, S. SAGIMOTO, AND M. UEMURA. *Org. Lett.*, **3**:2033, 2001. 24
- [125] H. RATNI AND E. P. KUENDIG. *Org. Lett.*, **1**:1997, 1999. 24
- [126] W. E. BACHMANN. *J. Am. Chem. Soc.*, **55**:391, 1933. 24
- [127] J. T. LI, J. H. YANG, J. F. HAND, AND T. S. LI. *Green Chem.*, **5**:433, 2003. 24
- [128] E. HAGGIAGE, E. E. COYLE, K. JOYCE, AND M. OELGEMOELLER. *Green Chem.*, **11**:318, 2009. 24
- [129] K. H. FUNKEN AND M. BECKER. *Renewable Energy*, **24**:469, 2001. 24
- [130] R. H. CRABTREE. *Chem. Rev.*, **85**:245, 1985. 25
- [131] V. RITLENG, C. SIRLIN, AND M. PFEFFER. *Chem. Rev.*, **102**:1731, 2002. 25
- [132] M. E. VAN DER BOOM AND D. MILSTEIN. *Chem. Rev.*, **103**:1759, 2003. 25
- [133] P. STEENWINKEL, R. A. GOSSAGE, AND G. VAN KOTEN. *Chem. Eur. J.*, **4**:759, 1998. 25
- [134] J. M. BROWN, P. H. DIXNEUF, A. FUERSTNER, L. S. HEGEDUS, P. HOFFMANN, P. KNOCHEL, G. VAN KOTEN, S. MURAI, AND M. REETZ. Springer, Berlin, 1999. 25
- [135] B. RYBTCHINSKI AND D. MILSTEIN. *Angew. Chem. Int. Ed.*, **38**:870, 1999. 25
- [136] C. PERTHUISOT AND W. D. JONES. *J. Am. Chem. Soc.*, **116**:3647, 1994. 25
- [137] W. D. JONES. *Nature*, **364**:676, 1993. 25
- [138] T. NISHIMURA AND K. OHE. *J. Am. Chem. Soc.*, **121**:11010, 1999. 25
- [139] T. C. FLOOD AND J. A. STATLER. *Organometallics*, **3**:1795, 1984. 25
- [140] J. A. M. SIMOES AND J. A. BEAUCHAMP. *Chem. Rev.*, **90**:629, 1990. 25
- [141] S. P. NOLAN, C. D. HOFF, P. O. STOUTLAND, L. J. NEWMAN, J. M. BUCHANAN, R. G. BERGMAN, G. K. YOUNG, AND K. S. PETERS. *J. Am. Chem. Soc.*, **109**:3143, 1987. 25
- [142] W. D. JONES AND F. J. FEHER. *J. Am. Chem. Soc.*, **106**:1650, 1984. 25
- [143] J. J. GARCIA AND W. D. JONES. *Organometallics*, **19**:5544, 2000. 25
- [144] J. W. SUGGS AND S. D. COX. *J. Organomet. Chem.*, **221**:199, 1981. 25
- [145] H. PETZOLD, T. WEISHEIT, H. GOERLS, H. BREITZE, G. BUNTROWSKY, D. ESCUDERO, L. GONZALEZ, AND W. WEIGAND. *Dalton Trans.*, page 1979, 2008. 25
- [146] J. J. LOW AND W. A. GODDARD III. *J. Am. Chem. Soc.*, **106**:8321, 1984. 25
- [147] P. E. M. SIEGBAHN AND M. R. A. BLOMBERG. *J. Am. Chem. Soc.*, **114**:10548, 1992. 25
- [148] A. GUNAY AND W. D. JONES. *J. Am. Chem. Soc.*, **129**:8729, 2007. 25, 64
- [149] B. O. ROOS, V. VERYAZOV, J. CONRADIE, P. R. TAYLOR, AND A. GHOSH. *J. Phys. Chem. B*, **112**:14099, 2008. 27
- [150] M. RADÓN, E. BROCLAWIK, AND K. PIERLOOT. *J. Phys. Chem. B*, **114**:1518, 2010. 27
- [151] A. GHOSH. *J. Biol. Inorg. Chem.*, **11**:712, 2006. 27
- [152] K. PIERLOOT, H. ZHAO, AND S. VANCOILLIE. *Inorg. Chem.*, **49**:10316, 2010. 27
- [153] B. A. HESS. *Phys. Rev. A*, **32**:756, 1985. 28
- [154] B. A. HESS. *Phys. Rev. A*, **33**:3742, 1986. 28
- [155] B. A. HESS. *Phys. Rev. A*, **39**:6016, 1989. 28
- [156] J. G. SNILDERS, E. VAN LENTHE AND E. J. BAERENDS. *J. Chem. Phys.*, **105**:6505, 1996. 28
- [157] C. J. CRAMER AND D. G. TRUHLAR. *Phys. Chem. Chem. Phys.*, **11**:10757, 2009. 29, 36
- [158] I. N. LEVINE. Prentice-Hall, New Jersey, 2000. 29
- [159] A. SZABO AND N. S. OSTLUND. Dover, New York, 1996. 29
- [160] J. B. FORESMAN, M. HEAD-GORDON, J. A. POPLE, AND M. J. FRISCH. *J. Phys. Chem.*, **96**:135, 1992. 31
- [161] B. O. ROOS, P. R. TAYLOR, AND P. E. M. SIEGBAHN. *Chem. Phys.*, **48**:157, 1980. 32
- [162] B. O. ROOS. *Int. J. Quantum Chem.*, **S14**:175, 1980. 32
- [163] J. OLSEN, B. O. ROOS, P. JØRGENSEN, AND H. J. AA. JENSEN. *J. Chem. Phys.*, **89**:2185–2192, 1988. 33
- [164] P.-Å. MALMQVIST, A. RENDELL, AND B. O. ROOS. *J. Phys. Chem.*, **94**:5477–5482, 1990. 33
- [165] K. ANDERSSON, P.-Å. MALMQVIST, B. O. ROOS, A. J. SADLEJ, AND K. WOLINSKI. *J. Phys. Chem.*, **94**:5483–5488, 1990. 34
- [166] K. ANDERSSON, P.-Å. MALMQVIST, AND B. O. ROOS. *J. Chem. Phys.*, **96**:1218–1226, 1992. 34
- [167] P. A. MALMQVIST, K. PIERLOOT, A. R. M. SHAHI, C. J. CRAMER, AND L. GAGLIARDI. *J. Chem. Phys.*, **128**:204109, 2008. 34
- [168] J. FINLEY, P.-Å. MALMQVIST, B. O. ROOS, AND L. SERRANO-ANDRÉS. *Chem. Phys. Letters*, **288**:299–306, 1998. 34
- [169] P. HOHENBERG AND W. KOHN. *Phys. Rev.*, **136**:B864, 1964. 34
- [170] W. KOHN AND L. J. SHAM. *Phys. Rev.*, **130**:A1133, 1965. 34

## REFERENCES

- [171] A. D. BECKE. *J. Chem. Phys.*, **98**:5648, 1993. 35
- [172] A. D. BECKE. *Phys. Rev. A.*, **38**:3098, 1988. 35
- [173] C. LEE, W. YANG, AND R. G. PARR. *Phys. Rev. B.*, **37**:785, 1988. 35
- [174] S. VOSKO, L. WILK, AND N. MUSAIR. *Can. J. Phys.*, **58**:1200, 1980. 35
- [175] Y. ZHANG AND W. YANG. *J. Chem. Phys.*, **109**:2604, 1998. 35
- [176] O. GRITSENKO, B. ENSING, P. R. T. SCHIPPER, AND E. J. BAERENDS. *J. Phys. Chem. A*, **104**:8588, 2000. 35
- [177] S. KRISTYAN AND P. PULAY. *Chem. Phys. Letters*, **229**:175, 1994. 35
- [178] P. HOBZA, J. SPONER, AND T. RESCHEL. *J. Phys. Chem.*, **16**:1315, 1995. 35
- [179] S. GRIMME. *J. Chem. Phys.*, **124**:034108, 2006. 35
- [180] T. SCHWABE AND S. GRIMME. *Phys. Chem. Chem. Phys.*, **9**:3397, 2007. 35
- [181] W. KOCH AND C. HOLTHAUSEN. Wiley-VCH, Weinheim, 2000. 35
- [182] R. G. PARR AND W. YANG. Oxford University Press, Oxford, 1989. 35
- [183] J. M SEMINARIO. Elsevier, Amsterdam, 1996. 35
- [184] T. ZIEGLER, A. RAUK, AND E. J. BAERENDS. *Theor. Chim. Acta*, **43**:877, 1977. 35
- [185] C. DAUL. *Int. J. Quantum Chem.*, **52**:867, 1994. 35
- [186] M. E. CASIDA. Elsevier, Amsterdam, 1996. 35
- [187] M. PARAC AND S. GRIMME. *J. Phys. Chem. A*, **106**:6844, 2002. 36
- [188] D. J. TOZER, R. D. AMOS, N. C. HANDY, B. O. ROOS, AND L. SERRANO-ANDRÉS. *Molec. Phys.*, **97**:859–868, 1999. 36
- [189] F. NEESE, T. PETRENKO, D. GANYUSHIN, AND G. OLBRICH. *Coord. Chem. Rev.*, **251**:288, 2007. 36
- [190] L. SERRANO-ANDRÉS, M. MERCHÁN, AND R. LINDH. *J. Chem. Phys.*, **122**:104107, 2005. 36
- [191] A. DREUW AND M. HEAD-GORDON. *Chem. Rev.*, **105**:4009, 2005. 36
- [192] A. DREUW, J. L. WEISMAN, AND M. HEAD-GORDON. *J. Chem. Phys.*, **119**:2943, 2003. 36
- [193] O. A. VYDROV AND G. E. SCUSERIA. *J. Chem. Phys.*, **125**:234109, 2006. 37
- [194] T. YANAI D. P. TEW AND N. C. HANDY. *Chem. Phys. Letters*, **393**:51, 2004. 37
- [195] N. L. DOLTSINIS. John von Neumann Institute for Computing, J 2006. 37
- [196] M. BARBATTI. *Comp. Mol. Sci.*, page DOI:10.1002/wcms.64, 2011. 37, 38
- [197] J. C. TULLY. *Faraday Discuss.*, **110**:407, 1998. 37
- [198] J. C. TULLY AND R. K. PRESTON. *J. Chem. Phys.*, **55**:562, 1971. 37
- [199] J. C. TULLY. *J. Chem. Phys.*, **93**:1061, 1990. 37
- [200] A. KARTON, A. TARNOPOLSKY, J.-F. LAMERE, G. C. SCHATZ, AND J. M. L. MARTIN. **112**:12868, 2008. 41
- [201] T. ROZGONYI AND L. GONZÁLEZ. *J. Phys. Chem. A*, **112**:5573, 2008. 41
- [202] J. BOSSERT AND C. DANIEL. *Coord. Chem. Rev.*, **23-24**:2493, 2008. 42
- [203] S. GRIMME AND M. WALETZKE. *J. Chem. Phys.*, **111**:5645, 1999. 46
- [204] D. JACQUEMIN, E. A. PERPÈTE, G. E. SCUSERIA, I. CIOFINI, AND C. ADAMO. *J. Chem. Theor. Comp.*, **4**:123, 2008. 46
- [205] D. JACQUEMIN, E. A. PERPÈTE, G. E. SCUSERIA, I. CIOFINI, AND C. ADAMO. *Chem. Phys. Letters*, **456**:226, 2008. 46
- [206] M. LEIN AND G. FRENKING. Wiley-VCH, Weinheim, Germany, 2005. 51
- [207] F. M. BICKELHAUPT AND E. J. BAERENDS. Wiley-VCH, Weinheim, Germany, 2000. 51
- [208] R. TONNER, G. HEYDENRYCH, AND G. FRENKING. *Chem. Asian J.*, **2**:1555, 2007. 51
- [209] G. S. M. TONG AND C. M. CHE. *Chem. Eur. J.*, **15**:7225, 2009. 54
- [210] G. S. M. TONG, P. K. CHOW, AND C. M. CHE. *Angew. Chem. Int. Ed.*, **49**:9206, 2010. 54
- [211] Z. A. SIDDIQUE, Y. YAMAMOTO, T. OHNO, AND K. NOZAKI. *Inorg. Chem.*, **42**:6366, 2003. 54
- [212] H. INUI AND S. MURATA. *J. Am. Chem. Soc.*, **127**:2628, 2005. 66
- [213] C. BORNEMANN AND M. KLESSINGER. *Chem. Phys.*, **259**:263, 2000. 66

## Declaration

Selbständigkeitserklärung:

Ich erkläre, dass die vorliegende Arbeit selbständig und unter Verwendung der angegebenen Hilfsmittel, persönlichen Mitteilungen und Quellen angefertigt habe.

Jena,

Daniel Escudero Masa

# Curriculum Vitae

**Daniel Escudero Masa**

Friedrich Schiller Universität Jena

Institute for Physical Chemistry

07743 Jena Germany

e-mail: [daniel.escudero@uni-jena.de](mailto:daniel.escudero@uni-jena.de)

[daniel.escudero.masa@googlemail.com](mailto:daniel.escudero.masa@googlemail.com)

Private address: Löbdergraben 6, D-07743 Jena

## 1 Personal details

Surname	Escudero Masa
Name	Daniel
Date/place of Birth	15.05.1984 in Mallorca (Spain)
Civil Status	Single

## 2 Degrees

July 2007	<b>Graduated</b> in Chemistry (Licenciado) by the University of the Balearic Islands (UIB), Spain. Major: Organic Physical Chemistry Grade: 97 %
June 2002	<b>University Entrance Degree in Spain (Selectividad)</b> Grade: 87%

## 3 Education

2002-2007	<b>Studies of Chemistry.</b> UIB, Spain.
1996-2002	<b>High School Studies.</b> Palma de Mallorca, Spain. Grade: 91%

## 4 Scientific Experience

Oct. 2007 -	<b>Institut für Physikalische Chemie</b> (Prof. Leticia González), Friedrich-Schiller Universität Jena.
Oct. 2006 - Sept. 2007	<b>Dept. of Organic Chemistry</b> (Prof. Antonio Frontera and Prof. Pere M. Deyà), UIB, Spain.
July 2006 - Oct. 2006	<b>Dept. of Peptide &amp; Protein Chemistry</b> (Prof. Isabel Haro), Spanish National Research Council (CSIC), Barcelona, Spain.
Nov 2003 - Febr. 2004	<b>Dept. of Organic Chemistry</b> (Prof. Ángel García-Raso), UIB, Spain.

## 5 Scholarships and Awards.

Aug. 2008 – Aug. 2011	<b>Carl-Zeiss-Stiftung scholarship</b>
2008	<b>Best oral presentation in Theoretical Chemistry</b> (5 <sup>a</sup> Meeting of Young Researchers of Catalonia (Vic, SPAIN, 28-29/01/2008))
Oct. 2007 - Aug. 2008	<b>Graduate scholarship</b> to extend studies abroad (Sa Nostra Foundation).

- 2007                                    **Award to the best graduate student in Chemistry** (UIB, Spain)
- Oct. 2006 - Sept. 2007            **Undergraduate scholarship:** Introduction to Research (Spanish Ministry of Education and Culture).
- July 2006 - Oct. 2006            **Undergraduate scholarship:** Introduction to Research (CSIC).

## **6 Scientific Contributions (see Attachment)**

30 Publications in International Journals  
11 Poster Presentations in Conferences  
3 Oral Presentation in Conferences

## **7 Languages**

Spanish :	Mother tongue
Catalan:	Mother tongue
English:	Fluent
German:	Intermediate

Jena, 1 July 2011

## Scientific contributions

### Publications:

1. C. Garau, D. Quiñonero, A. Frontera, D. Escudero, P. Ballester, A. Costa and P.M. Deyà.  
**MP2 study of anion- $\pi$  complexes of trifluoro-s-triazine with tetrahedral and octahedral anions**  
*Chem. Phys. Lett*, 438, 104-108 (2007)
2. D. Quiñonero, A. Frontera, D. Escudero, P. Ballester, A. Costa, P.M. Deyà.  
**A Theoretical Study of Anion- $\pi$  Interactions in Seven-Membered Rings**  
*Chem. Phys. Chem.*, 8, 1182-1187 (2007)
3. Á. García-Raso, F. Albertí, J. Fiol, A. Tasada, M. Barceló-Oliver, E. Molins, D. Escudero, A. Frontera, D. Quiñonero, P.M. Deyà.  
**Anion- $\pi$  interactions in bisadenine derivatives: a combined crystallographic and theoretical study**  
*Inorg. Chem.*, 46, 10724-10735 (2007)
4. Á. García-Raso, F. Albertí, J. Fiol, A. Tasada, M. Barceló-Oliver, E. Molins, D. Escudero, A. Frontera, D. Quiñonero, and P.M. Deyà.  
**A Combined Experimental and Theoretical Study of Anion- $\pi$  interactions in Bispyrimidine Salts**  
*Eur. J. Org. Chem.*, Issue 35, 5821-5825 (**Cover Picture**) (2007)
5. D. Quiñonero, A. Frontera, D. Escudero, P. Ballester, A. Costa, P.M. Deyà.  
**MP2 Study of Synergistic effects between X-H/ $\pi$  (X=C,N,O) and  $\pi$ - $\pi$  interactions.**  
*Theor. Chem. Accounts*, 120, 385-393 (2008)
6. H. Petzold, T. Weisheit, H. Görls, H. Breitzke, G. Buntkowsky, D. Escudero, L. González, W. Weigand.  
**Selective carbon-carbon bond cleavage of 2,2'-dibromotolane via photolysis of its appropriate (bisphosphine)Pt<sup>0</sup> complex in solid state.**  
*Dalton Trans.*, Issue 15, 1979-1981 (2008)
7. D. Escudero, A. Frontera, D. Quiñonero, A. Costa, P. Ballester, P.M. Deyà.  
**The Induced-Polarization Energy Map: a helpful tool for predicting geometric features of Anion- $\pi$  complexes**  
*J. Chem. Theory Comp.*, 3, 2098-2107 (2007)
8. D. Escudero, A. Frontera, D. Quiñonero, P. M. Deyà.  
**On the importance of the inclusion of the basis set superposition error counterpoise correction during optimization of ion- $\pi$  complexes**  
*Chem. Phys. Lett.* 455, 325-330 (2008)
9. D. Escudero, A. Frontera, D. Quiñonero, P. M. Deyà.  
**Interplay between cation- $\pi$  and hydrogen bonding interactions**  
*Chem. Phys. Lett.* 456, 257-261 (2008)

10. D. Escudero, A. Frontera, D. Quiñonero, P. M. Deyà.  
**Interplay between anion- $\pi$  and hydrogen bonding interactions.**  
*J. Comp. Chem.*, 30, 75-82 (2009)
11. D. Quiñonero, A. Frontera, D. Escudero, P. M. Deyà.  
**Molecular interaction potential with polarization (MIPp) study of the interplay between ion- $\pi$  and hydrogen bonding interactions**  
*The Open Chemical Physics Journal*, 1, 36-41 (2008)
12. D. Escudero, A. Frontera, D. Quiñonero, P. M. Deyà.  
**Interplay between edge-to-face aromatic and hydrogen bonding interactions**  
*J. Phys. Chem. A*, 112, 6017-6022 (2008)
13. I.A. Gural'skiy, D. Escudero, A. Frontera, P.V. Solntsev, E.B. Rusanov, A.N. Chernega, H. Krautscheid and K.V. Domasevitch  
**1,2,4,5-Tetrazine: An unprecedented  $\mu_4$ -coordination that enhances ability for anion/ $\pi$  interactions**  
*Dalton Trans.*, Issue 15, 2856-2864 (2009)
14. G. J. Mohr, H. Müller, B. Bussemer, A. Stark, T. Carofiglio, S. Trupp, R. Heuermann, T. Henkel, D. Escudero, and L. González  
**Design of acidochromic dyes for facile preparation of pH sensor layers**  
*Anal. Bioanal. Chem.*, 392, 1411-1418, (2008)
15. D. Escudero, C. Estarellas, A. Frontera, D. Quiñonero, P. M. Deyà.  
**Theoretical and Crystallographic Study of Edge-to-Face Aromatic Interactions between Pyridine Moieties and Benzene**  
*Chem. Phys. Lett.*, 30, 280-285 (2009)
16. C. Biswas, M.G.B. Drew, A. Ghosh, D. Escudero and A. Frontera.  
**Anion/ $\pi$ , lone-pair/ $\pi$ ,  $\pi/\pi$  and hydrogen bonding interactions in a coordination complex of protonated 4,4'-bipyridine: Crystal structure and theoretical studies**  
*Eur. J. Inorg. Chem.*, Issue 15, 2238-2246 (2009)
17. C. Estarellas, D. Escudero, A. Frontera, D. Quiñonero, P. M. Deyà.  
**Theoretical ab initio study of the interplay between hydrogen bonding, cation- $\pi$  and  $\pi$ - $\pi$  interactions**  
*Theor. Chem. Accounts*, 122, 325-332 (2009)
18. B. Beyer, C. Ulbricht, D. Escudero, C. Friebe, A. Winter, L. González, U. S. Schubert.  
**Phenyl-1H-[1,2,3]triazoles as new cyclometallating ligands for iridium(III) complexes**  
*Organometallics*, 28, 5478-5488 (2009)
19. X. Lucas, C. Estarellas, D. Escudero, A. Frontera, D. Quiñonero, P.M. Deyà.  
**Very long-range effects: cooperativity between anion- $\pi$  and hydrogen bonding interactions**  
*Chem. Phys. Chem.*, 10, 2256-2264 (2009)
20. D. Escudero, X. Lucas, C. Estarellas, A. Frontera, D. Quiñonero, P.M. Deyà.  
**Interplay between ion- $\pi$  and hydrogen bonding interactions**  
*Trends Phys. Chem.*, 13, 31-53(2009)



21. D. Escudero, C. Estarellas, A. Frontera, D. Quinonero, P.M. Deyà.  
**Cooperativity effects between non-covalent interactions: Are they important for Z-DNA stability?**  
*Chem. Phys. Lett.*, 485, 221-225 (2010)
22. M. Kahnes, J. Richthof, H. Görls, D. Escudero, L. González, M. Westerhausen.  
**Mechanistic studies on the alcoholysis and aminolysis of [(MeZn)<sub>2</sub>{μ-N(H)*t*Bu}{μ-N(CH<sub>2</sub>Py)<sub>2</sub>}**  
*J. Organomet. Chem.*, 695, 280-290 (2010)
23. S. Hazra, B. Sarkar, M. G. B. Drew, A. Frontera, D. Escudero, A. Ghosh.  
**Self-assembly of coordination polymers of Cd(II), hexamine and mono-carboxylates: Structural analysis and theoretical studies of supramolecular interactions**  
*Cryst. Growth Des.*, 10, 1667-1687 (2010)
24. B. Happ, D. Escudero, M.D. Hager, C. Friebe, A. Winter, H. Górls, E. Altuntas, L. González, U.S. Schubert.  
**N-heterocyclic donor- and acceptor-type ligands based on 2-(1H-[1,2,3]triazol-4-yl)pyridines and their ruthenium(II) complexes**  
*J. Org. Chem.* 75, 4025-4038 (2010)
25. D. Escudero, M. Assmann, A. Pospiech, W. Weigand, L. González.  
**Substituent effects on the light-induced C-C and C-Br bond activation in (bisphosphine)(eta(2)-tolane)Pt-0 complexes. A TD-DFT study**  
*Phys. Chem. Chem. Phys.*, 11, 4593-4600 (2009)
26. N. Tian, D. Lenkeit, S. Pelz, L.H. Fischer, D. Escudero, R. Schlewke, D. Klink, O. J. Schmitz, L. González, M. Schäferling, E. Holder.  
**Structure-property relationship of red- and green-emitting iridium(III) complexes with respect to their temperature and oxygen sensitivity**  
*Eur. J. Inorg. Chem.* 4875-4885 (2010)
27. T. Weisheit, D. Escudero, H. Petzold, H. Görls, L. González, W. Weigand.  
**Photochemical behaviour of (bisphosphine)(eta(2)-tolane)Pt-0 complexes in solution and in the solid state. Part A: Experimental considerations**  
*Dalton Trans.*, 39, 9493-9504 (2010)
28. D. Escudero, T. Weisheit, W. Weigand, L. González.  
**Photochemical behaviour of (bisphosphine)(eta(2)-tolane)Pt-0 complexes in solution and in the solid state. Part B: An insight from DFT calculations**  
*Dalton Trans.*, 39, 9505-9513 (2010)
29. B. Schulze, D. Escudero, C. Friebe, R. Siebert, H. Görls, U. Köhn, E. Altuntas, A. Baumgärtel, M. D. Hager, A. Winter, B. Dietzek, L. González, U.S. Schubert.  
**Long excited state lifetime and strong room temperature phosphorescence of a heteroleptic bis-tridentate ruthenium(II) complex: A pincer-ligand with click-derived triazolydenes as superior donors**  
*Chem. Eur. J.*, 11, 5494-5498 (**Back Cover**) (2011)
30. D. Escudero, S. Trupp, B. Bussemer, G. Mohr, L. González.  
**Spectroscopic properties of azobenzene-based pH indicator dyes: a quantum chemical and experimental study**  
*J. Chem. Theory Comp.*, 7, 1062-1072 (2011)

31. L. González, D. Escudero, L. Serrano-Andrés.

**Progress and challenges in the calculation of electronic excited states.**

*Chem. Phys. Chem. Submitted (2011)*

32. D. Escudero, L. González.

**RASPT2/RASSCF vs range-separated/hybrid DFT methods: assessing the excited states of a Ru(II)bipyridyl complex.**

*J. Chem. Theory Comp. Submitted (2011)*

**Presentations at Conferences:**

1. M. L. Pérez, D. Escudero, M. J. Gómara, I. Haro

**Poster: Citrullinated synthetic peptides for rheumatoid arthritis diagnosis.**

Jornada de Química de Catalunya i del Grand Sud-Oest Francès (Barcelona, SPAIN, 23/24-11-2006)

2. D. Escudero, A. Frontera, D. Quiñonero and P.M. Deyà.

**Poster: The Induced-Polarization Energy Map: a helpful tool for predicting geometric features of Anion- $\pi$  complexes.**

XXXI Meeting of the Spanish Royal Society of Chemistry (Toledo, SPAIN, 9-14/10/2007)

3. D. Escudero.

**Oral presentation: Synergistic effects between anion- $\pi$  and hydrogen bonding interactions.**

5<sup>a</sup> Meeting of Young Researchers of Catalonia (Vic, SPAIN, 28-29/01/2008)

4. D. Escudero, S. Rau, L. González.

**Poster: Photochemical studies on Ru(II) polypyridyl complexes: towards the profit of sun light.**

6th Congress on Electronic Structure: Principles and Applications - ESPA 2008 (Palma, SPAIN, 2-5/10/2008)

5. D. Escudero, A. Frontera, D. Quiñonero and P.M. Deyà.

**Poster: Cooperative effects between  $\pi$ - $\pi$  and hydrogen bonding interactions.**

6th Congress on Electronic Structure: Principles and Applications - ESPA 2008 (Palma, SPAIN, 2-5/09/2008)

6. D. Escudero, L. González.

**Poster: The performance of TD-DFT on organometallic complexes.**

XIVth European Seminar on Computational Methods in Quantum Chemistry (Elba, ITALY, 2-6/10/2008)

7. D. Escudero, L. González.

**Poster: Photochemical properties of iridium and platinum complexes.**

Molecular Properties '09, an ICQC 2009 Satellite Symposium (Oslo, NORWAY, 18-21/06/2009)

8. D. Escudero, L. González.

**Poster: 2H-Azirines: Quantum chemistry for excited states and non-adiabatic molecular dynamics.**

13<sup>th</sup> ICQC: International Congress of Quantum Chemistry (Helsinki, FINLAND, 22-27/06/2009)

9. X. Lucas, C. Estarellas, D. Escudero, A. Frontera, D. Quiñonero and P.M. Deyà.

**Poster: Very long range effects: cooperativity between anion- $\pi$  and hydrogen bonding interactions.**

Theoretical chemistry: Modeling reactivity from gas phase to biomolecules and solids (Barcelona, SPAIN, 29-3/06-07/2009)

10. D. Escudero, L. González.

**Poster: Quantum chemistry for excited states and surface hopping simulations in 2H-Azirines.**

45<sup>th</sup> Symposium on Theoretical Chemistry. Excited states: from photophysics to photobiology. (Neuss am Rhein, GERMANY, 8-12/09/2009)

11. D. Escudero, L. González.

**Poster: A theoretical insight into a complete photophysical picture of Ir(III) and Ru(II) organometallic complexes.**

International Bunsen Discussion Meeting on Light Harvesting and Solar Energy Conversion. (Stuttgart, GERMANY, 29-31/03/2010)

12. D. Escudero.

**Oral presentation: Emissive or non-emissive? TDDFT-CASSCF calculations to rationalize phosphorescence rates of Ru(II) polypyridyl complexes.**

24<sup>th</sup> Molecular Modelling Workshop 2010. (Erlangen, GERMANY, 15-16/03/2010)

13. D. Escudero, L. González.

**Poster: 2H-Azirines: Quantum chemistry for excited states and surface hopping dynamical simulations.**

8<sup>th</sup> European conference on computational chemistry. (Lund, SWEDEN, 25-28/08/2010)

14. D. Escudero.

**Oral presentation: Absorption, emission and deactivation mechanisms in light-harvesting antennas: RASPT2 and DFT studies on Ru(II)polypyridyl complexes.**

Modelling of biologically-inspired photoactive systems. BioPhotoChem Workshop (Marseille, FRANCE, 30-01/03-04/2011)